Transactions of the ASME, Journal of Heat Transfer (ISSN 0022-1481) is published monthly by The American Society of Mechanical Engineers, Three Park Avenue, New York, NY 10016. Periodicals postage paid at New York, NY and additional mailing offices. POSTMASTER: Send address changes to Transactions of the ASME, Journal of Heat Transfer, c/o THE AMERICAN SOCIETY OF MECHANICAL ENGINEERS, 22 Law Drive, Box 2300, Fairfield, NJ 07007-2300. **CHANGES OF ADDRESS** must be received at Society headquarters seven weeks before they are to be effective. Please send old label and new address. **STATEMENT from By-Laws.** The Society shall not be responsible for statements or opinions advanced in papers or ... printed in its publications (B7.1, Para. 3).

Journal of Heat Transfer

Published Monthly by ASME

VOLUME 133 • NUMBER 2 • FEBRUARY 2011

RESEARCH PAPERS

(**Contents continued on inside back cover**)

This journal is printed on acid-free paper, which exceeds the ANSI Z39.48-1992 specification for permanence of paper and library materials. ♾™
♻ 85% recycled content, including 10% post-consumer fibers.

TECHNICAL BRIEFS

The ASME Journal of Heat Transfer is abstracted and indexed in the following:

Applied Science and Technology Index, Chemical Abstracts, Chemical Engineering and Biotechnology Abstracts (Electronic equivalent of Process and Chemical Engineering), Civil Engineering Abstracts, Compendex (The electronic equivalent of Engineering Index), Corrosion Abstracts, Current Contents, E & P Health, Safety, and Environment, Ei EncompassLit, Engineered Materials Abstracts, Engineering Index, Enviroline (The electronic equivalent of Environment Abstracts), Environment Abstracts, Environmental Engineering Abstracts, Environmental Science and Pollution Management, Fluidex, Fuel and Energy Abstracts, Index to Scientific Reviews, INSPEC, International Building Services Abstracts, Mechanical & Transportation Engineering Abstracts, Mechanical Engineering Abstracts, METADEX (The electronic equivalent of Metals Abstracts and Alloys Index), Petroleum Abstracts, Process and Chemical Engineering, Referativnyi Zhurnal, Science Citation Index, SciSearch (The electronic equivalent of Science Citation Index), Theoretical Chemical Engineering

Temperature Created by a Tilted Moving Heat Source: Heating Line and Cylinder

Valerian Nemchinsky
Keiser University,
1500 Northwest 49 Street,
Fort Lauderdale, FL 33309
e-mail: nemchinsky@bellsouth.net

Temperatures created by a moving tilted line and a moving tilted cylinder are considered. Analytical expressions for low Peclet ($Pe \ll 1$) and high Peclet ($Pe \gg 1$) numbers are obtained for the whole range of possible tilt angles. These expressions almost overlap: It is shown that these analytical expressions describe very well the results of numerical calculations at any Peclet numbers except for a very narrow range of Pe close to unity. A method of calculation of the cut shape (variation of the tilt angle inside the cut) is discussed. [DOI: 10.1115/1.4002601]

Keywords: heat conduction, cutting, Peclet number, moving heat source, tilted heat source

1 Introduction

Cutting a metal with a moving heat source (MHS) is one of the most widely used technological processes: oxy-fuel cutting, plasma arc cutting, and laser and plasma assisted laser cutting. As a rule, the heat source (plasma jet, oxy-fuel flame, and laser beam) is perpendicular to the metal plate. However, the resulting cut is not perpendicular to the plate: It deflects from the vertical. At low cutting speeds, the tilt of the cut is low. In many cases, this low tilt is acceptable from the technological point of view. However, as the cutting speed increases, the cut starts to tilt more and more from the vertical. At some speeds, this phenomenon deteriorates the cut quality: the lower contour of the kerf doesn't reproduce the upper one. It is important to note that the phenomenon of the tilted cut exists with all the methods of metal cutting with MHS. Therefore, the phenomenon is a characteristic of heat transfer of cutting with MHS, regardless whether the cutting is with plasma, oxy-fuel, laser, or some other moving heat source.

Temperature fields created by nontilted MHS during cutting (the MHS that penetrates the object) were considered in many papers starting from the classical paper by Rosenthal [1]. Swift-Hook and Gick [2] calculated temperature distribution created by a one-dimensional moving heat source (1D MHS). Bunting and Cornfield [3] considered MHS in the form of an infinitely long cylinder while Baeva et al. [4], and Toshiyuki and Giedt [5] considered MHS in the form of an elliptic cylinder. The influence of the plate thickness on the temperature distribution was considered in Ref. [6]. In our work [7], we calculated temperature distribution created by a MHS in the form of a looking ahead section of surface of a cylinder.

Calculations in these papers, which dealt with nontilted MHS, demonstrated that only a small fraction of the total heat is transferred ahead of the MHS if its speed is high. Low effective heat transfer ahead of the MHS could be compensated, at least to some degree, by tilting the heat source as shown qualitatively in Ref. [8], the only paper we know of that considered tilted MHS. Here we consider heat transfer during cutting with tilted MHS in more detail. We consider steady-state, one-dimensional (infinitely thin) and two-dimensional cases.

The paper is organized as follows. In Secs. 2 and 3, we consider an approximate analytical approach in the cases of low and high Peclet numbers, namely, a one-dimensional approach in Sec. 2 and a two-dimensional approach in Sec. 3. In Sec. 4, we compare the results of these approximations with the results of numerical calculations. The difference between the heat transfer per unit cut length versus the heat transfer per unit cut thickness is discussed in Sec. 5. In Sec. 6, we give a brief outline of the approach on how to obtain the shape of the cut in the case where heat transfer efficiency decreases along the length of the cut.

2 Line Source

In this section, we consider an infinitely thin and infinitely long moving heat source in the form of a line. Besides the fact that this problem is interesting by itself, it provides a basis for two-dimensional consideration.

Assume that heat generation is distributed along the line uniformly. Intensity of this heat generation is Q (W/cm). The line is tilted from vertical by an angle β and moves with speed of U in the horizontal direction. Thermophysical properties of the medium are considered temperature independent. The medium is assumed as being isotropic and homogeneous. We are interested in the calculation of the temperature field created by this 1D MHS.

Since the line is not perpendicular to the plate, one cannot use the formula for vertical MHS [1]. We should start with the Green's function of the moving point source. The temperature distribution created by such a moving point heat source of unit power is [9]

$$G(x,r) = \frac{1}{4\pi\kappa\mathbf{R}}\exp\left(-\frac{U(X-\mathbf{R})}{2a}\right) \tag{1}$$

Here, $\mathbf{R}$ is the distance from the point of observation to the heat source, and $X=X_H-X_O$ is the distance of projections of these two points on the x-axis (direction of motion), and κ and a are the thermal conductivity and the thermal diffusivity, respectively. Here, X_H and X_O are the x-coordinates of heating point and point of observation, respectively. It is convenient to define the dimensionless temperature as

$$F_{1D} = \frac{4\pi\kappa T}{Q} \tag{2}$$

Let us introduce the following characteristics of the heating point and the point where we want to calculate the temperature (observation point). The heating point is characterized by L, its distance along the line counted from the origin of coordinates ($-\infty < L < +\infty$). The observation point O is $\mathbf{R}$ away from the origin of

Contributed by the Heat Transfer Division of ASME for publication in the JOURNAL OF HEAT TRANSFER. Manuscript received January 10, 2010; final manuscript received July 28, 2010; published online November 2, 2010. Assoc. Editor: Oronzia Manca.

coordinate, its azimuth angle is θ (see Fig. 1). We have

$$X_H = L\sin\beta, \quad Y_H = 0, \quad Z_H = L\cos\beta$$

$$X_O = \mathbf{R}\cos\theta, \quad Y_O = \mathbf{R}\sin\theta, \quad Z_O = 0 \tag{3}$$

The distance between heating and observation points is $\sqrt{L^2+\mathbf{R}^2-2L\mathbf{R}\sin\beta\cos\theta}$. For dimensionless temperature, we have

$$F_{1D} = \int_{-\infty}^{+\infty} \frac{\exp\left(-\frac{U}{2a}[L\sin\beta - \mathbf{R}\cos\theta - \sqrt{L^2+\mathbf{R}^2-2L\mathbf{R}\sin\beta\cos\theta}]\right)}{\sqrt{L^2+\mathbf{R}^2-2L\mathbf{R}\sin\beta\cos\theta}} dL \tag{4}$$

Let us introduce the number $\mathrm{Pe} = U\mathbf{R}/2a$ and dimensionless distances $x = X/\mathbf{R}$, $y = Y/\mathbf{R}$, $z = Z/\mathbf{R}$, and $l = L/\mathbf{R}$. Dimensionless temperature depends on the Peclet number Pe and angles β and θ.

The integral (Eq. (4)) cannot be calculated analytically for arbitrary number Pe.

When tilt angle $\beta = 0$, it can be reduced to the modified Bessel function of the second kind, zero order [1]:

$$F_{1D} = 2K_0(\mathrm{Pe})\exp(-\mathrm{Pe}\cos\theta) \tag{5}$$

Other important cases are small and large Peclet numbers $\mathrm{Pe} \ll 1$ and $\mathrm{Pe} \gg 1$ (conditions $\mathrm{Pe} \ll 1$ and $\mathrm{Pe} \gg 1$ for plasma cutting are discussed in Appendix A). As we will see, the results obtained under these conditions practically overlap. This allows one to calculate F_{1D} with a reasonable accuracy (a few percent) over the whole range of Pe.

It is convenient to write the integral (Eq. (4)) in the form

$$F_{1D} = \int_{-\infty}^{+\infty} \frac{\exp(-\mathrm{Pe}\, f)}{r} dl \tag{6}$$

The dimensionless distance between the observation and heating points can be written as

$$r = (l^2 + 1 - 2l\sin\beta\cos\theta)^{1/2} = (l'^2 + A^2)^{1/2}$$

where we introduced

$$A = \sqrt{1-(\sin\beta\cos\theta)^2} \tag{7}$$

and

$$l' = l - \sin\beta\cos\theta \tag{8}$$

With these variables, function f in Eq. (6) takes the form

$$f = l'\sin\beta - \cos\theta(\cos\beta)^2 - \sqrt{l'^2 + A^2} \tag{9}$$

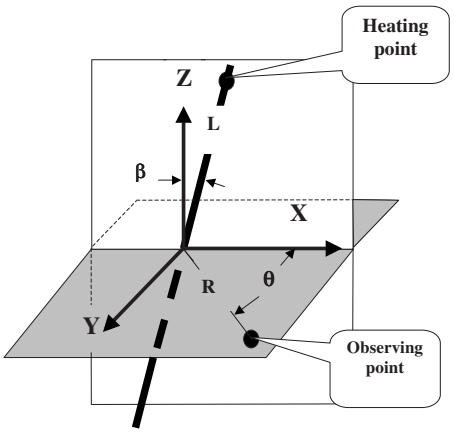

Fig. 1 Geometry used to calculate temperature in the case of 1D MHS (line), angle θ is the azimuth of the observation point

2.1 Heating Line: Small Peclet Number. Let us consider the case $\mathrm{Pe} \ll 1$ first. The integral diverges when $\mathrm{Pe} = 0$. At a nonzero Pe number, the convergence of the integral (Eq. (4)) is provided by the decrease of the exponential function at large distances on the order of $O(1/\mathrm{Pe})$. Therefore, one estimates F_{1D} by putting the exponential function equal to unity everywhere except at distances where the argument of the exponential function becomes equal to unity. Equating f to 1/Pe, one can find l'_1 and l'_2, the corresponding integration limits. Keeping in mind that their absolute value is large, function f could be written as $f \approx l'\sin\beta - \sqrt{l'^2} = l'\sin\beta \pm l'$, so we obtain approximately

$$l'_1 = -\frac{1}{\mathrm{Pe}(1-\sin\beta)} \tag{10a}$$

$$l'_2 = \frac{1}{\mathrm{Pe}(1+\sin\beta)} \tag{10b}$$

We have for Eq. (6) approximately

$$F_{1D} \approx \int_{l'_1}^{l'_2} \frac{dl'}{\sqrt{l'^2+A^2}} = \ln\left(\frac{4|l'_1 \times l'_2|}{A^2}\right) = \ln(l'_1 \times l'_2) + \ln(4/A^2) \tag{11}$$

We are considering the case of large absolute values of l'; therefore, the second term in the right-hand-side of Eq. (11) can be neglected. After putting Eq. (10) into Eq. (11), we finally have

$$F_{1D} \approx -2\ln(\mathrm{Pe}\cos\beta) = -2\ln\left(\frac{U\mathbf{R}\cos\beta}{2a}\right) \quad (U\mathbf{R}/2a \ll 1) \tag{12}$$

Note that in the limit $\mathrm{Pe} \ll 1$, the result does not depend on angle θ but on the $\mathbf{R}\cos\beta$, the distance of the observing point to the heating line. Since $K_0(z) \sim -\ln(z)$ at small argument, formula (5) becomes $F_{1D} \approx -2\ln(\mathrm{Pe})(1-\mathrm{Pe}\cos\theta)$. This coincides with Eq. (12) in the case of straight cut ($\beta = 0$). Also, one can see that Eq. (12) can be considered as the average of Eq. (5) when θ changes.

2.2 Heating Line: Large Peclet Number. When the Peclet number is large, $\exp(-\mathrm{Pe}\, f)$ is very small everywhere except for a small area around a specific length l'_0, where it is maximal (here, as before, we use the reduced length $l' = l - \sin\beta\cos\theta$). We, therefore, can use the steepest descent method. Taking a derivative of the argument of the exponential function and equating it to zero, we find $l'_0 = A\tan\beta$. One can see that the corresponding value of dimensionless distance from this point on the line to the observation point is $r_0(l'_0) = A/\cos\beta$. The second derivative of f at l'_0 is $d^2f/dl'^2 = -(\cos\beta)^3/A$. Function $f(l')$ can be approximated close to l'_0 as

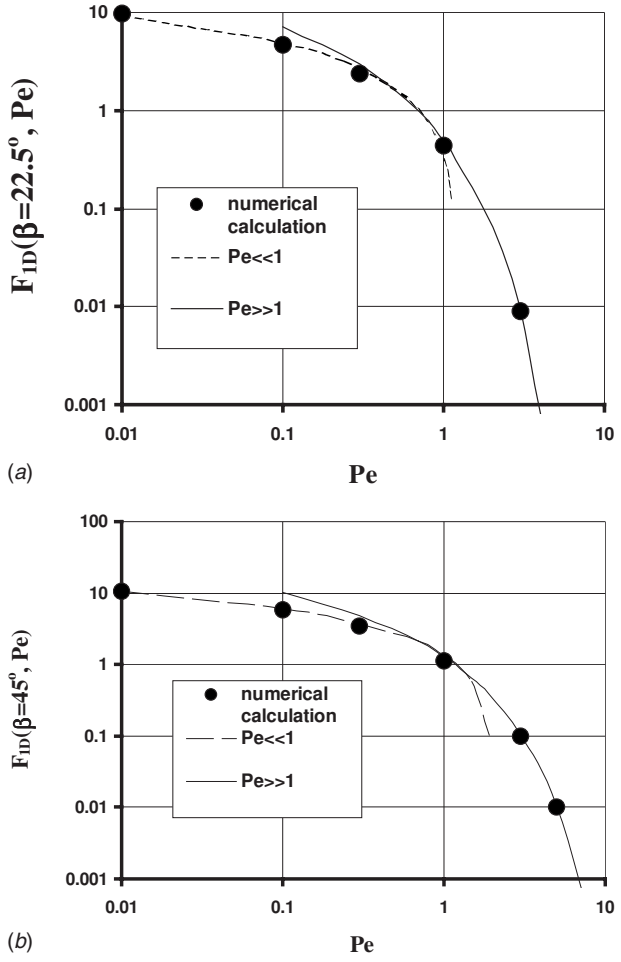

Fig. 2 (*a*) Nondimensional temperature created by 1D MHS: tilt angle $\beta=22.5$ deg, $\theta=0$; points are the numerical calculation of the integral (Eq. (4)), solid line is the approximation $Pe \gg 1$ (Eq. (15)); dashed line is the approximation $Pe \ll 1$ (Eq. (12)). (*b*) Nondimensional temperature created by 1D MHS: tilt angle $\beta=45$ deg, $\theta=0$; points are the numerical calculation of the integral (Eq. (4)); solid line is the approximation $Pe \gg 1$ (Eq. (15)); dashed line is the approximation $Pe \ll 1$ (Eq. (12)).

$$f = -A\cos\beta - \cos^2(\beta)\cos\theta - \frac{1}{2}\frac{(l' - l_0')^2\cos^3(\beta)}{A} \tag{13}$$

With this approximation of f, the integral (Eq. (6)) can be easily calculated, resulting in

$$F_{1D} = \sqrt{\frac{2\pi}{A\,\mathrm{Pe}\cos\beta}}\exp[-A\,\mathrm{Pe}\cos\beta - \mathrm{Pe}\cos\theta(\cos\beta)^2] \tag{14}$$

In the special case $\theta=0$ (straight ahead of the heating line), Eq. (14) reduces to

$$F_{1D} = \sqrt{\frac{2\pi}{\mathrm{Pe}}}\frac{\exp(-2\,\mathrm{Pe}(\cos\beta)^2)}{\cos\beta} \tag{15}$$

Comparison of results of numerical calculation integral (Eq. (6)) and those by approximation (formulas (12) and (15)) is given in Figs. 2(*a*) and 2(*b*). We see that the two approximations (Eqs. (12) and (15)) almost overlap. In a relatively narrow gap around $Pe=1$, one should use numerical integration.

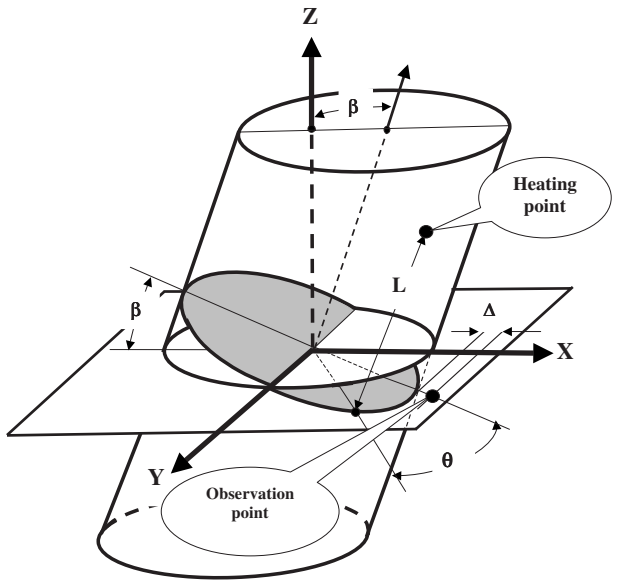

Fig. 3 Geometry used to calculate temperature in the case of 2D MHS (cylinder); observation point is by Δ ahead of the cylinder

3 MHS in Form of Hemicylinder's Surface

The results obtained in the previous section allow us to calculate temperature distribution created by a tilted moving cylinder with a cross-section of arbitrary shape. Below, we consider a moving cylinder with a circular cross section.

Consider a cylinder of radius R tilted by the angle β off the vertical. The cylinder moves with speed U in x-direction. The half of the cylinder's surface that is looking ahead is considered as a MHS. The heat released by this surface is evenly distributed over the half of a cylinder surface and is equal to Q (W/cm). We are most interested in the temperature created by this MHS at a distance Δ ahead of the cylinder (see Fig. 3). For the case of metal cutting, distance Δ represents thickness of a metal liquid film that separates the heating source from nonmelted metal.

The temperature distribution is described by generalization of the integral (Eq. (6)). In the coordinate system connected to the cylinder, the coordinates of the heating point (index H) are

$$X_H = \mathrm{R}\cos(\theta)\cos(\beta) + L\sin(\beta)$$

$$Y_H = \mathrm{R}\sin(\theta)$$

$$Z_H = -\mathrm{R}\cos(\theta)\sin(\beta) + L\cos(\beta) \tag{16}$$

Coordinates of the observation point (index O) are

$$X_O = R\cos(\beta) + \Delta$$

$$Y_O = 0$$

$$Z_O = -R\sin(\beta) \tag{17}$$

Here we introduced the azimuth angle θ to characterize the heating point (see Fig. 4).

Now that we have linear scale (cylinder radius), we can introduce dimensionless variables in a different way, namely,

$$x = X/R, \quad y = Y/R, \quad z = Z/R, \quad l = L/R, \quad \delta = \Delta/R \tag{18}$$

To characterize temperature distribution, we introduce dimensionless function $F_{2D}=4\pi\kappa T/Q$.

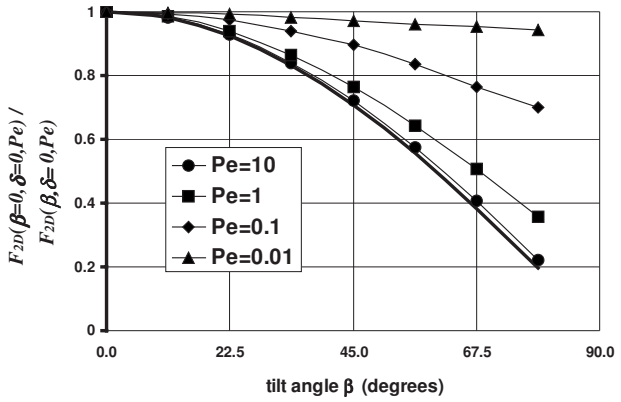

Fig. 4 Ratio of $F_{2D}(\mathrm{Pe},0,0)/F_{2D}(\mathrm{Pe},\beta,0)$ for different Peclet numbers; for $\mathrm{Pe}\gg 1$, this ratio should be proportional to $\cos\beta$ (formula (36)); bold line is $\cos\beta$

$$F_{2D} = \frac{4\pi\kappa T}{Q} = \frac{2}{\pi}\int_0^{\pi/2} d\theta \int_{-\infty}^{+\infty} \frac{dl}{r}\exp[-\mathrm{Pe}\, f] \tag{19}$$

where f, this time, is defined as $f = x_H - x_O - r$. Function F_{2D} depends on three parameters: angle β, Δ, the distance of the observation point from the heating cylinder, and the Peclet number defined here as $UR/2a$.

As before, r is the dimensionless distance between the point of observation and the heating point

$$r^2 = (x_H - x_O)^2 + (y_H - y_O)^2 + (z_H - z_O)^2. \tag{20}$$

One can calculate the integral (Eq. (19)) analytically in two extremes: $\mathrm{Pe}\ll 1$ and $\mathrm{Pe}\gg 1$. Let us start with the $\mathrm{Pe}\ll 1$ case.

3.1 Heating Cylinder: Small Peclet Number. Asymptotic formula for F_{2D} at low Peclet numbers could be easily found based on the fact that linear MHS depends on the distance between heating line and observation point only. First, consider case $\Delta = 0$ (observation point lies on the heating surface). The dimensionless distance from the point with coordinates $X_H = \mathrm{R}\sin\theta$, $Y_H = \mathrm{R}\cos\theta$, and $Z_H = 0$ to the point $X_O = \mathrm{R}$, $Y_O = 0$, and $Z_O = 0$ is $r = 2\sin(\theta/2)$.

Using formula (12) we find

$$F_{2D} = -\frac{2}{\pi}\int_0^{\pi/2} 2\ln\left[2\,\mathrm{Pe}\sin\left(\frac{\theta}{2}\right)\cos\beta\right]d\theta$$

$$= -2\ln(2\,\mathrm{Pe}\cos\beta) - \frac{4}{\pi}\int_0^{\pi/2}\ln\left[\sin\left(\frac{\theta}{2}\right)\right]d\theta \tag{21}$$

Numerical calculation shows that the last integral in Eq. (21) is equal to -2. Therefore, for F_{2D} ($\Delta = 0$, $\mathrm{Pe}\ll 1$), we have

$$F_{2D} = \frac{8}{\pi} - 2\ln(2\,\mathrm{Pe}\cos\beta) \tag{22}$$

This formula can be generalized for the case of nonzero Δ. The dimensionless distance between the heating and observation point is now

$$r = \sqrt{4(1+\delta)\sin^2\left(\frac{\theta}{2}\right) + \delta^2} \tag{23}$$

Using Eq. (12), we obtain

$$F_{2D} = \frac{4}{\pi}\Phi_1\left(\frac{\Delta}{R}\right) - 2\ln(2\,\mathrm{Pe}\cos\beta) \tag{24}$$

where we introduced the function

$$\Phi_1(x) = \int_0^{\pi/2} d\theta \ln\sqrt{(1+x)\sin^2\left(\frac{\theta}{2}\right) + x^2} \tag{25}$$

This function can be approximated by the expression $\Phi_1(x) \approx 2 - 1.6x^{0.84}$ ($x < 0.8$) with an accuracy better than 1.5%.

3.2 Heating Cylinder: Large Peclet Number. As in the one-dimensional case, if $\mathrm{Pe}\gg 1$, the main contribution to the integral is in a relatively narrow neighborhood around l_0 that corresponds to the maximum argument of the exponential function. Therefore, the steepest descent method can be used.

For the dimensionless distance between heating and observing point, we now have

$$r = \sqrt{4(1+\delta\cos\beta)\sin^2\left(\frac{\theta}{2}\right) + l'^2 + \delta^2(\cos\beta)^2} \tag{26}$$

where the reduced length was introduced as $l' = l - \delta\sin\beta$. For function f in formula (19), we have

$$f = \cos\theta\cos\beta - l'\sin\beta - \delta\cos^2\beta - \cos\beta - r \tag{27}$$

The maximum of this function corresponds to

$$l'_0 = A\tan\beta \tag{28}$$

where we introduced A as

$$A = \sqrt{4(1+\delta\cos\beta)\sin^2\left(\frac{\theta}{2}\right) + \delta^2\cos^2\beta} \tag{29}$$

Function f at l'_0 is

$$f(l'_0) = -2\cos\beta\sin^2\left(\frac{\theta}{2}\right) - \delta\cos^2\beta - A\cos\beta \tag{30}$$

And its second derivative at l'_0 is

$$\frac{d^2 f(l'_0)}{dl'^2} = -\frac{\cos^3\beta}{A} \tag{31}$$

For F_{2D}, we obtain the following approximation:

$$F_{2D} = \int_{-\infty}^{+\infty} dl' \frac{2}{\pi}\int_0^{\pi/2} \frac{d\theta}{r(l'_0)}\exp\left[\mathrm{Pe}\, f(l'_0) + \mathrm{Pe}\frac{1}{2}\frac{d^2 f(l'_0)}{dl'^2}(l' - l'_0)^2\right] \tag{32}$$

After integration, it takes the form

$$F_{2D} = \frac{2}{\pi}\sqrt{\frac{2\pi}{A\,\mathrm{Pe}\cos\beta}}\int_0^{\pi/2} d\theta \exp\left[\mathrm{Pe}\left(-2\cos\beta\sin^2\left(\frac{\theta}{2}\right) - \delta\cos\beta - A\cos\beta\right)\right] \tag{33}$$

At large Pe, only small angles θ contribute to this integral. Therefore, one can put $\sin\theta \approx \theta$ and neglect the term $2\,\mathrm{Pe}\cos\beta\sin^2(\theta/2)$ in comparison to $A\,\mathrm{Pe}\cos\beta$. After a few algebraic operations, one finally has

$$F_{2D} = \sqrt{\frac{8}{1+\delta\cos\beta}}\frac{1}{\mathrm{Pe}\cos\beta}\exp(-\mathrm{Pe}\,\delta\cos^2\beta) \times \Phi_2(\mathrm{Pe}\,\delta\cos^2\beta) \tag{34}$$

Here we introduced the function

$$\Phi_2(x) = \frac{1}{\sqrt{\pi}}\int_0^{\infty} \frac{\exp(-\sqrt{t^2+x^2})dt}{(t^2+x^2)^{1/4}} \tag{35}$$

For the case of $\delta = 0$, $\Phi_2(0) = 1$ and

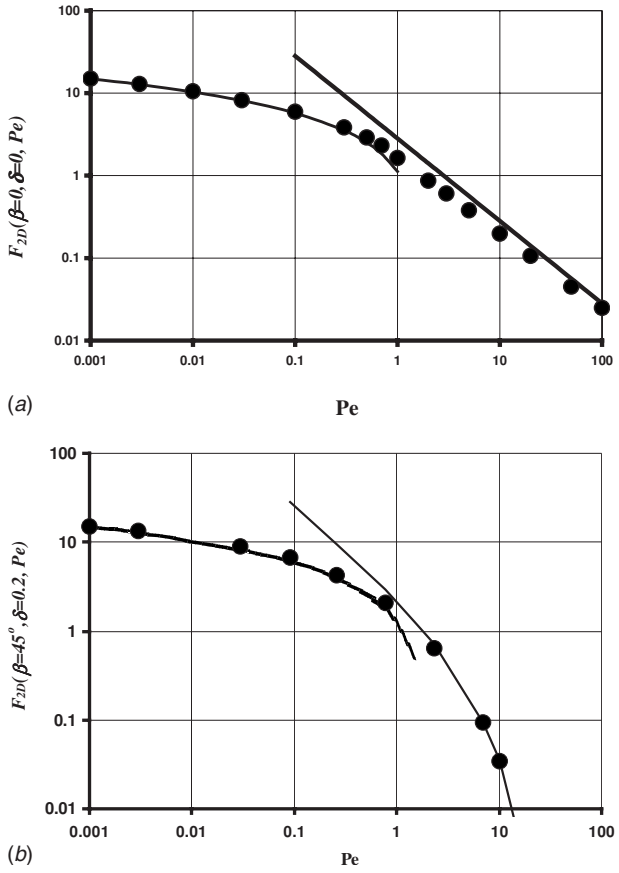

Fig. 5 (*a*) Nondimensional temperature created by a vertical MHS in the case of no liquid layer separating MHS and solid metal ($\Delta=0$); points are the numerical calculations of the integral (Eq. (19)); lines are the approximations (Eqs. (24) and (34)). (*b*) Nondimensional temperature created by a tilted MHS: tilt angle is 45 deg and thickness of the liquid layer separating MHS and solid metal is 20% of the cylinder radius ($\delta=0.2$). Points are the numerical calculations of the integral (Eq. (19)); lines are the approximations (Eqs. (24) and (34)).

$$F_{2D} = \frac{\sqrt{8}}{\mathrm{Pe}\cos\beta} \tag{36}$$

With accuracy better than 5%, function Φ_2 can be approximated as

$$\Phi_2(x) \approx \exp(-2x) \quad (x < 0.2)$$

$$\Phi_2(x) \approx 0.78\exp(-1.02x) \quad (x > 0.2) \tag{37}$$

4 Comparison With the Numerical Calculations

In this section, we compare the above approximate formulas with the results of the numerical calculations of the integral (Eq. (19)). Graphs in Fig. 4 are to check formula (36), which states that at $\mathrm{Pe}\gg 1$ and $\Delta=0$, $F_{2D}(\beta=0,\ \delta=0)/F_{2D}(\beta,0)$ is proportional to $\cos\beta$. The bold line in this figure represents $\cos\beta$. One can see that this proportionality perfectly holds at $\mathrm{Pe}=10$ and reasonably agreed with numerical calculations starting from $\mathrm{Pe}\sim 2$ and higher.

In Figs. 5(*a*) and 5(*b*), we compare approximate formulas (24) and (34) with the results of numerical calculations of the integral (Eq. (19)). Figure 5(*a*) shows this comparison for the case of a vertical cylinder ($\beta=0$) and different Peclet numbers. Figure 5(*b*) represents this comparison for tilted cylinder ($\beta=45$ deg) and $\Delta=0.2R$. It can be seen that analytical approximations almost overlap: At $\mathrm{Pe}<1$, approximation (24) can be used; at $\mathrm{Pe}>1$, approximation (34) can be used. Once again, one can see that two extreme approximations almost overlap.

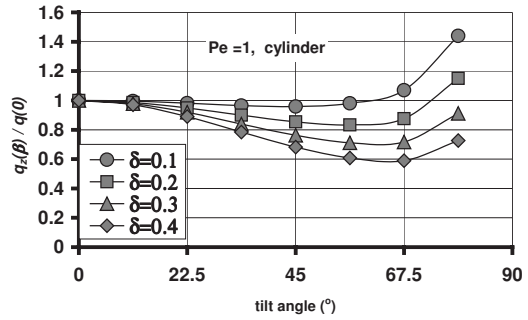

Fig. 6 Relative gain in heat per unit plate thickness by tilting the MHS (ratio of the heat per unit plate thickness to the one of the vertical MHS)

5 Heat Transfer Power Per Unit Cut Length and Per Unit Cut Thickness

It is convenient to present the results obtained above in a different form. Let us introduce dimensionless heat transfer power. One can define two heat transfer powers: one as per unit cut length $q_l=1/F$ and another as heat per unit cut thickness $q_z=1/F\cos\beta$. As was pointed above, tilted MHS always needs less heat transfer power per unit of the cut length than the vertical one. However, since the length of a tilted cut is longer than that of a vertical one, the total consumed power could by either lower or higher. For a practical point of view, when cutting a plate of a given thickness, it is important to know whether tilted MHS consumes higher or lower *total* power. In other words, whether $q_z(\beta)$ is higher or lower than $q_z(0)$.

Let us consider the two-dimensional case. In $\mathrm{Pe}\ll 1$ extreme, q_l depends on the tilt angle β in a weak, logarithmic way (see Eq. (22)). This means that although tilting MHS reduces q_l, the total consumed power increases when the heat source tilts from vertical. This conclusion is true for any thickness of a liquid film separating the heat source from nonmelted metal or if this film is negligibly thin.

Let us proceed to the $\mathrm{Pe}\gg 1$ case. In the absence of a liquid film ($\Delta=0$), q_z does not depend on the tilt angle (see Eq. (36)). The situation is different in the presence of a liquid film. When $\Delta>0$ and $\mathrm{Pe}\gg 1$, both q_l and q_z decrease with the tilt degree increase. The higher the Peclet number and the thicker the film, the higher is the power gain. The effect is exponential (see Eq. (34)).

The case of a moderate Peclet ($\mathrm{Pe}=1$) is shown in Fig. 6. One can see that for a small film thickness ($\Delta<0.1$), q_z is almost independent of the tilt angle up to a very steep tilt, about 50 deg. However, at thicker films and higher tilt angles, the tilted cut consumes considerable less total power than the vertical one.

6 On the Shape of a Cut

Above, we considered heat flux Q as constant throughout the cut. In reality, it decreases toward the bottom of the plate. As a result, the tilt angle changes throughout the cut, increasing toward the bottom. This determines the shape of the cut. Below, we give a brief outline of a possible approach to the problem. We use plasma arc cutting as an example.

One can consider two different situations regarding heat transfer from the plasma jet to the metal. In the first situation, power consumed by the whole process of the metal heating is substantially lower than the total power of the plasma jet. Plasma enthalpy does not change much along the cut depth. In this case, the tilt angle remains the same throughout the cut. It could be low or

high depending on efficiency of the heat transfer. Another situation happens when the plasma jet uses a substantial part of its initial enthalpy in cutting the metal. In this case, parameter Q, the heat flux per unit length of the cut, changes along the cut depth. The tilt angle changes also. Below, we consider this case.

Heat flux per unit of cut length can be expressed as [10]

$$Q = \mathrm{Nu} \times \kappa_{\mathrm{pl}}(T_{\mathrm{pl}} - T_m)$$

where κ_{pl} is the plasma thermal conductivity. T_{pl} and T_m are plasma and metal temperatures, respectively, and Nu is the appropriately defined Nusselt number. Let us assume that heat intensity decreases according to the rule

$$\frac{dQ}{dl} = -\alpha Q \tag{38}$$

where l is length of the cut measured from the top. Estimation of parameter α is presented in Appendix B. Thus, $Q(l)=Q_0 \exp(-\alpha l)$. Our goal is to find function $\beta(l)$, which determines the shape of the cut. The length of the cut (from the top down to the depth z) is

$$l(z) = \int_0^z \frac{dz'}{\cos\beta(z')} \tag{39}$$

The shape of the cut could be found from the following equation (combination of Eqs. (38) and (39)):

$$Q_0 \exp\left(-\alpha \int_0^z \frac{dz'}{\cos\beta(z')}\right) = \frac{4\pi\kappa T_m}{F_{iD}[\mathrm{Pe}, \cos(\beta)]} \tag{40}$$

Here, T_m is the melting point temperature. Index i in function F_{iD} could be 1 or 2, depending whether 1D or 2D approach is used. This equation is an integrodifferential equation that can be solved by step by step integration starting from $z=0$. The boundary condition at $z=0$ demands special consideration.

Strictly speaking, the approach developed in this paper is valid for infinitely thick plates. Using a method of successive reflections, we performed a few numerical calculations, which took into account the finite thickness of the plate. These calculations showed that starting from relatively low numbers $H/D \sim 2$ and higher, the obtained formulas describe the average heat transfer well (H is the plate thickness, and D is the cut width). Therefore, one can try (with some precaution), to use formula (40) at the top of the plate. After putting $z=0$ in Eq. (40), we obtain

$$Q_0 = \frac{4\pi\kappa T_m}{F_{iD}[\mathrm{Pe}, \cos\beta(z=0)]} \tag{41}$$

There are three unknowns in this condition: $\beta(z=0)$, Q_0, D, and the width of the cut. Two of them, Q_0 and D are determined by the particular system arrangement such as diameter of the nozzle, distance from the nozzle to the plate, initial enthalpy of the MHS, Nusselt number, and its dependence of the plasma velocity [10]. The condition in Eq. (41) could be solved for the initial cut tilt $\beta_0=\beta(z=0)$. Once β_0 is specified, the shape of the cut could be found as solution of the following equation:

$$\exp\left(-\alpha \int_0^z \frac{dz'}{\cos\beta(z')}\right) = \frac{F_{iD}[\mathrm{Pe}, \cos\beta_0]}{F_{iD}[\mathrm{Pe}, \cos\beta(z)]} \tag{42}$$

Let assume, for example, that (a) the width of the cut remains the same, (b) that liquid film separating MHS and solid metal is negligibly thin, and (c) that $\mathrm{Pe} \gg 1$. These assumptions mean that we can use formula (36). Then, Eq. (42) reduces to

$$\exp\left(-\alpha \int_0^z \frac{dz'}{\cos\beta(z')}\right) = \frac{\cos\beta}{\cos\beta_0} \tag{43}$$

The solution of Eq. (43) showing how the tilt angle increases with z and the distance from the plate top is

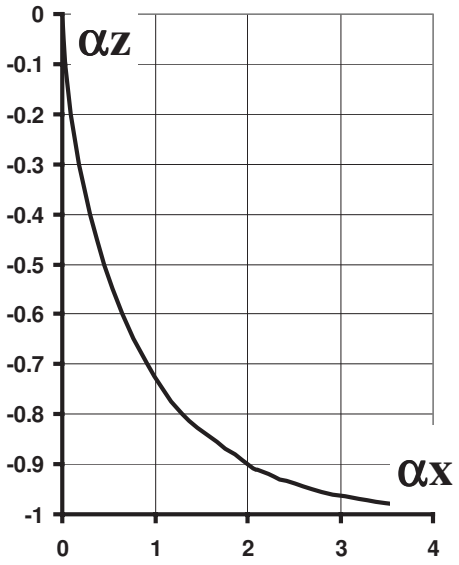

Fig. 7 Shape of a cut: distance of the front of the melting edge from the MHS center as a function of the cut depth; initial tilt of the cut $\beta_0=0$ and $\mathrm{Pe} \gg 1$

$$\cos\beta = \cos\beta_0 - \alpha z$$

One can see that in this approximation, the maximum plate thickness is $z_{\max}=\cos\beta_0/\alpha$. Let $x(z)$ be the decline of the kerf from its position at the top of the plate (lag of the cut from the vertical). This function defines the cut shape in an explicit way. To find this function, note that $\cos\beta=[1+(dx/dz)^2]^{-1/2}$. After solving for dx/dz, we find

$$x = \frac{1}{\alpha}\int_0^z dz' \frac{\sqrt{1-(\cos\beta_0 - \alpha z')^2}}{\cos\beta_0 - \alpha z} \tag{44}$$

After substituting $\theta=\cos^{-1}(\cos\beta_0 - \alpha z)$, this integral can be expressed as a combination of elementary functions, although it is a rather complex one. In Fig. 7, we present the result of the numerical calculations of function $x(z)$ in the case $\beta_0=0$.

Note that the above consideration was mostly for demonstration purposes. We neglected the influence of the liquid film. This could lead to a very substantial error even if the film is thin, especially in the case of large Peclet numbers. A more realistic approach should include consideration of the dynamics of the liquid film.

7 Conclusion

The temperature distribution created by a moving tilted line and a circular cylinder was considered qualitatively and quantitatively (analytically and numerically).

Analytical formulas for temperature distribution were obtained for linear MHS and for cylindrical moving heat sources for large and small Peclet numbers $\mathrm{Pe} \ll 1$ and $\mathrm{Pe} \gg 1$ and arbitrary tilt angles. Numerical calculations were performed to check these approximations and to obtain results for intermediate Peclet numbers. Both analytical approximations ($\mathrm{Pe} \ll 1$ and $\mathrm{Pe} \gg 1$) practically overlap. This allows one to use these approximations for the whole range of Peclet numbers.

The most attention was paid to calculating heat transfer, which is necessary to make a cut. For that purpose, the temperature straight ahead of the cut was considered. It was shown qualitatively and by calculations that the tilted moving heat source consumes less power per unit cut length than the vertical one. As for power consumed per unit cut thickness, a substantial power decrease could be achieved if the heat source and the solid metal are separated by a molten metal film.

An outline of an approach to calculate the cut shape is given.

Nomenclature

a = thermal diffusivity
C = plasma specific heat capacity
T = temperature
F_{1D}, F_{2D} = dimensionless functions (nondimensional temperature)
G = Green's function
H = plate thickness
K_0 = modified Bessel function of the second kind and zero order
Nu = Nusselt number
Pe = Peclet number
Q = heat source linear power
q = nondimensional linear power
U = heat source moving speed
$\mathbf{R}$ = distance between heating point and point of observation
R = radius of heating cylinder
X = projection of R on x-axis
Y = projection of R on y-axis
Z = projection of R on z-axis
L = coordinate along heating line or cylinder
r = nondimensional distance
x, y, z = nondimensional coordinates $(X/\mathrm{R}, Y/\mathrm{R}, Z/\mathrm{R})$
l = nondimensional coordinate along heating source (L/R)

Greek Symbols

α = parameter to characterize heat source power reduction along the cut
β = tilt angle
θ = azimuthal coordinate to characterize location of heating point with respect to moving direction
Δ = distance ahead of heating source
δ = nondimensional distance ahead heating source
Φ_1, Φ_2 = nondimensional functions
κ = thermal conductivity
ρ = plasma density

Subscripts

O = point of observation
H = heating point
pl = plasma
m = metal
z = per unit of thickness (heating power)
l = per unit of cut length (heating power)
1D = one-dimensional
2D = two-dimensional

Appendix A

One can see that $\mathrm{Pe} \ll 1$ and $\mathrm{Pe} \gg 1$ are important in the case of cutting such important materials as steel and aluminum. In fact, assuming the kerf radius to be on the order of 1 mm, we see that Pe becomes more than unity at cutting speeds of steel larger than 1–1.5 cm/s (the thermal diffusivity of steel at temperatures close to the melting point is about $0.05-0.075$ cm^2/s [11]). If plate thickness is not too thick, the highest cutting speed of steel occurs at $\mathrm{Pe} > 1$. In view of high thermal diffusivity of aluminum (at ~ 1 cm^2/s [11]), the situation is the opposite in the case of cutting this metal. The extreme case $\mathrm{Pe} < 1$ takes place when the cutting speed of an aluminum plate is less than ~ 20 cm/s, which occurs if the plate is not too thin.

Appendix B

Considering the equation for plasma temperature inside the kerf $d/dz(\rho \pi R^2 UCT_{\mathrm{pl}}) = -\mathrm{Nu} \times \kappa_{\mathrm{pl}} T_{\mathrm{pl}}$, we find that α can be estimated as $\alpha \sim \mathrm{Nu}(a/R^2 U)$. Here U, a, and C are the plasma velocity, the thermal diffusivity, and the specific heat capacity, respectively. Putting here $a \sim 10^{-2}$ m^2/s, $\mathrm{Nu} \sim 1$, $R \sim 10^{-3}$ m, and $U \sim 10^2$ m/s to 10^3 m/s, one obtains $\alpha \sim 10^2$ m^{-1} to 10 m^{-1}. This corresponds to a characteristic length on the order of 1–10 cm, the correct orders of magnitude.

References

[1] Rosenthal, D., 1941, "Mathematical Theory of Heat Distribution During Welding and Cutting," Welding J., **20**, pp. 220s–234s.
[2] Swift-Hook, D. T., and Gick, A. E. F., 1973, "Penetration Welding With Lasers," Weld. J., **52**, pp. 429s–499s.
[3] Bunting, K. A., and Cornfield, G., 1975, "Toward a General Theory of Cutting: A Relationship Between the Incident Power Density and the Cut Speed," ASME J. Heat Transfer, **97**, pp. 116–122.
[4] Baeva, M., Baev, P., and Kaplan, A., 1997, "An Analysis of the Heat Transfer From a Moving Elliptic Cylinder," J. Phys. D, **30**, pp. 1190–1196.
[5] Toshiyuki, M., and Geidt, W. H., 1982, "Heat Transfer From Elliptical Cylinder Moving Through an Infinite Plate Applied to Electron Beam Welding," Int. J. Heat Mass Transfer, **25**, pp. 807–814.
[6] Gariboldi, E., and Previtali, B., 2005, "High Tolerance Plasma Arc Cutting of Commercially Pure Titanium," J. Mater. Process. Technol., **160**, pp. 77–89.
[7] Nemchinsky, V. A., 1997, "Dross Formation and Heat Transfer During Plasma Arc Cutting," J. Phys. D, **30**, pp. 2566–2572.
[8] Nemchinsky, V. A., and Severance, W. S., 2009, "Plasma Arc Cutting: Speed and Cut Quality," J. Phys. D, **42**, p. 195204.
[9] Carslaw, H. S., and Jaeger, J. C., 1959, *Conduction of Heat in Solids*, 2nd ed., Oxford University, New York.
[10] Incropera, F. P., and DeWitt, D. P., 1996, *Fundamentals of Heat and Mass Transfer*, 4th ed., Wiley, New York.
[11] Touloukian. Y. S., 1970, *Thermal Conductivity: Metallic Elements and Alloys*, Plenum, New York.

T. K. Papathanasiou[1]
e-mail: thpapath@lycos.com

S. I. Markolefas
e-mail: markos34@gmail.com

S. P. Filopoulos
e-mail: sfilop@gmail.com

G. J. Tsamasphyros
e-mail: tsamasph@central.ntua.gr

School of Applied Mathematics and Physical Sciences,
Department of Theoretical and Applied Mechanics,
National Technical University of Athens,
9 Iroon Polytechniou Street,
Zografou Campus,
15773 Athens, Greece

Heat Transfer in Thin Multilayered Plates—Part I: A New Approach

We present a new model for the determination of temperature distributions in thin plates consisting of many different layers. The method uses both continuous and discrete approaches. The derived set of equations is based on a continuous representation of heat transfer phenomena at the midplane of each layer, whereas it facilitates a discrete process for introducing ply to ply, through thickness, heat transfer. For the steady state case, the resulting equations are of the Helmholtz type. Methods of solutions for the resulting system are discussed, and comparisons with the first order lamination theory are presented in a benchmark example. [DOI: 10.1115/1.4002630]

Keywords: heat transfer, composite materials, multilayered plates, first order lamination theory

1 Introduction

Composite materials have found numerous applications in both everyday and high technology applications. Among several types of composite structures, thin plates consisting of many layers of different materials have drawn special attention due to their extended use in low weight structures for the aircraft industry [1]. As new production techniques for these materials lead to decreased manufacturing costs [2,3], the applications of thin multilayered configurations extend to the vehicle and building construction industries as well. It is worth mentioning that such configurations are also used as reinforcing patches for the restoration of damaged structures, offering several advantages in comparison with classical metal patches [4–7].

The above-mentioned applications of thin multilayered plates have increased the demand of special models for the analysis of their properties and behavior. Many models have been proposed in order to simulate both the elastic and thermal behavior of such plates, all of which take advantage of the fact that the thickness of these configurations is small in comparison to their other dimensions. This last property justifies the selection of low order approximations to model the variation of mechanical and thermal fields through the thickness. In such a manner, first and second order lamination theories are in our days well established and used by many scientists and manufacturing industries. Several applications of these theories, for single layered plates, may be found in Refs. [8,9]. Furthermore, even higher order theories have been developed for special applications and increased accuracy [10–12]. Finally, we mention the use of the first order lamination (FOL) theory, by Argyris, Tenek, and Oberg for the construction of a special finite element, capable of modeling conduction, convection, and radiation phenomena in thin multilayered plates [13].

2 The First Order Lamination Theory

The construction of the FOL theory of heat transfer is based on the variational formulation of the classical heat diffusion equation and the assumption of a linear, through thickness variation of the temperature field. With reference to a Cartesian coordinate system *Oxyz*, we assume a thin multilayered plate and a temperature distribution described, independently of the number of layers, by the relation

$$T(x,y,z,t) = T_1(x,y,t) + zT_2(x,y,t) \tag{1}$$

The variation in this temperature distribution is

$$\delta T(x,y,z,t) = \delta T_1(x,y,t) + z\delta T_2(x,y,t) \tag{2}$$

If we multiply the heat diffusion equation by this temperature variation and integrate with respect to z through the total thickness of the plate, we get

$$\int_z \delta T\left[\mathrm{div}(\mathbf{K}\nabla T) + \Phi - \rho C_P \frac{\partial T}{\partial t}\right] dz = 0 \tag{3}$$

where $\mathbf{K}$ is the conductivity tensor, Φ is the internal heat generation term, ρ is the material density, and C_P is the specific heat capacity under constant pressure. Demanding that Eq. (3) holds for every δT_1 and δT_2 leads to a system of two partial differential equations, which must be solved for the determination of T_1 and T_2.

In this paper, we present a different approach in converting the 3D problem of heat diffusion in a thin multilayer composite plate to a system of 2D partial differential equations. As in the case of the FOL theory, we exploit the fact that the thickness of the plate is much smaller than all the other dimensions. The results of both approaches are compared with the use of some benchmark examples.

3 Derivation of the Model

3.1 Cartesian Coordinates. For a 3D anisotropic body, the Fourier law [14] of heat conduction is

$$\begin{bmatrix} q_x \\ q_y \\ q_z \end{bmatrix} = -\begin{bmatrix} k_{xx} & k_{xy} & k_{xz} \\ k_{yx} & k_{yy} & k_{yz} \\ k_{zx} & k_{zy} & k_{zz} \end{bmatrix} \begin{bmatrix} \partial_x T \\ \partial_y T \\ \partial_z T \end{bmatrix} \tag{4}$$

where ∂_i denotes the partial derivative with respect to variable i. In a more compact form, we may write Eq. (4) as

$$\underset{\sim}{q} = -\mathbf{K}\nabla T \tag{5}$$

where

[1]Corresponding author.

Contributed by the Heat Transfer Division of ASME for publication in the JOURNAL OF HEAT TRANSFER. Manuscript received July 23, 2009; final manuscript received September 23, 2010; published online November 2, 2010. Assoc. Editor: Cholik Chan.

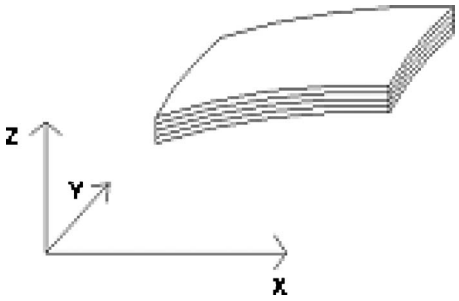

Fig. 1 Thin multilayered plate

$$\mathbf{K} = \begin{bmatrix} k_{xx} & k_{xy} & k_{xz} \\ k_{yx} & k_{yy} & k_{yz} \\ k_{zx} & k_{zy} & k_{zz} \end{bmatrix}$$

is the symmetric [15–17] conductivity tensor and $\tilde{q}$ is the heat flux vector.

Let us now consider a thin solid, consisting of many different layers along its thickness, as shown in Fig. 1. We state the following assumptions:

(A0) The solid consists of N distinct parallel layers, perfectly bonded on each other. The thickness of each layer is b_i, $i=1,2,\ldots,N$.
(A1) The curvature of the solid body is very small, so that the body may be considered as a plate.
(A2) For each layer $i=1,2,\ldots,N$, we assume ${}^{i}k_{xz}={}^{i}k_{yz}=0$, so that there is no coupling between the flow along directions x,y and the temperature gradient component along z.
(A3) Within each layer, the components of the conductivity matrix are constant.
(A4) The thermal contact resistance between two successive layers is negligible.

Besides these assumptions, the general case would involve convection and radiation heat loses from the upper and lower surfaces and finally internal heat generation $\Phi_i(x,y,z)$ $(\mathrm{W/m^3})$ in each layer.

We now consider a volume of the form $dV=\Sigma_{i=1}^{N}dV_i=dxdy\Sigma_{i=1}^{N}b_i$ (see Fig. 2). Under the assumption that $\partial\Phi_i(x,y,z)/\partial z=0$, the energy balance for each layer separately results in the following system of equations:

$$\Phi_1 b_1 + q_{o1} = b_1\frac{\partial q_{1x}}{\partial x} + b_1\frac{\partial q_{1y}}{\partial y} + q_{1,2} + q_{\mathrm{conv}1} + q_{\mathrm{rad}1} + b_1\rho_1 C_{P1}\frac{\partial T_1}{\partial t}$$

$$\Phi_2 b_2 + q_{1,2} = b_2\frac{\partial q_{2x}}{\partial x} + b_2\frac{\partial q_{2y}}{\partial y} + q_{2,3} + b_2\rho_2 C_{P2}\frac{\partial T_2}{\partial t}$$

$$\Phi_i b_i + q_{i-1,i} = b_i\frac{\partial q_{ix}}{\partial x} + b_i\frac{\partial q_{iy}}{\partial y} + q_{i,i+1} + b_i\rho_i C_{Pi}\frac{\partial T_i}{\partial t}$$

$$\Phi_N b_N + q_{N-1,N} + q_{oN} = b_N\frac{\partial q_{Nx}}{\partial x} + b_N\frac{\partial q_{Ny}}{\partial y} + q_{\mathrm{conv}N} + q_{\mathrm{rad}N} + b_N\rho_N C_{PN}\frac{\partial T_N}{\partial t} \quad (6)$$

where q_{o1}, q_{oN} $(\mathrm{W/m^2})$ are the external thermal loadings charging the lower and upper surfaces, respectively (e.g., laser beams). Convection losses from those two surfaces are $q_{\mathrm{conv}1}, q_{\mathrm{conv}N}$ $(\mathrm{W/m^2})$, whereas $q_{\mathrm{rad}1}, q_{\mathrm{rad}N}$ $(\mathrm{W/m^2})$ are possible losses from radiation phenomena. The density and specific heat at constant pressure, for each layer, are denoted by ρ_i $(\mathrm{kg/m^3})$ and C_{Pi} $(\mathrm{J/kg\ K})$, respectively. The terms $q_{i-1,i}$ represent heat transfer

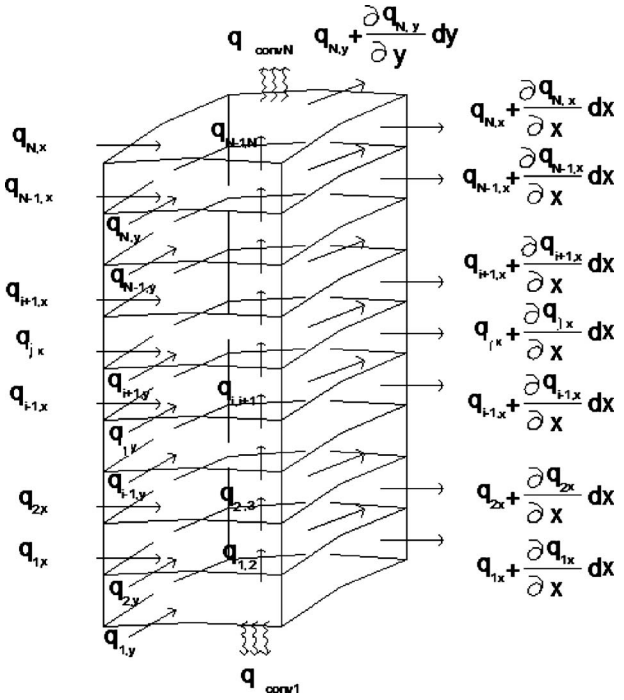

Fig. 2 Energy conservation for a characteristic volume of the plate

from ply $i-1$ to ply i, $\forall i$.

In the following analysis, we will ignore all radiation related heat transfer phenomena. The application of the Fourier law of heat conduction along directions x and y in Eq. (6) and the use of (A2) and (A3) lead to

$$\Phi_1 b_1 + q_{o1} = -b_1\left({}^{1}k_{xx}\frac{\partial^2 T_1}{\partial x^2} + 2({}^{1}k_{xy})\frac{\partial^2 T_1}{\partial x\,\partial y} + {}^{1}k_{yy}\frac{\partial^2 T_1}{\partial y^2}\right) + q_{1,2} + q_{\mathrm{conv}1} + b_1\rho_1 C_{P1}\frac{\partial T_1}{\partial t}$$

$$\Phi_2 b_2 + q_{1,2} = -b_2\left({}^{2}k_{xx}\frac{\partial^2 T_2}{\partial x^2} + 2({}^{2}k_{xy})\frac{\partial^2 T_2}{\partial x\,\partial y} + {}^{2}k_{yy}\frac{\partial^2 T_2}{\partial y^2}\right) + q_{2,3} + b_2\rho_2 C_{P2}\frac{\partial T_2}{\partial t}$$

$$\Phi_i b_i + q_{i-1,i} = -b_i\left({}^{i}k_{xx}\frac{\partial^2 T_i}{\partial x^2} + 2({}^{i}k_{xy})\frac{\partial^2 T_i}{\partial x\,\partial y} + {}^{i}k_{yy}\frac{\partial^2 T_i}{\partial y^2}\right) + q_{i,i+1} + b_i\rho_i C_{Pi}\frac{\partial T_i}{\partial t}$$

$$\Phi_N b_N + q_{N-1,N} + q_{oN} = -b_N\left({}^{N}k_{xx}\frac{\partial^2 T_N}{\partial x^2} + 2({}^{N}k_{xy})\frac{\partial^2 T_N}{\partial x\,\partial y} + {}^{N}k_{yy}\frac{\partial^2 T_N}{\partial y^2}\right) + q_{\mathrm{conv}N} + b_N\rho_N C_{PN}\frac{\partial T_N}{\partial t} \quad (7)$$

In order to model ply to ply heat transfer, we employ a discrete method known as the "energy balance" method [18,19]. This is similar to the finite volume method when applied to the heat transfer equations.

For two plies of different materials, as shown in Fig. 3(*a*), we suppose the temperature at the midpoint of each ply to be T_A and T_B. Let the temperature at the interface (see Fig. 3(*a*)) be T^*. Then, the heat flow between those plies may be approximated as

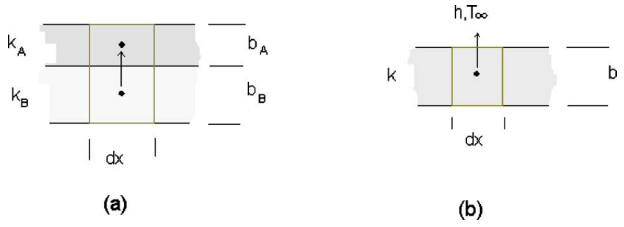

Fig. 3 (*a*) Ply to ply heat transfer approximation. (*b*) Convection loses approximation.

$$q_{B,A} = -2k_B \frac{T^* - T_B}{b_B} \tag{8a}$$

$$q_{B,A} = -2k_A \frac{T_A - T^*}{b_A} \tag{8b}$$

The latter two relations may be combined to yield

$$q_{B,A} = 2\frac{k_B k_A}{k_B b_A + k_A b_B}(T_B - T_A) \tag{9}$$

From relation (9), a new coefficient is defined:

$$s_{B,A} = 2\frac{k_B k_A}{k_B b_A + k_A b_B} \tag{10}$$

This is a coefficient used to describe ply to ply heat transfer in a way similar to that of Newton's law of cooling.

In the same manner, we may approximate the heat leaving a ply from its upper (or lower) surface by means of convection, as shown in Fig. 3(*b*), by using relations

$$q_{\text{conv}} = -2k\frac{T^* - T}{b} \tag{11a}$$

$$q_{\text{conv}} = h(T^* - T_\infty) \tag{11b}$$

where we have assumed that the terms q_{o1}, q_{oN} (W/m^2) are negligible or zero. Moreover, h denotes the convection coefficient. From these relations, we have

$$q_{\text{conv}} = h\left(1 + \frac{bh}{2k}\right)^{-1}(T - T_\infty) \tag{12}$$

An equivalent convection coefficient is defined through relation (12):

$$\bar{h} = \frac{h}{1 + \text{Bi}} \tag{13}$$

where $\text{Bi} = bh/2k$ is a Biot (nondimensional) number. For practical applications and when the thickness of a ply is small, $\text{Bi} \ll 1$. In that case, $\bar{h} \approx h$. In view of relations (9) and (12), system (7) becomes

$$b_1\left({}^1k_{xx}\frac{\partial^2 T_1}{\partial x^2} + 2({}^1k_{xy})\frac{\partial^2 T_1}{\partial x\,\partial y} + {}^1k_{yy}\frac{\partial^2 T_1}{\partial y^2}\right) + s_{1,2}(T_2 - T_1)$$
$$- \bar{h}_1(T_1 - T_\infty) + \Phi_1 b_1 + q_{o1} = b_1\rho_1 C_{P1}\frac{\partial T_1}{\partial t}$$

$$b_2\left({}^2k_{xx}\frac{\partial^2 T_2}{\partial x^2} + 2({}^2k_{xy})\frac{\partial^2 T_2}{\partial x\,\partial y} + {}^2k_{yy}\frac{\partial^2 T_2}{\partial y^2}\right) + s_{2,3}(T_3 - T_2)$$
$$- s_{1,2}(T_2 - T_1) + \Phi_2 b_2 = b_2\rho_2 C_{P2}\frac{\partial T_2}{\partial t}$$

$$b_i\left({}^ik_{xx}\frac{\partial^2 T_i}{\partial x^2} + 2({}^ik_{xy})\frac{\partial^2 T_i}{\partial x\,\partial y} + {}^ik_{yy}\frac{\partial^2 T_i}{\partial y^2}\right) + s_{i,i+1}(T_{i+1} - T_i)$$
$$- s_{i-1,i}(T_i - T_{i-1}) + \Phi_i b_i = b_i\rho_i C_{Pi}\frac{\partial T_i}{\partial t}$$

$$b_N\left({}^Nk_{xx}\frac{\partial^2 T_i}{\partial x^2} + 2({}^Nk_{xy})\frac{\partial^2 T_N}{\partial x\,\partial y} + {}^Nk_{yy}\frac{\partial^2 T_N}{\partial y^2}\right) - s_{N-1,N}(T_N - T_{N-1})$$
$$- \bar{h}_N(T_N - T_\infty) + \Phi_N b_N + q_{oN} = b_N\rho_N C_{PN}\frac{\partial T_N}{\partial t} \tag{14}$$

where $s_{i-1,i} = 2{}^ik_{zz}{}^{i-1}k_{zz}/({}^ik_{zz}b_{i-1} + {}^{i-1}k_{zz}b_i)$ (see relation (10)).

Relations (8*a*) and (8*b*) may be used for the determination of interlaminar temperatures, whereas relation (11*a*) or (11*b*) may provide the temperatures at the upper or lower surface of the plate.

Equations (14), along with boundary conditions of Dirichlet, Neumann, and Robin types along the perimeter of the plate and one initial condition for the temperature of each ply, form an initial-boundary value problem. If we introduce the plane conductivity tensor for each ply,

$${}^i\mathbf{K} = \begin{bmatrix} {}^ik_{xx} & {}^ik_{xy} \\ {}^ik_{yx} & {}^ik_{yy} \end{bmatrix} \tag{15}$$

and consider the plane gradient operator, this problem may be written in a more compact form as follows:

$$\left.\begin{aligned} &\nabla\cdot({}^i\mathbf{K}\,\nabla\,\vartheta_i) + \frac{1}{b_i}\sum_{j=1}^{N}\ell_{ij}\vartheta_j + \Phi_i = \rho_i C_{Pi}\frac{\partial\vartheta_i}{\partial t} \\ &i = 1,2,\ldots,N \\ &\text{in } \Omega\times(0,\tau)\subset\mathbb{R}^3 \end{aligned}\right\}$$

$$\vartheta_i = g_i(\text{Dirichlet conditions}) \quad \text{on } \partial\Omega_D^i\times(0,\tau)$$

$$-({}^i\mathbf{K}\,\nabla\,\vartheta_i)\cdot\mathbf{n} + p_i\vartheta_i = q_i(\text{Neumann or Robin conditions}) \quad \text{on } \partial\Omega_N^i\times(0,\tau)$$

$$\vartheta_i(\bullet,0) = \vartheta_{i0}(\text{initial conditions}) \quad \text{in } \Omega \tag{16}$$

where no summation on index i is implied. In problem (16), Ω is the spatial domain, g_i, p_i, q_i are known functions of time, $\mathbf{n}$ is the unit vector normal to the boundary, and ϑ_{i0} is the initial temperature distribution. Furthermore, $(0,\tau)$ is the temporal domain, where $\tau > 0$ is a constant. In addition, we define

$$\vartheta_i = T_i - T_\infty \tag{17a}$$

$$\ell_{11} = -s_{1,2} - \bar{h}_1 \tag{17b}$$

$$\ell_{NN} = -s_{N-1,N} - \bar{h}_N \tag{17c}$$

$$\ell_{ii} = -s_{i-1,i} - s_{i,i+1}, \quad i = 2,3,\ldots,N-1 \tag{17d}$$

$$\ell_{i,i+1} = s_{i,i+1}, \quad i = 1,2,\ldots,N-1 \tag{17e}$$

$$\ell_{i,i-1} = s_{i-1,i}, \quad i = 2,3,\ldots,N \tag{17f}$$

$$\ell_{ij} = 0, \quad |j-i| > 1, \quad i = 1,2,\ldots,N, \quad j = 1,2,\ldots,N \tag{17g}$$

and $\partial\Omega_D^i \cap \partial\Omega_N^i = \varnothing$, $\partial\Omega_D^i \cup \partial\Omega_N^i = \partial\Omega$.

3.2 Cylindrical Coordinates. If we consider cylindrical coordinates, the plane gradient operator becomes:

$$\nabla_{r\theta} \doteq \begin{bmatrix} \dfrac{\partial}{\partial r} & \dfrac{1}{r}\dfrac{\partial}{\partial\theta} \end{bmatrix}^T \tag{18}$$

Furthermore, we define the operator

$$\mathbf{J} \doteq \begin{bmatrix} v_1 \cdot \nabla_{r\theta} & v_2 \cdot \nabla_{r\theta} \end{bmatrix}^T \tag{19}$$

where $v_1=[\cos\theta \ -\sin\theta]^T$ and $v_2=[\sin\theta \cos\theta]^T$.

The resulting partial differential equation system and boundary and initial value problem may be written in the form

$$\left.\begin{aligned} &\mathbf{J}\cdot({}^i\mathbf{K}\mathbf{R}^T\nabla_{r\theta}\vartheta_i)+\frac{1}{b_i}\sum_{j=1}^{N}\ell_{ij}\vartheta_j+\Phi_i=\rho_i C_{Pi}\frac{\partial\vartheta_i}{\partial t}\\ &i=1,2,\ldots,N\\ &\text{in } \Omega\times(0,\tau)\subset\mathbb{R}^3 \end{aligned}\right\}$$

$$\vartheta_i = g_i(\text{Dirichlet conditions}) \quad \text{on} \quad \partial\Omega_D^i\times(0,\tau)$$

$$-({}^i\mathbf{K}\mathbf{R}^T\nabla_{r\theta}\vartheta_i)\cdot\mathbf{n}+p_i\vartheta_i=q_i(\text{Neumann or Robin conditions}) \quad \text{on} \quad \partial\Omega_N^i\times(0,\tau)$$

$$\vartheta_i(\bullet,0)=\vartheta_{i0}(\text{initial conditions}) \quad \text{in} \quad \Omega \tag{20}$$

where

$$\mathbf{R}=\begin{bmatrix} \cos\theta & \sin\theta \\ -\sin\theta & \cos\theta \end{bmatrix}$$

is the plane rotation matrix.

4 Heat Transfer in a Set of Isotropic Plies

In this section, we will focus on the equations governing heat transfer in a plate consisting of N isotropic plies. For the case of steady state conditions, we will discuss a general method for decoupling the resulting system and some properties of the solutions. We will first treat the formulation in Cartesian coordinates. The analysis in cylindrical coordinates is similar.

4.1 Cartesian Coordinates. In Cartesian coordinates, for the case that ${}^ik_{xx}={}^ik_{yy}={}^ik$ and ${}^ik_{xy}={}^ik_{yx}=0$ (isotropic plies), problem (16) becomes

$$\left.\begin{aligned} &\left(\frac{\partial^2}{\partial x^2}+\frac{\partial^2}{\partial y^2}\right)\vartheta_i+\frac{1}{{}^ikb_i}\sum_{j=1}^{N}\ell_{ij}\vartheta_j+\frac{\Phi_i}{{}^ik}=\frac{\rho_i C_{Pi}}{{}^ik}\frac{\partial\vartheta_i}{\partial t}\\ &i=1,2,\ldots,N\\ &\text{in } \Omega\times(0,\tau)\subset\mathbb{R}^3 \end{aligned}\right\}$$

$$\vartheta_i = g_i \quad \text{on} \quad \partial\Omega_D^i\times(0,\tau)$$

$$-{}^ik\nabla\vartheta_i\cdot\mathbf{n}+p_i\vartheta_i=q_i \quad \text{on} \quad \partial\Omega_N^i\times(0,\tau)$$

$$\vartheta_i(\bullet,0)=\vartheta_{i0} \quad \text{in} \quad \Omega \tag{21}$$

Under steady state conditions, system (21) may be uncoupled and some a priori qualitative results may easily be stated for the nature of its solutions. Steady state analysis results into the system:

$$\left.\begin{aligned} &\left(\frac{\partial^2}{\partial x^2}+\frac{\partial^2}{\partial y^2}\right)\vartheta_i+\frac{1}{{}^ikb_i}\sum_{j=1}^{N}\ell_{ij}\vartheta_j+\frac{\Phi_i}{{}^ik}=0\\ &i=1,2,\ldots,N\\ &\text{in } \Omega\subset\mathbb{R}^3 \end{aligned}\right\}$$

$$\vartheta_i = g_i \quad \text{on} \quad \partial\Omega_D^i$$

$$-{}^ik\nabla\vartheta_i\cdot\mathbf{n}+p_i\vartheta_i=q_i \quad \text{on} \quad \partial\Omega_N^i \tag{22}$$

For uniform heat generation, a partial solution of system (22) may be obtained by the formula

$$\underset{\sim}{\vartheta}_p=-\mathbf{A}^{-1}\underset{\sim}{\Phi} \tag{23}$$

where $\underset{\sim}{\vartheta}_P=[\vartheta_1 \ \vartheta_2 \ \cdots \ \vartheta_N]^T$, $\underset{\sim}{\Phi}=[\Phi_1/{}^1k \ \Phi_2/{}^2k \ \ldots \ \Phi_N/{}^Nk]^T$, and $\mathbf{A}=[({}^ikb_i)^{-1}\ell_{ij}]_{i,j=1}^{N,N}$.

The homogeneous form of system (22) may be uncoupled by expressing the homogeneous partial differential equation system as

$$\nabla^2\underset{\sim}{\vartheta}+\mathbf{A}\underset{\sim}{\vartheta}=\underset{\sim}{0} \tag{24}$$

The following result may be derived for the eigenvalues of matrix A.

PROPOSITION 1. *The spectrum* $\sigma(\mathbf{A})$ *of matrix* $\mathbf{A}=[({}^ikb_i)^{-1}\ell_{ij}]_{i,j=1}^{N,N}$ *is a subset of* $\mathbb{R}^-$ *, and the eigenvalues are discrete.*

The proof of Proposition 1 is given in Appendix A. In view of Proposition 1, Eq. (19) may be written in the form

$$\nabla^2\underset{\sim}{\vartheta}+\mathbf{U}\mathbf{D}\mathbf{U}^{-1}\underset{\sim}{\vartheta}=\underset{\sim}{0} \tag{25}$$

where $\mathrm{A}=\mathbf{U}D\mathbf{U}^{-1}$, $\mathrm{D}=\mathrm{diag}(\lambda_1,\lambda_2,\ldots,\lambda_N)$, λ_i being the eigenvalues of $\mathbf{A}$, and $\mathbf{U}$ is the matrix of eigenvectors of $\mathbf{A}$. If we set $\mathbf{U}^{-1}\underset{\sim}{\vartheta}=\underset{\sim}{y}$, system (25) takes the uncoupled form:

$$\nabla^2\underset{\sim}{y}+\mathbf{D}\underset{\sim}{y}=\underset{\sim}{0} \tag{26}$$

The ith equation of system (26) has the form

$$\nabla^2 y_i-|\lambda_i|y_i=0 \tag{27}$$

since all eigenvalues of $\mathbf{A}$ are negative (see Proposition 1). Equation (27) is of the Helmoltz type and may in general be easily solved. The fact that the coefficient in Eq. (27) is negative rules out the presence of oscillating solutions, as already expected by the physics of the problem. The general form of temperature distribution in each ply is given by the following relation:

$$\underset{\sim}{\vartheta}=\underset{\sim}{\vartheta}_P+\mathbf{U}\underset{\sim}{y} \tag{28}$$

4.2 Cylindrical Coordinates. In the case of cylindrical coordinates when ${}^ik_{xx}={}^ik_{yy}={}^ik$ and ${}^ik_{xy}={}^ik_{yx}=0$, we have from problem (20)

$$\left.\begin{aligned} &\left(\frac{\partial^2}{\partial^2 r}+\frac{1}{r}\frac{\partial}{\partial r}+\frac{1}{r^2}\frac{\partial^2}{\partial^2\theta}\right)\vartheta_i+\frac{1}{{}^ikb_i}\sum_{j=1}^{N}\ell_{ij}\vartheta_j+\frac{\Phi_i}{{}^ik}=\frac{\rho_i C_{Pi}}{{}^ik}\frac{\partial\vartheta_i}{\partial t}\\ &i=1,2,\ldots,N\\ &\text{in } \Omega\times(0,\tau)\subset\mathbb{R}^3 \end{aligned}\right\}$$

$$\vartheta_i = g_i \quad \text{on} \quad \partial\Omega_D^i\times(0,\tau)$$

$$-{}^ik(\mathbf{R}^T\nabla_{r\theta}\vartheta_i)\cdot\mathbf{n}+p_i\vartheta_i=q_i \quad \text{on} \quad \partial\Omega_N^i\times(0,\tau)$$

$$\vartheta_i(\bullet,0)=\vartheta_{i0} \quad \text{in} \quad \Omega \tag{29}$$

Under steady state conditions, the results obtained for Cartesian coordinates (see Proposition 1) are valid for the uncoupling of the equations of problem (29) as well.

5 Numerical Examples

In this section, we will test the present method in a benchmark example and compare the results with those obtained by the FOL theory.

Let us consider a plate composed of two plies, each one of a different isotropic material. The thicknesses of the plies are b_A and b_B, respectively. The plate is considered to be of infinite length normal to the page, and the heat transfer phenomena are 2D (see Fig. 4). We assume no internal heat generation. Moreover, the plate experiences convection losses due to the interaction with the surrounding medium of temperature $T_{\infty A}$ for the lower surface and $T_{\infty B}$ for the upper surface. The convection and conduction coefficients for the lower ply are h_A, k_A, respectively. For the upper ply the corresponding values are h_B, k_B.

The application of the present method results to the system

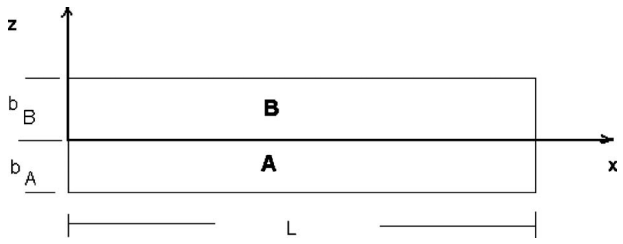

Fig. 4 A thin plate consisting of two different plies A and B

$$k_A b_A \frac{d^2T_A}{dx^2} - (\bar{h}_A + s_{A,B})T_A + s_{A,B}T_B = -\bar{h}_A T_{\infty A}$$

$$k_B b_B \frac{d^2T_B}{dx^2} + s_{A,B}T_A - (\bar{h}_B + s_{A,B})T_B = -\bar{h}_B T_{\infty B} \tag{30}$$

where $T(x,z=-b_A/2)=T_A$ and $T(x,z=b_B/2)=T_B$ (see Fig. 4).

The FOL theory uses the approximation $T(x,z)=T_1(x)+zT_2(x)$. When applied to the same problem, it produces the system (see relations (1)–(3))

$$G_1\frac{d^2T_1}{dx^2} + G_2\frac{d^2T_2}{dx_2} - (h_A+h_B)T_1 - h_B(b_A+b_B)T_1 = -h_A T_{\infty A} - h_B T_{\infty B}$$

$$G_2\frac{d^2T_1}{dx^2} + G_3\frac{d^2T_2}{dx^2} - h_B(b_A+b_B)T_1 + G_4T_2 = -h_B T_{\infty B}(b_A+b_B) \tag{31}$$

where

$$G_1 = k_A b_A + k_B b_B \tag{32a}$$

$$G_2 = k_A\frac{b_A^2}{2} + k_B\left(\frac{(b_B+b_A)^2}{2} - \frac{b_A^2}{2}\right) \tag{32b}$$

$$G_3 = k_A\frac{b_A^3}{2} + k_B\left(\frac{(b_B+b_A)^3}{2} - \frac{b_A^3}{2}\right) \tag{32c}$$

$$G_4 = -h_B(b_B+b_A)^2 - k_A b_A - k_B b_B \tag{32d}$$

We now assume that the temperature is prescribed at both the vertical sides of the plate and has the values

$$T_A(0) = T_B(0) = T(x=0,z) = T_0 \quad \text{and}$$

$$T_A(L) = T_B(L) = T(x=L,z) = T_L$$

Example 1 (consistency result). We will first show a consistency result for the present method. We assume that the upper and lower surfaces of the plate are insulated and that both plies are of the same material ($k_A=k_B=k$). Under these assumptions, heat flow is 1D inside the plate and the temperature distribution is independent of z:

$$T(x,z) = T_0\left(1-\frac{x}{L}\right) + T_L\left(\frac{x}{L}\right) \tag{33}$$

System (30) becomes

$$\frac{d^2T_A}{dx^2} - \frac{2}{b_A(b_A+b_B)}T_A + \frac{2}{b_A(b_A+b_B)}T_B = 0$$

$$\frac{d^2T_B}{dx^2} + \frac{2}{b_B(b_A+b_B)}T_A - \frac{2}{b_B(b_A+b_B)}T_B = 0 \tag{34}$$

The solution of system (34) is

$$T_A = C_1 + C_2x + C_3e^{\sqrt{2/(b_Ab_B)}x} + C_4e^{-\sqrt{2/(b_Ab_B)}x}$$

$$T_B = C_1 + C_2x - C_3\frac{b_B}{b_A}e^{\sqrt{2/(b_Ab_B)}x} - C_4\frac{b_B}{b_A}e^{-\sqrt{2/(b_Ab_B)}x} \tag{35}$$

Application of the boundary conditions leads to the exact solution:

$$T_A = T_B = T_0 + \left(\frac{T_L-T_0}{L}\right)x \tag{36}$$

Example 2. We now return to system (30) and set $T_{\infty A}=T_{\infty B}=293$ K and $b_A=b_B=b$. The essential boundary conditions are set to $T(x=0,z)=373$ K and $T(x=L,z)=323$ K. The length is $L=0.5$ m. We will examine two different cases:

(i) $k_A=150$ W/m K, $h_A=30$ W/m^2 K, $k_B=7.5$ W/m K, $h_B=6$ W/m^2 K
(ii) $k_A=150$ W/mK, $h_A=30$ W/m^2 K, $k_B=75$ W/mK, $h_B=15$ W/m^2 K

The exact solution for the problem, solving the Laplace equation in the 2D domain, may be found based on the variable splitting technique,

$$T_A = T_0 - \frac{T_L-T_0}{L}x + \sum_{n=0}^{\infty}(D_{1n}e^{-n\pi z/L} + D_{2n}e^{n\pi z/L})\sin\frac{n\pi x}{L} \tag{37a}$$

$$T_B = T_0 - \frac{T_L-T_0}{L}x + \sum_{n=0}^{\infty}(E_{1n}e^{-n\pi z/L} + E_{2n}e^{n\pi z/L})\sin\frac{n\pi x}{L} \tag{37b}$$

For the determination of the constants $D_{1n},D_{2n},E_{1n},E_{2n}$, we use the following boundary and interface conditions. Convection condition at the lower surface:

$$k_A\left.\frac{\partial T_A}{\partial z}\right|_{z=b_A} - h_A(T_A|_{z=b_A} - T_{\infty A}) = 0$$

Convection condition at the upper surface:

$$k_B\left.\frac{\partial T_B}{\partial z}\right|_{z=b_B} + h_B(T_B|_{z=b_B} - T_{\infty B}) = 0$$

Equality of temperatures at the interface:

$$T_A(x,0) = T_B(x,0)$$

Equality of thermal fluxes at the interface:

$$k_A\left.\frac{\partial T_A}{\partial z}\right|_{z=0} = k_B\left.\frac{\partial T_B}{\partial z}\right|_{z=0}$$

These four conditions yield a sequence of linear systems of the form $\mathbf{A_n}\underset{\sim}{x}_n=\underset{\sim}{f}_n$. The solution of these systems $\forall n\in\mathbb{N}$ provides the four constants required for each term of the infinite Fourier series. Matrix $\mathbf{A_n}$ and vector $\underset{\sim}{f}_n$ are given in Appendix B.

In Figs. 5 and 6, we present the temperature distribution along the interface of plies A and B as well as the percentage relative error with respect to the exact solution for both the present method and the results obtained from the FOL theory. The results are obtained for the ratio $b/L=0.04$.

We see in those two figures that both methods provide solutions of high accuracy, with errors of less than 0.015%.

Figures 7 and 8 are diagrams of the temperature distribution along the depth of the plate at four different cross sections. Figure 7 corresponds to case (i), whereas Fig. 8 corresponds to case (ii). In all cases, $b/L=0.04$. The temperature variation is nondimensionalized with respect to the maximum value of the exact solution. Again, both the present method and the FOL theory yield results of high accuracy. The present method seems to approximate more closely the form of the exact solution along the depth

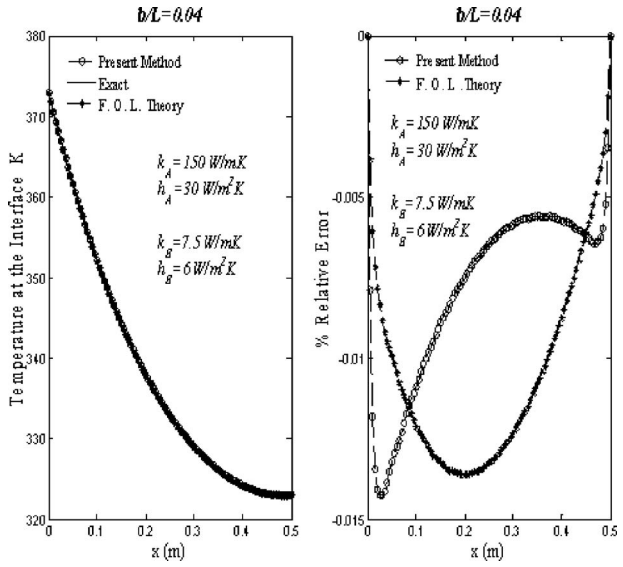

Fig. 5 Temperature profile at the interface and comparison of the present method with the FOL theory (case I)

of the plate. For the present method, the interlaminar and upper and lower surface temperatures have been calculated by formulas (8*a*), (8*b*), (11*a*), and (11*b*), which take the form

$$T(x,z=0)=\frac{k_B b_A T(x,z=b/2)+k_A b_B T(x,z=-b/2)}{k_B b_A+k_A b_B} \tag{38}$$

$$T(x,z=-b)=\frac{2k_A T(x,z=-b/2)-h_A b_A T_{\infty A}}{2k_A+h_A b_A} \tag{39}$$

$$T(x,z=b)=\frac{2k_B T(x,z=b/2)-h_B b_B T_{\infty B}}{2k_B+h_B b_B} \tag{40}$$

As general observations, we may state the following:

Remark 1. The FOL theory, when applied to the problems of multilayered plates, always produces a system of two equations and two unknowns. Contrary to that, the present method will yield an $N\times N$ system for the case of N plies, which is certainly a drawback. However, if higher order lamination theories are used, the number of equations and unknowns will increase as well.

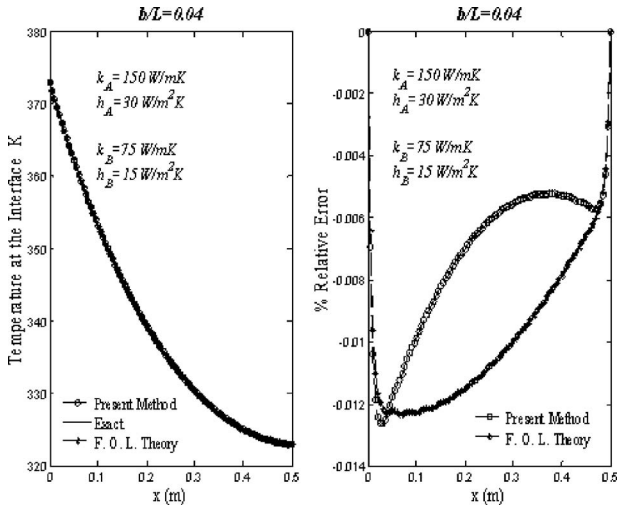

Fig. 6 Temperature profile at the interface and comparison of the present method with the FOL theory (case II)

Remark 2. The system produced by the FOL theory is coupled not only in the unknown functions values but in higher order derivatives as well. The present method results in the coupling of the unknown function values only. Furthermore, the procedure needed for the derivation of the equations of the first order lamination theory is much lengthier than that demanded for the present method as it involves the calculation of several integrals.

Finally, in order to study the performance of the method as the plate becomes thicker, we define the discrete L^2 norm,

$$\|\bullet\|_{DL}=100\frac{\sqrt{\sum_{i=1}^{M}(T_i-T_{i-\text{exact}})^2}}{\sqrt{\sum_{i=1}^{M}(T_{i-\text{exact}})^2}} \tag{41}$$

where M is a number of points in the domain and its boundary where the solution is calculated. The norm is calculated first for T_i the solution produced by the present method and then for the solution provided by the FOL theory. The results are plotted in log-log plots for $M=150$. Figure 9 corresponds to case (i), and Fig. 10 corresponds to case (ii). We can see that with respect to norm $\|\bullet\|_{DL}$, the present method produces better results than the FOL theory. The observed rate of convergence seems to be the same for both methods. The difference is that for the present method the line is displaced toward smaller values of the error norm.

6 Conclusions

We have presented a new method for modeling heat transfer in thin multilayered plates. This new approach, similar to lamination theories, reduces the general 3D problem into a coupled system of 2D partial differential equations. The method utilizes a discrete approximation for ply to ply heat transfer while using the classical continuous heat transfer theory to simulate the phenomena in the midplane of each layer. In a discrete manner, thermal losses due to convection from the upper and lower surfaces of the plane are introduced into the differential equations. The general form of the resulting boundary and initial value problems has been presented in both Cartesian and cylindrical coordinates. The efficiency of this new approach is tested with application to some benchmark problems, and comparisons are made with the first order lamination theory. The present model is found to yield more realistic results and produce smaller overall errors when compared with the FOL theory. The application of the proposed model to more complex cases is currently under investigation.

Appendix A

Proof of Proposition 1. The proof will be performed in three steps. We will first show that all eigenvalues of $\mathbf{A}=[({}^{i}kb_i)^{-1}\ell_{ij}]_{i,j=1}^{N,N}$ are real and discrete. We will use a standard result of linear algebra [20,21] presented here as Lemma 1.

LEMMA 1. *A tridiagonal matrix* $\mathbf{M}=[m_{ij}]_{i,j=1}^{N,N}$ *is similar to a Hermitian matrix if its elements have the property* $m_{i,i+1}m_{i+1,i}>0$, $i=1,2,\ldots,N-1$.

In view of Lemma 1, we have the following.

PROPOSITION 1.1. *For the matrix* $\mathbf{A}=[({}^{i}kb_i)^{-1}\ell_{ij}]_{i,j=1}^{N,N}$ *,, it holds that* $\sigma(\mathbf{A})\subset\mathbb{R}$ *and the eigenvalues are discrete.*

Proof of Proposition 1.1. By the definition of the elements of $\mathbf{A}$, we have $({}^{i}k^{-1}b_i^{-1})({}^{i+1}k^{-1}b_{i+1}^{-1})s_{i,i+1}s_{i+1,i}>0$, $i=1,2,\ldots,N-1$. Since $\mathbf{A}$ is tridiagonal, the use of Lemma 1 implies that $\mathbf{A}$ is similar to a Hermitian matrix and that all its eigenvalues are real and discrete.

We will now show the following.

PROPOSITION 1.2. *For the spectrum of matrix* $\mathbf{A}=[({}^{i}kb_i)^{-1}\ell_{ij}]_{i,j=1}^{N,N}$ *, we have* $\sigma(\mathbf{A})\subset\mathbb{R}_0^-$.

Proof of Proposition 1.2. For the proof, we will use the following:

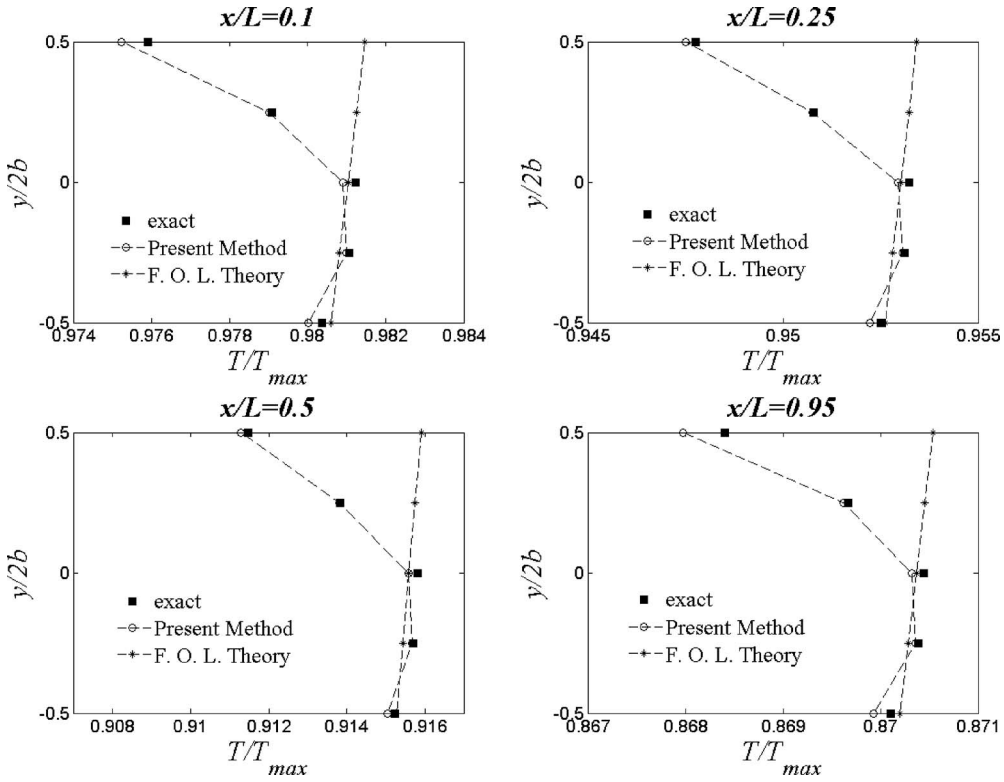

Fig. 7 In depth temperature distribution at four different cross sections (case I)

LEMMA 2 (Gerschgorin [20,21]). *Each eigenvalue of a matrix* $\mathbf{K}=[k_{ij}]_{i,j=1}^{N,N}$ *lies in at least one of the disks* $D_i=\{z:|z-k_{ii}| \le r_i\}$, $i=1,2,\ldots,N$ *of the complex plain, where* $r_i=\Sigma_{j=1,j\neq 1}^{N}|k_{ij}|$.

For matrix **A**, the following hold:

$$D_1=\left\{z:\left|z+\frac{h_1+s_{1,2}}{{}^1kb_1}\right| \le \frac{s_{1,2}}{{}^1kb_1}\right\}$$

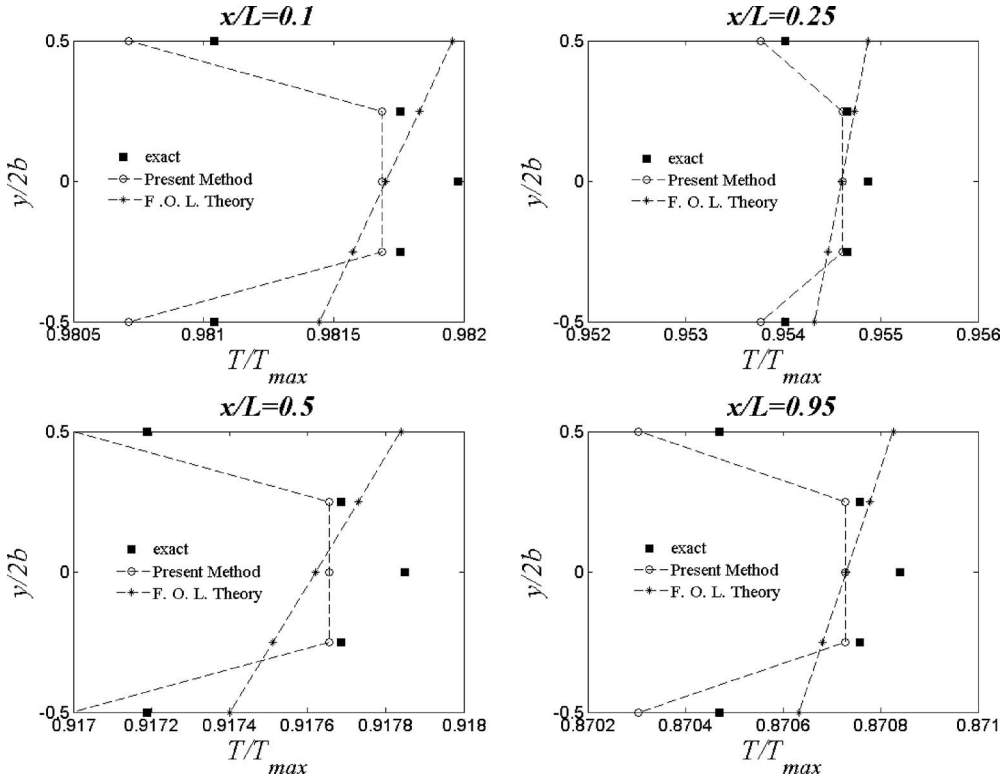

Fig. 8 In depth temperature distribution at four different cross sections (case II)

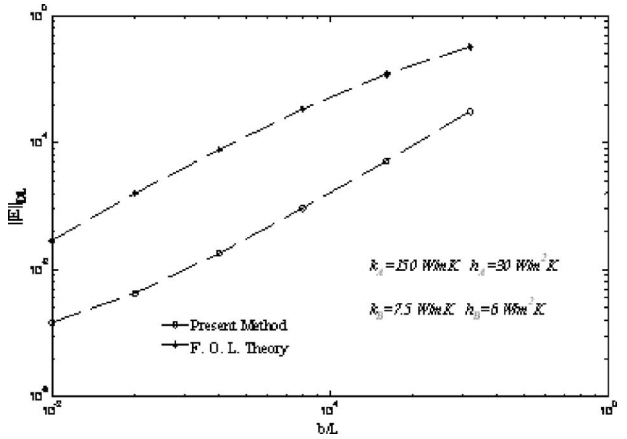

Fig. 9 Performance of the present method and FOL theory with respect to $\|\bullet\|_{DL}$ norm (case I)

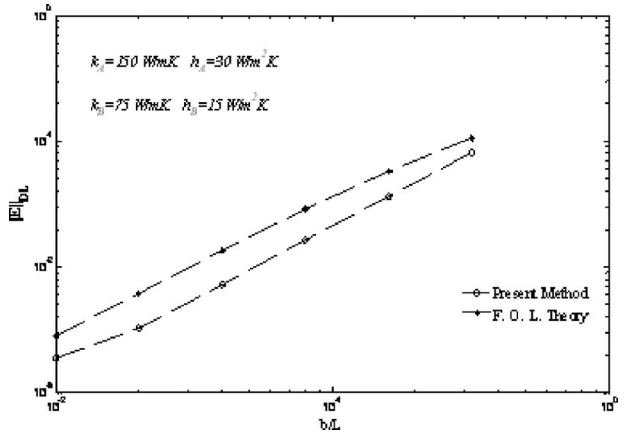

Fig. 10 Performance of the present method and FOL theory with respect to $\|\bullet\|_{DL}$ norm (case II)

$$D_i = \left\{ z: \left| z + \frac{s_{i-1,i} + s_{i,i+1}}{{}^{i}kb_i} \right| \le \frac{s_{i-1,i} + s_{i,i+1}}{{}^{i}kb_i} \right\}, \quad i = 2, \ldots, N-1$$

$$D_N = \left\{ z: \left| z + \frac{h_N + s_{N-1,N}}{{}^{N}kb_N} \right| \le \frac{s_{N-1,N}}{{}^{N}kb_N} \right\}$$

It is obvious that disks D_1, D_N lie exclusively in the left complex half plane. Disk D_i also lies in the left complex half plane, but it also includes point $z_0=0$ in its perimeter. So, $\sigma(\mathbf{A}) \subset \mathbb{R}_0^-$.

It remains to show that $0 \notin \sigma(\mathbf{A})$. We have

$$\det(\mathbf{A}) = \det([{}^{i}k^{-1}b_i^{-1}\ell_{ij}]_{i,j=1}^{N,N}) = \det([\ell_{ij}]_{i,j=1}^{N,N}) \prod_{i=1}^{N} {}^{i}k^{-1}b_i^{-1}$$

Since $\Pi_{i=1}^{N} {}^{i}k^{-1}b_i^{-1} \neq 0$, we need to show that $\det([\ell_{ij}]_{i,j=1}^{N,N}) \neq 0$. This last condition is equivalent with the condition $0 \notin \sigma([\ell_{ij}]_{i,j=1}^{N,N})$. It is sufficient to show that the symmetric matrix $[\ell_{ij}]_{i,j=1}^{N,N}$ is negative definite. We have the following.

PROPOSITION 1.3. *The symmetric matrix* $\mathbf{\Lambda} = [\ell_{ij}]_{i,j=1}^{N,N}$ *is negative definite.*

Proof of Proposition 1.3. If we consider the nonzero vector $\underset{\sim}{x} = [x_1 \ x_2 \ \ldots \ x_N]^T$, by the definition of the components of $\mathbf{\Lambda}$, we have

$$\underset{\sim}{x}^T \mathbf{\Lambda} \underset{\sim}{x} = -\bar{h}_1 x_1^2 - \sum_{i=1}^{N-1} s_{i,i+1}(x_i - x_{i+1})^2 - \bar{h}_N x_N^2$$

For $\underset{\sim}{x} \neq \underset{\sim}{0}$, it is $\underset{\sim}{x}^T \mathbf{\Lambda} \underset{\sim}{x} < 0$ since $\bar{h}_1 > 0$, $s_{i,i+1} > 0$, $i = 1, 2, \ldots, N$, $\bar{h}_N > 0$. Hence, $\mathbf{\Lambda}$ is negative definite and $\det(\mathbf{A}) \neq 0$.

This completes the proof of Proposition 1.

Appendix B

The determination of the constants of each term in the Fourier series in (37*a*) and (37*b*) representing the analytical solution of the problem in the numerical example may be performed, $\forall n \in \mathbb{N}_0$, from the solution of the system $\mathbf{A}_{\mathbf{n}} \underset{\sim}{x}_n = \underset{\sim}{f}_n$, where

$$\mathbf{A}_{\mathbf{n}} = \begin{bmatrix} -\left(h_A + \frac{n\pi}{L}k_A\right)e^{\frac{n\pi b_A}{L}} & \left(-h_A + \frac{n\pi}{L}k_A\right)e^{\frac{n\pi b_A}{L}} & 0 & 0 \\ 0 & 0 & \left(h_B - \frac{n\pi}{L}k_B\right)e^{-\frac{n\pi b_B}{L}} & \left(h_B + \frac{n\pi}{L}k_B\right)e^{\frac{n\pi b_B}{L}} \\ 1 & 1 & -1 & -1 \\ -k_A & k_A & k_B & -k_B \end{bmatrix}$$

$$\underset{\sim}{f}_n = \begin{bmatrix} h_A(T_0 - T_{\infty A})\frac{2}{\pi}\left(\frac{(-1)^{n+1}+1}{n}\right) + h_A\left(\frac{T_L - T_0}{L}\right)\frac{(-1)^{n+1}2L}{\pi n} \\ h_B(T_{\infty B} - T_0)\frac{2}{\pi}\left(\frac{(-1)^{n+1}+1}{n}\right) - h_B\left(\frac{T_L - T_0}{L}\right)\frac{(-1)^{n+1}2L}{\pi n} \\ 0 \\ 0 \end{bmatrix}$$

and the vector of the unknown constants is determined:

$$\underset{\sim}{x}_n = \begin{bmatrix} D_{1n} \\ D_{2n} \\ E_{1n} \\ E_{2n} \end{bmatrix}$$

References

[1] Niu, M., 1992, *Composite Airframe Structures*, Conmilit, Hong Kong.
[2] Mazumbar, S. K., 2002, *Composites Manufacturing*, CRC, Washington, D.C..
[3] Potter, K., 1997, *Resin Transfer Molding*, Chapman and Hall, London.
[4] Baker, A. A., and Jones, R., eds., 1988, *Bonded Repair of Aircraft Structures*, Martinus Nijhoff, Dordrecht.
[5] Jones, R., and Pitt, S., 2006, "Crack Patching Revisited," Compos. Struct., **76**, pp. 218–223.
[6] Caliskan, M., 2006, "Evaluation of Bonded and Bolted Repair Techniques With the Finite Element Method," Mater. Des., **27**, pp. 811–820.
[7] Marioli-Riga, Z. P., Tsamasphyros, G. J., and Kanderakis, G. N., 2001, "Design of Emergency Aircraft Repairs Using Composite Patches," Mech. Compos. Mater. Struct., **8**, pp. 199–204.
[8] Kovalenko, A. D., 1969, *Thermoelasticity*, Wolters-Noordhoff, Groningen, translated from Russian.
[9] Kern, D. Q., and Kraus A. D., 1972, *Extended Surface Heat Transfer*, McGraw-Hill, New York.
[10] Noor, A. K., and Tenek, L. H., 1992, "Steady-State Nonlinear Heat Transfer in Multilayered Composite Panels," J. Eng. Mech., **118**(8), pp. 1661–1678.
[11] Rolfes, R., 1991, "Higher Order Theory and Finite Element for Heat Conduction in Composites," *Numerical Methods in Thermal Problems, Proceedings of the Seventh International Conference*, R. W. Lewis, et al., eds., Pineridge, Swansea, UK, pp. 880–889.
[12] Surana, K. S., and Abusaleh, G., 1990, "Curved Shell Elements for Heat Conduction With p-Approximation in the Shell Thickness Direction," Comput. Struct., **34**(6), pp. 861–880.
[13] Argyris, J., Tenek, L., and Oberg, F., 1995, "A Multilayer Composite Triangular Element for Steady-State Conduction/Convection/Radiation Heat Transfer in Complex Shells," Comput. Methods Appl. Mech. Eng., **120**, pp. 271–301.
[14] Fourier, J. B. J., 1822, *Theorie Analytique de la Claleur*, Gauthier-Villars, Paris.
[15] Onsager, L., 1931, "Reciprocal Relations in Irreversible Processes I," Phys. Rev., **37**(4), pp. 405–426.
[16] Onsager, L., 1931, "Reciprocal Relations in Irreversible Processes I," Phys. Rev., **38**(12), pp. 2265–2279.
[17] Machlup, S., and Onsager, L., 1953, "Fluctuations and Irreversible Processes II," Phys. Rev., **91**(6), pp. 1512–1515.
[18] Incropera, F. P., and De Witt, D. P., 1990, *Fundamentals of Heat and Mass Transfer*, Wiley, New York.
[19] Mikhailov, M. D., and Özişik, M. N., 1984, *Unified Analysis and Solutions of Heat and Mass Diffusion*, Dover, New York.
[20] Horn, P., and Johnson, C., 1985, *Matrix Analysis*, Cambridge University Press, Cambridge, UK.
[21] Horn, P., and Johnson, C., 1991, *Topics in Matrix Analysis*, Cambridge University Press, Cambridge, UK.

T. K. Papathanasiou[1]
e-mail: thpapath@lycos.com

S. I. Markolefas
e-mail: markos34@gmail.com

S. P. Filopoulos
e-mail: sfilop@gmail.com

G. J. Tsamasphyros
e-mail: tsamasph@central.ntua.gr

Department of Theoretical and Applied Mechanics,
School of Applied Mathematics and Physical Sciences,
National Technical University of Athens,
9 Iroon Polytechniou Street,
Zografou Campus,
15773 Athens, Greece

Heat Transfer in Thin Multilayered Plates—Part II: Applications to the Composite Patch Repair Technique

This second part of our contribution entitled, "Heat Transfer in Thin Multilayered Plates," refers to the modeling of an advanced repair technique, known as the composite patch repair (CPR). Thermal analysis of this particular application is highly complicated due to the geometry of the domains and the fact that many different materials participate in the implementation. In this paper, we take advantage of the fact that both the composite patch and the damaged plate to be repaired are of very small thickness. In that way, the whole domain may be treated as a thin multilayer area of extended surface. These properties make the thermal analysis of CPR an ideal field for using the method presented in the previous part of our analysis. [DOI: 10.1115/1.4002631]

Keywords: heat transfer, extended surfaces, composite patch repair, multilayered plates

1 Introduction

Current economic world conditions force the operation of both military and civilian aircrafts well beyond their original design life, resulting in the necessity of innovative repair techniques. The recent development of high strength fibers and adhesives has led to the invention of a new methodology for the repair of structures by adhesive bonding of patches manufactured using composite materials [1–3]. Bonded repairs are mechanically efficient, cost effective, and can be applied rapidly to produce an inspectable damage tolerant repair. The actual objective of the repair of a cracked or corroded metallic structure by an adhesively bonded composite patch is the transfer of loads from the one side of the intact material to the other (via the patch), deviating the damaged area. Traditionally, structural problems due to fatigue or corrosion have been repaired by the addition of a metallic patch manufactured from aluminum or steel, which was mechanically joined to the cracked structure using fasteners or bolts [4]. This kind of repair causes stress concentration areas at the vicinity of the fasteners, which may lead to further structural problems, such as reduction of the fatigue life. With the new technique, the patch is manufactured using carbon/epoxy or boron/epoxy composite materials, while its bonding on the structure is performed with the use of high strength adhesives. The load transfer from the component to the patch and vice versa is achieved by the shear stresses applied on the adhesive layer [5,6]. Subsequently, no extra holes are required in the vicinity of the crack and no stress concentration points are created. Moreover, the application of such repair is faster than a traditional one while the performance of nondestructive inspections of the main structure is possible without removing the patch.

Despite the long list of advantages offered by this new repair technique, there are certain drawbacks. Because of the different nature and properties of the materials that form the repair (metals, composites, and adhesives), residual thermal stresses [7,8] are generated during the repair procedure, while the calculation of the overall heat distribution during curing is quite complex. In this paper, a heat transfer analysis is performed, in order to calculate the temperature distribution in patches during the process of their curing and simultaneous bonding on metal plates by means of conduction heating. The method derived in the first part of our contribution is employed and analytical solutions of the temperature distribution during the most significant stage of the repair process, the so-called plateau stage of the curing cycle, are derived for two different repair configurations.

2 Definition of the Problem

Let us consider a thin damaged plate that is to be reinforced with a patch. The bonding process consists of applying a thin adhesive film over the damaged area of the plate and then placing the patch over the adhesive. The patches examined in this paper are made of multiple pre-impregnated (prepreg) layers of carbon or boron fibers into epoxy resin. Similar materials are frequently used for repairs in actual aircraft structures. After the patch has been placed over the adhesive, the necessary heat for curing of both the epoxy resin and the adhesive is supplied to the system by means of conduction heating. Because of the heating, the polymer matrix cures and toughens and the patch becomes rigid and able to receive the loading of the structure. As the degree of cure of the polymer is temperature dependent, it is essential to be able to predict the temperature along the patch in order to be sure that the patch is completely cured at every point and therefore, guarantee the structural integrity of the repair.

Several ways of supplying heat for patch bonding exist. Conduction heating with the use of heating blankets is among the most common procedures. Heating blankets are composed of two thin plies of some flexible, high conductive materials with a thin metal grid among them. They are placed above the composite patch and the damaged plate underneath it. As electric current passes through the metal grid, heat is generated due to the Joule phenomenon. The heat is further conducted to the patch and the adhesive and leads to the increase of their temperature. The whole configuration is placed inside a vacuum bag. The vacuum is necessary in order to provide pressure over the area of the patch so as to achieve proper bonding. Further, in order to adequately bond the patch and achieve complete cure of the resin, the system must be retained at a certain temperature for a given time period. Both

[1]Corresponding author. Present address: Department of Mechanics, 9 Iroon Polytechniou St., Zografou Campus, Athens 15773, Greece.

Contributed by the Heat Transfer Division of ASME for publication in the JOURNAL OF HEAT TRANSFER. Manuscript received July 23, 2009; final manuscript received September 23, 2010; published online November 2, 2010. Assoc. Editor: Cholik Chan.

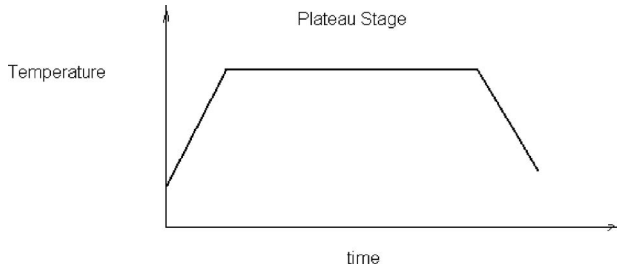

Fig. 1 Typical curing cycle for composite patch repair

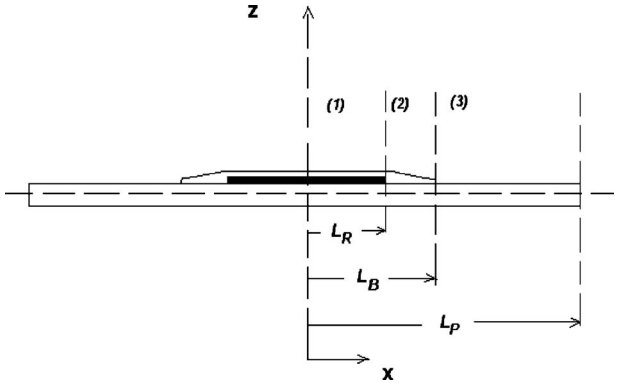

Fig. 2 Composite patch repair configuration (Cartesian coordinates)

of these characteristics are determined by a time-temperature profile, which is especially designed to guarantee complete curing of the resin and optimality of the properties of the final product. This profile is called a curing cycle and refers to constant pressure. A typical curing cycle is shown in Fig. 1.

The curing cycle involves three distinct periods. During the first one, heat is supplied through the heating blanket until the temperature reaches a critical value. For the following stage, the so-called plateau stage, the temperature remains constant at the level reached in the end of the first stage. During this stage, the heat supplied from the blanket balances heat losses mainly due to convection, so as to maintain the temperature of the patch constant. This is the most crucial stage of the whole cycle. The plateau temperature is such that it guarantees proper curing if sustained for a certain time, defined as the plateau stage duration. A notably lower temperature would result to incomplete curing and therefore to reduced strength. A much higher temperature would lead to increased thermal stresses or thermal degradation of the composite patch. The third part of the curing cycle describes the cooling of the repair when heat generation inside the blanket stops.

The whole process is controlled by thermocouples. Once a thermocouple senses a temperature decrease, additional heat is supplied by the blanket. Respectively, if the temperature is found to be greater than a certain limit, heat generation inside the blanket reduces. The main problem with this control system is that one cannot actually place thermocouples onto the patch, as they would form slits on it and therefore stress concentration. Common practice is to put thermocouples at the perimeter of the patch and onto the thermal blanket. However, this approach does not provide a full insight to the phenomena. Due to convection losses, temperature gradients are formed along the plane of the blanket, the patch, and the damaged plate. In this way, even if the heat supply is uniform, the resulting temperature fields will decline as we move from the center of the repair toward the edges.

The models presented in this paper aim at simulating the latter phenomena. We will show that, even though several simplifying assumptions are made, the form of the resulting temperature fields during the steady-state conditions of the plateau stage is adequately represented and furthermore, some quantitative results may be obtained.

At this point, we should mention that the plateau stage is, in realistic situations, nonisothermal. This is mainly due to the fact that the cure reaction of epoxy resins is exothermal. This exothermal reaction leads to heat generation inside the patch itself. As a result, an increase in the temperature is expected. However, for materials and temperature conditions commonly employed in practice, the heat generated due to the exothermal cure reaction is negligible compared with the amount supplied externally from the heating blanket. That is because the total mass of resin in composite patches is no more than a few grams. The use of this assumption enables the uncoupling of the heat diffusion equation from the cure rate kinetic model.

3 Plateau Stage Thermal Analysis

3.1 First Configuration. We consider a repair configuration, as shown in Fig. 2, which is considered to be very long in the direction normal to the page. We denote this dimension by W.

We decompose the above configuration in three distinct parts. The first one includes three layers (metal plate, reinforcing composite patch, and heating blanket) and it represents our structure up to length L_R. The second part extends from L_R to L_B and contains two layers, the metal plate and the heating blanket above it. This part of the structure is of major technical importance. The extension of the overlap $L_B - L_R$ has severe influence on the uniformity of the temperature distribution during the repair process. The third part is the remaining metal plate from point L_B up to L_P.

Since $b_i \ll W$, $L_i \ll W$ for $i=B,R,P$ and due to the fact that the conditions normal to the page are unaltered, temperature gradients along that direction are negligible. Applying the energy conservation principle in a characteristic volume of the first part of the structure, we obtain (see also Sec. 3 of Part I)

$$\Phi_B b_B W dx = b_B W \frac{dq_{Bx}}{dx} dx + W dx q_{B,R} + (W + 2b_B) dx q_{\text{conv}B} + W dx b_B \rho_B C_{PB} \frac{\partial T_B}{\partial t}$$

$$\Phi_{\text{cure}} b_R W dx + q_{B,R} = b_R W \frac{dq_{Rx}}{dx} dx + W dx q_{R,P} + W dx b_R \rho_R C_{PR} \frac{\partial T_R}{\partial t}$$

$$W dx q_{R,P} = b_P W \frac{dq_{Px}}{dx} dx + (W + 2b_P) dx q_{\text{conv}P} + W dx b_P \rho_P C_{PP} \frac{\partial T_P}{\partial t} \tag{1}$$

In system (1), q_i, $i=B,R,P$ represents the in-plane heat flux for the blanket, the reinforcing patch, and the plate, respectively, ρ_i, $i=B,R,P$ are the densities and C_{Pi} $i=B,R,P$ are the specific heat capacities. The heat generation rate inside the blanket is denoted by Φ_B, while the heat generation rate due to the exothermic cure reaction is denoted by Φ_{cure}.

Applying the energy balance to each layer of the differential volume and using the approximate relationships $W+2b_i \approx W$, $i=B,R,P$, leads to the following systems of equations:

$$\left\{\begin{array}{c} k_{Bxx}b_B\dfrac{\partial^2\vartheta_B}{\partial x^2}-(\bar{h}_B+s_{R,B})\vartheta_B+s_{R,B}\vartheta_R+b_B\Phi_B=b_B\rho_BC_{PB}\dfrac{\partial\vartheta_B}{\partial t} \\ k_{Rxx}b_R\dfrac{\partial^2\vartheta_R}{\partial x^2}+s_{R,B}\vartheta_B-(s_{R,B}+s_{P,R})\vartheta_R+s_{P,R}\vartheta_P+b_R\rho_RH\dfrac{\partial a}{\partial t}=b_R\rho_RC_{PR}\dfrac{\partial\vartheta_R}{\partial t} \\ k_{Pxx}b_P\dfrac{\partial^2\vartheta_P}{\partial x^2}-(\bar{h}_P+s_{P,R})\vartheta_P+s_{P,R}\vartheta_R=b_P\rho_PC_{PP}\dfrac{\partial\vartheta_P}{\partial t} \end{array}\right\}$$

$$x\in(0,L_R),\quad t\in(0,t_{\text{tot}})$$

$$\left\{\begin{array}{c} k_{Bxx}b_B\dfrac{\partial^2\vartheta_B}{\partial x^2}-(\bar{h}_B+s_{P,B})\vartheta_B+s_{P,B}\vartheta_P+b_B\Phi_B=b_B\rho_BC_{PB}\dfrac{\partial\vartheta_B}{\partial t} \\ k_{Pxx}b_P\dfrac{\partial^2\vartheta_P}{\partial x^2}+s_{P,B}\vartheta_B-(\bar{h}_P+s_{P,B})\vartheta_P=b_P\rho_PC_{PP}\dfrac{\partial\vartheta_P}{\partial t} \end{array}\right\}$$

$$x\in(L_R,L_B),\quad t\in(0,t_{\text{tot}})$$

$$k_{Pxx}b_P\frac{\partial^2\vartheta_P}{\partial x^2}-2\bar{h}_P\vartheta_P=b_P\rho_PC_{PP}\frac{\partial\vartheta_P}{\partial t}\quad x\in(L_B,L_P),\quad t\in(0,t_{\text{tot}}) \tag{2}$$

where each set of equations corresponds to one of the three distinct parts of the structure (see Fig. 2).

The definition of the coefficients $s_{i,j}$, $i,j=B,R,P$ is (see also part I)

$$s_{i,j}=2\frac{k_{izz}k_{jzz}}{k_{izz}b_j+k_{jzz}b_i} \tag{3}$$

Obviously, $s_{i,j}=s_{j,i}$.

The term $b_R\rho_RH(\partial a/\partial t)$ denotes heat generation inside the reinforcing patch due to the cure exothermic reaction [9]. Moreover, H is the cure reaction specific enthalpy, whereas $\partial a/\partial t$ is the rate of degree of cure. In most cases, the rate of degree of cure is characterized by an equation of the form

$$\frac{\partial a}{\partial t}=f(a,T) \tag{4}$$

where T^oK is the temperature profile. This equation is derived by the kinetics of the cure reaction [10–12].

As already mentioned, the plateau stage of the curing cycle is of crucial importance. During this stage, the temperature of the composite patch and the adhesive must be held constant at a predefined level and for a certain period of time, referred to as the plateau stage duration. It is at this stage where the curing process of the resin takes place. Strictly speaking, due to the exothermal nature of the curing reaction, the temperature during the plateau stage is also time dependent. However, the temperature values needed for the plateau stage are usually of such a magnitude that the heat generated from the cure reaction is negligible when compared with the heat supplied by the blanket. Having that in mind, we are able to perform a steady-state analysis of the plateau stage by decomposing the heat transfer and cure reaction equations. The equation system to be solved for the determination of the temperature and the degree of cure during the plateau stage is

$$\left\{\begin{array}{c} k_Bb_B\dfrac{\partial^2\vartheta_B}{\partial x^2}-(\bar{h}_B+s_{R,B})\vartheta_B+s_{R,B}\vartheta_R+b_B\Phi_B=0 \\ k_Rb_R\dfrac{\partial^2\vartheta_R}{\partial x^2}+s_{R,B}\vartheta_B-(s_{R,B}+s_{P,R})\vartheta_R+s_{P,R}\vartheta_P=0 \\ k_Pb_P\dfrac{\partial^2\vartheta_P}{\partial x^2}-(\bar{h}_P+s_{P,R})\vartheta_P+s_{P,R}\vartheta_R=0 \end{array}\right\}$$

$$x\in(0,L_R),\quad t\in(0,t_{\text{tot}})$$

$$\left\{\begin{array}{c} k_Bb_B\dfrac{\partial^2\vartheta_B}{\partial x^2}-(\bar{h}_B+s_{P,B})\vartheta_B+s_{P,B}\vartheta_P+b_B\Phi_B=0 \\ k_Pb_P\dfrac{\partial^2\vartheta_P}{\partial x^2}+s_{P,B}\vartheta_B-(\bar{h}_P+s_{P,B})\vartheta_P=0 \end{array}\right\},$$

$$x\in(L_R,L_B),\quad t\in(0,t_{\text{tot}})$$

$$k_Pb_P\frac{\partial^2\vartheta_P}{\partial x^2}-2\bar{h}_P\vartheta_P=0,\quad x\in(L_B,L_P)\quad(t\in0,t_{\text{tot}}) \tag{5}$$

We can see from equations in problem (5) that under this perspective, only the degree of cure is time dependent during the plateau stage. The temperature profile of the configuration is unaltered during the plateau, steady-state analysis.

For the heat transfer problem, the solution of the homogenous system of equations is

$$\begin{aligned}\vartheta_{oB}&=C_1X_{11}e^{\lambda_1x}+C_2X_{11}e^{-\lambda_1x}+C_3X_{12}e^{\lambda_2x}+C_4X_{12}e^{-\lambda_2x}\\&\quad+C_5X_{13}e^{\lambda_3x}+C_6X_{13}e^{-\lambda_3x}\\ \vartheta_{oR}&=C_1X_{21}e^{\lambda_1x}+C_2X_{21}e^{-\lambda_1x}+C_3X_{22}e^{\lambda_2x}+C_4X_{22}e^{-\lambda_2x}\\&\quad+C_5X_{23}e^{\lambda_3x}+C_6X_{23}e^{-\lambda_3x}\\ \vartheta_{oP}&=C_1X_{31}e^{\lambda_1x}+C_2X_{31}e^{-\lambda_1x}+C_3X_{32}e^{\lambda_2x}+C_4X_{32}e^{-\lambda_2x}\\&\quad+C_5X_{33}e^{\lambda_3x}+C_6X_{33}e^{-\lambda_3x}\end{aligned} \tag{6}$$

for $x\in[0,L_R]$.

$$\begin{aligned}\vartheta_{oB}&=D_1Y_{11}e^{\mu_1x}+D_2Y_{11}e^{-\mu_1x}+D_3Y_{12}e^{\mu_2x}+D_4Y_{12}e^{-\mu_2x}\\ \vartheta_{oP}&=D_1Y_{21}e^{\mu_1x}+D_2Y_{21}e^{-\mu_1x}+D_3Y_{22}e^{\mu_2x}+D_4Y_{22}e^{-\mu_2x}\end{aligned} \tag{7}$$

for $x\in[L_R,L_B]$. And finally

$$\vartheta_{oP}=E_1e^{\rho x}+E_2e^{-\rho x} \tag{8}$$

for $x\in[L_B,L_P]$, where λ_i, X_{ij}, $i,j=1,2,3$ are the eigenvalues and the eigenvectors of the matrix $\mathbf{M}_{(1)}^{-1}\mathbf{N}_{(1)}$, with

$$\mathbf{M}_{(1)}=\begin{bmatrix}k_Bb_B & 0 & 0\\ 0 & k_Rb_R & 0\\ 0 & 0 & k_Pb_P\end{bmatrix}\quad\text{and}$$

$$\mathbf{N}_{(1)} = \begin{bmatrix} -h_B - s_{R,B} & s_{R,B} & 0 \\ s_{R,B} & -s_{R,B} - s_{P,R} & s_{P,R} \\ 0 & s_{P,R} & -h_P - s_{P,R} \end{bmatrix}$$

where μ_i, Y_{ij}, $i,j=1,2$ are the eigenvalues and the eigenvectors of the matrix $\mathbf{M}_{(2)}^{-1}\mathbf{N}_{(2)}$, with

$$\mathbf{M}_{(2)} = \begin{bmatrix} k_B b_B & 0 \\ 0 & k_P b_P \end{bmatrix} \quad \text{and} \quad \mathbf{N}_{(2)} = \begin{bmatrix} -h_B - s_{P,B} & s_{P,B} \\ s_{P,B} & -h_P - s_{P,B} \end{bmatrix}$$

and $\rho = 2h_P/k_P b_P$.

In the case of uniform heat generation rate in the blanket, partial solutions for the first and second parts are given by

$$\underline{\vartheta}_{\text{Part}} = \mathbf{K}_{(1)}^{-1}\mathbf{\Omega}_{(1)} \quad x \in [0, L_R] \tag{9}$$

where $\mathbf{\Omega}_{(1)} = [-\Phi_B b_B \ 0 \ 0]^T$

$$\underline{\vartheta}_{\text{Part}} = \mathbf{K}_{(2)}^{-1}\mathbf{\Omega}_{(2)} \quad x \in [L_R, L_B] \tag{10}$$

where $\mathbf{\Omega}_{(2)} = [-\Phi_B b_B \ 0]^T$.

The partial solution for the third part is the zero one. Moreover, C_i, D_j, E_k, $i=1,2,\ldots,6$, $j=1,2,3,4$, $k=1,2$ are constants to be determined by the boundary conditions. In order to define the 12 boundary conditions needed for the determination of the solution of our problem, we make the following observations.

Due to the symmetry of the structure with respect to the vertical axis, we have the following.

For $x=0$,

$$\left.\frac{d\vartheta_B}{dx}\right|_{x=0} = 0 \tag{11a}$$

$$\left.\frac{d\vartheta_R}{dx}\right|_{x=0} = 0 \tag{11b}$$

$$\left.\frac{d\vartheta_P}{dx}\right|_{x=0} = 0 \tag{11c}$$

For the heating blanket and the plate, both the temperature and heat flux must be continuous at the shared point of the first part (three layers) and the second part (two layers). These conditions may be written as

$$\vartheta_B(L_R^-) = \vartheta_B(L_R^+) \tag{12a}$$

$$k_B \left.\frac{d\vartheta_B}{dx}\right|_{x=L_R^-} = k_B \left.\frac{d\vartheta_B}{dx}\right|_{x=L_R^+} \tag{12b}$$

$$\vartheta_P(L_R^-) = \vartheta_P(L_R^+) \tag{12c}$$

$$k_P \left.\frac{d\vartheta_P}{dx}\right|_{x=L_R^-} = k_P \left.\frac{d\vartheta_P}{dx}\right|_{x=L_R^+} \tag{12d}$$

In the case of the reinforcing patch, an adiabatic boundary condition may be assumed at point $x=L_R$,

$$\left.\frac{d\vartheta_R}{dx}\right|_{x=L_R} = 0 \tag{13}$$

Such an assumption is valid due to the small thickness of the patch. In addition, it is a common practice to gradually reduce the thickness of the patch at the edges, in order to reduce the stress concentration at these areas (tapering [5]).

At the end of the heating blanket (point L_B), a convection boundary condition is applied:

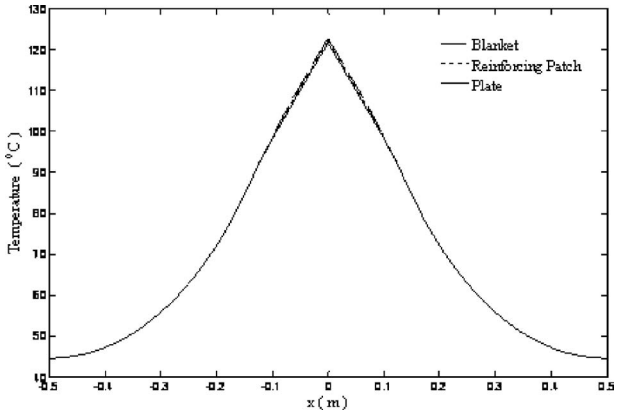

Fig. 3 Temperature distribution for example 1 (L_B=0.125 m)

$$-k_B \left.\frac{d\vartheta_B}{dx}\right|_{x=L_B} = h_B \vartheta(L_B) \tag{14}$$

At the same point, the temperature and the heat flux must be continuous between the second and the third part of the structure, leading to

$$\vartheta_P(L_B^-) = \vartheta_P(L_B^+) \tag{15a}$$

$$k_P \left.\frac{d\vartheta_P}{dx}\right|_{x=L_B^-} = k_P \left.\frac{d\vartheta_P}{dx}\right|_{x=L_B^+} \tag{15b}$$

Finally, at the end of the plate, a convection boundary condition is applied:

$$-k_P \left.\frac{d\vartheta_P}{dx}\right|_{x=L_P} = h_P \vartheta(L_P) \tag{16}$$

Equations (11*a*) to (16) define the 12 boundary conditions needed. For the first configuration, we will present two different examples.

3.2 Example 1. As a first example, we consider the bonding of a composite patch made of four plies of graphite fiber (25 vol %) reinforced epoxy material onto a 2024-T6 aluminum alloy plate [13]. The fibers of all plies are assumed to be along the direction of the x axis. The whole patch is assumed to be a single layer. The properties of the materials are as follows:

$$L_R = 0.1 \text{ m}, \quad L_P = 0.5 \text{ m}$$

$$k_B = 130 \text{ W/m K}, \quad h_B = 5 \text{ W/m}^2\text{K}$$

$$k_{R\|(\text{parallel to fibre})} = 11.1 \text{ W/m K},$$

$$k_{R\perp(\text{perpendicular to fibre})} = 0.87 \text{ W/m K}$$

$$k_P = 130 \text{ W/m K}, \quad h_P = 10 \text{ W/m}^2 \text{ K}$$

$$b_B = 0.0015 \text{ m}, \quad b_R = 0.001 \text{ m}, \quad b_P = 0.005 \text{ m}$$

$$\Phi_B = 10^6 \text{ W/m}^3, \quad T_\infty = 22 \,^\circ\text{C}$$

Figure 3 shows the resulting temperature fields for a total heating blanket length $2L_B = 0.25$ m (Figs. 3 and 4).

3.3 Example 2. As a second example, we present a repair, which involves bonding a composite patch over a composite panel. The geometry of the repair is identical to that in the first example. The plate is made of 16 plies of boron fiber/epoxy of total thickness 4 mm. The direction of the fibers is assumed to be perpendicular to the x axis, for all plies. The composite patch is composed of 4 plies boron fiber/epoxy with the fibers oriented parallel to the x axis.

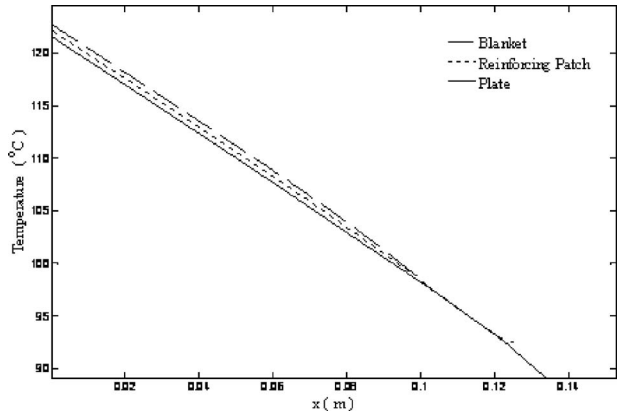

Fig. 4 Zoom of Fig. 3 at the area of the repair (L_B=0.125 m)

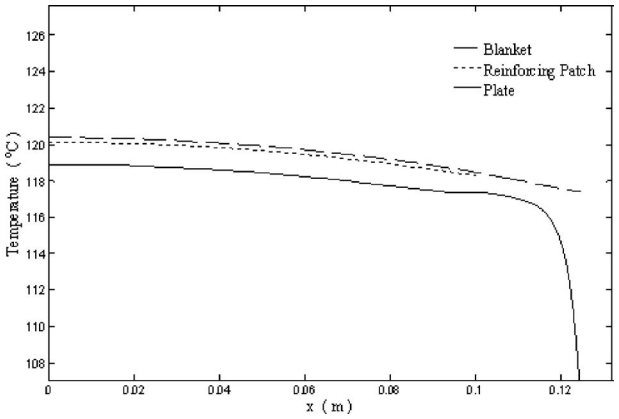

Fig. 6 Zoom of Fig. 5 at the area of the repair (L_B=0.125 m)

$$L_R = 0.1 \text{ m}, \quad L_P = 0.5 \text{ m}$$

$$k_B = 130 \text{ W/m K}, \quad h_B = 5 \text{ W/m}^2 \text{ K}$$

$$k_{R\|(\text{parallel to fibre})} = 2.29 \text{ W/m K},$$

$$k_{R\perp(\text{perpendicular to fibre})} = 0.59 \text{ W/m K}$$

$$k_{R\|(\text{parallel to fibre})} = 2.29 \text{ W/m K},$$

$$k_{R\perp(\text{perpendicular to fibre})} = 0.59 \text{ W/m K}, \quad h_P = 3 \text{ W/m}^2 \text{ K}$$

$$b_B = 0.0015 \text{ m}, \quad b_R = 0.001 \text{ m}, \quad b_P = 0.004 \text{ m}$$

$$\Phi_B = 0.57 \times 10^6 \text{ W/m}^3, \quad T_\infty = 22 \,^\circ\text{C}$$

A number of observations may be stated from the comparison between bonding composite over aluminum alloy and composite over composite. First of all, the heat generation rate inside the blanket, needed in order to achieve a temperature of about 120°C in the middle of the patch, is approximately half in the case of bonding composite over composite. This is due to the fact that the conduction and convection coefficients of epoxy resin matrix composites are much smaller than those of aluminum alloys. In that way, heat is more easily conducted, from the repair area, through a metal plate and then diffused in the form of convection losses. In the case of the epoxy resin matrix composite plate, heat is "retained" in the repair area and the temperature drop between the center of the patch and the edges is much smaller than in the case of the metal plate. Another observation is that the temperature of the composite plate drops extremely fast after the end of the heating blanket. This has been observed in realistic repairs including bonding patches over plates of composite materials. In such cases, a drop from 120°C to approximately environmental temperature within a few centimeters of the ends of the heating blanket has been observed (Figs. 5 and 6).

Under the assumptions made for the uncoupling of the heat and cure equations, it is possible to obtain the plateau stage duration needed for the complete curing of the composite patch. For the second example, we will calculate the time-degree of cure profile of the point of the patch with the lowest temperature. Obviously, once the complete curing of this point is ensured, we can conclude that the whole patch is properly cured. This is due to the fact that the higher the temperature, the fastest the cure reactions are.

For the epoxy resin of the patch, we adopt the autocatalytic mode of reaction described by the equation [12]

$$\frac{\partial a}{\partial t} = k_2 a^m (1-a)^n \tag{17}$$

where a is the degree of cure, $m \in \mathbb{R}_+$, $n \in \mathbb{R}_+$, and $k_2 = K_2 e^{-Q_2/RT}$ is an Arrhenius term. The nominator Q_2 represents the reaction activation energy, K_2 is a pre-exponential factor, and R is the universal gas constant. For the purposes of our example, we use the following values:

$$K_2 = 6 \times 10^5 \text{ s}^{-1}, \quad Q_2 = 55 \text{ kJ mol}^{-1}, \quad m = 0.4,$$

$$n = 1.6, \quad H = 500 \text{ J g}^{-1}$$

The time integration of Eq. (17) is performed with the use of an explicit fourth order Runge–Kutta scheme. We assume that the

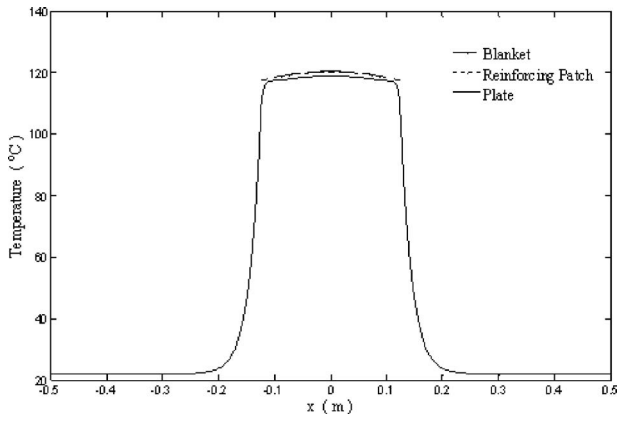

Fig. 5 Temperature distribution for example 2 (L_B=0.125 m)

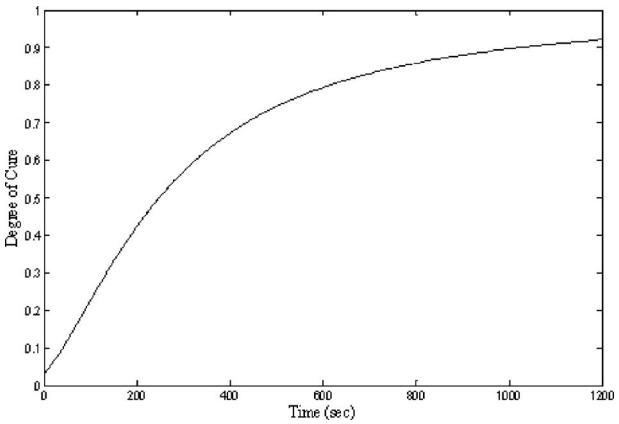

Fig. 7 Time-degree of cure profile during the plateau stage for the point of the patch with the lowest temperature

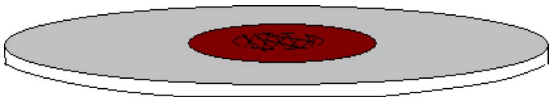

Fig. 8 Axially symmetric repair geometry

degree of cure of the whole patch at the beginning of the plateau is 0.03. The results are shown in Fig. 7.

3.4 Second Configuration. The second configuration to be modeled is an axially symmetric repair. In that repair, a circular patch is covered by a circular heating blanket (Fig. 8). Circular patches are sometimes used instead of rectangular ones in order to avoid the stress concentration that appears at the corners of the latter. In our analysis, we will also assume that the damaged plate is circular in shape. This scenario, although unrealistic, may simulate a true repair if we choose the diameter of the plate to be large enough compared with those of the reinforcing patch and blanket. In that case, the results are similar to those of bonding a circular patch over a large, practically infinite, surface. That is because the temperature reduces fast to the environment temperature as we move away from the repair area.

If we denote the radius of the heating blanket by R_B, the radius of the reinforcing patch as R_R and finally, the radius of the plate by R_P, the boundary value problem describing steady-state heat transfer in the geometry shown in Fig. 9 is governed by the following equations (due to the axial symmetry, the equations need to be defined only over one radius of the configuration):

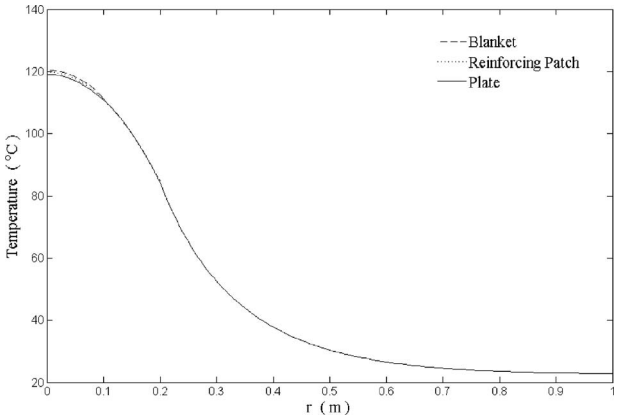

Fig. 9 Temperature distribution along the radius of the repair

$$\left\{\begin{array}{c} k_B b_B \dfrac{\partial^2 \vartheta_B}{\partial r^2} + k_B b_B \dfrac{1}{r}\dfrac{\partial \vartheta_B}{\partial r} - (\bar{h}_B + s_{R,B})\vartheta_B + s_{R,B}\vartheta_R + b_B \Phi_B = 0 \\ k_R b_R \dfrac{\partial^2 \vartheta_R}{\partial r^2} + k_R b_R \dfrac{1}{r}\dfrac{\partial \vartheta_R}{\partial r} + s_{R,B}\vartheta_B - (s_{R,B} + s_{P,R})\vartheta_R + s_{P,R}\vartheta_P = 0 \\ k_P b_P \dfrac{\partial^2 \vartheta_P}{\partial r^2} + k_P b_P \dfrac{1}{r}\dfrac{\partial \vartheta_P}{\partial r} - (\bar{h}_P + s_{P,R})\vartheta_P + s_{P,R}\vartheta_R = 0 \end{array}\right\}, \quad r \in (0, R_R), \quad t \in (0, t_{\text{tot}})$$

$$\left\{\begin{array}{c} k_B b_B \dfrac{\partial^2 \vartheta_B}{\partial r^2} + k_B b_B \dfrac{1}{r}\dfrac{\partial \vartheta_B}{\partial r} - (\bar{h}_B + s_{P,B})\vartheta_B + s_{P,B}\vartheta_P + b_B \Phi_B = 0 \\ k_P b_P \dfrac{\partial^2 \vartheta_P}{\partial r^2} + k_P b_P \dfrac{1}{r}\dfrac{\partial \vartheta_P}{\partial r} + s_{P,B}\vartheta_B - (\bar{h}_P + s_{P,B})\vartheta_P = 0 \end{array}\right\}, \quad r \in (R_R, R_B), \quad t \in (0, t_{\text{tot}})$$

$$k_P b_P \frac{\partial^2 \vartheta_P}{\partial r^2} + k_P b_P \frac{1}{r}\frac{\partial \vartheta_P}{\partial r} - 2\bar{h}_P \vartheta_P = 0, \quad r \in (R_B, R_P), \quad t \in (0, t_{\text{tot}}) \tag{18}$$

The solution of this system of equations is

$$\begin{aligned} \vartheta_{oB} &= C_1 X_{11} I_0(\lambda_1 r) + C_2 X_{11} K_0(\lambda_1 r) + C_3 X_{12} I_0(\lambda_2 r) \\ &\quad + C_4 X_{12} K_0(\lambda_2 r) + C_5 X_{13} I_0(\lambda_3 r) + C_6 X_{13} K_0(\lambda_3 r) \\ \vartheta_{oR} &= C_1 X_{21} I_0(\lambda_1 r) + C_2 X_{21} K_0(\lambda_1 r) + C_3 X_{22} I_0(\lambda_2 r) \\ &\quad + C_4 X_{22} K_0(\lambda_2 r) + C_5 X_{23} I_0(\lambda_3 r) + C_6 X_{23} K_0(\lambda_3 r) \\ \vartheta_{oP} &= C_1 X_{31} I_0(\lambda_1 r) + C_2 X_{31} K_0(\lambda_1 r) + C_3 X_{32} I_0(\lambda_2 r) \\ &\quad + C_4 X_{32} K_0(\lambda_2 r) + C_5 X_{33} I_0(\lambda_3 r) + C_6 X_{33} K_0(\lambda_3 r) \end{aligned} \tag{19}$$

for $x \in [0, L_R]$.

$$\begin{aligned} \vartheta_{oB} &= D_1 Y_{11} I_0(\mu_1 r) + D_2 Y_{11} K_0(\mu_1 r) + D_3 Y_{12} I_0(\mu_2 r) \\ &\quad + D_4 Y_{12} K_0(\mu_2 r) \\ \vartheta_{oP} &= D_1 Y_{21} I_0(\mu_1 r) + D_2 Y_{21} K_0(\mu_1 r) + D_3 Y_{22} I_0(\mu_2 r) \\ &\quad + D_4 Y_{22} K_0(\mu_2 r) \end{aligned} \tag{20}$$

for $x \in [L_R, L_B]$. And finally

$$\vartheta_{oP} = E_1 I_0(\rho r) + E_2 K_0(\rho r) \tag{21}$$

for $x \in [L_B, L_P]$, where I_0, K_0 are the zero order modified Bessel functions of the first and second kind respectively.

For the determination of the constants appearing in the general solution of this problem, 12 boundary conditions are needed. The demand that the temperature remains bounded for $r=0$, as well as the fact that its first derivative at that particular point equals to zero, leads to the conditions

$$C_2 = C_4 = C_6 = 0 \tag{22}$$

The remaining boundary conditions are identical to those of the problem in Cartesian coordinates described in Sec. 3.1.

We now consider an application involving bonding a particle reinforced-epoxy resin matrix composite to be bonded onto an aluminum alloy plate. The particle reinforced composite is considered macroscopically isotropic. The parameters of the particular case are

$$R_R = 0.1 \text{ m}, \quad R_B = 0.2 \text{ m}$$

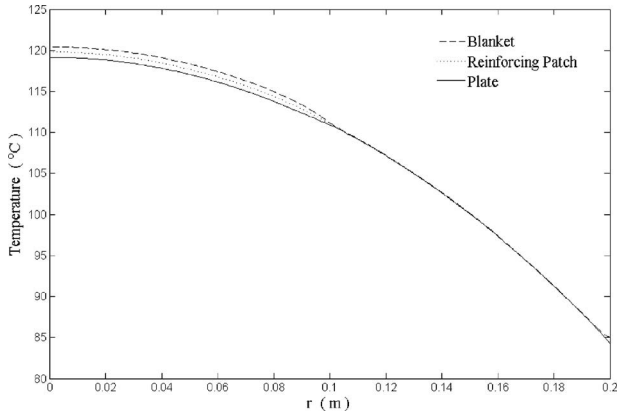

Fig. 10 Zoom of Fig. 9 at the area of the repair

$$k_B = 130 \text{ W/m K}, \quad h_B = 5 \text{ W/m}^2 \text{ K}$$

$$k_R = 4.75 \text{ W/m K}$$

$$k_P = 177 \text{ W/m K}, \quad h_P = 10 \text{ W/m K}$$

$$b_B = 0.0015 \text{ m}, \quad b_R = 0.001 \text{ m}, \quad b_P = 0.004 \text{ m}$$

$$\Phi_B = 3 \times 10^6 \text{ W/m}^3, \quad T_\infty = 22 \,^\circ\text{C}$$

The resulting temperature distribution as a function of the temperature is shown in Fig. 9. A zoom of the area covered by the blanket is shown in Fig. 10.

4 Conclusions

We have presented some simplified models describing heat transfer phenomena during the process of composite patch repairs for thin configurations. The derivation of these models is based on a continuous-discrete approach for heat transfer. More precisely, we have assumed the classical continuous heat diffusion equations for the in-plane heat transfer inside each ply, whereas we employ a discrete approach in order to model heat fluxes through the thickness. A steady-state analysis has been performed, for which the resulting differential systems have been solved analytically. Three different examples involving Cartesian and axially symmetric problems have been presented, involving a variety of materials participating in the repair. Fully coupled heat transfer analysis and cure reaction modeling within the perspective of the above presented models are currently under development. However, the solution to such problems is attainable only with the use of numerical techniques.

References

[1] Baker, A. A., and Jones, R., eds., 1988, *Bonded Repair of Aircraft Structures*, Martinus Nijhoff, Dordrecht.
[2] Jones, R., and Pitt, S., 2006, "Crack Patching Revisited," Compos. Struct., **76**, pp. 218–223.
[3] Marioli-Riga, Z. P., Tsamasphyros, G. J., and Kanderakis, G. N., 2001, "Design of Emergency Aircraft Repairs Using Composite Patches," Mech. Compos. Mater. Struct., **8**, pp. 199–204.
[4] Caliskan, M., 2006, "Evaluation of Bonded and Bolted Repair Techniques With the Finite Element Method," Mater. Des., **27**, pp. 811–820.
[5] Hart-Smith L. S., 1973, "Adhesive-Bonded Scarf and Stepped-Lap Joints," NASA Technical Report No. CR-112237.
[6] Da Silva, L. F. M., and Adams, R. D., 2007, "Techniques to Reduce the Peel Stresses in Adhesive Joints With Composites," Int. J. Adhes. Adhes., **27**, pp. 227–35.
[7] Albat, A. M., 1998, "Thermal Residual Stresses in Bonded Composite Repairs on Cracked Metal Structures," Ph.D. thesis, University of British Columbia, Vancouver, BC, Canada.
[8] Djokic, D., Johnston, A., Rogers, A., Lee-Sullivan, P., and Mrad, N., 2002, "Residual Stress Development During the Composite Patch Bonding Process: Measurement and Modeling," Composites, Part A, **33**, pp. 277–288.
[9] Vergnaud, J. M., and Bouzon, J., 1992, *Cure of Thermosetting Resins: Modelling and Experiments*, Springer, New York.
[10] Kamal, M. R., and Sourour, S., 1973, "Kinetics and Thermal Characterization of Thermoset Cure," Polym. Eng. Sci., **13**, pp. 59–64.
[11] Kamal, M. R., 1974, "Thermoset Characterization for Moldability Analyis," Polym. Eng. Sci., **14**(3), pp. 231–239.
[12] Martin, J. L., and Salla, J. M., 1992, "Models of Reaction Commonly Employed in the Curing of Thermosetting Resins," Thermochim. Acta, **207**, pp. 279–304.
[13] Papathanassiou, Th. K., Filopoulos, S. P., and Tsamasphyros, G. J., 2010, "Optimization of Composite Patch Repair Processes with the Use of Genetic Algorithms," Optim. Eng., to be published.10.1007/s11081-010-9116-0

Boundary Control of Temperature Distribution in a Rectangular Functionally Graded Material Plate

Hossein Rastgoftar
MSc. Graduate
Department of Mechanical Engineering,
Shiraz University,
Shiraz,
Fars 71348-51154, Iran

Mohammad Eghtesad
Associate Professor

Alireza Khayatian
Associate Professor

Departments of Mechanical and Electrical Engineering,
Shiraz University,
Shiraz,
Fars 71348-51154, Iran

In this paper, an analytical method and a partial differential equation based solution to control temperature distribution for functionally graded (FG) plates is introduced. For the rectangular FG plate under consideration, it is assumed that the material properties such as thermal conductivity, density, and specific heat capacity vary in the width direction, and the governing heat conduction equation of the plate is a second-order partial differential equation. Using Lyapunov's theorem, it is shown that by applying controlled heat flux through the boundary of the domain, the temperature distribution of the plate will approach a desired steady-state distribution. Numerical simulation is provided to verify the effectiveness of the proposed method such that by applying the boundary transient heat flux, in-domain distributed temperature converges to its desired steady-state temperature. [DOI: 10.1115/1.4002437]

1 Introduction

In all engineering sciences, modeling and control of distributed parameter systems (DPSs) which are presented by partial differential equations (PDEs) are of great importance. DPSs are dynamical systems whose state depends both on time and on the spatial coordinate variables. These systems are encountered in many practical engineering problems such as thermal systems, thermo-elastic problems, vibration, and acoustic systems. Heat transfer problems of distributed parameter systems have numerous applications in industrial and high-tech processes. Distribution of a desired temperature in a given material, which requires control of heat flux to be carried out through the manipulation of a PDE system, is one obvious application [1]. Some situations arise in semiconductor manufacturing where it is required that a uniform temperature is distributed for a rectangular shape wafer; in glass industries, desired temperature distribution is also needed.

From some researchers' point of view, control of temperature distribution in a body is an "inverse heat problem." Solution to this problem requires the heat flux to be found such that it satisfies the governing equations of the thermal PDE [2]. The inverse heat conduction problem (IHCP) has been widely used in different practical engineering problems such as estimation of surface conditions, initial conditions, and thermal properties of a body from known information at some predefined positions. For example, in Ref. [2], an inverse boundary design of square enclosures with natural convection is studied; in Ref. [1], the conjugate gradient method with an adjoint equation was applied to a three dimensional optimal control for determining the boundary heat fluxes. So far, in the literature, most of the research has been focused on the use of a numerical method to solve the heat transfer problems, and it should be noted that the implementation of the numerical method to solve the inverse problem is associated with certain difficulties [3]. It is well known that these problems are mathematically ill-posed and small changes in the input data can result in large changes in a computed solution. Hence, the numerical inverse methods require efficient optimization tools for their solution [4,5].

Contributed by the Heat Transfer Division of ASME for publication in the JOURNAL OF HEAT TRANSFER. Manuscript received July 11, 2009; final manuscript received May 21, 2010; published online November 3, 2010. Editor: Yogesh Jaluria.

The inverse heat transfer analysis based on boundary control is an elegant method that exploits the governing equations of transient heat transfer problems without discretizing PDE equations. Boundary control can present an exact solution to temperature distribution control problem that is not based on approximating the governing equations. In spite of great attention to the control design of distributed parameter systems, in the past two decades, little analytical control synthesis work for PDE-based systems is available compared with the abundance of control design techniques for a continuous domain, which rely on discretizing the PDE model to a set of ordinary differential equations. In Ref. [6], boundary feedback control of an unstable heat equation via measurement domain-averaged temperature for a thin rod is studied. Also, the boundary control of vibration for symmetric composite materials is presented in Refs. [7,8]. One advantage of the boundary control method, which is shown in these papers, is utilizing the control actuators and sensors only at the boundaries of the system under study; thus, it is not necessary to use distributed sensors and actuators to feedback the output information. This is a benefit of boundary control, which can be exploited for a temperature distribution problem since it avoids insertion of the in-domain point temperature measurement of the plate.

In contrast to ceramics, which are brittle and have low fracture toughness, functionally graded materials (FGMs), which are ceramics with reinforced metallic fibers, are tougher with excellent mechanical and thermal properties. They have found numerous applications in a high temperature environment, such as turbine, aircraft, and space engineering [9,10]. One complexity with the FGMs is that their material properties, such as thermal conductivity and specific heat capacity, are spatially varying. More specifically, the governing heat transfer equations of FGMs have spatially dependent coefficients. For FGM strips and plates, these coefficients vary along the thickness or width direction. There are two common models for determining the material properties of a FGM plate, the continuum models and the micromechanics models. In the continuum models, analytical functions such as exponential and power law are used to describe the continuous varying material properties of FGMs. Due to high mathematical complexity caused by the material nonhomogeneity, analysis and control of thermal systems that involve this kind of materials are more complicated than those of other thermal systems.

In Ref. [11], the transient heat conduction problem in function-

ally graded materials by the meshless local boundary integral equation method is investigated, and it is shown that for a finite strip with unidirectional exponential variation in the thermal conductivity and diffusivity, the meshless method solution of temperatures at the steady state agrees with the analytical solution, which is a spatially exponential temperature distribution. Most of the researches on the heat transfer analysis of FGMs are focused on the numerical solution of the transient heat conduction problem using different methods such as graded finite element [10,12–14], integral equation method [11], boundary element method [15], Petrov–Galerkin method [16], and others [17,18]. In almost all of these papers, exponentially varying thermal conductivity has been assumed and only analyses problem is considered. The work on the control of temperature distribution of FGM is almost rare. For example, in Ref. [19], temperature control of functionally graded plates using a feedforward-feedback controller based on the inverse solution is presented. In this paper, the authors have solved a direct and inverse heat problem numerically to control two dimensional and three dimensional plate temperature distributions. An interesting study on the thermal-stress characteristics of FGMs is presented in Ref. [20].

In this paper, we use boundary heat flux to control the temperature distribution at in-domain points of the FGM plate. In contrast to the dominant application of the numerical method to solve the PDE heat transfer problem, our method is analytic, which is not based on approximating the governing equation. The objective is to design a control strategy that the transient distribution temperature of the plate, $T(x,y,t)$, converges to a desired temperature distribution, $T_d(x,y)$, at any point of the plate. One of the main applications of this approach can be the simultaneous control of vibrations and stresses in FGM plates by utilizing control heat fluxes at the boundary of a plate. As mentioned earlier, the study of the thermal-stress characteristics of FGM plates is an interesting open problem that needs more work. As the thermal stress has a direct relationship with shear and normal stresses in FGM plates, vibration in a FGM plate can be suppressed, and normal and shear stresses can be controlled by exerting boundary heat flux control. Another interesting application of our method can be in the material manufacturing process, where the temperature control is a very effective technique to obtain a magnetically graded material with a suitable gradient of magnetization; for example, see Ref. [21]

The structure of the paper is as follows: In Sec. 2, the governing heat transfer equations of the FGM plate are discussed, and the appropriate boundary conditions that produce a temperature distribution in the plate is also presented. The analytical method of the Lyapunov technique, which shows that the desired temperature will be achieved with boundary control, is discussed in Sec. 3. In Sec. 4, numerical simulations are provided, and it is shown that the proposed method achieves expected results. The conclusions are presented in Sec. 5.

2 Governing Equations

Consider a thin rectangular FGM plate with spatially varying properties, as shown in Fig. 1. The plate is considered to be with a size of a (m) in length and b (m) in width. The heat diffusion equation for a FGM rectangular plate is obtained as follows [22]:

$$\frac{\partial}{\partial x}\left(k(y)\frac{\partial T(x,y,t)}{\partial x}\right)+\frac{\partial}{\partial y}\left(k(y)\frac{\partial T(x,y,t)}{\partial y}\right)=\rho(y)C(y)\frac{\partial T(x,y,t)}{\partial t} \tag{1}$$

where $T(x,y,t)$ is the temperature function, $\rho(y)$ is the mass density of the plate, $k(y)$ is the conductivity of the plate, and $C(y)$ is the specific heat capacity of the plate.

The desired distributed temperature of the plate is denoted by a function $T_d(x,y)$, and it is assumed that this steady-state solution exists. It is shown in the literature that [23] if functions $\rho(y)$, $k(y)$, and $C(y)$ satisfy a certain smoothness property known as the Lipschitz condition, the solution of the heat diffusion equation (Eq. (1)) exists and is unique. The desired temperature $T_d(x,y)$ is the final and steady temperature for the plate. So, it should satisfy the steady-state heat transfer equation:

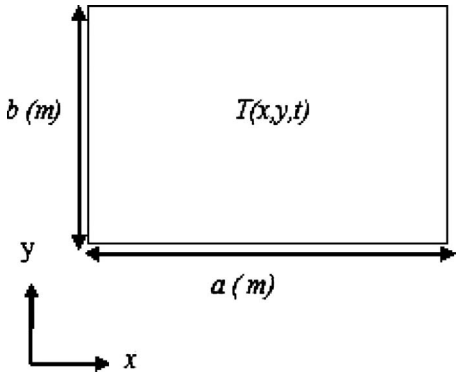

Fig. 1 Geometry and coordinates of the FGM plate

$$\frac{\partial}{\partial x}\left(k(y)\frac{\partial T_d(x,y)}{\partial x}\right)+\frac{\partial}{\partial y}\left(k(y)\frac{\partial T_d(x,y)}{\partial y}\right)=0 \tag{2}$$

and

$$\frac{\partial T_d(x,y)}{\partial t}=0 \tag{3}$$

By subtracting Eq. (2) from Eq. (1) and considering Eq. (3), one can obtain the dynamics in temperature difference $\theta(x,y,t)=T(x,y,t)-T_d(x,y)$ as

$$\frac{\partial}{\partial x}\left(k(y)\frac{\partial \theta(x,y,t)}{\partial x}\right)+\frac{\partial}{\partial y}\left(k(y)\frac{\partial \theta(x,y,t)}{\partial y}\right)=\rho(y)C(y)\frac{\partial \theta(x,y,t)}{\partial t} \tag{4}$$

Our goal is to find appropriate control inputs at the boundaries of the rectangular FGM plate that the error distributed function $\theta(x,y,t)$ converges to zero at any point of the plate.

2.1 Boundary Conditions. In this paper, we consider the boundary conditions as given in Table 1. The boundary conditions in Eqs. (5)–(8) should be selected such that the desired steady-state temperature distribution is achieved.

3 Boundary Control

For boundary control of the plate, Lyapunov's theorem is used, and a Lyapunov functional that is positive definite is introduced. The time derivative of the Lyapunov functional defined on the internal domain will be studied on the boundary of the plate by using some lemmas that are based on the integration by-part method. It is shown that by exerting the boundary control heat fluxes, the time derivative of the Lyapunov functional is made negative definite functional at any in-domain point of plate; therefore, the desired temperature distribution can be achieved.

Table 1 Defined boundary conditions for the rectangular plate

$x=0$	$y=0$
$q=-k(y)\left.\frac{\partial T}{\partial x}\right\|_{(0,y)}=U_{x0}(0,y)$	$q=-k(0)\left.\frac{\partial T}{\partial y}\right\|_{(x,0)}=U_{y0}(x,0)$
$x=a$	$y=b$
$q=k(y)\left.\frac{\partial T}{\partial x}\right\|_{(a,y)}=U_{xa}(a,y)$	$q=k(b)\left.\frac{\partial T}{\partial y}\right\|_{(x,b)}=U_{yb}(x,b)$

In this section, the Lyapunov theorem is used to show the convergence of the distributed temperature $T(x,y,t)$ to the desired distributed temperature $T_d(x,y)$. Consider the following Lyapunov candidate:

$$V = \frac{1}{2}\int_0^b \int_0^a \left\{ k(y)\left(\frac{\partial\theta}{\partial x}\right)^2 + k(y)\left(\frac{\partial\theta}{\partial y}\right)^2 \right\} dxdy \tag{9}$$

Here, for the sake of brevity, the dependence of θ on x, y, and t has been suppressed. The Lyapunov candidate is a positive definite functional, so it satisfies the assumption of Lyapunov's theorem. The time derivative of the Lyapunov functional is obtained as

$$\dot{V} = \int_0^b \int_0^a \left\{ k(y)\left(\frac{\partial\theta}{\partial x}\right)\left(\frac{\partial^2\theta}{\partial x\,\partial t}\right) + k(y)\left(\frac{\partial\theta}{\partial y}\right)\left(\frac{\partial^2\theta}{\partial y\,\partial t}\right) \right\} dxdy \tag{10}$$

By using lemmas (A1) and (A2) in the Appendix, the integration on the domain can be converted to integration on the boundary of the FGM rectangular plate:

$$\dot{V} = \int_0^b \int_0^a \left\{ -\frac{\partial}{\partial x}\left(k(y)\left(\frac{\partial\theta}{\partial x}\right)\right) - \frac{\partial}{\partial y}\left(k(y)\left(\frac{\partial\theta}{\partial y}\right)\right) \right\}\left(\frac{\partial\theta}{\partial t}\right) dxdy + \int_0^a \left(\frac{\partial\theta}{\partial t}\right)\left(k(y)\left(\frac{\partial\theta}{\partial y}\right)\right)\Big|_{y=0}^{y=b} dx + \int_0^b \left(\frac{\partial\theta}{\partial t}\right)\left(k(y) \times \left(\frac{\partial\theta}{\partial x}\right)\right)\Big|_{x=0}^{x=a} dy \tag{11}$$

Replacing Eq. (4) into Eq. (11) gives us

$$\dot{V} = \int_0^b \int_0^a \left\{ -\rho(y)C(y)\left(\frac{\partial\theta}{\partial t}\right)^2 \right\} dxdy + \int_0^a \left(\frac{\partial\theta}{\partial t}\right)\left(k(y) \times \left(\frac{\partial\theta}{\partial y}\right)\right)\Big|_{y=0}^{y=b} dx + \int_0^b \left(\frac{\partial\theta}{\partial t}\right)\left(k(y)\left(\frac{\partial\theta}{\partial x}\right)\right)\Big|_{x=0}^{x=a} dy \tag{12}$$

Rearranging Eq. (12) gives us

$$\dot{V} = \int_0^b \int_0^a \left\{ -\rho(y)C(y)\left(\frac{\partial\theta}{\partial t}\right)^2 \right\} dxdy + \int_0^a \left(\frac{\partial\theta}{\partial t}\right)\left(k(y) \times \left(\frac{\partial\theta}{\partial y}\right)\right)\Big|_{y=b} dx + \int_0^b \left(\frac{\partial\theta}{\partial t}\right)\left(k(y)\left(\frac{\partial\theta}{\partial x}\right)\right)\Big|_{y=0} dy + \int_0^b \left(\frac{\partial\theta}{\partial t}\right) \times \left(k(y)\left(\frac{\partial\theta}{\partial x}\right)\right)\Big|_{x=a} dy - \int_0^b \left(\frac{\partial\theta}{\partial t}\right)\left(k(y)\left(\frac{\partial\theta}{\partial x}\right)\right)\Big|_{x=0} dy \tag{13}$$

Applying the boundary conditions in Eqs. (5)–(8), the following relationship is obtained:

$$\dot{V} = \int_0^b \int_0^a \left\{ -\rho(y)C(y)\left(\frac{\partial\theta}{\partial t}\right)^2 \right\} dxdy + \int_0^a \left(\frac{\partial\theta}{\partial t}\right)\left(k(y)\left(\frac{\partial T}{\partial y} - \frac{\partial T_d}{\partial y}\right)\right)\Big|_{y=b} dx - \int_0^a \left(\frac{\partial\theta}{\partial t}\right)\left(k(y)\left(\frac{\partial T}{\partial y} - \frac{\partial T_d}{\partial y}\right)\right)\Big|_{y=0} dx + \int_0^b \left(\frac{\partial\theta}{\partial t}\right)\left(k(y)\left(\frac{\partial T}{\partial x} - \frac{\partial T_d}{\partial x}\right)\right)\Big|_{x=a} dy - \int_0^b \left(\frac{\partial\theta}{\partial t}\right)\left(k(y) \times \left(\frac{\partial T}{\partial x} - \frac{\partial T_d}{\partial x}\right)\right)\Big|_{x=0} dy = \int_0^b \int_0^a \left\{ -\rho(y)C(y)\left(\frac{\partial\theta}{\partial t}\right)^2 \right\} dxdy + \int_0^a \left(\frac{\partial\theta}{\partial t}\right)\left(U_{yb} - k(y)\frac{\partial T_d}{\partial y}\right)\Big|_{y=b} dx + \int_0^a \left(\frac{\partial\theta}{\partial t}\right)\left(U_{y0} - k(y)\frac{\partial T_d}{\partial y}\right)\Big|_{y=0} dx + \int_0^b \left(\frac{\partial\theta}{\partial t}\right)\left(U_{xa} - k(y)\frac{\partial T_d}{\partial x}\right)\Big|_{x=a} dy + \int_0^b \left(\frac{\partial\theta}{\partial t}\right)\left(U_{x0} - k(y)\frac{\partial T_d}{\partial x}\right)\Big|_{x=0} dy \tag{14}$$

The boundary control inputs are selected as follows:

$$U_{x0} = k(y)\left.\frac{\partial T_d}{\partial x}\right|_{x=0} f_{x0}(0,y,t) \tag{15}$$

$$U_{xa} = k(y)\left.\frac{\partial T_d}{\partial x}\right|_{x=a} f_{xa}(a,y,t) \tag{16}$$

$$U_{y0} = k(y)\left.\frac{\partial T_d}{\partial y}\right|_{y=0} f_{y0}(x,0,t) \tag{17}$$

$$U_{yb} = k(y)\left.\frac{\partial T_d}{\partial y}\right|_{y=b} f_{yb}(x,b,t) \tag{18}$$

where

$$f_{y0}(x,0,t) = 1, \quad |\theta(x,0,t)| > 10^{-3}$$

$$f_{y0}(x,0,t) = 0, \quad \frac{\partial\theta(x,0,t)}{\partial t} = 0, \quad |\theta(x,0,t)| < 10^{-3} \tag{19}$$

$$f_{yb}(x,b,t) = 1, \quad |\theta(x,b,t)| > 10^{-3}$$

$$f_{yb}(x,b,t) = 0, \quad \frac{\partial\theta(x,b,t)}{\partial t} = 0, \quad |\theta(x,b,t)| < 10^{-3} \tag{20}$$

$$f_{x0}(0,y,t) = 1, \quad |\theta(0,y,t)| > 10^{-3}$$

$$f_{x0}(0,y,t) = 0, \quad \frac{\partial\theta(0,y,t)}{\partial t} = 0, \quad |\theta(0,y,t)| < 10^{-3} \tag{21}$$

$$f_{xa}(a,y,t) = 1, \quad |\theta(a,y,t)| > 10^{-3}$$

$$f_{xa}(a,y,t) = 0, \quad \frac{\partial\theta(a,y,t)}{\partial t} = 0, \quad |\theta(a,y,t)| < 10^{-3} \tag{22}$$

Then, $\dot{V}$ will be simplified as

$$\dot{V} = \int_0^b \int_0^a \left\{ -\rho(y)C(y)\left(\frac{\partial\theta}{\partial t}\right)^2 \right\} dxdy \le 0 = -\int_0^b \int_0^a \frac{1}{\rho(y)C(y)}\left(\frac{\partial}{\partial x}\left(k(y)\frac{\partial\theta}{\partial x}\right) + \frac{\partial}{\partial y}\left(k(y)\frac{\partial\theta}{\partial y}\right)\right) dxdy \tag{23}$$

Therefore, the equilibrium state must satisfy

$$\dot{\theta} = 0 \ \text{ or } \ \frac{\partial}{\partial x}\left(k(y)\frac{\partial\theta}{\partial x}\right) + \frac{\partial}{\partial y}\left(k(y)\frac{\partial\theta}{\partial y}\right) = 0 \tag{24}$$

As a result of Eq. (24) and by the invariant set theorem, there is no heat transfer interaction in the plate. The solution of $\dot{V}=0$ is θ = const for all $x \in [0,a]$ and $y \in [0,b]$. Now, since θ is equal to zero (see Eqs. (19)–(22)) at the boundaries of the plate, it must be equal to zero at any in-domain point of the plate. This means that the distributed temperature $T(x,y,t)$ converges to the desired distributed temperature $T_d(x,y)$ at any arbitrary point (x,y) for all $x \in [0,a]$ and $y \in [0,b]$.

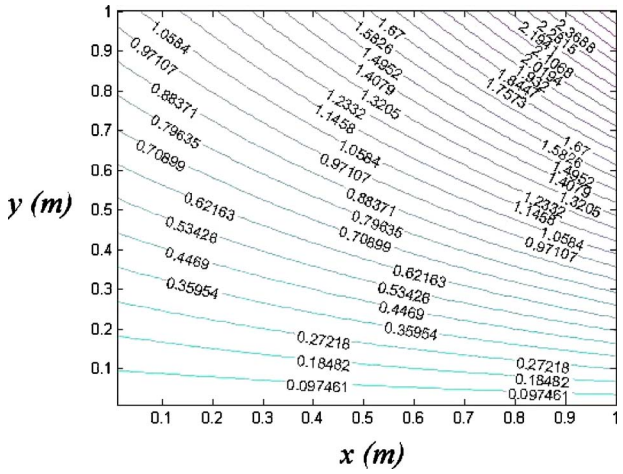

Fig. 2 Desired temperature distribution in rectangular FGM plate with spatially varying property

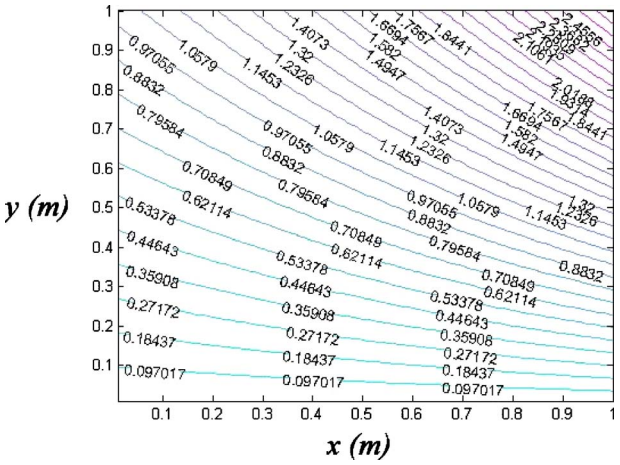

Fig. 3 Final (steady-state) temperature distribution *T* in °C after application of boundary control heat fluxes for $\Delta x=0.01$, $\Delta y=0.01$, and $\Delta t=0.01$ (plate with spatially varying thermal properties)

4 Numerical Results

In order to show the capability of the method to control the temperature distribution of a domain with appropriate heat fluxes on its boundaries, a typical plate with a simple rectangular geometry and spatially varying thermal property in the exponential form in the width direction is considered.

As shown in the previous section, every temperature distribution that satisfies the steady-state heat equation can be achieved by control of heat fluxes at the boundaries of the plate. Complicated temperature distributions are not common to be utilized in applied heat transfer analysis, but to prove the rigorousness of our approach a mathematically elegant temperature distribution is considered. The numerical results are presented as follows.

4.1 Numerical Results for the Plate With Varying Properties Along the Width. Consider a rectangular FGM plate such as the one shown in Fig. 1. Each of the four edges is 1 m long. The properties of the plate are assumed to be

$$k(y) = k_0 e^{-y/b}, \quad k_0 = 1, \quad b = 1 \text{ m}, \quad \rho(y) = 7800 \ \frac{\text{kg}}{\text{m}^3}, \quad C(y) = 470 \ \frac{\text{J}}{\text{kg K}}$$

The initial temperature of the plate is assumed to be $T(x,y,0) = 0\,^\circ\text{C}$. We suppose $T_d(x,y)$ to be

$$T_d(x,y) = xe^{y/b}, \quad b = 1 \text{ m} \tag{25}$$

It is obvious that $T_d(x,y)$ satisfies the steady-state heat transfer equation,

$$\frac{\partial}{\partial x}\left(k(y)\frac{\partial T_d(x,y)}{\partial x}\right) + \frac{\partial}{\partial y}\left(k(y)\frac{\partial T_d(x,y)}{\partial y}\right) = 0 \tag{26}$$

The desired temperature distribution contour $T_d(x,y)$ is illustrated in Fig. 2.

According to Eqs. (5)–(8), the appropriate boundary conditions should be considered as follows:

$$q|_{x=0} = 1 \tag{27}$$

$$q|_{x=1} = 1 \tag{28}$$

$$q|_{y=0} = x \tag{29}$$

$$q|_{y=1} = x \tag{30}$$

A thorough analysis of the grid and time step sizes of the written numerical program and also the convergency of the proposed control method has been carried out. The results, not all reported here to save space, confirm the method's convergency and verify our mathematical rationale of using boundary heat flux to control temperature distribution in a rectangular FGM plate.

To study the effects of different grid and time step sizes, a variety of distinct sets of grid sizes and time steps have been used in the written numerical program. Among them, to show the grid and time step independency of the solution, we have chosen five sets of Δx, Δy, and Δt. A threshold of $\Delta = 0.0008$ is chosen as the maximum allowable difference between the desired and the actual temperature at each node. The results are illustrated in Figs. 3–7.

Numerical results demonstrate that the desired temperature distributed function that satisfies the steady-state heat diffusion equation in the rectangular FGM plate is approached by appropriate boundary control heat fluxes.

Table 2 shows the resulting errors for different gird sizes and time steps in the numerical simulation. It is apparent from this table that mean absolute error (mae) and root mean squared error

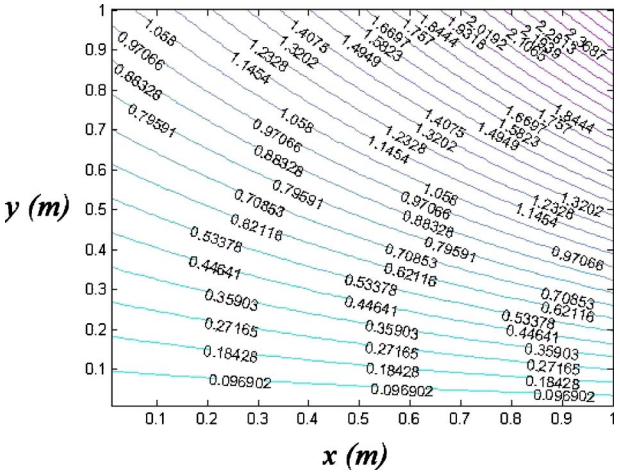

Fig. 4 Final (steady-state) temperature distribution *T* in °C after application of boundary control heat fluxes for $\Delta x=0.01$, $\Delta y=0.005$, and $\Delta t=0.01$ (plate with spatially varying thermal properties)

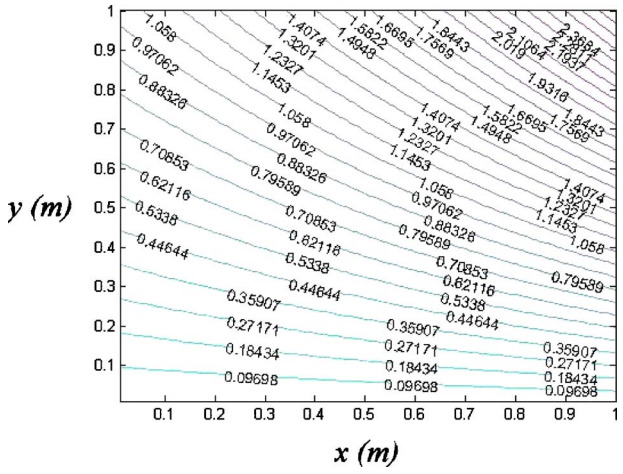

Fig. 5 Final (steady-state) temperature distribution T in °C after application of boundary control heat fluxes for $\Delta x=0.005$, $\Delta y=0.01$, and $\Delta t=0.005$ (plate with spatially varying thermal properties)

(rmse) for different combinations of gird sizes and time steps are all small, and the sets of numbers are close to each other.

5 Conclusions

In summary, the boundary control method was proposed to control temperature distribution in FGM plates. A positive definite Lyapunov candidate was introduced for this purpose. Integration by parts was used to convert integration on the rectangular domain to the integration on the boundary, so the time derivative of the Lyapunov functional defined on the rectangular domain could be studied on the boundary of the plate. The control inputs, consisting of heat fluxes at the boundary of the plate, were applied to make the time derivative of the Lyapunov functional negative definite. The convergence of the in-domain temperature distribution to the desired temperature distribution and also the grid size and time step independency of the numerical simulation for a rectangular FGM plate with spatially varying thermal property were demonstrated.

Nomenclature

$\rho(y)$ = mass density varying in the width direction

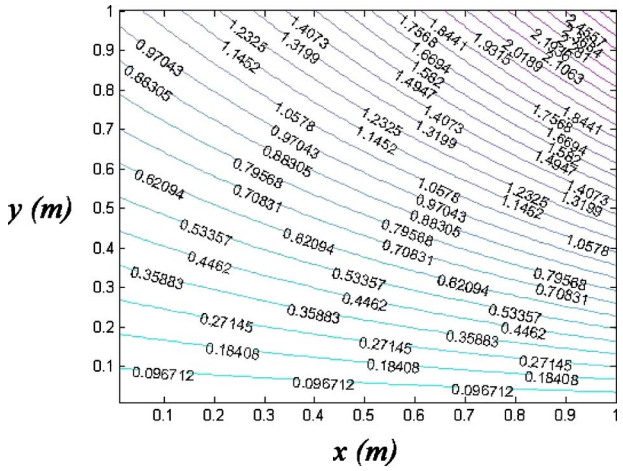

Fig. 6 Final (steady-state) temperature distribution T in °C after application of boundary control heat fluxes for $\Delta x=0.005$, $\Delta y=0.005$, and $\Delta t=0.01$ (plate with spatially varying thermal properties)

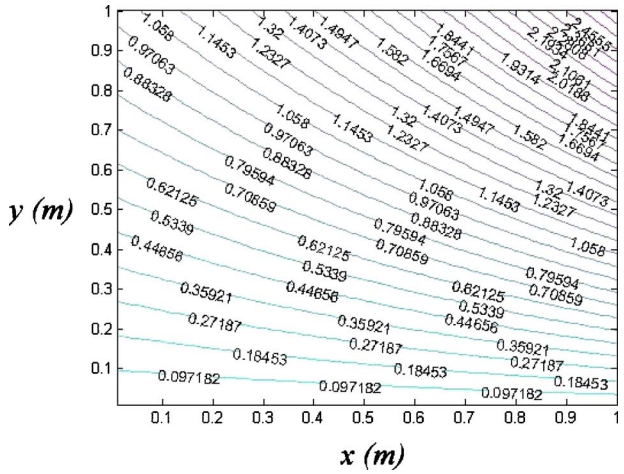

Fig. 7 Final (steady-state) temperature distribution T in °C after application of boundary control heat fluxes for $\Delta x=0.005$, $\Delta y=0.005$, and $\Delta t=0.005$ (plate with spatially varying thermal properties)

$C(y)$ = specific heat capacity varying in the width direction
$k(y)$ = conductivity of the plate varying in the width direction
$T(x,y,t)$ = transient temperature distribution
$T_d(x,y)$ = desired temperature distribution
$\theta(x,y,t)$ = difference between transient and desired temperature distributions
$V(t)$ = Lyapunov function
a = length of the plate
b = width of the plate

Appendix

The following are the required theorems, definitions, and lemmas related to the boundary control approach.

1 Theorems and Definitions

In order to apply Lyapunov's stability theorem to distributed parameter systems, it is necessary to introduce some definitions and lemmas. Furthermore, a basic theorem on which the stability proof is based will be presented.

DEFINITION 1. *An equilibrium state x_{eq} of a dynamic system is an element of the state space Ξ such that $\eta(\phi(t,t_0)x_{eq},x_{eq})=0$ for all $t\geq 0$ (the distance of its corresponding trajectory to that state is zero), where $\phi(t,t_0)$ is a continuous operator on Ξ and for any fixed $[t,t_0]$ it maps Ξ into itself. The set of all equilibrium states will be called the equilibrium set.*

DEFINITION 2. *An invariant set M of a dynamic system is a subset of Ξ so that for any initial state $\mathbf{x}(t_0)\in M$, its corresponding trajectory will remain in Ξ for all $t\geq t_0$.*

DEFINITION 3. *An asymptotically invariant set, M, of a distrib-*

Table 2 The resulting errors for different gird sizes and time steps in the numerical simulation

Grid and time step	Root mean squared error	Mean absolute error
$\Delta x=0.01$, $\Delta y=0.01$, $\Delta t=0.01$	4.63580×10^{-4}	4.01904×10^{-4}
$\Delta x=0.01$, $\Delta y=0.005$, $\Delta t=0.01$	4.62661×10^{-4}	4.00558×10^{-4}
$\Delta x=0.005$, $\Delta y=0.01$, $\Delta t=0.005$	4.60804×10^{-4}	3.98961×10^{-4}
$\Delta x=0.005$, $\Delta y=0.005$, $\Delta t=0.01$	4.65992×10^{-4}	4.04123×10^{-4}
$\Delta x=0.005$, $\Delta y=0.005$, $\Delta t=0.005$	4.62244×10^{-4}	4.00408×10^{-4}

uted parameter dynamic system is uniformly asymptotically stable if

$$R(\phi(t,t_0)\mathbf{x_0},M)\to 0 \quad \text{as} \quad t-t_0\to+\infty$$

uniformly with respect to $t_0\geq 0$, *where* δ_2 *is sufficiently small and* $\phi(t,t_0)\mathbf{x}(t_0)$ *is the solution of the dynamic system at time* t, *starting at* t_0.

THEOREM 1 (Zubov [23]). *In order for an invariant set* M *of a dynamic system to be stable, it is necessary and sufficient that there exists a one-parameter family of functions* $V(t)$, *having the following properties:*

1. On any element $\mathbf{x}\in S$, there is defined a function $V(\mathbf{x},t)$ of the real argument t, defined for $t\geq t_0$, where $S=\{\mathbf{x}\in\Xi^{=}0<\eta(\mathbf{x},M)<r\}$.
2. For any sufficiently small $\alpha_1>0$, it is possible to find a quantity $\alpha_2>0$ such that $V(\mathbf{x},t)>\alpha_2$ for $\eta(\mathbf{x}(t_0),M)>\alpha_1$ and all $t\geq 0$.
3. $V(\mathbf{x},t)\to 0$ uniformly relative to $t\geq 0$ as $R(\mathbf{x},M)\to 0$.
4. The functional $V(t)$ evaluated along the solution of the system does not increase for all $t\geq t_0$, for which it is defined, $\dot{V}\leq 0$.
5. Furthermore, if the functional $V(t)$ evaluated along the solution of the dynamic system tends to zero as $t\to+\infty$ for all $t_0\geq 0$ and $\eta(\mathbf{x},M)<\delta_1$, where $\delta_1>0$ is sufficiently small, then the invariant set of the dynamic system will be asymptotically stable, and, conversely, if the invariant set is asymptotically stable, this holds, $\dot{V}\leq 0$.

Note that condition 2 in the above theorem indicates positive definiteness of the function $V(\mathbf{x},t)$. Condition 3 requires that the function $V(\mathbf{x},t)$ admit an infinitesimally upper limit. To prove the stability of a distributed parameter system, one has to show that there exists a functional with the following properties:

1. The functional is positive definite with respect to a specified metric.
2. The functional admits an infinitesimally upper limit.
3. The time derivative of the functional along the solutions of the underlying system is negative definite.

2 Required Lemmas

For converting the integration on the domain to the integration on the boundary, we use the integration by-part method. Based on this method, we can establish the following lemmas:

$$\int_0^b\int_0^a\left\{k(y)\left(\frac{\partial\theta}{\partial x}\right)\left(\frac{\partial^2\theta}{\partial x\,\partial t}\right)\right\}dxdy=\int_0^b\int_0^a\left\{-\left(\frac{\partial}{\partial x}\left(k(y)\times\left(\frac{\partial\theta}{\partial x}\right)\right)\right)\left(\frac{\partial\theta}{\partial t}\right)\right\}dxdy+\int_0^b\left(\frac{\partial\theta}{\partial t}\right)\left(k(y)\left(\frac{\partial\theta}{\partial x}\right)\right)\Bigg|_0^a dy \tag{A1}$$

$$\int_0^b\int_0^a\left\{k(y)\left(\frac{\partial\theta}{\partial y}\right)\left(\frac{\partial^2\theta}{\partial y\,\partial t}\right)\right\}dxdy=\int_0^b\int_0^a\left\{-\left(\frac{\partial}{\partial y}\left(k(y)\times\left(\frac{\partial\theta}{\partial y}\right)\right)\right)\left(\frac{\partial\theta}{\partial t}\right)\right\}dxdy+\int_0^a\left(\frac{\partial\theta}{\partial t}\right)\left(k(y)\left(\frac{\partial\theta}{\partial y}\right)\right)\Bigg|_0^b dx \tag{A2}$$

References

[1] Huang, C. H., and Li, C. Y., 2003, "A Three-Dimensional Optimal Control Problem in Determining the Boundary Control Heat Fluxes," Heat Mass Transfer, **39**, pp. 589–598.

[2] Payan, S., Sarvari, S., and Ajam, H., 2009, "Inverse Boundary Design of Square Enclosures With Natural Convection," Int. J. Therm. Sci., **48**(4), pp. 682–690.

[3] Beck, J. V., Blackwell, B., and Clair, C. R., 1985, *Inverse Heat Conduction*, Wiley, New York.

[4] Scheuing, J., and Tortorelli, D., 1996, "Inverse Heat Conduction Problem Solution via Second-Order Design Sensitivities and Newton's Method," Inverse Probl. Sci. Eng., **2**(3), pp. 227–262.

[5] Duilkravich, G., and Martin, T., 1996, Inverse Shape and Boundary Condition Problem and Optimization in Heat Conduction, *Advances in Numerical Heat Transfer*, W. J. Minkowycz, and E. M. Sparrow, eds., Taylor and Francis, New York.

[6] Boskovic, D. M., and Kirstic, M., 2001, "Boundary Control of an Unstable Heat Equation via Measurement of Domain-Advanced Temperature," IEEE Trans. Autom. Control, **46**(12), pp. 2022–2028.

[7] Rastgoftar, H., Eghtesad, M., and Khayatian, A., 2008, "Boundary Control of Vibration of Symmetric Composite Laminated Plate," *Proceedings of the 17th IFAC World Congress*, Seoul, Korea.

[8] Rastgoftar, H., Eghtesad, M., and Khayatian, A., 2008, "Boundary Control of Vibration of General Composite Laminated Plate," *Proceedings of the 12th IEEE Conference INES*, Miami, FL.

[9] Suresh, S., and Mortensen, A., 1998, *Fundamentals of Functionally Graded Materials*, IOM Communications, London, UK.

[10] Miyamoto, Y., Kaysser, W. A., Rabin, B. H., Kawasaki, A., and Ford, R. G., 1999, *Functionally Graded Materials: Design, Processing and Applications*, Kluwer, Dordrecht, The Netherlands.

[11] Sladek, J., Sladek, V., and Zhang, C. H., 2003, "Transient Heat Conduction Analysis in Functionally Graded Materials by the Meshless Local Boundary Integral Equation Method," Comput. Mater. Sci., **28**, pp. 494–504.

[12] Marin, L., 2005, "Numerical Solution of the Cauchy Problem for Steady-State Heat Transfer in Two-Dimensional Functionally Graded Materials," Int. J. Solids Struct., **42**, pp. 4338–4351.

[13] Chen, B., Tong, L., Gu, Y., Zhang, H., and Ochoa, O., 2004, "Transient Heat Transfer Analysis of Functionally Graded Materials Using Adaptive Precise Time Integration and Graded Finite Elements," Numer. Heat Transfer, Part B, **45**, pp. 181–200.

[14] Wang, B. L., and Tian, Z. H., 2005, "Application of Finite Element-Finite Difference Method to the Determination of Transient Temperature Field in Functionally Graded Materials," Finite Elem. Anal. Design, **41**, pp. 335–349.

[15] Sutradhar, A., and Paulino, G. H., 2004, "The Simple Boundary Element Methods for Transient Heat Conduction Analysis in Functionally Graded Materials," Comput. Methods Appl. Mech. Eng., **193**, pp. 4511–4539.

[16] Qian, L. F., and Batra, R. C., 2005, "Three-Dimensional Transient Heat Conduction in a Functionally Graded Thick Plate With a Higher-Order Plate Theory and a Meshless Local Petrov-Galerkin Method," Comput. Mech., **35**, pp. 214–226.

[17] Ching, H. K., and Yen, S. C., 2006, "Transient Thermoelastic Deformations of 2-D Functionally Graded Strips Under Nonuniformly Convective Heat Supply," Compos. Struct., **73**, pp. 381–393.

[18] Wang, H., Qin, Q. H., and Kang, Y. L., 2006, "A Meshless Model for Transient Heat Conduction in Functionally Graded Materials," Comput. Mech., **38**, pp. 51–60.

[19] Golbahar Haghighi, M. R., Eghtesad, M., Necsulescu, D. S., and Malekzade, P., 2010, "Temperature Control of Functionally Graded Plates Using a Feedforward-Feedback Controller Based on the Inverse Solution and Proportional-Derivative Controller," Engineering Conversion and Management, **51**, pp. 140–146.

[20] Cho, J. R., and Oden, J. T., 2000, "Functionally Graded Material: A Parametric Study on Thermal-Stress Characteristics Using the Crank-Nicolson-Galerkin Scheme," Comput. Methods Appl. Mech. Eng., **188**, pp. 17–38.

[21] Watanabe, Y., and Momose, I., 2003, "Magnetically Graded Materials Fabricated by Inhomogeneous Heat Treatment of Deformed Stainless Steel," Ironmaking Steelmaking, **31**, pp. 265–268.

[22] Incropera, F. P., and Dewitt, D. P., 2002, *Fundamentals of Heat and Mass Transfer*, Wiley, New York.

[23] Zubov, V. L., 1964, *Methods of A. M. Liapunov and Their Application*, Noordhoff, Gorning, The Netherlands.

Dropwise Condensation Underneath Chemically Textured Surfaces: Simulation and Experiments

Basant Singh Sikarwar

Nirmal Kumar Battoo

Sameer Khandekar[1]
e-mail: samkhan@iitk.ac.in

K. Muralidhar

Department of Mechanical Engineering,
Indian Institute of Technology Kanpur,
Kanpur 208016, India

Experimental observations of dropwise condensation of water vapor on a chemically textured surface of glass and its detailed computer simulation are presented. Experiments are focused on the pendant mode of dropwise condensation on the underside of horizontal and inclined glass substrates. Chemical texturing of glass is achieved by silanation using octyl-decyl-tri-chloro-silane ($C_{18}H_{37}C_{13}Si$) in a chemical vapor deposition process. The mathematical model is built in such a way that it captures all the major physical processes taking place during condensation. These include growth due to direct condensation, droplet coalescence, sliding, fall-off, and renucleation of droplets. The effects arising from lyophobicity, namely, the contact angle variation and its hysteresis, inclination of the substrate, and saturation temperature at which the condensation is carried out, have been incorporated. The importance of higher order effects neglected in the simulation is discussed. The results of model simulation are compared with the experimental data. After validation, a parametric study is carried out for cases not covered by the experimental regime, i.e., various fluids, substrate inclination angle, saturation temperature, and contact angle hysteresis. Major conclusions arrived at in the study are the following: The area of droplet coverage decreases with an increase in both static contact angle of the droplet and substrate inclination. As the substrate inclination increases, the time instant of commencement of sliding of the droplet is advanced. The critical angle of inclination required for the inception of droplet sliding varies inversely with the droplet volume. For a given static contact angle, the fall-off time of the droplet from the substrate is a linear function of the saturation temperature. For a given fluid, the drop size distribution is well represented by a power law. Average heat transfer coefficient is satisfactorily predicted by the developed model. [DOI: 10.1115/1.4002396]

Keywords: dropwise condensation, chemical texturing, pendant droplets, modeling and simulation, imaging

1 Introduction

It is well known that the heat transfer coefficient during dropwise condensation is several times larger than other modes of condensation. Dropwise condensation could be promoted by introducing a nonwetting chemical into the vapor, by special physical treatment of the condensation surface/substrate, or by chemical coating of the solid substrate with a low surface-energy substance [1–3]. These techniques have been known for many years; the last technique holds considerable promise and has been an active area of research. Marto et al. [4] tested several polymer coatings, gold and silver, for sustaining dropwise condensation of steam and reported the heat transfer coefficients in dropwise condensation as high as six times when compared with filmwise condensation. Zhao et al. [5] reported that the heat transfer coefficients of dropwise condensation on Langmuir–Blodgett treated surfaces are more than 30 times higher than that of filmwise condensation on bare surfaces. Vemuri et al. [6] experimentally investigated the effects of various chemical coatings and their long term durability on the dropwise mode of heat transfer. They reported a decrease in heat transfer coefficient with the elapsed condensation time, suggesting possible leaching of the chemical coating. Rausch et al. [7] reported that the heat transfer coefficient on an ion-implantation surface is more than five times that of filmwise condensation. In recent years, with the advent of newer coating/manufacturing and nanoscale fabrication techniques, promoting long term sustainability of dropwise condensation by chemical coating now holds considerable prospect for enhancing heat transfer in a variety of industries [2,6,8]. An example of enhanced performance of compact steam condensers having chemically coated flow passages of only a few millimeter width is demonstrated by Majumdar and Mezic [9].

Apart from the dropwise condensation process for heat transfer applications, the formation of distinct drops on horizontal/inclined lyophobic surfaces and their subsequent dynamics is also of considerable interest in many other industrial and engineering applications such as microfluidics, lab-on-chip device, ink jet printing systems, spraying of insecticide on crops, and several biochemical processes [10]. The understanding of the dynamics of the droplet ensemble also gains importance if droplet-substrate interaction leads to physico-chemical leaching of the substrate, for example, during (i) estimation of the life cycle of a heat exchanger textured by promoter layers and (ii) estimation of substrate life on which heavy liquid metals are being deposited under closed vacuum conditions [11].

The phenomenon of droplet formation and the exact mechanism of enhancement of heat transfer by condensation on chemically textured surfaces have been a matter of debate and discussion. It depends not only on the thermophysical properties of the fluid

[1]Corresponding author.

Contributed by the Heat Transfer Division of ASME for publication in the JOURNAL OF HEAT TRANSFER. Manuscript received April 29, 2010; final manuscript received July 23, 2010; published online November 3, 2010. Assoc. Editor: Giulio Lorenzini.

getting condensed, but also on the physico-chemical properties of the substrate, time scales involved, process control parameters, external body forces other than gravity (such as electro-wetting), orientation and texture of the cold substrate, applicable subcooling, etc. Leach et al. [12] reported that the contribution of small drops to the overall heat transfer coefficient exceeds that of the largest drops by a factor of 15. McCormick and Baer [13] reported that the droplet nucleation, growth patterns, and subsequent droplet dynamics have important practical consequences on high heat transfer rates. Experimental determination of the heat transfer coefficient is also a challenging task because of the many intricacies involved in the process. Mainly, the driving temperature difference is very small in dropwise condensation, essentially resulting in a very high heat transfer coefficient. Second, required spatio-temporal resolutions are also quite demanding, as recently demonstrated by Bansal et al. [14], who have experimentally determined the local wall heat transfer coefficient below a condensing single-droplet and multidroplet pendant system by liquid crystal thermography. They reported the variation in local heat flux at the base of the droplet as a function of its diameter (similar work on single-droplet and multidroplet systems evaporating on a heated surface in the context of spray cooling has been shown by Tartarini et al. [15] using high resolution infrared thermography). Heat transfer rates are also affected by sessile/pendant mode and global orientation of the substrate. On an inclined substrate, continuous sweeping of critically sized droplets and renewal of drop growth cycle is responsible for the higher heat transfer coefficient associated with dropwise condensation, as summarized by Leipertz and Fröba [2]. Briscoe and Galvin [16] and Lawal and Brown [17] experimentally compared the performance of sessile and pendant droplets and attributed the instability of the pendant mode for its better heat transfer coefficient.

Modeling of the dropwise condensation process based on nucleation hypothesis has been attempted by various investigators. Glicksman and Hunt [18] simulated the dropwise condensation cycle in a number of stages, covering the equilibrium drop size to the departing drop size, to achieve a large nucleation site density. The initial stage consisted of a nucleation site density of 10^8 m^{-2} by taking 1000 sites on a surface of size 33×33 μm^2. The area of the second stage was increased ten times, and the droplets from the first stage were redistributed on this surface. In this way, the simulation was repeated until the departure droplet size was reached. Thus, a high nucleation site density was achieved, but an artificial redistribution between two consecutive stages destroyed the natural distribution of the drops. Wu and Maa [19] and Maa [20] used the population balance method to find the drop size distribution of small drops, which grow mainly by direct condensation. They estimated the heat transfer coefficient by considering only the conduction resistance through the drop. Abu-Orabi [21] incorporated the resistance due to heat conduction through the promoting layer; curvature resistance was also included. Rose and Glicksman [22] proposed a universal form of the distribution function for large drops, which grow primarily by coalescence with smaller drops, though smaller drops themselves mainly grow by direct condensation. Gose et al. [23] carried out computer simulation on a 100×100 grid with 200 randomly distributed nucleation sites. Burnside and Hadi [24] simulated dropwise condensation of steam from an equilibrium droplet to a detectable size on 240×240 μm^2 surface with 60,000 randomly spaced nucleation sites. Later, Vemuri and Kim [25] modeled dropwise condensation for hemispherical drops, which mainly grow by direct condensation, by the population balance method. The primary resistances to heat transfer, such as conduction through the drop and vapor-liquid interface resistance, were considered in developing the model. The derivation of a steady state distribution for small drops within the size range of negligible coalescence was based on the conservation of the number of drops with no accumulation. Contact angle other than 90 deg was not considered in this model. Leach et al. [12] experimentally observed drop growth kinetics: The smallest drops grow principally by the accretion of liquid molecules diffusing along the substrate surface, while drops larger than about 50 μm in diameter grow principally by the accretion of condensing vapor directly onto the drop surface. Their model incorporated these growth mechanisms. They also reported the effect of contact angles, degree of subcooling, and inclination of a substrate on nucleation site densities onto a hydrophobic polymer film and a silanized glass surface for sessile droplets.

A complete simulation of dropwise condensation from the equilibrium droplet size to the departing droplet size, accounting for the effect of saturation temperature, contact angle and its hysteresis, and the inclination of the substrate along with its experimental validation, has not been explicitly reported. Against this background, the present study aims at (a) experimentally observing dropwise condensation on a chemically textured surface and (b) simulating the entire spatio-temporal process of dropwise condensation. The methodology adopted for the experimental study is

(i) recording high quality video images at sufficiently high speeds to capture the complete cycle of dropwise condensation, under controlled conditions, on the underside (pendant mode) of chemically textured horizontal and inclined surfaces. Silanes, which are known promoters of hydrophobicity, are used for coating the glass substrate; the corresponding static contact angles have been determined under laboratory conditions.
(ii) digital processing of the video data obtained in step (i) above to extract relevant spatio-temporal quantities of interest such as drop size distribution, area of coverage, droplet merger dynamics, coalescences, and fall-off and slide-off times.

The quantitative experimental data thus obtained, along with the observed qualitative behavior of dropwise condensation, are used for comparison with the developed simulation model. After code validation, parametric studies of dropwise condensation have been done incorporating the numerical code. While the broad outline of the model has been taken from Ref. [3], we have now substantially enriched its originally proposed simplistic approach, not only in the details of the relevant droplet force fields under any substrate inclination but also on the generic extent of the applicability of the model. The simulation of the process proceeds from the equilibrium droplet size to the departing droplet size underneath a horizontal and an inclined substrate, respectively. The extended transient model incorporates the effect of contact angle and its hysteresis and substrate inclination; it accounts for continuous droplet fall-off/slide-off, droplet coalescence and merger dynamics, and renucleation of droplets; thus, all the major physical phenomena seen in experiments have been incorporated in the present model.

Section 2 of the paper describes the design details of the experiment setup and its methodology. Section 3 describes the mathematical model in detail, including the assumptions involved. Section 4 describes the results obtained from the simulation and their comparison with the experiments. Finally, major conclusions of the present study are reported in Sec. 5.

2 Experimental Setup and Methodology

The experimental apparatus was designed to study dropwise condensation under controlled conditions on the underside of a cold substrate and is schematically shown in Fig. 1. The setup primarily consisted of the main cylindrical stainless steel vacuum chamber (better than 10^{-6} mbar abs.) of 180 mm inner diameter and 120 mm length (Figs. 1(*a*) and 1(*b*)). It was closed from the two ends by specially designed flanges. The lower flange was fitted with a $\lambda/4$ optical viewing window (view A; typical photographs of condensing droplets are shown in Fig. 1(*c*)). In addition, it also had an annular space around this viewing window wherein the working fluid inventory (distilled and de-ionized water) was

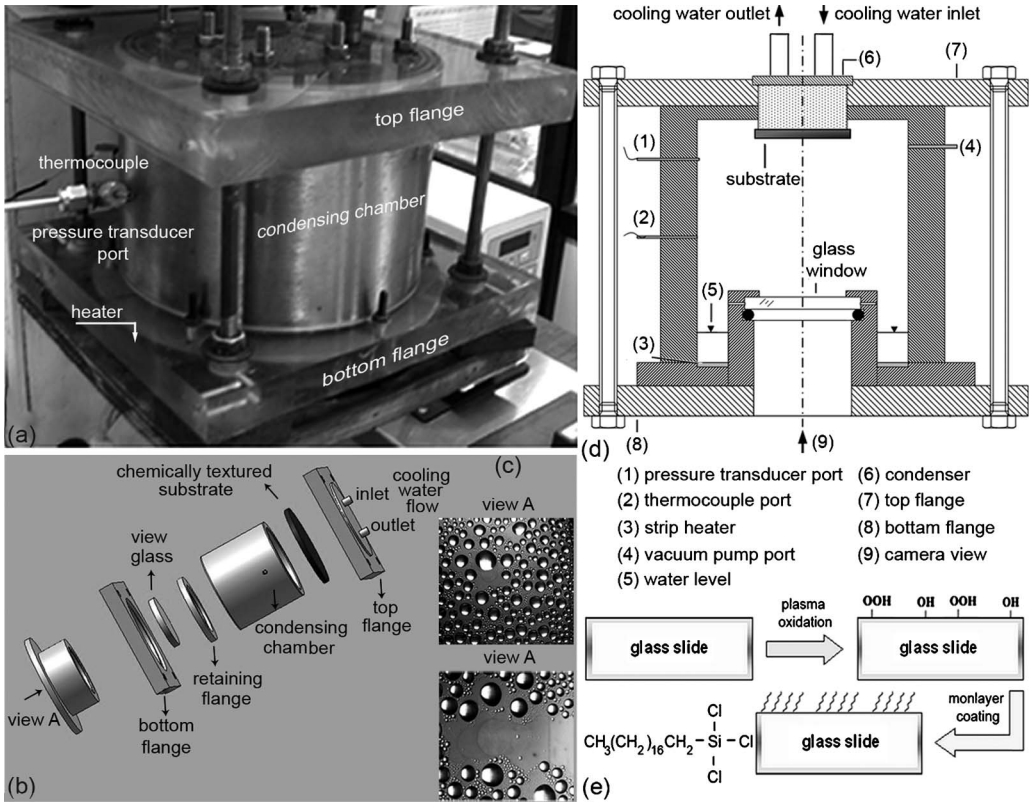

Fig. 1 Details of the experimental setup to study dropwise condensation under controlled conditions underneath a substrate. (*a*) Photograph shows the details of the main condensing chamber; (*b*) exploded view of the condensing chamber showing all the components. (*c*) Typical images of the condensing droplets at two different times, as captured from view A. (*d*) Cross-sectional view of condensing chamber. (*e*) Schematic diagram explaining the chemical vapor deposition process.

stored. A circular, 1.5 mm thick mica strip heater (o.d.=70 mm, i.d.=40 mm) was attached outside this annular space to give the necessary heat input, as shown in the cut section of the experimental setup in Fig. 1(*d*). The upper end of the main vacuum chamber was closed with a polycarbonate square flange with an inbuilt cavity wherein cold water was circulated to maintain constant temperature boundary conditions. The condenser capacity was at least 20 times that of the expected heat transfer rate. The chemically coated glass substrate (methodology of substrate preparation is explained in the next section) of 100×100 mm^2 was integrated on the upper flange, as shown. Connections for evacuation, pressure transducer, and temperature sensors were provided on the main condensing chamber wall. The temperature of the condensing vapor was measured with one K-type thermocouple (Omega®, 0.5 mm diameter) of accuracy of ±0.2°C after calibration. It was placed centrally in the chamber at a distance of 25 mm from its side wall. The condensing chamber pressure was measured by an absolute pressure transducer (Honeywell, accuracy 0.1% FS, NIST traceable calibration, range of 0–1.2 bars). Online data acquisition was carried out with 16 bit PCI-4351 card (National Instruments®). The entire assembly could be tilted to any desired inclination at 0–25 deg. A color charge coupled device (CCD) video camera (Basler® A202KC with 1024×1024 pixels at 100 fps) was used to capture the images of the drops forming on the underside of the chemically textured substrate (view A, Fig. 1(*b*)). Size scales were calibrated by imaging a grid with known periodicity. Diffused white light source symmetrically placed around the camera was directed on the substrate from the optical window on the bottom flange so as to maintain a near parallel and symmetric beam on the droplets, ensuring a proper contrast level for subsequent edge detection.

Dropwise condensation was achieved at the desired saturation pressure by controlling the coolant temperature and the heat throughput. Once a quasi-steady state was reached, the correspondence between the saturation pressure and the condensing vapor chamber temperature was continuously monitored. The high quality video images recorded were digitally processed (using IMAGE J® software) to get the relevant parameters of interest, i.e., area of coverage, droplet size distribution, fall-off/slide-off, coalescence/merger events, etc. The primary steps in finding the area of coverage were (a) digital image acquisition, (b) contrast thresholding and binning to reduce pixel noise, (c) droplet detection with geometry attributes, (d) measurement of total digitized pixel area covered by the droplets, and (e) finding the area of coverage by dividing the total pixel area of all the droplets by the total area of the acquired image. Droplets below a diameter of around 0.1 mm could not be resolved with the imaging hardware used. The image processing software is first tested against benchmark images before applying it on actual experimental images.

Surface Preparation (Chemical Texturing). The substrate preparation involved coating the glass surface using chemical vapor deposition (CVD) of silane molecules. The chemical vapor deposition setup consisted of a vacuum pump (rotary vane rougher pump coupled with diffusion pump, ultimate vacuum level $\sim10^{-5}$ mbar), a plasma oxidizer (with a rf generator having power levels of 6–18 W and frequencies of 8–12 MHz), and a desiccator. Inside the reactor, which was maintained at low vacuum pressure, the high frequency oscillating electromagnetic field ionized the silane molecules forming plasma. This interacted with the glass substrate by the following: (i) Removing organic contamination from its surface. The high energy plasma particles

combine with the contaminant to form carbon dioxide (CO_2) or methane (CH_4), and (ii) modifying the physico-chemical characteristics of surfaces by adsorption or chemisorption, etc. The silanation process is explained schematically in Fig. 1(*e*). Octyldecyl-trichloro-silane ($C_{18}H_{37}C_{13}Si$ supplied by M/s Sigma Aldrich®) was used as the coating material on the glass substrate. Before keeping the substrate for 30 min inside the CVD reactor, the substrate was cleaned by dipping it in a pirani solution (sulfuric acid and hydrogen peroxide in the ratio 3:1 by volume) for 2 h, thereafter washing it with distilled water and drying it in nitrogen. Nascent oxygen released when sulfuric acid reacts with hydrogen peroxide cleans the surface. The silane molecules attached themselves to the plasma cleaned glass plate, which was kept inside the CVD chamber, by a self-assembled monolayer process. After preparing the surface, the static, advancing, and receding contact angles of a pendant water drop for horizontal and inclined substrates were measured by a goniometer that had a special attachment for inclining the substrate.

3 Model Description

The simulation presented in this work is based on the postulate that droplet embryos form and grow at nucleation sites, while the portion of the surface between the growing droplets remains dry [26,27].[1] The nucleation sites are randomly distributed on the substrate. According to the Clausis–Claperyon equation, the size of the initial thermodynamically stable drop formed at a nucleus is of the order of magnitude of a few nanometers for the usual heat transfer fluids. Therefore, from an engineering standpoint, it is difficult to experimentally capture the initial nucleation density on freshly exposed surfaces. This necessitates the use of theoretical models for estimating the number of initial nucleation sites, for example, the proposal of Rose [28] and Mu et al. [29]. Leach et al. [12] reported that the initial drop nucleation density is a function of the degree of subcooling $\Delta T_{\text{sat}} = T_{\text{sat}} - T_w$ but is a weak function of the physico-chemical properties (resultant contact angle) of the cold substrate. Following the literature on the initial nucleation density and in view of the ensuing temperature difference for the range of interest, the nucleation density is assumed to be 10^9 m^{-2} in the present model. Initially, all the sites are occupied by the droplet of the smallest radius as determined from thermodynamic considerations. These droplets are allowed to grow by direct condensation followed by subsequent coalescence until, depending on the substrate inclination, the droplet attains critical size for either fall-off or slide-off. The simulation is confined to condensation underneath cold substrates with pendant drops.

3.1 Condensation Underneath a Horizontal Substrate. A pendant drop underneath a flat horizontal substrate is shown in Fig. 2(*a*). The drop is considered as a portion of a sphere of radius r making a contact angle θ. From the geometry, the drop volume V, area of liquid-vapor interface A_{lv}, and area of solid-liquid interface A_{sl} are given by

$$V = \frac{\pi r^3}{3}(2 - 3\cos\theta + \cos^3\theta) \tag{1}$$

$$A_{\text{lv}} = 2\pi r^2(1 - \cos\theta) \tag{2}$$

$$A_{\text{sl}} = 2\pi r^2(1 - \cos^2\theta) \tag{3}$$

For a specified wall subcooling $(T_s - T_w)$, the smallest stable droplet size possible can be found form thermodynamic considerations as [3]

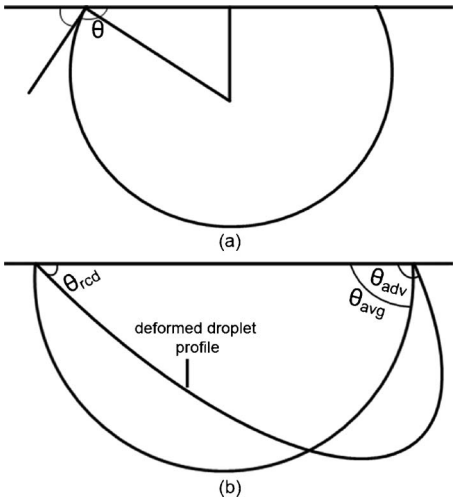

Fig. 2 (*a*) Schematic drawing of a pendant drop underneath a horizontal substrate with contact angle θ. (*b*) Drawing of a deformed drop with unequal advancing and receding angles, and its equivalent spherically approximated profile.

$$r_{\min} = \frac{2\sigma \cdot \nu_l \cdot T_w}{h_{\text{lv}}[T_{\text{sat}} - T_w]} \tag{4}$$

Although the arguments leading to this equation do not include the substrate surface energy, Leach et al. [12] showed that such effects are of higher order and can be neglected for engineering calculations on the microscale. As droplets grow in size, the meso-/macroscale droplet dynamics cannot neglect the bulk contact angle ensuing from the surface energy of the substrate. The maximum drop diameter is calculated from balancing the surface tension with the weight of the drop and is derived as[2]

$$r_{\max} = \sqrt{\left(\frac{6\sin^2\theta}{2 - 3\cos\theta + \cos^3\theta}\right) \cdot \left(\frac{\sigma}{g \cdot (\rho_l - \rho_v)}\right)} \tag{5}$$

The temperature drop due to various resistances to heat transfer is calculated as follows:

(i) Conduction resistance: The drop in temperature due to conduction heat transfer is determined as

$$\Delta T_{\text{cond}} = \frac{q \cdot r}{4\pi \cdot r^2 \cdot k_c(1 - \cos\theta)} \tag{6}$$

(ii) The temperature drop due to interfacial heat transfer is

$$\Delta T_{\text{int}} = \frac{q}{2\pi \cdot r^2 \cdot h_i(1 - \cos\theta)} \tag{7}$$

(iii) Curvature resistance: This resistance includes the loss of driving temperature potential due to the droplet interface curvature and is given by [3]

$$\Delta T_{\text{curv}} = \frac{2\nu_l \cdot \sigma \cdot T_w}{h_{\text{lv}} \cdot r} = \frac{(T_{\text{sat}} - T_w)r_{\min}}{r} \tag{8}$$

The interfacial heat transfer coefficient is given by

[1]Another postulation suggests that condensation initially occurs in a filmwise manner, forming an extremely thin film on the solid surface. As condensation continues in time, this film ruptures forming distinct droplets which subsequently grow. This mechanism is not followed in the present work.

[2]Eq. (5) can be interpreted as modified Bond number criterion, applicable for a pendant droplet which takes into account the effect of contact angle in the force balance. In case of a horizontal substrate, there is no contact angle hysteresis. The usual definition of Bond number is given by, $Bo = (2 \cdot r)(\sqrt{(g(\rho_l - \rho_v))/\sigma})$

$$h_i = \left(\frac{2\hat{\sigma}}{2-\hat{\sigma}}\right)\cdot\left(\frac{h_{lv}^2}{T_s \nu_{lv}}\right)\cdot\left(\frac{\bar{M}}{2\pi \bar{R} T_{sat}}\right)^{1/2} \quad (9)$$

Here, h_i is the interfacial heat transfer coefficient and k_c is the condensate thermal conductivity.

The temperature drop will balance the total available subcooling, and so,

$$\Delta T_t = \Delta T_{cond} + \Delta T_{int} + \Delta T_{curv} = \Delta T_{sat} \quad (10)$$

The heat flux through a single droplet is derived as

$$q = (\pi r^2 \rho_l h_{lv}) \cdot (2 - 3\cos\theta + \cos^3\theta) \cdot \left(\frac{dr}{dt}\right) \quad (11)$$

From the above equation, the rate of growth of individual droplets is as follows:

$$\frac{dr}{dt} = \left(\frac{4\Delta T_t}{\rho_l \cdot h_{lv}}\right)\cdot\left[\frac{\left(1-\frac{r_{min}}{r}\right)}{\left(\frac{2}{h_i}+\frac{r}{k_c}\right)}\right]\cdot\left(\frac{(1-\cos\theta)}{(2-3\cos\theta+\cos^3\theta)}\right) \quad (12)$$

Equation (12) has been integrated to determine the growth of the droplet due to direct condensation. Along with the direct condensation growth loop in the simulator, a parallel coalescence loop is also monitored at each time step. The time for coalescence is taken to be much smaller than the other time scales of the condensation process. Hence, as soon as two droplets contact each other (or three droplets or, very rarely, four droplets contact each other simultaneously), they are substituted with an equivalent single droplet with a conserved volume, located at the weighted center of mass of the individual coalescing droplets.[3] At each time step, the nucleation sites, which are covered by drops, are checked and flagged as hidden sites. In this manner, the randomly distributed droplets are allowed to grow to a stage where their weight exceeds the retention surface force, yielding the critical Bond number criterion given by Eq. (5). At this juncture, droplets fall off. The drop is then removed, and all hidden nucleation sites underneath the drop become active and instantaneously supplied with thermodynamically stable droplets of minimum radius. It is to be noted that the simulation needs to track multiple generations of the droplets—nucleating, growing by direct condensation and by coalescence, and some falling-off when the virgin surface thus exposed is renucleated. The cycle thus begins again and is repeated for a long duration until a dynamic quasi-steady state is reached.

3.2 Condensation Underneath an Inclined Substrate. Inclining the substrate causes imbalance in the forces and results in drop deformation to achieve necessary static balance. As the droplet grows in size, the gravity force component parallel to the substrate exceeds the force component due to surface tension and will eventually cause the droplet to slide underneath the substrate. As droplets slide, they encounter other growing droplets on their path. This process results in a very rapid mass accumulation, as the sliding droplet sweeps away a large population of drops located ahead of it. The critical drop diameter at which sliding commences depends not only on the thermophysical properties of the liquid but also on the contact angle hysteresis and physicochemical properties of the substrate. Moreover, under dynamic conditions of dropwise condensation, the applicability of static force balances is questionable due to the presence of capillary waves, distortion in local equilibrium droplet shapes, droplet pinning, variation in dynamic contact angle due to inertia effects, local sudden acceleration, and three dimensional flow structures inside the droplets [33–35]. Therefore, there is a considerable debate in the literature on the applicability of static conditions on the real-time condensation process [36]. The bulk composite effect of these real-time dynamic situations and local contact line perturbations is usually manifested in the form of varying hysteresis of advancing and receding angles. Therefore, the static force balance conditions are assumed to be representative of the dynamic situation as absolute contact angles and hysteresis are accounted for.

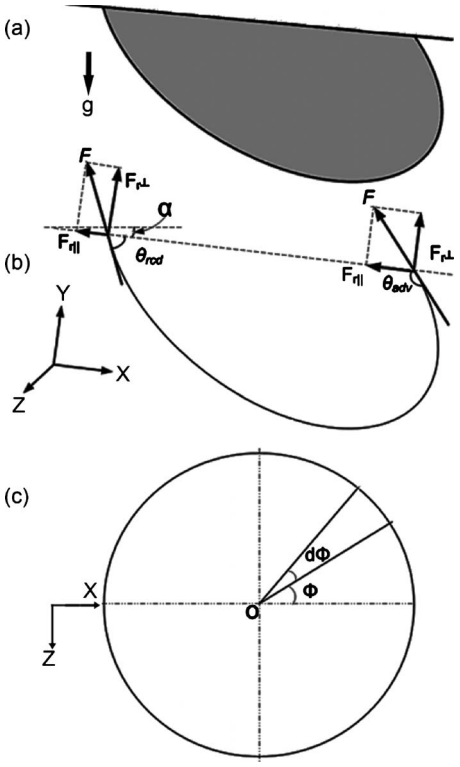

Fig. 3 (*a*) A deformed pendant drop underneath an inclined substrate. (*b*) Free body diagram of a static drop underneath an inclined surface. (*c*) Base of droplet on the substrate taken as a circle.

The contact angle hysteresis, namely, the variation in the advancing to the receding contact angle, is taken to vary linearly along the contact line (refer Fig. 3). While alternative strategies are available [37,38], this approach has been adopted earlier [39]. The variation in contact angle, with respect to azimuthal angle along the contact line, is formulated as

$$\theta = \theta_{adv} + \frac{(\pi - \theta_{rcd} - \theta_{adv})}{\pi}\phi \quad (13)$$

Figure 3(*a*) shows a deformed pendant droplet underneath an inclined substrate, and Fig. 3(*b*) highlights the relevant forces at the contact line. The base of the drop is assumed to be circular, as shown in Fig. 3(*c*), and its volume is calculated using the spherical cap approximation, as shown in Fig. 2(*b*).[4] With known advancing and receding contact angles, the geometric reconstruction

[3]Typically droplet mergers happen in a time scale of 5–300 ms, depending on their respective sizes and thermophysical properties [30–32]. In contrast, the entire experiment of dropwise condensation, from a virgin surface to the first fall-off or a slide-off is typically of the order of one hour. This justifies our assumption of 'instantaneous coalescence.

[4]There is some conflict in the calculation of volume and its experimental validation for sessile drops on inclined surfaces, as reported in [40–43]. Some reports [40–42] suggest that approximating the drop shape as a spherical cap can lead to 10%–25% error in volume. Based on experimental evidence, others [43] believe that such an approximation is quite valid. To the best of the knowledge of the authors, there is no corresponding literature on the calculation of pendant drop volumes. Therefore, the spherical cap approximation has been used in the present work.

of the entire droplet is possible.

The retention forces perpendicular and parallel to the substrate are calculated as

$$F_{r\|} = 2\int_0^{\pi} \sigma \cos\theta \cos\phi \cdot r_b \cdot d\phi \tag{14}$$

$$F_{r\|} = \sigma r_b \left[\frac{\pi}{2\pi - \theta_{rcd} - \theta_{adv}} \{\sin(2\pi - \theta_{rcd}) - \sin\theta_{adv}\} + \frac{\pi}{\theta_{adv} + \theta_{rcd}} \{\sin\theta_{rcd} + \sin\theta_{adv}\} \right] \tag{15}$$

As noted earlier, the drop is assumed as a segment of a sphere with a contact angle θ_{avg}, where θ_{avg} is evaluated at the base of the drop. Hence,

$$\theta_{avg} = (\theta_{rcd} + \theta_{adv})/2 \tag{16}$$

The volume of the equivalent spherically capped droplet is given by

$$V_{sc} = \frac{\pi \cdot r_b^3 (2 - 3\cos\theta_{avg} + \cos^3\theta_{avg})}{3\sin^3\theta_{avg}} \tag{17}$$

The force component due to gravity that is parallel to the substrate is

$$F_{g\|} = \frac{\pi r_b^3 (2 - 3\cos\theta_{avg} + \cos^3\theta_{avg})}{3\sin^3\theta_{avg}} \rho \cdot g \sin\alpha \tag{18}$$

Finally, the critical radius of the droplet at slide-off on the inclined substrate is calculated as

$$r_{crit} = \sqrt{\left(\frac{3\sin^3\theta_{avg}}{\pi(2 - 3\cos\theta_{avg} + \cos^3\theta_{avg})}\right)\left[\frac{\pi}{2\pi - \theta_{rcd} - \theta_{adv}}\{\sin(2\pi - \theta_{rcd}) - \sin\theta_{adv}\} + \frac{\pi}{\theta_{adv} + \theta_{rcd}}\{\sin\theta_{rcd} + \sin\theta_{adv}\}\right]\left(\frac{\sigma}{(g\sin\alpha)(\rho_l - \rho_v)}\right)} \tag{19}$$

The surface tension component perpendicular to the inclined substrate is calculated as

$$F_{r\perp} = 2\int_0^{\pi} \sigma \sin\theta \cdot r_b \cdot d\phi \tag{20}$$

$$F_{r\perp} = 2\sigma \cdot r_b \left(\frac{\pi}{\pi - \theta_{rcd} - \theta_{adv}}\right) \cdot (\cos\theta_{rcd} + \cos\theta_{adv}) \tag{21}$$

The gravity force component perpendicular to the substrate is

$$F_{g\perp} = \frac{\pi r_b^3 (2 - 3\cos\theta_{av} + \cos^3\theta_{av})}{3\sin^3\theta_{av}} \rho \cdot g \cos\alpha \tag{22}$$

The maximum radius of the drop at fall-off is obtained by balancing the forces perpendicular to the substrate as

$$r_{max} = \sqrt{\left(\frac{6(\sin^3\theta_{avg})(\cos\theta_{rcd} + \cos\theta_{adv})}{(2 - 3\cos\theta_{avg} + \cos^3\theta_{avg})(\pi - \theta_{rcd} - \theta_{adv})}\right)\left(\frac{\sigma}{(g\cos\alpha)(\rho_l - \rho_v)}\right)} \tag{23}$$

On an inclined surface, critical sized droplets first begin to slide-off, rather than fall, as on a horizontal substrate. Criticality is achieved by direct condensation growth or, alternatively, by coalescence with the adjoining drops. Thus, depending on the length scale of the substrate and the time scales of direct growth and growth due to coalescence, there are various possibilities on an inclined substrate. These include the following:

(i) Slide-off criticality is achieved, and during the entire slide-off on the substrate, fall-off criticality is not achieved.
(ii) Slide-off criticality is achieved, and during the slide-off on the substrate, fall-off criticality is also achieved before the droplet traverses the complete substrate length scale.

Both these possibilities have been incorporated in the mathematical model.

During slide-off, the body forces accelerate the droplets, and in the process many droplets on the path are swept away. The acceleration of the droplet is calculated by computing force components. Those parallel to the substrate are

(i) gravity force, $F_{g\|}$
(ii) force due to shear at the wall, F_s
(iii) retention force due to surface tension, $F_{r\|}$

A linear velocity distribution is assumed inside the moving drop, and the maximum velocity is taken to appear at its center of mass [33,34,44,45], which is at a distance of L from the substrate. The velocity gradient and shear stress are thus calculated as

$$\frac{du}{dy} = \frac{U}{L} \tag{24}$$

$$\tau = \mu_l \frac{du}{dy} = \mu_l \frac{U}{L} \tag{25}$$

The viscous force on the droplet is calculated as

$$F_s = \tau \cdot \pi \cdot r_b^2 \tag{26}$$

From these forces, the acceleration and velocity of the droplet are calculated as

$$a = \frac{F_{g\|} - F_s - F_{r\|}}{m} \tag{27}$$

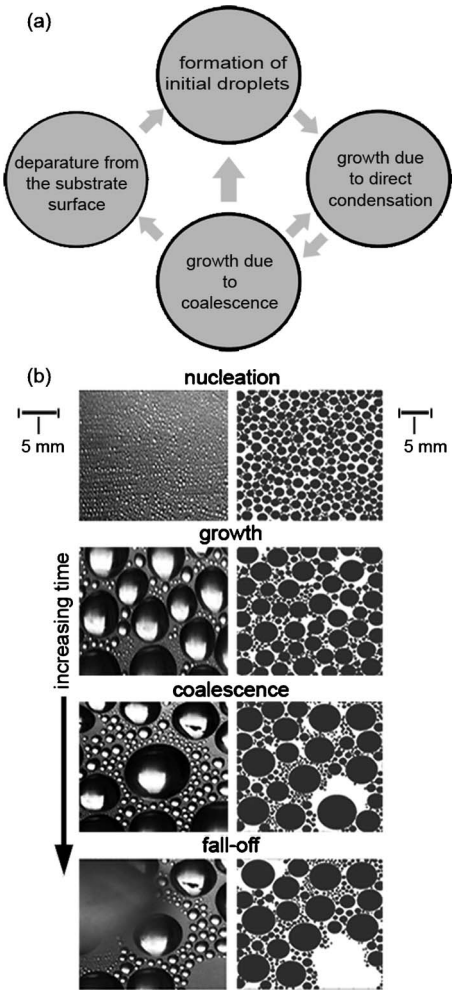

Fig. 4 (*a*) The cycle of major physical processes observed in the pendant mode of dropwise condensation on a horizontal substrate. (*b*) Qualitative comparison of experimental images of dropwise condensation on silanated glass substrate of area 25×25 mm² (coated with octyl-decyl-tri-chloro-silane, $C_{18}H_{37}C_{13}Si$) with corresponding images generated by simulation. The hazy patch seen in the top-left section of the last experimental image is due to the fact that the droplet has fallen on the viewing glass (view A) through which images are being recorded.

$$U_{\text{curr}} = U_{\text{prev}} + a \cdot dt \tag{28}$$

Finally, closure is obtained by externally supplying the wettability characteristics of the substrate, i.e., its average contact angle for a horizontal substrate and the advancing-receding angles for the inclined substrate, both from experimental data. Using these equations, the entire dropwise condensation process is simulated underneath an inclined substrate from initial nucleation to a dynamic quasi-steady state.

3.3 Model Assumptions. The following are the main assumptions considered during the development of the mathematical model.

1. Nucleation sites are randomly distributed on the surface. The initial nucleation site density of 10^9 m^{-2} is assumed [12].
2. The thermodynamically constrained smallest radius is taken as the minimum radius in the simulation. Initially, the substrate is virgin, and all nucleation sites are instantaneously occupied by the droplet of minimum radius.
3. Prior to reaching the critical volume for fall-off or slide-off, all drops are located at the weighted center of mass of the coalescing droplets.
4. Heat transfer resistance arises due to the liquid-vapor interface, curvature, and conduction, driven by subcooling of the substrate. Constriction resistance and convective transport of heat inside the drop are neglected.
5. The accommodation coefficient is taken to be 0.02 for water and 0.21 for sodium [3]. Although literature suggests that the accommodation coefficient is also a function of temperature, we have not changed its value in the simulations.
6. Droplet coalescence is assumed to be instantaneous and smooth (refer to footnote 4); inertia effects and change in the shape of the droplet due to acceleration are neglected.
7. An equivalent spherical cap approximation has been incorporated to model droplet shapes.
8. The dynamic variation in contact angle is neglected. For a particular surface-liquid combination, its value is taken to be constant and prescribed.
9. Partial fall-off of droplets is neglected; complete volume of the critical drop is removed.
10. The entire substrate is assumed to be at constant temperature; any local variation due to drop dynamics is neglected.

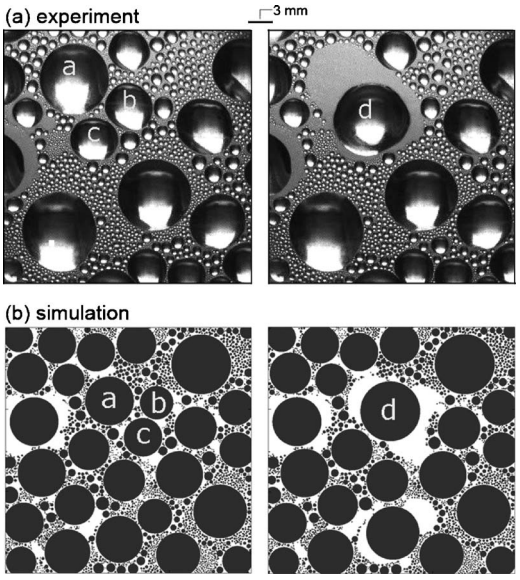

Fig. 5 Sequence of two images observed during experiment and corresponding simulation, showing coalescence of three droplets a, b, and c, resulting in the formation of a composite drop d

4 Results and Discussion

Dropwise condensation of distilled and de-ionized water, underneath a horizontal substrate and an inclined substrate having an angle of inclination of 15 deg, has been carried out on a glass substrate, which is coated by octyl-decyl-tri-chloro-silane ($C_{18}H_{37}C_{13}Si$). The saturation temperature is maintained at 27°C in all experiments with a cold substrate always maintained at 22°C. The static contact angle of water underneath the chemically textured substrate was measured to be 96 ± 0.5 deg for the droplet volume range of 50–100 μl. The experimental process is simulated by the mathematical model for both horizontal and inclined arrangements of the substrate, subject to features, assumptions, and limitations outlined in Sec. 3.3. Section 4.1 first reports the experimental observations of dropwise condensation on chemically textured horizontal and inclined surfaces. The data are compared against the simulation model presented in Sec. 3. After validation, simulations are performed for the range of parameters not covered in the experiments. Here, the effect of the static contact

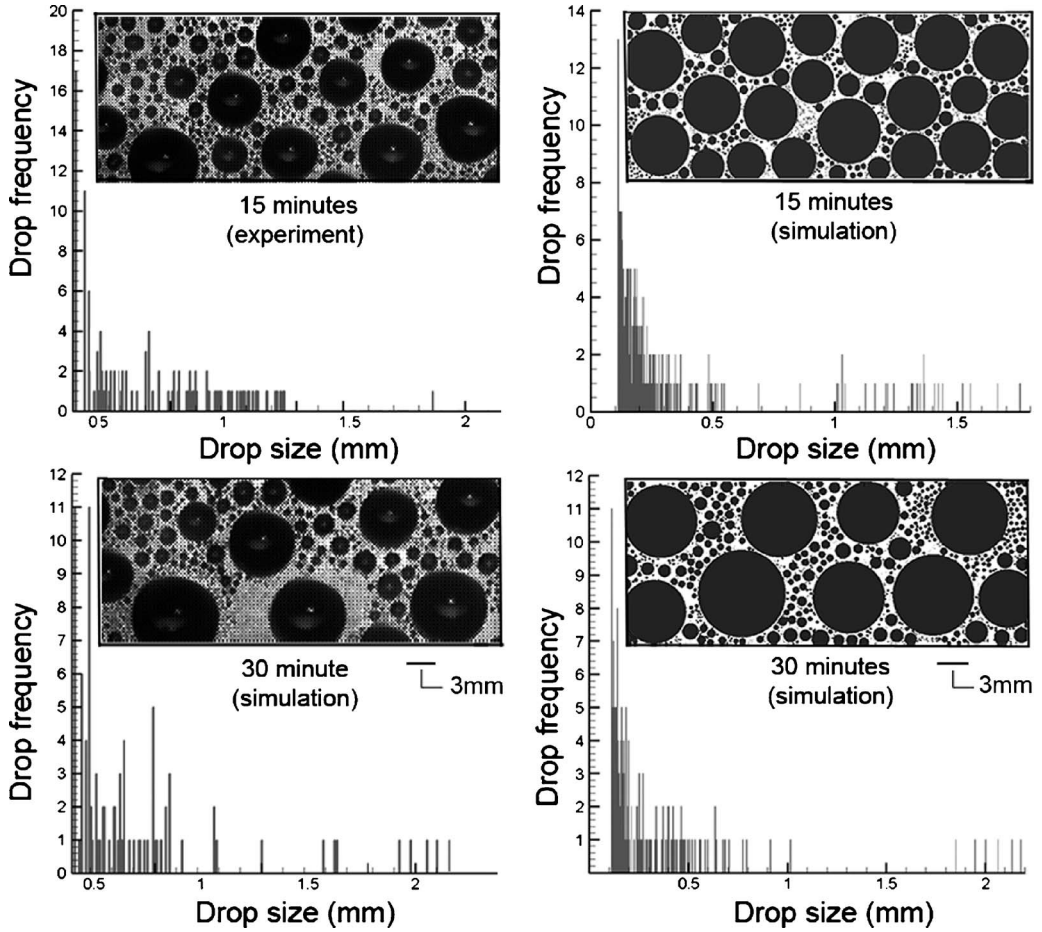

Fig. 6 Visual and statistical comparison of experimental and simulated spatial drop distribution patterns and the corresponding histograms of droplet frequency at the dynamic steady state

angle, thermophysical properties of the working fluid, physicochemical properties of the substrate, and the angle of inclination of the substrate are considered.

4.1 Experimental Observations and Comparison With Simulation. The experimental results and the corresponding numerical simulation of condensation of water at saturation temperature of 27°C ($\Delta T_{sat}=5°C$) are compared both on qualitative and quantitative terms. Major results are summarized in Figs. 4–11. Figure 4(*a*) schematically depicts the major observable processes of dropwise condensation underneath a horizontal substrate. These are nucleation, growth, coalescence, and fall-off of droplets. Figure 4(*b*) visually and qualitatively highlights these processes, as observed experimentally (view A in Fig. 1(*b*)) and captured in the computer simulation. The statistical nature of the overall process, with multiple generations of droplets in different stages of their respective growth phase and present simultaneously on the substrate, is clearly visible. Contrary to the perfect circular footprints of the droplet bases assumed in the simulation, local phenomena such as pinning of the contact line [10], capillary waves, contact line inertia during droplet merging, and the dynamics of the liquid-vapor interface cause deviations that are observable in the experiments. Specifically, droplet pinning and the noncircular base of the footprint can be clearly seen in the experimental images. Thus, the mathematical model can be further refined to cover local disturbances. However, major phenomena related to dropwise condensation underneath horizontal substrates are well simulated by the model.

Figure 5 depicts coalescence of three drops (marked as a, b, and c) as observed during the experiment and as revealed in the simulation. In the simulation, the center of the new resulting drop (after coalescence, i.e., drop d) is determined by a mass weighted average of centroids of constituent droplets before coalescence (i.e., droplets a, b, and c). The assumption that the coalesced volume takes up the weighted center of mass of the original droplets is vindicated by this representative comparison. The merger results in the exposure of virgin areas around the drop where renucleation of the new generation droplets will commence. Droplet mergers bring about near instantaneous changes in the total area coverage as well as the drop size distribution. A closer look at the edges of the droplets during experiments, especially the larger droplets, also reveals that the shapes of their bases are not exactly circular, showing local pinning phenomenon of the contact line at certain locations (e.g., see drop d in the experimental image). As droplets merge, experimental images show that it takes a certain finite time (of the order of 0.1–300 ms, depending on the respective sizes of the coalescing droplets) for the surface and body forces to redistribute the fluid in the coalesced drop and come to the state of minimum possible energy level; the new contact line shrinks and tends to be as circular as possible in a finite relaxation time; local pinning can distort its circularity.

Figure 6 shows the spatial drop size distributions underneath the horizontal substrate at 15 min and 30 min, respectively, after the commencement of the condensation process. No fall-off has yet taken place. The strong temporal variation in size distribution of droplets is clearly visible. As can be seen, after a 15 min time interval, the distribution shows moderately sized droplets with the maximum diameter of about ~2.0 mm. As time progresses, droplets merge, exposing virgin areas; an increase in the number den-

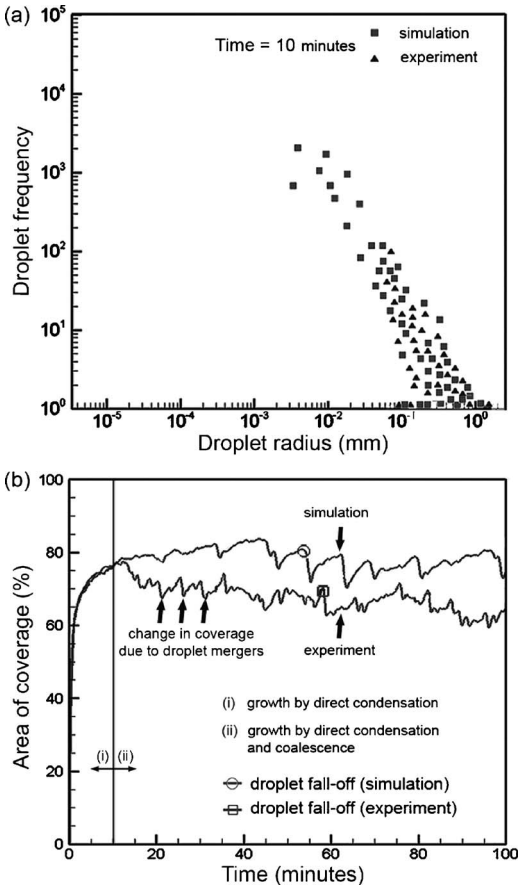

Fig. 7 (*a*) Drop size distribution from experiments and simulation at a time of 10 min after the commencement of dropwise condensation. (*b*) Time-wise variation in the area coverage of droplets over the substrate.

sity of very small droplets (below ~0.5 mm) is clearly visible at 30 min. In addition, the number density of larger droplets (greater than ~2.0 mm has increased substantially). The simulated histograms are denser than the experimental counterpart due to the loss

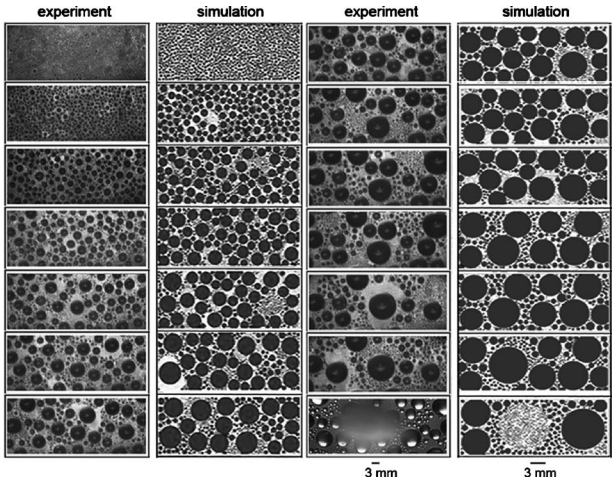

Fig. 8 Comparison of experiments and corresponding simulation for the complete sequence of dropwise condensation process, from the appearance of drops of minimum radius to the drops of critical radius underneath a horizontal silanated glass substrate of 25×10 mm^2 area

of information in experimental data during image processing of droplets below about 0.1 mm. For the same reason, the experimental and simulation histograms of the 15 min data are more dissimilar than those at 30 min. Initially, as condensation commences, the number of smaller sized droplets is quite large. At later times, droplets of higher diameter are greater in number, as noted earlier, and are captured well by the digital camera. In the latter part of the process, the growth is chiefly dominated by coalescence, and the number density distribution shifts toward larger sized drops.

Figure 7(*a*) compares the experimental and simulated droplet frequencies plotted as a function of the drop radius 10 min after the commencement of the condensation process. The experimental fall-off time for the first drop was approximately 58–62 min, while the simulation predicted a number in the range of 48–54 min. It is clear that drops whose radius is less than ~0.1 mm have not been recorded by the camera. The corresponding range of drop sizes that could be included in the simulation is 10^{-3}–1.0 mm. Although the order of magnitude of $r_{\min}$ (at time $t=0$) is $\sim10^{-4}$ mm, nearly all the original drops have since grown to the order of 10^{-3} mm at 10 min, mostly by direct condensation growth. Droplet coalescence has not yet started, as can be clearly seen in Fig. 7(*b*), where the temporal change in area coverage of drops is presented. Initially, there is a rapid increase in the coverage, and later, it approaches a dynamic quasi-steady state. Two distinct zones clearly seen in the experimental and simulation data are (i) growth due to direct condensation in the initial period and (ii) growth due to coalescence. Large local fluctuations in area coverage represent time instants when drops either coalesce to form larger drops or a large drop fall-off/slide-off. The fact that smaller drops could not be accounted due to imaging limitations explains the higher values of coverage area in simulation (73.1%) compared with experimental data (64.5%).

Figure 8 shows the complete sequence of experimental and simulated drop distributions, from the appearance of drops of minimum radius to the formation of drops of critical radius, underneath a horizontal substrate of 25×10 mm^2 area. The first image is at a time instant of 1 min, and thereafter the images are at 4 min intervals. The last image is presented at 59 min for the experiment and 50 min for the simulation. For this experiment, the first fall-off occurred at 58.5 min, while in the corresponding simulation, the first instance of fall-off was observed at 48 min and 10 s. This discrepancy may arise due to the following factors: (a) Noncondensable gases in the experimental chamber can deteriorate the heat transfer coefficient and delay the drop growth rate. (b) The local effects of pinning and contact line dynamics lead to higher frictional stresses, which enhance surface forces and delay fall-off. The comparisons shown in Fig. 8 for a horizontal substrate, however, show that the simulator satisfactorily captures the major processes of dropwise condensation, both from qualitative and quantitative standpoints.

4.1.1 Inclined Substrate. Various attributes of dropwise condensation of water at a saturation temperature of 27°C ($\Delta T_{\text{sat}}=5$°C) underneath an inclined substrate (15 deg from horizontal; $\theta_{\text{adv}}=111$ deg, $\theta_{\text{rcd}}=81$ deg), recorded in experiments and observed in numerical simulation, are shown in Figs. 9–11.

Major physical processes observed on an inclined substrate are similar to those of the horizontal substrate, except that the simple fall-off mechanism is replaced by a more complex combination of slide-off and fall-off. On an inclined substrate, a critically sized sliding droplet, while sweeping other droplets on its path, may either (i) reach the end of the substrate without falling off or (ii) acquire enough mass to be pulled in the downward direction, thus falling off from the substrate before actually reaching the edge of the substrate. The scenario realized will depend on the rate of growth of the drop, coalescence, and the length of the substrate itself. The other physical processes of nucleation, direct condensation growth, coalescence, and merger dynamics are quite similar

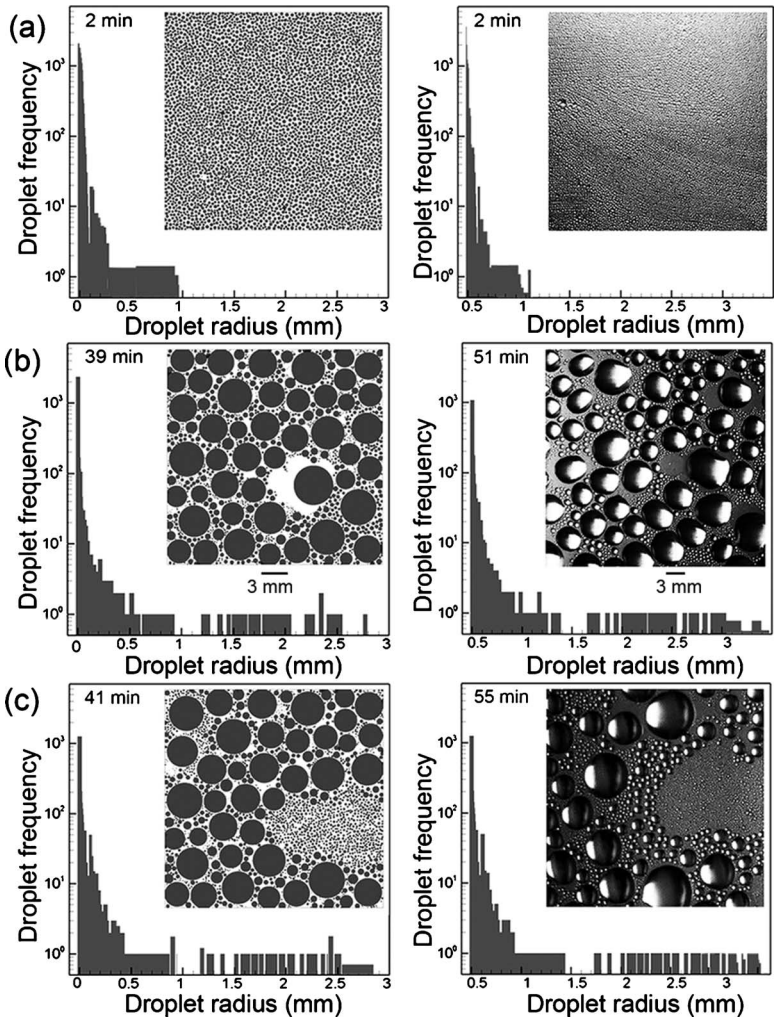

Fig. 9 Size distribution of drops condensing underneath an inclined (15 deg) silanated glass substrate of size 25×25 mm^2 as recorded in experiments and in the simulation: (*a*) at time=2 min from the commencement of dropwise condensation, (*b*) at critical state of slide-off, and (*c*) just after a complete sweeping action is completed by a sliding drop

to those of the horizontal substrate. The fact that the gravity vector now acts at an angle to the growing droplets leads to unsymmetrical drop deformation. The contact angle hysteresis plays a role in the static force balance, as explained in Sec. 3.

Figure 9 depicts the experimental images and histograms of droplet frequency along with the corresponding simulation data for the hydrophobic surface of 15 deg inclination. The critical stage of slide-off is also pictorially compared; a discrepancy in the actual time of slide-off in experiments as opposed to simulation is again observed. Soon after slide-off, virgin areas are created, nucleation sites are exposed, and renucleation commences, as shown in Fig. 9(*c*). Moreover, repeated removal of drops leads to the time averaged area of coverage being smaller for the inclined substrate when compared with the horizontal. At the instant of the first slide-off, the area coverage is 58.8% in simulation and 49.5% from experiments. The discrepancy is again primarily attributed to the loss of data pertaining to small sized droplets during experimental observations.

Figures 10 and 11 show the complete temporal sequence of events on the inclined substrate. Unlike a horizontal substrate, the drop dynamics on an inclined substrate is unique because the criticality of droplet motion and the series of events soon thereafter (sweeping and/or fall-off) happen extremely quickly leading to a sudden reduction in area coverage. It is clear from the histograms of Fig. 9 that the drop slide-off underneath the inclined substrate occurs earlier than the corresponding time instant of fall-off underneath a horizontal substrate. Figure 11 depicts the complex sequence of slide-off, rapidly followed by sweeping, fall-off, and renucleation. After the first instance of slide-off, it is interesting to note that the subsequent slide-offs and sweeping actions occur at a greater frequency. The mathematical model satisfactorily captures these processes.

4.2 Parametric Study. The effect of the static contact angle, namely, the wettability and substrate inclination, and the effect of the thermophysical properties of the working fluid on dropwise condensation patterns are parametrically explored in the present section at a condensation temperature of 30°C and a cold substrate temperature of 25°C. The mathematical model of Sec. 3 is used for data generation. During simulation, the nucleation site density has again been taken as 10^9 m^{-2}.

The effect of the wettability of the condensing liquid on the substrate is explored in Fig. 12(*a*), where the spatial drop distribution underneath a horizontal chemically textured substrate of 20×20 mm^2 area, just before fall-off, is pictorially depicted. A reduction in wettability increases the contact angle and leads to a smaller base circle of the drop and, therefore, smaller surface forces holding the drop. Thus, two effects are clearly visible. (i)

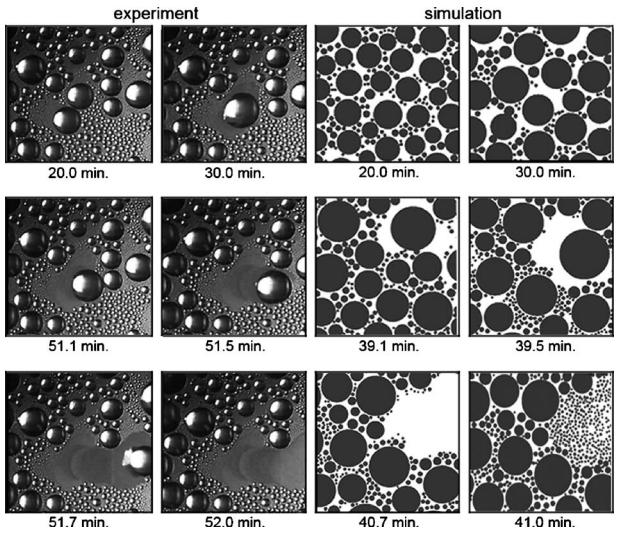

Fig. 10 Various temporal stages of droplet condensation on the inclined substrate (15 deg) recorded during experiments and simulation. The commencement of sliding and sweeping actions of the drop as it gathers mass during transit and renucleation of the virgin exposed surface, when the sweeping action is complete, are clearly seen.

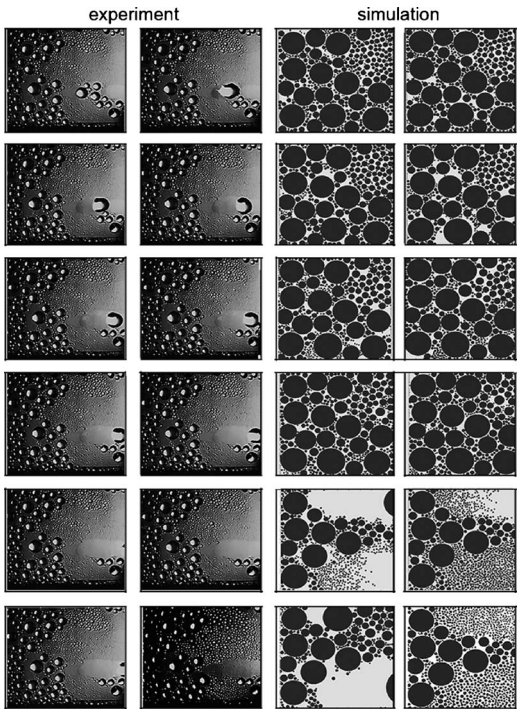

Fig. 11 Sequence of images from experiments as well as simulation showing drop slide-off and the subsequent sweeping action on a 15 deg inclined 25×25 mm^2 substrate. A dynamic steady state in the process has been achieved. Once slide-off commences, the drop quickly gathers mass during the sweeping action and subsequently falls off.

The droplet volume at the time of fall-off is smaller. The area coverage of the drops, seen in Fig. 12(*b*), is smaller as well. The quasi-steady state area coverage varies with contact angle from 73.3% for 90 deg, 67.1% for 105 deg, and 52.4% for 120 deg. (ii) With increasing contact angle, the drops achieve fall-off criticality earlier in the cycle, as shown in Fig. 12(*c*). All other conditions remaining unchanged, the fall-off time for a pendant drop is seen

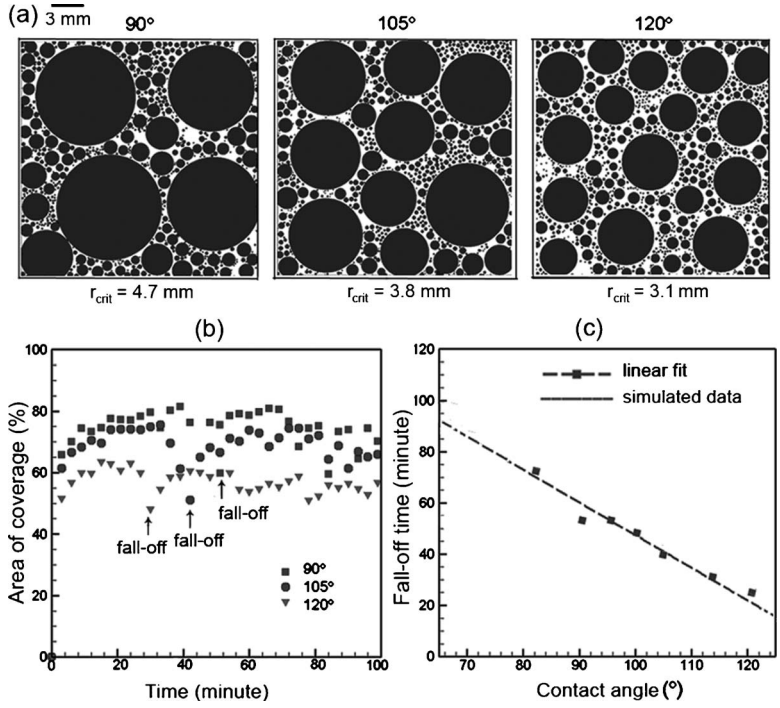

Fig. 12 Effect of wettability: (*a*) Simulated spatial droplet distribution just before fall-off of a drop underneath a horizontal substrate of 20×20 mm^2 area for contact angles of 90 deg, 105 deg, and 120 deg. (*b*) Temporal variation in coverage area of drops. (*c*) Fall-off time of the drop as a function of the contact angle (for all cases working fluid: water; T_{sat}=30°C, ΔT_{sat}=5°C).

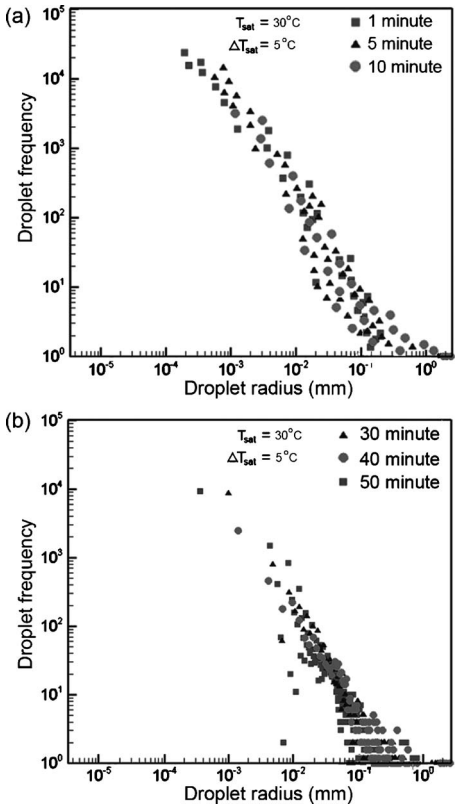

Fig. 13 ((*a*) and (*b*)) Temporal variation in drop size distribution for condensing water vapor underneath a horizontal silanated glass substrate (contact angle of 90 deg). For clarity, data for 1–10 min are separately plotted from the data of 30–50 min. The fall-off time for the first drop was equal to 48 min in this simulation. Immediately after fall-off (at 50 min), very small drops reappear because of the virgin area created after fall-off.

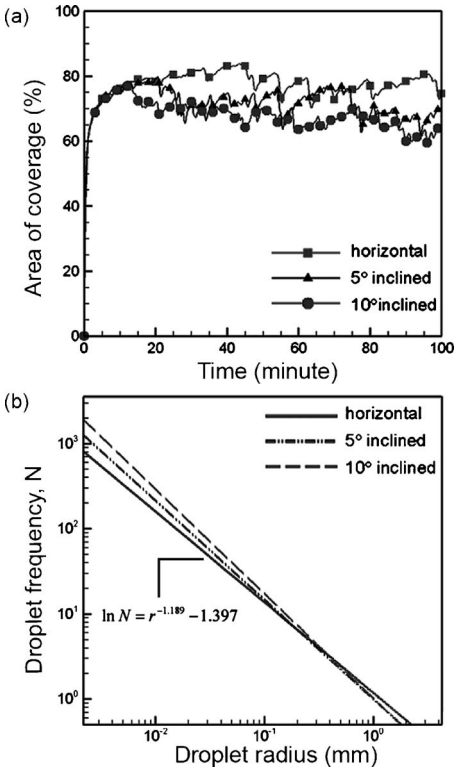

Fig. 14 Effect of substrate inclination: (*a*) Temporal variation in area coverage of drops during condensation of water in the pendant mode. (*b*) Drop size distribution just before fall-off (for horizontal substrate) or slide-off (inclined substrate). For this simulation, the wettability of the substrate is such that θ_{adv} =106 deg and θ_{rcd}=74 deg for angle of inclination of 5 deg and θ_{adv}=110 deg and θ_{rcd}=61 deg for angle of inclination of 10 deg; the droplet is assumed to be hemispherical on a horizontal surface; T_{sat}=30°C, ΔT_{sat}=5°C.

to be a linear function of the contact angle.

Figure 13(*a*) shows the frequency (namely, the number of drops) as a function of the drop radius, 10 min after commencement of condensation. At later times, drops of higher sizes are to be seen. For the present simulation, the fall-off time of the first drop was 48 min. Figure 13(*b*) shows that very small droplets nucleate on the substrate at $t=50$ min, immediately after the first drop falls off at $t=48$ min.

The effect of substrate inclination on the temporal distribution of area coverage is presented in Fig. 14(*a*). Inclination of the substrate facilitates easier movement of drops by sliding, leading to a droplet sweeping action. Therefore, the effective steady state coverage is smaller for inclined substrates, changing from 67.4% for the substrate with 10 deg inclination to 71.2% for 5 deg inclination, and 76.1% for a horizontal substrate. At the instant of the first fall-off (for the horizontal substrate) and the first slide-off (for the inclined substrate), Fig. 14(*b*) depicts the drop size distribution as a function of radius for various inclination angles. The distribution follows a power law with the negative slope increasing with the substrate angle, reflecting the repeated appearance of small drops at fresh nucleation.

For a given degree of subcooling ($\Delta T_{sat}=5°C$), the effect of saturation temperature on drop departure time is shown in Fig. 15 (working fluid: water). It is seen that increasing the saturation temperature reduces the fall-off time (and hence the size of the largest drop), indicating an increase in the overall heat transfer coefficient. The diffusional thermal resistance within the drop is a major limiting factor of condensation heat transfer. Hence, increasing the saturation temperature increases the thermal conductance of the water drop in the applicable range of the simulation. A marginal increase in the overall resistance is also noticed due to a reduction in the interfacial heat transfer coefficient; it essentially proves to be inconsequential as the overall thermal resistance is dominated by the conduction resistance of the droplet [14,46,47].

The effect of Prandtl number on convective heat transfer is well

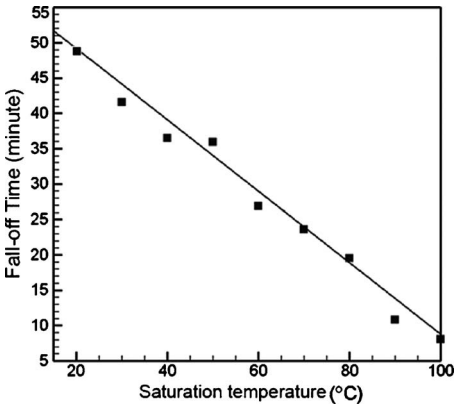

Fig. 15 Variation in drop departure time (time required for first fall-off) on a horizontal substrate with respect to the saturation temperature. Fluid employed is water, subcooling ΔT_{sat}=5°C, contact angle=90 deg, and nucleation site density=10^9 m^{-2}. For a given nucleation site density, the fall time has an uncertainty of ±3 min, depending on the random assignment of initial droplet centers on the substrate.

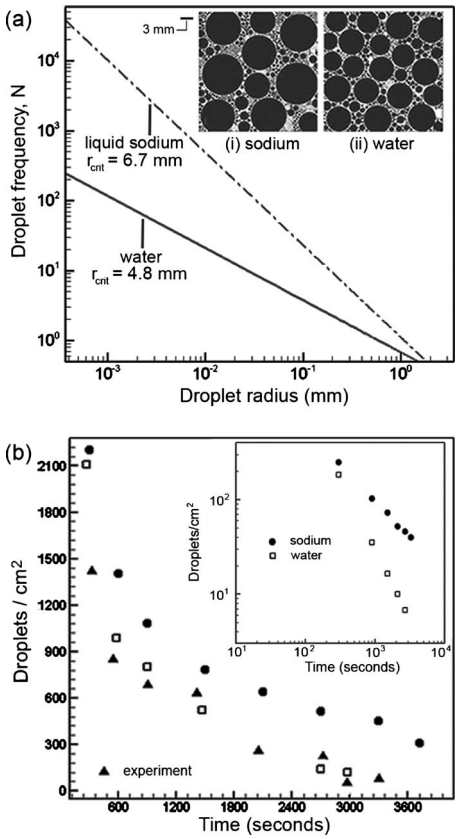

Fig. 16 (*a*) **Spatial drop distribution for condensation underneath horizontal stainless steel substrate just before fall-off for (i) liquid sodium (T_{sat}=342°C, ΔT_{sat}=5°C, θ=108 deg) and (ii) water (T_{sat}=30°C, ΔT_{sat}=5°C, θ=73 deg), with the corresponding pictorial depiction in the inset. For liquid sodium, the fall-off time is 66 min, and for water it is 48.** (*b*) **The temporal variation in the number density of drops of water and sodium from the commencement of condensation until 60 min.**

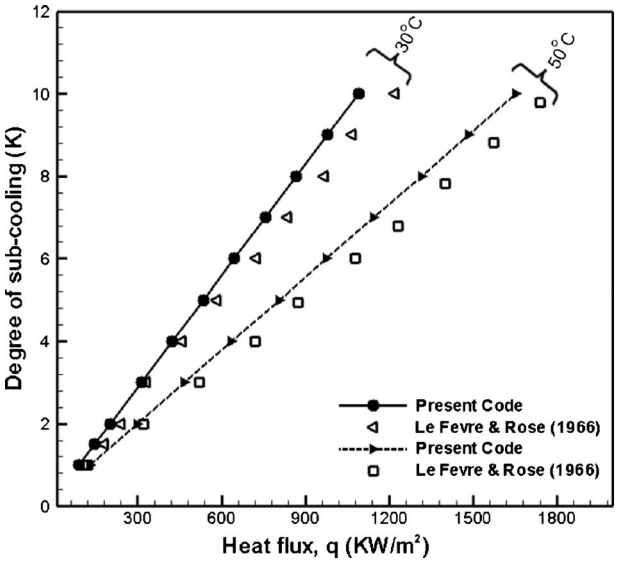

Fig. 17 Variation in heat transfer coefficient for dropwise condensation of water on a horizontal substrate at T_{sat}=30°C and T_{sat}=50°C with the degree of subcooling. The results from the present simulator are compared with the prediction model of Le Fevre and Rose for dropwise condensation of water on a promoter layer, as reported by Rose [1].

documented. In many situations, a singular behavior is observed for low Prandtl number systems, for example, liquid metals where $Pr \sim 10^{-2}$. Moreover, condensation of liquid metals also plays an important role in many engineering processes.

The results obtained by extending the present model to dropwise condensation of liquid metals are depicted in Figs. 16(*a*) and 16(*b*). The spatial distributions of drops underneath a horizontal substrate, just before fall-off, are compared in Fig. 16(*a*) for water and liquid sodium. Owing to the higher surface tension of liquid sodium, the departing drop size, as governed by critical Bond number, is considerably larger for sodium, being ~6.7 mm, as against ~4.8 mm for water. In liquid metals, a large number of small drops are present on the substrate, whereas the number density of small drops for condensing water is smaller (see inset of Fig. 16(*a*)). Figure 16(*b*) shows the temporal variation in the number density of drops of water and sodium from the commencement of condensation until 60 min. As condensation proceeds from time t=0, the droplet distribution and density continuously change; this variation follows a power law with time ($t \sim^{-\alpha}$) with α=1.54 for water and 0.76 for sodium. Experimental data for water condensing on chemically textured silanated glass are also shown for comparison. The inset shows these data on a log-log scale.

The variation in the average heat transfer coefficient for dropwise condensation of water with respect to the degree of subcooling (T_{sat}-T_w) at condensation temperatures 30°C and 50°C, respectively, on a horizontal chemically textured substrate is shown in Fig. 17. To calculate the average heat transfer coefficient, the simulation is continued for a period of 3 h. The amount of condensate collected, namely, the net summation of the fall-off volume in the entire period is tracked to determine the total latent heat transfer. The comparison of the present simulation with the theory put forward by Le Fevre and Rose for dropwise condensation of water on a monolayer promoter layer, as reported by Rose [1], is also shown.

The variation in the critical angle of inclination for the commencement of sliding with respect to the droplet radius for various liquid metals is shown in Fig. 18(*a*). The advancing and receding angles are taken to be known quantities for the purpose of simulation. For a given drop radius, the ordinate represents the angle that the substrate makes with the horizontal. At this stage of criticality, the weight of the drop exceeds the surface force holding it, resulting in either a fall-off or a slide-off. Increasing the angle of substrate inclination decreases the radius at which droplet slide-off commences. The critical angle of inclination also depends on the surface tension of the liquid; larger surface tension liquids have a greater critical inclination angle before sliding starts. The effect of the contact angle hysteresis on the critical angle of inclination is seen in Fig. 18(*b*). As the contact angle hysteresis is reduced, the critical angle of inclination for sliding motion reduces.

5 Conclusions

The heat transfer coefficient during dropwise condensation is two to three orders of magnitude higher than in filmwise condensation and is a preferred mode in many processes. Prediction of the heat transfer coefficient in dropwise condensation poses many challenges. Most heat transfer models proposed in the literature require a priori knowledge of the drop size distribution and the number density of condensing droplets after cyclic quasi-steady state is reached. These data are also required to calculate the average shear stress on the substrate arising from continuous cycles of dropwise condensation. Comprehensive inclusion of all forces affecting the droplet dynamics is thus essential for the prediction of transport properties of interest.

Against this background, a detailed simulation of dropwise condensation is proposed from first principles. The simulator is applicable for condensation underneath horizontal and inclined substrates. It accounts for growth by direct condensation and

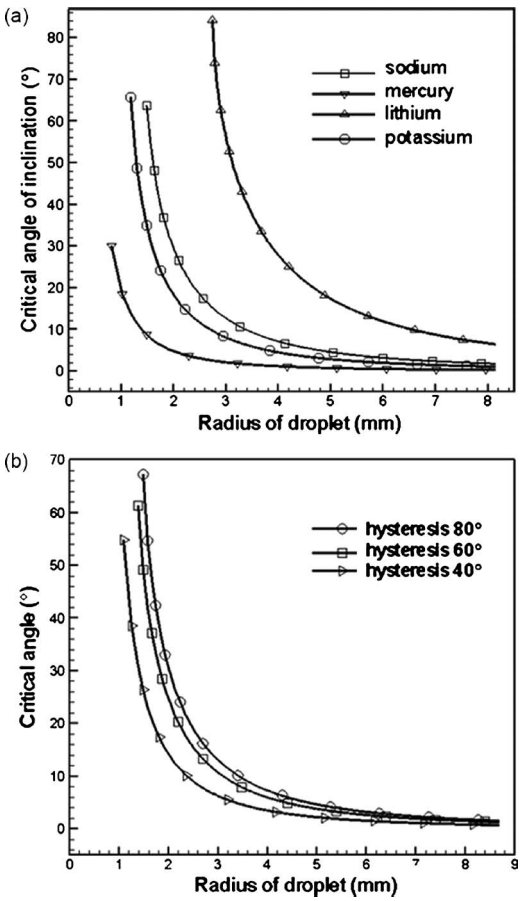

Fig. 18 (*a*) Critical angle of inclination of the substrate as a function of the drop size with respect to fall-off (horizontal substrate)/slide-off (inclined substrate). (*b*) Effect of contact angle hysteresis on the critical radius of the drop.

coalescence, subsequently resulting in drop motion due to force imbalances. Specific experiments have been carried out on a salinated glass substrate to understand the mechanisms of droplet growth, coalescence, and fall-off and slide-off behaviors. The data recorded in experiments are compared with those of the simulation. Post-validation, the simulator is extended for contexts not covered by the experiments. The effects of the contact angle, contact angle hysteresis, inclination of the substrate, thermophysical properties of the working fluid, and the saturation temperature of condensation are investigated. The following conclusions have been arrived at in the present study:

1. The mathematical model presented captures the major constituents of the dropwise condensation process quite satisfactorily. While there may be many reasons for the discrepancy between the predictions of the model and experimental data, some of which have been discussed in the paper, looking at the experiments closely we do believe that highly localized three-phase contact line dynamics, related to the anisotropic distribution of surface energy and surface roughness distribution, are likely candidates for further scrutiny and need to be incorporated in the model.
2. Essentially two distinct growth phases of droplet growth are observed: (a) growth due to direct condensation and (ii) growth primarily due to coalescence. The area fraction covered by the drops increases as the drops grow and finally achieves a dynamic quasi-steady state after many cycles of coalescence and fall-off/slide-off.
3. An increase in static contact angle (decrease in wettability of the substrate) reduces the droplet area coverage. Reduction of coverage is also observed by increasing the substrate inclination.
4. A decrease in wettability also results in earlier fall-off (horizontal substrate)/earlier slide-off (inclined substrate). In all cases, the simulations predict earlier fall-off than in experiments.
5. Inclining the substrate results in a larger number of small drops and hence in a higher heat transfer coefficient. This is because the resistance to heat transfer per unit area is smaller in smaller drops compared with larger drops.
6. At a higher saturation temperature, the rate of growth of the drop is higher. Heat transfer coefficient increases with an increase in the degree of subcooling of the substrate and is a strong function of the Prandtl number of the fluid. This is primarily due to the fact that diffusional resistance of the liquid drop constitutes the major thermal resistance in the flow of heat from the vapor to the substrate.
7. The critical radius of droplet, at which commencement of sliding takes place, is a function of the thermophysical properties of the fluid, inclination of the substrate and contact angle hysteresis. Fluids with higher surface tension show a larger critical radius. Reduction in contact angle hysteresis reduces the critical radius of the droplet at fall-off for a given angle of inclination.

Acknowledgment

The authors are grateful to the Board of Research in Nuclear Sciences (BRNS), Department of Atomic Energy, Government of India for providing the financial assistance to carry out this research work. Help provided by Dr. Animangsu Ghatak in coating glass substrates is acknowledged.

Nomenclature

A = area of cross section (m^2)
a = acceleration of the moving droplet (m^2/s)
F = force (N)
h = latent heat of vaporization of the liquid (kJ/kg)
k = thermal conductivity (W/m K)
L = length (m)
$\bar{M}$ = molecular weight of the condensing liquid (kg/kmol)
q = surface heat flux (W/m^2)
$\bar{R}$ = universal gas coefficient (J/kmol K)
r = radius of droplet (m)
T = temperature (K)
ΔT = temperature drop (K)
Δt = time step (s)
U = velocity of the moving droplet (m/s)
V = volume of the drop (m^3)

Greek Symbols

α = inclination angle (deg)
η = dynamic viscosity (Pa s)
λ = wavelength of light (m)
ν = specific volume at the saturation temperature (m^3/kg)
ϕ = azimuthal angle (deg)
ρ = density (kg/m^3)
σ = surface tension of liquid (N/m)
$\hat{\sigma}$ = accommodation coefficient
τ = shear stress (N/m^2)
θ = contact angle (deg)

Subscripts

adv = advancing
avg = average

b = base
c = condensate
cond = conduction
crit = critical
curr = current
curv = curvature
d = droplet
g = gravity
int = interfacial heat and mass transfer
l = liquid
lv = liquid-vapor interface
max = maximum
min = minimum
prev = previous
r = retention
rcd = receding
sat = saturation
sl = solid-liquid interface
s = shear
sc = spherical cap
t = total
v = vapor
w = wall
$\parallel$ = parallel to the substrate
$\perp$ = perpendicular to the substrate

References

[1] Rose, J. W., 2002, "Dropwise Condensation Theory and Experiments: A Review," Proc. Inst. Mech. Eng., Part A, **216**, pp. 115–128.
[2] Leipertz, A., and Fröba, A. P., 2006, "Improvement of Condensation Heat Transfer by Surface Modification," *Proceedings of the Seventh ASME, Heat and Mass Transfer Conference*, IIT Guwahati, India, K7, pp. k85–k99.
[3] Carey, V. P., 1992, *Liquid-Vapor Phase-Change Phenomena*, Hemisphere, New York, pp. 342–351.
[4] Marto, P. J., Looney, D. J., and Rose, J. W., 1986, "Evaluation of Organic Coating for the Promotion of Dropwise Condensation of Steam," Int. J. Heat Mass Transfer, **29**, pp. 1109–1117.
[5] Zhao, Q., Zhang, D. C., Lin, J. F., and Wang, G. M., 1996, "Dropwise Condensation on L-B Film Surface," Chem. Eng. Process., **35**, pp. 473–477.
[6] Vemuri, S., Kim, K. J., Wood, B. D., Govindaraju, S., and Bell, T. W., 2006, "Long Term Testing for Dropwise Condensation Using Self-Assembled Monolayer Coating of N-Octadecyl Mercaptan," Appl. Therm. Eng., **26**, pp. 421–429.
[7] Rausch, M. H., Fröba, A. P., and Leipertz, A., 2008, "Dropwise Condensation Heat Transfer on Ion Implanted Aluminum Surfaces," Int. J. Heat Mass Transfer, **51**, pp. 1061–1070.
[8] Ma, X.-H., and Wang, B.-X., 1999, "Life Time Test of Dropwise Condensation on Polymer-Coated Surfaces," Heat Transfer Asian Res., **28**(7), pp. 551–558.
[9] Majumdar, A., and Mezic, I., 1999, "Instability of Ultra-Thin Water Film and the Mechanism of Droplet Formation on Hydrophobic Surfaces," ASME Trans. J. Heat Transfer, **121**, pp. 964–970.
[10] Bertier, J., 2008, *Microdrops and Digital Micro-Fluidics*, William Andrew, Norwich, NY, pp. 130–135.
[11] Sikarwar, B. S., Muralidhar, K., and Khandekar, S., 2010, "Flow and Thermal Fields in a Pendant Droplet Moving on Lyophobic Surface," 14th International Heat Transfer Conference, Washington, D.C., Paper No. IHTC14-22520.
[12] Leach, R. N., Stevens, F., Langford, S. C., and Dickinson, J. T., 2006, "Experiments and Simulations of Nucleate and Growth of Water Drops in a Cooling System," Langmuir, **22**, pp. 8864–8872.
[13] McCormick, J. L., and Baer, E., 1963, "On the Mechanism of Heat Transfer in Dropwise Condensation," J. Colloid Sci., **18**, pp. 208–216.
[14] Bansal, G. D., Khandekar, S., and Muralidhar, K., 2009, "Measurement of Heat Transfer During Dropwise Condensation of Water on Polyethylene," Nanoscale Microscale Thermophys. Eng., **13**, pp. 184–201.
[15] Tartarini, P., Lorenzini, G., and Randi, M. R., 1999, "Experimental Study of Water Droplet on Hot, Non-Porous Surfaces," Heat Mass Transfer, **34**(6), pp. 437–447.
[16] Briscoe, B. J., and Galvin, K. P., 1991, "The Sliding of Sessile and Pendent Droplets the Critical Condition," J. Colloid Interface Sci., **52**, pp. 219–229.
[17] Lawal, A., and Brown, R. A., 1982, "The Stability of an Inclined Pendent Drop," J. Colloid Interface Sci., **89**, pp. 332–345.
[18] Glicksman, R. L., and Hunt, W. A., 1972, "Numerical Simulation of Dropwise Condensation," Int. J. Heat Mass Transfer, **15**, pp. 2251–2269.
[19] Wu, W. H., and Maa, J. R., 1976, "On the Heat Transfer in Dropwise Condensation," Chem. Eng. J., **12**, pp. 225–231.
[20] Maa, J. R., 1978, "Drop-Size Distribution and Heat Flux of Dropwise Condensation," Chem. Eng. J., **16**, pp. 171–176.
[21] Abu-Orabi, M., 1998, "Modeling of Heat Transfer in Dropwise Condensation," Int. J. Heat Mass Transfer, **41**, pp. 81–87.
[22] Rose, J. W., and Glicksman, L. R., 1973, "Dropwise Condensation—The Distribution of Drop Sizes," Int. J. Heat Mass Transfer, **16**, pp. 411–425.
[23] Gose, E., Mucciordi, A. N., and Baer, E., 1967, "Model for Dropwise Condensation on Randomly Distributed Sites," Int. J. Heat Mass Transfer, **10**, pp. 15–22.
[24] Burnside, B. M., and Hadi, H. A., 1999, "Digital Computer Simulation of Dropwise Condensation From Equilibrium Droplet to Detectable Size," Int. J. Heat Mass Transfer, **42**, pp. 3137–3146.
[25] Vemuri, S., and Kim, K. J., 2006, "An Experimental and Theoretical Study on the Concept of Dropwise Condensation," Int. J. Heat Mass Transfer, **49**, pp. 649–657.
[26] Eucken, A., 1937, "Energie Und Stoffaustausch an Grenzflächen," Naturwiss., **25**, pp. 209–218.
[27] Briscoe, B. J., and Galvin, K. P., 1991, "Growth With Coalescences During Condensation," Phys. Rev. A, **43**, pp. 1906–1917.
[28] Rose, J. W., 1976, "Further Aspects of Dropwise Condensation Theory," Int. J. Heat Mass Transfer, **19**, pp. 1363–1370.
[29] Mu, C., Pang, J., and Liu, T., 2008, "Effect of Surface Topography of Material on Nucleation Site Density of Dropwise Condensation," Chem. Eng. Sci., **63**, pp. 874–880.
[30] Narhe, R., Beysens, D., and Nikolayev, V. S., 2004, "Contact Line Dynamics in Drop Coalescence and Spreading," Langmuir, **20**, pp. 1213–1221.
[31] Wu, M., Cubaud, T., and Ho, C. M., 2004, "Scaling Law in a Liquid Drop Coalescence Driven by Surface Tension," Phys. Fluids, **16**(7), pp. L51–L54.
[32] Liao, Q., Zhu, X., Xing, S. M., and Wang, H., 2008, "Visualization Study on Coalescence Between Pair of Water Drops on Inclined Surfaces," Exp. Therm. Fluid Sci., **32**(8), pp. 1647–1654.
[33] Das, A. K., and Das, P. K., 2009, "Simulation of Drop Movement of an Inclined Surface Using Smoothed Particle Hydrodynamics," Langmuir, **25**, pp. 11459–11466.
[34] Sikarwar, B. S., Muralidhar, K., and Khandekar, S., 2010, "Flow and Heat Transfer in a Pendant Liquid Drop on an Inclined Plane," *Proceedings of the Ninth ASME Heat and Mass Transfer Conference*, IIT Mumbai, India, Paper No. 345, pp. 1322–1329.
[35] Grand, N. L., Daerr, A., and Limit, L., 2005, "Shape and Motion of Drops Sliding Down an Inclined Plane," J. Fluid Mech., **541**, pp. 253–315.
[36] Pierce, E., Carmona, F. J., and Amirfazli, A., 2008, "Understanding of Sliding and Contact Angles Results in Tilted Plate Experiments," Colloids Surf., A, **323**, pp. 73–82.
[37] ElSherbini, A. I., and Jacobi, A. M., 2004, "Liquid Drops on Vertical and Inclined Surfaces: I. An Experimental Study of Drop Geometry," J. Colloid Interface Sci., **273**, pp. 556–565.
[38] Dimitrakopoulos, P., and Higdon, J. J. L., 1999, "On the Gravitational Displacement of Three-Dimensional Fluid Droplets From Inclined Solid Surfaces," J. Fluid Mech., **395**, pp. 181–209.
[39] Korte, C. M., and Jacobi, A. M., 2001, "Condensate Retention Effects on the Performance of Plain-Fin and Tube Heat Exchangers: Retention Data and Modeling," ASME J. Heat Transfer, **123**, pp. 926–936.
[40] Dussan, E. B., V, and Chow, R. T., 1983, "On the Ability of Drops or Bubbles to Stick to Non-Horizontal Surfaces of Solids," J. Fluid Mech., **137**, pp. 1–29.
[41] Bouteau, M., Cantin, S., Benhabib, F., and Perrot, F., 2008, "Sliding Behavior of Liquid on Tilted Langmuir-Blodgett Surfaces," J. Colloid Interface Sci., **317**, pp. 247–254.
[42] ElSherbini, A. I., and Jacobi, A. M., 2004, "Liquid Drops on Vertical and Inclined Surfaces: II. A Method for Approximating Drop Shapes," J. Colloid Interface Sci., **273**, pp. 566–575.
[43] Extrand, C. W., and Kumara, Y., 1995, "Liquid Drop on an Inclined Plane: The Relation Between Contact Angles, Drop Shape and Retentive Forces," J. Colloid Interface Sci., **170**, pp. 515–521.
[44] Sakai, M., Hashimoto, A., Yoshida, N., Suzuki, S., Kameshima, Y., and Nakajima, A., 2006, "Direct Observation of Internal Fluidity in a Water Droplet During Sliding on Hydrophobic Surfaces," Langmuir, **22**, pp. 4906–4909.
[45] Kim, H. Y., Lee, H., and Kang, B. H., 2002, "Sliding of Drops Down an Inclined Solid Surface," J. Colloid Interface Sci., **247**, pp. 372–380.
[46] Sadhal, S. S., 1997, *Transport Phenomena With Drops and Bubbles* (Mechanical Engineering Series), Springer, New York, pp. 218–230.
[47] Koch, G., Kraft, K., and Leipertz, A., 1998, "Parameter Study on the Performance of Dropwise Condensation," Int. J. Therm. Sci., **37**, pp. 539–548.

Heat and Mass Transfer on the MHD Fluid Flow Due to a Porous Rotating Disk With Hall Current and Variable Properties

Mustafa Turkyilmazoglu
Department of Mathematics,
Hacettepe University,
06532 Beytepe, Ankara, Turkey
e-mail: turkyilm@hacettepe.edu.tr

The steady magnetohydrodynamics (MHD) laminar compressible flow of an electrically conducting fluid on a porous rotating disk is considered in the present paper. The governing equations of motion are reduced to a set of nonlinear differential equations by means of similarity transformations. The fluid properties are taken to be strong functions of temperature and Hall current that also readily accounts for the viscous dissipation and Joule heating terms. Employing a highly accurate spectral numerical integration scheme, the effects of viscosity, thermal conductivity, Hall current, magnetic field, suction/injection, viscous dissipation, and Joule heating on the considered flow are examined. The quantities of particular physical interest, such as the torque, the wall shear stresses, the vertical suction velocity, and the rate of heat transfer are calculated and discussed.
[DOI: 10.1115/1.4002634]

Keywords: rotating disk, conducting fluid, variable properties, Joule heating, shear stress, heat transfer

1 Introduction

A considerable effort has been spent in the recent research for the study of MHD fluid flow and heat transfer over a rotating disk. Rotating disk flows of conducting fluids are not only of theoretical interest, but they are also of practical significance in many areas, such as rotating machinery, computer storage devices, gas turbine rotors, and crystal growth processes. The present study thus deals with the steady laminar compressible MHD fluid flow over a rotating disk along with heat transfer, when the flow variables are considered as strongly depended on the temperature field.

The hydrodynamic flow due to an infinite rotating disk was first introduced in the pioneering work by Von-Kármán. The following studies, Refs. [1,2], to investigated the impacts of a uniform suction or injection of fluid through the surface of a rotating disk. Among many others, Kumar et al. [3] and Ariel [4] examined the hydromagnetic extension and the influence of an external uniform magnetic field on the steady flow due to a rotating disk. When strong magnetic field is effectively taken into account, Hall current becomes a driving force of the magnetohydrodynamic flow as pointed out in Refs [5,6]. Taking into consideration that the physical properties may significantly change with the temperature of the flow, Maleque and Sattar [7] solved the problem when the fluid properties were varying function of the temperature. An asymptotic model was presented in Ref. [8], which was used for heat transfer analysis from a rotating disk to fluids for a wide range of Prandtl numbers. Exact solutions corresponding to the viscous incompressible and conducting fluid flow due to a porous rotating disk were recently presented by Turkyilmazoglu [9].

In the current paper, we consider the viscous, steady, and compressible permeable rotating disk boundary layer flow of an electrically conducting fluid (specifically flue gas). Our prime motivation is to extend the variable properties study of Ref. [7] to incorporate into the viscous dissipation and Joule heating in the corresponding energy equation. It is then intended to work out the effects of these physical features on the behavior of mean flow, skin-friction coefficients, torque, and heat transfer. For this purpose, the governing nonlinear partial differential equations are integrated numerically by means of a highly accurate spectral technique. During the numerical computations, it was spotted that a numerical error was made in Ref. [7], which substantially changes some of the conclusions they reached.

The outline of this paper is as follows. In Sec. 2, the governing equations are highlighted. The numerical solutions are presented in Sec. 3. Finally, Sec. 4 contains the conclusions.

2 Formulation of the Problem

Our concern here is with the three-dimensional, steady MHD laminar boundary layer flow of a compressible, electrically conducting viscous fluid over an infinitely rotating disk in the presence of an external magnetic field and Hall current. The flow description and geometrical coordinates are depicted in Fig. 1. Since similar equations are also given in Ref. [7], after the usual assumptions we only present the equations in subsequent dimensionless form

$$H' + 2F + d\gamma(1+\gamma\theta)^{-1}\theta' H = 0$$

$$F'' + a\gamma(1+\gamma\theta)^{-1}\theta' F' - [F^2 - G^2 + HF'](1+\gamma\theta)^{d-a} - \frac{M}{1+m^2}(F - mG)(1+\gamma\theta)^{-a} = 0$$

$$G'' + a\gamma(1+\gamma\theta)^{-1}\theta' G' - [2FG + HG'](1+\gamma\theta)^{d-a} - \frac{M}{1+m^2}(G + mF)(1+\gamma\theta)^{-a} = 0$$

$$\theta'' + b\gamma(1+\gamma\theta)^{-1}\theta'^2 - \mathrm{Pr}(1+\gamma\theta)^{d-b}\theta' H + \mathrm{Ec}(1+\gamma\theta)^{a-b}(F'^2 + G') + \mathrm{Ec}\frac{M}{1+m^2}(1+\gamma\theta)^{-b}(F^2+G^2) = 0 \quad (1)$$

The boundary conditions appropriate to the flow geometry of the problem considered are given as

Contributed by the Heat Transfer Division of ASME for publication in the JOURNAL OF HEAT TRANSFER. Manuscript received January 19, 2010; final manuscript received September 24, 2010; published online November 2, 2010. Assoc. Editor: Joon Sik Lee.

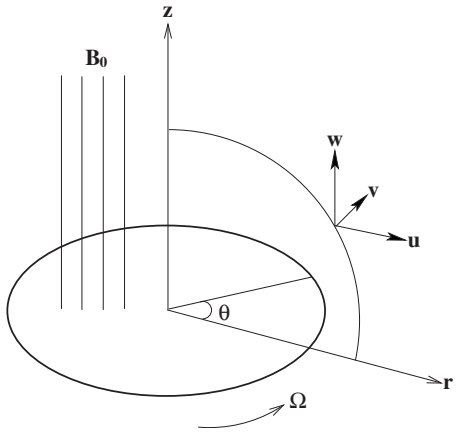

Fig. 1 Configuration of the flow and geometrical coordinates

$$F = G - 1 = H - s = \theta - 1 = 0, \quad \text{at} \quad \eta = 0$$
$$F = G = \theta = 0, \quad \text{as} \quad \eta \to \infty \tag{2}$$

In Eqs. (1) and (2), a, b, and d in general are arbitrary exponents, which are taken for the flue gas as $a=0.7$, $b=0.83$, and $d=-1.0$.

Upon solution of the mean flow quantities from Eqs. (1) and (2), the tangential shear stress τ_θ and radial shear stress τ_r can be computed from

$$\tau_\theta = \left[\mu\left(\frac{\partial v}{\partial z} + \frac{1}{r}\frac{\partial w}{\partial \theta}\right)\right]\Bigg|_{z=0} = \mu_\infty(1+\gamma)^a \Omega \mathrm{Re} G'(0)$$
$$\tau_r = \left[\mu\left(\frac{\partial u}{\partial z} + \frac{\partial w}{\partial r}\right)\right]\Bigg|_{z=0} = \mu_\infty(1+\gamma)^a \Omega \mathrm{Re} F'(0) \tag{3}$$

Evaluation of the scaled torque involves the quantity $G'(0)$. In addition to this, the rate of heat transfer is computed by the application of Fourier's law as given below

$$q = -\left(\kappa\frac{\partial T}{\partial z}\right)\Bigg|_{z=0} = -\kappa_\infty T_\infty \gamma(1+\gamma)^b \frac{\mathrm{Re}}{r}\theta'(0) \tag{4}$$

from which the Nusselt number can be obtained.

To briefly outline the method of numerical solution of the mean flow Eqs. (1) and (2), a spectral Chebyshev collocation method based on the Chebyshev polynomials is employed. More details of the integration scheme can be found in Ref. [10]. Moreover, a double check on the solutions obtained here was performed first by employing a classical fourth-order Runge–Kutta integrating scheme and next via the built-in numerical algorithms in the contemporary tool of MATHEMATICA.

3 Results and Discussion

We first of all emphasize that we do not intend to duplicate the results of Ref. [7]. However, during the numerical integration of Eqs. (1) and (2), we came across with the unfortunate fact that a numerical error was committed in the calculations of Ref. [7], thus affecting some of their conclusions. Actually, their numerical procedure was already open to questions since the comparisons made in Ref. [7] with Ref. [11] on Table 1 clearly indicated this reality. We therefore, recalculate the same parameters as in Ref. [7] and see how the results will change.

The validity of the numerical computations adopted in the present investigation has been implemented by comparisons with those of Kumar et al. [3], Kelson and Desseaux [11], and Maleque and Sattar [7] (besides those of Refs. [12,4]) in the case of constant properties in Tables 1–3. Without the variable property effects considered in the present investigation, it is seen from the tables that comparisons with literature show perfect agreements, unlike to the report of Ref. [7], which we believe that a numerical mistake deteriorated their findings.

Effects of the temperature difference parameter γ on the radial, azimuthal, and axial velocities and temperature profiles are shown in Figs. 2(*a*)–2(*d*). In Fig. 2(*a*), it is seen that due to the existence of the centrifugal force the radial velocity attains a maximum value close to the surface of the disk and an inflexion point slightly above the disk for the values of γ considered. The largest maximum value of the radial velocity is attained for the wall heating case ($\gamma=0.5$). For this reason, the conclusion made in Ref. [7] that the largest maximum value of the velocity is attained in the case of constant property is misleading. Figure 2(*a*) also shows that very close to the disk surface in a short interval (shorter as compared with the result of Ref. [7]), an increase in the values of γ leads to the decrease in the values of the radial velocity followed by an increase in most part of the boundary layer. In Fig. 2(*b*), it is found that the tangential velocity decreases fast (even faster as compared with the result of Ref. [7]) with the decreasing values of γ in whole of the boundary layer. A large deviation from the results of Ref. [7] takes place for the axial velocity profiles as depicted in Fig. 2(*c*). Cooling the surface totally removes the inflectional character of the axial velocity (but not in the calculations of Ref. [7]), whereas sufficient heating gives rise to the occurrence of two inflexion points, in contrast to the result of Ref. [7]. We also point out that the conclusion made in Ref. [7] that the thermal boundary layer is not affected much by the consideration of variable properties is also misleading. On the contrary, Fig. 2(*d*) shows that variable property has a substantial influence on the development of thermal boundary layer, as compared with the constant property case.

The effects of Lorentz force are depicted in Figs. 3(*a*)–3(*d*) by the decreases in the velocity profiles and increases in the temperature profiles as M increases. Additionally, the increases in the temperature profiles as M increases are accompanied by increases in the thickness of thermal boundary layer. Although Figs. 3(*a*), 3(*b*), and 3(*d*) exhibit close graphical similarities, the behavior of axial velocity in Fig. 3(*c*) absolutely deviates from the results shown in Fig. 5 of Ref. [7]. First, we see that the variable property ($\gamma=0.1$) reduces the axial flow in the vicinity of the wall to lower values than the value of suction, which is more prominent as the magnetic field is strengthened. Second, as the magnetic interaction parameter increases, an overshoot occurs in the axial velocity pro-

Table 1 Values of $F'(0)$ and $-G'(0)$ for $M=m=\gamma=0$

s	$F'(0)$ [a]	$-G'(0)$ [a]	$F'(0)$ [b]	$-G'(0)$ [b]	$F'(0)$ [c]	$-G'(0)$ [c]
−4	0.12473749	4.00518061	0.127661	4.009988	0.124737	4.005180
−2	0.24241618	2.03852681	0.243280	2.041367	0.242416	2.038530
0	0.51023261	0.61592201	0.510143	0.615960	0.510235	0.615922
1	0.48948122	0.30217348	0.489477	0.302172	0.489481	0.302173
5	0.19756596	0.01547064	-	-	0.197565	0.015471

[a]From present work.
[b]From Ref. [7].
[c]From Ref. [3].

Table 2 Values of $-\theta'(0)$ for Pr=0.71 and $M=m=\gamma=0$

s	$-\theta'(0)$ [a]	$-\theta'(0)$ [b]	$-\theta'(0)$ [c]
−4	2.84238189	2.864478	2.842381
−2	1.43778304	1.450654	1.437782
0	0.32586064	0.329527	0.325856
2	0.01101389	0.011052	0.011013
4	0.00001073	0.000011	0.000011

[a]From present work.
[b]From Ref. [7].
[c]From Ref. [11].

Table 3 Values of $H(\infty)$ and $-\theta'(0)$ for Pr=1, $M=0.5$, and $m=\gamma=0$

s	$H(\infty)$ [a]	$-\theta'(0)$ [a]	$H(\infty)$ [b]	$-\theta'(0)$ [b]
−4	−4.00700706	4.00239513	−4.00700	4.002395
−3	−3.01528894	3.00532198	−3.01530	3.005322
−2	−2.04131653	2.01505125	−2.04130	2.015051
−1	−1.14101328	1.05911937	−1.14100	1.059119
0	−0.45888005	0.28265593	−0.45888	0.282656
1	−0.03213052	0.00343275	−0.03213	0.003433

[a]From present work.
[b]From Ref. [3].

files before approaching an asymptotic value for large distances. It should be reminded that these features were missed from the calculations of Ref. [7]. Therefore, even though it is well-known that the magnetic field tends to act in the way to stabilize the hydromagnetic boundary layer flow in the case of constant properties, as observed in Fig. 3(*c*), this might not be the circumstance for the case of wall heating, an open issue that requires a linear stability analysis.

The parameter m has a marked effect on the velocity profiles as seen in Figs. 4(*a*)–4(*d*). It is observed that, due to an increase in the magnitude of $m>0$ within some interval, both the radial and axial velocity profiles increase. However, if the magnitude of $m>0$ is increased beyond some limit, the velocity profiles show a decreasing effect. The contribution of small positive values of m is to reduce the magnetic damping on the three velocity components by increasing their values initially, followed by a decrease for large positive values of m. A small negative value of m (which was omitted in Ref. [7]) has a reversed effect, decreasing the value of the radial velocity and yielding a reverse inward radial flow toward the center. In the case of negative Hall parameter, a similar effect is observed on the axial velocity profile while the azimuthal velocity keeps increasing as for the positive values of m in Figs. 4(*b*) and 4(*c*). Figure 4(*d*) shows the small variation of temperature profiles for different values of Hall parameter m; as a result of which, the thermal boundary layer gets thinned. Unlike in the case of positive Hall parameter, an increase in the temperature profile is observed for negative values of Hall parameter, pointing to a thickening effect in the thermal boundary layer.

Figure 5 demonstrates the influences of Eckert number Ec on the temperature distributions for a variety of parameters. The dotted line is for $Ec=0$ and the increase and decrease in the value of Ec are in 1 unit. A common characteristic feature pertinent to all parts revealed is that positive Eckert number increases the temperature, but negative Eckert number decreases it, making the profiles inflectional in both cases. Figure 5(*a*) shows the effects of viscous dissipation only when the constant properties are taken into account. Additionally, Fig. 5(*b*) shows the impacts of both viscous and Joule heating terms again for the constant property case. It can thus be deduced that Joule heating enhances the temperature distribution near the wall region. The influences of variable properties can be visualized in Figs. 5(*c*) and 5(*d*). It is clear

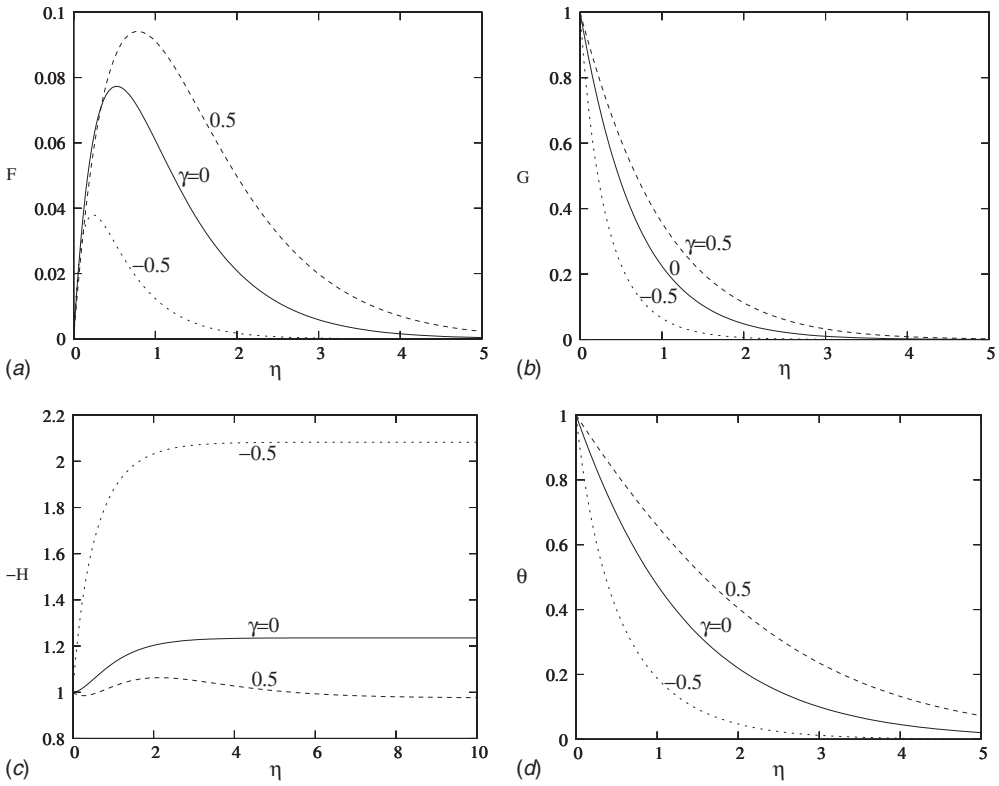

Fig. 2 (*a*) Effect of γ on the radial velocity profiles, (*b*) effect of γ on the azimuthal velocity profiles, (*c*) effect of γ on the minus axial velocity profiles, and (*d*) effect of γ on the temperature profiles, for $M=m=0.5$, $s=-1$, Pr=0.64, and Ec=0

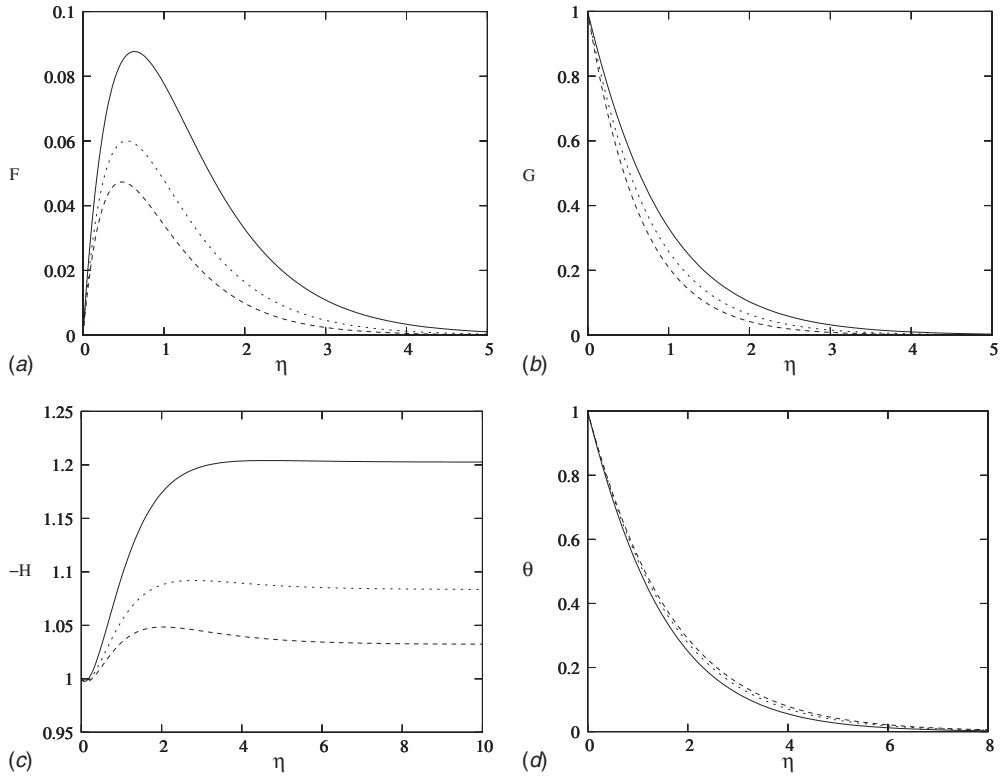

Fig. 3 (*a*) **Effect of** *M* **on the radial velocity profiles,** (*b*) **effect of** *M* **on the azimuthal velocity profiles,** (*c*) **effect of** *M* **on the axial velocity profiles, and** (*d*) **effect of** *M* **on the temperature profiles, for** $m=\gamma=0.1$, $s=-1$, Pr=0.64, **and** Ec=0, **the straight line corresponding to** $M=0$, **the dotted line to** $M=0.5$ **and the dashed line to** $M=1$

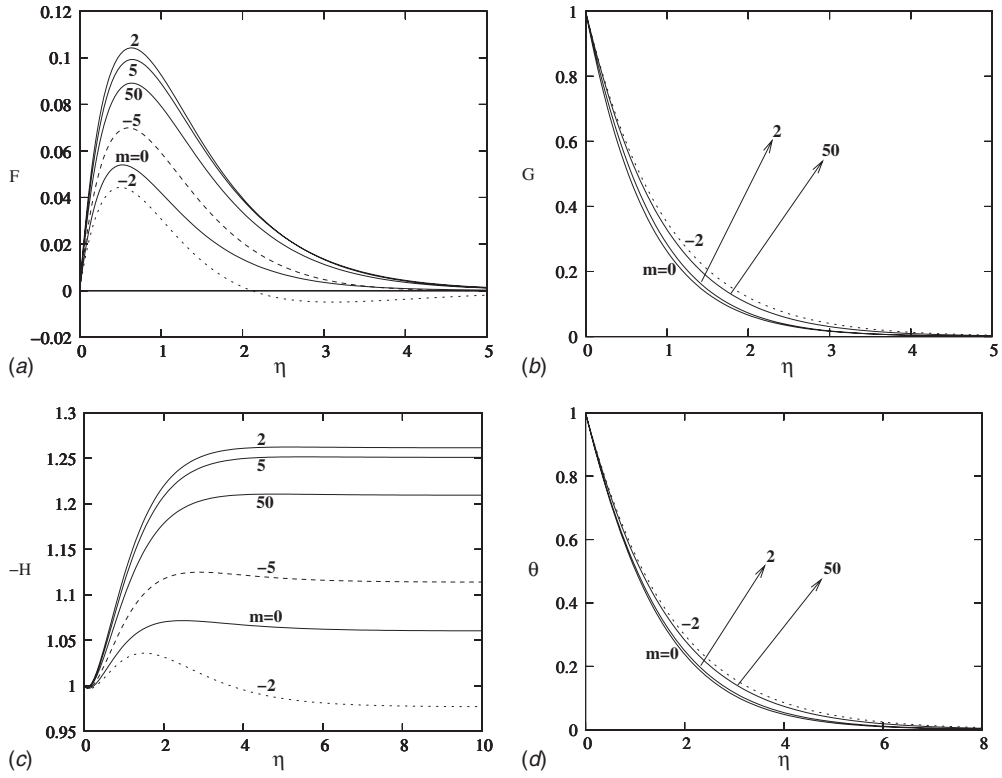

Fig. 4 (*a*) **Effect of** *m* **on the radial velocity profiles,** (*b*) **effect of** *m* **on the azimuthal velocity profiles,** (*c*) **effect of** *m* **on the axial velocity profiles, and** (*d*) **effect of** *m* **on the temperature profiles, for** $M=0.5$, $\gamma=0.1$, $s=-1$, Pr=0.64, **and** Ec=0, **the dotted line corresponding to** $m=-2$ **and the dashed line to** $m=-5$

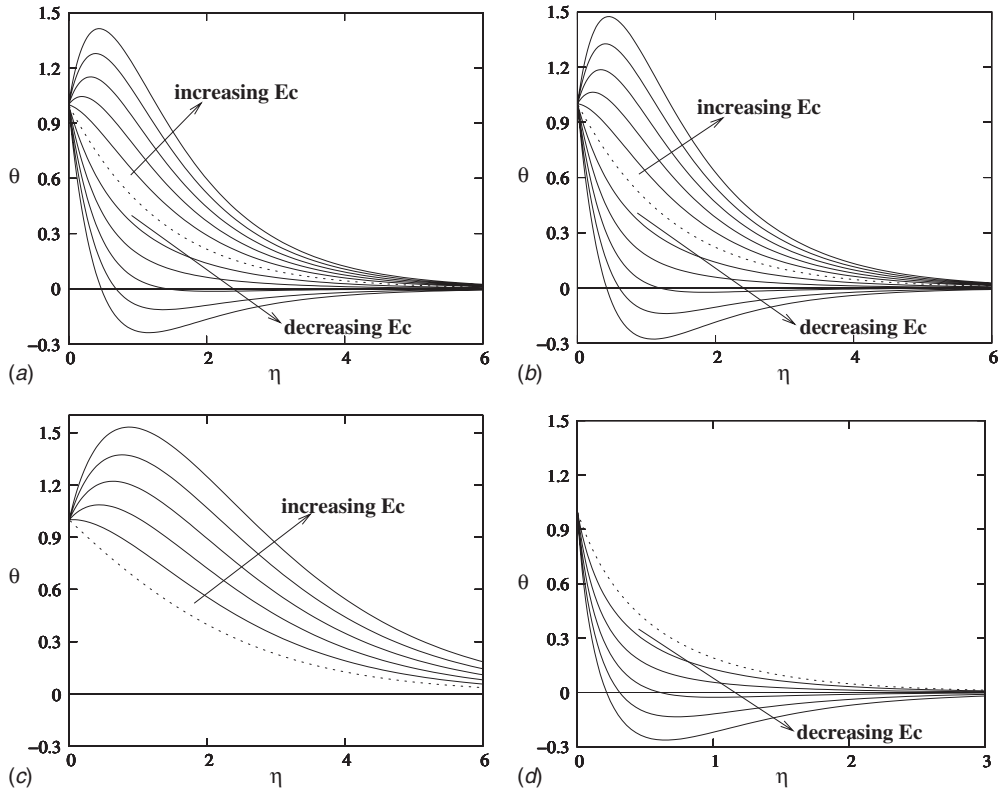

Fig. 5 Effect of Ec on the temperature distribution for Pr=0.64 and $s=-1$ corresponding to: (*a*) $M=m=\gamma=0$, (*b*) $M=m=0.1$ and $\gamma=0$, (*c*) $M=m=0.1$ and $\gamma=0.5$, and (*d*) $M=m=0.1$ and $\gamma=-0.5$

Table 4 Values of $F'(0)$, $-G'(0)$, and $-\theta'(0)$ for $M=m=0.1$, $s=-1$, Pr=0.64, and Ec=0

γ	$F'(0)$ [a]	$-G'(0)$ [a]	$-\theta'(0)$ [a]	$F'(0)$ [b]	$-G'(0)$ [b]	$-\theta'(0)$ [b]
−0.5	0.44663079	3.38299447	2.31044793	0.468276	2.086653	0.867656
−0.2	0.40859354	1.66800628	1.02560032	0.421738	1.538455	0.779307
0.0	0.37223022	1.23335228	0.71311078	0.372331	1.233757	0.720557
0.2	0.33724141	0.98021736	0.53643904	0.306259	0.966984	0.655588
0.5	0.29219345	0.75437701	0.38408764	0.168678	0.622670	0.559004
0.8	0.25611053	0.61789611	0.29540990	0.109027	0.518923	0.516888
1.0	0.23616658	0.55361833	0.25476724	−0.000367	0.370817	0.442873

[a]From present work.
[b]From Ref. [7].

that a positive temperature difference parameter broadens the interval of temperature distribution acting like a blowing parameter, whereas a negative temperature difference parameter shrinks the interval of temperature acting like a suction. The effect of Joule heating seems to be preserved for the parameters chosen in Fig. 5.

As we have already remarked before and also presented in Tables 1 and 2, the accuracy of the results of Ref. [7] is poor in the case of constant properties. The accuracy becomes even more questionable (as also discussed in Figs. 2–5) when the variable properties are taken into consideration in Table 4. Although the general trend of both results occurs in the same manner, the rate of change of increase and decrease in the quantities as the temperature difference parameter varies differs quite dramatically, the best agreement is for $\gamma=0$. It can be concluded from Table 4 that slight changes happen in the radial skin friction, unlike the larger changes in the azimuthal skin friction (or the torque requirement) and the rate of heat transfer, for increasing or decreasing γ as compared with $\gamma=0$.

We finally present the influences of addition of viscous dissipation and Joule heating into the energy equation on the parameters of physical interest at the fixed values of Pr=0.64 and $s=-1$. To serve this purpose, Table 5 tabulates the effects of just viscous dissipation on the rate of heat transfer for the chosen values $M=m=\gamma=0$. In compliance with Fig. 5(*a*), the smaller the value of Eckert number Ec is, the higher the heat transfer rate gets increased. Table 6 presents the effects of Joule heating along with the viscous dissipation on the rate of heat transfer for the selected values $M=m=0$ and the three values of γ. Table 6 shows that the infinity value of axial velocity is slowly affected and the rate of heat transfer is enhanced even more by the presence of the Joule heating as compared with the just viscous dissipation term. Moreover, decreasing γ slows down the occurrence of heat transfer unlike the great increase by positive values of γ.

Table 5 Values of $-\theta'(0)$ for $M=m=\gamma=0$, $s=-1$, Pr=0.64, and different Ec

Ec=−4	Ec=−2	Ec=0	Ec=2	Ec=4
3.16533851	1.94250280	0.71966709	−0.50316862	−1.72600433

Table 6 Values of $-H(\infty)$ and $-\theta'(0)$ for $M=m=0.1$, $s=-1$, Pr=0.64, and different Ec

Ec	$-H(\infty)$ [a]	$-H(\infty)$ [b]	$-H(\infty)$ [c]	$-\theta'(0)$ [a]	$-\theta'(0)$ [b]	$-\theta'(0)$ [c]
−4	-	1.23303654	2.05633339	-	3.41550640	9.90461839
−2	-	1.23303654	2.06061757	-	2.06430859	6.10141458
0	1.00520298	1.23303654	-	0.38408764	0.71311078	-
2	0.99121255	1.23303654	-	−0.45627526	−0.63808703	-
4	0.97847624	1.23303654	-	−1.30186432	−1.98928482	-

[a]Corresponding to $\gamma=0.5$.
[b]Corresponding to $\gamma=0$.
[c]Corresponding to $\gamma=-0.5$.

4 Conclusions

In this paper, the effects of variable properties in combination with the influences of uniform suction/blowing, uniform vertical magnetic field, Hall current, viscous dissipation, and Joule heating on the three-dimensional steady MHD conducting boundary layer flow of a flue gas induced by an infinite rotating porous disk have been investigated.

Our results show that the radial velocity reaches a maximum value close to the surface of the disk, whose largest maximum value is attained for the wall heating case, not for the constant property case as claimed in Ref. [7]. The tangential velocity decreases rapidly (much faster as compared with the finding of Ref. [7]) with the decreasing values of the temperature difference parameter γ. As opposed to the calculations of Ref. [7], cooling the surface completely removes the inflectional character of axial velocity profiles, whereas sufficient heating results in the appearance of two critical points. In contrast to the conclusion made in Ref. [7], the thermal boundary layer thickness increases for wall heating but decreases for wall cooling.

The effects of the magnetic field on the velocity profiles are seen to be stabilizing. The contribution of small positive values of Hall current is found to delay the effect of magnetic damping. A small negative value of the Hall parameter (which was not studied in Ref. [7]), on the other hand, has a reversed effect, causing a further inward radial flow toward the disk center. This effect is later diminished with an infinite increase in the Hall parameter.

Temperature is found to increase with a positive Eckert number but it decreases with a negative Eckert number. As compared with the viscous dissipation, Joule heating is found to enhance the temperature distribution near the wall. The effect of a positive temperature difference parameter γ is found to broaden the interval of temperature acting like a surface injection, whereas a negative temperature difference parameter shrinks the interval of temperature acting like the wall suction. In the case of only viscous dissipation, higher heat transfer rates take place when smaller values of Ec are taken into account. The addition of the Joule heating term further enhances the rate of heat transfer, causing the infinity axial velocities slightly changed. Decreasing γ reduces the rate of heat transfer unlike in the case of increasing γ.

Nomenclature

Roman Symbols

(a,b,d) = constants of flue gas
Ec = Eckert number
(F,G,H) = self-similar radial, azimuthal, and normal velocities
m = Hall current parameter
M = magnetic interaction parameter
P = self-similar pressure
Pr = Prandtl number
q = heat flux
r = radial direction in cylindrical polar coordinates
s = suction or injection parameter
T = temperature
(u,v,w) = velocity components in radial, azimuthal, and normal directions
z = normal direction in cylindrical polar coordinates

Greek Symbols

γ = relative temperature difference parameter
η = a scaled boundary layer coordinate
θ = azimuthal direction in cylindrical polar coordinates
τ_r = radial shear stress on the wall
τ_θ = azimuthal shear stress on the wall

References

[1] Stuart, J. T., 1954, "On the Effect of Uniform Suction on the Steady Flow Due to a Rotating Disc," Q. J. Mech. Appl. Math., **7**, pp. 446–457.
[2] Kuiken, H. K., 1971, "The Effect of Normal Blowing on the Flow Near a Rotating Disk of Infinite Extent," J. Fluid Mech., **47**, pp. 789–798.
[3] Kumar, S. K., Thacker, W. I., and Watson, L. T., 1988, "Magnetohydrodynamic Flow and Heat Transfer About a Rotating Disk With Suction and Injection at the Disk Surface," Comput. Fluids, **16**, pp. 183–193.
[4] Ariel, P. D., 2002, "On Computation of MHD Flow Near a Rotating-Disk," Z. Angew. Math. Mech., **82**, pp. 235–246.
[5] Cramer, K., and Pai, S., 1973, *Magnetofluid Dynamics for Engineers and Applied Physicists*, McGraw-Hill, New York.
[6] Attia, H. A., 2001, "Effect of Hall Current on the Unsteady MHD Flow Due to a Rotating Disk With Uniform Suction or Injection," Appl. Math. Model., **25**, pp. 1089–1098.
[7] Maleque, Kh. A., and Sattar,Md. A., 2005, "The Effects of Variable Properties and Hall Current on Steady MHD Laminar Convective Fluid Flow Due to a Porous Rotating Disk," Int. J. Heat Mass Transfer, **48**, pp. 4963–4972.
[8] Awad, M. M., 2008, "Heat Transfer From a Rotating Disk to Fluids for a Wide Range of Prandtl Numbers Using the Asymptotic Model," J. Heat Transfer, **130**, p. 014505.
[9] Turkyilmazoglu, M., 2009, "Exact Solutions Corresponding to the Viscous Incompressible and Conducting Fluid Flow Due to a Porous Rotating Disk," ASME J. Heat Transfer, **131**, p. 091701.
[10] Turkyilmazoglu, M., 1998, "Linear Absolute and Convective Instabilities of Some Two- and Three-Dimensional Flows," Ph.D. thesis, University of Manchester, Manchester, UK.
[11] Kelson, N., and Desseaux, A., 2000, "Note on Porous Rotating Disk Flow," ANZIAM J., **42**, pp. C837–C855.
[12] Sparrow, E. M., and Gregg, J. L., 1959, "Heat Transfer From a Rotating Disk to Fluids of Any Prandtl Number," ASME J. Heat Transfer, **81**, pp. 249–251.

Benjamin Latour
e-mail: benjamin.latour@hei.fr

Pascale Bouvier
Assistant Professor
e-mail: pascale.bouvier@hei.fr

Département EEA HEI,
F-59000 Lille, France;
Université de Lille Nord de France,
F-59000 Lille, France;
TEMPO/DF2T,
UVHC,
F-59313 Valenciennes, France

Souad Harmand[1]
Professor
Université de Lille Nord de France,
F-59000 Lille, France;
TEMPO/DF2T,
UVHC,
F-59313 Valenciennes, France
e-mail: souad.harmand@univ-valenciennes.fr

Convective Heat Transfer on a Rotating Disk With Transverse Air Crossflow

In this study, the local convective heat transfer from a rotating disk with a transverse air crossflow was evaluated using an infrared thermographic experimental setup. Solving the inverse conduction heat transfer problem allows the local convective heat transfer coefficient to be identified. We used the specification function method along with spatio-temporal regularization to develop a model of local convective heat transfer in order to take lateral conduction and 2D geometry into account. This model was tested using rotational Reynolds numbers (based on the cylinder diameter and the peripheral speed) between 0 and 17,200 and air crossflow Reynolds numbers between 0 and 39,600. In this paper, the distribution of the local heat transfer on the disk allows us to observe the combined effect of the rotation and air crossflow on heat exchanges. This coupling is able to be taken into account in a correlation of mean Nusselt number relative to both Reynolds numbers. [DOI: 10.1115/1.4002603]

Keywords: rotating fins, air crossflow, forced convection, local heat transfer, infrared thermography

1 Introduction

Heat exchanges by convection between rotating disk and surrounding fluid are important in some engineering applications such as turbomachinery, electrical devices, disk brake cooling, or even computer-disk drives. In spite of the large application field of rotating devices, relatively not enough studies of local convective phenomena on rotating disk in air crossflow are available. The first studies dealing with rotating systems in still air were linked to the single disk case. The flow and heat transfer around a disk principally depend on friction and centrifugal forces. They have been studied by many authors [1–8].

In the case of rotational disks in still air (Pr=0.72), Dorfman [3] was able to identify the zones on the disk surface corresponding to laminar, transitional, and turbulent regimes, according to disk radius and rotational speed. Concerning the convective heat transfer around rotating disks in the laminar regime in all of the investigations [3–8], a general formulation for Nusselt number correlation has been highlighted (Eq. (1)):

$$\overline{\mathrm{Nu}}_{\mathrm{re}} = C_1 \cdot \mathrm{Re}_{\omega,\mathrm{re}}^{0.5} \tag{1}$$

The value of coefficient C_1 varies from 0.28 to 0.40 according to the different studies [3–8]. aus der Wiesche [9] numerically studied convective heat exchanges around a rotating disk in still air by large-eddy-simulation (LES). The rotational Reynolds numbers $\mathrm{Re}_{\omega,\mathrm{re}}$ considered vary from 10^3 to 10^6. In the laminar regime ($\mathrm{Re}_{\omega,\mathrm{re}} < 2\times10^5$), results of aus der Wiesche agree well with Eq. (1) for $C_1=0.33$, whereas in the fully turbulent regime ($\mathrm{Re}_{\omega,\mathrm{re}} > 5\times10^5$), his results of simulation are well correlated by Eq. (2) with $C_2=0.015$,

$$\overline{\mathrm{Nu}}_{\mathrm{re}} = C_2 \cdot \mathrm{Re}_{\omega,\mathrm{re}}^{0.8} \tag{2}$$

In the case of a stationary disk in air crossflow, aus der Wiesche [9] also studied local convective heat transfer for air crossflow Reynolds numbers $\mathrm{Re}_{U,\mathrm{re}}$ varying from 10^3 to 10^6. His results are in accordance with those of the flat plate characterized by a symmetric Nusselt number (Fig. 1(*a*)). Indeed, a high convective heat transfer occurs at the beginning of the disk in the developing boundary layer and decreases along the disk diameter. The flow is laminar up to a critical value of $\mathrm{Re}_{U,\mathrm{re}}=5\times10^4$ for which the transition into turbulence begins, whereas the turbulent regime is fully reached at an air crossflow Reynolds number of about $\mathrm{Re}_{U,\mathrm{re}}=10^5$. By replacing $\mathrm{Re}_{\omega,\mathrm{re}}$ with $\mathrm{Re}_{U,\mathrm{re}}$ in Eqs. (1) and (2), the LES data are correlated by Eq. (1) with $C_1=0.417$ for the laminar case and by Eq. (2) with $C_2=0.0127$ for the turbulent regime. Dennis et al. [8] also proposed a correlation for the turbulent case with an experimental value of $C_2=0.027$.

In the case of a rotating disk in an air crossflow, there are a few studies dealing with the combined effect of rotation and air crossflow on convective heat transfer. The most detailed one has been realized by aus der Wiesche [9] who studied the flow field and the corresponding local Nusselt number distributions on the disk for $10^3<\mathrm{Re}_{\omega,\mathrm{re}}<10^6$ and $10^3<\mathrm{Re}_{U,\mathrm{re}}<10^6$. By comparing the results obtained with and without disk rotation, aus der Wiesche analyzed the rotation effect on convective heat transfer. From his results, he highlighted a domain characterized by high values of airflow Reynolds in which convective exchanges are governed by the crossflow since no additional heat transfer augmentation due to the rotation was observed. Then, for low rotational and airflow Reynolds numbers, disk rotation slightly affects the flow field and local temperature distribution, whereas the mean heat transfer relative to the disk surface remains constant. Indeed, rotation increases heat convection on the ascending (comoving) side and diminishes it on the descending (counter-moving) side in such a way that the mean heat transfer is almost unaffected. With increasing $\mathrm{Re}_{\omega,\mathrm{re}}$, the increase in the flow turbulence leads to higher variations in the local Nusselt number even if the typical flat plate distribution can still be identified. From sufficient high values of $\mathrm{Re}_{\omega,\mathrm{re}}$, the local Nusselt number distribution becomes uniform and mainly governed by rotational effects (Fig. 1(*b*)). In order to evaluate the relative influence of rotation and air crossflow, aus der Wiesche proposed a method consisting in plotting the ratio $\overline{\mathrm{Nu}}_{\mathrm{re}}/\overline{\mathrm{Nu}}_{\mathrm{re},\omega=0}$ against the ratio $\mathrm{Re}_{\omega,\mathrm{re}}/\mathrm{Re}_{U,\mathrm{re}}$. As a result, he highlighted two zones separated by a critical value $(\mathrm{Re}_{\omega,\mathrm{re}}/\mathrm{Re}_{U,\mathrm{re}})_{\mathrm{crit}}=1.4$. In the first one, corresponding to $\mathrm{Re}_{\omega,\mathrm{re}}/\mathrm{Re}_{U,\mathrm{re}}<1.4$, there is

[1]Corresponding author.

Contributed by the Heat Transfer Division of ASME for publication in the JOURNAL OF HEAT TRANSFER. Manuscript received February 11, 2010; final manuscript received August 23, 2010; published online November 3, 2010. Assoc. Editor: Frank Cunha.

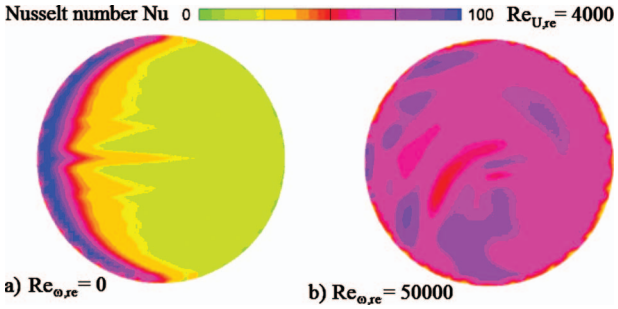

Fig. 1 Local Nusselt number on a rotating disk in air crossflow [9]

a dominant influence of air crossflow on the convective heat transfer characterized by a ratio $\overline{\mathrm{Nu}}_{\mathrm{re}}/\overline{\mathrm{Nu}}_{\mathrm{re},\omega=0}$ constant. In the second zone, corresponding to $\mathrm{Re}_{\omega,\mathrm{re}}/\mathrm{Re}_{U,\mathrm{re}}>1.4$, there is a significant increase in the ratio due to some instability created between rotational and plane flows, which tend to increase the convective heat transfer. Based on the LES study, the author proposed different correlations (Eqs. (3)–(6)) in order to predict convective exchanges on the disk:

$$\overline{\mathrm{Nu}}_{\mathrm{re}} = \overline{\mathrm{Nu}}_{\mathrm{re},\omega=0} \quad \text{for } 0 < \frac{\mathrm{Re}_{\omega,\mathrm{re}}}{\mathrm{Re}_{U,\mathrm{re}}} < 1.4 \tag{3}$$

$$\overline{\mathrm{Nu}}_{\mathrm{re}} = \overline{\mathrm{Nu}}_{\mathrm{re},\omega=0} \cdot \left[1 + 0.32 \cdot \left(\frac{\mathrm{Re}_{\omega,\mathrm{re}}}{\mathrm{Re}_{U,\mathrm{re}}} - 1.4\right)^{1/2}\right] \quad \text{for } 1.4 < \frac{\mathrm{Re}_{\omega,\mathrm{re}}}{\mathrm{Re}_{U,\mathrm{re}}} < 5 \tag{4}$$

$$\overline{\mathrm{Nu}}_{\mathrm{re}} = \sqrt{(0.0127 \cdot \mathrm{Re}_{U,\mathrm{re}}^{0.8})^2 + (0.015 \cdot \mathrm{Re}_{\omega,\mathrm{re}}^{0.8})^2} \quad \text{for } \mathrm{Re}_{\omega,\mathrm{re}} > 2 \times 10^5 \text{ and } \mathrm{Re}_{U,\mathrm{re}} > 5 \times 10^4 \tag{5}$$

$$\overline{\mathrm{Nu}}_{\mathrm{re}} = \sqrt{(0.0127 \cdot \mathrm{Re}_{U,\mathrm{re}}^{0.8})^2 + (0.33 \cdot \mathrm{Re}_{\omega,\mathrm{re}}^{0.5})^2} \quad \text{for } \mathrm{Re}_{\omega,\mathrm{re}} < 2 \times 10^5 \text{ and } \mathrm{Re}_{U,\mathrm{re}} > 5 \times 10^4 \tag{6}$$

Our study deals with a rotating disk mounted on a shaft perpendicular to an air crossflow. In the case of a fixed disk mounted on a cylinder and submitted to an air crossflow, the presence of the cylinder generates flow perturbations at the disk/cylinder junction, as studied by different authors [10–15]. From experimental observations, they detected a boundary layer development from the leading edge of the disk associated to a reduction of velocity due to the adverse pressure gradient in the stagnation zone upstream of the cylinder. This causes the flow to separate and to form a horseshoe vortex system (Fig. 2) consisting of counter-rotating vortices swept around the cylinder base. Zones of lower convective heat

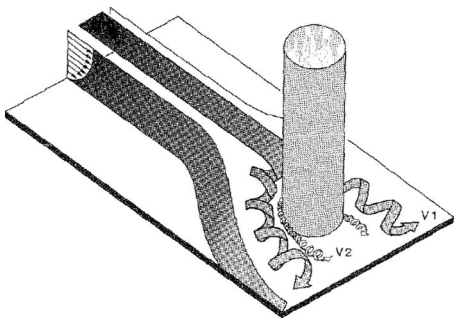

Fig. 2 3D boundary layer separation and horseshoe vortex system in the region of interaction between mainstream boundary layer and cylinder [10]

transfers correspond to the wake and to the flow separation located at $\theta = \pm 90$ deg from the front stagnation point. On the other hand, zones of higher heat transfers are located at $+110 \text{ deg} < \theta < +150$ deg and $-110 \text{ deg} < \theta < -150$ deg, where the legs of the horseshoe vortex system appears. Experimental studies [16–18] dealing with the visualization of the horseshoe vortex system by particle image velocimetry highlighted a significant influence of Re_U on the size of the vortex horseshoe. Moreover, Fu and Rockwell [17] showed that (i) the instability of the horseshoe vortex generates flow perturbations in the near wake, (ii) fluctuation level increasing in the horseshoe vortex leads to the development of coherent vortices earlier in the separating shear layer, and (iii) rotational perturbation of a vertical cylinder can destabilize the wake flow structure.

To the best of our knowledge, there is only one previous study about the mean convective exchanges around a rotating disk mounted on a cylinder in airflow [19]. In the case of a disk of 21 mm height and 1 mm wide mounted on a 58-mm-diameter cylinder, Watel determined a general correlation of the mean Nusselt number depending on Re_U and Re_ω (Eq. (7)). From this equation, she could determine the different domains of influence (rotation, air crossflow, and combined rotation/air crossflow) on convective heat transfer,

$$\overline{\mathrm{Nu}} = (0.03 \cdot \mathrm{Gr} + 0.053 \cdot \mathrm{Re}_U^2 + 9.1 \cdot 10^3 \cdot \mathrm{Re}_\omega^2)^{0.275} \tag{7}$$

The experimental setup presented in this paper allows the influence of rotational and air crossflow speeds on the convective heat transfer to be studied. A transient method for identifying heat transfers using infrared (IR) thermography is proposed. In this method, the infrared camera measures the temperature variation of the disk at eight angular locations in the radial direction over time. Solving the inverse conduction heat transfer problem allowed us to identify the local and mean Nusselt numbers in all the tests carried out while taking into account both conductive and radiative fluxes [20].

2 Experimental Study

2.1 Experimental Setup. Local convective exchange coefficients on the surface of a rotating disk in air crossflow were obtained by measuring the spatio-temporal temperature variations on the disk (Fig. 3(*a*)). The 2-mm-wide and 60-mm-high disk was made of aluminum ($\lambda_{\mathrm{al}}=200$ W m^{-1} K^{-1}, $\rho_{\mathrm{al}}=2700$ kg m^{-3}, and $C_{\mathrm{al}}=0.96$ kJ kg^{-1} K^{-1}) and was mounted on a 58-mm-diameter cylinder (Fig. 3(*b*)). The chosen disk height, higher than the 21 mm one used by Watel, allows us to observe the height influence on mean heat transfer as well as the radial variations of the convective heat transfer coefficient. The disk and cylinder were covered with a thin coat of black paint, which relatively high emissivity allowed the radiative heat flux emitted to be more accurately determined, thus improving the accuracy of the relationship between the camera exit signal and the disk temperature. The disk was driven by an electric motor coupled to a frequency variator, which allowed us to vary the rotational speed from 0 rpm to 2000 rpm. The experiments were performed in a 2.4-m-long wind tunnel. The test disk was positioned at a distance of 2 m from the fan in order to obtain a straightened airflow upstream from the disk. A diaphragm allows us to vary airflow speed from 0 m s^{-1} to 14 m s^{-1}. In order to measure disk temperatures by thermography, the front wall of the wind tunnel included a porthole made up of an infrared transparent film. The calibration law was determined with an extended black body at the laboratory.

A radiant panel emitting short infrared waves was placed horizontally above the disk, heating them uniformly to temperatures about 120 °C. Once the steady thermal state was reached, the heat source was shut off. The disk then cooled through radiative and convective heat transfers, depending on the rotational and air crossflow speeds. The surface temperatures during the cooling of the disk were recorded using an IR camera (JADE 3 from Cedip

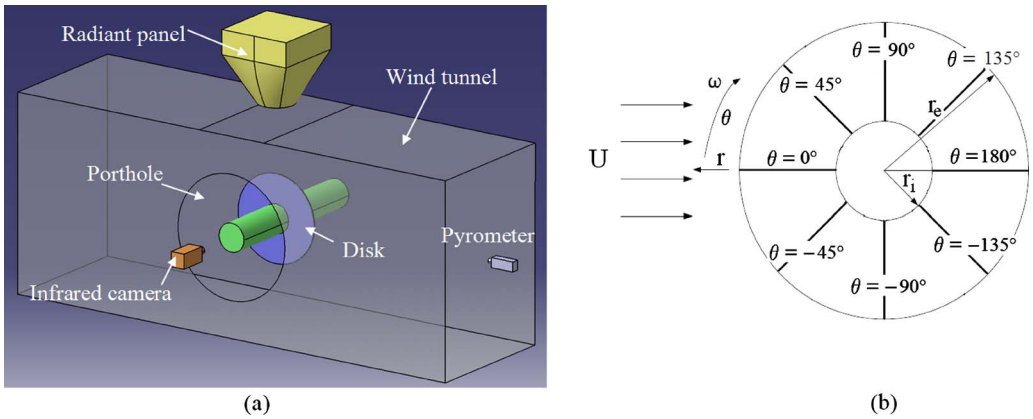

Fig. 3 Representation of the test facility: (*a*) experimental setup and (*b*) disk geometry

Infrared Systems) without a filter. A photoelectric sensor was used to detect the eight reflective bands stuck on the cylinder. Once the sensor had detected the bands, it triggered the IR camera, which then scanned the whole disk. In our study, the camera was placed 2.50 m in front of the disk with an acquisition frequency of 600 Hz and a window of 160×120 pixels, where each pixel corresponds to almost 2.5 mm^2 of the disk surface. Figure 4 shows the real image taken by the camera. The dashed lines correspond to the other locations taken at each turn of the disk.

The camera exit signals obtained during the cooling were collected and processed with the software MATLAB to determine the radial temperature profiles of the disk. They were expressed in thermal levels; their processing is explained in detail in the following section. An infrared pyrometer was placed perpendicular to the cylinder's rotational axis in order to measure the cylinder's temperature evolution over time. The air temperature measured by a K-thermocouple 0.5 m from the disk while they were cooling was used as the reference temperature.

2.2 Disk Temperatures. The infrared image taken by the IR camera shows the "thermal levels" (I_{meas}) of all the pixels. We converted these levels into temperatures using the camera calibration law and the expression of the radiative heat flux density J_{disk} emitted by the disk. The flux J_{meas} reaching the camera is, in fact, weakened by the atmosphere, thus yielding

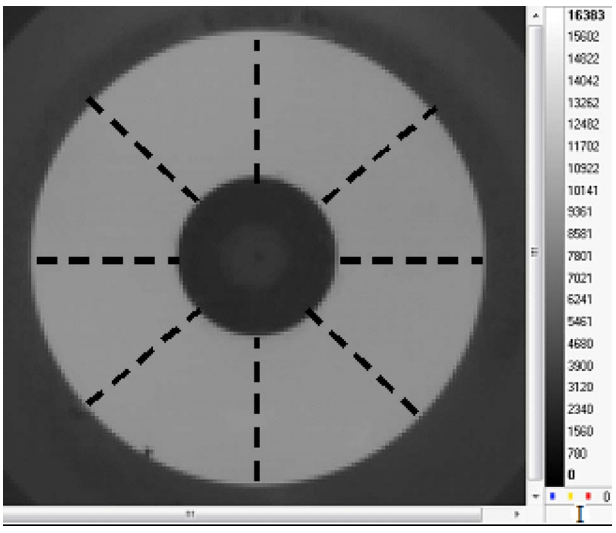

Fig. 4 The eight angular locations of measurement at each turn

$$J_{meas} = \tau_{amb} J_{disk} + (1 - \tau_{amb}) J_{amb} \tag{8}$$

In this equation, the radiosity J_{disk} depends on the radiosity of all the surfaces around it. Thus, the radiosity J_{disk} can be expressed as follows:

$$J_{disk} = \varepsilon_n \sigma T_{disk}^4 + (1 - \varepsilon_n) \sum_{j=1}^{n} F_{disk-j} J_j \tag{9}$$

The cylinder's temperature T_{cyl} is measured by the pyrometer and the ambient temperature $T_{amb} = T_\infty$ is measured by a K-type thermocouple. The emissivity of the black paint was determined experimentally in the laboratory [19] and depends on temperature T as follows:

$$\varepsilon_n = 0.93 \quad \text{for } 293 \text{ K} \le T \le 353 \text{ K}$$

$$\varepsilon_n = 0.98 - 5.7829 \cdot 10^{-4}(T - 273) \quad \text{for } 353 \text{ K} \le T \le 413 \text{ K} \tag{10}$$

Equation (9) leads to the following equation:

$$J_{disk} = a_1 \cdot \sigma \cdot T_{disk}^4 + a_2 \cdot \sigma \cdot T_{cyl}^4 + a_3 \cdot \sigma \cdot T_\infty^4 \tag{11}$$

where coefficients a_1, a_2, and a_3 are functions of the view factors between the different surfaces and the black paint emissivity. The thermal level $I(T)$ is the camera exit signal corresponding to a black body at temperature T, which makes the level proportional to σT^4. Thus, we can express the thermal level I_{disk} of the disk as follows:

$$J_{disk} = a_1 \cdot I(T_{disk}) + a_2 \cdot I(T_{cyl}) + a_3 \cdot I(T_\infty) \tag{12}$$

Using Eqs. (8) and (11), it is possible to write

$$I_{meas} = \tau_{amb}[a_1 \cdot I(T_{disk}) + a_2 \cdot I(T_{cyl}) + a_3 \cdot I(T_\infty)] + (1 - \tau_{amb}) \cdot I(T_\infty) \tag{13}$$

The disk temperature is obtained from Eq. (13) and the camera calibration law, determined using the reference temperature of the extended black body (Eq. (14)),

$$I(T) = \frac{I_{meas} - (1 - \varepsilon_n) \cdot I_a}{\tau \cdot \varepsilon_n} \tag{14}$$

Indeed, the camera calibration law I depends on the following data: the thermal level I_{meas} ($I_{meas} = \pm 4\% I_{meas}$) of the extended black body measured by the camera, the transmittivity τ_{amb} ($\Delta\tau_{amb} = \pm 0.001$ [19]), the black paint emissivity ε_n ($\varepsilon_n = 0.93 \pm 0.02$ [19]), and the thermal level corresponding to the environment I_a ($\Delta I_a = \pm 0.58\% I_a$). Finally, the uncertainty of the calibration law is $\Delta I(T) = \pm 6\% I(T)$. The temperature T_{disk} depends on the following data: the camera calibration law (Eq. (14)),

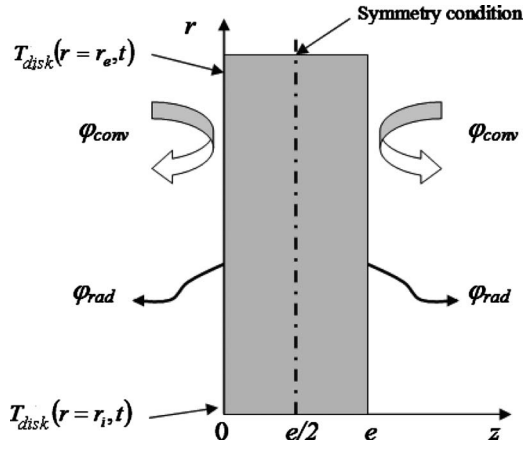

Fig. 5 Perpendicular view of the disk

the temperature of extended black body T_{CN} ($\Delta TCN = \pm 0.5$ K), the air temperature T_∞ ($\Delta T_\infty = \pm 3\% T_\infty$, T_∞ in °C), the cylinder temperature T_{cyl} ($\Delta T_{cyl} = \pm 2$ K), the emissivity, the transmittivity, and the view factors F_{i-j} ($\Delta F_{i-j} = \pm 3\% F_{i-j}$). Taking into account all of these uncertainties led to an absolute error on T_{disk} evaluated at about 1 °C.

2.3 Radiative Heat Flux Computation. Since the disk was cooled by convection and radiation, it was necessary to determine radiative heat flux in order to identify the convective heat transfer coefficient. The radiative heat flux depends on ambient and cylinder temperatures that were measured experimentally. This flux is computed from radiative balance of the forward surface of the disk. If the forward face radiosity is denoted as $J_{disk,f}$, the radiative heat flux rad can be expressed as follows:

$$\varphi_{rad} = \frac{\varepsilon_n}{1-\varepsilon_n}(\sigma T_{disk}^4 - J_{disk,f}) \tag{15}$$

We thus obtained an equation similar to Eq. (11), which depends on temperatures T_{disk}, T_{cyl}, and T_∞. By introducing the uncertainties of emissivity, disk temperature, and view factors into the calculation of the radiative heat flux, the φ_{rad} uncertainty was evaluated at about 25 W m^{-2}. In the case in which $Re_\omega = 12,900$ and $Re_U = 22,650$, it represents an error of about $\pm 4\%$.

3 Convective Heat Transfer Identification Method

Unlike disk temperature and radiative heat flux, the convective heat flux cannot be determined directly from measurements because convective phenomena depend on unknown flow characteristics. This type of problem is an inverse heat conduction problem that has been described by Beck et al. [21]. In such problems, temperature measurements can be exploited to identify surface conditions such as convective heat flux using the direct and inverse models described below.

3.1 Direct Model. The direct model involves solving partial differential equations related to the cooling of the disk. This model allows the spatio-temporal evolution of the disk temperature ($T_{cal}(r,z,t)$) to be computed. Figure 5 presents the perpendicular view of the disk with its boundary conditions. The 2D equation system used in the direct model is

$$\frac{\rho_{al}\cdot C_{al}}{\lambda_{al}}\cdot\frac{\partial T_{cal}(r,z,t)}{\partial t} = \frac{\partial^2 T_{cal}(r,z,t)}{\partial r^2} + \frac{1}{r}\cdot\frac{\partial T_{cal}(r,z,t)}{\partial r} + \frac{\partial^2 T_{cal}(r,z,t)}{\partial z^2}$$

$$T_{cal}(r,z,t=0) = T_{disk}(r,t=0)$$

$$T_{cal}(r=r_i,z,t) = T_{disk}(r=r_i,t)$$

$$T_{cal}(r=r_e,z,t) = T_{disk}(r=r_e,t)$$

$$-\lambda_{al}\cdot\left.\frac{\partial T_{cal}(r,z,t)}{\partial z}\right|_{z=e/2} = 0$$

$$-\lambda_{al}\cdot\left.\frac{\partial T_{cal}(r,z,t)}{\partial z}\right|_{z=0} = \varphi_{rad}(t) + h(r)\cdot(T_{cal}(r,z=0,t) - T_\infty) \tag{16}$$

In this model, the temperature distribution at the initial time and the boundary conditions on the inner and outer radii (r_i and r_e) of the disk are obtained from IR camera thermal levels. As shown in Fig. 5, at $z=0$ in the perpendicular direction, there is a convective heat flux density $\varphi_{conv}(r,t) = h(r)(T_{cal}(r,z=0,t) - T_\infty)$, characterized by a local time-averaged heat transfer coefficient $h(r)$ and a radiation heat flux density $\varphi_{rad}(t)$ given by Eq. (15). At $z=e/2$, the temperature gradient is null. To solve the direct model, the radial distribution of heat transfer coefficient $h(r)$ is assumed to be known. The equations in the system (Eq. (16)) are discretized and then solved by finite differences with an implicit scheme using right differences for first-order terms and central differences for second-order terms. A sensitivity study allowed us to better determine the fixed steps Δr and Δz. The temporal step Δt was fixed using the camera acquisition frequency.

3.2 Inverse Model. The inverse model allows the distribution $h(r)$ to be determined by comparing the computed and measured temperature evolutions during the cooling process. In order to reduce the effect of measurement noise on the parameter to be identified, we used spatio-temporal regularization. As explained by Beck et al. [21], this model involves searching for the distribution $h(r)$ that will minimize the following function:

$$S = \underbrace{\sum_t\sum_r [T_{cal}(r,t) - T_{disk}(r,t)]^2}_{F} + \underbrace{\alpha\cdot\sum_r [\vec{\nabla}(h(r))]^2}_{S_1} \tag{17}$$

where α is the regularization parameter of the model. The regularization term S_1 is added to a function specification method in order to obtain a stable solution in spite of the measurement noise. The S_1 term that we used was a first-order term that reduces the wide variation of the solution due to the noise [22,23]. To minimize S, we added a correction to the imposed distribution $h_{imp}(r)$ (which was arbitrarily chosen) using an iterative identification process that stops when the derivative with h of Eq. (17) tends to zero [22,23].

The procedure to validate this method is the following: A spatial variation of the heat transfer coefficient was chosen and the direct model was used to calculate the temperature histories at radial locations. Then, these data were contaminated by noise to simulate real temperature measurements. Next, these simulated measurements were introduced in the inverse model to recover the evolution of the heat transfer coefficient. The correctness of the inversion was evaluated by comparing the exact and estimated heat transfer coefficients [23]. Figure 6 presents the results obtained from temperatures contaminated by the noise of standard deviation $\sigma = 0.1$ with and without regularization. Adding the regularization term S_1 to the specification function allowed us to recover the theoretical profile of the heat transfer coefficient in spite of the measurement noise. The choice of the value of hyperparameter α will be explained in Sec. 4.

3.3 Convective Heat Transfer Uncertainty. When calculating the convective heat transfer uncertainty, it is necessary to evaluate the influence of measurement uncertainties on the convective heat transfer. The computation of the radial distribution $h(r)$ depends on the parameters ρ_{al}, C_{al}, λ_{al}, T_{disk}, T_∞, and φ_{rad} in

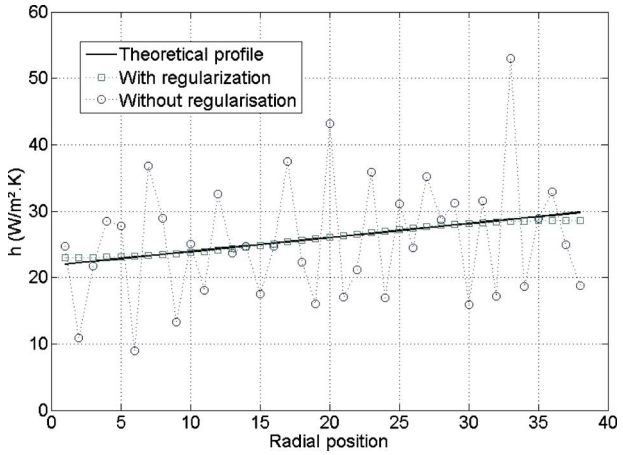

Fig. 6 Influence of regularization on heat transfer coefficient identification

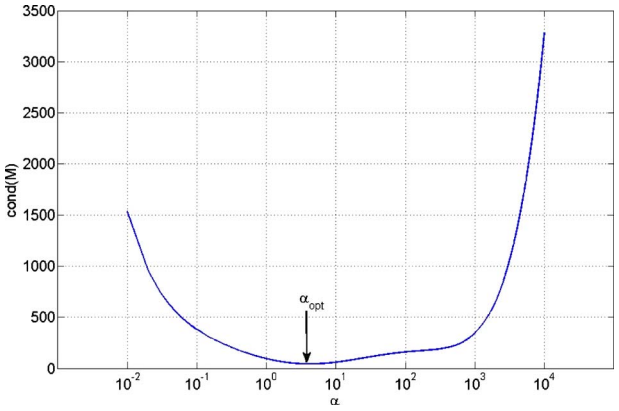

Fig. 7 Determination of α_{opt}

addition to the boundary conditions and the initial state. Since we did not have an explicit expression for $h(r)$ as a function of all these parameters, we used a sequential disturbance method [24] to determine the disturbance induced by entry parameter variations due to uncertainty. Since these variations do not depend on the radial and angular positions, we considered the global uncertainty $\Delta\bar{h}$ of the mean convective heat exchange coefficient $\bar{h}$ based on the quadratic sum of differences due to these variations. If $\Delta\bar{h}$ depends on n parameters x_i with uncertainty dx_i, the following equation can be used to find

$$\frac{\Delta\bar{h}}{\bar{h}} = \left[\frac{1}{\bar{h}^2}\cdot\sum_{i=1}^{n}\left(\frac{\partial\bar{h}}{\partial x_i}\cdot dx_i\right)^2\right]^{1/2} \tag{18}$$

Knowing that the eight angular surfaces corresponding to angles θ_i (see Fig. 3(*b*)) are equal to $(r_i - r_e)\Delta\theta/2$, the averaged convective heat coefficient is

$$\bar{h} = \frac{\sum_{i=1}^{8}\bar{h}_{\theta_i}}{8} \tag{19}$$

where

$$\bar{h}_{\theta_i} = \frac{\varphi_{\theta_i}(t)}{\bar{T}_{\text{disk},\theta_i}(t) - T_\infty} \tag{20}$$

with

$$\varphi_{\theta_i}(t) = \frac{1}{\pi\cdot(r_e^2 - r_i^2)}\cdot\int_{r_i}^{r_e} h(r,\theta_i)\cdot[T_{\text{disk}}(r,\theta_i,t) - T_\infty]\cdot 2\cdot\pi\cdot r\cdot dr \tag{21}$$

For example, in the case in which $\text{Re}_\omega = 12,900$ and $\text{Re}_U = 22,650$, we obtained $\Delta\bar{h}/\bar{h} = 0.169$.

4 Results and Discussion

The results reported in this section are expressed both in terms of local and mean Nusselt numbers (Nu and $\overline{\text{Nu}}$), which are characteristics of convective heat transfers, and in terms of rotational and air crossflow Reynolds numbers (Re_ω and Re_U) based on the diameter of the cylinder, which are characteristics of rotation and air crossflow, respectively.

Physical properties were evaluated at the air film temperature. To study the influence of rotation and air crossflow on convective heat transfers over the disk, we performed tests using the following parameter values: Re_ω between 0 and 17,200 and Re_U between 0 and 39,600. In all of the tests carried out, the value of the hyperparameter α occurred in Eq. (16) was determined from the "U-curve" presented in Fig. 7. This method explained by Blanc et al. in Ref. [25] consists of tracing the condition number (cond(M)) of the matrix to be inversed versus α. The optimal value is located at the minimum of the U-curve that has a parabolic shape (Fig. 7).

The identification method presented in Sec. 3 allows the determination of the local convective heat transfer coefficient, leading to the construction of a representative image of the local heat transfer on the disk for $36.5\ \text{mm} < r < 81.5\ \text{mm}$ by interpolating our data according to θ. In order to test the influence of the angular sectors number scanned by the camera, we compared the results obtained from eight and 16 radial profiles of temperature. Even if the 16-locations treatment would lead to a better observation of the phenomenon in the rear wake region, differences with the eight-location case could be considered negligible. Indeed, for both cases, convective exchanges obtained downstream from the cylinder and the mean heat transfer coefficients are similar (difference smaller than 2%). So, the results presented in the following sections concern an eight-location treatment.

4.1 Rotating Disk in Still Air. For the case of a rotating disk in still air (Fig. 8), local convective exchanges are uniform on the entire disk whatever the rotational speed is. Indeed, rotational convection is predominant in the considered domain of Re_ω variations compared with natural convection [19]. These results agree with those published for a single rotating disk by Dorfman [3] and aus der Wiesche (Fig. 1(*b*)) [9]. Our operational conditions, $r_e = 89\ \text{mm}$ and $2150 < \text{Re}_\omega < 17,200$, correspond to the single disk laminar flow domain. These initial observations verified on all the tests carried out for $\text{Re}_U = 0$ allow us to conclude that the radial and angular locations have a negligible influence on the local convective coefficient for a rotating disk in still air. From Eqs. (19)–(21), we determined the mean Nusselt number $\overline{\text{Nu}}$ that is plotted (Fig. 9) against the rotational Reynolds number Re_ω. The correlated relationship of the mean Nusselt number and the rotational Reynolds number for our tests is expressed as follows:

$$\overline{\text{Nu}}_{U=0} = 0.556\cdot\text{Re}_\omega^{0.5} \tag{22}$$

In Fig. 9, we added the experimental values obtained by Watel [19] corresponding to a disk of 21 mm height and 1 mm wide mounted on a 58-mm-diameter cylinder. The observed averaged difference of about 22.5% between our and her results could come from the conductive fluxes that are not taken into account in Watel's model. Indeed, in her model, which considered the disk thermally thin, the conductive flux toward the cylinder was taken equal to zero. At the cooling beginning, the disk and the cylinder are at the same temperature but the temperature decrease of the

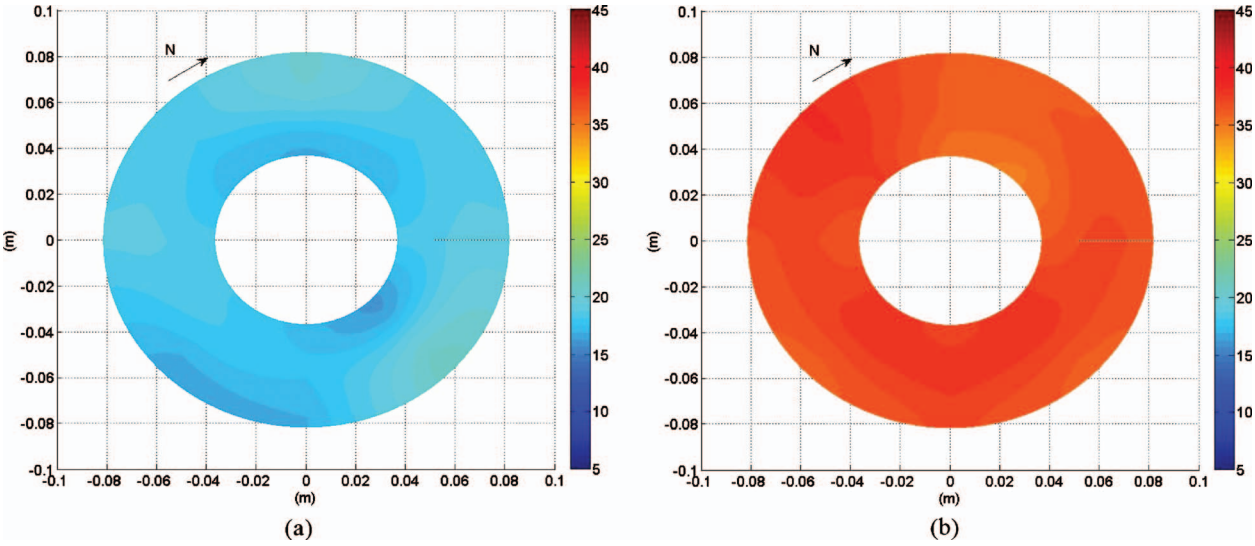

Fig. 8 Local heat transfer coefficient in W m^{-2} K^{-1} from a rotating disk in still air: (*a*) Re_ω=4300 and Re_U=0 and (*b*) Re_ω =17,200 and Re_U=0

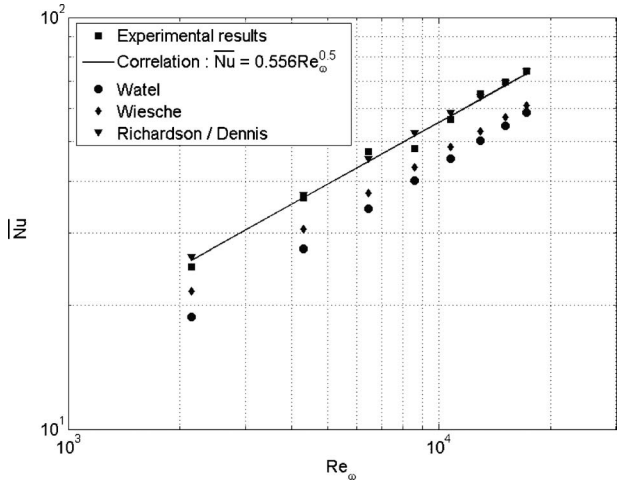

Fig. 9 $\overline{Nu}$ against Re_ω for a rotating disk in still air

disk is more rapid than the cylinder's since they do not have the same thermal inertia. When the cylinder becomes warmer than the disk, a conductive flux occurred at the disk base. Moreover, for highly conductive materials, neglecting lateral conduction could lead to important errors on heat transfer coefficient [20].

Correlations of Richardson and Saunders [7] and Dennis et al. [8] plotted in Fig. 9 are in accordance with our results with a gap of 1.6%. However, comparing to mean Nusselt numbers of aus der Wiesche's study [9], our results are 16% higher. Relative to the uncertainty on Nusselt numbers, we can conclude that the cylinder presence in our configuration does not greatly influence the mean convective exchanges compared with the disk plane.

4.2 Stationary Disk in Air Crossflow. For the case of a stationary disk in an air crossflow, a convective exchanges symmetry according to the horizontal axis is observed in Fig. 10. Upstream from the cylinder, the higher heat transfers are located at the disk leading edge, whereas the lower heat transfers appear at θ=0° near the cylinder and in angular sectors delimited by 80 deg$<\theta$ $<$100 deg and −100 deg$<\theta<$−80 deg (with the convention of

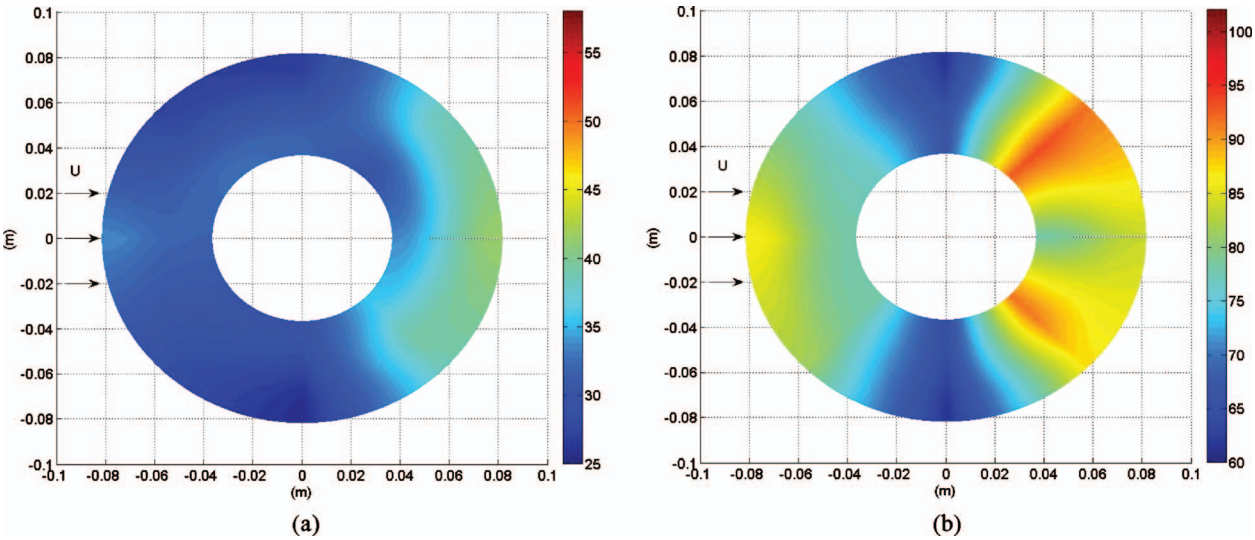

Fig. 10 Local heat transfer coefficient in W m^{-2} K^{-1} from a stationary disk in air crossflow: (*a*) Re_ω=0 and Re_U=11,350 and (*b*) Re_ω=0 and Re_U=33,950

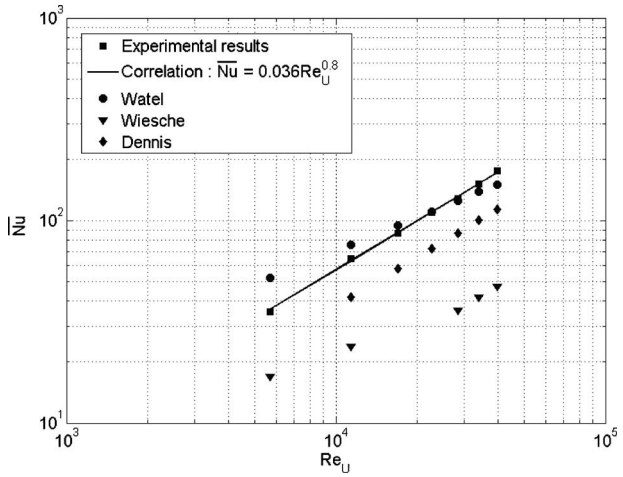

Fig. 11 $\overline{\mathrm{Nu}}$ **against** Re_U **for a stationary disk in air crossflow**

Fig. 3(*b*)). The zone of high heat transfers occurring at the disk leading edge corresponds to the boundary layer development, whereas the zones of the lower ones are linked to the separation of the boundary layer as well as to the augmentation of the boundary layer thickness up to the stagnation point. Indeed, in both cases, the flow is retarded by the pressure gradient [12,13]. Downstream from the cylinder, a second zone of high heat transfers located in angular sectors delimited by $130\ \mathrm{deg} < \theta < 150\ \mathrm{deg}$ and $-150\ \mathrm{deg} < \theta < -130\ \mathrm{deg}$ corresponds to the legs of the horseshoe vortex systems, which is a characteristic of the flow around the finned cylinder (Fig. 2) [10–14]. A second zone of low convective heat transfers comprised between both sectors is observed near the cylinder, in the zone of weak recirculation generated by the presence of the cylinder. The slighter the airflow speed, the more extended this zone (Figs. 10(*a*) and 10(*b*)). Indeed, the generation of new vortices for high speed increases the disk area exposed to an intensive heat transfer. Furthermore, for higher airflow speeds, the transition toward turbulent boundary layers destabilizes the vortex system, creating a highly turbulent wake behind the cylinder, which leads to a great increase in convective heat transfer. For the local analysis of our stationary disk in airflow, we conclude that (i) the convective heat transfer coefficient obtained by our identification method is nonuniform and greatly depends on both angular and radial position; (ii) the thermal results presented in Figs. 8(*a*) and 8(*b*) agree with flow observations stemming from bibliography [10–18].

The mean value of the heat transfer coefficient on a stationary disk in air crossflow can be calculated from its local variations (Eqs. (18)–(21)). The corresponding mean Nusselt number evolution Nu against the air crossflow Reynolds number Re_U is plotted in Fig. 11. These results obtained for the case of an airflow ($\mathrm{Pr} = 0.7$) are correlated by

$$\overline{\mathrm{Nu}}_{\omega=0} = 0.036 \cdot \mathrm{Re}_U^{0.8} \tag{23}$$

The correlation of Watel [19] plotted in Fig. 11 comes from measures realized with low rotational and high air crossflow velocities, a domain where convective heat transfers are supposed to be governed exclusively by the air crossflow according to Watel. However, for $\mathrm{Re}_U < 22{,}650$, the higher values obtained by Watel could be explained by the increasing influence of rotation with the decreasing of airflow speed for her tests. On the contrary, for $\mathrm{Re}_U > 22{,}650$, an inversion operates. Indeed, our local analysis shows us (i) a zone of lower convective heat transfer downstream from the cylinder for radial positions near the cylinder and (ii) an increase in the high convective exchanges area on the rear part of the disk with the increase in the airflow speed (Fig. 10). So, for a 21-mm-high disk, corresponding to Watel study, the convective phenomena downstream the cylinder are mainly governed by the observation (i), whereas for a 60-mm-high fin, corresponding to our study, they could be explained by the observation (ii). So, mean convective exchanges seem to increase with the disk height.

Results of aus der Wiesche [9] and Dennis et al. [8] plotted in Fig. 11 correspond to the stationary disk in an air crossflow. The important difference between their results and ours can be explained by the high convective exchanges zone on the rear part of the disk due to the presence of a cylinder (Fig. 10). Indeed, in the case of the disk plane presented in Fig. 1(*a*), local variations of the heat transfer coefficient are only due to the boundary layer development at the leading edge of the disk. So, the presence of a cylinder on the disk generates important local variations of the heat transfer coefficient, leading to a higher mean Nusselt number value than the case of the disk plane.

4.3 Rotating Disk in Air Crossflow. Local results of the convective heat transfer on a rotating disk in air crossflow are represented in Fig. 12 for four couples of values ($\mathrm{Re}_\omega, \mathrm{Re}_U$). For the couples $\mathrm{Re}_\omega = 4300$ and $\mathrm{Re}_U = 11{,}350$ (Fig. 12(*a*)) and $\mathrm{Re}_\omega = 17{,}200$ and $\mathrm{Re}_U = 33{,}950$ (Fig. 12(*d*)), in comparison with the case of a stationary disk in air crossflow, a relative uniformity of the convective coefficient is observed. However, contrary to the rotating disk in still air case, a zone of higher transfer is observed on the ascending side, where the airflow and rotation speeds are in the same direction (comoving), whereas a zone of weaker transfers appears on the descending side, where the airflow and rotation speeds are in opposite directions (counter-moving) (as in Ref. [9]). Finally, in comparison with the case of the stationary disk in airflow, the rotation effect tends to increase the mean convective coefficient by about 9% for $\mathrm{Re}_\omega = 4300$ and $\mathrm{Re}_U = 11{,}350$ up to about 16% for $\mathrm{Re}_\omega = 17{,}200$ and $\mathrm{Re}_U = 33{,}950$.

For $\mathrm{Re}_\omega = 4300$ and $\mathrm{Re}_U = 33{,}950$ (Fig. 12(*b*)), a symmetry according to the horizontal axis is observed, similar to the one observed in Fig. 10 relative to the fixed disk in an air crossflow. However, three zones of higher heat transfer are observed at other angular locations. Both of them occur at $\theta \cong \pm 90$ deg, whereas the last one is exactly behind the cylinder ($\theta \cong 180$ deg) in the wake zone. Moreover, a convective coefficient decrease is observed for $\theta \cong \pm 130$ deg. However, observed gradients are smaller than the ones in Fig. 10(*b*)). Indeed, the comparison between Figs. 12(*b*) and 10(*b*) allows us to observe both totally different maps of convective heat transfers at the disk surface, whereas the computed mean convective coefficients are almost identical. In fact, the increase in the mean heat transfer coefficient due to the rotation is about 6% relative to the stationary disk. In conclusion, even for the lowest rotational Reynolds numbers, the rotation tends to modify the local distribution of h without affecting significantly its mean value.

For $\mathrm{Re}_\omega = 17{,}200$ and $\mathrm{Re}_U = 11{,}350$ (Fig. 12(*c*)), the convective exchanges tend to be uniform on the entire disk area with a slighter transfer zone at $\theta = 0$ deg. This zone is influenced by the stagnation point that should substantially move in the rotation direction. However, our eight-location treatment according to θ does not allow us to identify the real location of the stagnation point. For this case, rotation greatly influences local distribution of the convective coefficient as well as the mean coefficient since its value increases by about 67% compared with the stationary disk in the air crossflow case.

From the analysis of the local convective coefficient, it appears that the thermal behavior of the disk and the mean value of the convective coefficient greatly depend on the couple Re_ω and Re_U. In order to identify the influence zones of rotation, airflow, and coupling rotation/airflow, we compare all the mean Nusselt numbers computed with the one corresponding to the stationary disk in an airflow. So, the evolution of the ratio $\overline{\mathrm{Nu}}/\overline{\mathrm{Nu}}_{\omega=0}$ against the ratio $\mathrm{Re}_\omega/\mathrm{Re}_U$ is studied as in Ref. [9]. From the plot of our experimental results (Fig. 13), three zones are underlined. For $\mathrm{Re}_\omega/\mathrm{Re}_U < 0.18$, our experimental values fluctuate around the

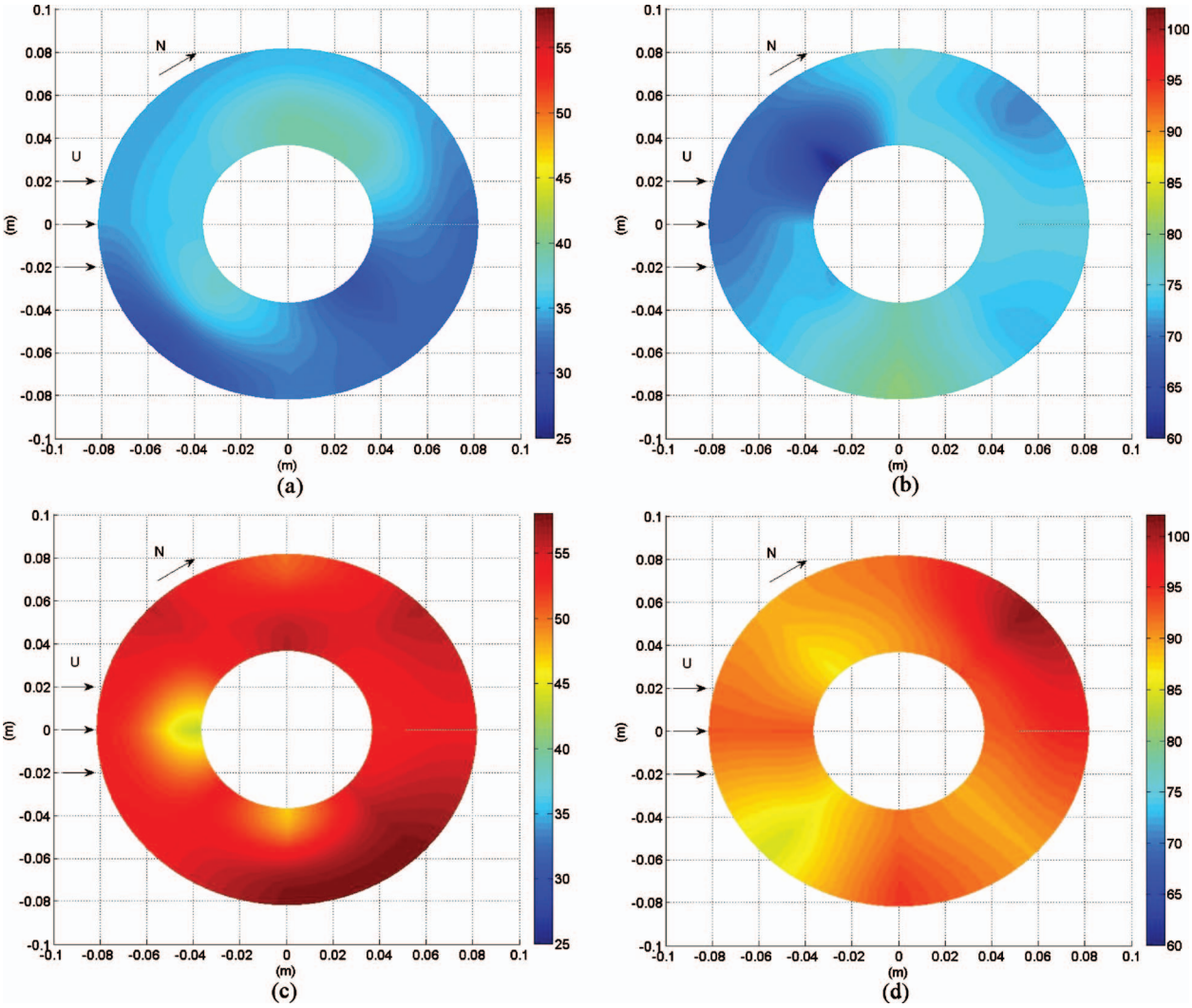

Fig. 12 Local heat transfer coefficient in W m^{-2} K^{-1} from a rotating disk in air crossflow: (*a*) Re_ω=4300 and Re_U=11,350, (*b*) Re_ω=4300 and Re_U=33,950, (*c*) Re_ω=17,200 and Re_U=11,350, and (*d*) Re_ω=17,200 and Re_U=33,950

horizontal axis $\overline{Nu}/\overline{Nu}_{\omega=0}=1$, corresponding to a mean Nusselt number independent of rotation. Therefore, this first zone corresponds to the domain of airflow influence. For $0.18<Re_\omega/Re_U<0.77$, the mean Nusselt number is slightly influenced by the rotation up to a value of $1.3\overline{Nu}_{\omega=0}$ at $Re_\omega/Re_U=0.77$. From $Re_\omega/Re_U>0.77$, rotation influence on the mean convective exchanges increases. In order to quantify convective exchanges augmentation engendered by the rotation, two correlations similar to Eqs. (3) and (4) are proposed:

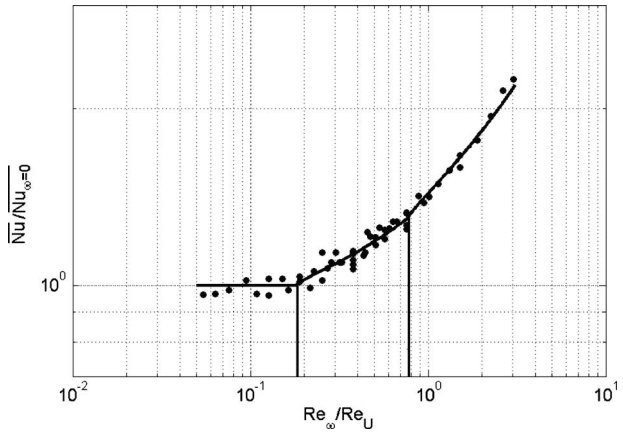

Fig. 13 Ratio of mean Nusselt numbers against Reynolds number ratio

$$\overline{Nu}=\overline{Nu}_{\omega=0}\cdot\left[1+0.45\cdot\left(\frac{Re_\omega}{Re_U}-0.18\right)^{0.77}\right]$$

$$\text{for } 0.18<\frac{Re_\omega}{Re_U}<0.77 \tag{24}$$

$$\overline{Nu}=\overline{Nu}_{\omega=0}\cdot\left[1.3+0.45\cdot\left(\frac{Re_\omega}{Re_U}-0.77\right)^{0.82}\right] \quad \text{for } \frac{Re_\omega}{Re_U}>0.77 \tag{25}$$

It is also possible to predict convective exchanges by considering Re_ω and Re_U separately, as in Eqs. (5) and (6). For $Re_\omega/Re_U<0.18$, our results are correlated by Eq. (23). To correlate our results for $Re_\omega/Re_U>0.18$, the following equation is proposed:

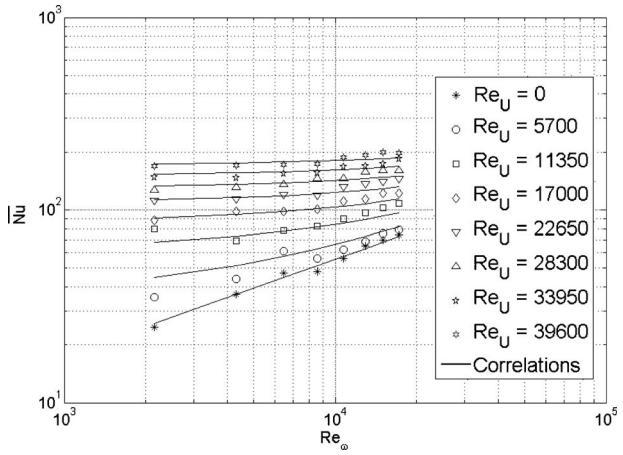

Fig. 14 Evolution of $\overline{\mathrm{Nu}}$ with Re_ω for various Re_U values

$$\overline{\mathrm{Nu}} = \sqrt{(0.036 \cdot \mathrm{Re}_U^{0.8})^2 + (0.556 \cdot \mathrm{Re}_\omega^{0.5})^2} \quad \text{for} \quad \frac{\mathrm{Re}_\omega}{\mathrm{Re}_U} > 0.18 \tag{26}$$

Figure 14 presents the experimental and correlated mean Nusselt numbers against Re_ω varying from 2150 to 17,200 for all of the Re_U values varying from 5700 to 39,600. The agreement between correlations (Eqs. (23) and (26)) and our experimental values is better than 10%. The highest steps are observed for the higher rotational Reynolds numbers. It would be due to the stronger influence of the rotation observed (Fig. 13) from the value $\mathrm{Re}_\omega/\mathrm{Re}_U > 0.77$. In conclusion, correlations (Eqs. (24) and (25)) allow us to predict the global thermal behavior of a rotating disk mounted on a shaft in an air crossflow by taking into account the combined effects of rotation and airflow. However, simpler correlations like Eqs. (23) and (26) could be used for practical applications to determine convective exchanges on the disk with a precision of 10%.

5 Conclusion

The experimental setup presented in this paper allowed us to evaluate the local distribution of the convective heat transfer coefficient on a rotating disk mounted on a shaft in air crossflow. In each test, the evolution of the thermal levels was recorded by the IR camera every 0.5 cm on the disk radius while the system was cooling for eight angular positions. The thermal levels were converted to temperature values using the camera calibration law and the radiative balance of the surface scanned. An inverse model based on spatio-temporal regularization allowed us to take both the radial conduction and radiative fluxes into account. This method allows us to determine local variations of the convective heat transfer coefficient. Concerning the case of the rotating disk in still air for $2150 < \mathrm{Re}_\omega < 17,200$, local heat transfers are uniform on the disk surface and a correlation between $\overline{\mathrm{Nu}}$ and Re_ω is proposed to predict its mean thermal behavior. In these conditions, the shaft influence can be considered negligible since obtained results do not differ much from the ones corresponding to the case of a shaftless disk given in literature. For the case of the stationary disk in air crossflow for $5700 < \mathrm{Re}_U < 39,600$, zones of higher heat transfers are located at the leading edge of the disk and where the legs of the horseshoe vortex systems appear. The lower ones occur at the stagnation point in front of the cylinder and at the flow separation, behind it. A correlation between $\overline{\mathrm{Nu}}$ and Re_U is proposed. When the disk rotates in air crossflow, physical phenomena depend on the couple of values $(\mathrm{Re}_\omega/\mathrm{Re}_U)$. For the lowest values of Re_ω considered, the rotation tends to strongly reduce gradients of heat transfer coefficient on the disk surface without having a significant effect on the mean Nusselt number. Conversely, for highest Re_ω and lowest Re_U, the rotation greatly influences local distribution of the convective coefficient as well as the mean Nusselt number, which can be increased up to 67%. In fact, in all of the cases, the rotation homogenizes convective heat transfers at the disk surface. Concerning the mean Nusselt numbers in order to quantify rotation influence, the evolution of the ratio $\overline{\mathrm{Nu}}/\overline{\mathrm{Nu}}_{\omega=0}$ against the ratio $\mathrm{Re}_\omega/\mathrm{Re}_U$ has been studied. In this way, three zones were highlighted. In the first one, there is no rotation influence, in the second one, it is slight, whereas in the last one, it becomes stronger. The proposed correlations of mean Nusselt numbers allows us to characterize mean convective exchanges of the rotating disk in air crossflow in all the conditions studied.

Nomenclature

C = specific heat
D_i = cylinder outer diameter
e = fin thickness
F_{a-b} = view factor between a and b
H = $(r_e - r_i)$ disk height
h = convective coefficient
I = thermal level
J = radiosity
L = cylinder length
Nu = $(h\,D_i/\lambda_a)$ Nusselt number
$\overline{\mathrm{Nu}}$ = $(\bar{h}\,D_i/\lambda_a)$ Nusselt number
Re_U = $(U\,D_i/\nu_a)$ airflow Reynolds number
$\mathrm{Re}_{U,\mathrm{re}}$ = $(U\,r_e/\nu_a)$ airflow Reynolds number
Re_ω = $(\omega r_i\,D_i/\nu_a)$ rotational Reynolds number
$\mathrm{Re}_{\omega,\mathrm{re}}$ = $(\omega r_e^2/\nu_a)$ rotational Reynolds number
r = radial coordinate
r_i = disk inner radius
r_e = disk outer radius
t = time
T = temperature
U = airflow speed
z = axial coordinate

Greek

ε = emissivity
φ = heat flux density
λ = heat conductivity
ν = kinematic viscosity
ρ = density
θ = angular coordinate
σ = Stefan Boltzmann constant
τ = transmittivity
ω = rotational speed

Subscripts

al = aluminum
amb = ambiance
cal = computed value
conv = convective heat transfer
cyl = cylinder
disk = disk
meas = measured value
n = black paint
rad = radiative heat transfer
∞ = outside the boundary layer
$\bar{A}$ = average A

References

[1] Gregory, N., Stuart, J., and Walker, W., 1955, "On the Stability of Free Dimensional Boundary Layer With Application to the Flow Due to Rotating Disk," Philos. Trans. R. Soc. London, **248**, pp. 155–199.
[2] Kreith, F., 1967, *Transmission de la Chaleur et Thermodynamique, Masson et*

Cie Editeurs, Traduction Franaise de l'Ouvrage de Frank Kreith: Principles of Heat Transfer, International Textbook Company, Paris.
[3] Dorfman, L., 1963, *Hydrodynamic Resistance and Heat Loss From Rotating Solids*, Oliver & Boyd, Edinburgh.
[4] Millsaps, K., and Polhausen, K., 1952, "Heat Transfer by Laminar Flow From a Rotating Plate," J. Aeronaut. Sci., **19**, pp. 120–126.
[5] Wagner, C., 1948. "Heat Transfer From a Rotating Disk to Ambient Air," J. Appl. Phys., **19**, pp. 837–839.
[6] Goldstein, S., 1935, "On the Resistance to the Rotation of a Disk Immersed in a Fluid," Proc. Cambridge Philos. Soc., **31**, pp. 232–241.
[7] Richardson, P., and Saunders, O., 1963, "Studies of Flow and Heat Transfer Associated With a Rotating Disk," J. Mech. Eng. Sci., **5**, pp. 336–342.
[8] Dennis, R., Newstead, C., and Ede, A., 1970. "The Heat Transfer From a Rotating Disc in an Air Crossflow," Proceedings of the Fourth International Heat Transfer Conference, Paper No. FC 7.1.
[9] aus der Wiesche, S., 2007. "Heat Transfer From a Rotating Disk in a Parallel Air Crossflow," Int. J. Therm. Sci., **46**, pp. 745–754.
[10] Goldstein, R., and Karni, J., 1984, "The Effect of a Wall Boundary Layer on Local Mass Transfer From a Cylinder in Crossflow," ASME J. Heat Transfer, **106**, pp. 260–267.
[11] Sung, H., Yang, J., and Park, T., 1996, "Local Convective Mass Transfer on Circular Cylinder With Transverse Annular Fins in Crossflow," Int. J. Heat Mass Transfer, **39**, pp. 1093–1101.
[12] Schüz, G., and Kottke, V., 1987. "Visualization of Flow, Heat, and Mass Transfer on Finned Tubes in Cross Flow," *Proceedings of the Fourth International Symposium on Flow Visualization*, Hemisphere, Washington, D.C..
[13] Schüz, G., and Kottke, V., 1992, "Local Heat Transfer and Heat Flux Distributions in Finned Tube Heat Exchangers," Chem. Eng. Technol., **15**, pp. 417–424.
[14] Sparrow, E., and Preston, C., 1986, "Heat Transfer From Rotating Annular Fins," Int. J. Heat Mass Transfer, **29**, pp. 831–839.
[15] Fisher, E., and Eibeck, P., 1990, "The Influence of a Horseshoe Vortex on Local Convective Heat Transfer," ASME J. Heat Transfer, **112**, pp. 329–335.
[16] Roulund, A., Mutlu Sumer, B., Fredsoe, J., and Michelsen, J., 2005, "Numerical and Experimental Investigation of Flow and Scour Around a Circular Pile," J. Fluid Mech., **534**, pp. 351–401.
[17] Fu, H., and Rockwell, D., 2005, "Shallow Flow Past a Cylinder: Transition Phenomena at Low Reynolds Number," J. Fluid Mech., **540**, pp. 75–97.
[18] Sahin, B., Ozturk, N., and Gurlek, C., 2008, "Horseshoe Vortex Studies in the Passage of a Model Plate-Fin-and-Tube Heat Exchanger," Int. J. Heat Fluid Flow, **29**, pp. 340–351.
[19] Watel, B., 1997. "Etude des Échanges Convectifs sur un Cylindre Aileté en Rotation Soumis un Courant d'Air Parallèle aux Ailettes," Ph.D. thesis, Université de Valenciennes et du Hainaut Cambrésis, Valenciennes, France.
[20] Bougeard, D., 2007, "Infrared Thermography Investigation of Local Heat Transfer in a Plate Fin and Two-Tube Rows Assembly," Int. J. Heat Fluid Flow, **28**, pp. 988–1002.
[21] Beck, J., Blackwell, B., and St. Clair, C., 1985, *Inverse Heat Conduction–Ill-Posed Problems*, Wiley Interscience, New York.
[22] Tikhonov, A., and Arsenin, V., 1977, *Solution of Ill-Posed Problems*, V. H. Winston & Sons, Washington.
[23] El Abbadi, A., 2005. "Dévelopement de Méthodes de Mesures des Transferts Convectifs par Thermographie Infrarouge: Application aux Ailettes d'Échangeurs Hautes Performances," Ph.D. thesis, Universit de Valenciennes et du Hainaut Cambrsis, Departement Energtique Industrielle de l'Ecole des Mines de Douai.
[24] Moffat, R., 1988, "Describing the Uncertainty in Experimental Results," Exp. Therm. Fluid Sci., **1**, pp. 3–17.
[25] Blanc, G., Raynaud, M., and Chau, T., 1998, "A Guide for the Use of the Function Specification Method for 2D Inverse Heat Conduction Problems," Rev. Gen. Therm., **37**, pp. 17–30.

Bi-Li Deng
Department of Energy and Resources Engineering,
College of Engineering,
Peking University,
Beijing 100871, China

Xin-Rong Zhang
Department of Energy and Resources Engineering,
College of Engineering,
Peking University,
Beijing 100871, China;
Department of Mechanical Engineering,
Energy Conversion Research Center,
Doshisha University,
Kyo-Tanabeshi, Kyoto 610-0321, Japan

Hiroshi Yamaguchi
Department of Mechanical Engineering,
Energy Conversion Research Center,
Doshisha University,
Kyo-Tanabeshi, Kyoto 610-0321, Japan

Bifurcated Forced Convective Heat Transfer of Supercritical CO_2 Flow in Plane Symmetric Sudden Expansion Duct

This study presents a computational investigation of forced convection of supercritical CO_2 flow in plane symmetric sudden expansion duct at an expansion ratio of 2 in flow asymmetric regime. Computations were conducted at various Reynolds numbers in flow asymmetric regime and low wall heat fluxes below 500 W/m^2 to examine the Reynolds number and thermal effects on the flow and heat transfer of the bifurcated flow. General flow features and temperature distributions are presented. The transitional Reynolds numbers above, which a third recirculation region will appear at different wall heat flux are presented, and thus thermal effects on the flow stability are discussed. Reynolds number and thermal effects on distributions of wall skin friction, pressure coefficient, and Nusselt number are presented and discussed. [DOI: 10.1115/1.4002440]

Keywords: supercritical CO_2, sudden expansion, bifurcated flow, forced convection

1 Introduction

CO_2 is widely considered to be the potential candidate of the next-generation refrigerant due to its unique combination of ecological and personal safety. Supercritical CO_2 have been widely applied as working fluid in supercritical boiler in nuclear engineering, extraction in chemical engineering, and during the last 2 decades, residential air-conditioning, vehicle air-conditioning, heat pumps [1], and solar collector [2] in HVAC engineering. As shown in Fig. 1, supercritical CO_2, as well as the other supercritical fluids, has the most remarkable characteristic that its thermophysical properties exhibit rapid variations with a change in temperature, especially near the pseudocritical point at which the specific heat reaches the peak at given pressure. This characteristic brings many different heat transfer features from the constant-property fluids. Heat transfer of supercritical fluids has been investigated extensively [3–13]; earlier studies [3–7] show that the heat transfer coefficient is affected significantly by local Reynolds number, pressure, and especially, wall heat flux. Many heat transfer correlations in the Dittus–Boelter form $Nu = C\,Re^m Pr^n$ are proposed. More recently, much attention [8–12] was paid on mini/micro channels to help design the heat exchangers in CO_2-based applications. However, to the best knowledge of the authors, the investigation on flow separation associated with heat transfer for supercritical CO_2 flow is very limited in open literature.

Flow separation caused by the change of flow passage exists widely in most types of engineering applications with working fluid inside. Compared with the conventional ones, heat exchangers in CO_2-based applications, especially in HVAC engineering, are smaller in size [8]. Owing to this downsizing and changes of flow passages in them, laminar separated supercritical CO_2 flow will appear if the Reynolds number is sufficient low. Being one of the classical models in the field of separated flow, sudden expansion flow has received extensive studies [14–28] for its simplicity in geometry and inclusion of flow and heat transfer features that exhibited in more complicated flow separation geometries. For two-dimensional laminar flows in symmetric sudden expansion, the main flow characteristic is the presence of recirculation regions (RRs) on the walls due to the sudden pressure drop at the enlargement. There exists a critical Reynolds number (Re_{cr}) above, which flow asymmetric occurs due to a pitchfork (symmetric-breaking) nature. This transitional phenomenon from flow symmetric steady to asymmetric steady state was confirmed by experimental investigations [14–17] in which detailed velocity distributions are measured at different cross sections using laser Doppler anemometer (LDA). Much attention of additional numerical studies [18–24] was paid on the nonlinear stability in this geometry. Nevertheless, results of these published works are limited to investigate the flow behavior under isothermal conditions. Studies on forced convection of sudden expansion flow are limited.

Nie and Armaly [25] provided a three-dimensional forced convection in the symmetric flow regime in which Reynolds number is below the critical value with steady and symmetric flow. For the same flow geometry, Thiruvengadam et al. [26] presented a forced convection regarding Reynolds number above the critical value, i.e., asymmetric regime, where flow is steady but asymmetric. In these two studies, as well as the abovementioned studies, thermophysical properties were all treated as constants. However, the variations of thermophysical properties should be involved for numerical studies on heat transfer of property-variation fluids. Guo et al. [27] examined the thermal effects on the RRs in sudden expansion gas flow in which the ideal gas state equation is solved as one of the governing equations. They demonstrated that the recirculation region length decreases with the increasing of heating intensity and pointed out that the heating-induced adverse pressure gradient in the flow direction resulted in the shrinkage of RRs. Zhang et al. [28] examined the bifurcation phenomenon and investigated the forced convection of supercritical CO_2 flow in plane symmetric sudden expansion in the symmetric regime. They presented that the RRs increased and the Re_{cr} decreased as the wall heat flux increased.

On the flow stability for flow in this sudden expansion geometry, Hawa and Rusak [24] utilized asymptotic analyses and numerical simulation to investigate the dynamics of two-dimensional disturbances on the flow stability. They reported that

Contributed by the Heat Transfer Division of ASME for publication in the JOURNAL OF HEAT TRANSFER. Manuscript received March 23, 2010; final manuscript received August 18, 2010; published online November 3, 2010. Assoc. Editor: W. Q. Tao.

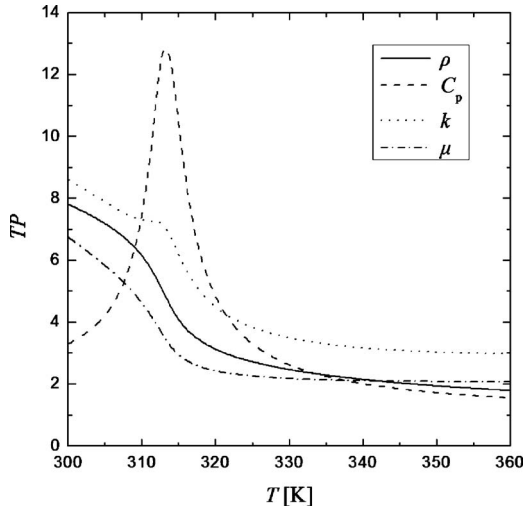

Fig. 1 Variations of thermophysical properties (TP) with temperature at 9 Mpa, density $\rho\times10^{-2}$(kg/m^3), specific heat $C_p\times10^{-3}$(J/kg K), thermal conductivity $k\times10^{2}$(W/m K), and dynamic viscosity $\mu\times10^{5}$(Pa s)

the loss of stability was caused by the interaction of the viscous dissipation, downstream convection of perturbation by the base symmetric flow, and upstream convection induced by two-dimensional asymmetric disturbance. The first two were the stabilizing effects and the last third was the destabilizing one. There was a critical balance among them when Reynolds number was at the critical value.

According to the above survey, we found limited study on heat transfer of bifurcated supercritical CO_2 flow in open literature, which motivated this study. In this work, bifurcated forced convection of supercritical CO_2 flow in plane symmetric sudden expansion is investigated in the flow asymmetric regime. The thermal effects on the transitional Reynolds numbers are presented, and thus thermal effects on the flow stability are discussed. Reynolds number and thermal effect on wall skin friction, pressure coefficient, and Nusselt number distributions are presented and discussed.

2 Problem and Solution Procedure

This work focuses on the flow and heat transfer features of the bifurcated flow in the asymmetric regime, which is an extension work in the symmetric regime by Zhang et al. [28]. A schematic diagram of the computation model for two-dimensional plane symmetric sudden expansion is shown in Fig. 2. The origin of the coordinate system is set at the bottom of the lower step. The streamwise (x) and transverse (y) direction is shown in the figure. The heights of the duct upstream d and downstream D provide a configuration with an expansion ratio (ER=D/d) of 2, which has received a lot of attention for this kind of geometry. The length downstream L is 60 times that of the step height S (S=0.5 mm) to ensure the flow can be treated as fully developed at the outlet. Typical operation and initial condition are utilized. Pressurized

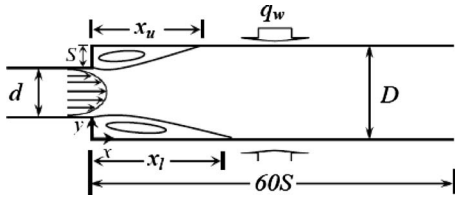

Fig. 2 Schematic diagram of the computation model

CO_2 flows in the duct at an operational supercritical pressure P of 9 MPa. The inlet of the supercritical CO_2 is fixed as hydrodynamically steady and fully developed with isothermal inlet temperature T_0 of 313.2 K at which the thermophysical properties are: density ρ=483.1 kg/m^3, specific heat C_p=12831 J/kg K, thermal conductivity k=0.070424 W/m K, and dynamic viscosity $\mu=3.46\times10^{-5}$ Pa s. The distribution of the streamwise velocity component u is set as laminar fully developed; the transverse velocity component v is equal to zero. The walls of the duct downstream are heated with constant uniform heat flux q_w below 500 W/m^2 and the other walls are all set as adiabatic. All walls are treated as no-slip ones. Moreover, the outflow boundary condition is utilized with a zero diffusion flux for all variables.

The thermophysical properties of the supercritical CO_2 are obtained based on the pressure and temperature values from the NIST Standard Reference Database 23 (REFPROP) version 8.0 [29]. Considering that the pressure drop between the inlet and outlet in this computation domain is negligible compared to the operational pressure, the properties of the supercritical CO_2 are treated temperature-based only in this study for the sake of numerical calculation. Thermophysical properties are arranged as piecewise polynomial functions of temperature at 9.0 MPa based on the data obtained from REFPROP database with an accuracy of more than 99%.

With the variations of thermophysical properties involved in the computation, governing equations for two-dimensional laminar flow without buoyancy are given by the following.

Continuity equation

$$\frac{\partial\rho}{\partial t}+\nabla\cdot(\rho\mathbf{V})=0 \tag{1}$$

Momentum equation

$$\frac{\partial(\rho\mathbf{V})}{\partial t}+\nabla\cdot(\rho\mathbf{V}\mathbf{V})=\nabla(\mu\nabla\mathbf{V})-\nabla P \tag{2}$$

Energy equation

$$\frac{\partial(\rho h)}{\partial t}+\nabla\cdot(\rho\mathbf{V}h)=\nabla\left(\frac{k}{C_p}\nabla h\right) \tag{3}$$

In Eq. (3), h is the specific enthalpy as

$$h=\int_{T_0}^{T}C_p dT+h_0 \tag{4}$$

where h_0=344420 J/kg is the reference specific enthalpy at T_0.

Code based on the finite volume method is utilized for the numerical solution to solve the continuity, momentum, and energy equations. Nonuniform mesh is generated in order to get more grids adjacent to the corners and walls. The SIMPLEC algorithm is used for the pressure velocity coupling and the momentum and energy equations are discretized with the second-order upwind scheme. The convergence criterion required that the scaled residuals be smaller than 10^{-8} for the energy and the momentum equations and smaller than 10^{-7} for the mass equation.

A test of grid independence and code validation were conducted. With difference in less than 1%, grid of $300(x)\times60(y)$ was selected for the computation. Computational results of u profiles at different cross sections are compared with the measurements by Durst et al. [14] in the symmetry and asymmetric regime, respectively. Very good agreements between the computational and experimental results are found. More details and illustrations for the numerical scheme, test of grid independence, and code validation could be found in Ref. [28].

3 Results and Discussion

Calculations were conducted for cases at various Reynolds number and wall heat fluxes. For the sake of examining the thermal effect, case of a zero wall heat flux (isothermal) with no

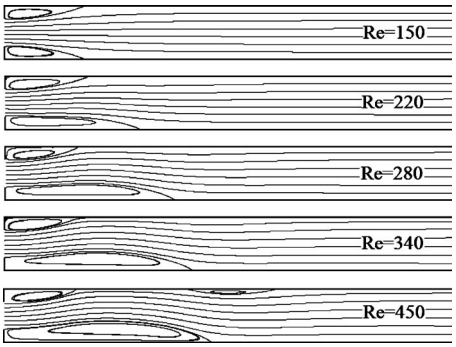

Fig. 3 Streamlines for general flow behaviors at $q_w = 250\ W/m^2$

variation of thermophysical properties is also calculated. Due to the similarity and space limitation of this paper, results are presented at Re=280 for cases of different wall heat flux and at $q_w = 250\ W/m^2$ for cases of different Reynolds numbers to illustrate the Reynolds number effects and thermal effects, respectively.

3.1 Compressibility and Buoyancy Effect. In order to examine compressibility and buoyancy effect, we calculate the Mach number Ma and Richardson number Ri for this study.

The Mach number is defined as

$$Ma = u_0/\sqrt{\gamma RT} \tag{5}$$

where γ is the ratio of specific heats (C_p/C_v) and R is the molar gas constant.

The definition of Richardson number is formulated as

$$\mathrm{Ri} = \frac{\mathrm{Gr}}{\mathrm{Re}^2} = \frac{(\rho_{ref} - \rho_w) g D^3}{\rho_{ref} \nu_{ref}^2 \mathrm{Re}^2} \tag{6}$$

where ρ_w and ρ_{ref} represent the density at wall temperature and reference temperature, respectively, and ν_{ref} denotes the kinetic viscosity at reference temperature. The reference temperature, $T_{ref} = (T_0 + T_w)/2$, is selected as the arithmetic mean value of inlet temperature and wall temperature.

For laminar forced convection flow in horizontal two-dimensional duct, the buoyancy effect becomes negligible when $\mathrm{Ri} < 10$ [30]. Let us examine the range of buoyancy effect. The maximum buoyancy effect exists in the case of the lowest Reynolds number Re=198 and highest wall heat flux $q_w = 500\ W/m^2$, and the minimum lies opposite in the case of Re=377 and $q_w = 100\ W/m^2$. The examination show that Ri ranges from 8×10^{-3} to 3×10^{-2}. Accordingly, the buoyancy effect on the flow and heat transfer is negligible [30] and forced convection dominates in the present study. Furthermore, the range of Ma is examined from 7×10^{-6} to 2×10^{-5}, the compressibility effect can be ignored [31] in this study.

3.2 Flow Behavior and Stability. Figure 3 shows the general flow behaviors of supercritical CO_2 in sudden expansion duct. At lower Re (i.e., Re=150), the flow is symmetric with two recirculation regions of equal size. Bifurcation phenomenon occurs when Re is at some critical value ($\mathrm{Re_{cr}}$). Flow becomes asymmetric (i.e., Re=220, 280, 340) as Re is above this value and the sizes of the two RRs on the two walls are unequal, one keeps increasing while the other shrinks as Re increases. At higher Re (i.e., Re=450), one more RR is found on the wall downstream, the shrinking one. Hence, there exist a critical Reynolds number ($\mathrm{Re_{cr}}$) above, which bifurcation phenomenon occurs and a transitional Reynolds number ($\mathrm{Re_{tr}}$) above, which a third RR appears. This study is limited between the $\mathrm{Re_{cr}}$ and the $\mathrm{Re_{tr}}$ in the flow asymmetric regime.

Table 1 shows the thermal effects on the critical Reynolds numbers [28] and transitional Reynolds numbers. With the increasing of wall heat fluxes, $\mathrm{Re_{tr}}$ decreases as well as $\mathrm{Re_{cr}}$, which means that at the same Re below the $\mathrm{Re_{tr}}$, the flow is less stable with higher wall heat flux. Because the bulk temperature increases as the wall heat flux increases, both of the density and viscosity decrease as shown in Fig. 1, which leads to a increase of local Reynolds number, and thus flow gets less stable. As a result, heating-induced interaction of property-variation has a destabilizing effect on the flow stability of supercritical CO_2 flow in sudden expansion duct.

Table 1 Comparisons of critical Reynolds number and transitional Reynolds number as wall heat flux increase

$q_w(W/m^2)$	0	100	250	500
$\mathrm{Re_{cr}}$ [29]	216	212.5	206	198
$\mathrm{Re_{tr}}$	383	377	370	360

Due to the symmetric geometry and boundary conditions of the computation, the RR on which wall is larger in flow asymmetric regime is absolutely random for all computational cases. For the purpose of discussion convenience, it should be mentioned that we treat the RR on the lower wall as the larger one in this work. For two-dimensional flow separation and reattachment x_r, location of reattachment point on the wall where the streamwise velocity gradient equal to zero $(\partial u/\partial y = 0)$, are usually utilized to characterize the size of RR on the wall. In order to identify the recirculation length and transitional Reynolds number, additional convergence criteria with high accuracy are adopted in this paper, namely, a steady solution was identified when the locations of reattachment points did not change any further. Integrated with the results of our previous results in flow symmetric regime [28], a bifurcation diagram for forced convection of supercritical CO_2 sudden expansion flow below the transitional Reynolds number is shown in Fig. 4. It is seen that bifurcation phenomenon occurs at some critical values of Re with different wall heat flux, the reattachment lengths of the lower wall (x_l) and the upper wall (x_u) turn unequal suddenly. The former increases while the latter decreases. When the Re increases, the larger one keeps increasing while the smaller one decreases slightly. As a result, the reattachment length difference between the upper wall and lower wall keep increasing. Let us examine the thermal effect, when wall heat flux increases at a fixed Reynolds number, x_l increases while x_u decreases slightly, and thus the difference of reattachment length between the two walls increases. These features can be illustrated and interpreted by the following results of the distribu-

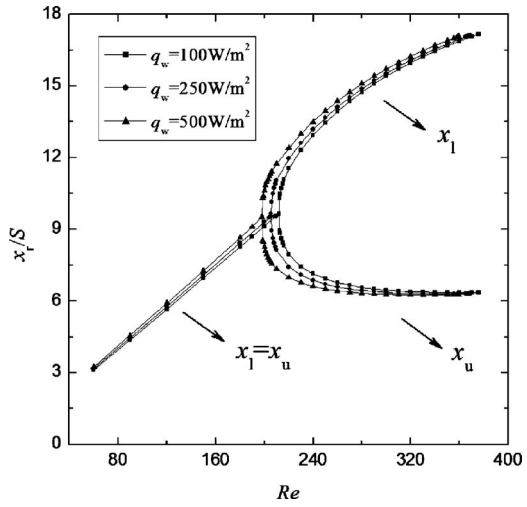

Fig. 4 Bifurcation diagram

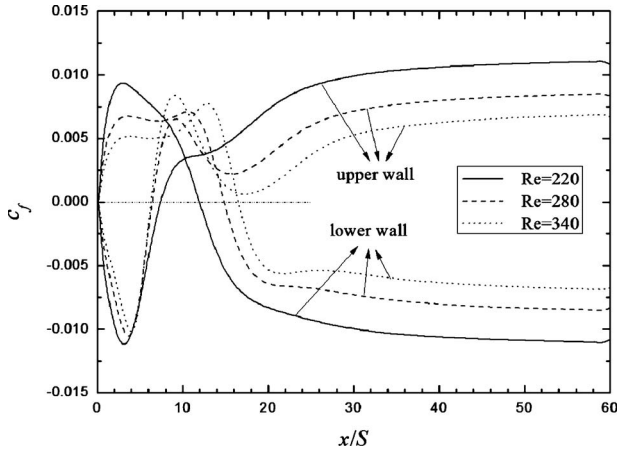

Fig. 5 Reynolds number effect on the variations of friction coefficient at $q_w=250$ W/m^2

tion of wall skin friction and pressure coefficient.

Figures 5 and 6 show the Reynolds number effects and thermal effects on the wall skin friction coefficient, $c_f=2\tau_w/\rho u_0^2$, where $\tau_w=\mu(\partial u/\partial y)$ is the wall shear stress. In these two figures, locations of reattachment point can be discerned where $c_f=0$. Asymmetric distribution according to the line $c_f=0$ between the upper wall and the lower wall is found. The locations of reattachment points locate at the intersection points of the curves of wall skin friction and the line $c_f=0$. At the same Reynolds number and wall heat flux, location of reattachment point of the lower wall locate downstream compared with that of the upper wall, and thus has larger reattachment length as shown in Fig. 4. It is seen in Fig. 5 that the reattachment point moves downstream for the lower wall while shifts upstream for the upper wall when Reynolds number increases, which behaves the increases and decreases of reattachment length for the two walls, respectively. Similar but less remarkable variations of reattachment point could be found as wall heat flux increases in Fig. 6, which correspond to the variations of reattachment length shown in Fig. 4.

Figures 7 and 8 show the Reynolds number effect and thermal effect on the pressure coefficient, defined as $c_p=2(P-P_0)/\rho u_0^2$, where P_0 is the pressure at the centerline of inlet. In the flow direction, the pressure coefficient increases first because of the sudden expansion in geometry and decreases afterward; there exist region of higher pressure coefficient (e.g., $0.2<c_p<0.25$) in the central part of the duct and region with highest pressure coefficient (e.g., $c_p>0.25$) close to the former one on the wall. It is the existence of adverse pressure difference gradient between the inlet and downstream regions that results in the formation of RR. The unequal size of RRs between the lower and upper wall arises from the asymmetric distribution of pressure coefficient of the bifurcated flow. As shown in Fig. 7, pressure coefficient redistribute when Reynolds number increases; the down stream regions with high pressure coefficient (regions of $c_p>0.2$) develop and move downstream and the lower half part of the pressure contour in the inlet region (see $c_p=0.01$ for example) bents downstream while the upper half part bents upstream slightly at the same time. Accordingly, the adverse pressure gradient between the inlet and downstream region increases for the lower half part while decreases slightly for the upper half. These variations of c_p result in the increase of RR on the lower wall and slight decrease on the upper wall. Let us examine the thermal effect in Fig. 8. As heating intensity increases, regions of highest pressure coefficient ($c_p>0.25$) develops, what is more, the opposite variations of pressure contour in the inlet region for the lower and upper half are intensified. These variations of the asymmetric distribution of pressure coefficient leads to an increase of RR on the lower wall and a decrease of RR on the upper wall.

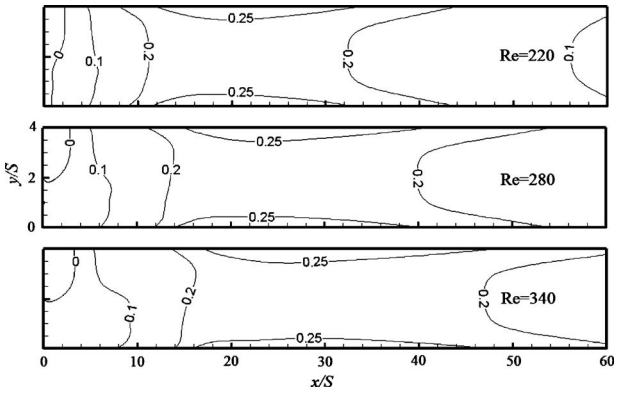

Fig. 7 Reynolds number effect on contour of pressure coefficient $q_w=250$ W/m^2

3.3 Convection Heat Transfer. Figure 9 presents the variations of wall temperature (T_w) as Reynolds number increase at $q_w=250$ W/m^2. It is seen that T_w decreases with the increasing of Re. Moreover, due to the flow in the RR brings heat from the wall to the central region in the transverse direction, the decrease of T_w is much more significant near the reattachment point (hollow circle on the curve). Because of the existence of RR, the wall temperature decreases to a minimum value and then increases

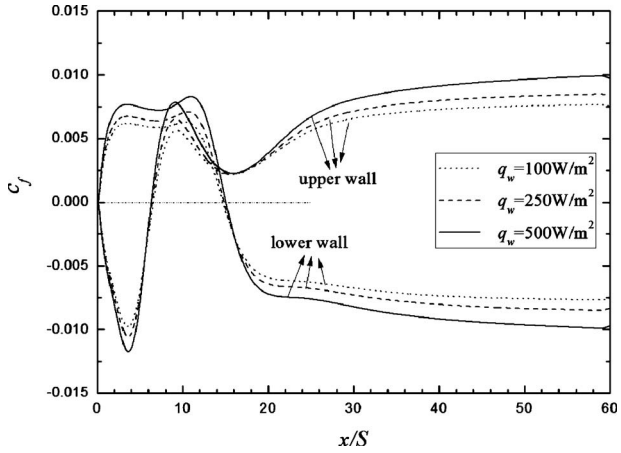

Fig. 6 Thermal effect on the variations of friction coefficient at Re=280

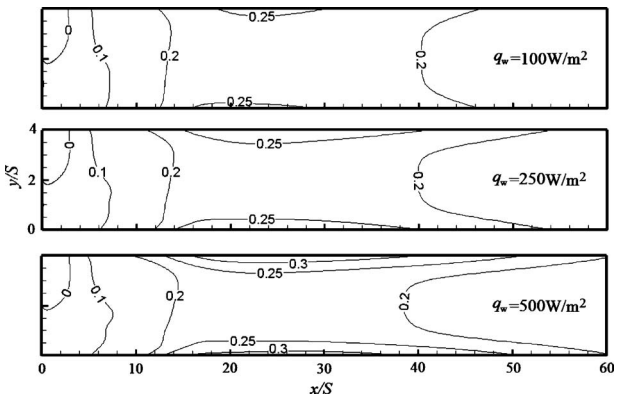

Fig. 8 Thermal effect on contour of pressure coefficient Re=280

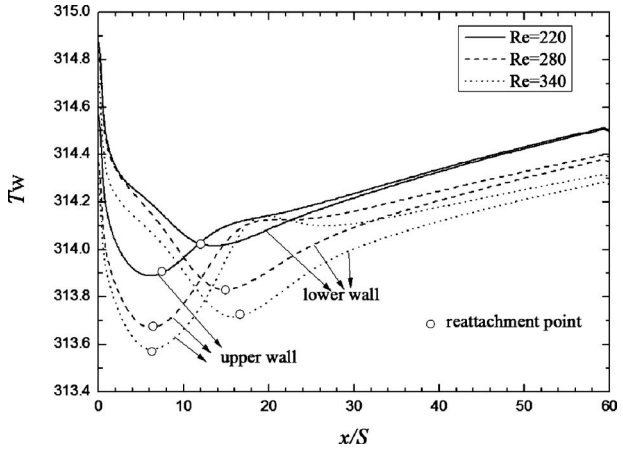

Fig. 9 Variations of wall temperature q_w=250 W/m^2

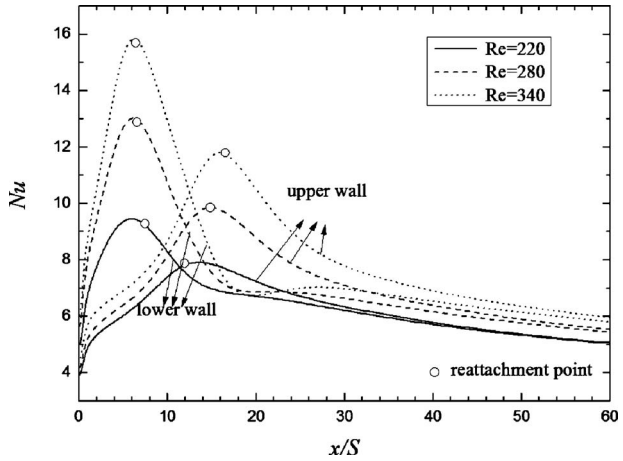

Fig. 11 Reynolds number effect on the variations of Nusselt number q_w=250 W/m^2

along the duct wall. This minimum value decreases as Reynolds number increases. In addition, the locations of the minimum value seem affected by the variations of RR, as shown in Fig. 4. First, compared with the upper wall, the location lies downstream for the lower wall, which has a larger RR. Second, as the Reynolds number increases, the location moves downstream for the lower wall and shifts upstream slightly for the upper wall.

Figure 10 shows the contours of dimensionless temperature, defined as $T^*=\lambda(T-T_0)/(q_w \cdot D)$ at q_w=250 W/m^2. The isothermal lines behave wavy in the RR. With the increasing of Reynolds number, on one hand, due to the decrease of wall temperature (see in Fig. 9), thermal conductivity and specific heat increase near the wall as shown in Fig. 1, which leads to a remarkable variation of dimensionless temperature in the RRs and increasing of temperature gradient near the wall in the RRs. On the other hand, corresponding to the variations of RRs on the lower and upper walls, the isothermal line in RR turns wavier in the RR and the wavy parts of isothermal lines develop downstream and shrink slightly upstream.

The Reynolds number effect and thermal effect on the distribution of Nusselt number, defined as $Nu=q_w D/k(T_w-T_0)$, are presented in Figs. 11 and 12, respectively. Due to the existence of RRs, the Nusselt number increases first and then decreases after reaching a peak value, which locates near the reattachment point. Compared with the upper wall, the peak value is smaller and its location lies downstream for the lower wall. It is found in Fig. 11 that the Nu increases with the increasing of Reynolds number; this is the same with most of the constant-property fluid. Dissimilarly, the change is very obvious near the reattachment point. This may be due to the increasing of temperature gradient near the wall in the RRs as shown in Fig. 10. Moreover, the peak value increases and its location moves downstream. Similarly, it is seen in Fig. 12 that the peak value increases but no obvious changes in its location could be found. The Reynolds number effects and thermal effects on the locations and values of peak Nuseelt number as well as the locations of reattachment point are presented in Tables 2 and 3, respectively. It is seen that the locations of Nu_p appear near the reattachment points but not always in the RRs. This may be due to the variation of thermophysical properties with the change of Reynolds number or wall heat flux. As presented in Table 2, with the increasing of Reynolds number, the relative location of Nu_p, defined as $(x_r-x_p)/x_r$, for the upper wall decreases but its value keep positive, which means that the location of Nu_p locates in the RR upstream the reattachment point. For the lower wall, the relative location of Nu_p changes from negative to positive and keep increasing; it moves into the recirculation region from downstream and its location relative to the reattachment point shifts upstream. In Table 3, similarity in the variations of the relative location of Nu_p for the lower wall and upper wall in Table 2 could be found as wall heat flux increases.

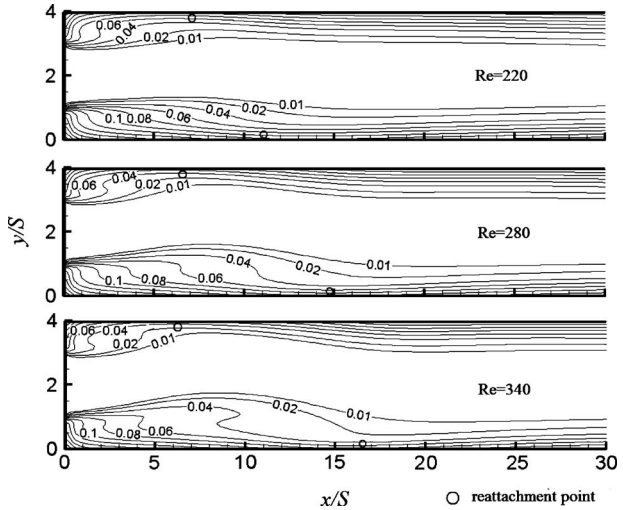

Fig. 10 Contours of dimensionless temperature q_w =250 W/m^2

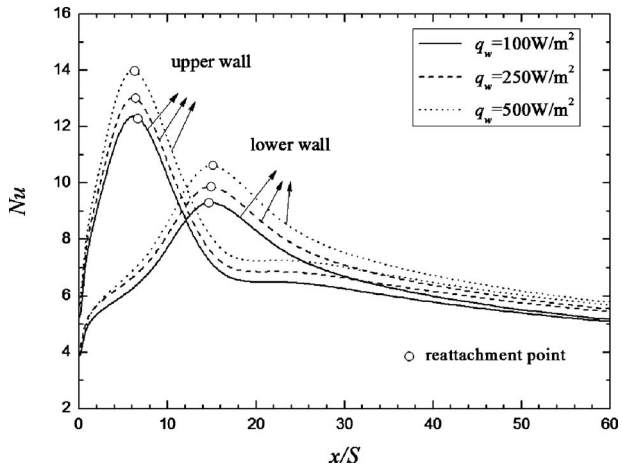

Fig. 12 Thermal effect on the variations of Nusselt number Re=280

Table 2 Reynolds number effect on locations and values of peak Nusselt numbers and locations of reattachment point

	Lower wall				Upper wall			
Re	Nu_p	x_p/S	x_r/S	$(x_r-x_p)/x_r$	Nu_p	x_p/S	x_r/S	$(x_r-x_p)/x_r$
220	7.91	13.48	11.97	−0.127	9.46	5.98	7.43	0.195
280	9.87	14.87	14.88	0.000	13.03	6.07	6.44	0.059
340	11.81	15.99	16.54	0.034	15.83	6.16	6.31	0.023

Table 3 Thermal effect on locations and values of peak Nusselt numbers and locations of reattachment point

	Lower wall				Upper wall			
q_w (W/m^2)	Nu_p	x_p/S	x_r/S	$(x_r-x_p)/x_r$	Nu_p	x_r/S	x_p/S	$(x_r-x_p)/x_r$
100	9.31	14.88	14.73	−0.009	12.37	6.16	6.57	0.063
250	9.87	14.87	14.88	0.000	13.03	6.07	6.44	0.059
500	10.61	14.87	15.09	0.014	13.99	5.98	6.33	0.057

4 Conclusion

The thermal-induced interaction of property-variation has a destabilizing effect on the flow stability. The transitional critical Reynolds number decreases as wall heat flux increases.

Due to the asymmetric distribution of pressure coefficient and its opposite variations of adverse pressure gradient as Reynolds number increases, the reattachment length on the lower wall increases while decreases slightly on the upper wall in flow asymmetric regime; heating can enhance this opposite variations.

As the Reynolds number or wall heat flux increases, both of the Nusselt number and its peak value increase. The variation of Nusselt number is more obvious near the reattachment point, which may due to the remarkable increasing of temperature gradient near the wall in the RRs. Compared with the upper wall, the peak Nusselt number is smaller and its location lies downstream for the lower wall. The location of peak Nusselt number appears near the reattachment point but not always in the RR.

Acknowledgment

The support of the National Natural Science Foundation of China (Grant No. 50706002) is gratefully acknowledged.

Nomenclature

c_f = streamwise skin friction coefficient, $c_f=2\tau_w/\rho u_0^2$
c_p = pressure coefficient, $c_p=2(P-P_0)/\rho u_0^2$
C_P = specific heat (at constant pressure), J/K kg
C_v = specific heat (at constant volume), J/K kg
d = upstream duct height, m
D = downstream duct height, m
ER = expansion ratio, $ER=D/d$
h = specific enthalpy, J/kg
Gr = Grashof number, $Gr=(\rho_w-\rho_{ref})gD^3/\rho_{ref}\nu_{ref}^2$
k = thermal conductivity, W/m K
Ma = Mach number, $Ma=u_0/\sqrt{\gamma RT}$
Nu = Nusselt number, $Nu=q_wD/k(T_w-T_0)$
P = pressure, Pa
q_w = wall heat flux, W/m^2
R = molar gas constant, J/K mol
Re = Reynolds number, $Re=\rho u_0 d/\mu$
Ri = Richardson number, $Ri=Gr/Re^2=(\rho_w-\rho_{ref})gD^3/\rho_{ref}\nu_{ref}^2\,Re^2$
S = step height, m
T = temperature, K
T^* = dimensionless temperature, $T^*=k(T-T_0)/(q_w\cdot D)$
u = velocity component in the x-coordinate direction, m/s
v = velocity component in the y-coordinate direction, m/s
x = streamwise coordinate
y = transverse coordinate
$\boldsymbol{V}$ = velocity vector
x_p = location of the peak Nusselt number on the wall, m
x_r = location of reattachment point on the wall where the streamwise velocity gradient equal to zero ($\partial u/\partial y=0$), m
x_R = dimensionless recirculation length, $x_R=x_r/S$

Greek Symbols

μ = dynamic viscosity, kg/m s
ν = kinematic viscosity, m^2/s
ρ = density, kg/m^3
γ = ratio of specific heat $=C_p/C_v$
τ_w = wall shear stress, $\tau_w=\mu(\partial u/\partial y)$, Pa

Subscripts

0 = central at inlet
cr = critical
p = peak
tr = transitional
w = wall
ref = value at reference temperature

References

[1] Lorentzen, G., and Pettersen, J., 1993, "A New Efficient and Environmentally Benign System for Car Air-Conditioning," Int. J. Refrig., **16**, pp. 4–12.
[2] Zhang, X. R., and Yamaguchi, H., 2008, "An Experimental Study on Evacuated Tube Solar Collector Using Supercritical CO_2," Appl. Therm. Eng., **28**, pp. 1225–1233.
[3] Petukhov, B. S., 1970, "Heat Transfer and Friction in Turbulent Pipe Flow With Variable Physical Properties," Adv. Heat Transfer, **6**, pp. 503–564.
[4] Hall, W. B., 1971, "Heat Transfer Near the Critical Point," Adv. Heat Transfer, **7**, pp. 1–87.
[5] Jackson, J. D., and Hall, W. B., 1979, *Forced Convection Heat Transfer to Fluids at Supercritical Pressure*, McGraw-Hill, New York, pp. 563–611.
[6] Kakaç, S., 1987, "The Effect of Temperature-Dependent Fluid Properties on Convective Heat Transfer," in *Handbook of Single-Phase Convective Heat Transfer*, S. Kakaç, R. K. Shah, and W. Aung, eds., John Wiley and Sons, New York, pp. 18.1–18.56.

[7] Polyakov, A. F., 1991, "Heat Transfer Under Supercritical Pressures," Adv. Heat Transfer, **21**, pp. 1–53.
[8] Pettersen, J., Rieberer, R., and Leister, A., 2000, "Heat Transfer and Pressure Drop Characteristics of Supercritical Carbon Dioxide in Microchannel Tubes Under Cooling," *Proceedings of the Fourth IIR-Gustav Lorentzen Conference on Natural Working Fluids*, Purdue, IN, pp. 99–106.
[9] Liao, S. M., and Zhao, T. S., 2002, "Measurements of Heat Transfer Coefficients From Supercritical Carbon Dioxide Flowing in Horizontal Mini/Micro Channels," ASME J. Heat Transfer, **124**, pp. 413–420.
[10] Liao, S. M., and Zhao, T. S., 2002, "An Experimental Investigation of Convection Heat Transfer to Supercritical Carbon Dioxide in Miniature Tubes," Int. J. Heat Mass Transfer, **45**, pp. 5025–5034.
[11] He, S., Jiang, P.-X., Xu, Y.-J., Shi, R.-F., Kim, W. S., and Jackson, J. D., 2005, "A Computational Study of Convection Heat Transfer to CO_2 at Supercritical Pressures in a Vertical Mini Tube," Int. J. Therm. Sci., **44**, pp. 521–530.
[12] Jiang, P. X., Zhang, Y., and Shi, R. F., 2008, "Experimental and Numerical Investigation of Convection Heat Transfer of CO_2 at Supercritical Pressures in a Vertical Mini-Tube," Int. J. Heat Mass Transfer, **51**, pp. 3052–3056.
[13] Zhang, X. R., and Yamaguchi, H., 2007, "Forced Convection Heat Transfer of Supercritical CO_2 in a Horizontal Circular Tube," J. Supercrit. Fluids, **41**, pp. 412–420.
[14] Durst, F., Melling, A., and Whitelaw, J. H., 1974, "Low Reynolds Number Flow Over a Plane Symmetric Sudden Expansion," J. Fluid Mech., **64**, pp. 111–128.
[15] Cherdron, W., Durst, F., and Whitelaw, J. H., 1978, "Asymmetric Flows and Instabilities in Symmetric Ducts With Sudden Expansions," J. Fluid Mech., **84**, pp. 13–31.
[16] Durst, F., Pereira, J. C. F., and Tropea, C., 1993, "The Plane Symmetric Sudden-Expansion Flow at Low Reynolds Numbers," J. Fluid Mech., **248**, pp. 567–581.
[17] Fearn, R. M., Mullin, T., and Cliffe, K. A., 1990, "Nonlinear Flow Phenomena in a Symmetric Sudden Expansion," J. Fluid Mech., **211**, pp. 595–608.
[18] Mizushima, J., and Shiotani, Y., 2000, "Structural Instability of the Bifurcation Diagram for Two-Dimensional Flow in a Channel With a Sudden Expansion," J. Fluid Mech., **420**, pp. 131–145.
[19] Shapira, M., Degani, D., and Weihs, D., 1990, "Stability and Existence of Multiple Solutions for Viscous Flow in Suddenly Enlarged Channel," Comput. Fluids, **18**, pp. 239–258.
[20] Alleborn, N., Nandakumar, K., Raszillier, H., and Durst, F., 1997, "Further Contributions on the Two-Dimensional Flow in a Sudden Expansion," J. Fluid Mech., **330**, pp. 169–188.
[21] Drikakis, D., 1997, "Bifurcation Phenomena in Incompressible Sudden Expansion Flows," Phys. Fluids, **9**, pp. 76–87.
[22] Battaglia, F., Travener, S. J., Kulkarni, A. K., and Merkle, C. L., 1997, "Bifurcation of Low Reynolds Number Flows in Symmetric Channels," AIAA J., **35**, pp. 99–105.
[23] Hawa, T., and Rusak, Z., 2000, "Viscous Flow in a Slightly Asymmetric Channel With a Sudden Expansion," Phys. Fluids, **12**, pp. 2257–2267.
[24] Hawa, T., and Rusak, Z., 2001, "The Dynamics of a Laminar Flow in a Symmetric Channel With a Sudden Expansion," J. Fluid Mech., **436**, pp. 283–320.
[25] Nie, J. H., and Armaly, B. F., 2004, "Three-Dimensional Forced Convection in Plane Symmetric Sudden Expansion," ASME J. Heat Transfer, **126**, pp. 836–839.
[26] Thiruvengadam, M., Nie, J. H., and Armaly, B. F., 2005, "Bifurcated Three-Dimensional Forced Convection in Plane Symmetric Sudden Expansion," Int. J. Heat Mass Transfer, **48**, pp. 3128–3139.
[27] Guo, Z. Y., Li, D. Y., and Liang, X. G., 1996, "Thermal Effect on the Recirculation Zone in Sudden-Expansion Gas Flows," Int. J. Heat Mass Transfer, **39**, pp. 2619–2624.
[28] Zhang, X. R., Deng, B. L., and Yamaguchi, H., 2010, "Bifurcation Phenomenon for Forced Convection of Supercritical CO_2 Sudden Expansion Flow and Heat Transfer in Symmetric Regime," Int. J. Heat Mass Transfer, **53**, pp. 4467–4473.
[29] Lemmon, E. W., Huber, M. L., and McLinden, M. O., 2007, NIST Reference Fluid Thermodynamic and Transport Properties—REFPROP, NIST Standard Reference Database 23—Version 8.0.
[30] Cebeci, T., 2002, *Convection Heat Transfer*, Springer, New York, pp. 242–243.
[31] White, F. M., 2003, *Fluid Mechanics*, McGraw-Hill, New York, pp. 599–600.

Cost and Entropy Generation Minimization of a Cross-Flow Plate Fin Heat Exchanger Using Multi-Objective Genetic Algorithm

Pouria Ahmadi
Department of Mechanical Engineering,
Sharif University of Technology,
11155–9567, Tehran, Iran
e-mail: pouryaahmadi81@gmail.com

Hassan Hajabdollahi
Department of Mechanical Engineering,
Iran University of Science and Technology (IUST),
11155–9567, Tehran, Iran
e-mail: hassan.hajabdollahi@gmail.com

Ibrahim Dincer[1]
Department of Mechanical Engineering,
Faculty of Engineering and Applied Science,
University of Ontario Institute of Technology (UOIT),
2000 Simcoe Street North,
Oshawa, ON, L1H 7K4, Canada
e-mail: ibrahim.dincer@uoit.ca

In the present work, a thermal modeling is conducted for optimal design of compact heat exchangers in order to minimize cost and entropy generation. In this regard, an $\varepsilon-NTU$ method is applied for estimation of the heat exchanger pressure drop, as well as effectiveness. Fin pitch, fin height, fin offset length, cold stream flow length, no-flow length, and hot stream flow length are considered as six decision variables. Fast and elitist nondominated sorting genetic algorithm (i.e., nondominated sorting genetic algorithm II) is applied to minimize the entropy generation units and the total annual cost (sum of initial investment and operating and maintenance costs) simultaneously. The results for Pareto-optimal front clearly reveal the conflict between two objective functions, the number of entropy generation units and the total annual cost. It reveals that any geometrical changes, which decrease the number of entropy generation units, lead to an increase in the total annual cost and vice versa. Moreover, for prediction of the optimal design of the plate fin heat exchanger, an equation for the number of entropy generation units versus the total annual cost is derived for the Pareto curve. In addition, optimization of heat exchangers based on considering exergy destruction revealed that irreversibilities, such as pressure drop and high temperature difference between cold and hot streams, play a key issue in exergy destruction. Thus, more efficient heat exchanger leads to have a heat exchanger with higher total cost rate. Finally, the sensitivity analysis of change in the optimum number of entropy generation units and the total annual cost with change in the decision variables of the plate fin heat exchanger is also performed, and the results are reported. [DOI: 10.1115/1.4002599]

Keywords: heat exchanger, heat transfer, $\varepsilon-NTU$, number of entropy generation units, cost, optimization, genetic algorithm

1 Introduction

Heat exchangers are considered a prominent component in industrial applications ranging from unit operations to power generation. They are used to transfer heat between two or more fluids, between a solid surface and a fluid, or between solid particulates and a fluid at different temperatures and in thermal contact. In heat exchangers, there are usually no external heat and work interactions. In heat exchangers, fins or extended surface elements are introduced to increase the heat transfer area [1]. Some of commonly used fins are wavy, offset strip, louver, perforated, and pin [2]. The schematic diagram of the mentioned heat exchanger is shown in Fig. 1. Also, rectangular offset strip fins, shown in Fig. 2, offset strip fins with high compactness, high heat transfer efficiency, and high reliability are widely employed in heat exchangers for cooling systems of aircrafts, automobiles, and heat ventilation air conditioning systems (HVACs) [3]. Offset strip fins have higher heat transfer performance than plain fins. Simultaneously, offset strip fins have higher strength and reliability than louver fins [4]. Wildi-Tremblay and Gosselin [5] used a procedure to minimize the cost of a shell-and-tube heat exchanger based on genetic algorithms (GAs). The cost function of their work was considered as operating cost (pumping power) and initial cost. Results showed that the procedure can properly and rapidly identify the optimal design for a specified heat transfer process. Guo et al. [6] employed a genetic algorithm to optimize the field synergy number, which is defined as the indicator of the synergy between the velocity field and the heat flow. Also, Guo et al. [7] performed an optimization of shell-and-tube heat exchangers based on the second law of thermodynamics. They introduced the modified entropy generation number and minimized it using a genetic algorithm. In addition, it was found that traditional optimization design with total cost as the objective function suffers from decrease in the heat exchanger effectiveness. Hilbert et al. [8] used a multiobjective optimization technique to maximize the heat transfer rate and to minimize the pressure drop in a tube bank heat exchanger. Xie et al. [9] minimized the total volume and the total annual cost of a compact heat exchanger by considering three shape parameters as decision variables. Wu et al. [10] used an evolutionary algorithm (i.e., genetic algorithm) method to obtain the maximum heat transfer surface area. Mishra et al. [11] minimized the entropy generation in cross-flow plate fin heat exchangers (PFHEs). Sahin et al. [12] optimized the design parameters of a heat exchanger with rectangular fins by Taguchi experimental-design method. The total annual cost of air cooled heat exchangers was minimized by Doodman et al. [13] using global sensitivity analysis. Foli et al. [14] estimated the optimum geometric parameters of microchannels in microheat exchangers by maximizing

[1]Corresponding author.

Contributed by the Heat Transfer Division of ASME for publication in the JOURNAL OF HEAT TRANSFER. Manuscript received December 15, 2009; final manuscript received March 18, 2010; published online November 3, 2010. Assoc. Editor: Giulio Lorenzini.

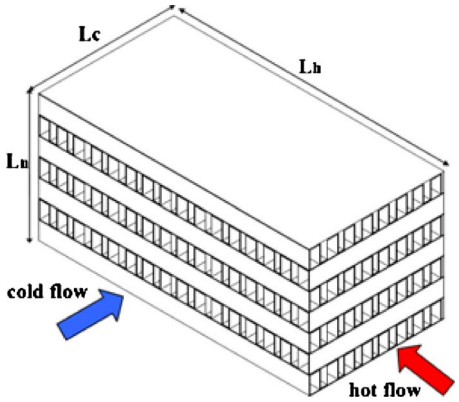

Fig. 1 Plate fin heat exchanger

the heat transfer rate and minimizing the pressure drop as two objective functions. Liu and Cheng [15] optimized a recuperator for the maximum heat transfer effectiveness, as well as minimum exchanger weight and pressure loss. Gholap and Khan [16] also studied air cooled heat exchangers by minimizing the energy consumption of fans and material cost as two objective functions.

The objective of the present study is to conduct a thermal modeling of a plate fin type heat exchanger, as well as multi-objective optimization of the heat exchanger. Therefore, two objective functions are considered here. The number of entropy generation units is optimized while total annual cost is minimized. In addition, a GA optimization technique is applied to provide a set of Pareto multiple optimum solutions. Moreover, the sensitivity analysis of changing the optimum values of number of entropy generation units and total annual cost with change in design parameters is performed and the results are reported.

In summary, the following are the specific objectives of the present paper.

- Thermal modeling of plate fin heat exchanger with rectangular offset strip fin by proposing a closed form of solution for predicting the heat transfer coefficient and total annual cost is considered.
- Multi-objective optimization of plate fin heat exchanger using for sets of objective functions, such as number of entropy generation units versus total annual cost, exergy efficiency versus total annual cost, exergy destruction versus total annual cost, and effectiveness and total annual cost, are performed using genetic algorithm.
- The following decision variables are selected: as the fin pitch, fin height, fin offset length, cold stream flow length, no-flow length, and hot stream flow.
- A closed form of solution for the total annual cost in terms of number of entropy generation units at the optimal design point is developed.

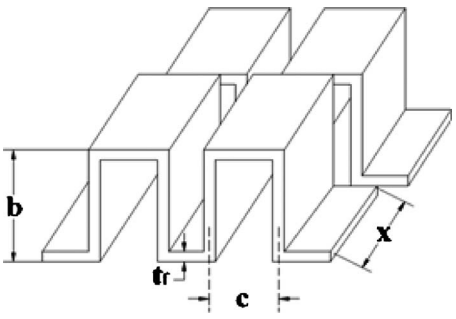

Fig. 2 Typical rectangular offset strip fin core

- A sensitivity analysis of changing the objective functions is performed for the varying optimum design parameters.

2 Modeling

2.1 Thermal Analysis. In this study, for thermal modeling of the heat exchanger, the $\varepsilon-\mathrm{NTU}$ method is applied to predict the heat exchanger performance. As we know, the effectiveness of cross-flow heat exchanger with both fluids unmixed is proposed as [17]

$$\varepsilon = 1 - \exp[-(1+C^*)\mathrm{NTU}] \times \left[I_0(2\mathrm{NTU}\sqrt{C^*}) + \sqrt{C^*} I_1(2\mathrm{NTU}\sqrt{C^*}) - \frac{1-C^*}{C^*} \sum_{n=2}^{\infty} C^{*n/2} I_n(2\mathrm{NTU}\sqrt{C^*}) \right] \quad (1)$$

in which I is the modified Bessel function. The number of transfer units (NTU) and the heat capacity ratio (C^*) are defined as follows [1]:

$$\mathrm{NTU}_{\max} = UA/C_{\min} \quad (2)$$

$$C^* = C_{\min}/C_{\max} \quad (3)$$

in which U is the overall heat transfer coefficient and A is the total heat transfer surface area computed from

$$U = \frac{1}{\dfrac{1}{h_c \eta_{s,c}} + \dfrac{1}{\dfrac{A_h}{A_c}(h_h \eta_{s,h})}} \quad (4)$$

and

$$A = (\beta V_p)_c + (\beta V_p)_h \quad (5)$$

In this formula, h is the heat transfer coefficient and β is the heat transfer area per unit volume [18].

Also, η_s in Eq. (4) is the overall surface efficiency defined as [1]

$$\eta_s = 1 - \frac{A_f}{A_{\mathrm{cell}}}(1-\eta_f) \quad (6)$$

where A_f is the fin heat transfer area (for a single fin without base area) and η_f is the efficiency of a single fin

$$\eta_f = \frac{\tanh(ml)}{ml} \quad (7)$$

in which

$$m = \sqrt{2h/k_f t_f} \quad \text{and} \quad l = \frac{b}{2} \quad (8)$$

where k_f is the fin conductivity.

To evaluate the actual exchanger effectiveness, reduction in cross-flow exchanger effectiveness ($\Delta\varepsilon/\varepsilon$) due to longitudinal wall heat conduction is considered by interpolation of tabular results given elsewhere [19].

In addition, the pressure drop is also estimated from [1]

$$\Delta p = \frac{G^2}{2} v_{\mathrm{in}} \left[(1+\sigma^2)\left(\frac{v_{\mathrm{out}}}{v_{\mathrm{in}}} - 1\right) + f\frac{4L}{D_h}\frac{v_{\mathrm{ave}}}{v_{\mathrm{in}}} \right] \quad (9)$$

where σ is the ratio of minimum free-flow area to frontal area and f is the friction factor.

The number of entropy generation units is defined as follows [11]:

$$NS = \frac{\dot{S}_{\text{gen}}}{C_{\max}} \tag{10}$$

where $\dot{S}_{\text{gen}}$ is the rate of entropy generation

$$\dot{S}_{\text{gen}} = \Delta\dot{S}_c + \Delta\dot{S}_h \tag{11}$$

and

$$\Delta\dot{S} = \dot{m}\left[c_p \ln\frac{T_{\text{out}}}{T_{\text{i}}} - R \ln\frac{P_{\text{out}}}{P_{\text{in}}} \right] \tag{12}$$

2.2 Exergy Analysis. Exergy analysis is a technique that combines the conservation of energy and the second law of thermodynamics. Exergy is defined as the maximum amount of work, which can be produced by a system or a flow of matter as it comes to equilibrium with the temperature, pressure, and chemical composition of a reference environment [20–22]. Exergy can be divided into four distinct components. The two important ones are the physical exergy and chemical exergy. Applying the first and second laws of thermodynamics, the following exergy balance is obtained:

$$\dot{\text{E}}\text{x}_Q + \sum_i \dot{m}_i \text{ex}_i = \sum_e \dot{m}_e \text{ex}_e + \dot{\text{E}}\text{x}_W + \dot{\text{E}}\text{x}_D \tag{13}$$

It should be noted that in Eq. (13), subscripts e and i are the specific exergies of control volume inlet and outlet flows and Ex_D is the exergy destruction. Other terms in this equation are as follows:

$$\dot{\text{E}}\text{x}_Q = \left(1 - \frac{T_0}{T_i}\right)\dot{Q}_i \tag{14}$$

$$\dot{\text{E}}\text{x}_W = \dot{W} \tag{15}$$

$$\text{ex}_{\text{ph}} = (h - h_0) - T_0(S - S_0) \tag{16}$$

where $\dot{\text{E}}\text{x}_Q$ and $\dot{\text{E}}\text{x}_W$ are the corresponding exergy of heat transfer and work, which cross the boundaries of the control volume and ex_{ph} is the physical exergy. Further, T is the absolute temperature (K) and (0) refers to the ambient conditions, respectively. It is worth mentioning that in this analysis, $\dot{\text{E}}\text{x}_Q$ and $\dot{\text{E}}\text{x}_W$ are considered negligible because the heat exchanger is isolated and does not produce work as well. Therefore, the exergy destruction for the heat exchanger is calculated as follows:

$$\dot{\text{E}}\text{x}_{D,\text{HE}} = \sum_i \dot{m}_i \text{ex}_i - \sum_e \dot{m}_e \text{ex}_e \tag{17}$$

Exergy efficiency of the heat exchanger is calculated as

$$\eta_{ex,\text{HE}} = 1 - \frac{\dot{\text{E}}\text{x}_{D,\text{HE}}}{\sum_{i,\text{HE}} \dot{\text{E}}\text{x}} \tag{18}$$

3 Genetic Algorithm for Multi-Objective Optimization

3.1 Multi-Objective Optimization. A multi-objective problem consists of optimizing (i.e., minimizing or maximizing) several objectives simultaneously with a number of inequality or equality constraint. The problem can be formally written as follows:

$$\text{find } x = (x_i), \quad \forall\, i = 1,2,\ldots,N_{\text{param}} \tag{19}$$

$f_i(x)$ is a minimum (respectively, maximum) $\forall i = 1,2,\ldots,N_{\text{obj}}$ subject to

$$g_j(x) = 0, \quad \forall\, j = 1,2,\ldots,M \tag{20}$$

$$h_k(x) \le 0, \quad \forall\, k = 1,2,\ldots,K \tag{21}$$

where x is a vector containing the N_{param} design parameters, $(f_i)_{i=1,\ldots,N_{\text{obj}}}$ are the objective functions, and N_{obj} is the number of objectives. The objective function $(f_i)_{i=1,\ldots,N_{\text{obj}}}$ returns a vector containing the set of N_{obj} values associated with the elementary objectives to be optimized simultaneously. The GAs are semistochastic methods based on an analogy with Darwin's laws of natural selection [23]. The first multi-objective GA called vector evaluated GA was proposed by Schaffer [24]. An algorithm based on nondominated sorting was proposed by Srinivas and Deb [25] and was called nondominated sorting genetic-algorithm (NSGA). This was later modified by Deb et al. [26] and Deb and Goel [27], which eliminated higher computational complexity, lack of elitism, and the need for specifying the sharing parameter. This algorithm is called NSGA-II, which is coupled with the objective functions developed in this study for optimization.

3.2 Nondominated Sorting. Following the definition by Deb [28], an individual $X^{(a)}$ is said to constrain-dominate an individual $X^{(b)}$ if any of the following conditions are true:

(1) $X^{(a)}$ and $X^{(b)}$ are feasible.
   (a) $X^{(a)}$ is no worse than $X^{(b)}$ in all objective.
   (b) $X^{(a)}$ is strictly better than $X^{(b)}$ in at least one objective.

(2) $X^{(a)}$ is feasible, while individual $X^{(b)}$ is not.
(3) $X^{(a)}$ and $X^{(b)}$ are both infeasible, but $X^{(a)}$ has a smaller constraint violation.

Here, the constraint violation $\ell(X)$ of an individual X is defined to be equal to the sum of the violated constraint function values.

3.3 Tournament Selection. Each individual competes in exactly two tournaments with randomly selected individuals, a procedure that imitates survival of the fittest in nature.

3.4 Controlled Elitism Sort. To preserve diversity, the influence of elitism is controlled by choosing the number of individuals from each subpopulation according to the geometric distribution to form a parent search population P_{t+1} (t denotes the generation) of size S [27],

$$S_q = S\frac{1-c}{1-c^w}c^{q-1} \tag{22}$$

where c is a controlled elitism value as considered in the range of $0 < c < 1$ and w is the total number of ranked nondominated.

3.5 Crowding Distance. The crowding distance metric proposed by Deb [28] is utilized, where the crowding distance of an individual is the perimeter of the rectangle with its nearest neighbors at diagonally opposite corners. So, if individuals $X^{(a)}$ and $X^{(b)}$ have same rank, each one having a larger crowding distance is better. Figure 3 shows the details about each step of the multi-objective genetic algorithm.

3.6 Crossover and Mutation. Uniform crossover and random uniform mutation are employed to obtain the offspring population Q_{t+1}. The integer-based uniform crossover operator takes two distinct parent individuals and interchanges each corresponding binary bits with a probability $0 < p_c \le 1$. Following crossover, the mutation operator changes each of the binary bits with a mutation probability $0 < p_m < 0.5$ [28].

3.7 Historical Archive. The NSGA-II algorithm is modified to include an archive of the historically nondominated individual H_t. Archive is used to update the data at each iteration.

4 Optimization Study

In the present study, number of entropy generation, total annual cost, heat exchanger effectiveness, heat exchanger exergy effi-

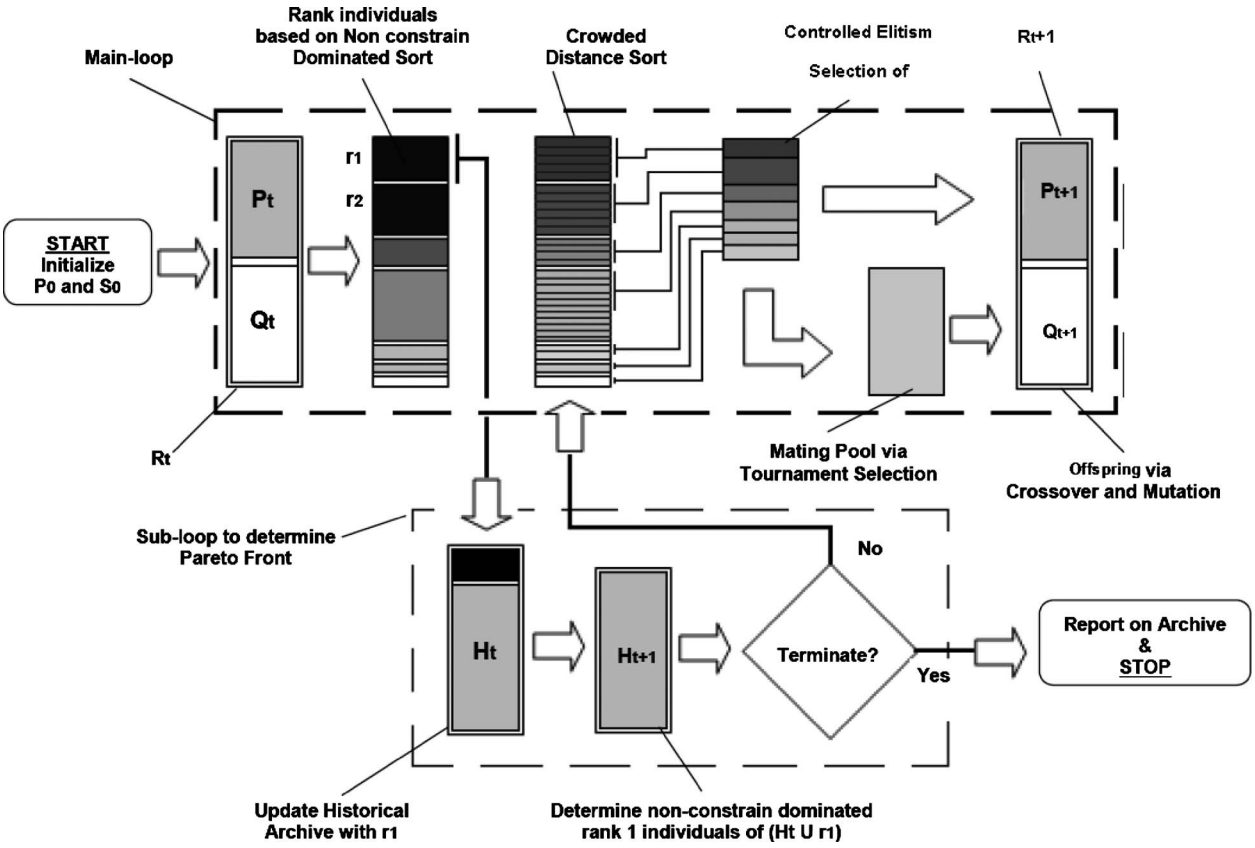

Fig. 3 The schematic diagram for the controlled elitist nondominated sorted multi-objective genetic algorithm with historical archive

ciency, and heat exchanger exergy destruction are considered as objective functions. Total annual cost includes investment cost (the annualized cost of the heat transfer surface area) and operating cost of compressor to flow the fluid. The relations are defined as follows [9]:

$$C_{\text{total}} = aC_{\text{in}} + C_{\text{op}} \tag{23}$$

$$C_{\text{in}} = C_A \times A^n \tag{24}$$

$$C_{\text{op}} = \left(k_{\text{el}}\tau\frac{\Delta pV_t}{\eta}\right)_c + \left(k_{\text{el}}\tau\frac{\Delta pV_t}{\eta}\right)_h \tag{25}$$

where C_A and k_{el} are the heat exchanger investment cost per unit surface area and the electricity unit cost, respectively, n is a constant, and τ is the operation hours of the exchanger per year (as 6000 h). Δp, V_t, and η are pressure drop, volume flow rate, and compressor efficiency, respectively. Also, a is the annual cost coefficient, which is defined as

$$a = \frac{r}{1-(1+r)^{-y}} \tag{26}$$

where r and y are interest rate and depreciation time, respectively.

In this study, fin pitch (c), fin height (b), fin offset length (x), cold stream flow length (L_c), no-flow length (L_n), and hot stream flow length (L_h) were considered as six decision parameters. Moreover, the constrains are introduced to insure that α, δ, and γ are in the range of $0.134<\alpha<0.997$, $0.012<\delta<0.048$, and $0.041<\gamma<0.121$, where $\alpha=c/b$, $\delta=t_f/x$, and $\gamma=t_f/c$, respectively.

It is worth mentioning that the relations for friction coefficient and Colburn factor used in this paper are valid in the mentioned ranges. Also, they can be considered as constraints.

5 Case Study

The PFHE optimum design parameters are obtained for a gas furnace in Almas Kavir Tile Factory located in northwest of Kerman City. Furnace temperature is about 380 K in initial stages and about 1200 K in last stages. The hot gas (hot stream) exits from middle stages of furnace with the mass flow rate of 1.8 kg/s and passes through the heat exchanger at 658.15 K. The fresh air (cold stream) with 2 kg/s mass flow rate passes through the exchanger at 306.15 K. Schematic diagram of the furnace including the studied heat exchanger is shown in Fig. 4. The PFHE metal is made of stainless steel with thermal conductivity $k_w=18$ W/m K. Operating conditions and cost function constant values are listed in Table

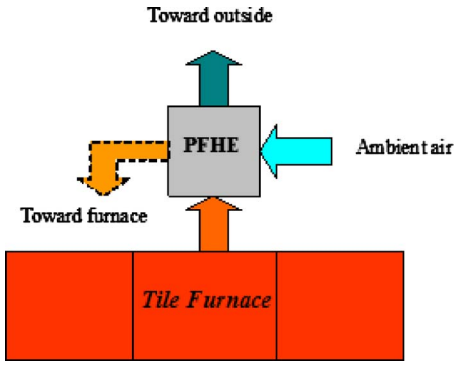

Fig. 4 The schematic diagram of a tile furnace with a plate fin heat exchanger as preheater

Table 1 The operating conditions of the PFHE (input data for the model)

Mass flow rate of hot flow (kg/s)	1.8
Mass flow rate of cold flow (kg/s)	2
Inlet hot temperature (K)	658.15
Inlet cold temperature (K)	306.15
Inlet pressure (hot side) (kPa)	180
Inlet pressure (cold side) (kPa)	120
Price per unit area ($/m^2)	100
Exponent of nonlinear increase with area increase	0.6
Hours of operation per year (h/yr)	6000
Price of electrical energy ($/MWh)	25
Compressor efficiency	0.65

1. Moreover, the thermophysical properties of air, such as Prandtl number, viscosity, and specific heat, were considered as temperature dependent.

6 Results and Discussion

6.1 Modeling Verification and Optimization Results. To verify the modeling results, the simulation output are compared with the corresponding reported results given in literature. The comparison of our modeling results and the corresponding values from Ref. [19] for the same input values is shown in Table 2. Results show that the difference percentage points of two mentioned modeling output results are acceptable for two objective functions (number of entropy generation units and annual cost). Furthermore, the optimization results using the procedure presented in this paper for the same case study and the same input values of Ref. [9] are listed in Table 3. The optimization results show 14.3% decrease in total annual cost at a fixed number of entropy generation units and 3.5% decrease in number of entropy generation units for a fixed total annual cost, which is a significant improvement.

Table 2 The comparison of modeling output and the corresponding results from Ref. [19]

Output variables	Unit	Ref. [19]	Present study	Difference (%)
j_h		0.017	0.01749	2.88
f_h		0.0669	0.0684	2.242
j_c		0.0134	0.0149	11.19
f_c		0.0534	0.055	2.996
h_h	(W/m^2 K)	360.83	370.50	2.68
h_c	(W/m^2 K)	336.81	371.49	10.3
ε		0.8381	0.8444	0.75
C_{total}	($)	1518.78	1530.82	0.79
NS		0.1304	0.1345	3.14
Δp_{total}	(kPa)	17.425	16.84	−3.357
A_{total}	(m^2)	169.208	174.3	3.01

Table 3 Input values from Ref. [9]

Mass flow rate of hot flow (m^3/s)	1.2
Mass flow rate of cold flow (m^3/s)	0.6
Inlet hot temperature (K)	513.15
Inlet cold temperature (K)	277.15
Inlet pressure (hot side) (kPa)	110
Inlet pressure (cold side) (kPa)	110
Fin material	Aluminum
Price per unit area ($/m^2)	100
Exponent of nonlinear increase with area increase	0.6
Hours of operation per year (h/yr)	6500
Price of electrical energy ($/MWh)	30
Compressor efficiency	0.5

Table 4 The design parameters, their range of variation, and their change step

Variables	From	To	Change step
Fin pitch (mm)	1	2.5	0.01
Fin height (mm)	2.5	8	0.01
Fin length (mm)	2	3.5	0.01
Hot stream flow length (m)	0.2	0.4	0.001
Cold stream flow length (m)	0.7	1.2	0.001
No-flow length (m)	0.2	0.4	0.001

6.2 Optimization Results. To minimize the number of entropy generation unit and the total annual cost and to maximize the heat exchanger exergy efficiency and heat exchanger effectiveness, six design parameters including fin pitch, fin height, fin offset length, cold stream flow length, no-flow length, and hot stream flow length are selected. Design parameters (decision variables) and range of their variations are listed in Table 4. The number of iterations for finding the global extremum in the whole searching domain was about 2.9×10^{14}. System was optimized for depreciation time $y=10$ yrs and interest rate $r=0.1$. The genetic algorithm optimization has been performed for 250 generations using a search population size of $M=100$ individuals, crossover probability of $p_c=0.9$, gene mutation probability of $p_m=0.035$, and controlled elitism value of $c=0.55$. The results for Pareto-optimal front are shown in Fig. 5, which clearly reveal the conflict between two objective functions, the number of entropy generation units and the total annual cost. Any geometrical changes, which decrease the number of entropy generation units, lead to an increase in the total annual cost and vice versa. It reveals the need for multi-objective optimization techniques in optimal design of a PFHE. As shown in Fig. 5, the minimum number of entropy generation units exists at design point A (0.0939) while the total annual cost is the biggest at this point. On the other hand, the minimum total annual cost occurs at design point E (1031.0 $) with the greatest number of entropy generation units value (0.13) at that point. Design point A is the optimal situation at which number of entropy generation units is a single objective function while design point E is the optimum condition at which total annual cost is a single objective function.

Optimum values of two objectives for five typical points from A to E (Pareto-optimal fronts) for input values are given in Table 1 and are listed in Table 5.

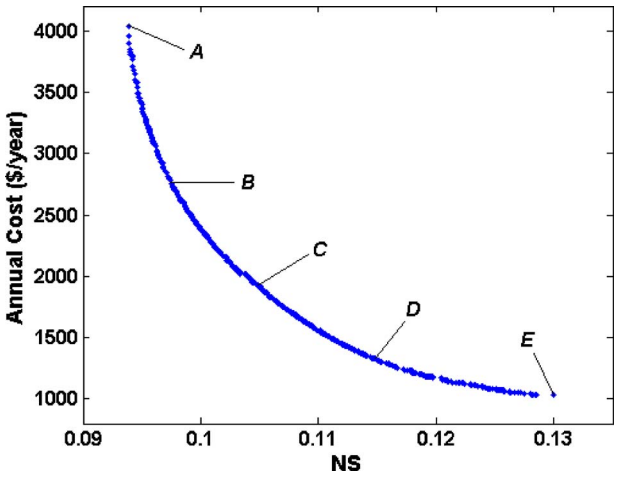

Fig. 5 The distribution of Pareto-optimal points solution for entropy generation units and annual cost using NSGA-II

Table 5 The optimum values of number of entropy generation units and the total annual cost for the design points *A–E* in Pareto-optimal fronts for input values given in Table 1

	A	B	C	D	E
NS	0.0939	0.0975	0.1048	0.1148	0.1300
Total annual cost ($/yr)	4031.3	2754.9	1924.6	1327.4	1031.0

For prediction of the optimal design of the PFHE, the following equation for number of entropy generation units versus total annual cost is derived for the Pareto curve (Fig. 5),

$$C_{\text{total}}(\$) = \frac{-2.819NS^3 - 4.311NS^2 + 1.728NS - 0.04891}{NS^2 + 21.84NS - 1.867} \times 10{,}000 \tag{27}$$

Equation (27) is valid in the range of $0.0939 < NS < 0.1300$. The interesting point in Eq. (27) is that considering a numerical value for the number of entropy generation units in mentioned range provides the minimum total annual cost for that optimal point along with other optimal design parameters.

In addition, the change in effectiveness versus annual cost for the set of optimal points (Fig. 5) is shown in Fig. 6. As shown in this figure, it can be predicted that considering the entropy generation unit and a distinguished objective function leads to the thermodynamic optimization as well (optimization of effectiveness).

Moreover, in Fig. 6, the Pareto-optimal front for another two objective functions is shown (i.e., annual cost and effectiveness). This figure shows that any geometrical changes, which increase the effectiveness, lead to an increase in the total annual cost and vice versa. The results of Fig. 6 show that by considering the entropy generation and annual cost, we can predict the optimization results when effectiveness and annual cost are considered as two objective functions.

On the other hand, the Pareto-optimal front for heat exchanger exergy efficiency and exergy destruction versus annual cost rate are shown in Fig. 7. This figure shows that when the exergy efficiency of the heat exchanger increases, the total cost of the heat exchanger increases, respectively. It means that higher heat exchanger exergy efficiency leads to have efficient heat exchangers in both thermodynamic and thermo-economic points of view. The same conclusion can be obtained by considering another two objective functions (i.e., exergy destruction, exergy efficiency, and annual cost) shown in Fig. 7. It is so clear from this figure that

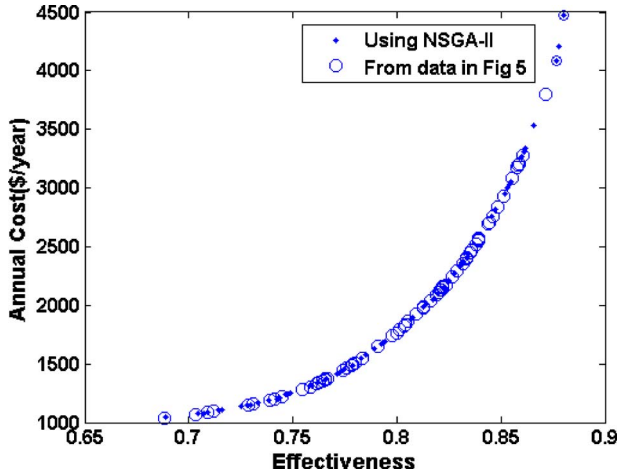

Fig. 6 Distribution of annual cost versus effectiveness for points of Pareto front in Fig. 5 using NSGA-II

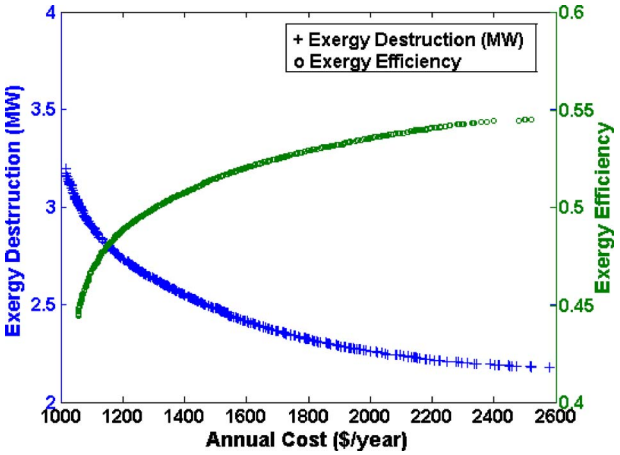

Fig. 7 The distribution of Pareto-optimal points solution for the exergy destruction and exergy efficiency versus annual cost using NSGA-II

when the exergy destruction of the heat exchanger increases, the total cost decreases due to the fact that the design parameters are not selected in the best case in which the exergy destruction is less. On the other hand, by decrease in exergy destruction, the total annual cost increases, respectively. It reveals that irreversibility, such as pressure drop and high temperature difference between cold and hot streams, play a key issue in exergy destruction. Thus, more efficient heat exchanger leads to have a heat exchanger with higher total cost rate.

In the present work, a new and interesting thing is done. Therefore, to have a good insight into this analysis, the distribution of decision variables for the optimal points on Pareto front (Fig. 5) is shown in Figs. 8(*a*)–8(*f*). The lower and upper bounds of the variables are illustrated by dotted lines. The following points for the optimal variables in Fig. 8 can be concluded.

1. The fin pitch and plate spacing have the values distributed equally in its whole allowable domain.
2. The numerical values of the fin offset length, cold stream flow length, hot stream flow length, and no-flow length are at their maximum level.

Since the optimum values of fin pitch and plate spacing, which have scattered distribution in their whole allowable domains, one may predict that these parameters have important effects on the conflict between the lower values of number of entropy generation units and total annual cost. The other parameters, which are situated at its maximum value, show that these parameters have no effect on the conflict between two objective functions. The variations in the optimum value of the number of entropy generation units with the total annual cost for various values of optimum design parameters in cases *A–E* (Pareto front) are shown in Figs. 9(*a*)–9(*f*).

It is observed that the variation of two objective functions at other points on the Pareto-optimal front has the same trend as the five points (*A–E*).

The effect of design variables on objective functions are investigated and explained as follows.

6.2.1 Fin Pitch. By increasing the fin pitch, the number of entropy generation units increases while the total annual cost decreases for the whole design points of *A–E* (Fig. 9(*a*)). Therefore, variations in fin pitch causes a conflict between two objective functions, and values of fin pitch have a distribution in the whole allowable domain (Fig. 8(*a*)).

6.2.2 Fin Height. Like the fin pitch, by increasing the fin height, the number of entropy generation units increases while the

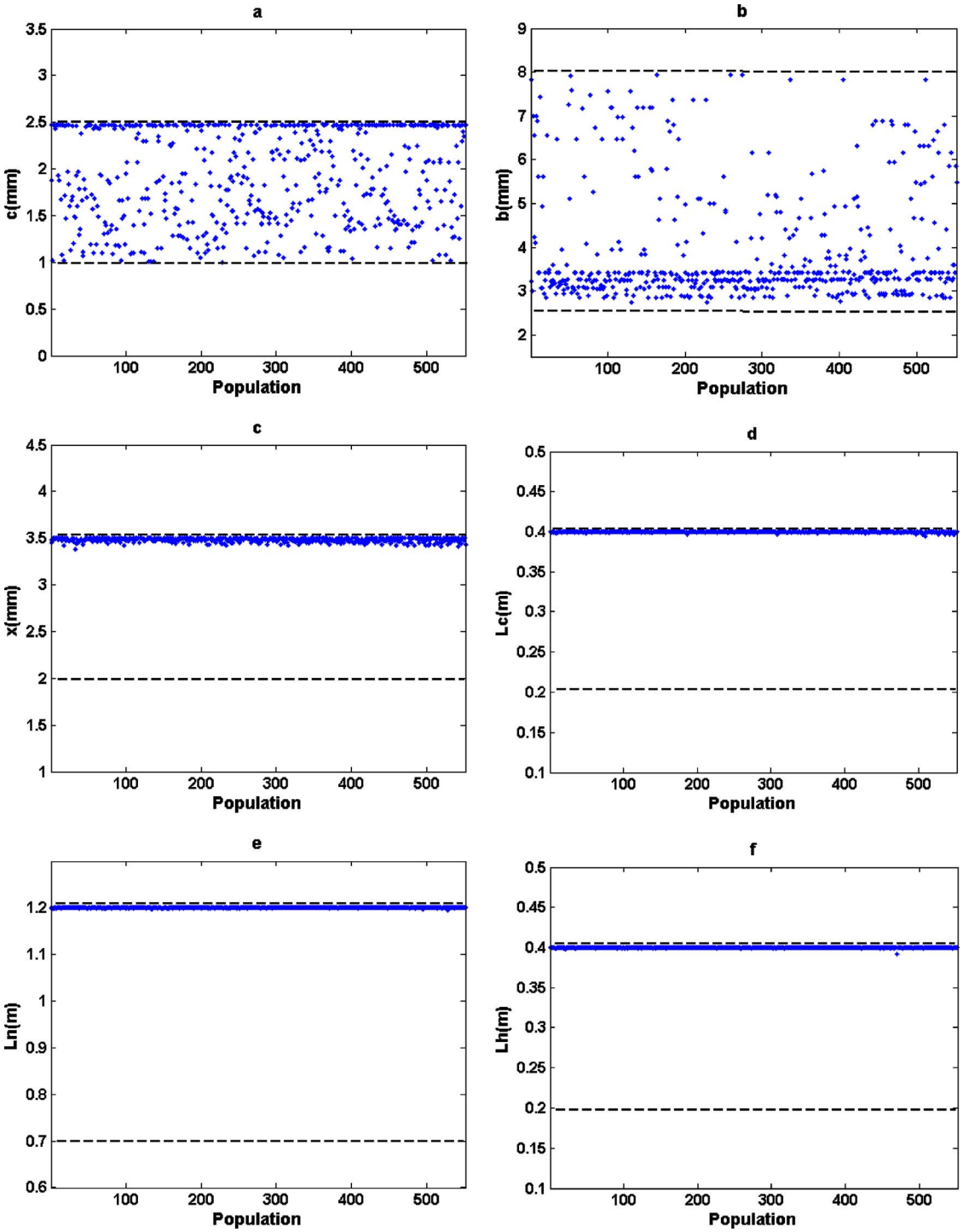

Fig. 8 Scattering of variables for the Pareto-optimal front in Fig. 5: (*a*) fin pitch, (*b*) fin height, (*c*) fin offset length, (*d*) cold stream flow length, (*e*) no-flow length, and (*f*) hot stream flow length

total annual cost decreases for the whole design points of $A-E$ (Fig. 9(*b*)). Therefore, the fin height caused a conflict between two objective functions and fin height values obtained on Pareto-optimal front have scattered distribution, as shown in Fig. 8(*b*).

6.2.3 Fin Offset Length. An increase in fin length increases the number of entropy generation units and decreases the total annual cost (Fig. 9(*c*)). However, Fig. 9(*c*) shows that there is a region in design points $A-B$ that has no effect on conflict in objective function.

6.2.4 Cold Stream Flow Length and Hot Stream Flow Length. An increase in the cold stream flow length and hot stream flow length decreases both the number of entropy generation units and the total annual cost (Figs. 9(*d*) and 9(*f*)). In fact, the investment cost of the heat exchangers is increased with respect to the increase in these two parameters due to the increment in the thermal surface area. On the other hand, operational cost decreases due to the fact that in this case, the pressure drop decreases by increasing these two parameters. Therefore, in this case, by increase in these

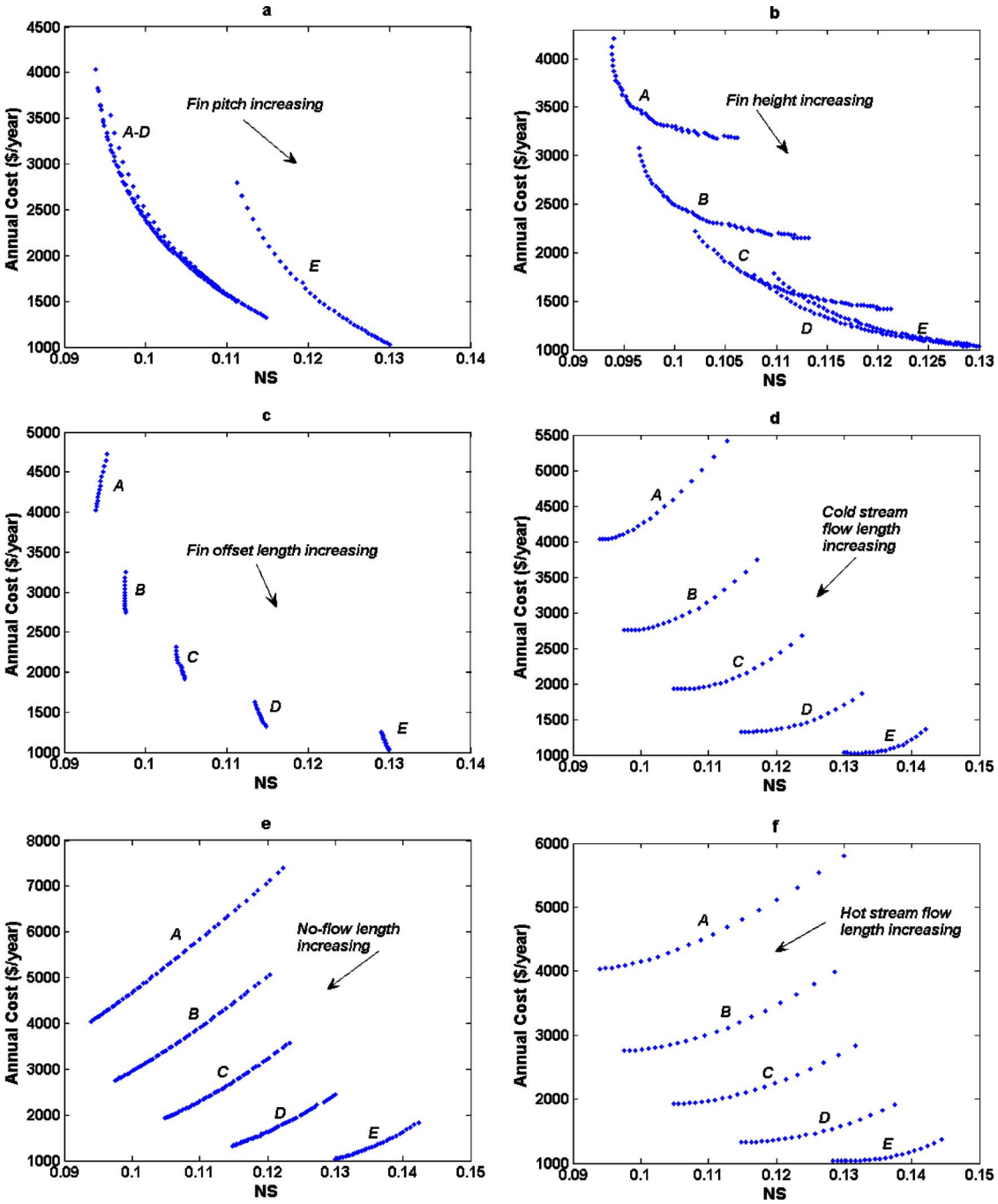

Fig. 9 The variation of number of entropy generation units with annual cost for six optimum design parameters in five cases of *A–E* in Fig. 5: (*a*) fin pitch, (*b*) fin height, (*c*) fin offset length, (*d*) cold stream flow length, (*e*) no-flow length, and (*f*) hot stream flow length

two parameters, the total annual cost decreases first and then it reaches to a fixed value. Therefore, the maximum value of these parameters is desired to improve both objective functions simultaneously (Figs. 8(*d*) and 8(*f*)).

6.2.5 No-Flow Length. Increasing the no-flow length has the same effect with the cold stream and hot stream flow lengths, which decreases both number of entropy generation units and total annual cost (Fig. 9(*e*)). As a result, no-flow length has no effect on conflict between two objective functions. The distribution of no-flow length around its maximum value verifies this point (Fig. 8(*e*)).

7 Conclusions

In this work, a PFHE is optimally designed using multi-objective optimization technique. In the present optimization problem, some objective functions were considered by using the multi-objective genetic algorithm; the design parameters were selected. In this analysis, the number of entropy generation units and total annual cost were considered as the first two objective functions (the number of entropy generation units and total annual cost were minimized). Another set of objective functions was heat exchanger effectiveness versus annual cost. The last set of objective functions was selected as heat exchanger exergy destruction and

exergy efficiency versus annual cost. The results from exergy analysis revealed that when the exergy efficiency of the heat exchanger increases, the total cost of the heat exchanger increases, respectively. It can be concluded that higher exergy efficiency leads to have efficient heat exchangers in both thermodynamic and thermo-economic points of view. The same results are obtained from exergy destruction. Results showed that by decrease in exergy destruction, the total annual cost increases, respectively. Moreover, results showed that irreversibility such as pressure drop and high temperature difference between cold and hot streams play a key issue in exergy destruction. Also, a set of Pareto-optimal front points was shown. Furthermore, the correlation between the optimal values of two objective functions was proposed. Fin pitch and fin height were found to be major design parameters, which caused a conflict between two objective functions. On the other hand, cold stream flow length, no-flow length, and hot stream flow length had no effect on the conflict between two optimized objective functions, and their maximum allowable value improved both objective functions simultaneously.

Nomenclature

A_{cell} = total heat transfer area for one fin (m^2)
A = total heat transfer area (m^2)
A_f = fin heat transfer area (m^2)
b = fin height (m)
c_p = heat capacity (J/kg K)
c = fin pitch (m)
C = heat capacity rate (W/K)
C^* = heat capacity rate ratio (C_{min}/C_{max})
C_{in} = annual cost of investment ($/yr)
C_{op} = annual cost of operation ($/yr)
C_{total} = total annual cost ($/yr)
D_h = hydraulic diameter (m)
$\dot{E}x$ = exergy rate (W)
$\dot{E}x_D$ = exergy destruction (W)
f = friction factor (dimensionless)
G = mass flux (kg/m^2 s)
h = heat transfer coefficient (W/m^2 K)
j = Colburn number (dimensionless)
k_{el} = price of electrical energy ($ MW h^{-1})
k_f = fin thermal conductivity (W/m K)
L_c = cold stream flow length (m)
L_h = hot stream flow length (m)
L_n = no-flow length (m)
$\dot{m}$ = mass flow rate of fluid (kg/s)
n = exponent of nonlinear increase with area increase
NS = number of entropy generation units (dimensionless)
NTU = number of transfer units (dimensionless)
P = pressure (Pa)
r = interest rate (dimensionless)
R = specific gas constant (J/kg K)
Re = Reynolds number (dimensionless)
$\dot{S}$ = rate of entropy generation (W/K)
t_f = fin thickness (m)
t_w = plate thickness (m)
U = overall heat transfer coefficient (W/m^2 K)
V_t = volumetric flow rate (m^3/s)
V_{cell} = single fin volume (m^3)
V_p = heat exchanger volume between plates (m^3)
x = fin length (m)
y = depreciation time (yr)

Greek Letters

ε = thermal effectiveness (dimensionless)
τ = hours of operation per year
η_s = overall surface efficiency (dimensionless)
η_f = fin efficiency (dimensionless)
η = compressor efficiency (dimensionless)
μ = viscosity (Pa s)
ν = specific volume (m^3/kg)
ΔP = pressure drop (Pa)
σ = ratio of minimum free-flow area to frontal area (dimensionless)
β = heat transfer area per unit volume (m^2/m^3)

Subscripts

c = cold
h = hot
HE = heat Exchanger
in = inlet
e = outlet
f = fin

References

[1] Kays, W. M., and London, A. L., 1984, *Compact Heat Exchangers*, 3rd ed., McGraw-Hill, New York.
[2] Kim, B., and Sohn, B., 2006, "An Experimental Study of Flow Boiling in a Rectangular Channel With Offset Strip Fins," Int. J. Heat Fluid Flow, **27**, pp. 514–521.
[3] Guo, L., Qin, F., Chen, J., and Chen, Z., 2008, "Lubricant Side Thermal–Hydraulic Characteristics of Steel Offset Strip Fins With Different Flow Angles," Appl. Therm. Eng., **28**, pp. 907–914.
[4] Lihua, G., Jiangping, C., Feng, Q., and Zhijiu, C., 2007, "Geometrical Optimization and Mould Wear Effect on HPD Type Steel Offset Strip Fin Performance," Energy Convers. Manage., **48**, pp. 2473–2480.
[5] Wildi-Tremblay, P., and Gosselin, L., 2007, "Minimizing Shell-and-Tube Heat Exchanger Cost With Genetic Algorithms and Considering Maintenance," Int. J. Energy Res., **31**, pp. 867–885.
[6] Guo, J., Xu, M., and Cheng, L., 2009, "The Application of Field Synergy Number in Shell-and-Tube Heat Exchanger Optimization Design," Appl. Energy, **86**, pp. 2079–2087.
[7] Guo, J., Cheng, L., and Xu, M., 2009, "Optimization Design of Shell-and-Tube Heat Exchanger by Entropy Generation Minimization and Genetic Algorithm," Appl. Therm. Eng., **29**, pp. 2954–2960.
[8] Hilbert, R., Janiga, G., Baron, R., and Thevenin, D., 2006, "Multi-Objective Shape Optimization of a Heat Exchanger Using Parallel Genetic Algorithms," Int. J. Heat Mass Transfer, **49**, pp. 2567–2577.
[9] Xie, G. N., Sunden, B., and Wang, Q. W., 2008, "Optimization of Compact Heat Exchangers by a Genetic Algorithm," Appl. Therm. Eng., **28**, pp. 895–906.
[10] Wu, Z., Ding, G., Wang, K., and Fukaya, M., 2008, "Application of a Genetic Algorithm to Optimize the Refrigerant Circuit of Fin-and-Tube Heat Exchangers for Maximum Heat Transfer or Shortest Tube," Int. J. Therm. Sci., **47**, pp. 985–997.
[11] Mishra, M., Das, P. K., and Sarangi, S., 2009, "Second Law Based Optimisation of Crossflow Plate-Fin Heat Exchanger Design Using Genetic Algorithm," Appl. Therm. Eng., **29**, pp. 2983–2989.
[12] Sahin, B., Yakut, K., Kotcioglu, I., and Celik, C., 2005, "Optimum Design Parameters of a Heat Exchanger," Appl. Energy, **82**, pp. 90–106.
[13] Doodman, A. R., Fesanghary, M., and Hosseini, R., 2009, "A Robust Stochastic Approach for Design Optimization of Air Cooled Heat Exchangers," Appl. Energy, **86**, pp. 1240–1245.
[14] Foli, K., Okabe, T., Olhofer, M., Jin, Y., and Sendhoff, B., 2006, "Optimization of Micro Heat Exchanger: CFD, Analytical Approach and Multi-Objective Evolutionary Algorithms," Int. J. Heat Mass Transfer, **49**, pp. 1090–1099.
[15] Liu, Z., and Cheng, H., 2008, "Multi-Objective Optimization Design Analysis of Primary Surface Recuperator for Microturbines," Appl. Therm. Eng., **28**, pp. 601–610.
[16] Gholap, A. K., and Khan, J. A., 2007, "Design and Multi-Objective Optimization of Heat Exchangers for Refrigerators," Appl. Energy, **84**, pp. 1226–1239.
[17] Franco, A., and Giannini, N., 2005, "Optimum Thermal Design of Modular Compact Heat Exchangers Structure for Heat Recovery Steam Generators," Appl. Therm. Eng., **25**, pp. 1293–1313.
[18] Smith, E. M., 2005, *Advances in Thermal Design of Heat Exchangers*, Wiley, New York.
[19] Shah, R. K., and Sekulic, P., 2003, *Fundamental of Heat Exchanger Design*, Wiley, New York.
[20] Rosen, M. A., and Dincer, I., 2001, "Exergy as the Confluence of Energy, Environment and Sustainable Development," Exergy, An International Journal, **1**(1), pp. 3–13.
[21] Orhan, M. F., Erek, A., and Dincer, I., 2009, "Entropy Generation During a Phase-Change Process in a Parallel Plate Channel," Thermochim. Acta, **489**(1–2), pp. 70–74.
[22] Haseli, Y., Dincer, I., and Naterer, G. F., 2008, "Optimum Temperatures in a

Shell and Tube Condenser With Respect to Exergy," Int. J. Heat Mass Transfer, **51**, pp. 2462–2470.
[23] Goldberg, D. E., 1989, *Genetic Algorithms in Search, Optimization and Machine Learning*, Addison-Wesley, Reading, MA.
[24] Schaffer, J. D., 1985, "Multiple Objective Optimization With Vector Evaluated Genetic Algorithms," *Proceedings of the International Conference on Genetic Algorithm and Their Applications*.
[25] Srinivas, N., and Deb, K., 1994, "Multi-Objective Optimization Using Non-Dominated Sorting in Genetic Algorithms," Evol. Comput., **2**(3), pp. 221–248.
[26] Deb, K., Pratap, A., Agarwal, S., and Meyarivan, T., 2002, "A Fast and Elitist Multi-Objective Genetic Algorithm: NSGA-II," IEEE Trans. Evol. Comput., **6**(2), pp. 182–197.
[27] Deb, K., and Goel, T., 2001, "Controlled Elitist Non-Dominated Sorting Genetic Algorithms for Better Convergence," *Proceedings of the First International Conference on Evolutionary Multi-Criterion Optimization*, Zurich, pp. 385–399.
[28] Deb, K., 2001, *Multi-Objective Optimization Using Evolutionary Algorithms*, Wiley, Chichester.

The Physical Mechanism of Heat Transfer Augmentation in Stagnating Flows Subject to Freestream Turbulence[1]

Andrew R. Gifford

Thomas E. Diller

Pavlos P. Vlachos

Department of Mechanical Engineering,
AEThER Laboratory,
Virginia Polytechnic Institute and State University,
Blacksburg, VA 24061

Experiments have been performed in a water tunnel facility to examine the physical mechanism of heat transfer augmentation by freestream turbulence in classical Hiemenz flow. A unique experimental approach to studying the problem is developed and demonstrated herein. Time-resolved digital particle image velocimetry (TRDPIV) and a new variety of thin-film heat flux sensor called the heat flux array (HFA) are used simultaneously to measure the spatiotemporal influence of coherent structures on the heat transfer coefficient as they approach and interact with the stagnation surface. Laminar flow and heat transfer at low levels of freestream turbulence ($\overline{Tu_x}=0.5-1.0\%$) are examined to provide baseline flow characteristics and heat transfer coefficients. Similar experiments using a turbulence grid are performed to examine the effects of turbulence with mean streamwise turbulence intensity of $\overline{Tu_x}=5.0\%$ and an integral length scale of $\overline{\Lambda_x}=3.25$ cm. At a Reynolds number of $\overline{Re_D}=\overline{U_\infty}D/\nu=21,000$, an average increase in the mean heat transfer coefficient of 64% above the laminar level was observed. Experimental studies confirm that coherent structures play a dominant role in the augmentation of heat transfer in the stagnation region. Calculation and examination of the transient physical properties for coherent structures (i.e., circulation, area averaged vorticity, integral length scale, and proximity to the surface) shows that freestream turbulence is stretched and vorticity is amplified as it is convected toward the stagnation surface. The resulting stagnation flow is dominated by dynamic, counter-rotating vortex pairs. Heat transfer augmentation occurs when the rotational motion of coherent structures sweeps cooler freestream fluid into the laminar momentum and thermal boundary layers into close proximity of the heated stagnation surface. Evidence in support of this mechanism is provided through validation of a new mechanistic model, which incorporates the transient physical properties of tracked coherent structures. The model performs well in capturing the essential dynamics of the interaction and in the prediction of the experimentally measured transient and time-averaged turbulent heat transfer coefficients.
[DOI: 10.1115/1.4002595]

Keywords: coherent structures, digital particle image velocimetry, heat flux sensor, heat transfer augmentation, Hiemenz flow, mechanistic model, turbulence

1 Introduction

It has long been known that freestream turbulence has a pronounced effect on boundary layer heat transfer, particularly in regions of stagnating flow. Very high levels of surface heat transfer augmentation, or increase in mean heat transfer rate above laminar levels, have been observed for relatively small changes in freestream turbulence parameters. The importance of understanding and accurately modeling this phenomenon cannot be understated. Turbomachinery airfoils, for instance, are routinely operated at temperatures close to or exceeding their maximum material temperature limits. Being able to predict the peak heating loads on these airfoils is therefore crucial in maintaining structural integrity and achieving peak efficiency.

1.1 Background and Related Studies. There is to date a large body of experimental and theoretical work spanning over 65 years devoted to the topic of freestream turbulence and its effects on boundary layer heat transfer. Much of this work has focused on the effects of freestream turbulence on laminar flow in the stagnation region of various geometries. Hiemenz [1] was the first to solve the governing equations for laminar flow. Goldstein [2] and others examined the laminar heat transfer solutions for various heat transfer boundary conditions.

Much of the experimental work dealing with the problem prior to 1965 has been summarized by Kestin [3]. Subsequent experiments by Kestin and Wood [4], Smith and Kuethe [5], Lowery and Vachon [6], and others succeeded in determining the local and overall variation of heat transfer augmentation on cylinders. Correlations for the time-averaged stagnation region heat transfer as a function of Reynolds number, Prandtl number, and turbulence intensity were developed, although no single correlation could capture all available experimental data. Analytical work by Traci and Wilcox [7] and others using various turbulence models were somewhat successful in predicting the augmentation of heat transfer. The effects of turbulence parameters such as turbulence length scale have gained recent attention. Yardi and Sukhatme [8] showed that for a given turbulence intensity and Reynolds number, a decreasing length scale served to increase heat transfer augmentation. Experiments by Dullenkopft and Mayle [9], Van Fos-

[1]Preliminary studies published in ASME 2008 Summer Heat Transfer Conference, Paper No. HT2008-56329.

Contributed by the Heat Transfer Division of ASME for publication in the JOURNAL OF HEAT TRANSFER. Manuscript received September 5, 2008; final manuscript received July 23, 2010; published online November 2, 2010. Assoc. Editor: Cholik Chan.

sen et al. [10,11], and recently by Sak et al. [12] and Peyrin and Kondjoyan [13] confirm that turbulence length scale is an important parameter in correlating stagnation point heat transfer.

Beginning with the works of Sutera et al. [14,15], a clearer picture of the mechanism of heat transfer augmentation emerged including the effects of turbulent length scale. It was shown numerically that freestream vorticity with scale greater than a certain neutral scale and orientation set parallel to the stagnation streamlines could be amplified near the boundary layer by the mean flow strain rate. This induced changes in the thermal and momentum boundary layers, which led to significantly increasing surface heat transfer over laminar cases. A pair of recent numerical studies by Bae et al. [16,17] provided yet another picture of how Reynolds number, disturbance intensity, and length scale affect heat transfer in the stagnation region. For a fixed disturbance amplitude and Reynolds number, the augmentation of heat transfer increases with the disturbance length scale up to a maximum length scale of $\lambda/\delta \sim 5.3$ and then decreases. A numerical study by Zhongmin and Lele [18] examined the effects of unsteady 3D fluctuations upstream of a Hiemenz boundary layer. Results similar to Bae et al. [17] were observed.

A number of experimental studies [19–21] have examined the behavior of freestream turbulence in the stagnation region, many providing evidence for the vorticity amplification theory. Nearly all of these studies were performed in air using classic flow visualization and hot-wire methods. An early digital particle image velocimetry (DPIV) study of the problem was done by Sakakibara et al. [22]. DPIV and laser induced fluorescence (LIF) were used to simultaneously measure flow field velocity and temperature near the stagnation point of a rectangular water jet impinging on a heated flat plate. In agreement with previous studies, maximum local increases in surface heat transfer coincided with the presence of coherent vortical structures, which are stretched and amplified by the mean flow strain rate. Full flow field temperature measurements reveal that these structures create an "up-wash" region pulling cold fluid into the plate from the freestream while warmer fluid is ejected from the surface. This agrees qualitatively with the analytical results of Ref. [17]. With the exception of the work in Ref. [22], particle image velocimetry has not been used to thoroughly study the problem. In this work, time-resolved DPIV techniques are used to examine the transient physics of the interaction of freestream turbulence and the heated Hiemenz boundary layer while simultaneously measuring transient surface heat transfer.

1.2 Hypothetical Mechanism. In a recent paper by Nix et al. [23], a mechanistic model was developed that successfully predicted experimentally measured values of the time-averaged heat transfer to surfaces subjected to large-scale, high-intensity freestream turbulence. The model has been compared with several existing data sets from the literature with good agreement for a variety of surface geometries, boundary layers, and freestream turbulence conditions. In this model, it is assumed that the main mechanism responsible for heat transfer augmentation is the penetration of high energy turbulent eddies in the freestream through the existing boundary layer. This serves to bring freestream fluid directly into contact with the surface, increasing heat transfer above and beyond normal levels.

It is suggested that an overall time-averaged turbulent heat transfer coefficient $\overline{h_{\text{turb}}}$ at the surface can be described as a linear superposition of contributions from the normal flow without freestream turbulence $\overline{h_o}$ and is due solely to the freestream turbulence interacting with the surface $\overline{\Delta h_{\text{turb}}}$:

$$\overline{h_{\text{turb}}} = \overline{h_o} + \overline{\Delta h_{\text{turb}}} \tag{1}$$

To model the augmentation or turbulent interaction term, the one-dimensional, transient conduction heat transfer solution for semi-infinite medium with constant surface and freestream temperatures has been used by Nix et al. [23]. As shown in Eq. (2), the heat transfer augmentation term is found by transforming the original solution from transient to time-averaged by using an overall interaction time scale, $t_{\text{int}} = \overline{\Lambda_x}/u'_{\text{rms}}$. The ratio of mean streamwise integral length scale to streamwise rms fluctuating velocity represents the average time the turbulent structure resides on the surface,

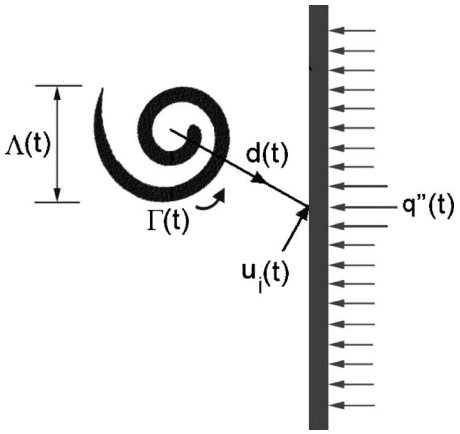

Fig. 1 A hypothetical mechanism for heat transfer augmentation at a stagnation surface

$$h(t) = \frac{k}{\sqrt{\pi\alpha t}} \Rightarrow \overline{\Delta h_{\text{Turb}}} = \frac{k}{\sqrt{\pi\alpha t_{\text{int}}}} = \frac{k}{\sqrt{\pi\alpha \overline{\Lambda_x}/u'_{\text{rms}}}} \tag{2}$$

In Eq. (2), the constants k and α are the thermal conductivity and thermal diffusivity of the fluid, respectively. The values of these constants are typically evaluated at the freestream temperature. This relatively simple mechanistic model only requires knowledge of the local turbulence quantities in the vicinity of the surface, where there is high coherence between the fluctuating velocity and surface heat transfer. However, it is important to note that Eq. (2) includes no explicit information about the surface geometry, although this may affect the interaction time scale. Likewise, no information about the state of the boundary layer without freestream turbulence is included in the model. This may lead to error in the mechanistic model predictions since a transitional or fully turbulent boundary layer could prevent freestream turbulence from penetrating all the way to the surface. Freestream turbulence with energy distributed in a variety of scales would also contribute to error in the mechanistic model predictions since this is formulated for only the integral or most energetic scale.

Given the overall success of the mechanistic model, it is hypothesized that a new mechanistic model based on Eqs. (1) and (2) could be used to predict not only the time-averaged, but also the *transient* heat transfer for stagnation flow subject to large-scale, high-intensity freestream turbulence. This will be accomplished by incorporating the transient physical properties of coherent structures into the model. A hypothetical coherent structure interaction mechanism is depicted in Fig. 1.

As shown in Fig. 1, a coherent structure of given size or integral length scale $\Lambda(t)$ and circulation or strength $\Gamma(t)$ approaches the stagnation surface at a core-to-surface distance $d(t)$. The rotational motion of the coherent structure brings a proportional amount of cooler freestream fluid directly into the heated surface with induced velocity, $u_i(t)$. The resulting surface temperature gradient, being locally larger than that found under turbulence-free or laminar conditions, leads to heat transfer augmentation. The new mechanistic model derivation begins with an identical but transient version of Eq. (1) following the same general assumption of linear superposition:

$$h_{\text{Turb}}(t) = \overline{h_{\text{Lam}}(t)} + \Delta h_{\text{Turb}}(t) \tag{3}$$

In this work, the normal level of heat transfer without freestream turbulence is the time-averaged value for laminar stag-

nation point flow $\overline{h_{\text{lam}}(t)}$. The turbulent heat transfer or augmentation term $\Delta h_{\text{turb}}(t)$ is in the same form as the original time-averaged mechanistic model. The corresponding interaction time for a single event is the ratio of coherent structure integral length scale to induced fluid velocity,

$$t_{\text{int}} = \Lambda(t)/u_i(t) \tag{4}$$

Each event, however, may not bring the freestream fluid completely to the surface. Consequently, an interaction scaling factor F is added to account for this. After substitution and simplification, the final form of the transient mechanistic model is

$$\Delta h_{\text{turb}}(t) = \frac{Fk}{\sqrt{\pi\alpha\dfrac{\Lambda(t)}{u_i(t)}}} = \frac{Fk}{\sqrt{\pi\Lambda^2(t)\dfrac{\alpha}{\nu}\dfrac{\nu}{\Lambda(t)u_i(t)}}}$$

$$= \frac{Fk}{\Lambda(t)\sqrt{\pi}}\text{Pr}^{0.5}\ \text{Re}_\Lambda(t)^{0.5} \tag{5}$$

The Reynolds number is based on the induced velocity at the plate surface due to the coherent structure and the integral length scale:

$$\text{Re}_\Lambda(t) = \frac{\Lambda(t)u_i(t)}{\nu} \tag{6}$$

The induced velocity $u_i(t)$ is calculated by approximating the coherent structure as an infinite line vortex with total circulation $\Gamma(t)$. The radial velocity distribution is approximated using the Biot–Savart law:

$$u_i(t) \cong \frac{\Gamma(t)}{2\pi d(t)} \tag{7}$$

Later in this work, the identification, tracking, and analysis of coherent structures using time-resolved digital particle image velocimetry (TRDPIV) data is discussed. Transient data from this analysis is used with Eqs. (3)–(7) to predict both the transient and time-averaged heat transfer coefficients measured experimentally with the heat flux array (HFA) sensor.

2 Experimental Methods and Facilities

2.1 Water Tunnel Facility. The Virginia Tech AEThER Laboratory low speed water tunnel facility was used to conduct the current experiments. This variable speed, closed loop tunnel is impeller driven from approximately 0.05–1.0 m/s. The tunnel has a clear acrylic test section with dimensions of 0.61×0.61 m^2 and a length of 1.77 m. A series of screens is used in the upstream contraction to reduce freestream turbulence $\overline{Tu_x}$ to around 0.5–1% over the length of the test section at low speeds.

2.2 Turbulence Generation. A simple biplane grid was designed, constructed, and tested with the intent of generating homogenous, isotropic turbulence possessing both high turbulence intensity and large integral length scale in the water tunnel facility. Grid sizing was based on correlations by Baines and Peterson [24]. The grid was constructed of rigid PVC pipe with a nominal diameter $b = 2.14$ cm. The center-to-center pipe spacing was set at $Mu = 4.8$ cm, which gave a grid solidity of $\sigma \cong 70\%$. The performance of the grid design was evaluated using the two-dimensional TRDPIV data reduction techniques described later in this work. With the time-averaged freestream velocity downstream of the grids set at 10 cm/s, flow data were acquired at several locations downstream of the center of the grid. The time-averaged streamwise turbulence intensity and streamwise integral length scales were computed across the TRDPIV flow field region of interest. As expected, some spatially periodic variations in these properties were observed within the flow fields. These variations diminished with increasing distance downstream of the grid face as the turbulence became fully developed into the power-law region. When

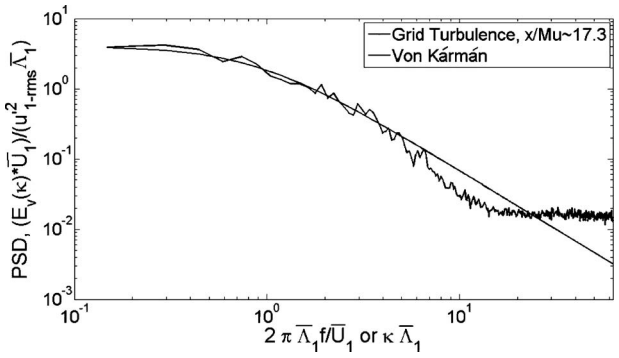

Fig. 2 Normalized grid turbulence power spectral density versus von Kàrmàn spectrum

spatiotemporally averaged, the streamwise turbulence intensity and streamwise integral length scales are in good qualitative agreement with the Baines and Peterson correlations.

In this study, all turbulent flow experiments were performed with the grid situated solely at a distance $x/Mu = 17.5$ upstream of the stagnation surface. At this distance and with a mean freestream velocity of $\overline{U_\infty} = 10$ cm/s, the grid generated turbulence has a spatiotemporally averaged streamwise turbulence intensity of $\overline{Tu_x} = 5.0\%$ and streamwise integral length scale of $\overline{\Lambda_x} = 3.25$ cm. The spatiotemporally averaged power spectral density (Fig. 2) for the grid turbulence data near $x/Mu = 17.5$ compares reasonably well with the theoretical one-dimensional energy spectrum for isotropic turbulence of Von Kàrmàn [25]. Hence, the turbulence is approximately homogenous and isotropic approaching the stagnation plate surface. Using the Von Kàrmàn relation [25], it may also be shown that the frequency of the most energetic turbulent structures is approximately $f_{\text{turb}} \cong 3\overline{U_1}/8\pi\overline{\Lambda_1}$. Given the aforementioned flow and turbulence parameters, this frequency is approximately $f_{\text{turb}} \cong 0.37$ Hz.

2.3 Experimental Model and Heat Transfer Instrumentation. A basic flat plate model was constructed to create a classic Hiemenz stagnation flow. As shown in Fig. 3, the model is comprised of a smooth, removable face-plate mounted to a water-tight rectangular housing. Two long square tubes are used to hold the model rigidly in the flow and double as conduits to carry heater and sensor wires safely out of the water. The model spans the entire 0.61 m width of the tunnel with the instrumentation conduits against the tunnel sidewalls. Flow visualization using the TRDPIV laser plane showed that these conduits create small standing vortices on the tunnel walls. The influence of these structures on the stagnation flow at the center of the stagnation

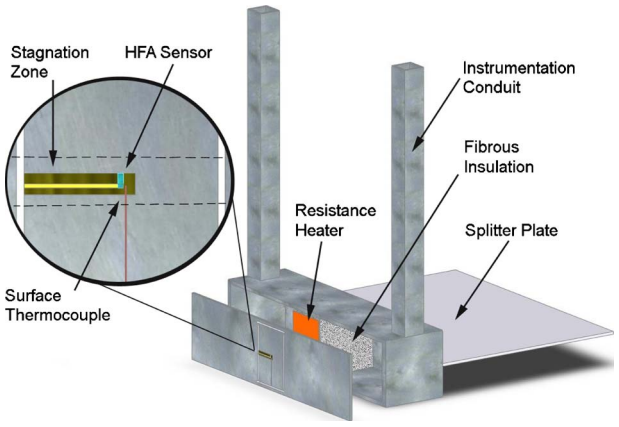

Fig. 3 Hiemenz flow model and instrumentation

plate was negligible. A long splitter plate is attached aft of the rectangular housing to eliminate vortex shedding interactions with the stagnation region. This was also verified by flow visualization.

The measurement area (inset Fig. 3) on the face plate is limited to a section approximately 10 cm wide by 15 cm tall at the center of the plate. This section is isolated thermally from the rest of the face-plate by a series of channels machined through the surface. The entire testing area is heated to a uniform power density of 1.5 W/cm^2 using a thin-film resistance heating element applied with adhesive to the back of the plate. Low thermal conductivity fibrous insulation is applied to the back of the heater to force heat conduction through the face-plate and into the oncoming flow.

The heat transfer instrumentation includes three fine wire thermocouples and one thin-film heat flux sensor. The first type K thermocouple monitors heater core temperature. A second type K thermocouple is embedded in the face-plate adjacent to the heat flux sensor for measurements of fluctuating surface temperature. A final type K thermocouple is used to monitor the freestream temperature in the water tunnel facility. Measurements of the transient surface heat flux are made using a prototype sensor called the heat flux array or HFA. This thin-film, direct-measurement sensor is based on a differential thermocouple design. Details of the design, fabrication, calibration, and performance of the HFA are found in Refs. [26,27]. The HFA used in this study is hot pressed with thin plastic and epoxy onto the center of the measurement area in the stagnation line region, as shown in Fig. 3. The mean sensitivity of the HFA in convective heat transfer conditions was found to be $S_q = 42.6$ $\mu V/W/cm^2$ measured in situ on the stagnation plate surface. In all experiments discussed in this work, the heat transfer data were sampled at a fixed frequency of $F_s = 1$ kHz using a National Instruments 6015 DAQ and SCB-16 block with 16 bit resolution. The resulting data were downsampled to the sampling frequency of the TRDPIV images. The microvolt signal of the HFA was first amplified using a custom fabricated amplifier with fixed gains of 1000 Hz and 480 Hz antialiasing filter. Error analysis for the AEThER convection calibration facility [27] shows the measurement uncertainty of the HFA to be $\pm 6.6\%$.

2.4 Flow Measurements: Time-Resolved Digital Particle Image Velocimetry and Setup. This study examines the full two-dimensional velocity field in front of the experimental model using time-resolved digital particle image velocimetry. This technique delivers noninvasive, full-flow-field velocity measurements with high spatial resolution and high sampling frequencies.

In DPIV, a laser is used to illuminate a thin two-dimensional plane within a chosen flow field. Particles or tracers seeded in the flow become highly visible as they interact with and scatter light. In this case, Spherical® glass microspheres with a mean diameter of 11 μm were used. A digital camera oriented normal to the laser plane captures images of the particles at precise intervals of time within a region of interest (ROI). The velocity field within the ROI may then be inferred by calculating the displacement of particle patterns between two or more images in the predetermined time interval. References [28,29] provide details on the general method.

As shown in Fig. 4, the TRDPIV system used here employs a New Wave Research (Portland, OR) *Pegasus* dual head laser. The laser light is guided by an optical train and spread into a thin ($\sim$1 mm) plane, which is aligned perpendicular to the stagnation flow model along the stagnation line. A Photron (San Diego, CA) *Fastcam* digital camera is used to acquire images and is located underneath the water tunnel. Timing of the laser and camera are controlled via a timing hub and software by Integrated Design Tools Inc. (Tallahassee, FL). A central PC is used to control the camera, laser, and timing hub and to acquire and store images and heat transfer data.

The region of interest for these experiments was fixed at 8.75 cm tall by 10.75 cm wide centered on the HFA sensor junction

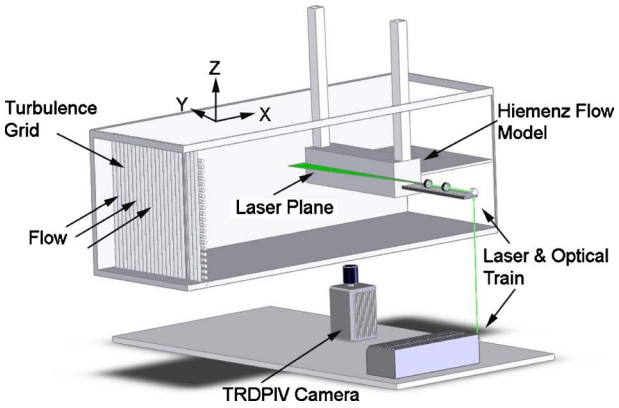

Fig. 4 Water Tunnel Facility and experimental setup

along the stagnation line of the plate surface. The ROI was imaged using 1024×832 pixels, giving an image magnification of $M = 105.25$ μm/pixel. With a 4 pixel $\times$ 4 pixel vector spacing, this ROI contains 53,248 vectors with 421 μm between vectors. TRDPIV data were continuously sampled in single pulsing fashion at $F_s = 125$ Hz (i.e., one laser pulse per image at a fixed time interval of 0.008 s). The total uncertainty in TRDPIV velocity measurements using the aforementioned experimental setup and image processing techniques is estimated to be $\pm 5\%(30)$.

Sampling times were maximized to fill the available memory of the camera. This gave roughly 3200 images per trial or 60 s of data. As mentioned previously, the frequency of the most energetic turbulent structures is approximately $f \cong 0.37$ Hz. The sampling time is therefore long enough to calculate meaningful average flow quantities since upwards of 20 major interactions can be expected in a given trial and three identical trials are taken successively. Given the freestream turbulence parameters, the estimated Kolmogorov length and time scales are 665 μm and 0.2 s, respectively. The TRDPIV configuration described above is therefore sufficient to accurately capture fluid motion across the turbulent energy range. However, uncertainty and random noise would have a greater effect on measurements in the low-end of the dissipative range. Higher spatiotemporal resolution, though possible with this DPIV system, was sacrificed to allow for a larger field of view and longer sampling times. This was done because existing evidence suggests that the highest-energy, large-scale structures are responsible for major increases in heat transfer and they occur over long time scales.

2.5 Experimental Procedure. In this work, a single mean Reynolds number of $\overline{Re}_D = 21{,}000$ is used, which corresponds to a mean freestream velocity $\overline{U}_\infty = 10$ cm/s and plate width in the z-direction of $D = 15.25$ cm An initial series of three laminar stagnation flow trials was completed to validate the experimental approach and provide baseline flow and heat transfer quantities for comparison with turbulent flow scenarios. Three trials were then completed to study the effects of freestream turbulence with the face of the turbulence grid fixed at a distance $x/Mu = 17.5$ upstream of the stagnation surface.

To begin an experiment, the unheated stagnation plate was allowed to reach thermal equilibrium with the water tunnel. The heater was then turned on to full power and the system was allowed to reach steady state conditions. The TRDPIV system was then initiated and images were acquired. The laser pulse and camera signals were synchronized with the heat transfer data so precise comparison of the two data sets in time could be performed. A total of 60 s of concurrent TRDPIV and heat transfer data were acquired. The heater was then turned off.

3 Data Reduction and Analysis

Sections 4.1–4.3 describe the data reduction procedures used to reduce the raw heat transfer and TRDPIV flow data for analysis.

3.1 Heat Transfer. All heat transfer raw voltage signals were first zero-phase-shift, low-pass filtered to 35 Hz, which is the highest frequency resolved by this particular HFA prototype. Transient surface temperature $T_s(t)$ and freestream temperature $T_\infty(t)$ were calculated in °C using NIST type K thermocouple tables. The transient surface heat flux $q_s''(t)$ was calculated according to Eq. (8)

$$q_s''(t) = \frac{V_q(t)}{S_q} \tag{8}$$

where $V_q(t)$ and S_q are the gain adjusted transient HFA voltage output and HFA sensitivity, respectively. The transient surface heat transfer coefficient $h(t)$ whether laminar or turbulent follows from Newton's law of cooling:

$$h(t) = \frac{q_s''(t)}{(T_s(t) - T_\infty(t))} \tag{9}$$

In comparing turbulent flow quantities to turbulent heat transfer quantities, it is customary to follow the Reynolds decomposition technique. Hence, the mean removed or fluctuating heat transfer coefficient becomes

$$h'(t) = h(t) - \sum_{k=1}^{N} \frac{h(t_k)}{N_k} \tag{10}$$

where $k=1,2,\ldots N_k$ is the number of samples in the data set.

3.2 TRDPIV: Image Processing, Proper Orthogonal Decomposition, and Turbulence Statistics. The reduction of TRDPIV data begins with processing of the raw particle image sequences. Image processing is done using a custom analysis software package developed and validated by researchers in the AEThER laboratory. The details of the various methods used in image processing and validation can be found in Refs. [29,30]. The focus here is on the postprocessing of the two-dimensional flow field images. All postprocessing were performed using customized codes in MATLAB.

A given TRDPIV data set is comprised of $k=1,2,\ldots,N_k$ time instances t_k of the flow field, each having a regularly spaced grid of $N_i x N_j$ total vectors:

$$\boldsymbol{U}(x_i,y_j,t_k) = \sum_{l=1,2} u_l(x_i,y_j,t_k)\hat{x_l} \tag{11}$$

where for reference, index $l=1$ corresponds to the x-direction and $l=2$ corresponds to the y-direction, which spans the ROI. Subscripts $i=1,2,\ldots,N_i$ and $j=1,2,\ldots,N_j$ are indices describing the x and y locations in the grid. Each of the TRDPIV flow fields contains a certain degree of noise dependent upon how the image sequences are processed and validated. Proper orthogonal decomposition (POD) is used in this study as a filtering tool to remove noise. As described by Smith et al. [31], POD seeks to reconstruct the original flow field $\boldsymbol{U}(x_i,y_j,t_k)$ in terms of N_p time dependent projection coefficients $a_p(t)$ and optimal basis functions or eigenmodes $\varphi_p(x_i,y_j)$ such that

$$\boldsymbol{U}(x_i,y_j,t_k) = \sum_{p=1}^{N_p} a_p(t_k)\phi_p(x_i,y_j) \tag{12}$$

Using Eq. (12), it is possible to reconstruct the flow field using any number of eigenmodes. In fact, using only the most energetic eigenmodes in the flow field reconstruction serves to eliminate high spatial frequency and low energy noise. Hence, reconstruction of the flow fields in this study was done using only the number of modes required to capture 90% of the total flow field energy. In this study, around 20 modes are sufficient. This typically results in a substantially less noisy flow field and one that better represents the flow structures of interest in this study.

The POD reconstructed flow field is divided into mean and fluctuating velocity fields using Reynolds decomposition. The fluctuating velocities at each grid point at time t_k become

$$u_l'(x_i,y_j,t_k) = u_l(x_i,y_j,t_k) - \frac{1}{N_k}\sum_{k=1}^{N_k} u_l(x_i,y_j,t_k) \tag{13}$$

The first turbulence quantities calculated from the fluctuating velocity fields are the rms velocity fields:

$$u'_{l-\mathrm{rms}}(x_i,y_j) = \sqrt{\frac{1}{N_k}\sum_{k=1}^{N_k} u'_l(x_i,y_j,t_k)^2} \tag{14}$$

The rms velocity fields are used to calculate the turbulence intensities:

$$Tu_l(x_i,y_j) = \frac{u'_{l-\mathrm{rms}}(x_i,y_j)}{\sum_{k=1}^{N_k} u_l(x_i,y_j,t_k)/N_k} \tag{15}$$

The integral length scale characterizes the largest, most energetic structures present in the turbulent flow field, which are important contributors to heat transfer augmentation. In this work, integral length scales are calculated by the integration of the longitudinal autocorrelation functions defined in Eq. (16). These autocorrelations use the fluctuating u'_1 and u'_2 velocities starting from the centroid (x_c,y_c) of the identified coherent structure at each time instance t_k. These functions are integrated up to the first zero crossing using Eq. (17):

$$R_{u'_l}(\varepsilon_1) = \frac{u'_l(x_c,y_c,t_k)u'_l(x_c+\varepsilon_1,y_c,t_k)}{u'_l(x_c,y_c,t_k)u'_l(x_c,y_c,t_k)} \quad \text{(longitudinal)} \tag{16}$$

$$\Lambda_{l,1}(x_c,y_c,t_k) = 2\int_0^{R_{u'_l}(\varepsilon_1)=0} R_{u'_l}(\varepsilon_1)d\varepsilon_1 \quad \text{(longitudinal)} \tag{17}$$

The average longitudinal length scale, $\overline{\Lambda(x_c,y_c,t_k)} = (\Lambda_{1,1}(x_c,y_c,t_k)+\Lambda_{2,1}(x_c,y_c,t_k))/2$ is used for analysis in the remainder of this work. This appears to be a reliable estimate of the coherent structure's overall size.

3.3 Coherent Structure Identification and Dynamic Tracking. A number of works have examined methods of coherent structure identification. In this study, the critical point method of Chong et al. [32] is used. Briefly, critical points in the given 2D flow field, which collectively identify a coherent structure, occur when the following function is strictly positive:

$$\Delta(x_i,y_j,t_k) = (Q(x_i,y_j,t_k)/3)^3 + (R(x_i,y_j,t_k)/2)^2 \tag{18}$$

where Q and R are invariants of the rate-of-deformation tensor for a particular point in the flow field at a particular time instance. Reference [33] provides more details on the method. Equation (18) is applied to each point in the TRDPIV flow field at each time instance. A constant, user defined threshold is then set on the $\Delta(x_i,y_j,t_k)$ magnitude. The threshold is chosen subjectively so that only clearly defined coherent structures remain identified in the flow field image. The area coverage of the $\Delta(x_i,y_j,t_k)$ magnitude threshold is typically on the order of the length scale of the coherent structure. Subjective filtering is also required to eliminate falsely identified structures, which result from noise in approximation of the rate-of-deformation tensor. The vortex strength or circulation, Γ, is calculated using the standard line integral method on the boundary of the area identified using Eq. (18). Knowing the coherent structure area and circulation also allows for estimation of the total area averaged vorticity ω_A. This approach is less susceptible to numerical errors from approximations

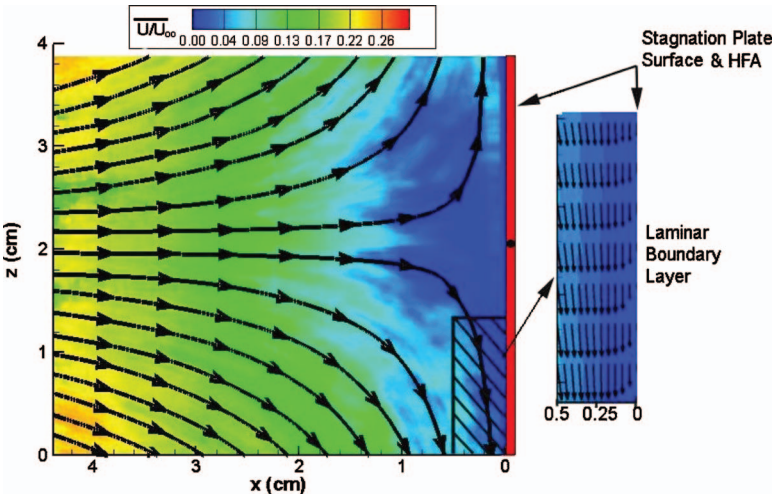

Fig. 5 Laminar flow and boundary layer

of velocity gradients.

The tracking of coherent flow structures has been the subject of a number of works. The method utilized in this study is based on a simplified combination of features from Samtaney et al. [33]. Briefly, each time step in the coherent structure analysis results in a certain number of identified structures. Key parameters are calculated for each structure including core location, integral length scale, circulation, and area averaged vorticity. With the dense spatiotemporal information given by TRDPIV, it is possible to track a particular structure in time without ambiguity by simply comparing these parameters at different time steps. This algorithm has proven reliable for tracking complex vortex motions in the stagnation region. However, this simple approach is limited since it does not account explicitly for the coalescence of multiple coherent structures.

4 Results

4.1 Laminar Flow and Heat Transfer. One of the interesting features of laminar Hiemenz flow is the fact that the fluid boundary layer thickness is constant across the stagnation region [1]:

$$\delta_{\text{lam}} = 2.40\sqrt{\frac{\nu}{a}} \tag{19}$$

where ν is the kinematic viscosity of the fluid and the parameter a depends on the characteristic width of the stagnating body and the freestream velocity. This parameter is found experimentally from TRDPIV measurements of laminar flow velocity along the stagnation streamline to be $a=0.59$ 1/s. This gives a predicted boundary layer thickness of $\delta_{\text{lam}}=2.8$ mm using Eq. (17). The film temperature was used to calculate thermodynamic properties as the plate was heated in all of the flow trials.

Figure 5 shows a contour plot of time-averaged velocity magnitude normalized by freestream velocity along with associated streamtraces. Note from the schematic in Fig. 3 that the laser plane in Fig. 5 is oriented in the x-z plane across the narrow dimension of the stagnation plate. The remainder of this study examines data in the x-y plane along the stagnation line of the plate. The comparison to classic Hiemenz flow is striking. The inset image in Fig. 5 shows a closer view of the laminar boundary layer. The measured laminar boundary layer thickness is approximately $\delta_{\text{Lam}}=3.0$ mm, which is slightly larger than that predicted using Eq. (17). Focusing now on the thermal aspects of the laminar flow cases, the mean laminar heat transfer coefficient for the three trials was found to be $\overline{h_{\text{lam}}(t)}=0.053$ W/cm^2 °C. The solution for the laminar heat transfer coefficient given by Goldstein [2] for stagnation point flow is

$$h_{\text{lam}} = 0.5421k\ \text{Pr}^{0.42}\sqrt{\frac{a}{\nu}} \tag{20}$$

where k is the thermal conductivity of the fluid, Pr is the Prandtl number of the fluid, and a and ν are defined previously. Using Eq. (18), the predicted heat transfer coefficient is $h_{\text{lam}}=0.058$ W/cm^2 °C. The value measured experimentally is slightly lower but near the experimental uncertainty.

4.2 Time-Averaged Turbulent Heat Transfer: Mean Augmentation. An example of the effect of freestream turbulence on stagnation heat transfer is shown in Fig. 6. This image compares the time-averaged laminar value to the turbulent heat transfer coefficient measured by the HFA for a representative trial.

It is clear that large-scale fluctuations in the heat transfer coefficient serve to shift the mean heat transfer levels above the mean laminar values. The average augmentation for the three trials was $\overline{\Delta h_{\text{Turb}}(t)}=0.034$ W/cm^2 °C or an increase of 64%. As discussed in Sec. 3, Nix et al. [23] developed a successful mechanistic model, which uses time-averaged turbulent flow information in the vicinity of the stagnation region to predict the augmentation of heat transfer. This model was applied to the TRDPIV data taken simultaneously with the turbulent heat transfer data shown in Fig. 6. Figure 7 shows the streamwise variations in the rms fluctuating velocity ($u'_{1-\text{rms}}$), time-averaged integral length scale ($\overline{\Lambda_1}$), and the time-averaged heat transfer augmentation according to Eq. (2) ($\overline{\Delta h_{\text{turb}}(t)}$). In this case, the rms fluctuating velocity and integral length scale in the streamwise direction are calculated in an identical manner as Ref. [23] using transient data at each point in the

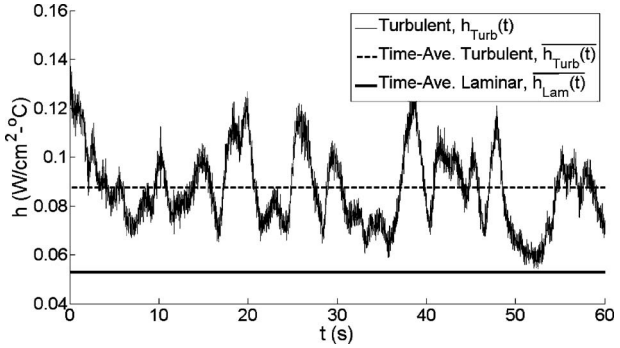

Fig. 6 The effects of freestream turbulence on time-averaged heat transfer

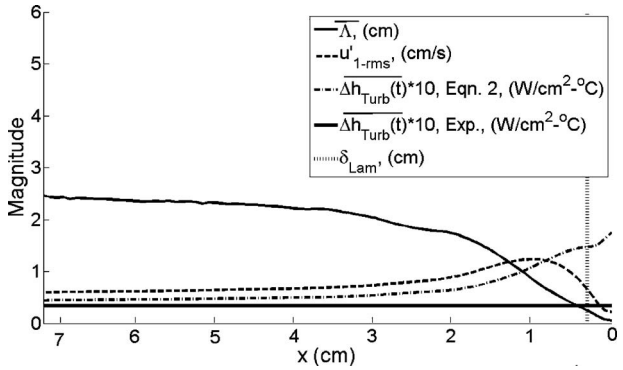

Fig. 7 Stream-wise variation in time-averaged flow properties and predicted heat transfer augmentation

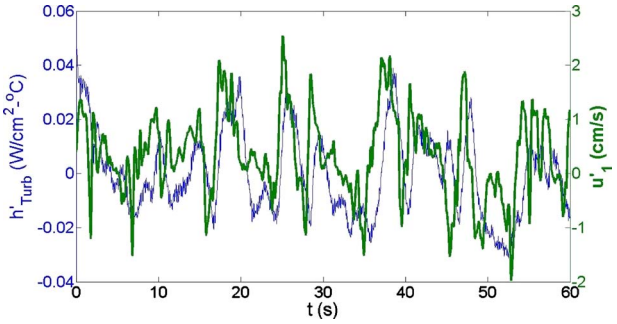

Fig. 9 Comparison of fluctuating velocity and heat transfer signals in a region of high coherence

flow field. Reported values are spatial averages across the width (y-direction) of the TRDPIV field-of-view at each stream-wise location along the x-direction.

As shown in Fig. 7, the time-averaged integral length scale begins lower than the freestream value and decreases to near zero at the stagnation plate surface. This demonstrates the influence of the stagnation plate upstream in the water tunnel facility beyond the TRDPIV field of view. The rms fluctuating velocity increases upon approaching $d \cong 3\delta_{\text{lam}}$, and then decreases near the stagnation plate surface. While this flow behavior is consistent with that observed by Nix et al. [23], the predicted heat transfer augmentation using Eq. (2) is shown to overpredict the experimentally measured value by around 30% across the TRDPIV field of view. One major difference between the current study and previous experiments is the use of water instead of air. It is possible that the order-of-magnitude higher Prandtl number of water plays a role in the overall heat transfer augmentation. For instance, in the current study, the thermal boundary layer is quite thin ($\sim .5\delta_{\text{lam}}$) compared with the laminar momentum boundary layer thickness. All of the work presented by Nix et al. [23] was completed in air with the thermal and fluid boundary layer thicknesses nearly equal.

4.3 Transient Flow and Heat Transfer: Insight Into the Mechanism of Heat Transfer Augmentation. To better understand the mechanism of heat transfer augmentation, the coherence between the flow field and the measured heat transfer coefficient are first examined. The coherence function is defined as

$$\gamma_{AB}(f) = \frac{|s_{AB}{}^2|}{s_{AA} \cdot s_{BB}} \tag{21}$$

The coherence function is defined as the magnitude of the squared cross-power spectrum between two signals A and B normalized by the product of the autopower spectrum for each signal. The resulting function of frequency has values on the interval [0,1]. If two signals have a high coherence, they share significant energy content at similar frequencies in time. Equation (21) was applied to the fluctuating velocity $u'_1(x_i, y_j, t_k)$ at every point in the transient flow field and the transient heat transfer coefficient, $h'_{\text{Turb}}(t)$ for the data shown in Fig. 6. Figure 8(*a*) shows a contour plot of the maximum coherence between signals, while Fig. 7(*b*) shows the corresponding frequency at the peak coherence.

It is clear from Figs. 8(*a*) and 8(*b*) that very high levels of coherence are present corresponding to very low frequencies ranging from 0.1 Hz to 1.5 Hz. These low frequencies are precisely the frequencies of the integral length scales determined in our turbulence grid analysis. Figure 9 compares $u'_1(x_i, y_j, t)$ and $h'_{\text{turb}}(t)$ in the region of high coherence, which is near the laminar boundary layer. It can be seen quite clearly that these low frequency, large-scale fluctuations in streamwise velocity correspond directly to large fluctuations in heat transfer. A small amount of time lag on the order of 1.0 s is also present.

The coherence analysis suggests that the mechanism responsible for heat transfer augmentation involves the large-scale motion of fluid, particularly in the stream-wise direction. Using animations of the TRDPIV flow field, it is immediately apparent that large increases in heat transfer and fluid velocity coincide with the

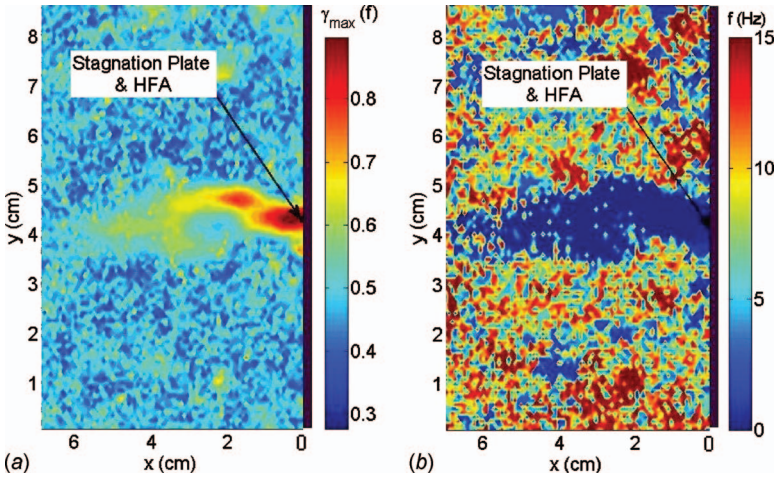

Fig. 8 Peak coherence and associated frequencies between fluctuating velocity and surface heat transfer

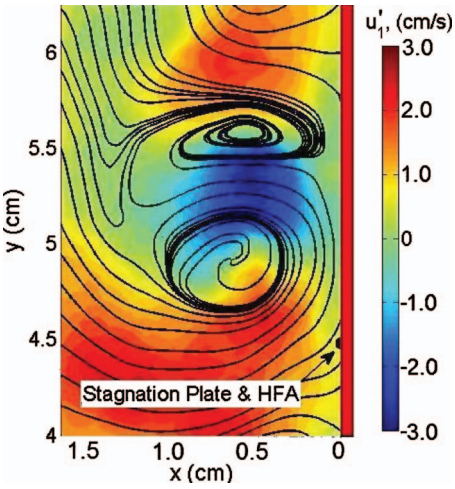

Fig. 10 A snapshot of TRDPV flow field animations showing coherent structures in the stagnation region

presence of coherent structures in close proximity to the HFA sensor. Using the data in Fig. 9 as an example, a large spike in fluctuating stream-wise velocity and heat transfer coefficient is seen to occur near $t=38$ s. The flow field in the stagnation region corresponding to $t=38$ s is shown in Fig. 10. The streamwise fluctuating velocity component has been color contoured in Fig. 10, and streamlines have been added to accentuate the rotational motion of the coherent structures. Notice the presence of a coherent structure with counterclockwise spin near the HFA sensor. This coherent structure is part of a counter-rotating vortex pair. It appears that the coherent structure is sweeping freestream fluid through the laminar boundary layer directly into the surface. This is fully consistent with the behavior of coherent structures and heat transfer reported in Ref. [22].

The mechanism by which coherent structures augment heat transfer becomes clearer after examining their general behavior in the stagnation region. This behavior is studied using the coherent structure identification analysis described in Sec. 4.3. Coherent structures within the flow fields are first identified at each time instance and analyzed before applying the tracking algorithm. The mean integral length scale ($\bar{\Lambda}$), circulation (Γ), area averaged vorticity (ω_A), and distance relative to the stagnation plate surface (d) are calculated for the core location, (x_c, y_c) of each structure at each time instance. This information is then combined into a four-dimensional histogram. An example is shown in Fig. 11.

Several immediate observations can be made from Fig. 11.

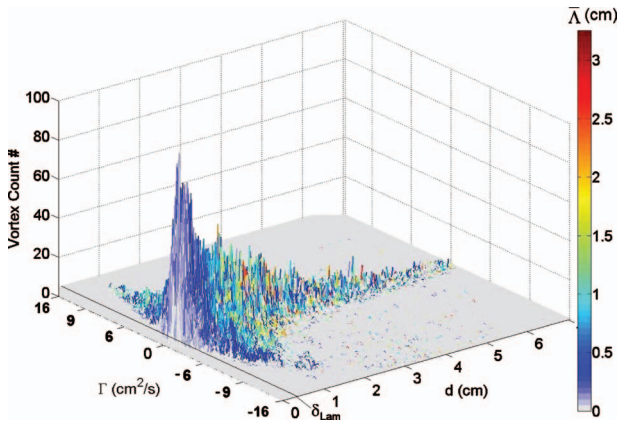

Fig. 11 Histogram of coherent structures identified in the stagnation region and corresponding physical properties

First, it is clear that a large degree of symmetry exists in the flow field. Similar numbers of coherent structures exist with either positive or negative circulation (spin). A portion of the symmetry is the result of many counter-rotating vortex pairs forming near the surface of the stagnation plate. Such a distribution of coherent structures can also be expected for isotropic grid generated turbulence. Secondly, there is a higher incidence of coherent structures just outside the laminar boundary layer thickness of $\delta_{lam}=0.03$ cm, suggesting a nominal stand-off distance for the coherent structures. The increased incidence of these coherent structures is a combination of factors. Structures tend to linger in the near wall region as they are stretched, amplified, and ultimately dissipated. There also appears to be a number of secondary, weaker coherent structures being generated near the surface by the larger, more energetic counter-rotating vortex pairs. Thirdly, the mean integral length scale generally decreases upon approaching the stagnation plate surface with circulation concentrated in a band ranging over ± 4 cm^2/s. This coincides with increasing area averaged vorticity approaching the stagnation plate surface. This behavior supports the theory of vorticity amplification proposed by Sutera [15] for turbulence approaching the stagnation region. Interestingly, for a small number of coherent structures the circulation increases substantially near $d \cong 3\delta_{lam}$. Note that a similar behavior for stream-wise integral length scale and fluctuating velocity was noted earlier in the time-averaged data of Fig. 7, including the location of a peak in fluctuating velocity around $d \cong 3\delta_{lam}$. The final and perhaps most important observation is that a large percentage of the identified structures have core-to-plate distances small enough, and integral length scales large enough, to completely penetrate both the laminar momentum and thermal boundary layers. It is likely that these coherent structures are directly responsible for heat transfer augmentation as they can bring cold freestream fluid directly into the heated stagnation surface.

4.4 Validation of the Transient Mechanistic Model. The coherent structure tracking algorithm was applied to the identified structures for all trials in an attempt to validate the transient mechanistic model and help identify the mechanism of heat transfer augmentation. Examinations of both the tracked structures and flow field animations reveal a complex flow pattern near the stagnation region along the x-y plane. Coherent structures may enter the stagnation region in more or less a straight trajectory (x-direction), but tend to move and translate in the transverse direction (y-direction). This is consistent with results reported in Ref. [22]. A close inspection reveals much of the transient coherent structure behavior discussed previously in Sec. 4.3. Validation of the transient mechanistic model is provided by examining the appropriately chosen coherent structure interactions. From the coherence analysis, the model may only be expected to work well in a region centered on the sensor, covering nearly the width of the TRDPIV field-of-view and the height of about 2.5 cm. The coherent structures used to validate the model should also be minimally influenced by other coherent structures existing over the same time interval. An example coherent structure interaction, which fit these criteria, was chosen for detailed study and used to validate the mechanistic model.

The results of the analysis are contained in Figs. 12(*a*)–12(*d*). The first plot, Fig. 12(*a*), provides a visualization of the trajectory and behavior of the coherent structure through time. The trajectory is shown as a black line on the x-y plane. The three dimensional plot, which accompanies the trajectory data, is a reconstruction of the coherent structures evolution through time and space, and is constructed as follows. At each time instance, the coherent structure is represented as a simple cylinder of diameter reflecting the integral length scale. The true size is not shown for the sake of clarity. The height of the cylinder is adjusted so that the volume of the cylinder is always in unity. The color of the cylinder corresponds to the normalized, area averaged vorticity magnitude contained in the coherent structure at each time instance (i.e., circulation divided by total coherent structure area). The second plot,

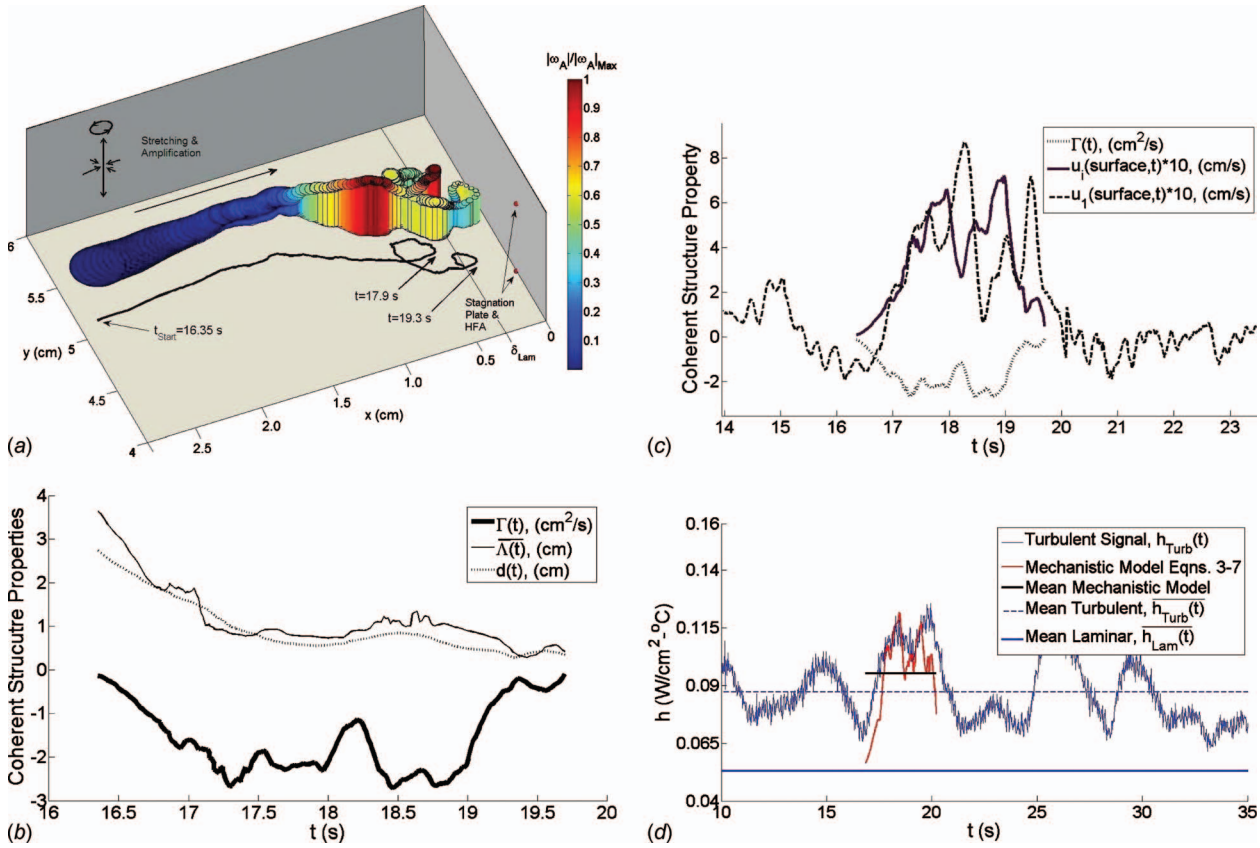

Fig. 12 Mechanistic model validations for an example streamwise coherent structure interaction

Fig. 12(*b*), shows the transient physical properties from the tracking analysis, which are used in the prediction of the measured transient heat transfer. Figure 12(*c*) demonstrates the ability of the simple model to predict the principle velocity magnitude at the stagnation plate surface. Finally, Fig. 12(*d*) compares the mechanistic model heat transfer predictions using Eqs. (3)–(7) to the experimentally measured values. Note that the interaction scaling factor for the transient mechanistic model was initially estimated to be $F=0.8$.

Figure 12(*a*) shows a single coherent structure with counterclockwise rotation enter the TRDPIV field-of-view with relatively large integral length scale and low area averaged vorticity. As the structure approaches the plate, the normalized area averaged vorticity increases to its peak value of $|\omega_A|/|\omega_A|_{max}\sim 1.0$ from $t=17.3$ to $t=17.9$ s. The amplification factor of area averaged vorticity is quite large, at around 15.0 times during the initial approach toward the stagnation surface. The strengthened coherent structure approaches closely to the stagnation plate surface at $t=17.9$ s and then turns abruptly away from the sensor. This motion is concurrent with a sharp rise in the experimentally measured turbulent heat transfer coefficient shown in Fig. 12(*d*) at $t=18.43$ s. As shown in Fig. 12(*b*), the integral length scale is nearly identical to the core-to-plate distance during this close passage. This implies that the coherent structure is likely perturbing and penetrating at least into the laminar momentum boundary layer. Although not shown in Fig. 12(*a*), a vortex of opposite spin is generated at the plate when this structure enters the stagnation region, forming a counter-rotating vortex pair. This generated structure appears to be short lived, and entrained by the primary coherent structure before a second close passage at $t=19.3$ s. A second close passage of the slightly weakened coherent structure at $t=19.3$ s causes a second, higher increase in heat transfer corresponding to the second peak seen in Fig. 12(*d*) at $t=19.76$ s. In this case, it is believed that the closer proximity leads to the higher heat transfer augmentation since it is more probable that the structure completely penetrates both the laminar momentum and thermal boundary layers.

The interplay of coherent structure physical properties is shown in Fig. 12(*b*). The mean integral length scale decreases in a smooth fashion from the freestream upon approaching the stagnation surface. The transient circulation strength, however, resembles the measured heat transfer coefficient. There are two regions of increasing strength corresponding roughly to the two peaks in heat transfer, all of this occurring when the coherent structure is within a distance of $d\cong 3\delta_{lam}$ where fluid motion is complex. This suggests that it is the strength of the vortex that plays one of the major roles in heat transfer augmentation. Figure 12(*c*) compares the predicted induced velocity $u_i(t)$ with the TRDPIV measured stream-wise velocity component $u_1(t)$ at a distance of $d=0.04$ cm from the surface. This is inside the laminar momentum boundary layer and directly in front of the HFA sensor. Notice that the induced velocity is generally close to the measured value, especially in the dynamic shape of the curves. Of course, some errors in the induced velocity calculation may be expected as the velocity induced by nearby structures is not accounted for in the analysis, and approximating the coherent structure as an infinite line vortex may not be the most accurate approach.

The mechanistic model prediction of the transient, turbulent heat transfer coefficient using the coherent structure properties of Figs. 12(*b*) and 12(*c*) is shown in Fig. 12(*d*). With an interaction scaling factor of $F=0.8$, the transient mechanistic model prediction matches the experimental curve well in terms of magnitude and dynamic shape. Note that a time lag of ~ 0.5 s is applied to the mechanistic model predictions for ease in comparison. The relatively simple mechanistic model performs well considering the complexity of the turbulent flow. As mentioned previously, there is some error associated with the heat transfer prediction

since other coherent structures could be contributing to the heat transfer over the same interaction time frame. An improved model would be able to predict the cumulative induced velocity at the surface due to multiple coherent structures at the same time instance. One final point may be made about this model. If it works well in predicting heat transfer augmentation for individual transient interactions, it would be expected to provide an accurate estimate of the time-averaged turbulent heat transfer. This is, in fact, the case as shown by the solid black line in Fig. 12(*d*), which is close to the overall time-averaged turbulent heat transfer (dashed blue line). The time average is, however, slightly biased toward a higher value because the tracking analysis results do not extend over a long enough time period.

5 Conclusions

This work successfully demonstrates the application of simultaneous TRDPIV and HFA measurements to the study of heat transfer in stagnating flows subject to freestream turbulence. Freestream turbulence is shown to have a pronounced effect on heat transfer at a stagnation point, producing large increases in both the transient and time-averaged surface heat transfer coefficient. These studies confirm that coherent structures are responsible for the observed increases in heat transfer. Coherent structures entering the stagnation region experience stretching and amplification of vorticity and may impinge on the stagnation surface with enough energy to penetrate the laminar momentum and thermal boundary layers. It appears that the rotational motion of the coherent structure brings freestream fluid into direct contact with the stagnation surface, thereby increasing the local heat transfer. Evidence for such an augmentation mechanism is provided by the successful validation of a new transient mechanistic model, which incorporates the properties of identified and tracked coherent structures.

Acknowledgment

The principal author would like to thank several AEThER laboratory members including David Hubble for their invaluable assistance during experimentation and Christopher Weiland for the vortex identification code development and assistance with analysis. This material is based upon work supported by the National Science Foundation under Grant No. CTS-0423013.

Nomenclature

a = stagnation flow parameter (1/s)
a_p = POD projection coefficient
b = grid bar diameter (cm)
d = coherent structure core-to-surface distance (cm)
D = characteristic width of stagnation plate (cm)
f = frequency (Hz)
F = interaction scaling factor
F_s = sampling frequency (Hz)
h = heat transfer coefficient ($W/cm^2\ ^\circ C$)
k = thermal conductivity ($W/cm\ ^\circ C$)
M = TRDPIV camera magnification ($\mu m/pixel$)
Mu = grid spacing (cm)
N_p = total number of POD projection coefficients
N_k = total number of TRDPIV time instances
Nu = Nusselt number
Pr = Prandtl number
q'' = heat flux (W/cm^2)
R = normalized autocorrelation function
S = power spectral density (power/Hz)
Re = Reynolds number
S_q = sensitivity of heat flux sensor ($\mu V/W/cm^2\ ^\circ C$)
t = time (s)
T = temperature (°C)
Tu = turbulence intensity (%)
U = total flow velocity (cm/s)
u' = fluctuating velocity component (cm/s)
V_q = heat flux sensor output voltage (μV)

Greek Symbols

α = thermal diffusivity (cm^2/s)
δ = boundary layer thickness (cm)
ε = TRDPIV vector spacing (cm)
Δh_{turb} = turbulent heat transfer augmentation
γ = coherence (%)
Γ = vortex circulation (cm^2/s)
Λ = integral length scale (cm)
ν = kinematic viscosity (cm^2/s)
ω_A = area averaged vorticity (1/s)
ϕ_p = POD eigenmode
σ = grid solidity (%)

Subscripts

c = coherent structure core
i = induced velocity
s = stagnation plate surface
x, 1 = stream-wise or longitudinal flow direction
y, 2 = cross-stream or transverse flow direction
∞ = freestream indicator
turb = turbulent flow
lam = laminar flow

References

[1] Hiemenz, K., 1911, "Die Grenzschicht an einem in den gleichformigen Flussigkeitsstrom eingetauchen geeraden Kreiszlinder," Dinglers Polytechnic J., **326**, p. 321–410.
[2] Goldstein, S., 1938, *Modern Developments in Fluid Dynamics*, Clarendon, Oxford.
[3] Kestin, J., 1966, "The Effect of Freestream Turbulence on Heat Transfer Rates," *Advances in Heat Transfer*, Vol. 3, Academic, New York, pp. 1–32.
[4] Kestin, J., and Wood, R. T., 1969, "Enhancement of Stagnation-Line Heat Transfer by Turbulence," Prog. Heat Mass Transfer, **2**, pp. 249–253.
[5] Smith, M. C., and Kuethe, A. M., 1966, "Effects of Turbulence on Laminar Skin Friction and Heat Transfer," Phys. Fluids, **9**, pp. 2337–2344.
[6] Lowery, G. W., and Vachon, R. I., 1975, "The Effect of Turbulence on Heat Transfer From Heated Cylinders," Int. J. Heat Mass Transfer, **18**, pp. 1229–1242.
[7] Traci, R. M., and Wilcox, D. C., 1974, "Analytical Study of Freestream Turbulence Effects on Stagnation Point Flow and Heat Transfer," *Proceedings of the AIAA Seventh Fluid and Plasma Dynamics Conference*, Paper No. 74-515.
[8] Yardi, N. R. and Sukhatme, S. P., 1978, "Effects of Turbulence Intensity and Integral Length Scale of a Turbulent Freestream on Forced Convection Heat Transfer From a Circular Cylinder in Cross Flow," *Proceedings of the Sixth International Conference on Heat Transfer*, Toronto, ON, Canada, Aug. 7–11.
[9] Dullenkopf, K., and Mayle, R. E., 1995, "An Account of Free-Stream-Turbulence Length Scale on Laminar Heat Transfer," ASME J. Turbomach., **117**, pp. 401–406.
[10] Van Fossen, G. J., Simoneau, R. J., and Ching, C. Y., 1995, "Influence of Turbulence Parameters, Reynolds Number, and Body Shape on Stagnation-Region Heat Transfer," ASME J. Heat Transfer, **117**, pp. 597–603.
[11] Van Fossen, G. J., and Ching, C. Y., 1997, "Measurements of the Influence of Integral Length Scale on Stagnation Heat Transfer," Int. J. Rotating Mach., **3**, pp. 117–132.
[12] Sak, C., Liu, R., Ting, D. S.-K., and Rankin, G. W., 2007, "The Role of Turbulence Length Scale and Turbulence Intensity on Forced Convection From a Heated Horizontal Circular Cylinder," Exp. Therm. Fluid Sci., **31**, pp. 279–289.
[13] Peyrin, F., and Kondjoyan, A., 2002, "Effect of Turbulent Integral Length Scale on Heat Transfer Around a Circular Cylinder Placed Cross to an Air Flow," Exp. Therm. Fluid Sci., **26**, pp. 455–460.
[14] Sutera, S. P., Maeder, P. F., and Kestin, J., 1963, "On the Sensitivity of Heat Transfer in the Stagnation-Point Boundary Layer to Free-Stream Vorticity," J. Fluid Mech., **16**, pp. 497–520.
[15] Sutera, S. P., 1965, "Vorticity Amplification in Stagnation-Point Flow and Its Effect on Heat Transfer," J. Fluid Mech., **21**, pp. 513–534.
[16] Bae, S., Lele, S. K., and Sung, H. J., 2000, "Influence of Inflow Disturbances on Stagnation-Region Heat Transfer," ASME J. Heat Transfer, **122**, pp. 258–265.
[17] Bae, S., Lele, S. K., and Sung, H. J., 2003, "Direct Numerical Simulation of Stagnation Region Flow and Heat Transfer With Free-Stream Turbulence," Phys. Fluids, **15**, pp. 1462–1484.
[18] Zhongmin, X., and Lele, S., 2004, "Distortion of Upstream Disturbances in a Hiemenz Boundary Layer," J. Fluid Mech., **519**, pp. 201–232.

[19] Sadeh, W., Sutera, S., and Maeder, P., 1970, "An Investigation of Vorticity Amplification in Stagnation Flow," ZAMP, **21**, pp. 717–742.
[20] Wei, C., and Miau, J., 1992, "Stretching of Freestream Turbulence in the Stagnation Region," AIAA J., **30**, pp. 2196–2203.
[21] Wei, C., and Miau, J., 1993, "Characteristics of Stretched Vortical Structures in Two-Dimensional Stagnation Flow," AIAA J., **31**, pp. 2075–2082.
[22] Sakakibara, J., Hishida, K., and Maeda, M., 1997, "Vortex Structure and Heat Transfer in the Stagnation Region of an Impinging Plane Jet (Simultaneous Measurements of Velocity and Temperature Fields by Digital Particle Image Velocimetry and Laser-Induced Fluorescence)," Int. J. Heat Mass Transfer, **40**, pp. 3163–3176.
[23] Nix, A. C., Diller, T. E., and Ng, W. F., 2007, "Experimental Measurements and Modeling of the Effects of Large-Scale Freestream Turbulence on Heat Transfer," ASME J. Turbomach., **129**, pp. 542–550.
[24] Baines, W.D. and E.G. Peterson., 1951, "An Investigation of Flow Through Screens," ASME J. Heat Transfer, **73**, pp. 467–480.
[25] Hinze, J. O., 1975, *Turbulence*, McGraw-Hill, New York.
[26] Ewing, J., Gifford, A., Hubble, D., Vlachos, P., Wicks, A., and Diller, T., 2010, "A Direct-Measurement Thin-Film Heat Flux Sensor Array," Meas. Sci. Technol., **21**(10), p. 105201.
[27] Gifford, A., Hoffie, A., Diller, T. E., and Huxtable, S., 2010, "The Convection Calibration of Heat Flux Sensors in Shear and Stagnation Flow," ASME J. Heat Transfer, **132**(3), p. 031601.
[28] Raffel, M., Willert, C., and Kompenhans, J., 1998, *Particle Image Velocimetry*, Spinger-Verlag, Berlin.
[29] Westerweel, J., 1997, "Fundamentals of Digital Particle Image Velocimetry," Meas. Sci. Technol., **8**, pp. 1379–1392.
[30] Eckstein, A. and P. Vlachos, 2009, "Digital Particle Image Velocimetry (DPIV) Robust Phase Correlation," Meas. Sci. Technol., **20**, p. 055401.
[31] Smith, T., Moehlis, J., and Holmes, P., 2005, "Low-Dimensional Modeling of Turbulence Using the Proper Orthogonal Decomposition: A Tutorial," Nonlinear Dyn., **41**, pp. 275–307.
[32] Chong, M. S., Perry, A. E., and Cantwell, B. J., 1990, "A General Classification of Three-Dimensional Flow Fields," Phys. Fluids A, **2**, pp. 765–777.
[33] Samtaney, R., Silver, D., Zabusky, N., and Cao, J., 1994, "Visualizing Features and Tracking Their Evolution," Computer, **27**, pp. 20–27.

Heat Transfer Enhancement of MHD Flow by Conducting Strips on the Insulating Wall

Hulin Huang[1]
e-mail: hlhuang@nuaa.edu.cn

Bo Li

Academy of Frontier Science,
Nanjing University of Aeronautics and Astronautics,
Nanjing 210016, P.R. China

Due to the magnetohydrodynamic (MHD) effect, which degrades heat transfer coefficients by pulsation suppression of the external magnetic field, on the electrically conducting flow, the wall with nonuniform electrical conductivity is employed in a MHD-flow system for heat transfer enhancement. The nonuniform electrical conductivity distribution of the channel wall could create alternate Lorentz forces along the spanwise direction, which can effectively produce flow disturbance, promote mixture, reduce the thickness of the boundary layer, and enhance heat transfer. So, the heat transfer performances enhanced by some conducting strips aligned with the mean flow direction on the insulating wall for free surface MHD flow are simulated numerically in this paper. The flow behaviors, heat transfer coefficients, friction factors, and pressure drops are presented under different Hartmann numbers. Results show that in the range of Hartmann numbers $30 \leq Ha \leq 100$*, the wall with nonuniform conductivity can achieve heat transfer enhancements* (Nu/Nu_0) *of about 1.2–1.6 relative to the insulating wall, with negligible friction augmentation. This research indicates that the modules with three or five conducting strips can obtain better enhancement effect in our research. Particularly, the heat transfer augmentation increases monotonically with increasing Hartmann numbers. Therefore, the enhancement purpose for high Hartmann number MHD flow is marked, which may remedy the depressing heat transfer coefficients by the MHD effect.*
[DOI: 10.1115/1.4002436]

Keywords: heat transfer enhancement, nonuniform electrical conductivity, free surface, magnetohydrodynamic, MHD flow

1 Introduction

The motion of electrically conducting fluid in a strong magnetic field generally induces electric currents, which interact with the magnetic field and generate electromagnetic forces that change the velocity distribution and turbulent pulsation characteristics and exhibit an integral retarding force on the flow. Those effects modify heat transfer performances, friction factor, pressure drop, and the required pumping power of the system in comparison with those of the cases without magnetic field. The external magnetic field suppresses turbulent pulsations even if it is not enough to substantially influence the average velocity profile, which leads in general to a decrease in heat transfer coefficient (Nusselt number, Nu) with an increase in magnetic fields. For many engineering applications, such as the first wall in fusion engineering, the heat transfer performance has to be improved to extract heat energy and reduce the friction loss as much as possible. Then, heat transfer enhancement methods, which maximize heat transfer augmentation with minimal friction penalty, are sought.

Recently, various surface topologies have been used to increase the disturbance in the fluid flow and enhance convective heat transfer in some engineering applications for magnetohydrodynamic (MHD) flow, as in the metallurgical processes, the continuous casting, and the first wall design of fusion blanket [1]. These surface topologies, such as pin-fin array and ribs, have an additional aspect; i.e., any design has to be sensitive to the friction penalty of achieving heat transfer enhancement. Meanwhile, a number of investigations have indicated that the enhancement purpose for high Hartmann number MHD flow is not marked [1,2].

Bühler [3] provided computational results of the instabilities in quasi-two-dimensional MHD flow, in which the walls contained a conducting strip aligned with the mean flow direction. In his study, the main flow exhibited wake character with the vortex street developing in the downstream. However, no attention has been paid to enhance the heat transfer of the MHD flow by the nonuniform electrical conductivity wall at present.

The objective of this paper is to investigate the heat transfer performance enhanced by the wall with nonuniform electrical conductivity for free surface MHD flow. Through the numerical analysis, the flow behaviors, heat transfer coefficients, friction factors, and pressure drops are presented under different Hartmann numbers.

2 Physical and Mathematical Models

Figure 1 shows the domain of the computational model. The configuration consists of a rectangular open channel containing several conducting strips aligned with the mean flow direction in the bottom insulating wall. The geometry scales are from Nygrena et al. [2], where the channel width is $d=0.027$ m, which is selected as a characteristic length. The dimensionless length of the channel is $L=3.7$. The liquid metal ($Re=11{,}650$, $Re_m=14.3$, and $Pr=0.05$) flows through the open channel with a uniform dimensionless thickness $H=0.185$ at the inlet, and the fluid above the liquid metal is taken as air. The applied external magnetic field is the z direction, normal to the bottom wall. The dimensionless width of each conducting strip is $S=0.1$, and the number of conducting strips is m.

The dimensionless variables based on the channel width d and the inlet velocity, U_{in}, are as follows:

[1]Corresponding author.

Contributed by the Heat Transfer Division of ASME for publication in the JOURNAL OF HEAT TRANSFER. Manuscript received March 29, 2009; final manuscript received July 31, 2010; published online November 2, 2010. Assoc. Editor: Patrick H. Oosthuizen.

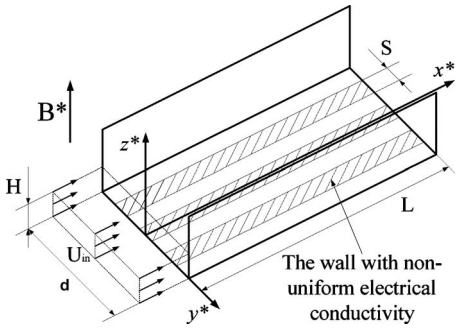

Fig. 1 Schematic of the physical model

$$(x^*,y^*,z^*)=\left(\frac{x}{d},\frac{y}{d},\frac{z}{d}\right),\quad t^*=\frac{tU_{\text{in}}}{d},\quad T^*=\frac{T-T_i}{T_w-T_i}$$

$$\boldsymbol{V}^*=\frac{\boldsymbol{V}}{U_{\text{in}}},\quad p^*=\frac{p}{\rho U_{\text{in}}^2},\quad k^*=\frac{k}{U_{\text{in}}^2},\quad \varepsilon^*=\frac{\varepsilon d}{U_{\text{in}}^2}$$

$$\boldsymbol{B}^*=\frac{\boldsymbol{B}}{B_0},\quad \mathbf{J}^*=\frac{\mathbf{J}}{\sigma_m U_{\text{in}} B_0}$$

$$\mu_t^*=\text{Re}\,C_\mu\frac{k^{*2}}{\varepsilon^*}[1-\exp(-C_3 y^{+*})],\quad y^{+*}=\sqrt{\text{Re}}\sqrt{\frac{\partial V^*}{\partial y^*}}y^*$$

The flow of an electrically conducting fluid under the influence of an external magnetic field is governed by the following dimensionless momentum equation:

$$\frac{\partial \boldsymbol{V}^*}{\partial t^*}+(\boldsymbol{V}^*\cdot\nabla)\boldsymbol{V}^*=-\nabla p^*+\nabla\cdot\left(\left(\frac{1}{\text{Re}}+\mu_t^*\right)\nabla\boldsymbol{V}^*\right)+\frac{1}{\text{Fr}}+\frac{k\boldsymbol{n}\delta(\phi)}{\text{We}}+\frac{\text{Ha}^2}{\text{Re}}(\boldsymbol{J}^*\times\boldsymbol{B}^*) \tag{1}$$

where $\delta(\phi)=|\nabla\phi|$ is the surface delta function and ϕ is the volume fraction. $\boldsymbol{B}^*$ is the magnetic field intensity, including both the applied ($\boldsymbol{B}_0^*$) and the induced magnetic field $\boldsymbol{b}^*$; $\boldsymbol{J}^*$ is the induced current density, which can be obtained by

$$\mathbf{J}^*=\frac{1}{\text{Re}_m}(\nabla\times b^*) \tag{2}$$

The induced magnetic field $\boldsymbol{b}^*$ may be derived from Maxwell's equations and Ohm's law for a uniform external magnetic field:

$$\frac{\partial \boldsymbol{b}^*}{\partial t}+(\boldsymbol{V}\cdot\nabla)\boldsymbol{b}^*=\nabla\cdot\left(\frac{1}{\text{Re}_m}\nabla\boldsymbol{b}^*\right)+(\boldsymbol{B}^*\cdot\nabla)\boldsymbol{V}^* \tag{3}$$

Turbulence properties are calculated by considering the $k-\varepsilon$ turbulence model governed by transport equations. The influences of magnetic fields on turbulence are realized in two ways. First, magnetic fields influence the redistribution of turbulence, and, second, magnetic fields have an effect on the dissipation of turbulence. The transport equations for the turbulent kinetic energy, κ^*, and the dissipation rate of the turbulent kinetic energy, ε^*, have been derived for liquid metal flow, including the additional MHD effects based on the Reynolds' analogy for low magnetic Reynolds number from Smolentsev et al. [4] and Kitamura and Hirata [5],

$$\frac{\partial k^*}{\partial t^*}+(\boldsymbol{V}^*\cdot\nabla)k^*=\nabla\cdot\left(\left(\mu^*+\frac{\mu_t^*}{\sigma_k}\right)\nabla k^*\right)+\mu_t^*\nabla^2\boldsymbol{V}^*+\frac{\varepsilon^*}{\text{Re}}-\frac{1}{\text{Re}}\frac{2k^*}{x_2^{*2}}-C_3\frac{\text{Ha}^2}{\text{Re}}k^* \tag{4}$$

$$\frac{\partial \varepsilon^*}{\partial t^*}+(\boldsymbol{V}^*\cdot\nabla)\varepsilon^*=\nabla\cdot\left(\left(\mu^*+\frac{\mu_t^*}{\sigma_\varepsilon}\right)\nabla\varepsilon^*\right)+C_1\frac{\varepsilon^*}{k^*}\mu_t^*\nabla^2\boldsymbol{V}^*-C_2\rho^*\frac{\varepsilon^{*2}}{k^*}-C_4\frac{\text{Ha}^2}{\text{Re}}\varepsilon^* \tag{5}$$

where C_1, C_2, and C_3 are constants chosen in accordance with Kitamura and Hirata [5], and σ_k and σ_ε are the turbulent Prandtl numbers for κ^* and ε^*, respectively. Here, C_3 and C_4 are adopted in the form of $1.9e^{-2N}$, $1.9e^{-4N}$.

With the introduction of turbulent viscosity for heat transfer and the ignorance of the viscous heating, the energy equation is written as

$$\frac{\partial T^*}{\partial t^*}+(\boldsymbol{V}^*\cdot\nabla)T^*=\frac{1}{\text{Pe}}\nabla\cdot\left[\left(1+\frac{\mu_t}{\sigma_t}\text{Pr}\right)\nabla T^*\right] \tag{6}$$

where $\sigma_t=0.7\times(1+\exp\{37\times(z^*/H-0.89)\})$ is the turbulent Prandtl number, which stands for the ratio between the eddy diffusivity for momentum and the eddy diffusivity for heat and the value obtained from Smolentsev et al. [4].

3 Boundary Conditions

A uniform velocity profile is employed at the inlet. An inlet turbulence intensity level of 1% is used, and the hydraulic diameter at the inlet is taken as equal to the width of the channel. According to experimental data on heat transfer in liquid metal MHD flow revealed in Nygrena et al. [2], constant temperature boundary conditions are employed at the bottom wall at $T_w^*=1$ and the temperature of liquid metal is $T_i^*=0$ at the channel inlet. Sidewalls are adiabatic; thus, no heat boundary conditions are given to them. The streamwise gradients of all variables such as velocity and temperature are set to zero at the outlet boundary to attain fully developed conditions.

4 Computational Method

The grid is made up of hexahedral elements aligned with the flow direction to reduce the numerical diffusion errors and thus to improve the quality of the numerical predictions. Meshes of these regions near the wall and the interface are fined to resolve the typical high gradients. In the near-wall regions, enhanced wall treatment, which combines a two-layer model with enhanced wall functions, is applied. The enhanced wall functions smoothly blend the law of an enhanced turbulent wall law with that of laminar wall law. So, near-wall meshes are fully resolved for y^{+*} values less than 1 to resolve the laminar sublayer. In order to check the grid convergence, simulations with six sets of different meshes are performed, and the concept of grid convergence index (GCI) [6] is introduced. The average Nusselt number Nu_{av} [7], mean friction factor f_m, and pressure drop ΔP are defined as monitors for each mesh. The grid convergence indices $\text{GCI}(\text{Nu}_{\text{av}})=|1-\text{Nu}_{\text{av}}(Mi)/\text{Nu}_{\text{av}}(M6)|$, $\text{GCI}(f_m)=|1-f_m(Mi)/f_m(M6)|$, and $\text{GCI}(\Delta P)=|1-\Delta P(Mi)/\Delta P(M6)|$ are calculated. Shown in Table 1, the values of $\text{GCI}(\text{Nu}_{\text{av}})$, $\text{GCI}(f_m)$, and $\text{GCI}(\Delta P)$ of M5 are all less than 2.7×10^{-3}, which indicates that grid M5 has good convergence. In order to save CPU time and keep a reasonable accuracy in our computations, all simulations are performed with the M5 mesh.

The Reynolds averaged Navier–Stokes equations are solved numerically in conjunction with the turbulent transport equations and MHD equations. The discretization of the combined convective and diffusive fluxes across the control volumes is modeled by using the QUICK scheme. The pressure-velocity coupling is handled with the PISO scheme. The calculations are carried out in a nonuniform staggered grid system. The calculation domain involves free surfaces; thus, the volume of fluid (VOF) method is adopted to capture its evolution.

Table 1 Grid convergence index values under different meshes

Mesh	M1	M2	M3	M4	M5	M6
Number of nodes	0.8×10^5	1×10^5	1.2×10^5	1.4×10^5	2.2×10^5	4.2×10^5
GCI(f_m)	2.1×10^{-2}	1.1×10^{-2}	6.9×10^{-3}	3.4×10^{-3}	2.7×10^{-3}	0
GCI(ΔP)	5.6×10^{-2}	2.3×10^{-2}	8.9×10^{-3}	5.6×10^{-3}	1.3×10^{-3}	0
Nu_{av}	11.41	10.83	10.40	10.21	10.16	10.15
GCI(Nu_{av})	0.12	6.7×10^{-2}	2.4×10^{-2}	5.9×10^{-3}	9.8×10^{-4}	0

5 Model Validation

For the validation of this model, a calculation is conducted to compare with the numerical study of heat transfer in a free surface MHD flow by Smolentsev et al. [4]. Figure 2 summarizes the comparisons. The distributions of the turbulence kinetic energy show excellent agreement with the results of Smolentsev et al. The maximum deviation detected is within a tolerable band of 10%.

6 Results and Discussion

In order to investigate the heat transfer performance enhanced by the wall with nonuniform electrical conductivity for free surface MHD flow, the flow behaviors, heat transfer coefficients, friction factors, and pressure drops have been performed numerically. The effect of magnetic fields normal to the bottom wall, corresponding with the Hartmann number varying from 30 to 100, is investigated. Baseline Nusselt numbers Nu_0 and friction factors f_0 are measured with a uniform insulating wall replacing the nonuniform electrical conductivity wall at the same Hartmann numbers. These baseline values are used to normalize the uniform insulating wall values and are thus used as a basis of comparison with nonuniform electrical conductivity wall values.

The interaction of the moving fluid with the magnetic field induces an electric field $\boldsymbol{V}^*\times\boldsymbol{B}^*$, which drives the electric current $\boldsymbol{J}^*$. The electric conductivity distribution of the channel walls influences the distribution of current in the fluid and determines the flow pattern. For a uniform insulating channel, the electric current distribution in the plane at $x^*=2.6$ can be seen in Fig. 3(*a*). Since no current can enter the wall, the induced currents in the bulk flow are blocked to go through the viscous boundary layers near the wall. However, as shown in Fig. 3(*b*), several current circuits are formed in the transverse section under the influence of the wall with electrical conductivity strips. In the conducting strip regions, almost all currents enter the conductivity strips. In contrast, in the insulating wall regions, no currents can enter the wall, and they cross through the viscous boundary layers near the wall. So, the current direction in the vicinity of the conducting strip is opposite to that in the vicinity of the insulating wall, as shown in Fig. 3(*b*).

The components of current, which are perpendicular to the magnetic field lines, generate a Lorentz force F_x under the normal magnetic fields. Figure 4 presents the Lorentz force F_x distribution in the $x^*=2.6$ plane for Ha=30. The negative sign in the figure indicates that the direction of the Lorentz force is opposite to the flow direction. It is obvious that the direction of the Lorentz force is inhomogeneous in different regions at the boundary layer, which is opposite to the main flow direction in the vicinity of the conducting strips but along the direction of the main flow near the insulating walls. This alternative distribution along the spanwise direction of the Lorentz force may break the boundary layer,

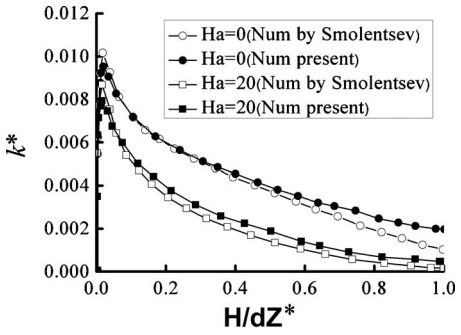

Fig. 2 Comparison between numerical and Smolentsev's results

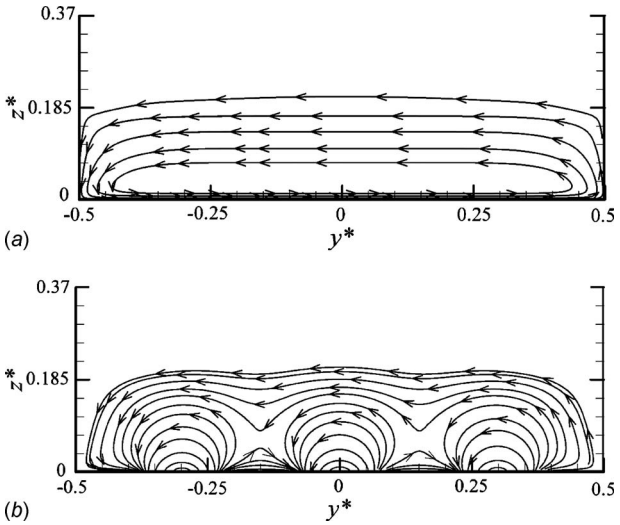

Fig. 3 Electric current paths in $x^*=2.6$ plane (Ha=30): (*a*) insulating wall and (*b*) nonuniform electrical conductivity wall

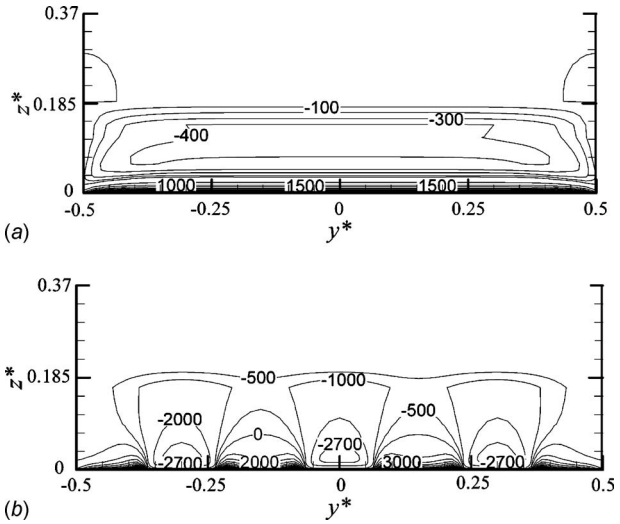

Fig. 4 Lorentz force F_x distribution in $x^*=2.6$ plane (Ha=30): (*a*) insulating wall and (*b*) nonuniform electrical conductivity wall

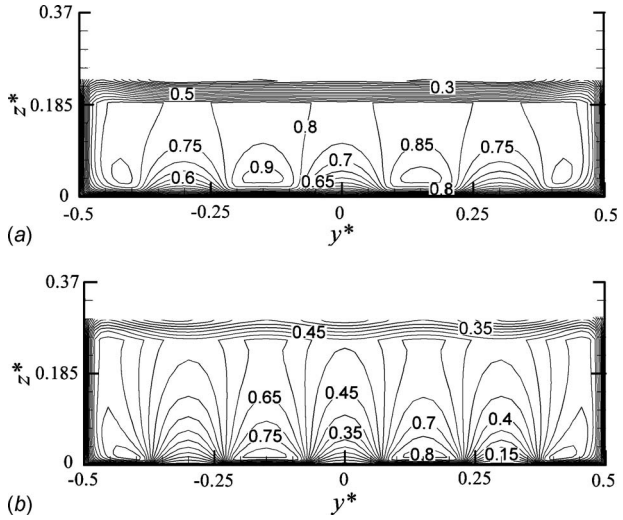

Fig. 5 Velocity distribution in $x^*=2.6$ plane: (*a*) Ha=30 and (*b*) Ha=70

which produces intermittent perturbation on the flow near the wall, promotes the mixing of the fluid, and enhances the heat transfer.

Figure 5 depicts the velocity distribution in the $x^*=2.6$ plane under different Hartmann numbers. The velocity distribution becomes inhomogeneous under the effect of the wall with nonuniform electrical conductivity. Obvious differences in velocity distribution appear with the increase in Hartmann numbers.

The perturbation by the nonuniform electrical conductivity wall may remedy the depressing turbulent pulsations by the MHD effect. The turbulent viscosity distribution in the $x^*=2.6$ plane is depicted in Fig. 6 for different Hartmann numbers. Under the effect of the nonuniform electrical conductivity wall, the turbulent viscosity exhibits a higher magnitude compared with that of an insulating wall and displays an inhomogeneous distribution along the spanwise direction. The difference in turbulent viscosity becomes more prominent with the increase in Hartmann numbers due to the greater perturbation by the nonuniform Lorentz force. Therefore, the turbulent pulsations become more furious, and the ability of convective heat transfer is greatly improved.

The employment of the wall with nonuniform electrical conductivity can efficiently enhance heat transfer for free surface

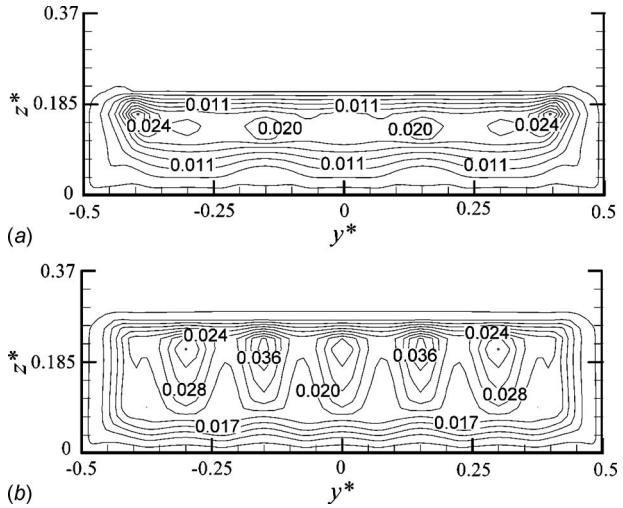

Fig. 6 Turbulent viscosity distribution in the $x^*=2.6$ plane: (*a*) Ha=30 and (*b*) Ha=70

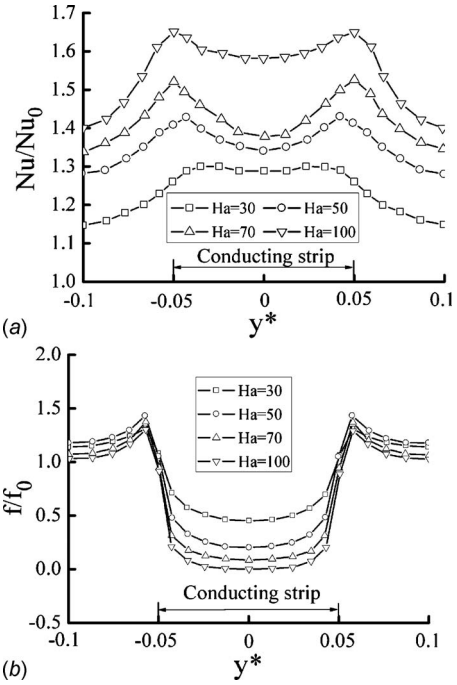

Fig. 7 Distribution of local Nu/Nu_0 and local f/f_0 (at $x^*=2.6$ plane): (*a*) local Nu/Nu_0 at different positions and (*b*) local f/f_0 at different positions

MHD flow. Figure 7(*a*) gives local Nusselt numbers at the $x^*=2.6$ plane. The Nu/Nu_0 magnitudes for all Hartmann numbers range from 1.16 to 1.65, and the enhancement effect is very obvious on the borders between the insulating walls and the conducting strips. From the results, it is evident that local Nu/Nu_0 values increase as the Hartmann number Ha increases in most regions because the nonuniform Lorentz force obviously modifies the velocity distribution near the bottom wall and increases turbulent pulsations with the increase in magnetic fields. Figure 7(*b*) shows the friction factor distribution in the $x^*=2.6$ plane for different Hartmann numbers. It is seen that the friction factor markedly decreases as the Hartmann number Ha increases in the regions of conducting strips. This is because the Lorentz force damps the motion of the flow near the conducting strips, and the velocity gradient is sharply decreased in these regions.

Figure 8 illustrates the variations in the mean Nusselt number, mean friction factor, and pressure drop with different Hartmann numbers. In the range of Hartmann numbers $30 \le Ha \le 100$, the wall with nonuniform conductivity can achieve heat transfer en-

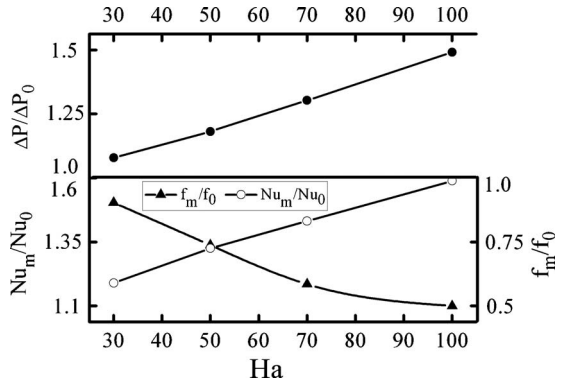

Fig. 8 Distribution of the mean Nusselt number, mean friction factor, and pressure drop

Table 2 Details of the models of nonuniform wall

Model	Number of conducting strips	Width of conducting strip S	Gap between conducting strips
1	m=1	0.1	–
2	m=3	0.1	0.17
3	m=5	0.1	0.075
4	m=7	0.1	0.028

hancements (Nu/Nu_0) of about 1.2–1.6, while the friction factors are only 0.50–0.84 relative to the insulating wall. The pressure drop increases by about 1.1–1.5 relative to the insulating wall due to the increasing second flow and turbulent pulsations. In addition, heat transfer augmentation (Nu/Nu_0) is found to increase monotonically with the increase in Hartmann numbers. This figure demonstrates that the enhancement purpose for MHD-free surface flow by the way at high Hartmann number is marked.

In order to investigate the heat transfer performance with different numbers of the conducting strips, four different models have been discussed in this paper. Table 2 shows the details of these models.

Figure 9 illustrates the variations in the mean Nusselt number, mean friction factor, and pressure drop with the number of the conducting strips. It is found that the Nu/Nu_0 is influenced by the number of conducting strips, which increases first and then decreases with the increasing number of conducting strips. The friction factor ratios f/f_0 decrease with the increasing number of the conducting strips, and the pressure drop appreciably increases as the number of conducting strips increases. These curves demonstrate that the number of conducting strips has great influence on heat transfer, and the models with three or five conducting strips can achieve better enhancement effect in our research.

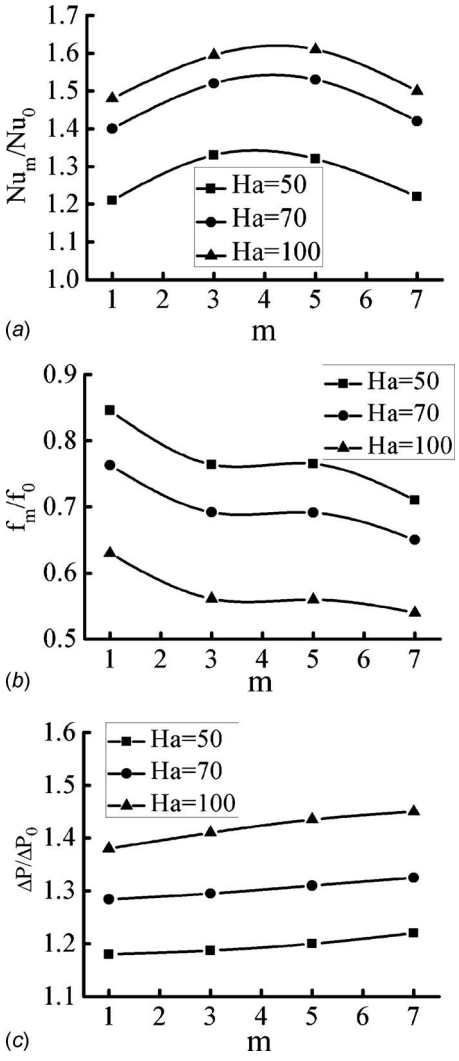

Fig. 9 Distribution of the mean Nusselt number, mean friction factor, and pressure drop: (*a*) mean Nusselt number, (*b*) mean friction factor, and (*c*) pressure drop

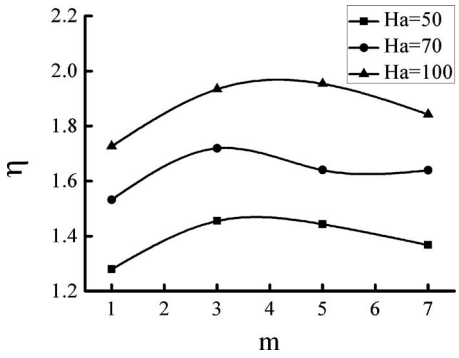

Fig. 10 Global thermal performance for different models

The performance analysis is important for the evaluation of the net energy gain to determine whether the method employed to enhance the heat transfer is effective from the viewpoint of energy. Here, the global thermal performance $\eta = (Nu/Nu_0)/(f/f_0)^{1/3}$ [8] is used as the overall enhancement ratio. The results for the several cases simulated in this paper are presented in Fig. 10. It is found that the thermal performance value increases with the number of conducting strips increasing up to about $m=3$ and starts to decrease when $m>5$. These curves indicate that there is an optimum strip number for heat transfer enhancement, and the maximum thermal performance values range from 1.45 to 1.95 under different Ha. In addition, the influence of magnetic fields on the thermal performance is marked, and η values increase with Hartmann number increasing. Thus, the enhancement heat transfer effect for the free surface MHD flow at high Hartmann numbers is very prominent.

7 Conclusions

The wall with nonuniform electrical conductivity employed in the free surface MHD-flow system to improve the heat transfer performance is performed numerically here. The conclusions are as follows:

(1) The employment of the wall with nonuniform electrical conductivity can efficiently enhance heat transfer for a free surface MHD flow and remedy the degrading heat transfer by the MHD effect.
(2) In the range of Hartmann numbers $30 \le Ha \le 100$, the wall with nonuniform conductivity can achieve heat transfer enhancements (Nu/Nu_0) of about 1.2–1.6, while the friction loss and pressure drop are about 0.50–0.84 and 1.1–1.5 times relative to the insulating wall, respectively.
(3) Heat transfer augmentation (Nu/Nu_0) increases as the Hartmann number Ha increases. Therefore, the enhancement purpose at a high Hartmann number MHD flow is marked.
(4) The number of conducting strips has great influence on heat transfer. The models with three or five conducting strips can achieve better enhancement effect in this paper.

Acknowledgment

This work was supported by National Nature Science Foundation of China under Grant Nos. 50306006 and 50710105050.

Nomenclature

$\boldsymbol{B}$ = magnetic field vector, T
$\boldsymbol{B}_0$ = application field vector, T
$\boldsymbol{b}$ = induced-magnetic-field vector, T
C_p = thermal capacity, W kg^{-1} K^{-1}
d = width of the channel, m
Fr = $Fr = U_{in}^2/gd$, Froude number
h = heat transfer coefficient, W m^{-2} K^{-1}
Ha = $Ha = B_0 d\sqrt{\sigma/\mu}$, Hartmann number
$\boldsymbol{J}$ = current density (vector), A m^{-2}
N = $N = Ha^2/Re$, interaction parameter
Nu = $Nu = hd/k$, Nusselt number
$\boldsymbol{n}$ = $\boldsymbol{n} = \nabla\phi/|\nabla\phi|$, free surface normal vector
p = pressure (N m^{-2})
Pe = $Pe = \rho C_p U_{in} d/\lambda$, Peclet number
Pr = Prandtl number
Re = $Re = \rho U_{in} d/\mu$, Reynolds number
Re_m = $Re_m = \sigma_m \mu_m U_{in} d$, magnetic Reynolds number
T = temperature, K
t = time, s
U_{in} = the velocity of inlet, m s^{-1}
We = $We = \rho U_{in}^2 d/\sigma$, Weber number
x, y, z = Cartesian coordinate, m

Greek

κ = turbulent kinetic energy, m^2 s^{-2}
λ = thermal conductivity, W m^{-1} K^{-1}
ε = dissipation rate of the turbulent kinetic energy
σ_m = electrical conductivity, Ω^{-1} m^{-1}
σ = surface tension, N m^{-1}
σ_t = turbulent Prandtl number
ϕ = volume fraction
μ = dynamic viscosity of liquid, kg m^{-1} s^{-1}
μ_m = magnetic conductivity
μ_t = the turbulent viscosity
ρ = density of liquid metal, kg m^{-3}
v = velocity vector, m s^{-1}
Δt = time step, s
$\mathfrak{y}$ = $\mathfrak{y} = (Nu/Nu_0)/(f/f_0)^{1/3}$, the global thermal performance

Subscripts

e = effective
m = magnetic field

References

[1] Kirillova, I. R., Reed, C. B., Barleon, L., and Miyazaki, K., 1995, "Present Understanding of MHD and Heat Transfer Phenomena for Liquid Metal Blankets," Fusion Eng. Des., **27**, pp. 553–569.
[2] Nygren, R. E., Cowgill, D. F., Ulrickson, M. A., Nelson, B. E., Fogarty, P. J., Rognlien, T. D., Rensink, M. E., Hassanein, A., Smolentsev, S. S., and Kotschenreuther, M., 2004, "Design Integration of Liquid Surface Divertors," Fusion Eng. Des., **72**, pp. 223–244.
[3] Bühler, L., 1996, "Instabilities in Quasi-Two-Dimensional Magnetohydrodynamic Flows," J. Fluid Mech., **326**, pp. 125–150.
[4] Smolentsev, S., Abdou, M., and Morley, N., 2002, "Application of the 'k-ε' Model for Open Channel Flow in a Magnetic Field," Int. J. Eng. Sci., **40**, pp. 693–711.
[5] Kitamura, K., and Hirata, M., 1978, "Turbulent Heat and Momentum Transfer for Electrically Conducting Fluid Flowing in Two-Dimensional Channel Under Transverse Magnetic Field," *Sixth International Heat Transfer Conference*, Vol. 3, Hemisphere, Toronto, pp. 159–164.
[6] Roache, P. J., 1997, "Quantification of Uncertainty in Computational Fluid Dynamics," Annu. Rev. Fluid Mech., **29**, pp. 123–160.
[7] Dousset, V., and Pothérat, V., 2008, "Numerical Simulations of a Cylinder Wake Under a Strong Axial Magnetic Field," Phys. Fluids, **20**, p. 017104.
[8] Gee, D. L., and Webb, R. L., 1980, "Forced Convection Heat Transfer in Helically Rib-Roughened Tubes," Int. J. Heat Mass Transfer, **23**, pp. 1127–1136.

Modeling of Heat Transfer in Microchannel Gas Flow

Tomasz Lewandowski
e-mail: tomasz.lewandowski@imp.gda.pl

Tomasz Ochrymiuk
e-mail: tomasz.ochrymiuk@imp.gda.pl

Institute of Fluid Flow Machinery,
Polish Academy of Sciences,
Fiszera 14,
80-952 Gdansk, Poland

Justyna Czerwinska
Artorg Center,
University of Bern,
Stauffacherstrasse 78,
CH-3014 Bern, Switzerland
e-mail: justyna.czerwinska@artorg.unibe.ch

Due to the existence of a velocity slip and temperature jump on the solid walls, the heat transfer in microchannels significantly differs from the one in the macroscale. In our research, we have focused on the pressure driven gas flows in a simple finite microchannel geometry, with an entrance and an outlet, for low Reynolds ($Re<200$) and low Knudsen ($Kn<0.01$) numbers. For such a regime, the slip induced phenomena are strongly connected with the viscous effects. As a result, heat transfer is also significantly altered. For the optimization of flow conditions, we have investigated various temperature gradient configurations, additionally changing Reynolds and Knudsen numbers. The entrance effects, slip flow, and temperature jump lead to complex relations between flow behavior and heat transfer. We have shown that slip effects are generally insignificant for flow behavior. However, two configuration setups (hot wall cold gas and cold wall hot gas) are affected by slip in distinguishably different ways. For the first one, which concerns turbomachinery, the mass flow rate can increase by about 1% in relation to the no-slip case, depending on the wall-gas temperature difference. Heat transfer is more significantly altered. The Nusselt number between slip and no-slip cases at the outlet of the microchannel is increased by about 10%. [DOI: 10.1115/1.4002438]

Keywords: microchannel gas flow, heat transfer, slip regime, turbomachinery

1 Introduction

The motivation behind this work was to find a more efficient cooling system for the first stages of gas turbine blades. In such configurations, the coolant is supplied by the set of small holes. The film cooling process has been widely adopted on the walls of a high temperature system, such as gas turbine blades and nozzles, and the walls of a combustion chamber to protect the surfaces from being overheated. Aircraft engine turbine airfoils are small and therefore require small flow passages and film holes. As an example, an average aircraft engine needs film hole diameters as small as 0.4 mm, while an average industrial power turbine can be limited to a minimum diameter of 1 mm [1]. The concept of microchannel cooling for gas turbine blades is the natural application of thermodynamics and heat transfer to accomplish two goals: first, to spread out the cooling network in a series of smaller and highly distributed channels to provide much better uniformity of cooling and thermal gradients; second, to bring the cooling fluid closer to the blade surface and create more efficient heat transfer. In the past, the film jet used in the film cooling process was so thick that the amount of cooling air used was so large that it could effectively reduce the performance of a gas turbine engine [2]. In addition, the relatively thick film jet is expected to rapidly mix with the hot gas in the freestream and to reduce its protection effectiveness [3]. Examples of the microchannel cooling technique of the overall cooling effectiveness and the film cooling are shown in Refs. [4,5]. The challenges of these applications include hole plugging, wall strength, film cooling, manufacturing, and costs. Up to now, no commercial use of such microchannel cooling solutions was utilized. Therefore, this is the motivation behind our computational investigation. In our simulations, temperature values are much smaller than the actual gas turbine blade temperature. It is related to the fact that for the experimental setup of the gas turbine section [6–9], the temperature values are limited by electrically operating heating foils. Hence, experiments are also performed for a much lower temperature range than the one in the real gas turbine engine. The principle of the measurement technique used in the blade cooling test sections is based on the heat flux that is generated at the surface as a result of measured wall temperature distribution and temperature of the main flow. The results are nevertheless comparable with the phenomenology in a real gas turbine by means of the heat transfer coefficient [10].

In this paper, we have focused on the influence of the hole's reduction in diameter and its connection to the heat transfer properties. The size of the hole is interlinked with the limit of the continuum flow regime. The current study is performed exactly on the border of the no-slip and slip regimes. We have shown that despite a very insignificant slip velocity value, the influence on the flow thermal behavior is pronounced.

Due to the small length scales for our simulations, the respective Knudsen numbers are comparably high and are often within the slip flow regime (between $Kn \approx 0.1$ and $Kn \approx 0.001$). Navier–Stokes equations are still applicable in this region, though it is necessary to incorporate changed boundary conditions for the fluid-solid interface. Maxwell and Smoluchowski proposed such boundary conditions derived from the kinetic theory of gases. These conditions allow evaluating values of the temperature jump T_s and slip velocity u_s on solid walls. We have implemented them into the finite volume fluid solver FLUENT® [11] by means of user defined functions. This formulation allows us to simulate complex systems within the slip flow regime. For larger Knudsen numbers (transition or free-molecular flows) only molecular based approaches disserting the Boltzmann equation can be used.

In this paper, we have studied two thermal configurations: *hot gas cold wall* and *cold gas hot wall*. It is shown that despite very similar flow patterns, the slip regime influences the temperature field in a very distinct manner. The configuration setup is shown in Fig. 1. To study entrance and outlet effects, the microchannel was embedded in a larger geometrical configuration. A similar configuration without heating was also studied by Refs. [12,13]. In the literature, most of the heat transfer aspects up to now were focused on an ideal microchannel without a finite length studied numerically [14–21] or theoretically [22,23] with wall roughness [24] and with a heated wall [25,26]. Such models are too approximate for industrial applications, where both the channel entrance and channel length have important roles.

Contributed by the Heat Transfer Division of ASME for publication in the JOURNAL OF HEAT TRANSFER. Manuscript received September 29, 2009; final manuscript received July 30, 2010; published online November 2, 2010. Assoc. Editor: Satish G. Kandlikar.

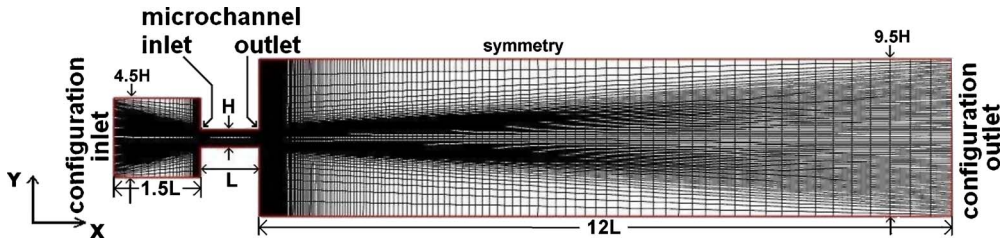

Fig. 1 Flow configuration geometry (L=1000 μm, H=300 μm). The pressure difference was applied between configuration inlet and outlet to drive the flow through the microchannel.

The physical model of the phenomena was described by conservation equations for mass, momentum, and energy,

$$\frac{\partial}{\partial t}\begin{bmatrix}\rho\\ \rho \mathrm{u}_i\\ e\end{bmatrix}+\frac{\partial}{\partial x_j}\begin{bmatrix}\rho \mathrm{u}_j\\ \rho \mathrm{u}_i \mathrm{u}_j + p\delta_{ji} - \sigma_{ji}\\ e\mathrm{u}_j + (p\delta_{ij} - \sigma_{ji})\mathrm{u}_i + q_i\end{bmatrix}=0 \tag{1}$$

where ρ and p are the gas density and pressure, respectively. The ideal gas assumption is used to determine pressure in terms of local density and temperature, i.e., $p=\rho R\mathrm{T}$, where R is the specific gas constant, and temperature is determined from the equation $e=\rho(C_V\mathrm{T}+\mathrm{u}_i\mathrm{u}_i/2)$.

The conservation equations (Eq. (1)) are valid for the continuum, slip flow regime and even for higher Knudsen numbers. However, the viscous stresses σ_{ij} and the heat flux q_i have to be determined separately for different flow regimes. For the first-order model, they have the familiar forms used in the Navier–Stokes equations,

$$\sigma_{ij}^{N-S}=\mu\left(\frac{\partial \mathrm{u}_j}{\partial x_i}+\frac{\partial \mathrm{u}_i}{\partial x_j}\right)-\frac{2}{3}\mu\frac{\partial \mathrm{u}_m}{\partial x_m}\delta_{ij} \tag{2}$$

where μ is the dynamic viscosity and δ_{ij} is the Kronecker delta. The heat flux is determined from the Fourier law $q_i=-\kappa(\partial\mathrm{T}/\partial x_i)$, where κ is the thermal conductivity. In the slip regime, boundary conditions for velocity and the temperature of the gas on the solid wall need to be altered. We have used the Maxwell–Smoluchowski [27,28] relation in the following form:

$$\mathrm{u}_\mathrm{s}=\mathrm{u}_\mathrm{g}-\mathrm{u}_\mathrm{w}=\frac{2-\sigma_\mathrm{v}}{\sigma_\mathrm{v}}\lambda\frac{\partial \mathrm{u}}{\partial y}+\frac{3}{4}\frac{\mu}{\rho\mathrm{T}}\frac{\partial \mathrm{T}}{\partial x} \tag{3}$$

$$\mathrm{T}_\mathrm{s}=\mathrm{T}_\mathrm{g}-\mathrm{T}_\mathrm{w}=\frac{2-\sigma_\mathrm{T}}{\sigma_\mathrm{T}}\frac{2\gamma}{\gamma+1}\frac{\lambda}{\mathrm{Pr}}\frac{\partial \mathrm{T}}{\partial y} \tag{4}$$

We have considered a very low Knudsen number and flat surfaces. Therefore, second order approximation was not necessary [29–31]. As can be seen in the Appendix, the continuum channel flow with the slip model, for such a regime, fits very well with the direct simulation Monte Carlo (DSMC) results. The extensive validation of implemented routines is available in Ref. [32]. Here, only several computational aspects are mentioned in the Appendix.

2 Simulation Results

To obtain an extensive parametric study, two-dimensional geometry and steady state flow simulations were performed. A three-dimensional study would be much more computationally expensive and in the case of the chosen geometry, which is axially symmetric, would not add much information. The following simulations gave information regarding the flow behavior and heat transfer in the microchannel. The grid used for these studies had 27200 nodes (for a detailed explanation, see the Appendix). The simulations were performed for an ideal gas (air). The geometry was fixed, following previous studies, which has shown a very small influence of the inlet shape on global parameters such as mass flow rate [33].

Simulations were performed for three Reynolds numbers corresponding to the well developed laminar flow, the border of the Stokes flow regime, and the Stokes flow regime for the following cases:

- no heating—the temperature of the gas was equal to the temperature of the wall,

$$\mathrm{T_{in}}=\mathrm{T_w}=300\ \mathrm{K}$$

- hot gas cold wall—$\Delta\mathrm{T}=\mathrm{T_{in}}-\mathrm{T_w}>0$ for differences,

$$\Delta\mathrm{T}=25\ \mathrm{K},50\ \mathrm{K},100\ \mathrm{K},150\ \mathrm{K}$$

- cold gas hot wall—$\Delta\mathrm{T}=\mathrm{T_{in}}-\mathrm{T_w}<0$ for differences,

$$\Delta\mathrm{T}=-25\ \mathrm{K},-50\ \mathrm{K},-100\ \mathrm{K},-150\ \mathrm{K}$$

The temperature was only applied on the microchannel walls. All studies were done twice: with slip and without slip boundary condition. This has allowed an estimation of the influence of the slip on flow behavior. Most of the cases were calculated for Kn=0.008. However, for the comparison of mass flow rate values, some additional simulations for Kn=0.004 and Kn=0.011 were performed. The detailed information such as inlet and outlet pressures, obtained average density, velocity, and Reynolds number are presented in Tables 1–3.

3 Microchannel Flow: Reynolds Number and Temperature Configuration Dependencies

This section focuses on velocity slip effects on the flow profile. Microchannel flow parameters were controlled by the inlet and outlet pressure differences. In Fig. 2, it can be seen that the general characteristics of the pressure field remain unchanged regardless of the specific values. Figure 2 shows pressure contours for the case of a zero temperature difference between the wall and gas ($\Delta\mathrm{T}=0$) for two Reynolds numbers, Re=0.55 and Re=120. Though it is not shown here, it was found that the pressure contours change very slightly with the temperature difference. Additionally, in Fig. 2(*c*), the pressure distribution is plotted for Re=25 for two extreme temperature difference cases $\Delta\mathrm{T}=-150$ K and $\Delta\mathrm{T}=150$ K. The values are taken at the wall, at one-fourth of the channel width, and in the middle of the channel. Changes across the channel are noticeable only at its entrance. Further along the channel, the pressure remains unaltered. The difference in applied temperature results in the variation in the pressure distribution in the microchannel. Continuum and noncontinuum behaviors remain very similar (the curves cover each other). The pressure distribution behaves that way since in the considered scale, Knudsen induced effects are relatively small, and flow largely behaves as a continuum. Within the slip regime, phenomena induced by a velocity slip are small and localized in the vicinity of the walls. Therefore, velocity slip induced effects on pressure distribution could be neglected.

Figure 3 shows velocity profiles for three different Knudsen numbers. The logarithmic scale is used to underline the fact that the wall slip velocity is relatively small in comparison to the mean flow. As expected, for a larger Knudsen number, the velocity slip

Table 1 Simulation parameters for various flow configurations

Test case	A0	AI1	AI2	AI3	AI4	AII1	AII2	AII3	AII4
T_{in} (K)	300	325	350	400	450	300	300	300	300
T_w (K)	300	300	300	300	300	325	350	400	450
Re	0.56	0.56	0.55	0.55	0.55	0.46	0.38	0.27	0.21
Ma	0.031	0.031	0.031	0.031	0.031	0.031	0.031	0.031	0.031
Kn	0.008	0.008	0.008	0.008	0.008	0.008	0.008	0.008	0.008
$p_{c,in}$ (Pa)	3000	3000	3000	3000	3000	3000	3000	3000	3000
$p_{c,out}$ (Pa)	2998	2998	2998	2998	2998	2998	2998	2998	2998
ρ_{avg} (kg/m^3)	0.035	0.035	0.035	0.035	0.035	0.032	0.030	0.026	0.023
	B0	BI1	BI2	BI3	BI4	BII1	BII2	BII3	BII4
T_{in} (K)	300	325	350	400	450	300	300	300	300
T_w (K)	300	300	300	300	300	325	350	400	450
Re	24.24	23.67	23.40	22.95	22.56	21.14	18.48	14.23	11.07
Ma	0.221	0.221	0.221	0.221	0.221	0.221	0.221	0.221	0.221
Kn	0.008	0.008	0.008	0.008	0.008	0.008	0.008	0.008	0.008
$p_{c,in}$ (Pa)	3000	3000	3000	3000	3000	3000	3000	3000	3000
$p_{c,out}$ (Pa)	2900	2900	2900	2900	2900	2900	2900	2900	2900
ρ_{avg} (kg/m^3)	0.034	0.034	0.033	0.032	0.031	0.320	0.030	0.027	0.024
	C0	CI1	CI2	CI3	CI4	CII1	CII2	CII3	CII4
T_{in} (K)	300	325	350	400	450	300	300	300	300
T_w (K)	300	300	300	300	300	325	350	400	450
Re	119.15	112.05	105.73	94.92	86.05	112.21	105.89	94.79	85.35
Ma	0.886	0.886	0.886	0.886	0.886	0.886	0.886	0.886	0.886
Kn	0.008	0.008	0.008	0.008	0.008	0.008	0.008	0.008	0.008
$p_{c,in}$ (Pa)	3000	3000	3000	3000	3000	3000	3000	3000	3000
$p_{c,out}$ (Pa)	1800	1800	1800	1800	1800	1800	1800	1800	1800
ρ_{avg} (kg/m^3)	0.026	0.024	0.023	0.022	0.020	0.025	0.024	0.023	0.022
	D0	DI4	DII4		E0	EI4	EII4		
T_{in} (K)	300	450	300		300	450	300		
T_w (K)	300	300	450		300	300	450		
Re	23.93	22.56	10.82		25.03	22.67	11.65		
Ma	0.108	0.108	0.108		0.347	0.347	0.347		
Kn	0.004	0.004	0.004		0.011	0.011	0.011		
$p_{c,in}$ (Pa)	6000	6000	6000		2000	2000	2000		
$p_{c,out}$ (Pa)	5951	5951	5951		1840	1840	1840		
ρ_{avg} (kg/m^3)	0.069	0.064	0.048		0.022	0.020	0.015		

increases. The second part of the same figure shows a velocity slip along the wall for three Reynolds numbers. The normalization of velocity is performed by the division of the values by their average slip velocity given in Table 3. The changes in velocity at the wall are most significant near the entrance of the microchannel. The velocity slip varies slightly further along the channel for a large Reynolds number. As expected, the velocity slip value is the largest for the high Reynolds number at the entrance,

$$u(x,y) = F\left(\frac{dp}{dx},\mu,\lambda,H\right)\left[-\left(\frac{y}{H}\right)^2+\left(\frac{y}{H}\right)+\left(\frac{2-\sigma_v}{\sigma_v}\right)\frac{Kn}{1-bKn}\right] \quad (5)$$

Equation (5), proposed in Ref. [34], represents a semi-empirical relation for the velocity profile as a function of a Knudsen number for an infinite channel ($b=-1$). According to Eq. (5), for the Knudsen number chosen in this paper, the values of the velocity are altered by about 3–6%. Similarly, as for the simple theory, the velocity for the microchannel inlet obtained from simulations changes insignificantly by about 3%. Only in the vicinity of the inlet and the outlet, velocity obtained from simulations is more sensitive to changes along the channel, which also include the raise in the value of the slip velocity.

The velocity slip effects in infinite microchannels are well investigated, as indicated, for example, in Refs. [34,16,11], and the result is in agreement with previous research. However, studies of the interaction between the velocity slip and temperature jump boundary conditions are much more limited. Figure 4 shows the influence of the temperature difference on the inlet and outlet velocity profiles across the channel. The microchannel inlet velocity depends largely on the Reynolds number. The temperature difference does not cause pronounced changes in the velocity field. The outlet velocity profiles for all the cases are almost identical.

The x-velocity field is mostly dominated by the difference in the pressure. The y-velocity is an interaction between the channel geometry, the slip effects, and the difference in the pressure. Hence, the changes manifest themselves very clearly for low Reynolds numbers, for which slip effects are less overshadowed by the main flow. That characteristic can be noted in Fig. 5.

Global characteristics of the microchannel flow field are significantly altered by the variations in the Reynolds number. Slip effects are restricted only to the vicinity of the walls and are reduced for larger Reynolds numbers. Temperature does not influence velocity flow in a visible manner. Hence, from the simulations, it can be concluded that the velocity field structure is almost insensitive to the induced temperature difference. For very low Reynolds numbers (Stokes flow regime $Re \ll 1$), this is not the case [35]. In this paper, however, we consider significantly larger Reynolds

Table 2 Resulting average velocities and temperatures for various flow configurations

Test case	A0	AI1	AI2	AI3	AI4	AII1	AII2	AII3	AII4
u_{max} (m/s)	0.983	0.982	0.981	0.978	0.976	0.927	0.879	0.800	0.740
$u_{in,avg}$ (m/s)	0.451	0.452	0.453	0.456	0.458	0.424	0.400	0.363	0.334
$u_{out,avg}$ (m/s)	0.450	0.449	0.448	0.446	0.445	0.424	0.403	0.367	0.339
$T_{in,avg}$ (K)	299.99	300.69	301.39	302.77	304.16	324.32	348.68	397.45	446.27
$T_{out,avg}$ (K)	300.00	300.00	300.00	300.00	300.00	325.00	350.00	400.00	450.00
$T_{mid,avg}$ (K)	300.00	300.37	300.73	301.46	302.19	324.65	349.31	398.68	448.07
	B0	BI1	BI2	BI3	BI4	BII1	BII2	BII3	BII4
u_{max} (m/s)	43.71	43.99	44.73	46.17	47.46	42.73	41.74	39.70	37.59
$u_{in,avg}$ (m/s)	21.57	21.18	22.77	23.85	24.83	20.08	18.79	16.69	15.09
$u_{out,avg}$ (m/s)	19.06	18.90	18.72	18.37	18.01	18.76	18.43	17.70	16.89
$T_{in,avg}$ (K)	299.72	308.09	316.40	332.65	348.56	316.68	334.35	371.84	412.13
$T_{out,avg}$ (K)	299.78	300.83	301.81	303.51	304.94	323.88	348.34	397.99	448.19
$T_{mid,avg}$ (K)	299.29	308.59	317.61	334.87	351.14	315.58	333.22	372.12	414.99
	C0	CI1	CI2	CI3	CI4	CII1	CII2	CII3	CII4
u_{max} (m/s)	274.97	280.28	284.94	292.59	298.49	275.33	275.91	277.63	279.92
$u_{in,avg}$ (m/s)	124.54	128.90	133.02	140.66	147.59	119.62	115.16	107.34	100.68
$u_{out,avg}$ (m/s)	129.48	131.18	132.74	135.44	137.66	129.86	130.31	131.36	132.55
$T_{in,avg}$ (K)	291.41	303.76	316.04	340.40	364.51	304.07	316.95	343.36	370.61
$T_{out,avg}$ (K)	288.31	294.16	299.84	310.74	321.06	306.98	325.87	364.30	403.58
$T_{mid,avg}$ (K)	276.01	295.08	313.91	350.87	386.96	280.82	285.96	297.25	309.99
	D0	DI4	DII4		E0	EI4	EII4		
u_{max} (m/s)	21.248	23.308	18.154		69.832	74.037	60.654		
$u_{in,avg}$ (m/s)	10.636	12.564	7.636		33.473	38.630	23.489		
$u_{out,avg}$ (m/s)	9.220	8.924	8.361		30.665	28.998	27.407		
$T_{in,avg}$ (K)	299.93	349.23	411.83		299.32	348.51	411.06		
$T_{out,avg}$ (K)	299.95	305.29	448.28		299.42	304.87	447.54		
$T_{mid,avg}$ (K)	299.830	352.47	414.82		298.22	350.92	412.85		

Table 3 Resulting slip velocities and temperature jump values for various flow configurations

Test case	A0	AI1	AI2	AI3	AI4	AII1	AII2	AII3	AII4
$u_{s,avg}$ (m/s)	0.0060	0.0059	0.0058	0.0055	0.0053	0.0063	0.0065	0.0071	0.0077
$u_{s,max}$ (m/s)	0.0121	0.0133	0.0145	0.0173	0.0202	0.0111	0.0102	0.0085	0.0069
$T_{s,avg}$ (K)	300.00	300.00	300.00	300.00	300.00	324.99	349.99	399.99	449.99
	B0	BI1	BI2	BI3	BI4	BII1	BII2	BII3	BII4
$u_{s,avg}$ (m/s)	0.2708	0.2774	0.2808	0.2870	0.2923	0.2796	0.2881	0.3043	0.3193
$u_{s,max}$ (m/s)	0.7259	0.8011	0.8742	1.0156	1.1492	0.6523	0.5865	0.4801	0.4078
$T_{s,avg}$ (K)	300.00	300.01	300.02	300.05	300.07	324.99	349.98	399.96	449,95
	C0	CI1	CI2	CI3	CI4	CII1	CII2	CII3	CII4
$u_{s,avg}$ (m/s)	1.844	1.911	1.977	2.107	2.234	1.897	1.979	2.138	2.294
$u_{s,max}$ (m/s)	7.581	8.529	9.437	11.305	13.131	6.864	6.142	4.689	3.238
$T_{s,avg}$ (K)	299.99	300.02	300.04	300.10	300.15	324.96	349.93	399.88	449.82
	D0	DI4	DII4		E0	EI4	EII4		
$u_{s,avg}$ (m/s)	0.1296	0.1414	0.1553		0.4288	0.4641	0.5126		
$u_{s,max}$ (m/s)	0.3453	0.5617	0.2808		1.1561	1.8516	0.9011		
$T_{s,avg}$ (K)	300.00	300.07	449.95		299.99	300.07	449.94		

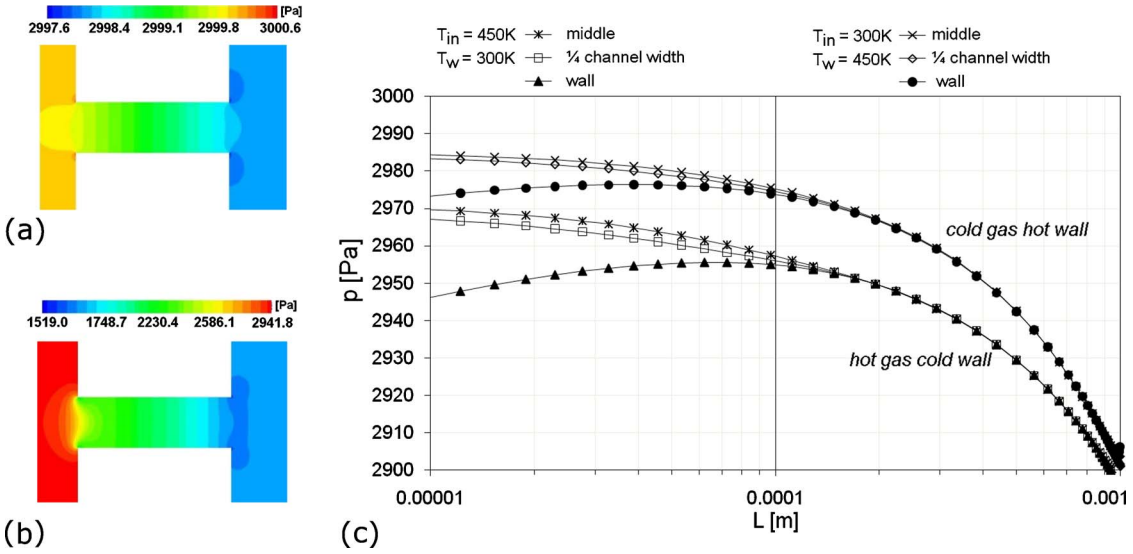

Fig. 2 Pressure distribution for various Reynolds numbers and temperature difference. General characteristics of the pressure drop do not change significantly. Flow velocity was controlled by pressure difference between configuration inlet and outlet. Therefore, the values are a result of fixed boundary conditions. In all cases, Kn=0.008. (*a*) Pressure distribution for Re=0.55. (*b*) Pressure distribution for Re=120. (*c*) Pressure plots for Re=25 and two cases of hot gas cold wall and hot wall cold gas. Values are obtained along the microchannel: at the wall, at 1/4th of the channel width, and in the middle of the channel. Pressure values vary from the entrance of the channel up to 10% of its length.

numbers. In such a configuration, the flow investigation can focus mainly on the temperature field.

4 Microchannel Flow: Temperature Distribution

In this section, we study temperature influence on the slip flow. Simulations were performed for three distinctive cases: no temperature difference between the inlet gas and the microchannel wall, a hot gas cold wall configuration, and a *hot wall cold gas* configuration. The latter configuration is the most interesting for turbomachinery application. Several values of the temperature differences were applied, and details were given in Tables 1–3.

Figure 6 shows all these cases for Knudsen number Kn =0.008 and for two different Reynolds numbers: Re=0.55 and Re=120. For the lowest Reynolds number (cases A), the temperature of the gas penetrates the microchannel only at its entrance. Therefore, no efficient cooling or heating can be obtained. As we have seen in the previous section, the flow is well developed along the channel. However, the heat transfer is restricted only to the area in the vicinity of the channel entrance. This phenomenon depends on the Reynolds number and channel geometry. The larger Reynolds number flow has a pronounced influence on the temperature field. The figure shows temperature contours for Re =120 for the hot gas cold wall and cold gas hot wall configurations and the temperature distribution along the center of the channel. In all computational cases for a high Reynolds number, the temperature varies significantly along the channel. The hot wall cold gas configuration shows that the temperature field penetrates the channel more extensively than the opposite configuration. It will be seen later that mass flow rate and slip induced effects for such a setup are much more apparent.

It has to be noted qualitatively that a very similar temperature drop across the channel for a low Reynolds number (Fig. 6(*c*)) was observed in Ref. [36]. For larger Reynolds numbers, the entrance effects dominate the flow, as seen in Fig. 6(*f*).

Figure 7 shows temperature profiles for all configurations at the inlet and at the outlet of the microchannel. The temperature is normalized over the average temperature. Therefore, the plots indicate how the temperature field relates to the average tempera-

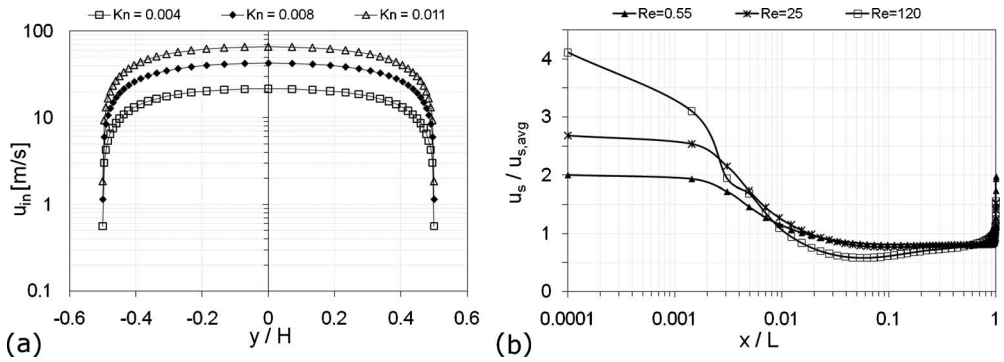

Fig. 3 Influence of the Knudsen and Reynolds numbers on the velocity profile in the microchannel. (*a*) Velocity at the inlet of the channel for three different Knudsen numbers and Re=25. The slip at the wall changes substantially, however, is still small in comparison to the average velocity. (*b*) Slip velocity along the wall for three different Reynolds numbers and Kn=0.008. The largest changes can be observed at the inlet of the channel up to 10% of channel length.

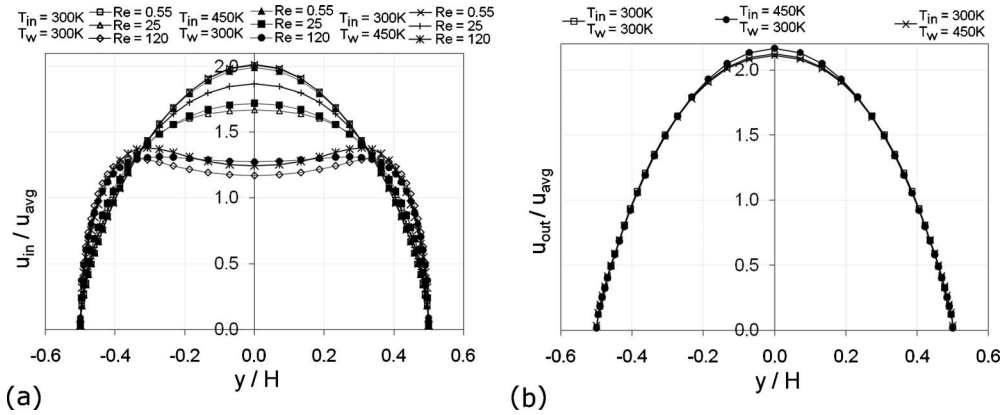

Fig. 4 Velocity profiles at the inlet and outlet of the microchannel for various Reynolds numbers and the temperature differences. It can be noted that only the inlet is significantly influenced by the Reynolds number. The difference between gas and wall temperature changes the flow insignificantly. (*a*) Inlet velocity profiles. (*b*) Outlet velocity profiles.

ture. Figure 7 only shows the values for Reynolds Re=120. At the inlet, the temperature field is as expected, a uniformly distributed and larger temperature difference ΔT result in a larger temperature profile. The outlet temperature behaves very differently. For the case of the hot gas cold wall, the slip induced phenomena influence the temperature penetration region. By the penetration region, we mean the area in which the gradient of the temperature field is significant. The balance between these two effects for a small ΔT leads to a smaller penetration. Only for sufficiently large temperature differences are these flow phenomena overshadowed by the temperature gradient. This process becomes more evident in Fig. 8, which plots temperature contours for the hot gas cold wall configuration. For a sufficiently large temperature difference, the penetration length changes drastically. The outlet temperature for a hot wall cold gas changes with the temperature difference and uniformly penetrates the channel outlet as predicted.

The difference in the gradient necessary to overcome the blocking behavior for temperature penetration can be easily estimated

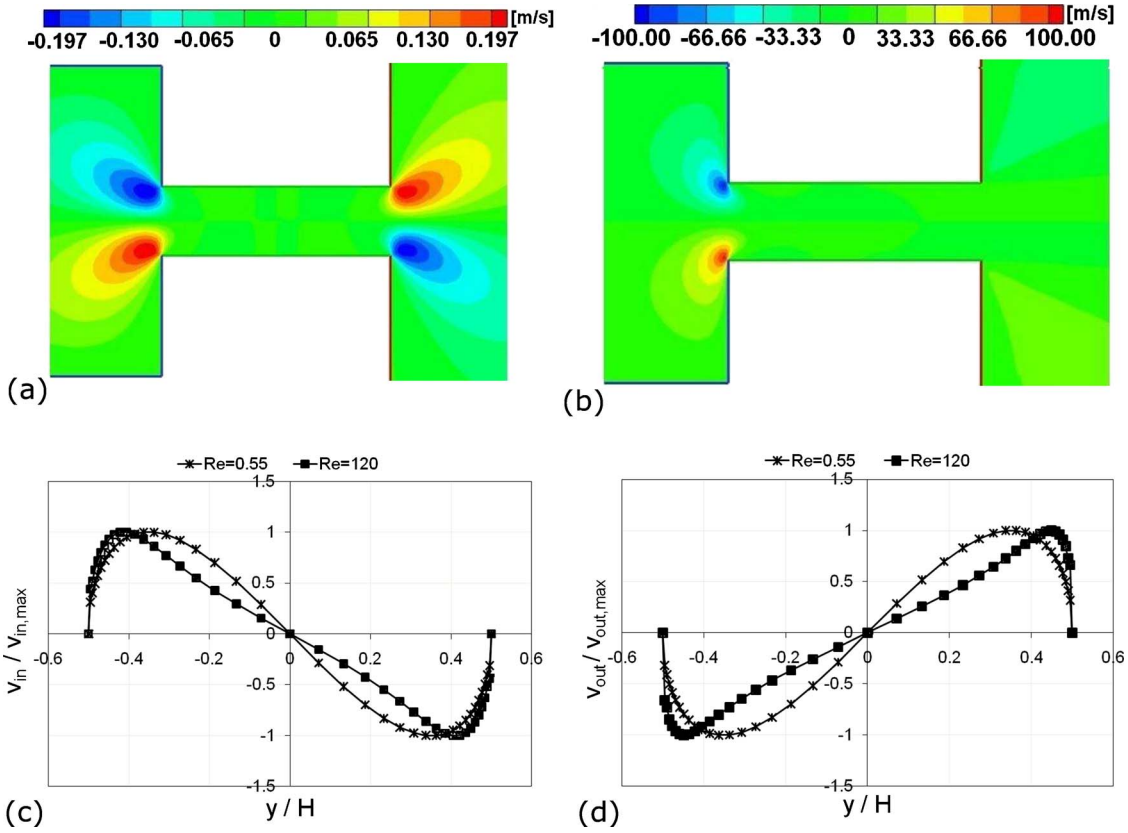

Fig. 5 Velocity in y-direction for Kn=0.008 and for the two Reynolds numbers. The changes across the channel in the relative velocity values are more pronounced for low Reynolds numbers. It is the best illustrated in normalized y-velocity profiles. (*a*) Velocity in y-direction for Re=0.55, $v_{in,max}$=0.118 m/s, and $v_{out,max}$ =0.0114 m/s. (*b*) Velocity in y-direction for Re=120, $v_{in,max}$=7.72 m/s, and $v_{out,max}$=71.53 m/s. (c) Inlet y-velocity profiles for two Reynolds numbers. (d) Outlet y-velocity profiles for two Reynolds numbers.

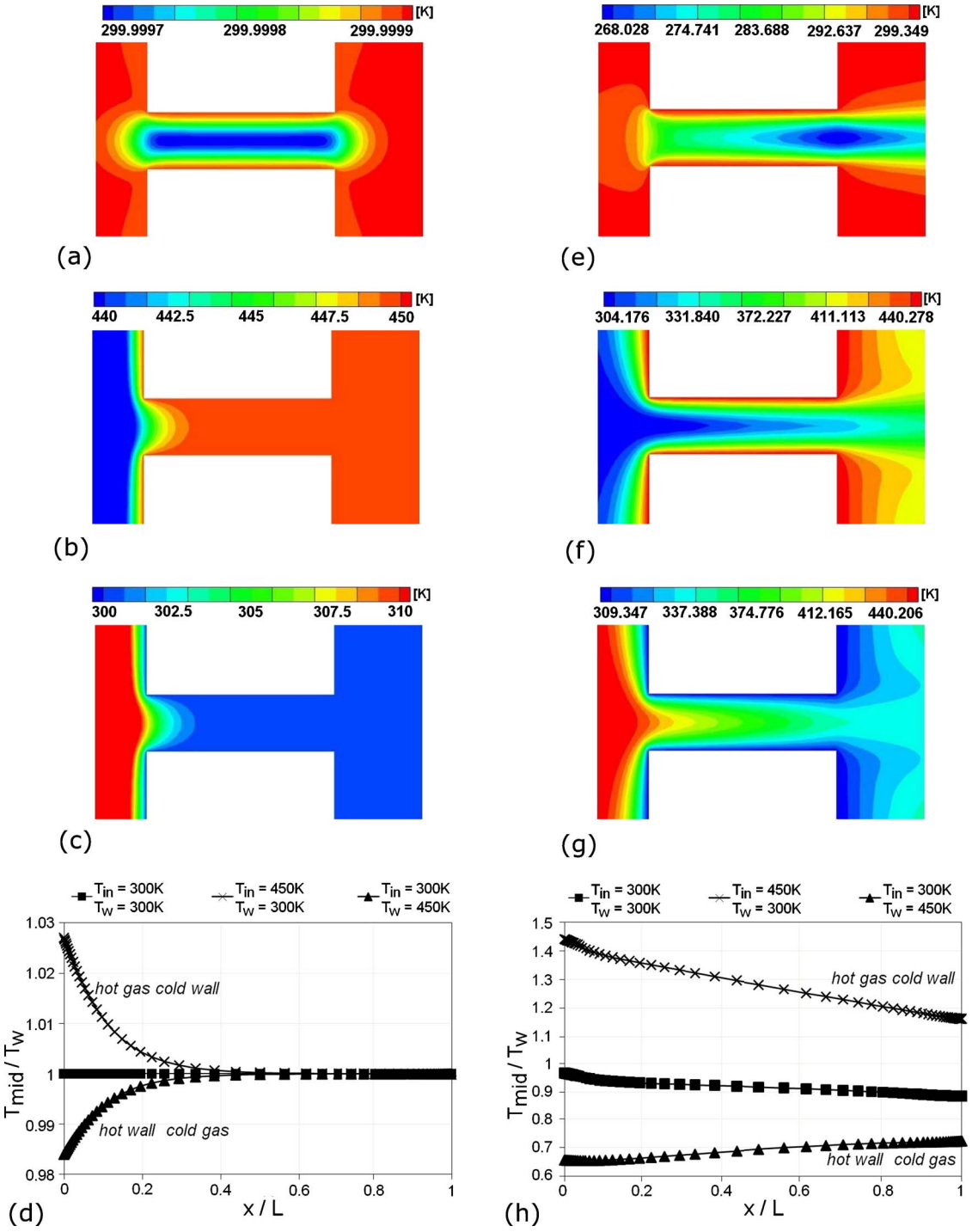

Fig. 6 Temperature distribution for Kn=0.008, two Reynolds numbers, and three different setups: no heating, cold gas hot wall, and hot gas cold wall. It is evident that the temperature field penetrates the microchannel much more extensively for a higher Reynolds number. (*a*) T_{in}=300 K, T_w=300 K, and Re=0.55. (*b*) T_{in}=300 K, T_w=450 K, and Re=0.55. (*c*) T_{in}=450 K, T_w=300 K, and Re=0.55. (*d*) Temperature distribution in the middle of the channel for Re=0.55. (*e*) T_{in}=300 K, T_w=300 K, and Re=120. (*f*) T_{in}=300 K, T_w=450 K, and Re=120. (*g*) T_{in}=450 K, T_w=300 K, and Re=120. (*h*) Temperature distribution in the middle of the channel for Re=120.

by analyzing the temperature field without heating. The inlet temperature is mostly uniform and changes only slightly near the wall. The outlet, however, has a parabolic profile (the middle point is lower than the average temperature). For hot gas cold wall, these flow phenomena need to be reduced by the temperature gradient. Hence, the heat transfer for such a case would be less efficient than that for a cold gas hot wall. In such circumstances, the temperature gradient and pressure induced flow work in the same direction to increase the mass flow rate in the microchannel. It can be seen in Eqs. (3) and (4) that the induced velocity slip is always in the direction of the flow. Temperature gradient, however, can be either in the same or in the opposite direction. From Eq. (3), it can be seen that temperature gradient influences slip. Hence, it can alter the mass flow rate.

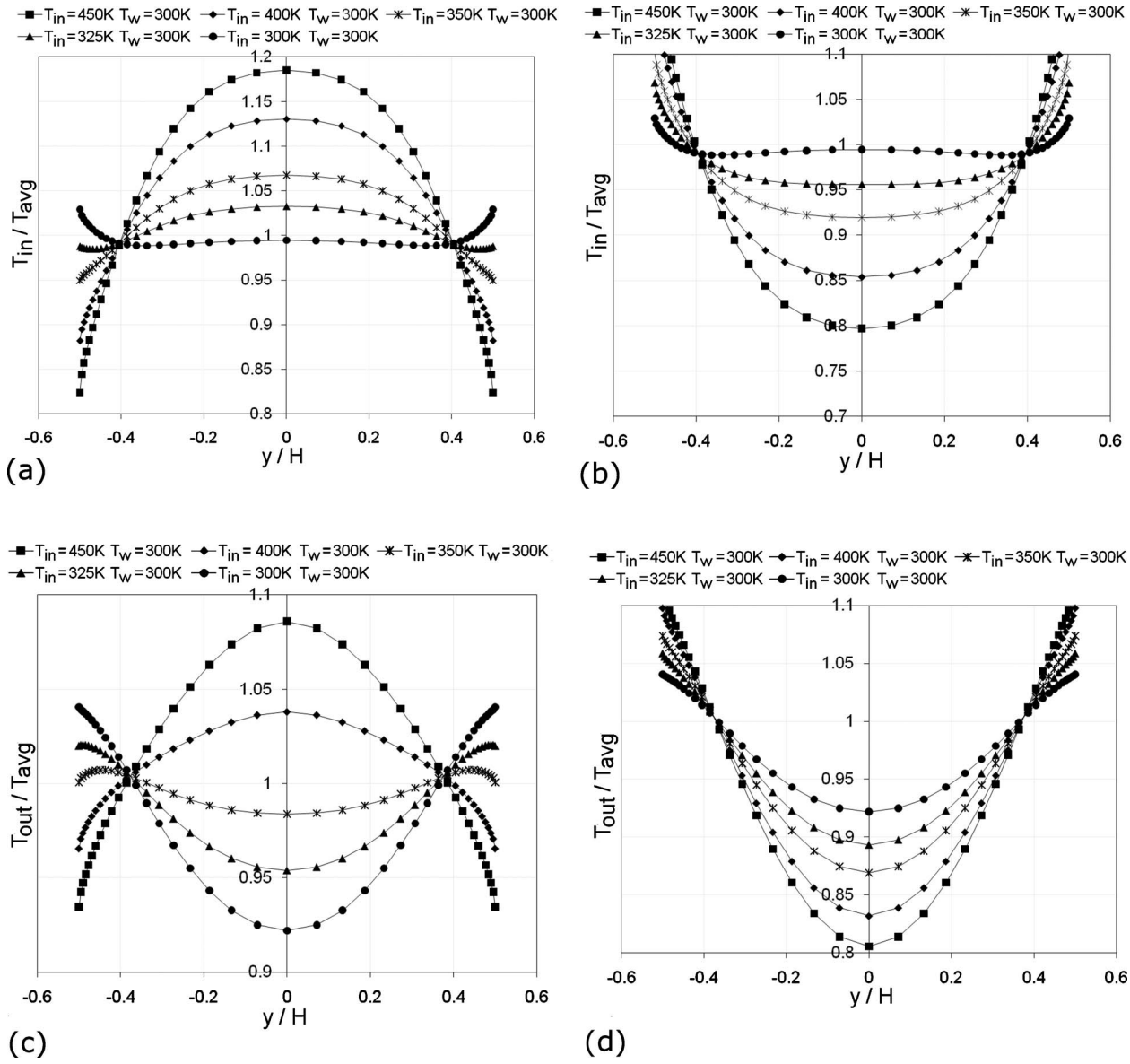

Fig. 7 Temperature profiles for the inlet and outlet of the microchannel for two configurations: hot gas cold wall and cold gas hot wall. Reynolds number is Re=120. Knudsen number is Kn=0.008. (*a*) Inlet temperature across the channel width for various temperature differences ($\Delta T=T_{in}-T_w$) for hot gas cold wall configuration. (*b*) Inlet temperature across the channel width for various temperature differences ($\Delta T=T_{in}-T_w$) for cold gas hot wall configuration. (*c*) Outlet temperature across the channel width for hot gas cold wall configuration. (*d*) Outlet temperature across the channel width for cold gas hot wall configuration. It can be noted that for cold wall hot gas configuration and for a small temperature difference, the field does not penetrate the microchannel outlet the same way as for a large temperature difference.

Figure 9 shows temperature distribution at the wall and the temperature in the middle of the channel for various ΔT for Re $=120$. As for the temperature jump, the majority of changes occur at the entrance.

The *cold wall hot gas* and cold gas hot wall configurations differ in the way the temperature relates to the average temperature in the microchannel. At the wall, the hot entrance leads to the cool outlet and vice versa. A similar tendency is present in the middle of the channel. Additionally, if the wall is hotter than average, the middle of the channel is cooler than average. These middle-channel effects could be used in connection with channel length. By altering that dimension, the heat transfer can be altered even when the Reynolds number is not favorable. However, in this work, the consideration has been restricted only to one length of the channel. Additionally, by the design of entrance geometry, the flow can be influenced [33] and can result in a heat transfer alteration.

5 Microchannel Flow: Slip Velocity Temperature Jump Interaction

The interaction between velocity slip effects induced by the curvature and the temperature gradient is very pronounced at low Reynolds numbers [37]. For $Re>1$, these phenomena cannot be distinguished from the average flow. The performed simulation does not differ in that respect. Only for very low Reynolds Re $=0.55$ and high temperature gradient, the flow at the inlet has been slightly affected. Figure 10 shows the velocity slip at the wall for the entrance of the microchannel and the x-velocity for both extreme cases of maximal temperature gradients $\Delta T=\pm 150$ K. The

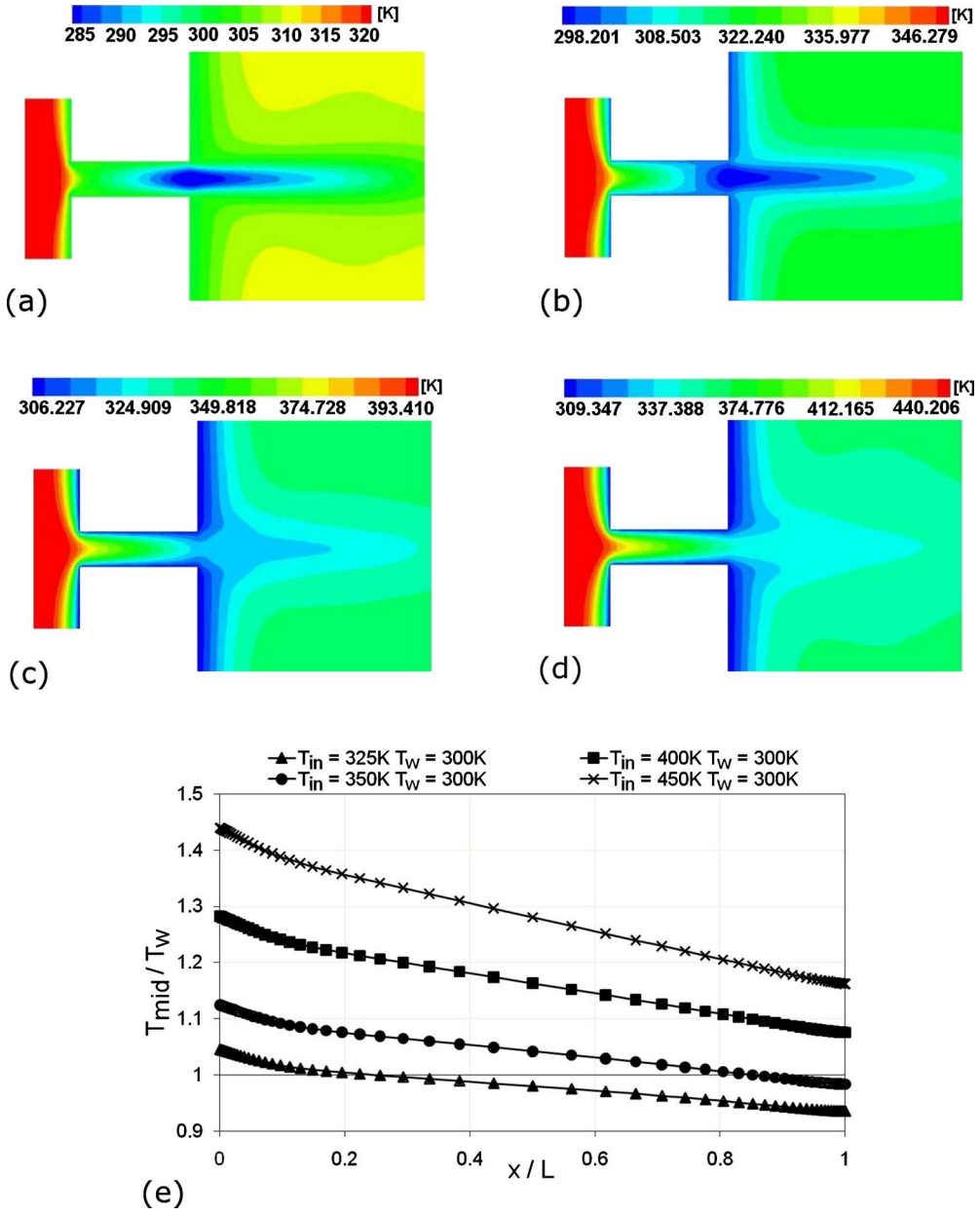

Fig. 8 Temperature field for Re=120 for hot gas cold wall (T_w=300 K) configuration and Kn =0.008. The inlet temperature is varied. Compared with Fig. 6, it can be noted that with small differences between the inlet and wall temperature, the inside of the microchannel gas is colder than the outside. For larger differences, the temperature field starts to penetrate the whole length of the channel and reaches the microchannel outlet. Simulations indicate that there is a temperature gradient for which the heat transfer between inlet and outlet regions can be blocked. (*a*) T_{in} =325 K. (*b*) T_{in}=350 K. (*c*) T_{in}=400 K. (*d*) T_{in}=450 K. (*e*) Temperature profile in the middle of the channel.

cold gas hot wall configuration seems to be more influenced by the entrance geometry. The velocity slip value is enlarged by the temperature gradient. Hot gas cold wall geometry results in the decrease in the local slip velocity at the entrance. The occurrence of this phenomenon is only dependent on the boundary conditions and is independent of the Reynolds number. However, the relative value is significantly reduced for a higher Reynolds number and is difficult to notice.

Simulations for Newtonian and non-Newtonian slip effects in a case of corner flow are presented in Ref. [38]. The qualitative comparison with Fig. 10 shows that the temperature difference has a prominent influence on the velocity at that region. In Ref. [38], the velocity field looks almost identical for Newtonian and non-Newtonian cases. It can be clearly seen in Figs. 10(*b*) and 10(*c*) that the temperature induces the tendency for separation. The x-velocity is plotted and varies significantly between two temperature difference cases.

It was shown that for an even smaller Reynolds number, the slip effects interacting with the thermal jump will lead to the slip induced separation structures. It is here, however, that the flow is too strong. Therefore, the flow reduces such tendency. The increase in the temperature difference could possibly utilize that property to alter mass or heat transfer by adjusting the entrance slip velocity.

As provided in this paper, the slip regime interaction between the velocity slip and the temperature jump is very limited and

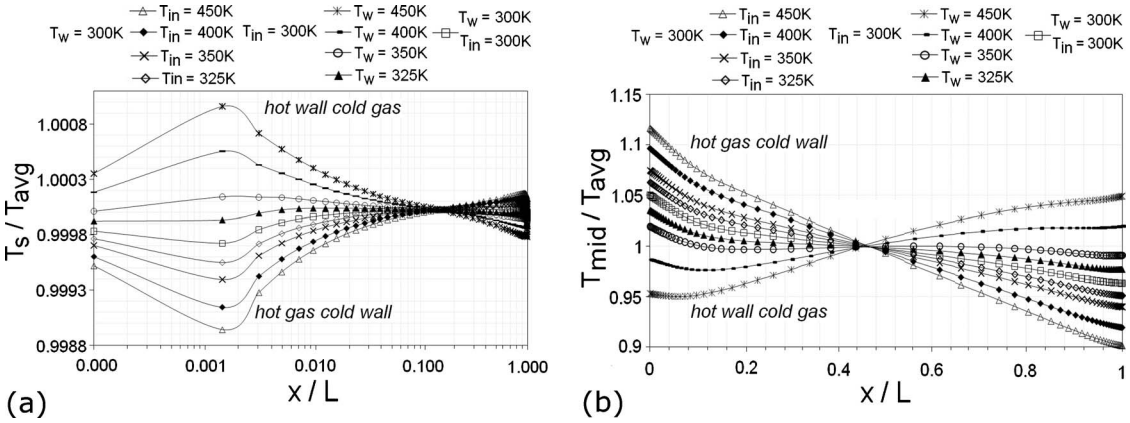

Fig. 9 Temperature values for various simulation cases, Re=120 and Kn=0.008. The temperature is normalized by its average value. (*a*) Temperature jump at the wall along the microchannel. It is apparent that the largest changes are present in the vicinity of the entrance of the microchannel. (*b*) The temperature in the middle of the channel. Concerning hot wall cold gas, the temperature is larger than average temperature near the entrance. However, in the middle of the channel length, the same quantity is smaller than average.

could not generally be used for flow and heat control. This is a result of the conclusion of slip effects, which at this scale are very small. For Knudsen numbers lower than 0.01, the slip in a very limited way changes global flow characteristics though only near the walls. However, as we will see in the next sections, the heat transfer along the microchannel is significantly altered by slip phenomena. That can be directly seen in Maxwell–Smoluchowski relations. The larger difference in the temperature increases addi-

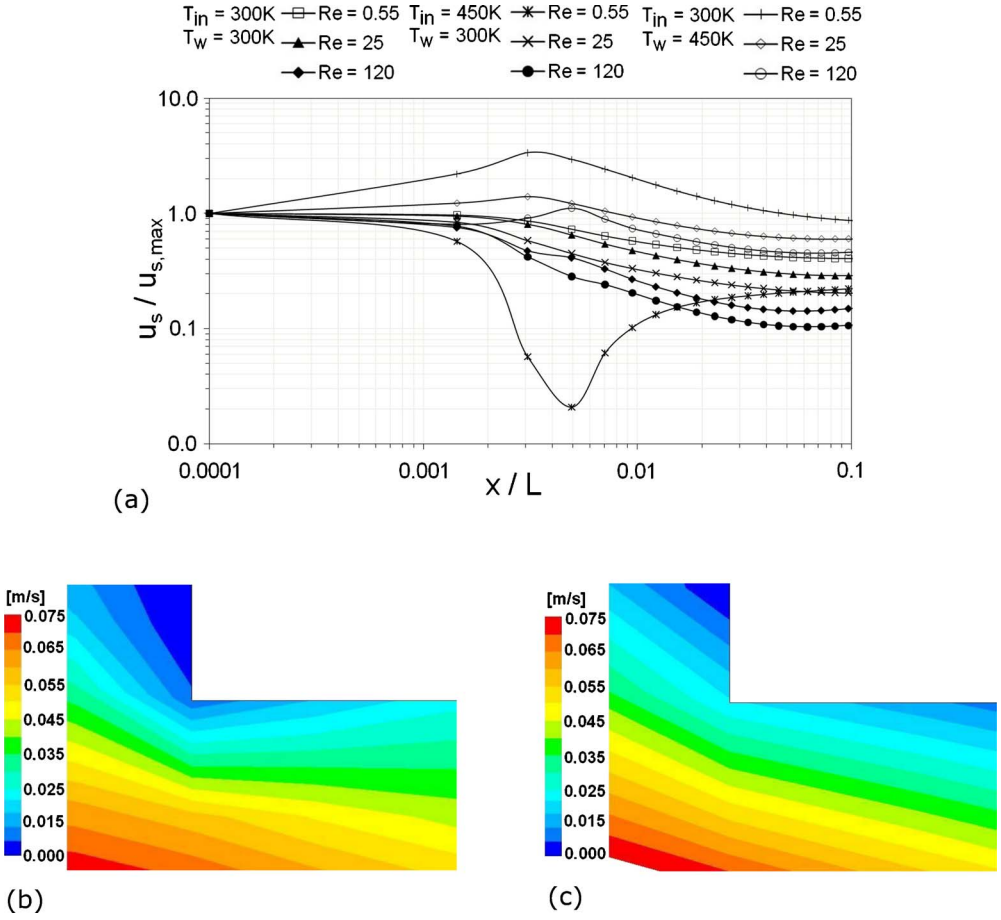

Fig. 10 Slip induced entrance effects. (*a*) The velocity slip along the microchannel wall for various temperature differences for Re=0.55 and Kn=0.008. (*b*) Velocity in the x-direction for cold gas hot wall (ΔT=−150 K). (*c*) Velocity in x-direction for hot gas cold wall (ΔT=150 K). The interaction between entrance geometry, velocity slip, and temperature jump creates changes in the x-direction of the velocity. Main stream velocity is still, however, sufficiently strong (large Reynolds number) to prevent flow separation.

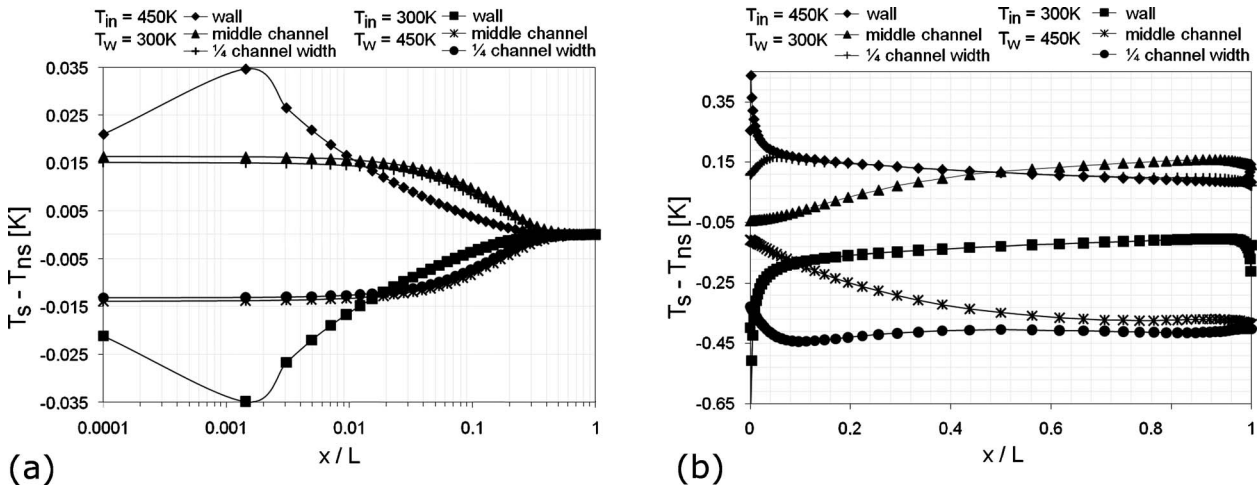

Fig. 11 Temperature difference between slip and no-slip simulations along the channel for Kn=0.008 and for two different Reynolds numbers: (*a*) Re=0.55 and (*b*) Re=120; for hot gas cold wall and cold gas hot wall configurations. The temperature is plotted on the wall, at 1/4th of the channel, and in the middle of the channel. For Re=0.55, the absolute value is taken. It can be noticed that for both cases temperature varies only slightly at the entrance of the microchannel. For the larger Reynolds number, the difference between the cold gas hot wall case and hot gas cold wall is much more pronounced and present all along the channel length.

tional velocity slip and leads to significant changes in the mean temperature field.

6 Microchannel Flow: Heat and Mass Transfer Properties

Figures 6 and 8 illustrate a temperature field behavior for a few computational cases. Figure 11 gives more insight into this characteristic. To answer the question whether the slip effects have important influence over the average temperature field, the two cases for a different Reynolds number were plotted. Both continuum and slip regime simulations were performed. The difference between temperature values along the channel at the wall, in 1/4th of the channel width, and in the middle of the channel is presented. The imposed temperature at the wall, for both cases of hot gas cold wall and hot wall cold gas, is the same, as it only depends on the temperature difference value. For a low Reynolds number, Re=0.55, the temperature between slip and no-slip computations varies only at the entrance and in a very small amount ~0.1%. A very different behavior can be observed for a high Reynolds number Re=120. The slip and no-slip temperatures in the middle of the channel differ from 1% to 3% of the temperature difference, and the amount depends on the configuration case. For the hot gas cold wall, it is smaller than that for the hot wall cold gas setup. The latter as mentioned earlier is more important for turbomachinery application. Hence, it is a very promising result to show that slip induced effects will drastically influence heat transfer performance for such configurations. The temperature penetration along the channel is set to be uniform and only slightly influenced by the microchannel entrance.

For the large Reynolds number and the configuration of hot wall cold gas, the slip induced temperature in the middle of the channel is smaller for about 0.45 K than for a no-slip case. This implies that colder gas penetrates further along the channel before heating up and that the longer channel can be cooled more uniformly by introduction of the slip phenomena (decrease in the microchannel diameter). The hot gas cold wall configuration behaves differently. At the entrance in the middle of the channel, the slip temperature is smaller than that for no-slip calculations, but further along the channel, the tendency is opposite. Therefore, the length of the channel can influence global temperature characteristics. A similar result was observed for such a case by a closer view of temperature profiles. Therefore, the channel length will be an important parameter for hot gas cold wall configuration and much less significant for cold gas hot wall setups. However, for a detailed investigation of the heat transfer, nonstationary flow should be considered.

Figure 12 illustrates the characteristic of the mass flow rate as a function of various physical properties. The mass flow rate increases linearly with the Reynolds number and for the presented simulation following the equation

$$\dot{Q} = 0.00001132\text{Re kg/s} + 0.00001768 \text{ kg/s} \tag{6}$$

As shown [14], this linear tendency can be generally described as

$$\dot{Q} = -\frac{H^3}{12\mu}\frac{dp}{dx}\left(1 + \frac{6\text{Kn}}{1 - b\text{Kn}}\right) \tag{7}$$

The equation again is valid for an ideal periodic channel. Therefore, it cannot be applied to the investigation. However, the linear tendency between mass flow rate and pressure gradient (or Reynolds number) is preserved even in the experiment in real bounded microchannels for helium and nitrogen [29]. Hence, the simulations presented here remain in agreement with other work. A more detailed comparison cannot be easily drawn as the geometry would have to be adequately adjusted, and different gas would have to be used for the simulation.

Mass flow rate dependency on the Knudsen number is much smaller, and due to the fact that too few simulations were performed, no empirical relation was found. The point of this work was not to study Knudsen effects independently, as this is a subject more common in literature, but in relation with other parameters. The focus has remained on the other issues in particular. One such problem is a mass flow rate relation based on the induced temperature gradient. Again, two configurations were considered. The mass flow rate for the hot wall cold gas setup is a bit smaller than that for the opposite case. However, the difference diminished with the increase in the Reynolds number.

The most interesting relation is the dependency of the normalized mass flow rate as a function of Reynolds number. The mass flow rate for slip simulations is reduced by the value for no-slip computations and is then normalized. These data illustrate clearly that for a no-heating case as well as for a hot gas cold wall configuration, the mass flow rate is insignificantly changed by slip induced effects. Hot wall cold gas, which is the most important configuration for turbomachinery, is profoundly altered by the slip

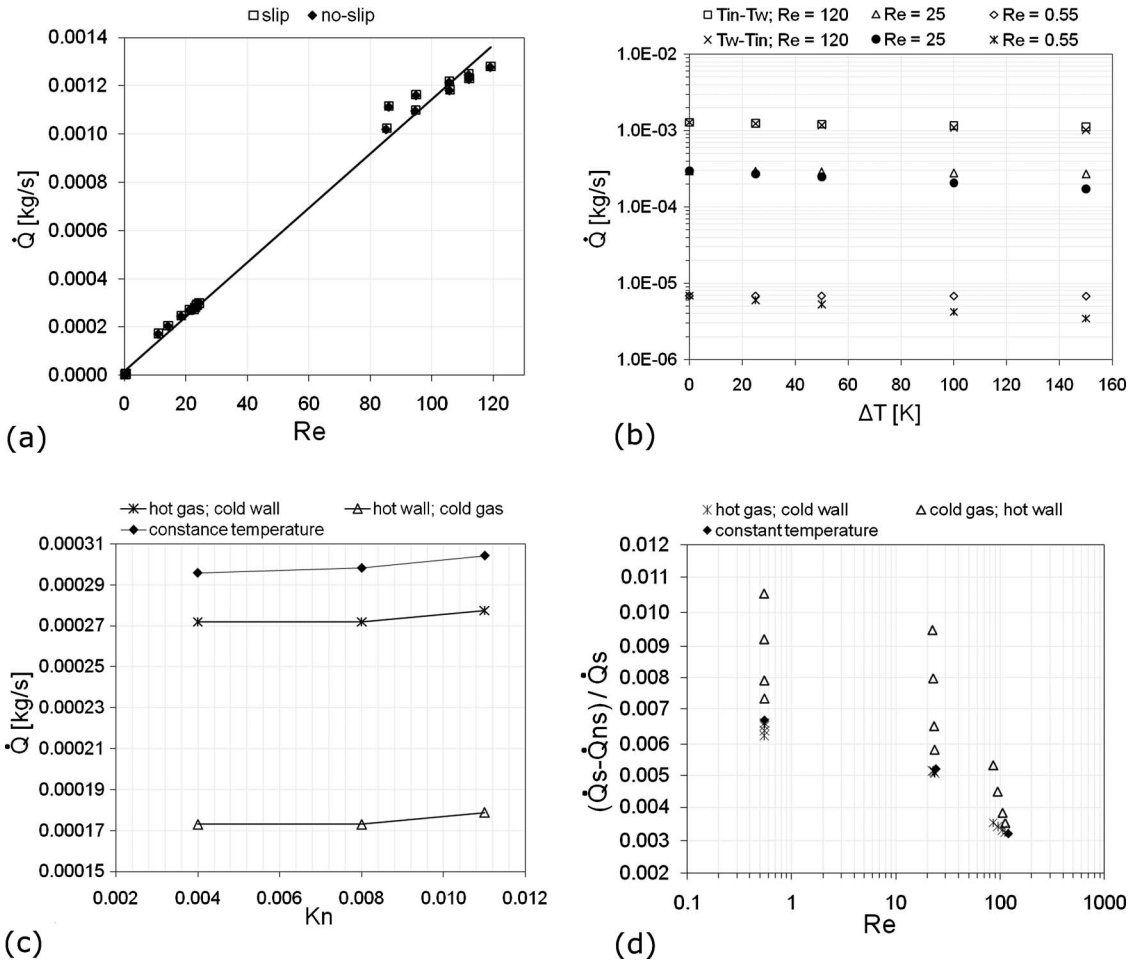

Fig. 12 Mass flow rate dependencies for different Reynolds and Knudsen numbers. (*a*) Mass flow rate as a function of Reynolds number for all calculated cases. Plotted line has equation: $\dot{Q}_s = 0.00001132\text{Re}$ kg/s $+0.00001768$ kg/s and depends on neither the temperature gradient nor the Knudsen number. (*b*) Mass flow rate as a function of the temperature difference between gas and wall ($\Delta T = T_{in} - T_w$). It can be seen that for cold gas hot wall configuration, the mass flow rate is significantly affected by the temperature gradient. The opposite configuration remains unchanged. (*c*) Mass flow rate for Re=25 as a function of Knudsen number. The influence of the Knudsen number is insignificantly small. (*d*) Difference of the mass flow rate for slip and no-slip ($(\dot{Q}_s - \dot{Q}_{ns})/\dot{Q}_s$) computations as a function of Reynolds number for three cases: no-temperature difference; hot gas cold wall and cold gas hot wall configurations. The latter one has the largest variation (triangles) in terms of applied temperature difference, which implies that slip effects are the most pronounced.

phenomena. The temperature gradient is also important as it increases the mass flow rate value. It is again seen that a larger Reynolds number leads to the reduction of slip induced effects.

Figure 12 is a conclusion for all performed simulations and can be a guideline for future experiments in that field. The mass flow rate is linearly dependent on the Reynolds number, the Knudsen number, and the temperature difference; however, the Reynolds effects are dominant. Though slip induced effects were insignificant for the velocity field, they play an important role for the mass flow rate and heat distribution. The temperature can vary as much as 3% due to that fact, which can be a very important advantage with regard to blade cooling. In the future, experimental confirmation of the theoretical prediction will be performed using perforated plates with a set of microchannels.

Figure 13 summarizes rarefaction and channel length effects in heat exchange. The Nusselt number is plotted as a function of the normalized length of the channel. The Nusselt number is given by the following equation, similarly as in Ref. [10],

$$\text{Nu} = \frac{\overline{\text{H}\left(\left(\frac{\partial \text{T}}{\partial n}\right)_{\text{w}}\right)_x}}{\text{T}_{\text{w}} - \text{T}_m} \tag{8}$$

where $\overline{(\partial \text{T}/\partial n)}_{\text{w}}$ is an average temperature gradient normal to the wall and $\text{T}_m(x)$ is a bulk mean temperature,

$$\text{T}_m = \frac{1}{\text{H}\ \text{u}_{\text{in}}} \int_y \text{T}V \cdot n dy \tag{9}$$

Figure 13(*a*) shows Nusselt number effects related to the channel length and various flow configurations. Similarly, as from temperature profile, it can be seen that hot gas cold wall and cold gas hot wall configurations have different heat exchange properties. Additionally, a corresponding theoretical solution for an infinite channel is plotted [21]. The theory fits well at the beginning of the channel, and relatively early the outlet and finite characteristic of the channel start to be important. This fact was also seen from

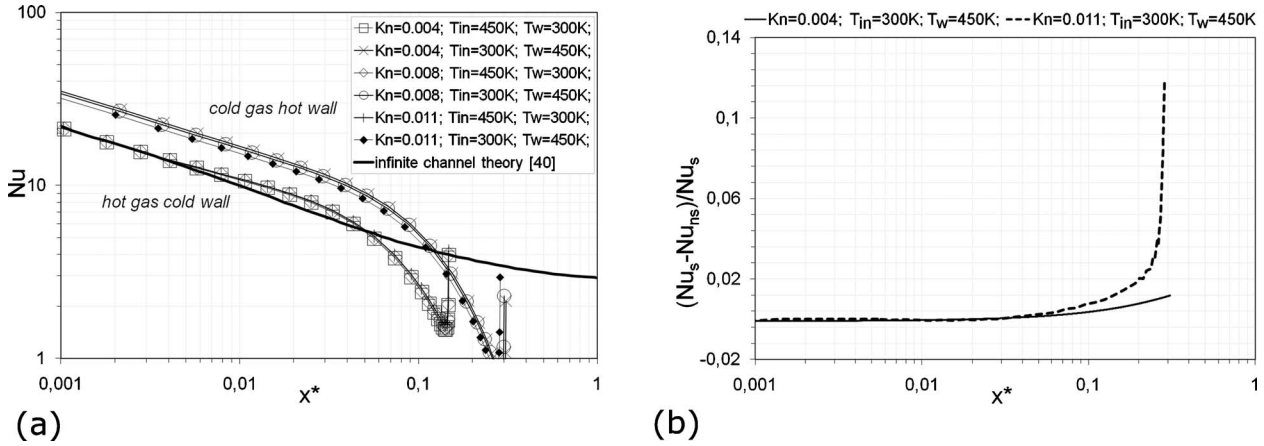

Fig. 13 Nusselt number at the wall as a function of normalized channel length. (*a*) Nusselt number for hot wall cold gas and cold gas hot wall case. Additionally, the theoretical value for infinite channel is plotted [40]. It can be seen that channel length has important role on Nusselt characteristics. (*b*) The difference between Nusselt at the wall for a slip and no-slip flow for two cases of Knudsen number. The rarefaction effects in Nusselt distribution are substantial especially for Kn = 0.011.

temperature distribution. Moreover, Fig. 13(*a*) shows that the cold gas hot wall configuration has better heat transfer characteristics. Combining that result with mass flow rate presented in Fig. 12(*d*), and additionally with Fig. 13(*b*), it can be concluded that an increase in heat exchange is related to rarefaction effects for such configuration. This is especially clearly seen in Fig. 13(*b*), where normalized Nusselt for slip and no-slip configurations for same flow parameters is plotted. With an increase in the channel length, the slip influence increases. As it was expected, this tendency will be especially pronounced for higher Knudsen numbers.

7 Conclusion

Microchannel gas flow has been investigated with the various temperature gradient configurations. It was shown that low Knudsen number flows within the slip regime are insignificantly affected by the slip itself but are largely influenced by the temperature gradient. The velocity slip alters the flow only near the wall. However, for the flows with a temperature gradient, slip phenomena globally change the flow behavior.

For the configuration of hot wall cold gas, which is important in turbomachinery application, the slip effects are very pronounced and show their presence along the entire microchannel length. Therefore, the mass flow rate changes significantly, with the difference lying in the temperature field. The most prominent results are shown in Figs. 12(*d*) and 13(*b*), presenting changes in mass flow rate and in Nusselt number. The plots underline the differences between no-slip and slip regimes for a hot wall cold gas configuration. Despite very low Knudsen numbers, the differences between those regimes are sufficiently large to be noticed. This had not been the case for the cold wall hot gas configuration. The obtained results promise that velocity slip and temperature jump effects can be utilized in turbomachinery cooling. However, the optimal hole configuration will also depend on issues such as the roughness of the walls, plate perforation parameters, and flow conditions. Therefore, more investigation is needed.

Additionally, it was shown that in the case of microchannels, Reynolds number has a pronounced role especially concerning intensification of heat transfer by an increase in the temperature penetration length. The changes in Knudsen number between Kn=0.004 and Kn=0.011 lead to very small changes in the flow global parameter.

These results are very promising for turbomachinery effective cooling applications, whereby concerning the reduction in the holes' diameter and the thickness of the cooling plate, the heat transfer phenomena can be intensified. The same coolant can also be used, but only if the geometric parameters are adjusted.

Acknowledgment

This investigation was supported by the Polish Ministry of Science and Education under the project "Efficient turbomachinery blade cooling with various outlet coolant configurations," Grant No. N501 367134.

Nomenclature

- b = coefficient
- C_V = specific heat at constant volume
- e = energy
- F = general unspecified function depending on flow parameters
- H = channel width
- Kn = Knudsen number ($\mathrm{Kn}=k_b\mathrm{T}/\sqrt{2}\sigma^2 p\mathrm{H}$) defined at the inlet
- k_B = Boltzmann constant
- L = channel length
- n = normal direction
- Nu = Nusselt number
- Pr = Prandtl number
- p = pressure
- q = heat flux
- $\dot{Q}$ = mass flow rate
- R = gas constant
- Re = Reynolds number ($\mathrm{Re}=\mathrm{Lu}\rho/\mu$) defined from average density, average viscosity, and maximal velocity of the flow
- t = time
- T = temperature
- u, v = velocity components
- V = velocity vector
- x, y = coordinate
- x^* = normalized channel length; $x^*=x/(H\mathrm{RePr})$
- δ_{ij} = Kronecker's delta
- σ = molecule diameter, stress tensor
- σ_v = tangential momentum coefficient
- σ_T = thermal accommodation coefficient;
- κ = thermal conductivity
- ρ = density
- μ = dynamic viscosity

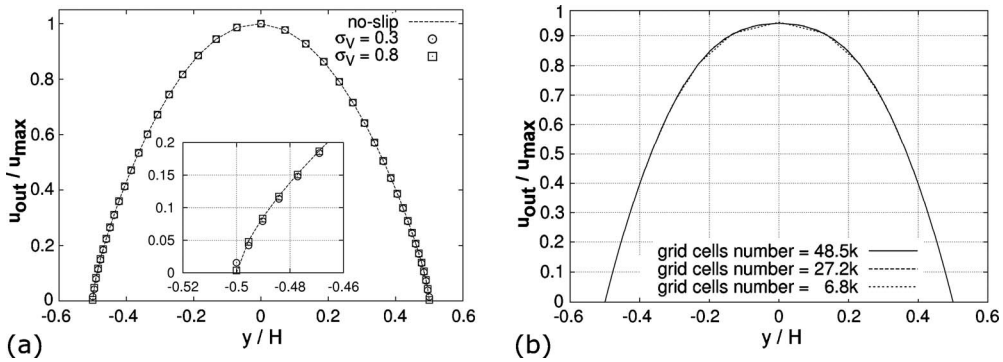

Fig. 14 Outlet velocity for Kn=0.008 and Re=120. (*a*) Outlet velocity for two accommodation coefficients. Line indicates solution with no-slip boundary conditions. Symbols refer to the solution with slip equations with two different accommodation coefficients σ_v=0.3 (circles) and σ_v =0.8 (squares). It can be noted that for considered cases, accommodation coefficient influences flow only near the walls and is the largest for σ_v=0.3. (*b*) Velocity profile for Kn=0.008 for three different grid sizes 48500, 27200, and 6800 elements. The solution does not demonstrate visible grid dependency for medium and fine meshes. Therefore, medium mesh was chosen for simulations.

γ = specific heat ratio
λ = mean free path

Indices

avg = average, the mean value over all considered values
c = configuration
g = gas
i = index
in = inlet
j = index
m = bulk mean temperature, index
max = maximum
mid = middle
ns = no slip
N-S = Navier–Stoke equations
out = outlet
s = slip
w = wall

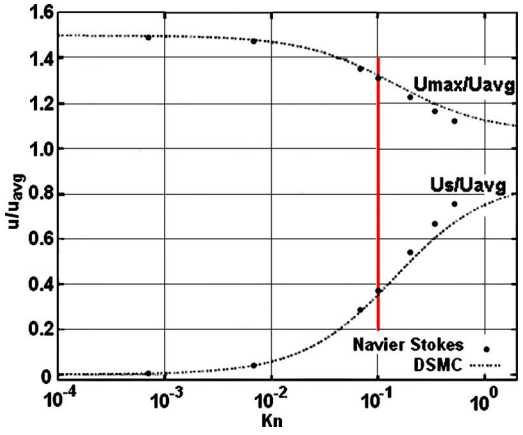

Fig. 15 Centerline (upper curve) and wall velocity (lower curve) in the function of Knudsen number for pressure driven flow in a channel; results of DSMC [34] compared with the Navier–Stokes slip flow approach [32]; vertical line marks the boundary between slip and transition flow regime

Appendix

To investigate the slip effect influence, three types of simulations were performed. In the first simulation, a no-slip boundary condition was assumed. The other two have differed in accommodation coefficient σ_v, which corresponded to the roughness of the channel walls. Two values were chosen: 0.3 and 0.8. The difference between all cases was very small. This is due to the fact that considered Knudsen numbers are relatively small. Figure 14(*a*) presents the distribution of the outlet velocity profile. The changes are visible only near the boundary and are the most prominent for σ_v=0.3. Additionally, it was shown in experiments [39] that for higher temperatures the accommodation coefficient tends to get lower. Due to that fact, in this paper all presented results are for the accommodation coefficient σ_v=0.3 and, similarly, energy accommodation coefficient σ_T=0.3.

Figure 14(*b*) shows velocity profiles in the middle of the channel for three different grid sizes: 48500, 27200, and 6800 elements. It can be seen that the difference in the obtained results is difficult to notice. The mass flow rate, however, exemplifies some of these differences. For the most refined grid, it is 0.002153901 kg/s; for the medium size grid, it is 0.002156794 kg/s; and for the less dense, it is 0.002163946 kg/s. It was for this reason that the medium grid was chosen to perform calculations. It gives satisfying values for mass flow rate and is less computationally expensive than the refined grid.

Figure 15 shows a comparison for the channel flow with no heating with theory and the direct simulation Monte Carlo presented in Ref. [34]. The upper curve is a middle velocity value, and the bottom is the velocity at the wall. The quantities are plotted as a function of Knudsen number, and our simulations agree perfectly with the one within the slip regime, as expected. More validations for the curved channel as well as heating and secondary slip effects can be found in Ref. [32].

References

[1] Bunker, R. S., 2007, "Gas Turbine Heat Transfer: Ten Remaining Hot Gas Path Challenges," ASME J. Turbomach., **129**(2), pp. 193–201.
[2] Gau, C., and Huang, W. B., 1990, "Effect of Weak Swirling Flow on Film Cooling Performance," ASME J. Turbomach., **112**(4), pp. 786–791.
[3] Li, P. L., Ko, H. S., Jeng, D. Z., Liu, C. W., and Gau, C., 2009, "Micro Film Cooling Performance," Int. J. Heat Mass Transfer, **52**(25–26), pp. 5889–5894.
[4] Hale, C. A., Plesniak, M. W., and Ramadhyani, S., 2000, "Film Cooling Effectiveness for Short Film Cooling Holes Fed by a Narrow Plenum," ASME J. Turbomach., **122**(3), pp. 553–557.
[5] Nakamata, C., Okita, Y., Matsuno, S., Mimura, F., Matsushita, M., Yamana, T.,

and Yoshida, T., 2005, "Spatial Arrangement Dependence of Cooling Performance of an Integrated Impingement and Pin Fin Cooling Configuration," ASME Paper No. GT-2005-68348.
[6] Kost, F., and Mullaert, A., 2006, "Migration of Film-Coolant From Slot and Hole Ejection at a Turbine Vane Endwall," ASME Paper No. GT2006-90355.
[7] Kost, F., and Nicklas, M., 2001, "Film-Cooled Turbine Endwall in a Transonic Flow Field: Part I—Aerodynamic Measurements," ASME J. Turbomach., **123**(4), pp. 709–719.
[8] Nicklas, M., 2001, "Film-Cooled Turbine Endwall in a Transonic Flow Field: Part II—Heat Transfer and Film Cooling Effectiveness," ASME J. Turbomach., **123**(4), pp. 720–729.
[9] Sundaram, N., and Thole, K. A., 2009, "Film-Cooling Flowfields With Trenched Holes on an Endwall," ASME J. Turbomach., **131**(4), p. 041007.
[10] Rehder, H. J., and Dannhauer, A., 2007, "Experimental Investigation of Turbine Leakage Flows on the 3D Flow Field and Endwall Heat Transfer," ASME J. Turbomach., **129**(3), pp. 608–618.
[11] Fluent Inc., 2006, FLUENT 6.3.26 Manual.
[12] Ewart, T., Firpo, J. L., Graur, I. A., Perrier, P., and Meolans, J. G., 2009, "DSMC Simulation: Validation and Application to Low Speed Gas Flows in Microchannels," ASME J. Fluids Eng., **131**, p. 014501.
[13] Yang, J. M., Yang, X., Ho, C. M., and Tai, Y.-C., 2001, "Micromachined Particle Filter With Low Power Dissipation," ASME J. Fluids Eng., **123**(4), pp. 899–908.
[14] Bar-Cohen, A., Arik, M., and Ohadi, M., 2006, "Direct Liquid Cooling of High Flux Micro and Nano Electronic Components," Proc. IEEE, **94**(8), 1549-1570.
[15] Bahukudumbi, P., Park, J. H., and Beskok, A., 2003, "A Unified Engineering Model for Steady and Quasi-Steady Shear-Driven Gas Microflows," Microscale Thermophys. Eng., **7**(4), pp. 291–315.
[16] Beskok, A., Karniadakis, G. E., and Trimmer, T., 1996, "Rarefaction and Compressibility Effects in Gas Microflows," ASME J. Fluids Eng., **118**(3), pp. 448–456.
[17] Jain, V., and Lin, C. X., 2006, "Numerical Modeling of Three-Dimensional Compressible Gas Flow in Microchannels," J. Micromech. Microeng., **16**(2), pp. 292–302.
[18] Jeong, N., Lin, Ch.-L., and Choi, D. H., 2006, "Lattice Boltzmann Study of Three-Dimensional Gas Microchannel Flows," J. Micromech. Microeng., **16**(9), pp. 1749–1759.
[19] Jeong, H. E., and Jeong, J. T., 2006, "Extended Graetz Problem Including Streamwise Conduction and Viscous Dissipation in Microchannel," Int. J. Heat Mass Transfer, **49**(13–14), pp. 2151–2157.
[20] Mackowski, D. W., Papadopoulos, D. H., and Rosner, D. E., 1999, "Comparison of Burnett and DSMC Predictions of Pressure Distributions and Normal Stress in One-Dimensional, Strongly Nonisothermal Gases," Phys. Fluids, **11**(8), pp. 2108–2116.
[21] Yang, J., Ye, J. J., Zheng, I., Wong, J. Y., Lam, C. K., Xu, P., Chen, R. X., and Zhu, Z. H., 2010, "Using Direct Simulation Monte Carlo With Improved Boundary Conditions for Heat and Mass Transfer in Microchannels," ASME J. Heat Transfer, **132**(4), pp. 041008.
[22] Bahrami, M., Tamayol, A., and Taheri, P., 2009, "Slip-Flow Pressure Drop in Microchannels of General Cross Section," ASME J. Fluids Eng., **131**, p. 031201.
[23] Duan, Z., and Muzychka, Y. S., 2010, "Slip Flow in the Hydrodynamic Entrance Region of Circular and Noncircular Microchannels," ASME J. Fluids Eng., **132**, p. 011201.
[24] Khadem, M. H., Shams, M., and Hossainpour, S., 2009, "Numerical Simulation of Roughness Effects on Flow and Heat Transfer in Microchannels at Slip Flow Regime," Int. Commun. Heat Mass Transfer, **36**(1), pp. 69–77.
[25] Renksizbulut, M., Niazmand, H., and Tercan, G., 2006, "Slip-Flow and Heat Transfer in Rectangular Microchannels With Constant Wall Temperature," Int. J. Therm. Sci., **45**(9), pp. 870–881.
[26] van Rij, J., Ameel, T., and Harman, T., 2009, "The Effect of Viscous Dissipation and Rarefaction on Rectangular Microchannel Convective Heat Transfer," Int. J. Therm. Sci., **48**(2), pp. 271–281.
[27] Maxwell, J. C., 1879, "On Stresses in Rarefied Gases Arising From Inequalities of Temperature," Philos. Trans. R. Soc. London, **170**, pp. 231–256.
[28] Smoluchowski, M., 1898, "Uber den Temperatursprung bei Warmeleitung in Gasen," Akad. Wiss. Wien, **CVII**, pp. 304–329.
[29] Lockerby, D. A., Reese, J. M., Emerson, D. R., and Barber, R. W., 2004, "Velocity Boundary Condition at Solid Walls in Rarefied Gas Calculations," Phys. Rev. E, **70**, p. 017303.
[30] Sone, Y., and Yoshimoto, M., 1997, "Demonstration of a Rarefied Gas Flow Induced Near the Edge of a Uniformly Heated Plate," Phys. Fluids, **9**(11), pp. 3530–3534.
[31] Sone, Y., 2000, "Flows Induced by Temperature Fields in a Rarefied Gas and Their Ghost Effect on the Behavior of a Gas in the Continuum Limit," Annu. Rev. Fluid Mech., **32**, pp. 779–811.
[32] Jebauer, S., and Czerwinska, J., 2007, "Implementation of Velocity Slip and Temperature Jump Boundary Conditions for Microfluidic Devices," Polish Academy of Sciences, IFTR Report.
[33] Lewandowski, T., Jebauer, S., Czerwinska, J., and Doerffer, P., 2009, "Entrance Effects in Microchannel Gas Flow," J. Therm. Sci., **18**(4), pp. 345–352.
[34] Beskok, A., and Karniadakis, G. E., 1999, "A Model for Flows in Channels, Pipes, and Ducts at Micro and Nano Scales," Microscale Thermophys. Eng., **3**(1), pp. 43–77.
[35] Jebauer, S., and Czerwinska, J., 2008, "Slip Flow Structures in Confined Geometries," Proceedings of the Sixth International ASME Conference ICNMM2008, Darmstadt, Germany.
[36] Shih, J. C., Ho, C. M., Liu, J., and Tai, Y. C., 1995, "Non-Linear Pressure Distribution in Uniform Microchannels," ASME AMD-MD, **238**, pp. 51–56.
[37] Hong, C., and Asako, Y., 2007, "Heat Transfer Characteristics of Gaseous Flows in a Microchannel and a Microtube With Constant Wall Temperature," Numer. Heat Transfer, Part A, **52**(3), pp. 219–238.
[38] Sunarso, A., Yamamoto, T., and Mori, N., 2007, "Numerical Analysis of Wall Slip Effects on Flow of Newtonian and Non-Newtonian Fluids in Macro and Micro Contraction Channels," ASME J. Fluids Eng., **129**(1), pp. 23–30.
[39] Rebrov, A. K., Morozov, A. A., Plotnikov, M. Yu., Timoshenko, N. I., and Maltsev, V. A., 2003, "Determination of Accommodation Coefficients of Translational and Internal Energy Using a Thin Wire in a Free-Molecular Flow," Rev. Sci. Instrum., **74**(2), pp. 1103–1106.
[40] Yu, S., and Ameel, T. A., 2001, "A Universal Entrance Nusselt Number for Internal Slip Flow," Int. Commun. Heat Mass Transfer, **28**(7), pp. 905–910.

F. X. Alvarez[1]
Departament de Física,
Universitat Autònoma de Barcelona,
08193 Bellaterra, Catalonia, Spain
e-mail: xavier.alvarez@uab.cat

D. Jou
Departament de Física,
Universitat Autònoma de Barcelona,
08193 Bellaterra, Catalonia, Spain;
Institut d'Estudis Catalans,
Carme 47,
08001 Barcelona, Catalonia, Spain
e-mail: david.jou@uab.cat

A. Sellitto
Department of Mathematics and Computer Science,
University of Basilicata, Campus Macchia Romana,
85100 Potenza, Italy
e-mail: ant.sellitto@gmail.com

Phonon Boundary Effects and Thermal Conductivity of Rough Concentric Nanowires

By using a phonon hydrodynamics model for heat flow complemented with boundary conditions for smooth or rough boundaries, we study the influence of boundary conditions on the longitudinal thermal conductivity for several kinds of nanowires (single, tubular, and core-shell). The effects of the boundaries are seen to be extremely important. [DOI: 10.1115/1.4002439]

Keywords: phonon hydrodynamic, nanowires, nanosystems, thermal conductivity, ballistic transport, heat transport

1 Introduction

Since the properties of nanosystems depend on temperature, it is logical to study their thermal properties, as for instance, thermal conductivity. In order to do that, one has to note that the classical Fourier law of diffusive regime is no longer applicable in nanosystems, but more general transport laws are needed [1–5]. To explore this transport regime, experiments have measured the effective thermal conductivity of silicon or metal layers with different widths or nanowires with different radii [6–14] and with different roughness [15,16]. The effective thermal conductivity of a D-length device with a total transversal area A through which flows a total heat flux $Q^{(\mathrm{tot})}$ when a thermal difference ΔT is applied through its ends is defined as

$$\kappa^{(\mathrm{eff})} \equiv \frac{Q^{(\mathrm{tot})}}{A}\frac{D}{\Delta T} \tag{1}$$

Some authors have tried to model these data from microscopic models [5,17–19] based on the Boltzmann equation for phonons or electrons or from macroscopic formalisms going beyond local equilibrium.

In this paper, we apply the formalism of phonon hydrodynamics to describe heat transport in these devices. These equations of heat transport are more general than the Fourier one and they explicitly incorporate nonlocal effects. Although they may be obtained by starting from the Boltzmann equation, these equations are much simpler than the Boltzmann equation itself. This makes them useful for practical applications in nanotechnology, in situations where one is not looking for microscopic details but only for applications.

The standard and well-known phonon hydrodynamics equations were derived by Guyer and Krumhansl [20,21] for bulk systems without considering the role of phonon collisions with the boundaries, which introduce anisotropic aspects. However, in very small systems, the boundary collisions are especially relevant and their effects must be incorporated in the description. These effects will be of two kinds: those of relatively smooth boundaries (i.e., specular reflection and diffusive scattering) and those arising from roughness (i.e., backscattering). The influence of roughness has seen to be very relevant in rough Si nanowires [15,16] and has stimulated new interest in the microscopic analysis of phonon boundary conditions [22,23].

In Ref. [24], we have paid special attention to the role of the slip heat flux in longitudinal heat flux along a nanowire. Here, we will also include the effects of the boundary roughness and will study single, tubular, and core-shell nanowires (where the internal boundaries between the core and the shell may have a decisive role in the effective thermal conductivity). We will also examine plane multilayers and will compare with results obtained from numerical simulations [25,26].

2 Phonon Hydrodynamic Equations and Boundary Conditions in Nanowires

Phonon hydrodynamics is a regime of phonon heat transfer in which the role played by nonlocal effects becomes as relevant as the heat flux itself as the size of a microdevice decreases. The form of the constitutive equation for the heat flow $\mathbf{q}$ derived from the kinetic theory of phonons [20,21], or from extended irreversible thermodynamics [18,27,28], or other generalized thermodynamic formalisms [29] is found to be

$$\tau\dot{\mathbf{q}} + \mathbf{q} = -\kappa^{(0)}\nabla T + l^2(\nabla^2\mathbf{q} + 2\nabla\nabla\cdot\mathbf{q}) \tag{2}$$

with $\kappa^{(0)}$ as the bulk thermal conductivity, τ as the relaxation time related to the resistive phonon collisions, and l as an average mean-free path. In the microscopic derivation of Eq. (2) by Guyer and Krumhansl, the term in $\kappa^{(0)}$ was related to the resistive phonon collisions, whereas the term in l^2 was related both to the normal and the resistive phonon collisions, being $l^2 = c\tau\tau_N$ with c as the phonon speed and τ_N as the normal time collision. Note that Eq. (2) allows to take into account both the relaxational and nonlocal effects, but the boundary effects are lacking in it. An equation of this form is not exclusive of phonons, but it could also be valid for electrons as it may be derived purely on macroscopic grounds.

[1]Corresponding author.

Contributed by the Heat Transfer Division of ASME for publication in the JOURNAL OF HEAT TRANSFER. Manuscript received December 13, 2009; final manuscript received August 20, 2010; published online November 2, 2010. Assoc. Editor: Patrick E. Phelan.

When τ and l vanish, Eq. (2) is simply the classical Fourier law. In steady-state situations ($\dot{\mathbf{q}}=0$ and $\dot{e}=-\nabla\cdot\mathbf{q}=0$ with e as the specific internal energy), instead, and when $\mathbf{q}\ll l^2\nabla^2\mathbf{q}$, Eq. (2) reduces to

$$\nabla^2\mathbf{q}=\frac{\kappa^{(0)}}{l^2}\nabla T \tag{3}$$

The condition $\mathbf{q}\ll l^2\nabla^2\mathbf{q}$ is satisfied, for instance, in thin layers or in nanowires of radius R, where $l^2\nabla^2\mathbf{q}\approx(l^2/R^2)\mathbf{q}$. When R is smaller than the mean-free path, the nonlocal term is more important than the overall heat flux $\mathbf{q}$. For $R\gg l$, instead of Eq. (3), the linear term in $\mathbf{q}$ appearing in Eq. (2) will become dominant. Equation (3) is analogous to the Navier–Stokes hydrodynamic equation for steady flow along a straight channel

$$\nabla^2\mathbf{v}=\frac{1}{\eta}\nabla p \tag{4}$$

with η as the shear viscosity, $\mathbf{v}$ as the velocity of the fluid, and p as the pressure.

From this formalism and for a thin cylinder of radius R, one obtains an effective thermal conductivity given by $\kappa^{(\mathrm{eff})}=(\kappa^{(0)}/8)(R^2/l^2)$, which vanishes when R tends to zero [30]. Since it is usually observed that $\kappa^{(\mathrm{eff})}$ vanishes as R, rather than as R^2, in Ref. [24] we included a slip flow on the boundary, leading to $\kappa^{(\mathrm{eff})}\propto R$, as we will comment below.

Thus, the effects of the boundaries are indeed relevant since they change the behavior of effective thermal conductivity from $\kappa^{(\mathrm{eff})}\propto R^2$ to $\kappa^{(\mathrm{eff})}\propto R$, as previously noted. It is expected that they will be farther more relevant in concentric nanowires when there is not only an external boundary but also an internal one. Studying this influence is the aim of the following sections.

In order to take into account boundary effects, here, we complement Eq. (2) with an expression for boundary conditions giving the tangential heat flux near the walls as

$$q_w=Cl\left(\frac{\partial q_b}{\partial r}\right)_{r=R}-\alpha l^2\left(\frac{\partial^2 q_b}{\partial r^2}\right)_{r=R} \tag{5}$$

where q_b is the bulk heat flow with C and α being suitable coefficients depending on the structure of the walls [31]. The higher-order model in Eq. (5) for boundary condition is analogous to the boundary expressions used in rarefied gas dynamics or in microfluidics. It goes up to the second order in l as well as Eq. (2). In other terms, we assume that full local heat flux will be $q(r)=q_b(r)+q_w$. Thus, we consider Eqs. (2) and (5) complementing each other: Eq. (2) giving the bulk contribution and Eq. (5) adding the contribution from collisions with the walls, which influence the whole volume because we will take the radius comparable or lower than the mean-free path l. As it will be seen, for smooth surfaces, $\alpha=0$ and C describes specular and diffusive collisions. For rough surfaces, the value of C is reduced and α becomes different from zero because of phonon backscattering.

We consider that the roughness of the wall is described by two parameters (see Fig. 1): Δ, which is the root-mean square value of the roughness fluctuations, and L, which is the average distance between roughness peaks [32]. In terms of these parameters, we suppose

$$C=C'\left(1-\frac{\Delta}{L}\right)$$

$$\alpha=\alpha'\frac{\Delta}{L} \tag{6}$$

where C' and α' are numerical constants independent on Δ/L. Indeed, when $\Delta/L\to 0$ (or in the limit case when $\Delta=0$), no backscattering is expected, but only specular and diffusive scattering. Therefore, $\alpha\to 0$ when $\Delta/L\to 0$. On the other side, when $L=\Delta$, the surface has no flat regions but it is completely rough in which case $C=0$ is expected.

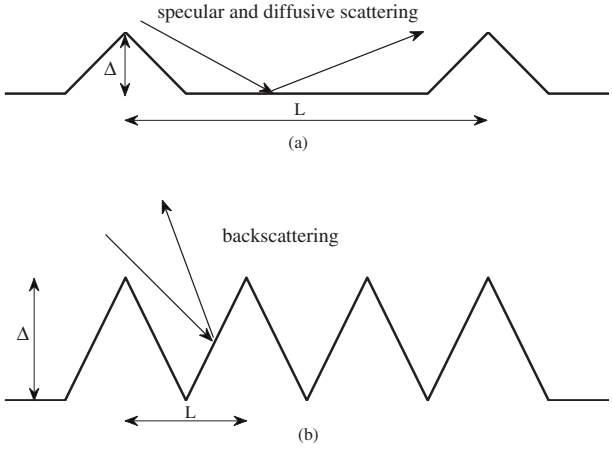

Fig. 1 Different degree of roughness of a wall described by the parameters Δ (height of the roughness peaks) and L (separation of neighboring roughness peaks). When the ratio $\Delta/L\to 0$ (or in the limit case when $\Delta=0$), only specular and diffusive scattering is expected (Fig. 1(*a*)). Otherwise, backscattering is expected (Fig. 1(*b*)). Furthermore, when $L=2\Delta$, the surface has no flat regions but it is completely rough in which case $C=0$ is expected.

Here, we have assumed the simplest dependence for C and α on terms of the ratio Δ/L. Further comparison with statistical physics of boundary conditions should give the detailed form of these functions on a deeper basis. Note, finally, that the coefficients C' and α' will depend on temperature because a surface is considered smooth (or rough) when the characteristic height Δ of the roughness is smaller (or higher) than the phonon wavelength, which depends on temperature [33]. To estimate the values of these coefficients and to study the suitability of our hypothesis, we compare the effective thermal conductivity derived from Eqs. (2) and (5) with experimental data.

By using Eq. (5) and in the case of validity of Eq. (3), i.e., $R\ll l$, in terms of the well-known Knudsen number ($\mathrm{Kn}=l/R$) in Ref. [31] we have obtained that the effective thermal conductivity is

$$\kappa^{(\mathrm{eff})}=\frac{\kappa^{(0)}}{8\ \mathrm{Kn}^2}(1+4C\ \mathrm{Kn}-4\alpha\ \mathrm{Kn}^2) \tag{7}$$

Once the assumptions in Eq. (6) for C and α have been made, the effective thermal conductivity above in terms of Kn and Δ/L becomes

$$\kappa^{(\mathrm{eff})}\left(\mathrm{Kn};\frac{\Delta}{L}\right)=\frac{\kappa^{(0)}}{8\ \mathrm{Kn}^2}(1+4C'\ \mathrm{Kn})-\frac{\kappa^{(0)}}{2\ \mathrm{Kn}}\left(\frac{\Delta}{L}\right)(C'+\alpha'\ \mathrm{Kn}) \tag{8}$$

In Refs. [13,15,22], the effective thermal conductivity for smooth and rough Si nanowires has been experimentally obtained. The nanowires are made by silicon and have different cross sections. The effective thermal conductivity results to be lowered by roughness. In the case of nanowires at 100 K ($\kappa_{\mathrm{Si}}^{(0)}=884\ \mathrm{W\ m^{-1}\ K^{-1}}$ and $l_{\mathrm{Si}}=557$ nm), the results of Tables 1 and 2 follow from Eq. (8) in the case that $C'=0.46$ and $\alpha'=0.08$. The results reasonably fit with experimental data from Refs. [13,15,22]. It is worth observing that the values for C' and α' do not follow from experimental observations but they have been obtained in an empirical way [33].

In particular, in Table 1, only specular and diffusive scattering are considered ($\Delta=0$ nm). It is seen that the influence of boundaries, as expressed by C, is extremely important and that the use

Table 1 Effective thermal conductivity in silicon nanowires at 100 K in the absence of backscattering (i.e., $\alpha=0$). Comparison between the experimental data (taken from Ref. [13]), the results predicted by Eq. (8), and those predicted by Eq. (2). The results for $C'=0$, in fact, follow directly from the Guyer–Krumhansl equation (Eq. (2)) in the case of high Kn without using Eq. (5) and are unacceptably different from experimental data.

	Experimental data	$C'=0.46$	$C'=0$
R (nm)	$\kappa^{(\mathrm{eff})}$ (W m^{-1} K^{-1})	$\kappa^{(\mathrm{eff})}$ (W m^{-1} K^{-1})	$\kappa^{(\mathrm{eff})}$ (W m^{-1} K^{-1})
115	45	45.5	4.7
56	23	20.9	1.1
37	14	13.6	0.5

of Guyer–Krumhansl equation (Eq. (2)) only does not provide a satisfactory description of the effective thermal conductivity in the case of high Kn, namely, if $l \gg R$.

In Table 2, instead, backscattering has been taken into account ($\Delta=3$ nm and $L=6$ nm). The results predicted by Eq. (8) are still in agreement with the results which we inferred from Refs. [15,22] at 100 K.

Thus, it is seen that the strong influence of the boundaries on the effective thermal conductivity is well represented by the phonon hydrodynamics approach at the condition to complement the Guyer–Krumhansl equation (Eq. (2)) with the boundary condition (5).

3 Core-Shell and Tubular Nanowires

In this section, we apply the phonon hydrodynamics model for heat flow complemented by Eq. (5) to discuss the thermal conductivity of cylindrical concentric nanowires such as core-shell nanowires or tubular nanowires (see Fig. 2).

In the limit of high Knudsen numbers, the heat flow profile for the inner core as a function of the radius following from Eqs. (3) and (5) is:

$$q_{ic}(r)=\frac{\kappa_{ic}^{(0)}}{4l_{ic}^2}\frac{\Delta T}{D}(R_{ic}^2-r^2+2C_{ic}l_{ic}R_{ic}-2\alpha_{ic}l_{ic}^2) \tag{9}$$

where the subscript ic indicates that all the mentioned values are referred to the inner core. Since total heat flow along the inner nanowire is defined as $Q_{ic}^{(\mathrm{tot})}=\int_0^{R_{ic}}2\pi r q_{ic}(r)dr$, direct calculations allow to obtain

$$\kappa_{ic}^{(\mathrm{eff})}=\frac{Q_{ic}^{(\mathrm{tot})}}{\pi R_{ic}^2}\frac{D}{\Delta T}=\frac{\kappa_{ic}^{(0)}}{8\ \mathrm{Kn}_{ic}^2}(1+4C_{ic}\ \mathrm{Kn}_{ic}-4\alpha_{ic}\ \mathrm{Kn}_{ic}^2) \tag{10}$$

for the inner core effective thermal conductivity being $\mathrm{Kn}_{ic}=l_{ic}/R_{ic}$ as the corresponding Knudsen number.

The local heat flow profile for the outer shell (os), instead, has the form [34]

Table 2 Effective thermal conductivity in silicon nanowires at 100 K in the presence of backscattering ($\Delta=3$ nm and $L=6$ nm). Comparison between the approximative experimental data inferred from Refs. [15,22] and the results predicted by Eq. (8).

	Experimental data	$C'=0.46$ and $\alpha'=0.08$
R (nm)	$\kappa^{(\mathrm{eff})}$ (W m^{-1} K^{-1})	$\kappa^{(\mathrm{eff})}$ (W m^{-1} K^{-1})
115	5.7	6.9
97	3.8	2.4

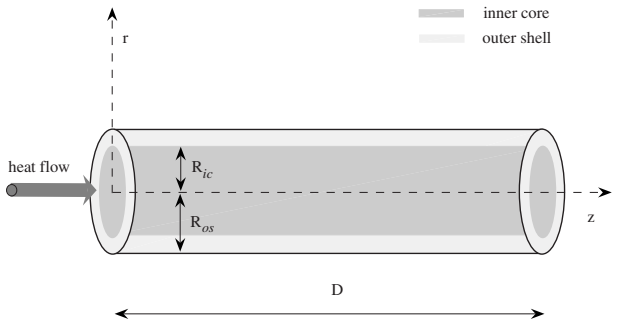

Fig. 2 Cylindrical and concentric nanowires with a longitudinal heat flow. The inner core may be made either by different material with respect to the outer shell (core-shell nanowire) or it may be vacuum (tubular nanowire).

$$q_{os}(r)=-\frac{\kappa_{os}^{(0)}}{4l_{os}^2}\frac{\Delta T}{D}r^2+a\ln r+b \tag{11}$$

In continuum hydrodynamic case, the parameters a and b are found by requiring that $q_{os}(r=R_{os})=0$ as well as $q_{os}(r=R_{ic})=0$. In the dilute case, instead, these coefficients are determined by the boundary conditions

$$q_{os}(R_{ic})=C_{os}l_{os}\left(\frac{\partial q_{os}}{\partial r}\right)_{r=R_{ic}}-\alpha_{os}l_{os}^2\left(\frac{\partial^2 q_{os}}{\partial r^2}\right)_{r=R_{ic}} \tag{12a}$$

$$q_{os}(R_{os})=-C_{os}l_{os}\left(\frac{\partial q_{os}}{\partial r}\right)_{r=R_{os}}+\alpha_{os}l_{os}^2\left(\frac{\partial^2 q_{os}}{\partial r^2}\right)_{r=R_{os}} \tag{12b}$$

The difference of signs in the equations above is due to the fact that at $r=R_{ic}$, $q_{os}(r)$ is an increasing function of r, whereas at $r=R_{os}$, it is a decreasing function of r. For this reason, we prefer to explicitly write both conditions in a separate way. Observe that the pairs of coefficients $\{C_{ic};\alpha_{ic}\}$ and $\{C_{os};\alpha_{os}\}$ in principle are different. This means that the surfaces at the two walls in contact with the outer shell are assumed to have the same roughness (namely, the same coefficient C_{os} and α_{os}) and the inner surfaces of the separation wall are assumed to have the coefficients C_{ic} and α_{ic}.

The solution of Eqs. (11) and (12) in the absence of backscattering (i.e., when $\alpha_{os}=0$) may be found in Ref. [35]. In the presence of backscattering, instead, we have

$$a=-\frac{\kappa_{os}^{(0)}}{16\ \mathrm{Kn}_{os}^2}\frac{\Delta T}{D}\Gamma \tag{13a}$$

$$b=\frac{\kappa_{os}^{(0)}}{32\ \mathrm{Kn}_{os}^2}\frac{\Delta T}{D}\left[\frac{1+\Phi^2}{(1-\Phi)^2}+4C_{os}\ \mathrm{Kn}_{os}\right]-\frac{a}{2}(\ln R_{os}+\ln R_{ic})+\frac{a}{\Phi^2}[\Phi(1-\Phi)^2C_{os}\ \mathrm{Kn}_{os}+(1+\Phi)(1-\Phi)^3 2\alpha_{os}\ \mathrm{Kn}_{os}^2] \tag{13b}$$

$$\Gamma=\frac{\Phi^2[(1+\Phi)(1+4C_{os}\ \mathrm{Kn}_{os})-(1-\Phi)16\alpha_{os}\ \mathrm{Kn}_{os}^2]}{(1-\Phi)[\Phi(1-\Phi^2)2C_{os}\ \mathrm{Kn}_{os}+(1+\Phi^2)(1-\Phi)^2 4\alpha_{os}\ \mathrm{Kn}_{os}^2-\Phi^2\ln\Phi]} \tag{13c}$$

where $\Phi=R_{ic}/R_{os}$ and $\mathrm{Kn}_{os}=l_{os}/2(R_{os}-R_{ic})$ is the Knudsen number for the outer shell. Since total heat flow along the inner nanowire is defined as $Q_{os}^{(\mathrm{tot})}=\int_{R_{ic}}^{R_{os}}2\pi r q_{os}(r)dr$, from Eq. (13), the following effective thermal conductivity for the outer shell arises:

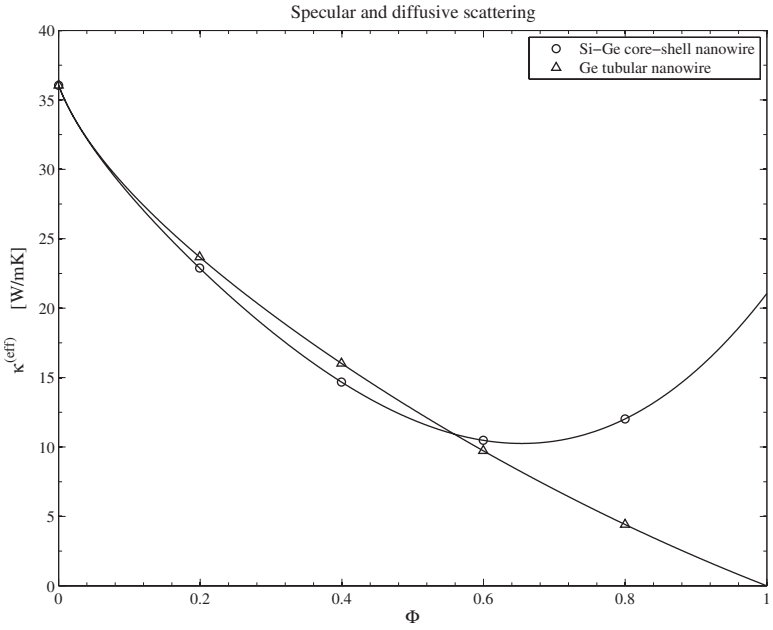

Fig. 3 Comparison between the behavior of the effective thermal conductivity of a Si–Ge core-shell composite nanowire and that of a Ge tubular nanowire in terms of the ratio $\Phi = R_{ic}/R_{os}$ at 100 K ($\kappa_{Si}^{(0)} = 884$ W m^{-1} K^{-1}, $\kappa_{Ge}^{(0)} = 232$ W m^{-1} K^{-1}, $l_{Si} = 557$ nm, and $l_{Ge} = 130$ nm). Only specular and diffusive scattering has been supposed on the walls, i.e., $\Delta = 0$ nm both in the silicon and in the germanium.

$$\kappa_{os}^{(\mathrm{eff})} = \frac{Q_{os}^{(\mathrm{tot})}}{\pi(R_{os}^2 - R_{ic}^2)}\frac{D}{\Delta T} = \frac{\kappa_{os}^{(0)}}{16\,\mathrm{Kn}_{os}}\left\{-\frac{\Gamma}{2}\left[1 + \left(\frac{1+\Phi^2}{1-\Phi^2}\right)\ln\Phi\right] + 2C_{os}\,\mathrm{Kn}_{os}\left[1 + \frac{\Gamma}{2}\frac{(1-\Phi)^2}{\Phi}\right] + 2\alpha_{os}\,\mathrm{Kn}_{os}\Gamma\frac{(1-\Phi^2)(1-\Phi)^2}{\Phi^2}\right\} \tag{14}$$

It is worth noticing that Eq. (14) also represents the effective thermal conductivity ($\kappa_t^{(\mathrm{eff})}$) of a tubular nanowire with R_{ic} as the inner radius and R_{os} as the outer radius.

Finally, the effective thermal conductivity of the core-shell nanowire may be obtained by Eqs. (10) and (14) as

$$\kappa_{nw}^{(\mathrm{eff})} = \kappa_{ic}^{(\mathrm{eff})}\Phi^2 + \kappa_{os}^{(\mathrm{eff})}(1-\Phi^2) \tag{15}$$

Figure 3, in terms of the ratio $\Phi = R_{ic}/R_{os}$, shows the effects of the boundary conditions on the effective thermal conductivity both in a Si–Ge core-shell nanowire and in a Ge tubular nanowire at 100 K ($\kappa_{\mathrm{Si}}^{(0)} = 884$ W m^{-1} K^{-1}, $\kappa_{\mathrm{Ge}}^{(0)} = 232$ W m^{-1} K^{-1}, $l_{\mathrm{Si}} = 557$ nm, and $l_{\mathrm{Ge}} = 130$ nm) in the absence of backscattering at walls. Furthermore, we have supposed that the couple of coefficients $\{C_{ic};\alpha_{ic}\}$ and $\{C_{os};\alpha_{os}\}$ still depend on Δ and L, as in Eq. (6). Note that since, in this case, we are aware of experimental data to infer, for the sake of illustration in Fig. 3, we have assumed $C'_{ic} = C'_{os} = 0.46$. As it is possible to observe, Fig. 3 points out that the presence of the silicon inner core does not always imply an effective thermal conductivity bigger than that one recovers when the inner core is vacuum. In particular, in our case, we have that $\kappa_{nw}^{(\mathrm{eff})} < \kappa_t^{(\mathrm{eff})}$ when $\Phi < 0.56$.

In Fig. 4, for the same systems as above, backscattering at walls has been considered ($\Delta = 3$ nm and $L = 6$ nm). For the sake of illustration, in Fig. 4, we have assumed $C'_{ic} = C'_{os} = 0.46$ and $\alpha'_{ic} = \alpha'_{os} = 0.08$. The same conclusions as above still hold in this case. In particular, for the system at hand, it seems that the presence of a silicon inner core is deleterious for the propagation of heat since $\kappa_{nw}^{(\mathrm{eff})} < \kappa_t^{(\mathrm{eff})}$ when $\Phi < 0.92$. Moreover, a comparison of Fig. 3 (no backscattering) with Fig. 4 (backscattering) shows larger effective thermal conductivities in the case of absence of backscattering, as it was expected.

Equation (12) allows us to illustrate the behavior of effective thermal conductivity for different combinations of the friction parameters, too. In particular, for a Si–Ge core-shell nanowire at 100 K, we show in Fig. 5(*a*) the behavior of the effective thermal conductivity when the effects of backscattering are felt only in the outer shell of germanium. This behavior may be compared with that in Fig. 5(*b*), i.e., when the effects of backscattering are felt only in the inner core of silicon. The comparison in Fig. 5 shows that the effects of the boundary conditions may indeed be very relevant as the values of the effective thermal conductivity and its qualitative dependence on the radii are considerably different in both cases. In order to compute the results of Fig. 5, we have assumed Eq. (6) still holding for $\{C_{ic};\alpha_{ic}\}$ and $\{C_{os};\alpha_{os}\}$ being $C'_{ic} = C'_{os} = 0.46$ and $\alpha'_{ic} = \alpha'_{os} = 0.08$.

4 Thin Layers

The results of the previous sections have been restricted to high values of the Knudsen number. In the general case of a steady-state situation, the condition $\mathbf{q} \ll l^2\nabla^2\mathbf{q}$ is not satisfied and, instead of Eq. (3), one should use the full steady-state version of Guyer–Krumhansl (Eq. (2)), namely,

$$\mathbf{q} = -\kappa^{(0)}\nabla T + l^2\nabla^2\mathbf{q} \tag{16}$$

The solution of this equation is cumbersome in cylindrical geometry, but results may be easily derived for thin layers. Thus, in this section, we will consider thin layers with a thickness h and a width b much longer than h. For this system, in Ref. [24] (see Eq. (18) therein), it has been derived that the bulk heat profile vanishing at $r = \pm h/2$ is

$$q_b(r) = -\kappa^{(0)}\left[1 - \frac{e^{r/l} + e^{-r/l}}{e^{1/2\,\mathrm{Kn}} + e^{-1/2\,\mathrm{Kn}}}\right]\frac{\Delta T}{D} \tag{17}$$

where the Knudsen number is defined now as $\mathrm{Kn} = l/h$.

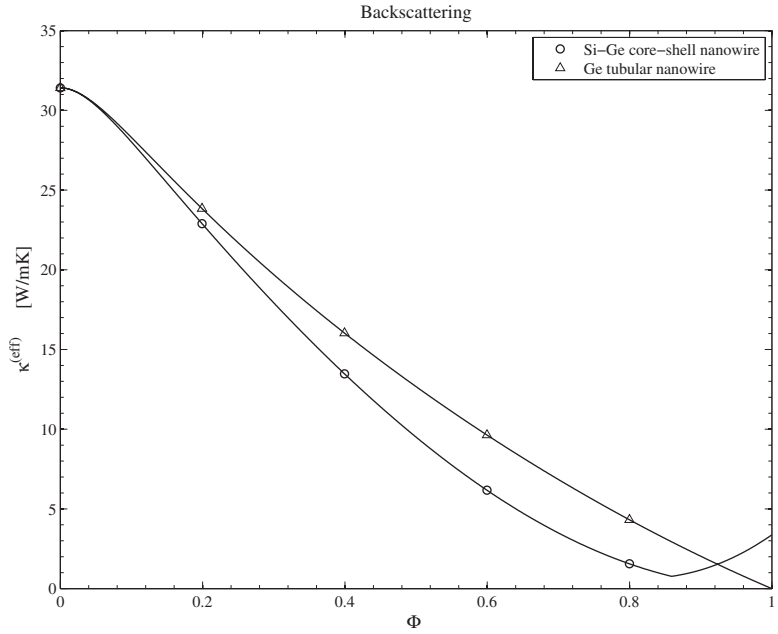

Fig. 4 Comparison between the behavior of the effective thermal conductivity of a Si–Ge core-shell composite nanowire and that of a Ge tubular nanowire in terms of the ratio $\Phi = R_{ic}/R_{os}$ at 100 K. The presence of backscattering on both walls has been supposed ($\Delta = 3$ nm and $L = 6$ nm).

If Eq. (5) is assumed as a boundary condition and Eq. (17) is introduced into it, the wall contribution is obtained. When added to the bulk contribution Eq. (17), straightforward calculations allow us to obtain the following effective thermal conductivity:

$$\frac{\kappa_{TL}^{(eff)}}{\kappa^{(0)}} = 1 - \alpha - (2\,\mathrm{Kn} - C)\tanh\left(\frac{1}{2\,\mathrm{Kn}}\right) \tag{18}$$

where the subscript TL stands for thin layers.

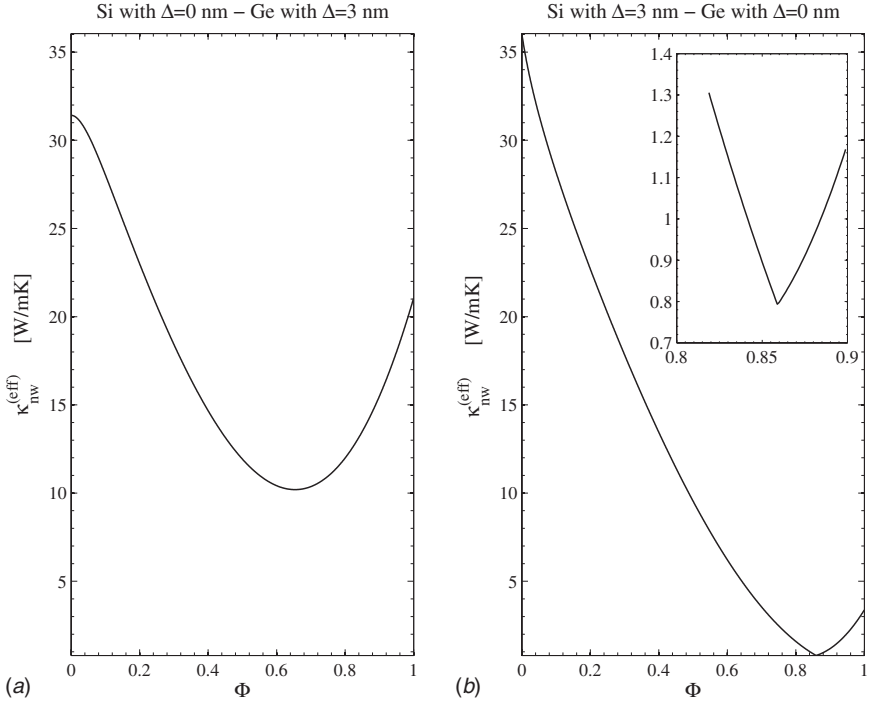

Fig. 5 Behavior of the effective thermal conductivity of a Si–Ge core-shell composite nanowire at 100 K in terms of the ratio $\Phi = R_{ic}/R_{os}$ in the case of backscattering only in the outer shell (Fig. 5(*a*)) and in the case of backscattering only in the inner core (Fig. 5(*b*)). The inset in Fig. 5(*b*), plotting the results in a shorter length scale, allows to show the behavior of $\kappa_{nw}^{(eff)}$ around the value $\Phi = 0.85$ clearer. The friction parameters characterizing backscattering are $\Delta = 3$ nm and $L = 6$ nm.

The results for a plane thin layer will be similar to those of tubular nanowires with radius R_{os} relatively big as compared with the thickness of the wall $R_\Delta=(R_{os}-R_{ic})$. Prasher [25] and Yang et al. [26] studied several situations arising in core-shell nanowires. In particular, for Si thin layers at room temperature ($\kappa_{\mathrm{Si}}^{(0)}=148$ W m^{-1} K^{-1} and $l_{\mathrm{Si}}=40$ nm) and in the absence of backscattering ($\Delta=0$ nm), in Refs. [25,26], it has been found that the values of the ratio $\kappa_{\mathrm{TL}}^{(\mathrm{eff})}/\kappa_{\mathrm{Si}}^{(0)}$ for layers of thickness of 20 nm and 50 nm are 0.17 and 0.31, respectively. Using the same values as in Sec. 2 for the coefficient describing the wall features (i.e., $C'=0.46$), from Eq. (18), we get, instead, 0.15 and 0.37, respectively. Thus, we are able to obtain again results matching satisfactorily with experimental data.

It would be interesting to determine the effective thermal conductivity of a thin layer of silicon in the presence of backscattering. For the sake of computing, we suppose $\Delta=3$ nm and $L=6$ nm as well as $\alpha'=0.08$. In this case, from Eqs. (18) and (6), it follows that $\kappa_{\mathrm{TL}}^{(\mathrm{eff})}/\kappa_{\mathrm{Si}}^{(0)}=0.04$ for a layer of thickness of 20 nm and $\kappa_{\mathrm{TL}}^{(\mathrm{eff})}/\kappa_{\mathrm{Si}}^{(0)}=0.12$ for a layer of thickness of 50 nm. As it is expected, backscattering produces a strong reduction of the effective thermal conductivity.

5 Conclusions

In this paper, we have exhibited the influence of the boundary conditions on the effective thermal conductivity of core-shell and tubular nanowires and for thin layers. It has been shown that the use of phonon hydrodynamic equations with vanishing heat flow on the walls leads to results which are incompatible with the experimental data. Instead, when phonon collisions with the walls are incorporated by means of the simple expression (5), the results arising from the model are in reasonable agreement with the observed results. The effects of the roughness are also considered and the effective thermal conductivity is reduced drastically.

Using the values of the parameters for the description of the collisions obtained by fitting the experimental data in cylindrical nanowires, we have generalized the hydrodynamic formalism to concentric core-shell nanowires, tubular nanowires, and thin layers. The results for thin layers are seen to agree with the observed values; the results for core-shell composite nanowires cannot be compared with experimental results yet but we have studied the expected trends of the effective thermal conductivity for several conditions (smooth inner and outer surfaces and rough inner and outer surfaces and rough inner and smooth outer surface and smooth inner and rough outer surface). In all cases, it is seen that the influence of the boundary conditions is very relevant.

Acknowledgment

D.J. and F.X.A. acknowledge the financial support from the Dirección General de Investigación of the Spanish Ministry of Education and Science under Grant No. FIS 2009-13370-C02-01 and the Direcció General de Recerca of the Generalitat of Catalonia under Grant No. 2009 SGR-00164. A.S. acknowledges the financial support from Italian Gruppo Nazionale della Fisica Matematica under grant Progetto Giovani 2010 and the University of Basilicata for logistic support.

Nomenclature

α = coefficient depending on wall's features
C = coefficient depending on wall's features
c = phonon speed, ms^{-1}
D = length, m
Δ = root-mean square value of the roughness fluctuations, m
κ = thermal conductivity, W m^{-1} K^{-1}
Kn = Knudsen number
L = average distance between roughness peaks, m
l = mean-free path, m
Q = total heat, W
$\mathbf{q}$ = heat flux, W m^{-2}
R = radius, m
r = radial coordinate, m
T = temperature, K
τ = resistive relaxation time, s
τ_N = normal relaxation time, s
Φ = ratio between inner core radius and outer shell radius

Superscripts

0 = bulk
eff = effective
tot = total

Subscripts

b = bulk
ic = inner core
N = normal collisions
os = outer shell
t = tubular
TL = thin layer
w = wall

References

[1] Wang, J., and Wang, J.-S., 2006, "Carbon Nanotube Thermal Transport: Ballistic to Diffusive," Appl. Phys. Lett., **88**, p. 111909.
[2] Fujii, M., Zhang, X., Xie, H., Ago, H., Takahashi, K., Ikuta, T., Abe, H., and Shimizu, T., 2005, "Measuring the Thermal Conductivity of a Single Carbon Nanotube," Phys. Rev. Lett., **95**, p. 065502.
[3] Jou, D., Casas-Vázquez, J., Lebon, G., and Grmela, M., 2005, "A Phenomenological Scaling Approach for Heat Transport in Nano-Systems," Appl. Math. Lett., **18**, pp. 963–967.
[4] Cahill, D. C., Ford, W. K., Goodson, K. E., Mahan, G. D., Majumdar, A., Maris, H. J., Merlin, R., and Phillpot, S. R., 2003, "Nanoscale Thermal Transport," J. Appl. Phys., **93**, pp. 793–818.
[5] Chen, G., 2001, "Ballistic-Diffusive Heat-Conduction Equations," Phys. Rev. Lett., **86**, pp. 2297–2300.
[6] Hao, Z., Zhichao, L., Lilin, T., Zhimin, T., Litian, L., and Zhijian, L., 2007, "Measurement of Thermal Conductivity of Ultra-Thin Single Crystal Silicon Film Using Symmetric Structure," Chin. J. Semicond., **27**, pp. 1961–1965.
[7] Liu, W., and Asheghi, M., 2005, "Thermal Conduction in Ultrathin Pure and Doped Single-Crystal Silicon Layers at High Temperatures," J. Appl. Phys., **98**, p. 123523.
[8] Liu, W., and Asheghi, M., 2004, "Phonon-Boundary Scattering in Ultrathin Single-Crystal Silicon Layers," Appl. Phys. Lett., **84**, pp. 3819–3821.
[9] Asheghi, M., Kurabayashi, K., Kasnavi, R., and Goodson, K. E., 2002, "Thermal Conduction in Doped Single-Crystal Silicon Films," J. Appl. Phys., **91**, pp. 5079–5088.
[10] Kim, P., Shi, L., Majumdar, A., and McEuen, P. L., 2001, "Thermal Transport Measurements of Individual Multiwalled Nanotubes," Phys. Rev. Lett., **87**, p. 215502.
[11] Ju, Y. S., and Goodson, K. E., 1999, "Phonon Scattering in Silicon Films With Thickness of Order 100 nm," Appl. Phys. Lett., **74**, pp. 3005–3007.
[12] Asheghi, M., Leung, Y. K., Wong, S. S., and Goodson, K. E., 1997, "Phonon-Boundary Scattering in Thin Silicon Layers," Appl. Phys. Lett., **71**, pp. 1798–1800.
[13] Li, D., Wu, Y., Kim, P., Shi, L., Yang, P., and Majumdar, A., 2003, "Thermal Conductivity of Individual Silicon Nanowires," Appl. Phys. Lett., **83**, pp. 2934–2936.
[14] Chen, R., Hochbaum, A. I., Murphy, P., Moore, J., Yang, P., and Majumdar, A., 2008, "Thermal Conductance of Thin Silicon Nanowires," Phys. Rev. Lett., **101**, p. 105501.
[15] Hochbaum, A. I., Chen, R., Delgado, R. D., Liang, W., Garnett, E. C., Najarian, M., Majumdar, A., and Yang, P., 2008, "Enhanced Thermoelectric Performance of Rough Silicon Nanowires," Nature (London), **451**, pp. 163–167.
[16] Boukai, A. I., Bunimovich, Y., Tahir-Kheli, J., Yu, J.-K., Goddard, W. A., III, and Heath, J. R., 2008, "Silicon Nanowires as Efficient Thermoelectric Materials," Nature (London), **451**, pp. 168–171.
[17] Alvarez, F. X., and Jou, D., 2007, "Memory and Nonlocal Effects in Heat Transports: From Diffusive to Ballistic Regimes," Appl. Phys. Lett., **90**, p. 083109.
[18] Jou, D., Casas-Vázquez, J., and Lebon, G., 2001, *Extended Irreversible Thermodynamics*, 3rd ed., Springer-Verlag, Berlin.
[19] Joshi, A. A., and Majumdar, A., 1993, "Transient Ballistic and Diffusive Phonon Heat Transport in Thin Films," J. Appl. Phys., **74**, pp. 31–39.
[20] Guyer, R. A., and Krumhansl, J. A., 1966, "Solution of the Linearized Phonon Boltzmann Equation," Phys. Rev., **148**, pp. 766–778.
[21] Guyer, R. A., and Krumhansl, J. A., 1966, "Thermal Conductivity, Second Sound and Phonon Hydrodynamic Phenomena in Nonmetallic Crystals," Phys.

Rev., **148**, pp. 778–788.
[22] Martin, P., Aksamija, Z., Pop, E., and Ravaioli, U., 2009, "Impact of Phonon-Surface Roughness Scattering on Thermal Conductivity of Thin Si Nanowires," Phys. Rev. Lett., **102**, p. 125503.
[23] Mingo, N., 2003, "Calculation of Si Nanowire Thermal Conductivity Using Complete Phonon Dispersion Relations," Phys. Rev. B, **68**, p. 113308.
[24] Alvarez, F. X., Jou, D., and Sellitto, A., 2009, "Phonon Hydrodynamics and Phonon-Boundary Scattering in Nanosystems," J. Appl. Phys., **105**, p. 014317.
[25] Prasher, R., 2006, "Thermal Conductivity of Tubular and Core/Shell Nanowires," Appl. Phys. Lett., **89**, p. 063121.
[26] Yang, R., Chen, G., and Dresselhaus, M. S., 2005, "Thermal Conductivity of Simple and Tubular Nanowire Composites in the Longitudinal Direction," Phys. Rev. B, **72**, p. 125418.
[27] Lebon, G., Jou, D., and Casas-Vázquez, J., 2008, *Understanding Nonequilibrium Thermodynamics*, Springer, Berlin.
[28] Jou, D., and Casas-Vázquez, J., 1990, "Nonequilibrium Absolute Temperature, Thermal Waves and Phonon Hydrodynamics," Physica A, **163**, pp. 47–58.
[29] Cimmelli, V. A., and Frischmuth, K., 2007, "Gradient Generalization to the Extended Thermodynamic Approach and Diffusive-Hyperbolic Heat Conduction," Physica B, **400**, pp. 257–265.
[30] Lacroix, D., Joulain, K., Terris, D., and Lemonnier, D., 2006, "Monte Carlo Simulation of Phonon Confinement in Silicon Nanostructures: Application to the Determination of the Thermal Conductivity of Silicon Nanowires," Appl. Phys. Lett., **89**, p. 103104.
[31] Sellitto, A., Alvarez, F. X., and Jou, D., 2010, "Second Law of Thermodynamics and Phonon-Boundary Conditions in Nanowires," J. Appl. Phys., **107**, p. 064302.
[32] Ferry, D. K., and Goodnick, S. M., 2009, *Transport in Nanostructures*, 2nd ed., Cambridge University Press, Cambridge.
[33] Sellitto, A., Alvarez, F. X., and Jou, D., 2010, "Temperature Dependence of Boundary Conditions in Phonon Hydrodynamics of Smooth and Rough Nanowires," J. Appl. Phys., **107**, p. 114312.
[34] Landau, L. D., and Lishitz, E. M., 1985, *Mechanics of Fluids*, Pergamon, Oxford.
[35] Duan, Z., and Muzychka, Y. S., 2008, "Slip Flow Heat Transfer in Annular Microchannels With Constant Heat Flux," ASME J. Heat Transfer, **130**, p. 092401.

Jae Hun Seol

Arden L. Moore

Li Shi[1]
e-mail: lishi@mail.utexas.edu

Department of Mechanical Engineering,
University of Texas at Austin,
Austin, TX 78712

Insun Jo

Zhen Yao

Department of Physics,
University of Texas at Austin,
Austin, TX 78712

Thermal Conductivity Measurement of Graphene Exfoliated on Silicon Dioxide

We have developed a nanofabricated resistance thermometer device to measure the thermal conductivity of graphene monolayers exfoliated onto silicon dioxide. The measurement results show that the thermal conductivity of the supported graphene is approximately 600 W/m K at room temperature. While this value is lower than the reported basal plane values for graphite and suspended graphene because of phonon leakage across the graphene-support interface, it is still considerably higher than the values for common thin film electronic materials. Here, we present a detailed discussion of the design and fabrication of the measurement device. Analytical and numerical heat transfer solutions are developed to evaluate the accuracy and uncertainty of this method for thermal conductivity measurement of high-thermal conductivity ultrathin films.
[DOI: 10.1115/1.4002608]

Keywords: thermal conductivity, supported graphene, phonon transport, measurement

1 Introduction

Graphene is a monatomic sheet of sp^2 bonded carbon atoms. After graphene was first mechanically exfoliated from graphite onto a dielectric substrate in 2004 [1], it has received intense interest for applications as future-generation electronic materials because of the superior electron mobility [2], mechanical strength [3], and thermal conductivity [4]. Thermal conductivity measurements of such ultrathin films present a challenge. In the past, several methods have been developed to measure the cross- and in-plane thermal conductivities of thin films. The 3-ω technique [5] and the time domain thermal reflectance (TDTR) method [6–8] are two widely used methods for measuring the cross-plane thermal conductivity as well as the thermal boundary conductance of thin films. With the use of various heater line widths on a supported thin film sample and a two-dimensional (2D) heat conduction model, the 3-ω technique can also yield the in-plane thermal conductivity of thin films [9]. For improving the accuracy for in-plane thermal conductivity measurements, suspended thin film membrane structures with a resistance thermometer line patterned on top has been developed [10]. In addition, suspended thin films with thickness on the order of 100 nm have been assembled between two suspended microthermometer devices to measure the in-plane thermal conductivity [11]. Thin films have also been evaporated on top of a membrane with built-in thermometers for in-plane thermal conductivity measurement [12]. However, these methods have not been demonstrated yet for monatomic films such as graphene.

Recently, a micro-Raman spectroscopy method has been reported for the measurement of the thermal conductivity of suspended graphene flakes. In this method, a laser beam is focused at the center of the suspended graphene flake. The temperature rise at the laser spot is determined from the position of the Raman G peak, which downshifts with increasing temperature because of anharmonic G phonon scattering processes. The laser absorption by the graphene was determined to be ~6% per pass of the laser beam by an optical absorption model in combination with a calibration on graphite. This method yielded a thermal conductivity value as high as 5000 W/m K near room temperature for an ~3 μm long suspended graphene flake [4]. Recent optical measurements of suspended graphene flakes yielded a lower optical absorption value of 2.3% for a clean mechanically exfoliated graphene [13]. Using the 2.3% value and a Raman thermometry method, Faugeras et al. obtained a thermal conductivity of ~630 W/m K for a 44-μm-diameter monolayer graphene flake when the graphene in the laser spot was heated to about 660 K [14]. In their measurement, the radius of the Gaussian laser beam focused by a 100× objective was estimated to be about 1 μm. The obtained thermal conductivity would exceed 850 W/m K if the radius was actually about 0.178 μm measured directly in another Raman measurement of thermal transport in both supported and suspended graphene grown by chemical vapor deposition (CVD) [15]. In that work, the optical absorption was measured to be 3.3% ± 1.1% for the CVD graphene flake that was transferred to cover a 3.8-μm-diameter hole. The obtained thermal conductivity of the suspended CVD graphene was found to increase from about $(1400+500/-480)$ W/m K to exceed $(2500+1100/-1050)$ W/m K when the graphene temperature at the laser spot was decreased from ~500 K to ~350 K and the substrate temperature was near 300 K. Moreover, they found that the thermal conductivity of the area of the graphene flake supported on a gold film is $(370+650/-320)$ W/m K near room temperature and considerably lower than values for the suspended graphene.

Despite the progress in Raman-based thermal measurements of suspended and supported graphene, the temperature sensitivity of these Raman measurements is limited to be about 50 K, and the uncertainty in the measured optical absorption can be rather large. Consequently, the thermal conductivity obtained by the Raman technique consists of a large uncertainty. Hence, the Raman technique is inherently inadequate for probing the temperature-thermal conductivity relation especially at low temperatures, which is important for understanding the low dimensional behavior of phonons in graphene.

It has been suggested that phonon transport in graphene as well as in carbon nanotubes (CNTs) can be influenced by interaction of the monatomic layer and the medium [16,17]. To investigate the effect of substrate in phonon transport in graphene in detail, we have developed a suspended resistance thermometer device to

[1]Corresponding author.

Contributed by the Heat Transfer Division of ASME for publication in the JOURNAL OF HEAT TRANSFER. Manuscript received April 29, 2010; final manuscript received August 27, 2010; published online November 3, 2010. Assoc. Editor: Pamela M. Norris.

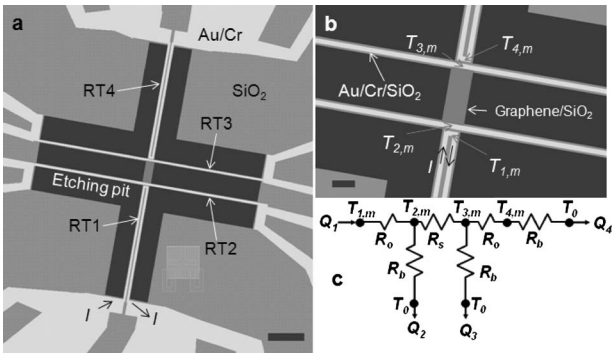

Fig. 1 ((*a*) and (*b*)) Layout schematic of the measurement device that consists of an Au/Cr layer (white), 300-nm-thick SiO_2 layer (gray), and an etching pit (black) under the Au/Cr/SiO_2 beams and the central graphene/SiO_2 beam. (*c*) Thermal circuit of the measurement device. $T_{1,m}$, $T_{2,m}$, $T_{3,m}$, and $T_{4,m}$ are the midpoint temperatures of RT1, RT2, RT3, and RT4, respectively, as indicated in (*b*). T_0 is the substrate temperature. R_s, R_b, and R_0 are the thermal resistances of the central graphene/SiO_2 beam, each RT line including the supporting SiO_2 beam, and the SiO_2 joint between the adjacent straight and U-shaped RT lines, respectively. Q_1 is the heat conducted from the self heated RT1 into the other three RT lines. Q_2, Q_3, and Q_4 are the heat conducted from RT2, RT3, and RT4 into the substrate, respectively. The scale bars are 20 μm and 5 μm in (*a*) and (*b*), respectively.

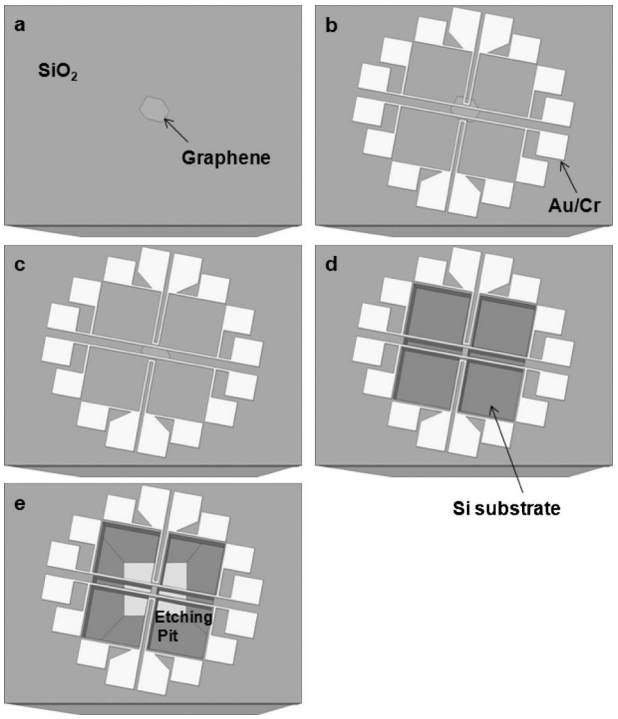

Fig. 2 Schematic diagram of the fabrication process. (*a*) A graphene flake was exfoliated on a 300-nm-thick SiO_2 film thermally grown on a Si wafer. (*b*) Au/Cr RT lines were patterned with the use of EBL and metal lift-off. (*c*) The graphene was patterned using EBL and oxygen plasma etching so that only the part of graphene flake between the two inner straight RTs was left after patterning. (*d*) Windows in the SiO_2 layer were patterned and etched to form Au/Cr/SiO_2 beams and graphene/SiO_2 beams. (*e*) The device was suspended by etching the underlying silicon substrate in a TMAH solution. All schematics are not to scale.

measure the temperature-thermal conductivity relation of graphene exfoliated on a silicon dioxide (SiO_2) support [18]. The measured thermal conductivity of the supported graphene flakes is lower than the reported value of the suspended graphene because of phonon leakage across the graphene-support interface but is still considerably higher than the values of common thin film electronic materials. The obtained temperature-thermal conductivity relation further supports a quantum mechanical calculation that shows a large thermal conductivity contribution in suspended graphene from the out-of-plane flexural modes, which are suppressed much more strongly by substrate interaction than the in-plane vibrational modes in supported graphene.

Thermal measurements of nanostructures are challenging and prone to errors. Although some details of this new measurement method for supported graphene have been reported in the supporting online materials of Ref. [18], we have received inquiries for additional details of the measurement method and associated uncertainty. The objective of the current paper is to examine this measurement method for high thermal conductivity ultrathin supported films in depth. The design and fabrication processes of the measurement device are discussed in detail. In addition to the analytical solution, numerical heat transfer analysis is used to understand the accuracy and uncertainty of the measurement method. By examining the effects of interface thermal conductance and radiation loss as well as the validity of the assumption of one-dimensional (1D) temperature profile along the graphene sample, the numerical results verify the accuracy of the analytical solution that was developed to obtain the thermal conductivity of the supported graphene.

2 Device Design and Fabrication

Figure 1 shows the layout schematic for electron beam lithography (EBL) patterning of the measurement device. In this device, the patterned monolayer graphene ribbon is supported on a 3-μm-wide and 12.5-μm-long suspended SiO_2 beam. Each of the two ends of the graphene/SiO_2 beam is connected to one 4-μm-wide and one 2-μm-wide suspended SiO_2 beams, which are parallel and perpendicular to the central graphene/SiO_2 beam, respectively, and are 60 μm long. One U-shaped and one straight Au/Cr resistance thermometer (RT) lines are patterned on the 4-μm- and 2-μm-wide SiO_2 beams, respectively. The Au/Cr RT lines are 1 μm wide and 120 μm long. The graphene ribbon on the central SiO_2 beam was electrically connected to the two straight RTs clamping the ribbon on the SiO_2 surface but separated from the two outer U-shaped RTs.

During the fabrication of the device, a monolayer graphene flake was mechanically exfoliated from graphite (NGS Naturagraphit GmbH, flake graphite, 99–99.9% carbon) on a 300-nm-thick SiO_2 film thermally grown on top of a silicon substrate, as illustrated in Fig. 2(*a*). The monolayer graphene can be differentiated from double- or few-layer flakes based on contrast difference through an optical microscope [19,20] and can be further verified with a micro-Raman spectroscopy measurement [21].

The device fabrication process consists of three EBL steps. In the first EBL step, a poly(methyl methacrylate) (PMMA) film was spun and patterned on the wafer piece containing the exfoliated graphene flake. Five-nm-thick Cr and 50-nm-thick Au were deposited on the patterned PMMA, followed by a metal lift-off process of soaking the sample in room temperature acetone to remove the PMMA and the metal on top, leaving only the metal RT lines and contact pads on the wafer surface. In the second EBL step, we patterned a PMMA etching mask and used oxygen plasma to etch the part of the graphene flake outside the region between the two straight RTs. This etching process is necessary in order to electrically separate the straight RTs from the U-shaped RTs. In the third EBL step, a 50-nm-thick PMMA layer and a 700-nm-thick ZEP resist layer were spun on the wafer. Windows were open in the double-layer resist and are shown as the dark regions in Fig. 1(*a*). The exposed SiO_2 film was removed by reactive ion etching (RIE)

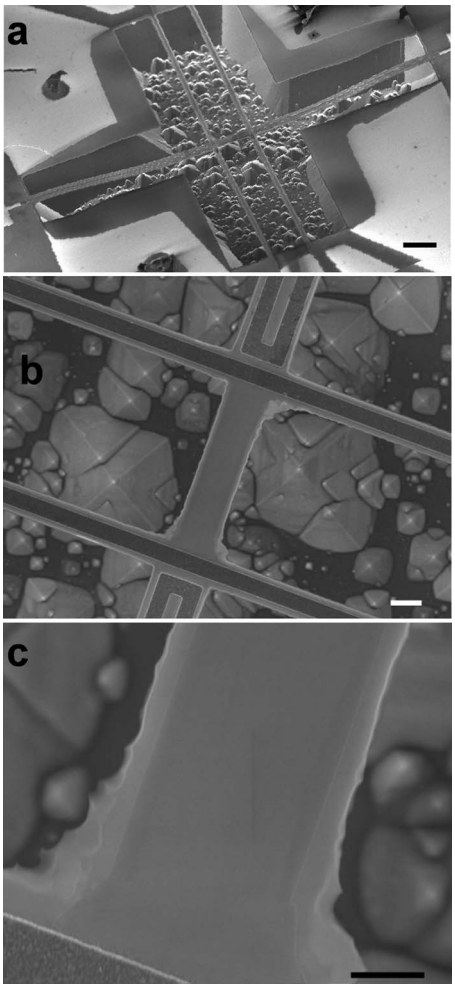

Fig. 3 SEM images of (*a*) the measurement device, (*b*) the central beam, and (*c*) the supported graphene ribbon near one straight Au/Cr RT line. The scale bars are 10 μm, 2 μm, and 1 μm in (*a*), (*b*), and (*c*), respectively.

with a CF_4 chemistry. The RIE etching rate for the ZEP layer was much lower than that for PMMA, providing good etching selectivity to SiO_2. Subsequently, the silicon substrate was etched with 4% tetramethylammonium hydroxide (TMAH) in deionized (DI) water at 90°C for 25 to 30 min immediately after the wafer was dipped in 5% hydrofluoric acid (HF) for 30 s to remove the native oxide on the Si surface. Because the patterned SiO_2 beams were at an angle to the ⟨111⟩ etching-stop plane, the silicon underneath the SiO_2 beams were removed by TMAH. After the TMAH etching, the device was soaked overnight in acetone to completely dissolve organic residue. The ZEP layer could not be dissolved in acetone readily, and was lifted off after the underlying PMMA layer was dissolved in acetone. In the final step, the device was rinsed in methanol and was dried in air.

Figure 3 shows the scanning electron microscopy (SEM) images of the fabricated device. The two side edges of the graphene ribbon were visible in Fig. 3(*c*). The width of the ribbon was measured to be 2.4 μm based on the SEM image, which is smaller than the 3 μm width of the underlying SiO_2 beam because of lateral undercutting during the oxygen plasma etching process in the third EBL step as well as some folding of the two side edges. Raman spectroscopy was used to verify that the sample is a monolayer graphene without the D band caused by defects [21].

3 Analytical Solution of the Measurement Method

Figure 1(*c*) shows the thermal circuit of the measurement device. In the thermal circuit, $T_{j,m}$ is the midpoint temperature of RT j for $j=1-4$, as shown in Fig. 1(*b*). R_s, R_b, and R_o are the thermal resistances of the central graphene/SiO_2 beam, each Au/Cr/SiO_2 beam, and the SiO_2 joint between a straight RT line and the adjacent U-shaped RT line, respectively. Because of the designed dimensions, the four RT lines have the same R_b value between its midpoint temperature ($T_{j,m}$) and the substrate temperature (T_0) in the thermal circuit.

For the measurement of the temperatures and thermal resistances in the thermal circuit, the sample was loaded in the evacuated sample space of a cryostat for thermal measurements. Prior to thermal measurement, the sample was annealed at 375 K in vacuum overnight in an attempt to outgas impurity species adsorbed on the sample surface. During the measurement, direct current (I) was flowed to one of the U-shaped RT shown as RT1 in Fig. 1(*a*). The current was ramped from zero to negative maximum ($-I_{\max}$), from $-I_{\max}$ to $I_{\max}$, and from $I_{\max}$ to zero. During the ramping cycle, a total of 203 measurements were taken at equal intervals of I and time delay of 3 s before each measurement. The time delay is much larger than the thermal time constant of the device that is calculated to be less than 2×10^{-4} s. The measured voltage drop (V) along RT1 in a four-terminal configuration can be fitted using a third order polynomial,

$$V = a_3 I^3 + a_2 I^2 + a_1 I + a_0 \tag{1}$$

where the residual a_0 term is a small number caused by the zero-point offsets in the measured V and I values. The electrical resistance of RT1 at different I level was obtained as

$$R_1(I) \equiv \frac{V - a_0}{I} = a_3 I^2 + a_2 I + a_1 \tag{2}$$

During the ramping process of the heating current, the four-probe electrical resistances of RT2, RT3, and RT4 were measured with a small sinusoidal current from a lock-in amplifier. Because RT2 and RT3 are electrically connected by the graphene ribbon in between, their electrical resistances were measured separately in two different ramping cycles at the same I levels.

As shown in Fig. 4, the measured electrical resistance (R) of each of the four RT lines shows a quadratic dependence on the heating current I when the sample stage temperature (T_0) was kept at 325 K. For each RT line, the measured R value during the I ramping up cycle agrees with that measured at the same I value during the I ramping down cycle, verifying that the 3 s delay time before each measurement is sufficiently long compared with the thermal time constant of the device. With $I=0$, the measured R increases linearly with T_0, as shown in Fig. 5, for RT1 and RT3. The slope of the measured R-T curve is $dR/dT=0.204$ Ω/K, 0.194 Ω/K, 0.195 Ω/K, and 0.202 Ω/K for RT1, RT2, RT3, and RT4, respectively. These values are used to convert the measured resistances of each RT line at different I values to the average temperature rise ($\overline{\Delta T_j}$) in the RT line. As shown in Fig. 6(*a*), the obtained $\overline{\Delta T_j}$ shows a linear dependence on the heating power ($Q=IV$) in RT1.

Because of negligible internal electrical heating, the temperature profile is linear between the midpoint and the junction with the substrate for RT2, RT3, and RT4. Hence,

$$\Delta T_{j,m} \equiv T_{j,m} - T_0 = 2\overline{\Delta T_j} \quad \text{for } j = 2,\ 3,\ \text{or } 4 \tag{3}$$

In comparison, Joule heating results in a parabolic temperature profile in RT1 given as [22]

$$\Delta T_1(x) \equiv T_1(x) - T_0 = -\frac{Q}{2\kappa_b LA}x^2 + C_1 x + C_2 \tag{4}$$

where L, A, and κ_b are the length, the cross section, and the effective thermal conductivity, respectively, of the Au/Cr/SiO_2

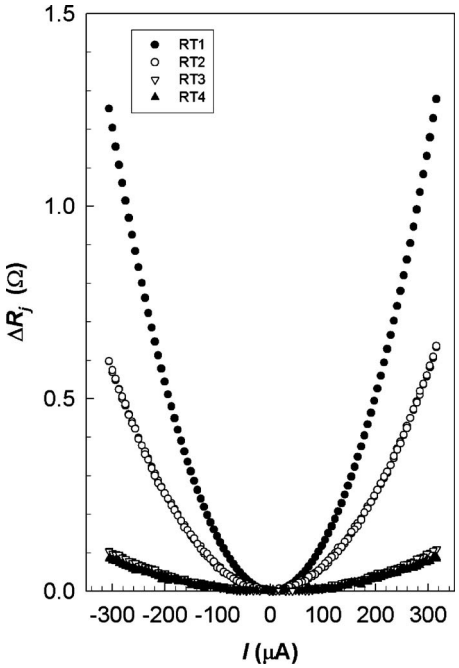

Fig. 4 Measured resistance increases ΔR_j (for $j=1$ to 4) of RT1,RT2, RT3, and RT4 as a function of heating current in RT1 when the sample stage temperature was kept at 325 K

beam of RT1. The two constants, C_1 and C_2, are determined using the following boundary conditions:

$$\Delta T_1(x=0)=0 \quad \text{and} \quad \Delta T_1(x=L)=T_{1,m} \tag{5}$$

The solution is

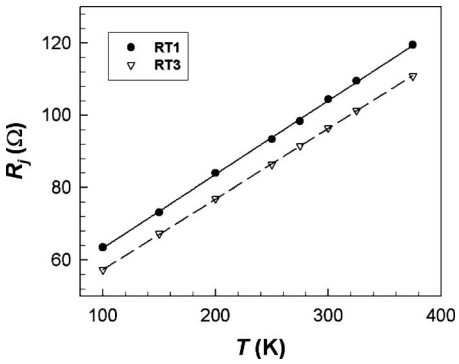

Fig. 5 Measured low-biased electrical resistances of RT1 and RT3 in RT1 as a function of the sample stage temperature. Lines are linear fits to the measurement data.

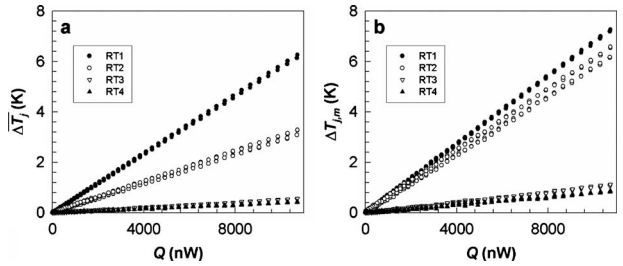

Fig. 6 Measured (*a*) average and (*b*) midpoint temperatures of RT1, RT2, RT3, and RT4 at $T_0=325$ K as function of the heating power in RT1

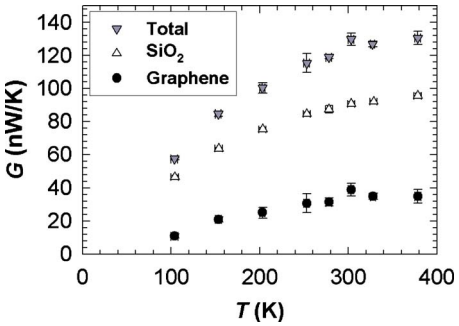

Fig. 7 Measured thermal conductance of the central beam before and after the graphene on top of the central SiO_2 beam was etched with the difference found as the thermal conductance of the graphene

$$\Delta T_1(x) = -\frac{Q}{2\kappa_b LA}x^2 + \left(\frac{\Delta T_{1,m}}{L} + \frac{R_b Q}{2L}\right)x \tag{6}$$

Here, $R_b \equiv L/\kappa_b A$ is the conduction thermal resistance of RT1 between $T_{1,m}$ and T_0 when there is no self heating in RT1, and is designed to be the same as the thermal resistance of each of the other three other RT lines. If radiation loss is ignored, the heat flow from RT1 to the other three RT lines is equal to the sum of the heat flows from the three RT lines to the environment. Hence,

$$Q_1 = -\kappa_b A \left.\frac{d\Delta T_1(x)}{dx}\right|_{x=L} = \frac{\Delta T_{2,m}+\Delta T_{3,m}+\Delta T_{4,m}}{R_b} \tag{7}$$

Equations (6) and (7) are used to obtain

$$R_b = 2\frac{\Delta T_{1,m}+\Delta T_{2,m}+\Delta T_{3,m}+\Delta T_{4,m}}{Q} \tag{8}$$

Using Eqs. (6) and (8), the average temperature rise in RT1 is obtained as

$$\overline{\Delta T_1} = \frac{1}{L}\int_0^L \Delta T_1(x)dx = \frac{4\Delta T_{1,m}+\Delta T_{2,m}+\Delta T_{3,m}+\Delta T_{4,m}}{6} \tag{9}$$

Therefore,

$$\Delta T_{1,m} = \tfrac{3}{2}\overline{\Delta T_1} - \tfrac{1}{2}(\overline{\Delta T_2}+\overline{\Delta T_3}+\overline{\Delta T_4}) \tag{10}$$

Figure 6(*b*) shows the obtained $\Delta T_{j,m}$ for $j=1-4$ as a function of the heating power.

Based on the thermal circuit in Fig. 1(*c*),

$$R_s = R_b\frac{\Delta T_{2,m}-\Delta T_{3,m}}{\Delta T_{3,m}+\Delta T_{4,m}} \tag{11}$$

In addition, the thermal resistance of the SiO_2 joint between the straight RT line and the adjacent U-shaped RT line is obtained from the thermal circuit as follows:

$$R_o = R_b\frac{\Delta T_{1,m}-\Delta T_{2,m}}{\Delta T_{2,m}+\Delta T_{3,m}+\Delta T_{4,m}} \tag{12}$$

Because of the much lower thermal conductivity of the SiO_2 joint than that of the Au/Cr RT, R_o is not negligible, as manifested in the appreciable difference between the measured $\Delta T_{1,m}$ and $\Delta T_{2,m}$ or between $\Delta T_{3,m}$ and $\Delta T_{4,m}$ based on Fig. 6.

The thermal conductance of the central graphene/SiO_2 beam ($G_s \equiv 1/R_s$) was measured before and after the graphene ribbon was etched away in oxygen plasma for 30 s. As shown in Fig. 7, the thermal conductance values before and after removing the graphene are $(129.8\pm3.8)\times10^{-9}$ W/K and $(90.8\pm0.8)\times10^{-9}$ W/K at 300 K, respectively. In comparison, no noticeable change in G_s could be observed after a device without the graphene on the central SiO_2 beam was etched in oxygen plasma

for 30 s. Hence, we attribute the $(39.0 \pm 3.9) \times 10^{-9}$ W/K decrease in G_s after the graphene was etched to the thermal conductance of the supported graphene ribbon (G_g). This measurement is feasible because G_g is appreciable at $T_0 > 100$ K compared with the thermal conductance of the underlying SiO_2 beam, although the thickness of graphene is three orders of magnitude smaller than that of the SiO_2 beam.

The symmetric design of the measurement devices makes it feasible for us to use either of the two U-shaped RT lines as the heater and switch the heat flow direction. The obtained thermal resistance values for the two opposite heat flow directions along the graphene are within the measurement uncertainties. This result verifies that the as-fabricated device was indeed symmetric according to the design.

We examine the influence of the interface thermal resistance on the measured G_s and G_g values. At near room temperature, the experimental interface resistance values are $\sim 2 \times 10^{-8}$ m^2 K/W and $(3.6+1.5/-1.9) \times 10^{-8}$ m^2 K/W between graphite and evaporated Al [23] and for CVD graphene supported on Au [15], respectively. While organic resist residues of one or a few monolayer thickness between the metal electrode and a CNT or graphene can cause large contact electrical resistance, thermal interface resistance between CNTs and PMMA has been found to be much lower than that between CNT and metals because of smaller phonon-mode overlapping between the CNT and the metals at low frequencies and the low phonon transmission coefficient at the metal-CNT interface in the intermediate and high frequency range [24]. In addition, the thermal interface resistance between Al and PMMA has been thought to be lower than 3×10^{-8} m^2 K/W in Ref. [25]. Moreover, we note that no PMMA residue is expected at the interface between the monolayer graphene ribbon and the SiO_2 surface under the metal electrode. Heat can be conducted not only between the metal electrode and the graphene but also across the SiO_2-graphene interface under the electrode. The interface thermal resistance for the graphene embedded in SiO_2 has been recently measured [26] to be 1.2×10^{-8} m^2 K/W at room temperature. Hence, the interface resistances are on the order of 10^{-8} m^2 K/W at the interfaces between the graphene and the top metal electrode and the bottom SiO_2. When these values are divided by the $\sim 1 \times 2.5$ μm^2 contact area at the two clamped ends of the graphene, the obtained contact resistance is on the order of 10^4 K/W, which is three orders of magnitude smaller than the total measured thermal resistance at room temperature. The negligible thermal interface resistance suggests that the temperatures at the two ends of the graphene/SiO_2 beam are rather uniform at the contact area.

4 Numerical Heat Transfer Modeling of the Measurement Device

In order to evaluate the accuracy of the analytical solution and especially the impact of radiation losses and interface thermal resistance, a three-dimensional (3D) numerical heat transfer model for this device design was built with the commercial finite element analysis software ANSYS using the known dimensions and thicknesses for each material. The thermal conductivity of the thin film Au used in the finite element simulation was determined from the measured electrical resistivity of the actual device and the Lorenz number for Au [27] to be 189 W/m K at 300 K, about 40% lower than the bulk value [22]. Thermal conductivity values for amorphous SiO_2 were taken from literature [28]. The maximum temperature rise in the converged simulations did not exceed 22 K above the specified substrate temperature at 300 K. Thus, the temperature dependence of the thermal conductivity of the materials was ignored.

Based on the measurement results [18], we take the thermal conductivity to be 616 W/m K for the monolayer graphene samples supported on SiO_2 and the thickness of the monolayer graphene as 0.335 nm, which is the interlayer spacing between the graphene sheets in graphite [29]. If the graphene monolayer was modeled to scale in the finite element model, achieving a reliable mesh would require a prohibitively large number of nodes not allowed within the ANSYS software. Instead, the graphene was represented by a thin solid film of equivalent thermal conductance achieved by increasing and decreasing, respectively, the thickness and thermal conductivity by a factor of 100. Using this approach, the sample film in the finite element model was assigned with a thickness of 33.5 nm and a thermal conductivity of 6.16 W/m K.

For the finite element simulation, we specified the substrate temperature at the ends of the supporting beams and an appropriate electrical heating rate for the heater line. Radiation loss was accounted for with the inclusion of an additional surface heat flux term, that is, $q''_{\text{rad}} = \varepsilon\sigma(T^4 - T_0^4)$, where ε is the emissivity of the device, σ is the Stefan–Boltzmann constant, T is the temperature at the simulation node, and T_0 is the temperature of the environment, which includes the Si substrate and a custom-made radiation shield thermally anchored to the sample stage of the cryostat. The addition of the custom-made radiation shield kept at temperature close to T_0 helps to maintain the suspended sample temperature at T_0 when $I = 0$.

In the experiment, the electrical resistance of each thermometer is measured to determine the average temperature rise during electrical heating of RT1. To follow this same approach in the case of the ANSYS simulation, the nodal temperatures for each of the respective resistance thermometers were averaged, thus giving the average temperature rise $\overline{\Delta T_j}$ of each thermometer. These values were then used along with the electrical heating rates in the conduction analysis of the device to obtain the thermal resistance of the supporting beams and the sample. To simulate the actual measurement, three heating rates were simulated and the thermal resistances of the beams and of the sample were taken from the slope of the three simulations. The applied electrical heating values were adjusted such that the resulting temperature differences between the two inner resistance thermometers were similar to those used in the actual measurements.

A point of interest was the effect of thermal interface resistance between the graphene and the device materials on the measured sample thermal resistance. To investigate this effect, the finite element analysis was performed for the device assuming perfect contacts and performed again using thermal interface resistance values from literature. For the graphene-Au interface, a thermal interface conductance of 5×10^7 W/m^2 K was used, as found between graphite and evaporated Al [23]. For the graphene-SiO_2 interface, a thermal interface conductance of 8.3×10^7 W/m^2 K was used, as found for graphene embedded in SiO_2 [26].

The numerical results of the finite element analyses are summarized in Table 1, whereas the representative temperature contours are shown in Fig. 8. In comparison to the R_s values calculated based on the specified thermal properties and dimensions, the R_s values obtained based on the calculated $\overline{\Delta T_j}$ values and the analytical solution contain errors less than 2% and 1% for the case of with and without graphene on the central SiO_2 beam, respectively, and perfect thermal contacts. For perfect thermal interfaces and interfaces with finite thermal interface resistances from literature, respectively, the relative errors in the obtained sample thermal resistance following subtraction of the bare bridge thermal conductance were $\sim -4.6\%$ and -1.5% in comparison with the value calculated based on the specified thermal properties and dimensions. In the associated conduction analysis, the temperature is assumed to be uniform across the contact areas. The simulation results verify nearly uniform temperatures in the contact area and approximately 1D temperature gradient along the central graphene/SiO_2 beam, as shown in Fig. 8. The small temperature nonuniformity at the contact area results in the less than 5% relative error in the thermal resistance obtained based on the analytical solution compared with the value calculated based on the specified thermal conductivity and dimension of the graphene sample. Including the radiation loss in the numerical calculation

Table 1 Relative error of the thermal resistance values determined using the analytical solution in comparison to the values calculated from the thermal conductivity and dimension of the SiO_2 beams and graphene ribbon specified in the numerical simulations. The substrate temperature is 300 K. Results with and without radiation considered are within the computational resolution of the simulation.

Device	Relative error in R_b (%)	Relative error in R_s (%)	Interface resistances
Before etching graphene	−1.0	−1.7	
After etching graphene	0.7	−0.1	Perfect thermal interfaces
Graphene	—	−4.6	
Before etching graphene	−1.0	−0.6	Literature thermal
After etching graphene	0.7	−0.1	Interface resistances
Graphene	—	−1.5	

leads to a negligible error within the computational resolution of the simulation. In addition, the numerical calculation also suggests that the differences between the measured $\Delta T_{1,m}$ and $\Delta T_{2,m}$ or between $\Delta T_{3,m}$ and $\Delta T_{4,m}$ could be reduced considerably if Pd/Cr or Pt/Cr instead of Au/Cr is used as the materials for the RT lines. This stems from the much lower thermal conductivity of Pd and Pt [30,31] compared with Au, which would make R_b much larger than R_0.

5 Measurement Results and Discussion

The thermal conductivity of the supported graphene is obtained as follows:

$$\kappa_g = L_g \frac{G_g}{t_g W_g} \tag{13}$$

where κ_g, L_g, W_g, and t_g are the thermal conductivity, the length, the width, and the thickness of the graphene ribbon, respectively. L_g and W_g were measured from the SEM images. On the other hand, the interlayer spacing between the graphene sheets in graphite was used as the thickness of the graphene, as discussed above, i.e., $t_g = 0.335$ nm [29].

The uncertainties in L_g and W_g, labeled as U_{L_g} and U_{W_g}, were 0.11 μm and 0.05 μm, respectively, for the sample shown in Fig. 3, and were included in the uncertainties of thermal conductivities. Based on uncertainty propagation, the uncertainty of G_g was calculated as follows:

$$U_{G_g} = \sqrt{(U_{G_{\text{total}}})^2 + (U_{G_{\text{oxide}}})^2} \tag{14}$$

where $U_{G_{\text{total}}}$ and $U_{G_{\text{oxide}}}$, respectively, are the uncertainties of the measured thermal conductance before and after the graphene was etched. Therefore, the uncertainty of thermal conductivity (U_{κ_g}) is obtained as follows:

$$\frac{U_{\kappa_g}}{\kappa_g} = \sqrt{\left(\frac{U_{G_{\text{total}}}}{G_{\text{total}}}\right)^2 + \left(\frac{U_{L_g}}{L_g}\right)^2 + \left(\frac{U_{W_g}}{W_g}\right)^2} \tag{15}$$

To reduce random uncertainties, we made between three and nine thermal measurements at each substrate temperature.

A total of three samples have been measured and found with similar thermal conductivity [18]. As shown in Fig. 9, the peak value of thermal conductivity of the sample shown in Fig. 3 is 616 ± 64 W/m K, which is about one-third of the highest basal plane thermal conductivity of pyrolytic graphite [32]. This suppression in thermal conductivity of the supported graphene results from the phonon leakage across the interface between graphene and SiO_2, as discussed in detail in Ref. [18]. The thermal conductivity gradually increases from 100 K to 300 K and decreases at temperatures above 300 K. In comparison, a peak thermal conductivity of 2832 W/m K was reported at 138 K for graphite. The considerably lower peak thermal conductivity value at a much higher temperature suggests that substrate scattering and umklapp phonon-phonon scattering are the dominant phonon scattering mechanism below and above 300 K, respectively, in the supported graphene.

In addition, we obtained the thermal conductivity of the central SiO_2 beam using G_{oxide} and geometries of the beam. As shown in Fig. 10, the obtained thermal conductivity values of SiO_2 agree well with the literature values, verifying the accuracy of this measurement method [18,28].

6 Conclusions

We have developed a method to measure the thermal conductivity of graphene monolayer exfoliated on SiO_2. The analytical solution for calculating the temperatures of the measurement device shows a good agreement with the numerical heat transfer simulation considering radiation loss and interface thermal resistance. The obtained thermal conductivity of the supported

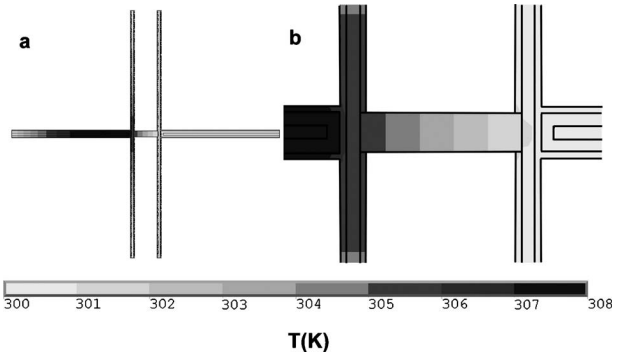

Fig. 8 Temperature distribution (*a*) on the entire device and (*b*) near the central graphene/SiO_2 beam obtained from numerical heat transfer analysis of the device

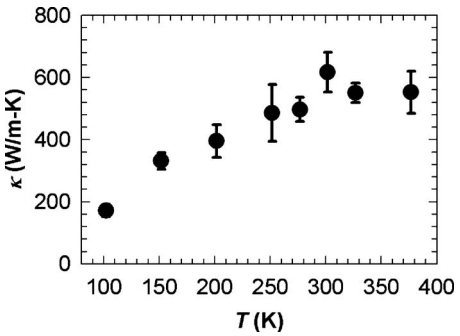

Fig. 9 Thermal conductivity of the supported graphene as a function of temperature

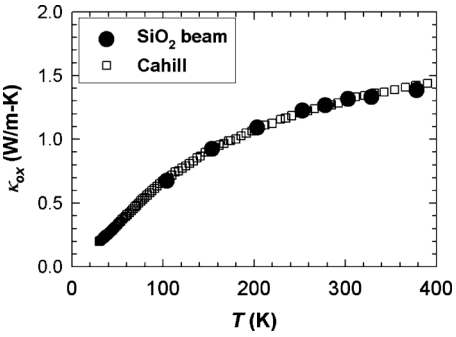

Fig. 10 Thermal conductivity of the central SiO_2 beam as a function of temperature. The error bars of the measurement results are smaller than the size of the symbols. Shown for comparison is the thermal conductivity for thermally grown SiO_2 reported by Cahill [28].

graphene was about a factor of three lower than the highest basal plane thermal conductivity of pyrolytic graphite because of phonon leakage across the graphene and SiO_2 interface. However, this value is still higher than other thin film electronic materials such as copper or silicon [33,34]. The high thermal conductivity of the graphene monolayer makes its thermal conductance comparable to that of the SiO_2 support that is 1000 times thicker than graphene. Interestingly, the feasibility of this measurement was envisioned by Klemens [16] even before graphene was first mechanically exfoliated from graphite.

Acknowledgment

This work is supported by the National Science Foundation Award No. CBET-0553649 and 0933454 (J.H.S and L.S.) and the Office of Naval Research Award No. N00014-08-1-1168 (A.L.M. and L.S.).

Nomenclature

A = area (m^2)
G = thermal conductance (W/K)
I = current (A)
κ = thermal conductivity (W/m K)
L = length (m)
Q = heat (W)
R_b, R_s, and R_o = thermal resistance of $Au/Cr/SiO_2$ beam, graphene/SiO_2 beam, and SiO_2 between the two adjacent thermometer lines, respectively, (K/W)
R = electrical resistance (Ω)
T = temperature (K)
t = thickness (m)
U = uncertainty of measured thermal conductance (W/K)
V = voltage (V)
W = width (m)
ε = emissivity
σ = Stefan–Boltzmann's constant ($W/m^2 T^4$)

References

[1] Novoselov, K. S., Geim, A. K., Morozov, S. V., Jiang, D., Zhang, Y., Dubonos, S. V., Grigorieva, I. V., and Firsov, A. A., 2004, "Electric Field Effect in Atomically Thin Carbon Films," Science, **306**(5696), pp. 666–669.
[2] Bolotin, K. I., Sikes, K. J., Jiang, Z., Klima, M., Fudenberg, G., Hone, J., Kim, P., and Stormer, H. L., 2008, "Ultrahigh Electron Mobility in Suspended Graphene," Solid State Commun., **146**(9–10), pp. 351–355.
[3] Lee, C., Wei, X., Kysar, J. W., and Hone, J., 2008, "Measurement of the Elastic Properties and Intrinsic Strength of Monolayer Graphene," Science, **321**(5887), pp. 385–388.
[4] Balandin, A. A., Ghosh, S., Bao, W., Calizo, I., Teweldebrhan, D., Miao, F., and Lau, C. N., 2008, "Superior Thermal Conductivity of Single-Layer Graphene," Nano Lett., **8**(3), pp. 902–907.
[5] Cahill, D. G., and Pohl, R. O., 1987, "Thermal Conductivity of Amorphous Solids Above the Plateau," Phys. Rev. B, **35**(8), pp. 4067–4073.
[6] Hostetler, J. L., Smith, A. N., and Norris, P. M., 1997, "Thin-Film Thermal Conductivity and Thickness Measurements Using Picosecond Ultrasounds," Nanoscale Microscale Thermophys. Eng., **1**(3), pp. 237–244.
[7] Cahill, D. G., 2004, "Analysis of Heat Flow in Layered Structures for Time-Domain Thermoreflectance," Rev. Sci. Instrum., **75**(12), pp. 5119–5122.
[8] Stevens, R. J., Smith, A. N., and Norris, P. M., 2005, "Measurement of Thermal Boundary Conductance of a Series of Metal-Dielectric Interfaces by the Transient Thermoreflectance Technique," ASME J. Heat Transfer, **127**(3), pp. 315–322.
[9] Ju, Y. S., Kurabayashi, K., and Goodson, K. E., 1999, "Thermal Characterization of Anisotropic Thin Dielectric Films Using Harmonic Joule Heating," Thin Solid Films, **339**(1–2), pp. 160–164.
[10] Jain, A., and Goodson, K. E., 2008, "Measurement of the Thermal Conductivity and Heat Capacity of Freestanding Shape Memory Thin Films Using the 3ω Method," ASME J. Heat Transfer, **130**(10), p. 102402.
[11] Mavrokefalos, A., Pettes, M. T., Zhou, F., and Shi, L., 2007, "Four-Probe Measurements of the In-Plane Thermoelectric Properties of Nanofilms," Rev. Sci. Instrum., **78**(3), p. 034901.
[12] Zink, B. L., Revaz, B., Cherry, J. J., and Hellman, F., 2005, "Measurement of Thermal Conductivity of Thin Films With a Si-N Membrane-Based Microcalorimeter," Rev. Sci. Instrum., **76**(2), p. 024901.
[13] Nair, R. R., Blake, P., Grigorenko, A. N., Novoselov, K. S., Booth, T. J., Stauber, T., Peres, N. M. R., and Geim, A. K., 2008, "Fine Structure Constant Defines Visual Transparency of Graphene," Science, **320**(5881), pp. 1308.
[14] Faugeras, C., Faugeras, B., Orlita, M., Potemski, M., Nair, R. R., and Geim, A. K., 2010, "Thermal Conductivity of Graphene in Corbino Membrane Geometry," ACS Nano, **4**(4), pp. 1889–1892.
[15] Cai, W., Moore, A. L., Zhu, Y., Li, X., Chen, S., Shi, L., and Ruoff, R. S., 2010, "Thermal Transport in Suspended and Supported Monolayer Graphene Grown by Chemical Vapor Deposition," Nano Lett., **10**(5), pp. 1645–1651.
[16] Klemens, P. G., 2001, "Theory of Thermal Conduction in Thin Ceramic Films," Int. J. Thermophys., **22**(1), pp. 265–275.
[17] Prasher, R., 2007, "Thermal Conductance of Single-Walled Carbon Nanotube Embedded in an Elastic Half-Space," Appl. Phys. Lett., **90**(14), p. 143110.
[18] Seol, J. H., Jo, I., Moore, A. L., Lindsay, L., Aitken, Z. H., Pettes, M. T., Li, X., Yao, Z., Huang, R., Broido, D., Mingo, N., Ruoff, R. S., and Shi, L., 2010, "Two-Dimensional Phonon Transport in Supported Graphene," Science, **328**(5975), pp. 213–216.
[19] Blake, P., Hill, E. W., Castro Neto, A. H., Novoselov, K. S., Jiang, D., Yang, R., Booth, T. J., and Geim, A. K., 2007, "Making Graphene Visible," Appl. Phys. Lett., **91**(6), p. 063124.
[20] Abergel, D. S. L., Russell, A., and Fal'ko, V. I., 2007, "Visibility of Graphene Flakes on a Dielectric Substrate," Appl. Phys. Lett., **91**(6), p. 063125.
[21] Ferrari, A. C., and Robertson, J., 2000, "Interpretation of Raman Spectra of Disordered and Amorphous Carbon," Phys. Rev. B, **61**(20), pp. 14095–14107.
[22] Incropera, F. P., DeWitt, P. D., Bergman, T. L., and Lavine, A. L., 2007, *Fundamentals of Heat and Mass Transfer*, Wiley, Hoboken, NJ.
[23] Schmidt, A. J., Chen, X., and Chen, G., 2008, "Pulse Accumulation, Radial Heat Conduction, and Anisotropic Thermal Conductivity in Pump-Probe Transient Thermoreflectance," Rev. Sci. Instrum., **79**(11), p. 114902.
[24] Li, Q. W., Liu, C. H., and Fan, S. S., 2009, "Thermal Boundary Resistances of Carbon Nanotubes in Contact With Metals and Polymers," Nano Lett., **9**(11), pp. 3805–3809.
[25] Persson, A. I., Koh, Y. K., Cahill, D. G., Samuelson, L., and Linke, H., 2009, "Thermal Conductance of InAs Nanowire Composites," Nano Lett., **9**(12), pp. 4484–4488.
[26] Chen, Z., Jang, W., Bao, W., Lau, C. N., and Dames, C., 2009, "Thermal Contact Resistance Between Graphene and Silicon Dioxide," Appl. Phys. Lett., **95**(16), p. 161910.
[27] Ashcroft, N. W., and Mermin, N. D., 1976, *Solid State Physics*, Saunders College Publishing, Fort Worth, TX.
[28] Cahill, D. G., 1990, "Thermal Conductivity Measurement From 30 to 750 K: The 3ω Method," Rev. Sci. Instrum., **61**(2), pp. 802–808.
[29] Al-Jishi, R., and Dresselhaus, G., 1982, "Lattice-Dynamical Model for Graphite," Phys. Rev. B, **26**(8), pp. 4514–4522.
[30] Zhang, Q. G., Cao, B. Y., Zhang, X., Fujii, M., and Takahashi, K., 2006, "Size Effects on the Thermal Conductivity of Polycrystalline Platinum Nanofilms," J. Phys.: Condens. Matter, **18**, pp. 7937–7950.
[31] Zhang, X., Xie, H., Fujii, M., Ago, H., Takahashi, K., Ikuta, T., Abe, H., and Shimizu, T., 2005, "Thermal and Electrical Conductivity of a Suspended Platinum Nanofilm," Appl. Phys. Lett., **86**, p. 171912.
[32] Slack, G. A., 1962, "Anisotropic Thermal Conductivity of Pyrolytic Graphite," Phys. Rev., **127**(3), pp. 694–701.
[33] Nath, P., and Chopra, K. L., 1974, "Thermal Conductivity of Copper Films," Thin Solid Films, **20**(1), pp. 53–62.
[34] Ju, Y. S., and Goodson, K. E., 1999, "Phonon Scattering in Silicon Films With Thickness of Order 100 nm," Appl. Phys. Lett., **74**(20), pp. 3005–3007.

Numerical Analysis of the Time-Dependent Energy and Momentum Transfers in a Rarefied Gas Between Two Parallel Planes Based on the Linearized Boltzmann Equation

Toshiyuki Doi
Assistant Professor
Department of Applied Mathematics and Physics,
Tottori University,
Tottori 680-8552, Japan
e-mail: doi@damp.tottori-u.ac.jp

Periodic time-dependent behavior of a rarefied gas between two parallel planes caused by an oscillatory heating of one plane is numerically studied based on the linearized Boltzmann equation. Detailed numerical data of the energy transfer from the heated plane to the unheated plane and the forces of the gas acting on the boundaries are provided for a wide range of the gas rarefaction degree and the oscillation frequency. The flow is characterized by a coupling of heat conduction and sound waves caused by repetitive expansion and contraction of the gas. For a small gas rarefaction degree, the energy transfer is mainly conducted by sound waves, except for very low frequencies, and is strongly affected by the resonance of the waves. For a large gas rarefaction degree, the resonance effects become insignificant and the energy transferred to the unheated plane decreases nearly monotonically as the frequency increases. The force of the gas acting on the heated boundary shows a remarkable minimum with respect to the frequency even in the free molecular limit. [DOI: 10.1115/1.4002441]

Keywords: Boltzmann equation, rarefied gas, microflow, oscillatory heating

1 Introduction

The flow of a rarefied gas has been studied extensively for more than five decades, and the behaviors of various fundamental flows have been clarified [1–4]. These results have been successfully applied to vacuum and micro-engineering and have made important contributions to modern technologies [1,3,4]. In the last two decades, studies of flows in micro-electromechanical systems (MEMS) have greatly developed. These studies were first developed by focusing on mass transfer. Energy transfer in a micro- or vacuum system is also important, for example, in the cooling of micro-electrical devices. The collective study of energy transfer is, however, not as extensive as that of mass transfer and is thus a currently developing field [3,5–8].

From a theoretical point of view, there is a comprehensive accumulation of the studies on the energy transfer in a rarefied gas [9–19]. These studies mainly focus on time-independent problems. In a microsystem, where the characteristic length is very small, a time-independent analysis is sufficient for many applications. In a vacuum system, on the other hand, where the characteristic length is arbitrary, studies based on the full time-dependent equation may be necessary. For an understanding of the basic properties of a flow, an analysis of the periodic time-dependent behavior of a gas between parallel planes is fundamental. To the knowledge of the author, however, no systematic analysis of this fundamental problem based on the Boltzmann equation has been conducted. Incidentally, a transient flow of a gas caused by a sudden change in the boundary temperature, which is the counterpart of the periodic time-dependent problem, is a type of basic problem of a rarefied gas flow [20–22]. In Refs. [20,21], a transient motion of a rarefied gas caused by a sudden change in the plate temperature is accurately analyzed, and the energy transferred from the infinite plate to the half space is studied. Analysis of a motion of a confined gas caused by a temperature disturbance of the boundary is conducted based on the classical fluid dynamics in Refs. [23,24].

In the present study, we will conduct a numerical analysis of the periodic time-dependent behavior of a rarefied gas between two parallel planes caused by an oscillatory heating of one plane based on the linearized Boltzmann equation for a hard-sphere molecular gas. The goals of this study are to provide detailed numerical data of the energy transfer from the heated wall to the other and to clarify the behavior of the gas for a wide range of the gas rarefaction degree and the oscillation frequency. As we will show in Sec. 5, the present flow is characterized by a coupling of heat conduction and sound waves and is more complicated than a time-independent heat transfer problem. Thus the behavior of the flow field is discussed in detail because it leads to an understanding of the energy transfer. Recently, Manela and Hadjiconstantinou [25,26] considered a similar flow and developed a numerical scheme for the gas motion for an arbitrary time variation of the boundary temperature based on the collisionless Boltzmann equation. The present study considers only the periodic time variation and, in turn, an arbitrary gas rarefaction degree.

2 Problem and Basic Equation

2.1 Problem. Consider a rarefied gas between two parallel planes placed at rest at $X_1=0$ and $X_1=L$, where X_i is the space rectangular coordinates. No external force such as gravitation is present. The temperature T_0 of the plane at $X_1=L$ is constant,

Contributed by the Heat Transfer Division of ASME for publication in the JOURNAL OF HEAT TRANSFER. Manuscript received March 27, 2010; final manuscript received July 22, 2010; published online November 3, 2010. Assoc. Editor: Pamela M. Norris.

while that T_w of the other plane at $X_1=0$ varies in time as $T_w(t)=T_0(1+\Delta\tau\cos\omega t)$ (t is the time). We study the periodic time-dependent behavior of the gas based on kinetic theory. We carry out the analysis under the following assumptions: (i) the gas behavior is governed by the Boltzmann equation for a hard-sphere molecular gas, (ii) the gas molecules make diffuse reflection on the boundaries, and (iii) the relative temperature variation $\Delta\tau$ of the plane is so small that the equation and the boundary condition may be linearized.

2.2 Basic Equation. The basic equation is the linearized Boltzmann equation for the spatially one dimensional case

$$\frac{\partial\phi}{\partial\hat{t}}+\zeta_1\frac{\partial\phi}{\partial x_1}=\frac{2}{\sqrt{\pi}\ \mathrm{Kn}}\mathcal{L}(\phi) \tag{1}$$

where $\hat{t}=t/[L(2RT_0)^{-1/2}]$, $x_i=X_i/L$, and $\zeta_i=\xi_i/(2RT_0)^{1/2}$ are, respectively, the nondimensional variables of the time t, space coordinates X_i, and the molecular velocity ξ_i. $\phi=f/[\rho_0(2RT_0)^{-3/2}E]-1$ is the perturbation of the velocity distribution function f from the equilibrium state at rest with the density ρ_0 and the temperature T_0, $E=\pi^{-3/2}\exp(-\zeta_i^2)$, R is the specific gas constant, and ρ_0 is the mean density of the gas. $\mathrm{Kn}=\ell/L$ is the Knudsen number, where $\ell=1/(\sqrt{2}\pi d_m^2\rho_0 m^{-1})$ is the mean free path of the gas in the equilibrium state at rest with the density ρ_0, and m and d_m are, respectively, the mass and the diameter of a molecule. $\mathcal{L}(\phi)$ is the linearized collision integral defined by

$$\mathcal{L}(\phi)=\int_{\text{all }\zeta_*}K(\boldsymbol{\zeta},\boldsymbol{\zeta}_*)\phi(\boldsymbol{\zeta}_*)\mathbf{d}\boldsymbol{\zeta}_*-\nu_L(\boldsymbol{\zeta})\phi(\boldsymbol{\zeta}) \tag{2}$$

where

$$K(\boldsymbol{\zeta},\boldsymbol{\zeta}_*)=\frac{1}{\sqrt{2}\pi}\left[\frac{1}{|\boldsymbol{\zeta}_*-\boldsymbol{\zeta}|}\exp\left(\frac{|\boldsymbol{\zeta}_*\times\boldsymbol{\zeta}|^2}{|\boldsymbol{\zeta}_*-\boldsymbol{\zeta}|^2}\right)-\frac{|\boldsymbol{\zeta}_*-\boldsymbol{\zeta}|}{2}\right]\exp(-\boldsymbol{\zeta}_*^2) \tag{3}$$

$$\nu_L(\boldsymbol{\zeta})=\frac{1}{2\sqrt{2}}\left[\exp(-\zeta^2)+\left(2\zeta+\frac{1}{\zeta}\right)\int_0^{\zeta}\exp(-\zeta_*^2)\mathrm{d}\zeta_*\right] \tag{4}$$

for a hard-sphere molecular gas and

$$K(\boldsymbol{\zeta},\boldsymbol{\zeta}_*)=\pi^{-3/2}\left[1+2\boldsymbol{\zeta}\cdot\boldsymbol{\zeta}_*+\tfrac{2}{3}\left(\boldsymbol{\zeta}^2-\tfrac{3}{2}\right)\left(\boldsymbol{\zeta}_*^2-\tfrac{3}{2}\right)\right]\exp(-\boldsymbol{\zeta}_*^2),\quad \nu_L=1 \tag{5}$$

for the Boltzmann-Krook-Welander (BKW) equation or Bhatnagar-Gross-Krook (BGK) model [27,28]l, with $\zeta=|\boldsymbol{\zeta}|$ and $\mathbf{d}\boldsymbol{\zeta}_*=\mathrm{d}\zeta_{1*}\mathrm{d}\zeta_{2*}\mathrm{d}\zeta_{3*}$.

The boundary condition is the diffuse reflection condition,

$$\phi=(\zeta_i^2-2)\Delta\tau\cos\Omega\hat{t}-2\sqrt{\pi}\int_{\zeta_1<0}\zeta_1\phi E\mathbf{d}\boldsymbol{\zeta}\quad(x_1=0,\zeta_1>0) \tag{6}$$

$$\phi=2\sqrt{\pi}\int_{\zeta_1>0}\zeta_1\phi E\mathbf{d}\boldsymbol{\zeta}\quad(x_1=1,\zeta_1<0) \tag{7}$$

where $\Omega=\omega L/(2RT_0)^{1/2}$ is the nondimensional frequency of the oscillation or the Strouhal number.

The macroscopic variables of the gas, the density ρ, the flow velocity v_i, the temperature T, the pressure p, the stress tensor p_{ij}, and the heat flow vector q_i, are given as

$$\rho/\rho_0=1+\int\phi E\mathbf{d}\boldsymbol{\zeta},$$

$$v_i/(2RT_0)^{1/2}=\int\zeta_i\phi E\mathbf{d}\boldsymbol{\zeta}$$

$$T/T_0=1+\frac{2}{3}\int\left(\zeta_i^2-\frac{3}{2}\right)\phi E\mathbf{d}\boldsymbol{\zeta},\quad p/p_0=1+\frac{2}{3}\int\zeta_i^2\phi E\mathbf{d}\boldsymbol{\zeta} \tag{8}$$

$$p_{ij}/p_0=\delta_{ij}+2\int\zeta_i\zeta_j\phi E\mathbf{d}\boldsymbol{\zeta},$$

$$q_i/[p_0(2RT_0)^{1/2}]=\int\zeta_i\left(\zeta_i^2-\frac{5}{2}\right)\phi E\mathbf{d}\boldsymbol{\zeta}$$

where $p_0=R\rho_0T_0$, $\mathbf{d}\boldsymbol{\zeta}=\mathrm{d}\zeta_1\mathrm{d}\zeta_2\mathrm{d}\zeta_3$, and the range of integration is the whole space of ζ_i.

In this problem, we can seek the solution in the form [1]

$$\phi(x_1,\zeta_i,\hat{t})/\Delta\tau=\mathrm{Re}[\exp(-\mathrm{i}\Omega\hat{t})\Phi(x_1,\zeta_1,\zeta_\rho)] \tag{9}$$

where $\zeta_\rho=(\zeta_2^2+\zeta_3^2)^{1/2}$, $\mathrm{i}=\sqrt{-1}$, and $\mathrm{Re}[*]$ denotes the real part of $*$. Substituting Eq. (9) into Eqs. (1), (6), and (7), we are led to the boundary value problem of the spatially one dimensional Boltzmann equation:

$$-\mathrm{i}\Omega\Phi+\zeta_1\frac{\partial\Phi}{\partial x_1}=\frac{2}{\sqrt{\pi}\mathrm{Kn}}\mathcal{L}(\Phi) \tag{10}$$

$$\Phi=(\zeta_1^2+\zeta_\rho^2-2)-4\int_{-\infty}^{0}\int_0^{\infty}\zeta_1\zeta_\rho\Phi\exp(-\zeta_1^2-\zeta_\rho^2)\mathrm{d}\zeta_\rho\mathrm{d}\zeta_1$$

$$(x_1=0,\zeta_1>0) \tag{11}$$

$$\Phi=4\int_0^{\infty}\int_0^{\infty}\zeta_1\zeta_\rho\Phi\exp(-\zeta_1^2-\zeta_\rho^2)\mathrm{d}\zeta_\rho\mathrm{d}\zeta_1\quad(x_1=1,\zeta_1<0) \tag{12}$$

This boundary value problem (10)–(12) is characterized by the two parameters, the Knudsen number Kn and the nondimensional frequency Ω. We will solve this problem numerically for various set of Kn and Ω.

The macroscopic variables of the gas are, correspondingly,

$$(\rho/\rho_0-1)/\Delta\tau=\mathrm{Re}[\exp(-\mathrm{i}\Omega\hat{t})\mathrm{D}(x_1)] \tag{13}$$

$$v_1/[(2RT_0)^{1/2}\Delta\tau]=\mathrm{Re}[\exp(-\mathrm{i}\Omega\hat{t})\mathrm{U}(x_1)],\quad v_2=v_3=0 \tag{14}$$

$$(T/T_0-1)/\Delta\tau=\mathrm{Re}[\exp(-\mathrm{i}\Omega\hat{t})\mathrm{T}(x_1)] \tag{15}$$

$$(p_{11}/p_0-1)/\Delta\tau=\mathrm{Re}[\exp(-\mathrm{i}\Omega\hat{t})\mathrm{P}(x_1)] \tag{16}$$

$$q_1/[p_0(2RT_0)^{1/2}\Delta\tau]=\mathrm{Re}[\exp(-\mathrm{i}\Omega\hat{t})\mathrm{Q}(x_1)],\quad q_2=q_3=0 \tag{17}$$

where D, U, T, P, and Q are the complex-valued functions of x_1 and are given by

$$\mathrm{D}=2\pi^{-1/2}\int_{-\infty}^{\infty}\int_0^{\infty}\zeta_\rho\Phi\exp(-\zeta_1^2-\zeta_\rho^2)\mathrm{d}\zeta_\rho\mathrm{d}\zeta_1 \tag{18}$$

$$\mathrm{U}=2\pi^{-1/2}\int_{-\infty}^{\infty}\int_0^{\infty}\zeta_1\zeta_\rho\Phi\exp(-\zeta_1^2-\zeta_\rho^2)\mathrm{d}\zeta_\rho\mathrm{d}\zeta_1 \tag{19}$$

$$\mathrm{T}=\frac{4}{3}\pi^{-1/2}\int_{-\infty}^{\infty}\int_0^{\infty}\zeta_\rho(\zeta_1^2+\zeta_\rho^2)\Phi\exp(-\zeta_1^2-\zeta_\rho^2)\mathrm{d}\zeta_\rho\mathrm{d}\zeta_1-\mathrm{D} \tag{20}$$

$$\mathrm{P}=4\pi^{-1/2}\int_{-\infty}^{\infty}\int_0^{\infty}\zeta_1^2\zeta_\rho\Phi\exp(-\zeta_1^2-\zeta_\rho^2)\mathrm{d}\zeta_\rho\mathrm{d}\zeta_1 \tag{21}$$

$$\mathrm{Q} = 2\pi^{-1/2}\int_{-\infty}^{\infty}\int_{0}^{\infty}\zeta_1\zeta_\rho(\zeta_1^2+\zeta_\rho^2)\Phi\,\exp(-\zeta_1^2-\zeta_\rho^2)\mathrm{d}\zeta_\rho\mathrm{d}\zeta_1 - \frac{5}{2}\mathrm{U} \tag{22}$$

The force $(F_1,0,0)$ of the gas acting on the walls per unit area and the energy flow vector $(W_1,0,0)$ at the walls per unit time and per unit area are expressed in terms of P and Q at $x_1=0$ and $x_1=1$ [1]:

$$(\nu F_1/p_0 - 1)/\Delta\tau = \mathrm{Re}[\exp(-\mathrm{i}\Omega\hat{t})\mathrm{P}] \tag{23}$$

$$W_1/[p_0(2RT_0)^{1/2}\Delta\tau] = \mathrm{Re}[\exp(-\mathrm{i}\Omega\hat{t})\mathrm{Q}] \tag{24}$$

where $\nu=-1(x_1=0)$ or $=1(x_1=1)$, since the flow velocity vanishes there due to the boundary conditions (6) and (7). Here we give some remarks on the energy flow W_1. In the present problem, according to the form (9) of the solution, all the perturbed variables make a sinusoidal variation in time, and thus all the variables integrated with respect to time over one period $2\pi/\omega$ vanish. The energy flow W_1 at $x_1=1$ expresses how the wall is subject to an oscillatory heating as the consequence of the heating of the other wall and the energy transfer through the gas. In this paper, we use the term *energy transfer*, although the energy goes and backs the same amount in one period and there is no one-way energy transfer as is present in the time-independent problem.

Multiplying Eq. (10) by E, $\zeta_1 E$, or $(\zeta_1^2+\zeta_\rho^2)E$, integrating the result with respect to ζ_1 and ζ_ρ for the range $-\infty<\zeta_1<\infty$ and $0<\zeta_\rho<\infty$, respectively, and then integrating with respect to x_1 from 0 to x_1 and taking the boundary condition Eq. (11) into account, we have

$$-\mathrm{i}\Omega\int_0^{x_1}\mathrm{D}(x_{1*})\mathrm{d}x_{1*} + \mathrm{U}(x_1) = 0 \tag{25}$$

$$-\mathrm{i}\Omega\int_0^{x_1}\mathrm{U}(x_{1*})\mathrm{d}x_{1*} + \frac{1}{2}[\mathrm{P}(x_1)-\mathrm{P}(0)] = 0 \tag{26}$$

$$-\frac{3}{2}\mathrm{i}\Omega\int_0^{x_1}[\mathrm{T}(x_{1*})+\mathrm{D}(x_{1*})]\mathrm{d}x_{1*} + \left[\mathrm{Q}(x_1)-\mathrm{Q}(0)+\frac{5}{2}\mathrm{U}(x_1)\right] = 0 \tag{27}$$

Equations (25)–(27) represent the conservation of mass, momentum, and energy. These equations will be used for the test of accuracy in Sec. 5.4.

3 Numerical Analysis

The boundary value problem (10)–(12) is solved using a finite difference method. The collision integral is evaluated with the aid of the numerical kernel method [29]. In this method, the distribution function Φ is expanded by a set of basis functions in (ζ_1,ζ_ρ). Then, the collision integral is reduced to the product of a matrix of known coefficients (basis functions operated upon by the collision integral) and that of the values of the distribution functions at the lattice points in (ζ_1,ζ_ρ). This method is well established and has been applied to various time-independent problems [16,30–34], etc. It is also applicable to the present time-dependent problem without any modification. The finite difference scheme is a spatially second order scheme, which is essentially the same as that used in Ref. [29].

As a characteristic of the present time-dependent problem, the velocity distribution function Φ varies rapidly in ζ_1 for a large Ω. The numerical kernel method was developed by assuming that the velocity distribution function is gentle except in the neighborhood of $\zeta_1=0$; thus this characteristic makes the application of the method invalid. To avoid this difficulty, we employ the method devised in Ref. [35]. That is, we deal with the difference $\Phi-\Phi_\#$ instead of directly dealing with Φ, where $\Phi_\#$ is the solution of the boundary value problem equations (10)–(12) with the collision gain term (the first term on the right-hand side of Eq. (2)) being dropped. Then, we have a problem similar to Eqs. (10)–(12) for $\Phi-\Phi_\#$ with an inhomogeneous term. The inhomogeneous term is a known function and can be accurately computed beforehand. Because the remainder $\Phi-\Phi_\#$ is considerably small, we can carry out an accurate numerical analysis up to considerably large values of Ω.

4 Navier–Stokes and Free Molecular Solutions

Before presenting the numerical results, we give the solutions of the Navier–Stokes equation and the collisionless Boltzmann equation.

The Navier–Stokes solution is easily obtained and we have

$$\mathrm{U} = \frac{3}{2\alpha_1}(\gamma_b\ \mathrm{Kn}\ \alpha_1^2-\mathrm{i}\Omega)(-A_1\sin\alpha_1x_1 + B_1\cos\alpha_1x_1 - \delta^{-1}A_2\sin\alpha_2x_1 + \delta^{-1}B_2\cos\alpha_2x_1) \tag{28}$$

$$\mathrm{T} = A_1\cos\alpha_1x_1 + B_1\sin\alpha_1x_1 + A_2\cos\alpha_2x_1 + B_2\sin\alpha_2x_1 \tag{29}$$

$$\mathrm{P} = \mathrm{T} + \mathrm{i}\frac{3}{2\Omega}(1-2\mathrm{i}\gamma_a\ \mathrm{Kn}\ \Omega)(\gamma_b\ \mathrm{Kn}\ \alpha_1^2-\mathrm{i}\Omega)\left(A_1\cos\alpha_1x_1 + B_1\sin\alpha_1x_1 + \frac{\alpha_2}{\delta\alpha_1}A_2\cos\alpha_2x_1 + \frac{\alpha_2}{\delta\alpha_1}B_2\sin\alpha_2x_1\right) \tag{30}$$

$$\mathrm{Q} = \tfrac{3}{2}\gamma_b\ \mathrm{Kn}(\alpha_1A_1\sin\alpha_1x_1 - \alpha_1B_1\cos\alpha_1x_1 + \alpha_2A_2\sin\alpha_2x_1 - \alpha_2B_2\cos\alpha_2x_1) \tag{31}$$

where

$$A_1 = \frac{\delta(\cos\alpha_1\cos\alpha_2-1)+\sin\alpha_1\sin\alpha_2}{2\delta(\cos\alpha_1\cos\alpha_2-1)+(\delta^2+1)\sin\alpha_1\sin\alpha_2} \tag{32}$$

$$B_1 = \frac{\delta\sin\alpha_1\cos\alpha_2-\cos\alpha_1\sin\alpha_2}{2\delta(\cos\alpha_1\cos\alpha_2-1)+(\delta^2+1)\sin\alpha_1\sin\alpha_2} \tag{33}$$

$$A_2 = 1-A_1, \quad B_2 = -\delta B_1 \tag{34}$$

$$\delta = \frac{\alpha_2}{\alpha_1}\frac{\gamma_b\ \mathrm{Kn}\ \alpha_1^2-\mathrm{i}\Omega}{\gamma_b\ \mathrm{Kn}\ \alpha_2^2-\mathrm{i}\Omega} \tag{35}$$

$$\gamma_a = \sqrt{\pi}\gamma_1/3, \quad \gamma_b = 5\sqrt{\pi}\gamma_2/12 \tag{36}$$

and α_1 and α_2 are the square roots $\sqrt{z_1}$ and $\sqrt{z_2}$ of the solutions z_1 and z_2 of the following quadratic equation:

$$z^2 - \mathrm{i}\frac{5\Omega}{3}\frac{1-(6/5)(\gamma_a+\gamma_b)\Omega\ \mathrm{Kn}}{\gamma_b(1-2\mathrm{i}\gamma_a\Omega\ \mathrm{Kn})\mathrm{Kn}}z + \frac{2\mathrm{i}\Omega^3}{\gamma_b(1-2\mathrm{i}\gamma_a\Omega\ \mathrm{Kn})\mathrm{Kn}} = 0 \tag{37}$$

In the solutions (28)–(31), we used the following relation between the viscosity μ, the thermal conductivity λ, and the mean free path ℓ [1]:

$$\mu = \gamma_1\frac{\sqrt{\pi}}{2}\frac{p_0}{(2RT_0)^{1/2}}\ell, \quad \lambda = \gamma_2\frac{5\sqrt{\pi}}{4}\frac{Rp_0}{(2RT_0)^{1/2}}\ell \tag{38}$$

where γ_1 and γ_2 are constants determined by the molecular model, e.g., $\gamma_1=1.270042$, $\gamma_2=1.922284$ for a hard-sphere gas and $\gamma_1=\gamma_2=1$ for the BKW model. As is well known, the spatial variations in α_1 and α_2 correspond to the sound mode and the thermal mode [36]. Incidentally, the solution of the heat conduction equation is given as

$$\mathrm{T} = \frac{\sinh\sqrt{\mathrm{i}}\beta_*(1-x_1)}{\sinh\sqrt{\mathrm{i}}\beta_*} \tag{39}$$

$$\mathrm{Q} = \sqrt{\mathrm{i}}\frac{3}{2}\gamma_b\beta_* \ \mathrm{Kn}\frac{\cosh\sqrt{\mathrm{i}}\beta_*(1-x_1)}{\sinh\sqrt{\mathrm{i}}\beta_*} \tag{40}$$

where

$$\beta_* = (4\Omega/\sqrt{\pi}\gamma_2 \ \mathrm{Kn})^{1/2} \tag{41}$$

is the Stokes number associated with the thermal diffusivity $a[=\lambda(5R\rho_0/2)^{-1}]$ and is expressed in terms of the dimensional quantities as $\beta_*=(\omega/a)^{1/2}L$.

Next we show the solution of the collisionless Boltzmann equation. When the Knudsen number Kn is large, the collision term may be neglected and the Boltzmann equation can be solved easily. On the other hand, when the frequency Ω is large compared with Kn^{-1}, the collision term is negligible compared with the time derivative term. In both cases, the solution is given by the following solution (free molecular solution). This situation is common to some periodic time-dependent problems [37,38]. The macroscopic variables are given as

$$\mathrm{U} = \frac{1}{\sqrt{\pi}}[J_3(-\mathrm{i}\Omega x_1) + (2CJ_* - 1)J_1(-\mathrm{i}\Omega x_1) - CJ_1(-\mathrm{i}\Omega(1-x_1))] \tag{42}$$

$$\mathrm{T} = \frac{2}{3\sqrt{\pi}}\left[J_4(-\mathrm{i}\Omega x_1) + \left(2CJ_* - \frac{3}{2}\right)J_2(-\mathrm{i}\Omega x_1) - \left(CJ_* - \frac{3}{2}\right) \times J_0(-\mathrm{i}\Omega x_1) + CJ_2(-\mathrm{i}\Omega(1-x_1)) - \frac{C}{2}J_0(-\mathrm{i}\Omega(1-x_1))\right] \tag{43}$$

$$\mathrm{P} = \frac{2}{\sqrt{\pi}}[J_4(-\mathrm{i}\Omega x_1) + (2CJ_* - 1)J_2(-\mathrm{i}\Omega x_1) + CJ_2(-\mathrm{i}\Omega(1-x_1))] \tag{44}$$

$$\mathrm{Q} = \frac{1}{\sqrt{\pi}}\left[J_5(-\mathrm{i}\Omega x_1) + \left(2CJ_* - \frac{5}{2}\right)J_3(-\mathrm{i}\Omega x_1) - \left(3CJ_* - \frac{5}{2}\right) \times J_1(-\mathrm{i}\Omega x_1) - CJ_3(-\mathrm{i}\Omega(1-x_1)) + \frac{3C}{2}J_1(-\mathrm{i}\Omega(1-x_1))\right] \tag{45}$$

where

$$C = 2\frac{J_3(-\mathrm{i}\Omega) - J_1(-\mathrm{i}\Omega)}{1 - 4J_1(-\mathrm{i}\Omega)^2}, \quad J_* = J_1(-\mathrm{i}\Omega)$$

and

$$J_n(\mathrm{z}) = \int_0^\infty \zeta^n \exp\left(-\zeta^2 - \frac{z}{\zeta}\right)\mathrm{d}\zeta \tag{46}$$

is the Abramowitz function [39]. In the limit of the infinitely large Ω, the macroscopic variables vanish except at $x_1=0$ and we have

$$\mathrm{P} \to 1/4 \quad \text{and} \quad \mathrm{Q} \to 1/\sqrt{\pi} \quad \text{at} \quad x_1 = 0 \tag{47}$$

5 Results and Discussion

5.1 Macroscopic Variables. We first show the profile of the macroscopic variables. As explained in Sec. 2.2 (Eqs. (13)–(17)), the flow velocity, normal stress, temperature, and heat flow are expressed in terms of the complex-valued functions U, P, T, and Q. We show the amplitudes (or absolute values) |U|, |P|, |T|, and |Q| for the Knudsen number Kn=0.01, 0.1, and 10 in Figs. 1–3, respectively. For the convenience of explanation, we also use the following ω/ω_0 as well as Ω:

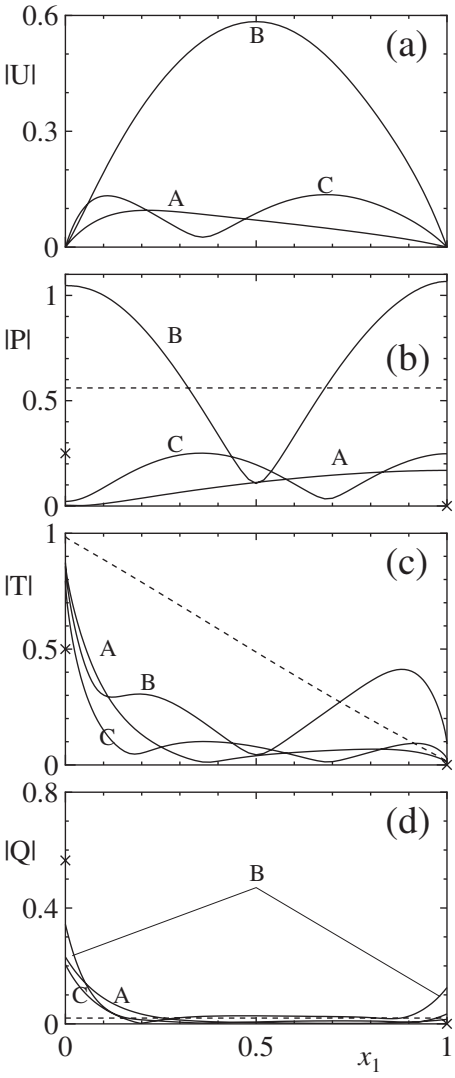

Fig. 1 The profile of the macroscopic variables (I) Kn=0.01. (A) ω/ω_0=1.032, (B) 1.939, and (C) 3.068. (*a*) The amplitude U of the flow velocity, (*b*) normal stress P, (*c*) temperature T, and (*d*) heat flow Q (see Eqs. (14)–(17)). Solid line (——): present result (hard-sphere gas), dotted line (- - -): time-independent solution (ω=0) [16], and cross (×): solution in the limit $\omega\to\infty$ (Eq. (47)).

$$\frac{\omega}{\omega_0} = \frac{2}{\pi}\left(\frac{6}{5}\right)^{1/2}\Omega \quad \text{where} \quad \omega_0 = \frac{\pi}{2L}\left(\frac{5}{3}RT_0\right)^{1/2} \tag{48}$$

is the fundamental standing-wave frequency of a pipe of length L with one closed end. In Figs. 1–3, the parameter ω/ω_0 (or Ω) is chosen such that the normal stress at $x_1=0$ takes local minima and local maxima with respect to ω/ω_0. The solid line is the present result for a hard-sphere gas. The dotted line is the solution of the time-independent heat transfer problem ($\omega=0$) [16], for which P and Q are uniform and U vanishes identically (see Eqs. (25)–(27)), and the cross × is the solution in the limit $\omega\to\infty$ (Eq. (47)), where the macroscopic variables vanish except at $x_1=0$.

Figure 1 shows the case where the Knudsen number Kn is relatively small (Kn=0.01). In this case, the gas behavior is understood with the aid of fluid dynamics. Due to the oscillatory heating of the wall at $x_1=0$, an oscillating heat flow arises from this wall. As the frequency increases, the decay of the heat flow becomes rapid as is inferred from the solution of the heat conduction equation (Eq. (40)). On the other hand, the gas is subject to a repetitive expansion and contraction by this heating so that sound waves are generated in the gas owing to this piston effect. The

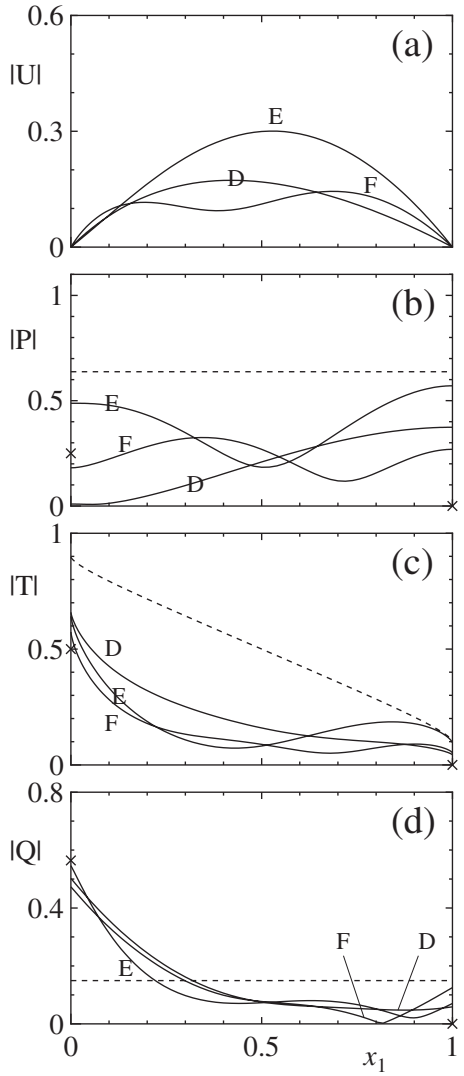

Fig. 2 The profile of the macroscopic variables (II) Kn=0.1. (D) ω/ω_0=1.165, (E) 1.953, and (F) 3.347. See the caption of Fig. 1.

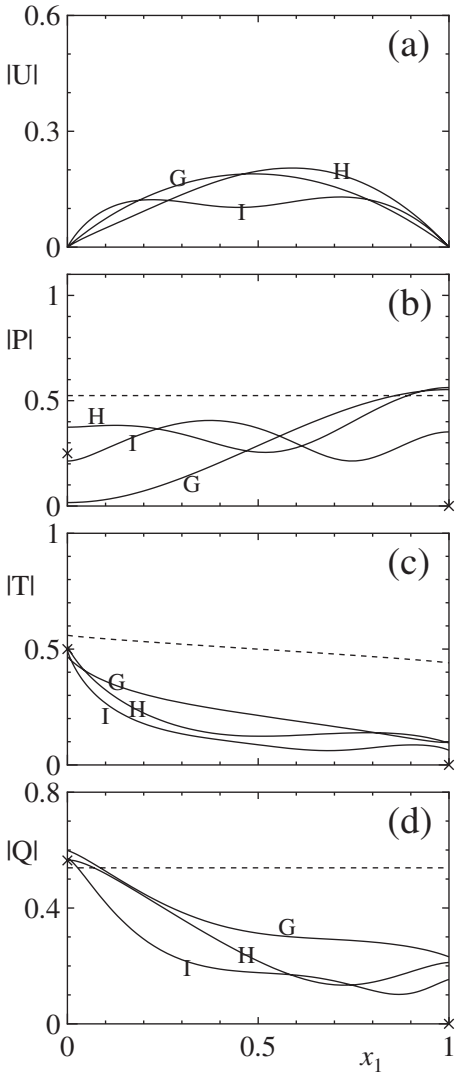

Fig. 3 The profile of the macroscopic variables (III) Kn=10. (G) ω/ω_0=1.541, (H) 2.580, and (I) 4.533. See the caption of Fig. 1.

sound waves propagate and reflect off the other wall at $x_1=1$, and forward and backward waves are superimposed. As is expected from acoustics, standing waves are formed when ω/ω_0 is close to an integer. Case A ($\omega/\omega_0=1.03$) is the state of the first standing wave with a wavelength of $\sim 4L$, or, in acoustic terms, a node is located at $x_1=1$ and an antinode (or loop) is found at about $x_1=0$. In this case, the normal stress on the wall at $x_1=0$ becomes considerably small. The gas motion is driven by the oscillatory heating at $x_1=0$, while the flow velocity should vanish at $x_1=0$ due to the boundary condition (6). Thus, an antinode cannot be located at $x_1=0$ and instead should be slightly within the gas region. Case B ($\omega/\omega_0=1.94$) is the state of the second standing wave, i.e., a wavelength of $\sim 4L/2$. In this case, the normal stress, as well as the flow velocity, is highly excited (resonant state). The flow velocity has nodes at $x_1=0$ and $x_1=1$ and an antinode at about $x_1=1/2$. In this case, the node at $x_1=0$ is consistent with the boundary condition (6) so the flow velocity and the normal stress are nearly symmetric with respect to $x_1=1/2$. Case C ($\omega/\omega_0=3.07$) is the state of the third standing wave, i.e., a wavelength of $\sim 4L/3$. In this case, the normal stress at $x_1=0$ has a small value as in case A. The flow velocity has another node in the gas at about $x_1\sim 1/3$. In these three cases, the heat flow in the central region of the gas is considerably small due to the small thermal conductivity. On the other hand, the heat flow at $x_1=1$, which is the same as the energy flow at that point, is considerably large compared with that in the middle of the gas. This is because most of the energy is transferred by sound waves rather than by heat conduction, except at very low frequencies. This characteristic is most remarkable in the resonant state (case B).

For a slightly larger Knudsen number Kn=0.1 (Fig. 2), the induced normal stress, as well as the flow velocity, in the resonant state (case E) is smaller than that of the corresponding case (case B) for the smaller Knudsen number Kn=0.01, while the heat flow in the central region of the gas is larger. For a large Knudsen number, Kn=10 (Fig. 3), the resonant character is less significant. However, it should be noted that the normal stress at $x_1=0$ for case G exhibits a considerably small value, although the behavior cannot be explained with the aid of fluid dynamics. As we will show in Sec. 5.2, this property holds even in the limit of the infinite Knudsen number. For the cases shown in Fig. 3, the energy flow at $x_1=1$ is considerably smaller than that of the time-independent heat transfer problem (dotted line). The normal stress and the energy flow at the two walls are important quantities and will be discussed in detail in Secs. 5.2 and 5.3.

5.2 Forces Acting on the Walls. In this subsection, we discuss the force of the gas acting on the two walls at $x_1=0$ and $x_1=1$ as a function of the two parameters Kn and ω/ω_0. As was explained in Sec. 2.2 (Eq. (23)), the force per unit area is ex-

pressed in terms of the values of P at the point. The numerical values of the amplitude $|P|$ and the phase lag φ_P are tabulated in Table 1, where the amplitude and phase lag are given by $P=|P|\exp(i\varphi_P)$. The phase lag has an arbitrariness by $2\pi\times$integer so that we choose such that $0\le\varphi_P<2\pi$. The amplitude $|P|$ is also depicted in Fig. 4 for Kn=0.01, 0.1, and 10. The open circles represent the present results for a hard-sphere gas. The letters A,B,... represent the cases shown in Figs. 1–3 with the same letter. The solid line is the result of the BKW model. For the BKW model, we follow the general rule of transformation of the Knudsen number $Kn_{BKW}=\gamma_1 Kn$ in order to compensate for the difference of the molecular model. The BKW result shows a fairly good agreement with the hard-sphere result through this transformation. The dotted line in Figs. 4(*a*) and 4(*b*) is the Navier–Stokes solution (Eq. (30)) for Kn=0.01, and the dot-dashed line is the limiting value of $|P|$ at $x_1=0$ as $\omega\to\infty$ (Eq. (47)); $|P|$ at $x_1=1$ vanishes in the same limit. In Figs. 4(*e*) and 4(*f*), the free molecular solution (44) is also shown in the dotted line, which is almost indistinguishable from the result for Kn=10.

When the Knudsen number is relatively small (Kn=0.01, Figs. 4(*a*) and 4(*b*)), the Navier–Stokes solution is a qualitatively reasonable result. The normal stress on the two walls exhibits local maxima at about $\omega/\omega_0=1.94,3.94,...$ (resonant state), and that on the wall at $x_1=0$ has local minima at about $\omega/\omega_0=1.03,3.07,...$. These points correspond to the standing-wave states. As is well known in fluid dynamics, an increase of the viscosity results in a decrease in the phase speed of the sound wave. Thus, one may infer that the frequency of the standing-wave condition decreases as the Knudsen number increases. As seen by a close examination of Fig. 4(*a*) and Table 1, the shift of the position of the peaks $\omega/\omega_0\sim 2,4,...$ is in agreement with this estimate, while that of the valleys $\omega/\omega_0\sim 1,3,...$ is in the opposite direction. As shown in Fig. 1, the position of the antinode in the first standing-wave state (case A) is a little distanced from the wall at $x_1=0$. This shift causes the effect of reducing the channel width and raising the standing-wave frequencies. The resultant frequency is determined by these two factors. The numerical results show that the frequencies of the first two of the local minima are slightly higher than those of the acoustic ones.

As the Knudsen number increases (Figs. 4(*c*)–4(*f*)), the peaks and valleys become insignificant, except for the first minimum at $x_1=0$. Clearly, this distinct minimum is the continuous transformation of that of the first standing-wave state for a small Knudsen number. This characteristic remains even in the limit of the infinite Knudsen number (Fig. 4(*e*)). This is a remarkable character of the present flow caused by an oscillatory heating, in contrast to the flow in a slab generated by a vibration of one plate [40]. The minimum point for Kn=∞ is $\omega/\omega_0=1.54$. The normal stress at $x_1=1$ for Kn=∞ has the only local maximum located at about $\omega/\omega_0\sim 2$ and vanishes in the limit of infinite ω (Fig. 4(*f*)).

5.3 Energy Transfer. Next, we discuss the energy flows at both of the walls. As we explained in Sec. 2.2 (see Eq. (24) and the subsequent remark), the energy flow at a boundary is expressed in terms of Q. We show the numerical results of the amplitude $|Q|$ and the phase lag φ_Q in Table 1. The amplitude $|Q|$ is also depicted in Fig. 5 as a function of the frequency ω/ω_0. The meanings of the lines and symbols in Fig. 5 are basically the same as those in Fig. 4. For the BKW result (solid line), we use the transformation $Kn_{BKW}=\gamma_2 Kn$ instead of that used in Sec. 5.2. The dotted line with the letters HC is the solution of the heat conduction (40) for Kn=0.01.

For a relatively small Knudsen number Kn=0.01 (Figs. 5(*a*) and 5(*b*)), the Navier–Stokes solution serves as a qualitatively reasonable estimate. The energy flow at $x_1=0$ initially increases rapidly as the frequency ω/ω_0 increases. This increase is due to the increase in the temperature gradient at $x_1=0$ because the behavior of $|Q|$ is qualitatively the same as that of the solution of the heat conduction equation. For the energy flow at $x_1=1$, however, the solution of the heat conduction equation is only valid for a very narrow range. As we demonstrated in Fig. 1, the heat flow near $x_1=0$ decays very rapidly for a large ω/ω_0 and thus the energy transfer due to the heat flow becomes very small. On the other hand, the generation of sound waves increases, causing an increase in the energy transfer. In this way, the energy flow at $x_1=1$ has a local minimum with respect to ω/ω_0 ($\sim$0.15 for Kn=0.01) that is independent of the standing waves. The solution of the heat conduction equation is valid only below this minimum point. For a large ω/ω_0, the energy transferred to $x_1=1$ is mainly caused by the sound waves, and thus it exhibits significant peaks at the resonant points, as the normal stress did in Fig. 4(*b*).

In the time-independent energy transfer problem ($\omega=0$), the energy flow Q is a monotonically increasing function of the Knudsen number [16]. Correspondingly, the energy flow for a small ω/ω_0 increases as the Knudsen number increases, while the peaks and valleys of $|Q|$ associated with the resonance become insignificant (Figs. 5(*c*)–5(*f*)). As a consequence, for a large Knudsen number, the energy flow $|Q|$ at $x_1=0$ becomes a very smooth function of the frequency ω/ω_0 (Fig. 5(*e*)). In the limit of the infinite Knudsen number, the energy flow $|Q|$ at $x_1=1$ becomes a nearly decreasing function of ω/ω_0; it is not a strictly decreasing function but slightly increases around $\omega/\omega_0\sim 2$ and vanishes in the limit $\omega/\omega_0\to\infty$ (Fig. 5(*f*)).

5.4 Computational Conditions and Accuracy Testing. Finally, we give a brief summary of the conditions of the numerical computation and the results of the accuracy testing.

The computation was carried out in the finite three-dimensional space $0\le x_1\le 1$, $-\zeta_D\le\zeta_1\le\zeta_D$, and $0\le\zeta_\rho\le\zeta_d$, where ζ_D and ζ_d are positive constants chosen such that the absolute value $|\Phi|E$ of the distribution function is sufficiently small around $\zeta_1=\pm\zeta_D$ or $\zeta_\rho=\zeta_d$. In the computation, $\zeta_D=4.4$ and $\zeta_d=4$ are chosen. The lattice system in ζ_1 space is nonuniform with 129 lattice points, with the minimum size of 0.002 around $\zeta_1=0$ and with the maximum size of 0.2 around $\zeta_1=\pm\zeta_D$. The lattice system in ζ_ρ is uniform with 41 points and the uniform size of 0.1. The lattice system in x_1 is as follows. The lattice size is smallest at $x_1=0$ and $x_1=1$ and is equal to d_1, uniform in the interval $0.3<x_1<0.7$ and is equal to d_2, and nonuniform otherwise. The number of lattice points N_x and the values of d_1 and d_2 are $(N_x,d_1,d_2)=(801,0.00016,0.0025)$ for Kn=0.01 and $=(401,0.00032,0.005)$ for Kn=0.1, 1, and 10.

The results of the accuracy tests are as follows: (i) The magnitude $|\Phi|E$ of the distribution function on the planes $\zeta_1=\pm\zeta_D$ or $\zeta_\rho=\zeta_d$ ($0\le x_1\le 1$) is less than 1.6×10^{-7}. (ii) The absolute values of the left hand side of Eqs. (25)–(27), which should vanish theoretically, are bounded by 2.2×10^{-3} (Kn=0.01), 1.9×10^{-4} (Kn=0.1), 1.3×10^{-4} (Kn=1), and 2.6×10^{-3} (Kn=10). (iii) For a test of accuracy, we have also carried out additional computations using a coarser lattice system (two times coarser in the x_1 lattice and about 1.5 times coarser in ζ_1 and ζ_ρ) for 16 typical cases of the set of (Kn, Ω). From a comparison of the values of $|Q(0)|$ and $|Q(1)|$ from the two computations, the numerical error of the present computation is estimated to be at most 0.04% for Kn=0.1 and 1, and 0.1% for Kn=0.01 and 10.

6 Conclusion

We have carried out a numerical analysis of the periodic time-dependent flow of a rarefied gas between two parallel planes caused by an oscillatory heating of one plane based on the linearized Boltzmann equation for a hard-sphere molecular gas. Detailed numerical data regarding the forces of the gas acting on the planes and the energy transferred from the heated plane to the other are provided for a wide range of the Knudsen number and the oscillation frequency. The behavior of the gas is studied from low to high Knudsen numbers. The flow is characterized by a coupling of the heat conduction and the sound waves caused by

Table 1 The amplitude $|P|$ and the phase lag φ_P of the normal stress (Eq. (23)) and those $|Q|$ and φ_Q of the energy flow (Eq. (24)) at the two planes $x_1=0$ and 1 as a function of the Knudsen number Kn and the nondimensional frequency Ω (hard-sphere gas). $\Omega=(\pi/2)(5/6)^{1/2}\omega/\omega_0$ (Eq. (48)). The cases A, B, ... correspond to those shown in Figs. 1–3.

Ω	$\lvert P(0)\rvert$	$\lvert P(1)\rvert$	$\frac{\varphi_P(0)}{\pi}$	$\frac{\varphi_P(1)}{\pi}$	$\lvert Q(0)\rvert$	$\lvert Q(1)\rvert$	$\frac{\varphi_Q(0)}{\pi}$	$\frac{\varphi_Q(1)}{\pi}$	Case
				Kn=0.01					
0	0.561	0.561	0	0	0.020	0.020	0	0	
1	0.076	0.155	0.290	0.274	0.193	0.012	1.79	0.067	
1.2	0.046	0.157	0.311	0.283	0.209	0.013	1.80	0.080	
1.48	0.003	0.169	0.880	0.298	0.231	0.016	1.81	0.099	A
1.6	0.024	0.179	1.27	0.306	0.240	0.017	1.81	0.108	
2	0.132	0.247	1.34	0.339	0.267	0.026	1.83	0.146	
2.2	0.224	0.320	1.37	0.368	0.280	0.034	1.84	0.177	
2.4	0.386	0.462	1.43	0.420	0.292	0.051	1.86	0.232	
2.6	0.719	0.772	1.55	0.542	0.287	0.089	1.91	0.355	
2.7	0.957	0.992	1.68	0.668	0.253	0.115	1.95	0.483	
2.78	1.047	1.066	1.82	0.805	0.205	0.125	1.93	0.620	B
3	0.679	0.684	0.089	1.08	0.224	0.083	1.80	0.895	
3.4	0.300	0.344	0.220	1.21	0.288	0.043	1.80	1.04	
3.6	0.216	0.288	0.244	1.24	0.303	0.037	1.81	1.07	
4	0.101	0.243	0.255	1.29	0.325	0.033	1.83	1.11	
4.4	0.022	0.248	1.82	1.33	0.344	0.034	1.84	1.16	C
5	0.217	0.354	1.51	1.44	0.363	0.051	1.87	1.27	
5.4	0.480	0.542	1.66	1.62	0.344	0.080	1.90	1.45	
5.6	0.587	0.607	1.81	1.77	0.309	0.091	1.90	1.61	
6	0.454	0.455	0.054	0.044	0.314	0.070	1.84	1.88	
				Kn=0.1					
0	0.6376	0.6376	0	0	0.1493	0.1493	0	0	
0.4	0.4203	0.4391	0.1600	0.1564	0.2667	0.1217	1.814	0.2160	
0.6	0.3528	0.3944	0.2192	0.2080	0.3298	0.0994	1.818	0.2893	
0.8	0.2861	0.3602	0.2669	0.2433	0.3781	0.0798	1.830	0.3344	
1	0.2225	0.3403	0.3085	0.2679	0.4160	0.0648	1.844	0.3502	
1.2	0.1602	0.3347	0.3490	0.2877	0.4471	0.0556	1.857	0.3377	
1.4	0.0960	0.3428	0.3967	0.3078	0.4735	0.0529	1.870	0.3075	
1.5	0.0622	0.3521	0.4319	0.3194	0.4853	0.0539	1.876	0.2923	
1.6	0.0271	0.3647	0.5132	0.3327	0.4962	0.0565	1.883	0.2808	
1.67	0.0090	0.3757	0.9580	0.3433	0.5034	0.0592	1.888	0.2761	D
1.7	0.0157	0.3810	1.234	0.3482	0.5063	0.0606	1.890	0.2749	
1.8	0.0550	0.4008	1.400	0.3664	0.5152	0.0659	1.898	0.2757	
2	0.1480	0.4509	1.489	0.4134	0.5289	0.0799	1.915	0.2983	
2.8	0.4880	0.5708	1.860	0.7627	0.4731	0.1252	1.958	0.6198	E
3	0.4762	0.5208	1.944	0.8511	0.4622	0.1177	1.946	0.7063	
4	0.2679	0.3211	0.113	1.122	0.5139	0.0794	1.923	0.9652	
4.8	0.1816	0.2692	0.028	1.293	0.5463	0.0703	1.938	1.123	F
5	0.1820	0.2607	1.992	1.340	0.5501	0.0690	1.943	1.167	
6	0.2449	0.2142	1.941	1.588	0.5490	0.0605	1.959	1.400	
				Kn=1					
0	0.6185	0.6185	0	0	0.4179	0.4179	0	0	
0.6	0.4072	0.4274	0.1509	0.1428	0.4933	0.3607	1.949	0.2089	
1	0.3234	0.3928	0.2185	0.1863	0.5293	0.3072	1.953	0.3152	
1.2	0.2792	0.3914	0.2515	0.2023	0.5410	0.2816	1.954	0.3609	
1.4	0.2302	0.4007	0.2858	0.2189	0.5519	0.2572	1.956	0.4016	
1.6	0.1744	0.4206	0.3204	0.2394	0.5638	0.2345	1.957	0.4362	
1.8	0.1103	0.4498	0.3485	0.2666	0.5776	0.2145	1.959	0.4636	
1.9	0.0753	0.4672	0.3489	0.2834	0.5851	0.2060	1.960	0.4744	
2.0	0.0397	0.4857	0.2995	0.3025	0.5927	0.1987	1.963	0.4834	
2.1	0.0195	0.5048	1.905	0.3240	0.6002	0.1930	1.966	0.4908	
2.4	0.1310	0.5571	1.628	0.4014	0.6171	0.1860	1.980	0.5107	
2.6	0.2090	0.5795	1.677	0.4610	0.6198	0.1882	1.991	0.5299	
2.8	0.2746	0.5872	1.736	0.5228	0.6143	0.1923	0.0017	0.5577	
3	0.3232	0.5809	1.793	0.5835	0.6021	0.1953	0.0102	0.5926	
3.6	0.3738	0.5180	1.934	0.7434	0.5578	0.1902	0.0156	0.7100	
4	0.3590	0.4718	1.997	0.8318	0.5403	0.1801	0.0081	0.7838	
4.5	0.3195	0.4248	0.0485	0.9308	0.5354	0.1669	1.996	0.8677	
5	0.2745	0.3886	0.0706	1.024	0.5428	0.1562	1.988	0.9460	
5.5	0.2372	0.3593	0.0631	1.116	0.5551	0.1478	1.985	1.023	
6	0.2172	0.337	0.0325	1.208	0.5664	0.1408	1.986	1.101	
6.2	0.2149	0.324	0.0180	1.245	0.5699	0.1383	1.987	1.132	
				Kn=10					
0	0.524	0.524	0	0	0.539	0.539	0	0	
1	0.351	0.415	0.198	0.161	0.536	0.397	1.99	0.321	

Table 1 (***Continued.***)

Ω	$\lvert P(0)\rvert$	$\lvert P(1)\rvert$	$\frac{\varphi_P(0)}{\pi}$	$\frac{\varphi_P(1)}{\pi}$	$\lvert Q(0)\rvert$	$\lvert Q(1)\rvert$	$\frac{\varphi_Q(0)}{\pi}$	$\frac{\varphi_Q(1)}{\pi}$	Case
1.4	0.266	0.429	0.272	0.199	0.542	0.333	1.98	0.415	
1.8	0.151	0.478	0.352	0.247	0.564	0.275	1.97	0.488	
2	0.079	0.514	0.375	0.282	0.581	0.251	1.97	0.513	
2.1	0.041	0.533	0.344	0.302	0.589	0.242	1.97	0.523	
2.21	0.016	0.553	1.88	0.326	0.599	0.231	1.98	0.534	G
2.4	0.085	0.587	1.61	0.373	0.613	0.222	1.98	0.548	
2.6	0.168	0.616	1.65	0.430	0.623	0.215	1.99	0.561	
2.8	0.238	0.626	1.71	0.489	0.622	0.218	0.003	0.580	
3	0.295	0.627	1.76	0.547	0.615	0.218	0.013	0.609	
3.5	0.368	0.586	1.89	0.682	0.579	0.216	0.025	0.693	
3.7	0.374	0.563	1.93	0.729	0.564	0.212	0.025	0.729	H
4	0.370	0.528	1.98	0.796	0.548	0.205	0.020	0.781	
4.5	0.338	0.478	0.037	0.895	0.535	0.190	0.008	0.862	
5	0.294	0.438	0.070	0.988	0.537	0.178	1.99	0.937	
5.5	0.252	0.405	0.075	1.08	0.548	0.168	1.99	1.01	
6	0.223	0.378	0.053	1.17	0.561	0.160	1.99	1.08	
6.5	0.214	0.352	0.018	1.26	0.571	0.153	1.99	1.16	I

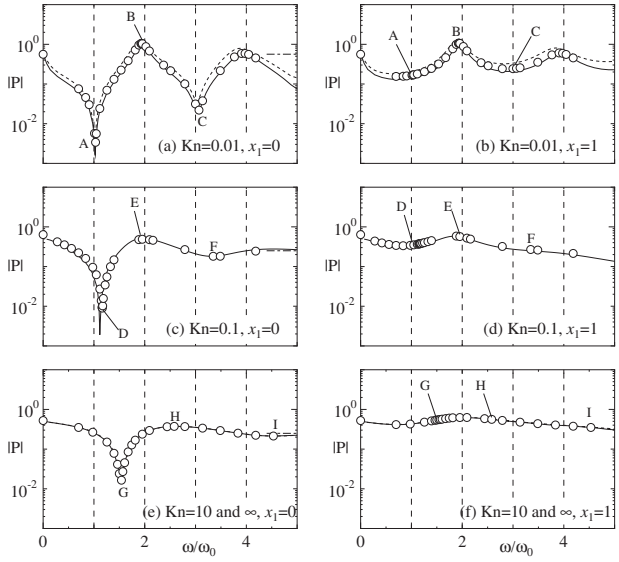

Fig. 4 Amplitude $|P|$ of the normal stress at the two walls as a function of ω/ω_0. ((*a*) and (*b*)) Kn=0.01, ((*c*) and (*d*)) Kn=0.1, and ((*e*) and (*f*)) Kn=10; ((*a*), (*c*), and (*e*)) $|P|$ at x_1=0 and ((*b*), (*d*), and (*f*)) $|P|$ at x_1=1. Open circle (○): hard-sphere gas, solid line (——): BKW model, dotted line (- - -) in (*a*) and (*b*): Navier–Stokes solution (Eq. (30)) for Kn=0.01, dotted line (- - -) in (*e*) and (*f*): free molecular solution for Kn=∞ (Eq. (44)), dot-dashed line (– - –): limiting value of $|P(0)|$ as $\omega\to\infty$ (Eq. (47)), and vertical dashed lines (– –): ω/ω_0=1,2,...,4.

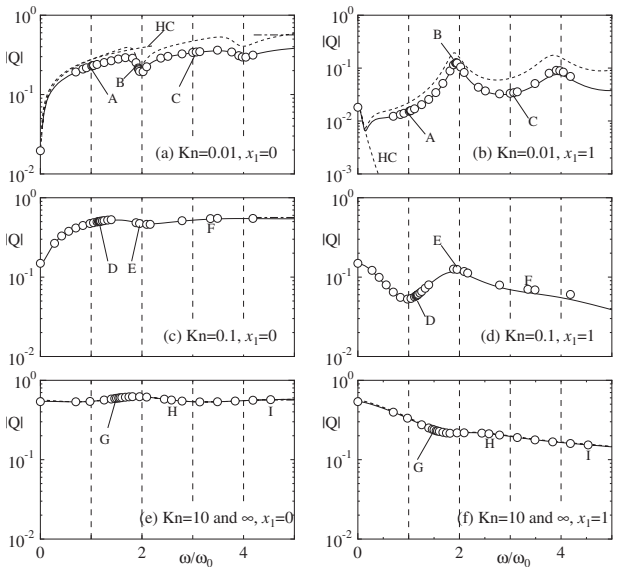

Fig. 5 Amplitude $|Q|$ of the energy flow at the two walls as a function of ω/ω_0. ((*a*) and (*b*)) Kn=0.01, ((*c*) and (*d*)) Kn=0.1, and ((*e*) and (*f*)) Kn=10; ((*a*), (*c*), and (*e*)) $|Q|$ at x_1=0 and ((*b*), (*d*), and (*f*)) $|Q|$ at x_1=1. Open circle (○): hard-sphere gas, solid line (——): BKW model, dotted line (- - -) in (*a*) and (*b*): Navier–Stokes solution (Eq. (31)) for Kn=0.01, dotted line (- - -) with the letters HC in (*a*) and (*b*): solution of heat conduction equation (Eq. (40)) for Kn=0.01, dotted line (- - -) in (*e*) and (*f*): free molecular solution for Kn=∞ (Eq. (45)), dot-dashed line (– - –): limiting value of $|Q(0)|$ as $\omega\to\infty$ (Eq. (47)), and vertical dashed lines (– –): ω/ω_0=1,2,...,4.

the repetitive expansion and contraction of the gas. For a small Knudsen number, the energy transfer is mainly conducted by the sound waves except for very low frequencies and is strongly affected by the resonance of the waves. For a large Knudsen number, the effect of the resonance becomes insignificant, and the energy transferred to the unheated plane decreases nearly monotonically as the frequency increases. The force of the gas acting on the heated boundary shows a remarkable minimum with respect to the frequency even for large and infinite Knudsen numbers.

Nomenclature

a = thermal diffusivity
d_m = diameter of a molecule
E = $\pi^{-3/2}\exp(-\zeta_i^2)$
ℓ = mean free path of the gas
$(F_1,0,0)$ = force of the gas acting on the walls per unit area
i = $\sqrt{-1}$
J_n = Abramowitz function
Kn = Knudsen number = ℓ/L
L = distance between the walls
m = mass of a molecule
P = normal stress (complex-valued function)
p_0 = $R\rho_0 T_0$
p_{ij} = stress tensor
Q = heat flow (complex-valued function)

q_i = heat flow vector
R = specific gas constant = Boltzmann constant/m
$\mathrm{Re}[*]$ = real part of $*$
T = temperature of the gas
T = temperature of the gas (complex-valued function)
t = time
$\hat{t}$ = time (dimensionless)
T_0 = temperature of the wall at $X_1 = L$
U = flow velocity (complex-valued function)
v_i = flow velocity
$(W_1, 0, 0)$ = energy flow at the wall per unit area and per unit time
X_i = space rectangular coordinates
x_i = space rectangular coordinates (dimensionless)

Greek Symbols

β_* = Stokes number associated with the thermal diffusivity
γ_1, γ_2 = transport coefficients (dimensionless)
$\Delta\tau$ = relative amplitude of the oscillation of the temperature of the wall
Φ = perturbation of the velocity distribution function (similarity solution)
ϕ = perturbation of the velocity distribution function
λ = thermal conductivity of the gas
μ = viscosity of the gas
Ω = nondimensional oscillation frequency or Strouhal number = $\omega L/(2RT_0)^{1/2}$
ω = oscillation frequency
ω_0 = fundamental standing-wave frequency = $(\pi/2L) \times (5RT_0/3)^{1/2}$
ρ_0 = mean density
ξ_i = molecular velocity
ζ_i = molecular velocity (dimensionless)
ζ_ρ = $(\zeta_2^2 + \zeta_3^2)^{1/2}$

References

[1] Sone, Y., 2007, *Molecular Gas Dynamics*, Birkhäuser, New York.
[2] Cercignani, C., 2000, *Rarefied Gas Dynamics*, Cambridge University Press, Cambridge.
[3] Karniadakis, G., Beskok, A., and Aluru, N., 2005, *Microflows and Nanoflows: Fundamentals and Simulation*, Springer-Verlag, New York.
[4] Cercignani, C., 2006, *Slow Rarefied Flows: Theory and Application to Micro-Electro-Mechanical Systems*, Birkhäuser, New York.
[5] Beskok, A., and Karniadakis, G. E., 1994, "Simulation of Heat and Momentum Transfer in Complex Microgeometries," J. Thermophys. Heat Transfer, **8**, pp. 647–655.
[6] Larrodé, F. E., Housiadas, C., and Drossinos, Y., 2000, "Slip-Flow Heat Transfer in Circular Tubes," Int. J. Heat Mass Transfer, **43**, pp. 2669–2680.
[7] Hadjiconstantinou, N. G., and Simek, O., 2002, "Constant-Wall-Temperature Nusselt Number in Micro and Nano-Channels," ASME J. Heat Transfer, **124**, pp. 356–364.
[8] Tunc, G., and Bayazitoglu, Y., 2002, "Heat Transfer in Rectangular Microchannels," Int. J. Heat Mass Transfer, **45**, pp. 765–773.
[9] Wang Chang, C. S., and Uhlenbeck, G. E., 1953, "The Heat Transport Between Two Parallel Plates as Functions of the Knudsen Number," Engineering Research Institute, University of Michigan, Project No. M999.
[10] Gross, E. P., and Ziering, S., 1959, "Heat Flow Between Parallel Plates," Phys. Fluids, **2**, pp. 701–712.
[11] Liu, C. Y., and Lees, L., 1961, "Kinetic Theory Description of Plane Compressible Couette Flow," in *Rarefied Gas Dynamics*, L. Talbot, ed., Academic, New York, pp. 391–428.
[12] Willis, D. R., 1963, "Heat Transfer in a Rarefied Gas Between Parallel Plates at Large Temperature Ratios," in *Rarefied Gas Dynamics*, J. A. Laurmann, ed., Academic, New York, pp. 209–225.
[13] Bassanini, P., Cercignani, C., and Pagani, C. D., 1967, "Comparison of Kinetic Analyses of Linearized Heat Transfer Between Parallel Plates," Int. J. Heat Mass Transfer, **10**, pp. 447–460.
[14] Asmolov, E. S., Makashev, N. K., and Nosik, V. I., 1979, "Heat Transfer Between Plane Parallel Plates in a Gas of Maxwellian Molecules," Sov. Phys. Dokl., **24**, pp. 892–894.
[15] Santos, A., Brey, J. J., and Garzó, V., 1986, "Kinetic Model for Steady Heat Flow," Phys. Rev. A, **34**, pp. 5047–5050.
[16] Ohwada, T., Aoki, K., and Sone, Y., 1989, "Heat Transfer and Temperature Distribution in a Rarefied Gas Between Two Parallel Plates With Different Temperatures: Numerical Analysis of the Boltzmann Equation for a Hard Sphere Molecule," in *Rarefied Gas Dynamics*, E. P. Muntz, D. P. Weaver, and D. H. Campbell, eds., AIAA, Washington, DC, pp. 70–81.
[17] Santos, A., and Garzó, V., 1995, "Exact Non-Linear Transport From the Boltzmann Equation," *Rarefied Gas Dynamics*, Vol. I, J. Harvey and G. Lord, eds., Oxford University Press, Oxford, pp. 13–21.
[18] Ohwada, T., 1996, "Heat Flow and Temperature and Density Distributions in a Rarefied Gas Between Parallel Plates With Different Temperatures. Finite-Difference Analysis of the Nonlinear Boltzmann Equation for Hard-Sphere Molecules," Phys. Fluids, **8**, pp. 2153–2160.
[19] Kosuge, S., Aoki, K., and Takata, S., 2001, "Heat Transfer in a Gas Mixture Between Two Parallel Plates," *Rarefied Gas Dynamics*, T. J. Bartel and M. A. Gallis, eds., AIP, Melville, NY, pp. 289–296.
[20] Sone, Y., 1965, "Effect of Sudden Change of Wall Temperature in a Rarefied Gas," J. Phys. Soc. Jpn., **20**, pp. 222–229.
[21] Aoki, K., Sone, Y., Nishino, K., and Sugimoto, H., 1991, "Numerical Analysis of Unsteady Motion of a Rarefied Gas Caused by Sudden Change of Wall Temperature With Special Interest in the Propagation of a Discontinuity in the Velocity Distribution Function," *Rarefied Gas Dynamics*, A. E. Beylich, ed., VCH, Weinheim, pp. 222–231.
[22] Wadsworth, D. C., Erwin, D. A., and Muntz, E. P., 1993, "Transient Motion of a Confined Rarefied Gas Due to Wall Heating and Cooling," J. Fluid Mech., **248**, pp. 219–235.
[23] Kassoy, D. R., 1979, "The Response of a Confined Gas to a Thermal Disturbance. I: Slow Transients," SIAM J. Appl. Math., **36**, pp. 624–634.
[24] Clarke, J. F., Kassoy, D. R., and Riley, N., 1984, "Shock Generated in a Confined Gas Due to Rapid Heat Addition at the Boundary. I: Weak Shock Waves," Proc. R. Soc. London, Ser. A, **393**, pp. 309–329.
[25] Manela, A., and Hadjiconstantinou, N. G., 2007, "On the Motion Induced in a Small-Scale Gap Due to Instantaneous Boundary Heating," J. Fluid Mech., **593**, pp. 453–462.
[26] Manela, A., and Hadjiconstantinou, N. G., 2008, "Gas Motion Induced by Unsteady Boundary Heating in a Small-Scale Slab," Phys. Fluids, **20**, p. 117104.
[27] Bhatnagar, P. L., Gross, E. P., and Krook, M., 1954, "A Model for Collision Processes in Gases. I. Small Amplitude Processes in Charged and Neutral One-Component Systems," Phys. Rev., **94**, pp. 511–525.
[28] Welander, P., 1954, "On the Temperature Jump in a Rarefied Gas," Ark. Fys., **7**, pp. 507–553.
[29] Sone, Y., Ohwada, T., and Aoki, K., 1989, "Temperature Jump and the Knudsen Layer: Numerical Analysis of the Linearized Boltzmann Equation for a Hard Sphere Gas," Phys. Fluids A, **1**, pp. 363–370.
[30] Sone, Y., Ohwada, T., and Aoki, K., 1989, "Evaporation and Condensation on a Plane Condensed Phase: Numerical Analysis of the Linearized Boltzmann Equation for Hard-Sphere Molecules," Phys. Fluids A, **1**, pp. 1398–1405.
[31] Ohwada, T., Sone, Y., and Aoki, K., 1989, "Numerical Analysis of the Shear and Thermal Creep Flows of a Rarefied Gas Over a Plane Wall on the Basis of the Linearized Boltzmann Equation for Hard-Sphere Molecules," Phys. Fluids A, **1**, pp. 1588–1599.
[32] Ohwada, T., Sone, Y., and Aoki, K., 1989, "Numerical Analysis of the Poiseuille and Thermal Transpiration Flows Between Two Parallel Plates on the Basis of the Boltzmann Equation for Hard-Sphere Molecules," Phys. Fluids A, **1**, pp. 2042–2049.
[33] Sone, Y., Takata, S., and Ohwada, T., 1990, "Numerical Analysis of the Plane Couette Flow of a Rarefied Gas on the Basis of the Linearized Boltzmann Equation for Hard-Sphere Molecules," Eur. J. Mech. B/Fluids, **9**, pp. 273–288.
[34] Takata, S., Sone, Y., and Aoki, K., 1993, "Numerical Analysis of a Uniform Flow of a Rarefied Gas Past a Sphere on the Basis of the Boltzmann Equation for Hard-Sphere Molecules," Phys. Fluids A, **5**, pp. 716–737.
[35] Sharipov, F., and Kalempa, D., 2008, "Oscillatory Couette Flow at Arbitrary Oscillation Frequency Over the Whole Range of the Knudsen Number," Microfluid. Nanofluid., **4**, pp. 363–374.
[36] Morse, P., and Ingard, K. U., 1968, *Theoretical Acoustics*, Princeton University Press, Princeton, NJ, Chap. 6.
[37] Park, J. H., Bahukudumbi, P., and Beskok, A., 2004, "Rarefaction Effects on Shear Driven Oscillatory Gas Flows: A Direct Simulation Monte Carlo Study in the Entire Knudsen Regime," Phys. Fluids, **16**, pp. 317–330.
[38] Hadjiconstantinou, N. G., 2005, "Oscillatory Shear-Driven Gas Flows in the Transition and Free-Molecular-Flow Regimes," Phys. Fluids, **17**, p. 100611.
[39] Abramowitz, M., and Stegun, I., 1965, *Handbook of Mathematical Functions*, Dover, New York, p. 1001.
[40] Sharipov, F., Marques, W., Jr., and Kremer, G. M., 2002, "Free Molecular Sound Propagation," J. Acoust. Soc. Am., **112**, pp. 395–401.

Modeling of Free Convection Heat Transfer to a Supercritical Fluid in a Square Enclosure by the Lattice Boltzmann Method

Mostafa Varmazyar

Majid Bazargan
e-mail: bazargan@kntu.ac.ir

Department of Mechanical Engineering,
K.N. Toosi University of Technology,
1999143344, Tehran, Iran

During the last decade, a number of numerical computations based on the finite volume approach have been reported, studying various aspects of heat transfer near the critical point. In this paper, a lattice Boltzmann method (LBM) has been developed to simulate laminar free convection heat transfer to a supercritical fluid in a square enclosure. The LBM is an ideal mesoscopic approach to solve nonlinear macroscopic conservation equations due to its simplicity and capability of parallelization. The lattice Boltzmann equation (LBE) represents the minimal form of the Boltzmann kinetic equation. The LBE is a very elegant and simple equation, for a discrete density distribution function, and is the basis of the LBM. For the mass and momentum equations, a LBM is used while the heat equation is solved numerically by a finite volume scheme. In this study, interparticle forces are taken into account for nonideal gases in order to simulate the velocity profile more accurately. The laminar free convection cavity flow has been extensively used as a benchmark test to evaluate the accuracy of the numerical code. It is found that the numerical results of this study are in good agreement with the experimental and numerical results reported in the literature. The results of the LBM-FVM (finite volume method) combination are found to be in excellent agreement with the FVM-FVM combination for the Navier–Stokes and heat transfer equations. [DOI: 10.1115/1.4002598]

Keywords: lattice Boltzmann method, energy equation, supercritical fluid flow, cavity enclosure, free convection

1 Introduction

A fluid exists in a single phase at pressures higher than its thermodynamic critical point. At supercritical pressure, the thermodynamic and transport properties of fluids change dramatically near the critical temperature. The fluid flow behavior at a supercritical environment is substantially different than its characteristics under normal conditions [1,2]. The idea of using fluids at their supercritical state to improve heat transfer has been given attention since more than half a century ago. The recent development of systems (e.g., supercritical water oxidation) operating at supercritical conditions necessitates a further understanding of heat transfer to supercritical fluids. In the last decade, much effort has been focused on the development of conventional numerical methods to simulate the convection heat transfer to the supercritical fluid flows [3].

The conventional computational fluid dynamics (CFD) methods are based on direct discretization of the Navier–Stokes equations. The kinetic methods for CFD, however, are derived from the Boltzmann equation. The distinctive features of the kinetic methods, because of which they have recently attracted much interest, are as follows. Since they are based on the kinetic theory, the kinetic methods are capable of treating a fluid dynamics problem with the aids of microscopic view. This helps in explaining some problems which are very difficult to explain, otherwise, on a pure macroscopic approach as it is the case with the traditional way of solving the Navier–Stokes equations. It is known that the Boltzmann equation provides the theoretical connection between hydrodynamics and the underlying microscopic physics. Kinetic methods are often called mesoscopic methods for they act between the macroscopic conservation laws and their corresponding microscopic dynamics. Furthermore, the Boltzmann equation is a first-order integropartial-differential equation with a linear advection term, whereas the Navier–Stokes equation is a second-order partial-differential equation with a nonlinear advection term. The nonlinearity in the Boltzmann equation resides in its collision term, which is local. This feature may lead to some computational advantages. Due to their mesoscopic nature, kinetic methods are particularly appealing in modeling and simulations of complex fluids [4].

There are a number of kinetic or mesoscopic methods, such as the lattice gas cellular automata, the lattice Boltzmann equation (LBE), the gas-kinetic schemes (GKSs), the smoothed particle hydrodynamics, and the dissipative particle dynamics. Among these methods, the LBE and GKS methods are specifically designed to simulate viscous heat transfer problems, shallow water equations, multiphase and multicomponent flows, magnetohydrodynamics, and microflows (see Ref. [4] and references therein). The LBE, in particular, has recently achieved considerable success in simulating various transport phenomena.

Near the critical point the variations of the fluid properties are very large. More accurate and complicated schemes are therefore needed to implement in conventional numerical simulations in order to model a laminar supercritical fluid flow. Accary and Raspo [3], for example, used a finite volume method to model the flow of a supercritical fluid in a square enclosure.

For the isothermal fluid flows, the LBM was found to be an accurate, stable, and computationally "economic" method compared with the conventional computational fluid dynamics methods [5].

At supercritical pressures, the convection heat transfer to a fluid is a single phase process. Near the pseudocritical point, however,

Contributed by the Heat Transfer Division of ASME for publication in the JOURNAL OF HEAT TRANSFER. Manuscript received September 23, 2009; final manuscript received August 10, 2010; published online November 2, 2010. Assoc. Editor: Patrick H. Oosthuizen.

the fluid behavior somehow resembles its two-phase state and the temperature variation is small. This is why the heat flux in boundaries may remain high. Házi and Márkus [6] recently employed the lattice Boltzmann equation to study the convection heat transfer to a supercritical fluid. They considered a one-dimensional supercritical viscous fluid layer between two plates heated from the bottom and investigated the onset of convection near the critical point.

In the present study the LBE is employed to simulate a two-dimensional laminar free convection heat transfer to a supercritical fluid in a square enclosure. The main purpose of the current study is to determine the streamlines and temperature fields with the LBE. The evaluation of the model will be made possible by the comparison of the results with the available data of the finite volume studies for perfect gases and SCFs (super-critical fluids).

2 Governing Equations and Modeling

2.1 Lattice Boltzmann Equation. The LBE is directly derived from the Boltzmann equation by discretization in both time and phase space [7]. The general form of the lattice Boltzmann equation in the *i*th direction with buoyancy force included is

$$f_i(x + \Delta t \cdot \mathbf{c}_i, t + \Delta t) - f_i(x,t) = \Omega_i + \Delta t \cdot F_{\text{buoyancy}} \tag{1}$$

where the x, t, Δt, and F_{buoyancy} are the location vector, time, time step, and buoyancy force, respectively. The term f_i is the one-particle velocity distribution function that travels with velocity c_i. The collision operator Ω_i, which represents the rate of change of f_i, resulting from collision, depends on the lattice Boltzmann method. In the lattice Boltzmann–Bhatnagher–Gross–Krook method [8], which has been used in this study, the particle distribution after propagation is relaxed toward the equilibrium distribution $f_i^{eq}(x,t)$, as

$$\Omega_i = \frac{1}{\tau}(f_i(x,t) - f_i^{eq}(x,t)) \tag{2}$$

The relaxation τ parameter has been calculated from the kinematic viscosity υ of the simulated fluid, according to

$$\tau = 3\upsilon + \tfrac{1}{2} \tag{3}$$

The SCF is a nonideal gas. So, the lattice Boltzmann formulation needs to be adjusted accordingly to simulate the nonideal gas. Assuming that the variation of temperature is small near the critical point, the van der Waals equation of state, presented below, may be used [9].

$$\left(P + \frac{a}{\nu^2}\right)(\nu - b) = RT \tag{4}$$

The interaction pseudopotential ψ and hence the intermolecular force $\mathbf{F}$ are calculated as follows [10]:

$$\psi^2 = 2\left(\frac{P - \rho RT}{GRT}\right) \tag{5}$$

$$\mathbf{F} = -G \times \Delta t \psi \nabla \psi \tag{6}$$

where the parameter G controls the strength of the interaction.

The equilibrium density $f_i^{eq}(x,t)$ is calculated as

$$f_i^{eq}(x,t) = w_i \rho(x,t) \times \left(1 + \frac{\mathbf{c}_i \cdot \mathbf{u}^{eq}}{c_s^2} + \frac{(\mathbf{c}_i \cdot \mathbf{u}^{eq})^2}{2c_s^4} - \frac{\mathbf{u}^{eq} \cdot \mathbf{u}^{eq}}{2c_s^2}\right) \tag{7}$$

where $\mathbf{u}^{eq} = \mathbf{u}' + (\mathbf{F}/\rho)\tau$, c_s is the speed of sound, $\mathbf{F}$ is the force between particles, and w_i is the corresponding equilibrium density for $\mathbf{u}^{eq} = 0$. Taking the moment of the distribution function, the $\mathbf{u}'$ may be obtained as follows:

$$\mathbf{u}'(x,t) = \frac{1}{\rho(x,t)} \sum_i f_i(x,t)\mathbf{c}_i \tag{8}$$

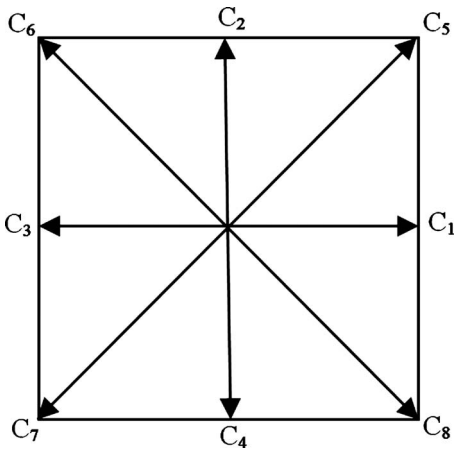

Fig. 1 The square lattice velocities D2Q9

The macroscopic quantities are calculated as follows [10]:

$$\rho(x,t) = \sum_i f_i(x,t) \tag{9}$$

$$\mathbf{u}(x,t) = \mathbf{u}'(x,t) + \frac{\mathbf{F}(x,t)}{2} \tag{10}$$

The two-dimensional nine-velocity model (D2Q9), the lattice vectors of which are shown in Fig. 1, is used.

The buoyancy force in the lattice Boltzmann model is calculated as follows:

$$F_{\text{buoyancy}} = \frac{3\mathbf{G} \cdot (\mathbf{c}_i - \mathbf{u})}{c_s^2} f_i^{eq} \tag{11}$$

$$\mathbf{G} = (\rho - \rho_m)\mathbf{g} \tag{12}$$

where ρ_m is the average fluid density. With the Boussinesq approximation, the buoyancy term in perfect gas simulation will be

$$\mathbf{G} = -\rho\beta(T - T_m)\mathbf{g} \tag{13}$$

where T_m is the average fluid temperature.

2.2 Equation of Temperature. The energy equation for the present system can be expressed by the following 2D equation:

$$\frac{\partial \rho T u_i}{\partial x_i} = \frac{\partial}{\partial x_i}\left(\frac{k}{c_p}\frac{\partial T}{\partial x_i}\right) \tag{14}$$

where k and c_p are the thermal conductivity and the specific heat capacity at constant pressure, respectively. Note that the subscript i in the above equation represents the tensorial index. We choose the finite volume method for solving the energy equation in order to compare the velocity-pressure coupling algorithm and the LBM in momentum equation. The power-law scheme of Patankar [11] is used to calculate the discretized temperature equation. In this method the Peclet number at each node specifies *to what extent* the temperature at each face is affected by the upstream node.

2.3 Boundary Conditions, Properties, and Dimensionless Parameters. The schematic diagram of the square enclosure and macroscopic boundary conditions are shown in Fig. 2. As illustrated, the walls at $x=0$ and $x=L$ are heated and cooled, respectively. Other walls are insulated. The fluid is initially at rest. Thermodynamic equilibrium at constant temperature T_0 is maintained. T_0 is slightly greater than the critical temperature T_c and follows the equation $T_0 = (1+\varepsilon)T_c$, where ε is a dimensionless parameter ($\varepsilon \ll 1$), reflecting the proximity to the critical point. The fluid is stratified in pressure and density because of its weight. The average density, ρ_0, is equal to the critical value of density. Once the

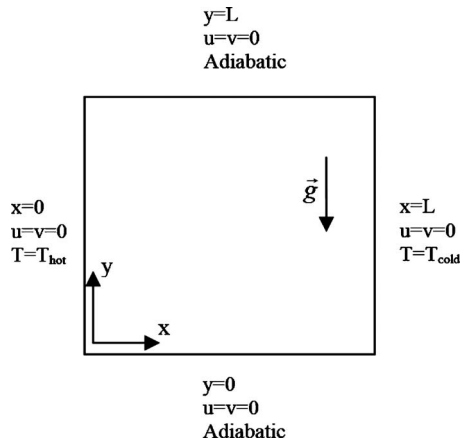

Fig. 2 Configuration of natural convection in a square cavity

simulation starts, the temperature of the heated wall is slightly increased by ΔT_h, ($\Delta T_h \sim$ few mK), and then maintained at $T_0 + \Delta T_h$. The opposite situation occurs at the cooled wall. It means that the temperature of the cooled wall is slightly decreased by ΔT_c ($\Delta T_c \sim$ few mK) and then maintained at $T_0 - \Delta T_c$. The critical temperature and density for carbon dioxide are as follows:

$$T_c = 304.13 \text{ K}, \quad \rho_c = 468 \text{ kg/m}^3 \tag{15}$$

Proper implementation of the microscopic boundary conditions is very essential. The distribution functions at the nodes located at the boundaries are needed to be determined. The method of Zou and He [12] has been used to support the no-slip condition at the boundaries. To accomplish this, they proposed a bounce-back rule of the nonequilibrium distribution function at the boundaries.

The density distribution functions may be determined at the boundary by means of the following equation:

$$f_i - f_i^{eq} = f_j - f_j^{eq} \tag{16}$$

where $\mathbf{e}_i$ (unit vector in the ith direction) represents the direction of the unknown distribution function and $\mathbf{e}_j$ (unit vector in the jth direction) has an opposite direction to $\mathbf{e}_i$, i.e., represents the direction of the known distribution function. The potential functions of the inner nodes have been used to obtain the potential functions at the walls via extrapolation. This leads to

$$\psi_i = 2\psi_{i-1} - \psi_{i-2}$$

where $i-1$ and $i-2$ refer to the inner domain of the fluid and i represents a wall node [6].

The CO_2 transport properties near the critical point in the SI system (International System of Units) are as follows [3]:

$$k = 0.01 \times \left[1 + 0.75\left(\frac{T}{T_c} - 1\right)^{-(1/2)}\right] \tag{17}$$

$$c_p = 472.15 \times \gamma\left[1 + \frac{\gamma - 1}{\gamma}\varepsilon^{-1}\right] \tag{18}$$

$$\mu = 3.44 \times 10^{-5} \tag{19}$$

The expression of thermal expansion coefficient is [3]

$$\beta = \frac{2}{3T_c}\varepsilon^{-1} \tag{20}$$

Thus, the Rayleigh number for the supercritical fluid flow can be written as follows:

$$\text{Ra}^c = \Pi g \ \text{Pr}\left(\frac{\rho_c}{\mu_0}\right)^2 L^3 \frac{\Delta T_h}{T_0} \tag{21}$$

Table 1 Comparison of the Nusselt number values for the natural convection inside a differentially heated square cavity filled with a perfect gas in the low Mach number approximation for Pr=0.71

	Nusselt number	
	$\text{Ra}=10^5$	$\text{Ra}=10^6$
Reference [13]	4.519	8.800
N=2050 (conventional numerical methods) [14]	-	8.8597
N=925 (conventional numerical methods) [15]	-	8.8598
N=256 (LBM) [16]	4.5463	-
N=512 (LBM) [16]	-	8.652
N=300 (present)	4.54413	8.73454

where $\Pi = 2\varepsilon^{-1}(\gamma + (\gamma - 1)\varepsilon^{-1})/3\gamma(1 + 0.75\varepsilon^{-0.5})$.

Pr and Nu are, respectively, the Prandtl number and the average Nusselt number at the isotherm walls defined as

$$\text{Pr} = \frac{k}{\rho c_p} \tag{22}$$

$$\text{Nu} = \frac{1}{2\Delta T}\int_0^L \left(\frac{\partial T}{\partial y}\right)_{y=0,L} dx \tag{23}$$

2.4 Method of Solution. A brief description on the procedure of the implementation of LBM and FVM in the current study is presented in this section. The first step is to generate a temperature profile in the computational domain. This is done by setting the temperature of the walls in $x=0$ and $x=L$ according to the boundary conditions stated in Sec. 2.3. The temperature distribution is calculated from the energy equation by the numerical method explained in Sec. 2.2. Since the fluid density changes with temperature, a free convection flow can be initiated near the walls. The LBM is used to simulate the compressible fluid flow field. This will be done in two steps, collision and streaming. The collision step is implemented by using Eq. (2). It is worthwhile to note that the velocity vector should be upgraded by the equation of $\mathbf{u}^{eq}$ to substitute in the equilibrium distribution function. In the second step, the particles (distribution functions) are streamed in all directions into the neighbor nodes, following $\mathbf{c}_i$. Finally, the macroscopic parameters are calculated using Eqs. (9) and (10). This algorithm will be continued until the changes of Nusselt number become less than 10^{-3} or 10^{-4}.

3 Results and Discussion

3.1 2D Low Mach Number. The steady natural convection benchmark tests for the perfect gas at low Mach number approximation in a square cavity are used to evaluate the results of the present study. The test conditions of the available data are as follows: $L=1$, $\rho_0=0.5884$ kg/m^3, $T_0=600$ K, $R=287$ J kg/K, Pr=0.71, and $\Delta T_h=\Delta T_c=0.6T_c$. The simulations were carried out for two values of the Rayleigh number, 10^5 and 10^6. The Rayleigh number is defined in this section as

$$\text{Ra} = \Pi g \ \text{Pr}\left(\frac{\rho_0}{\mu_0}\right)^2 L^3 \frac{\Delta T_h}{T_0} \tag{24}$$

The average Nusselt numbers (Table 1) obtained from the present model are compared with the results of other investigators in Table 1. As can be seen, the present model with the grid size of N=300 provides the compatible results with those of Refs. [13–16] for $\text{Ra}=10^6$. Meanwhile the conventional numerical methods with a much larger number of grids (925 and 2050) have been used in Refs. [14,15]. Note that the total number of grids is the squared values of the numbers mentioned above (i.e., 300×300, 925×925, or 2050×2050). Thus, considering the

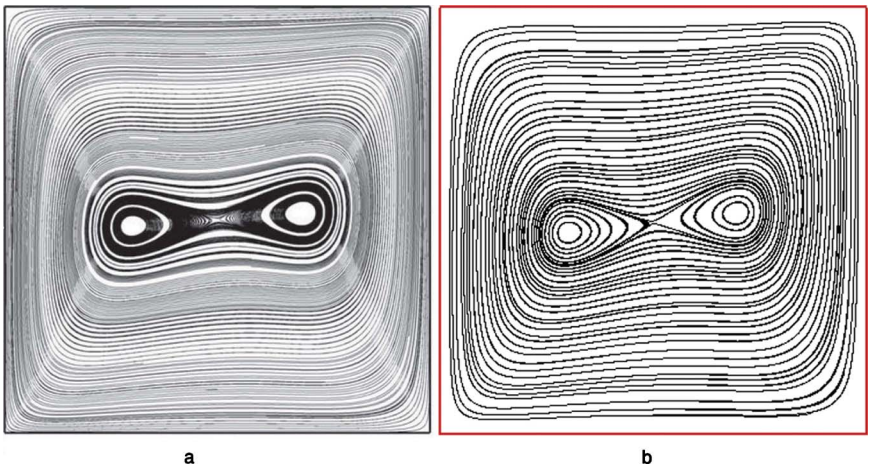

Fig. 3 Natural convection in a side heated cubical box filled with a SCF for $T_0-T_c=1$ K, $\Delta T_h=1$ mK, and $Ra^c=10^5$. (*a*) The results of Ref. [3] for streamlines in the vertical symmetry plane of the flow. (*b*) Streamlines (present study).

economy of computation, it can be concluded that the method of solution used in this study is much more efficient than the conventional numerical methods.

In addition, the comparison of the results for the case of a bigger value of $Ra=10^6$, as shown in Table 1, indicates that the method of the present solution provides compatible results with those of Ref. [16]. In Ref. [16] both the momentum and energy equations are solved by the LBM.

3.2 SCF in a Cavity Enclosure. The simulation results in a side heated cubical box filled with a SCF (CO_2) for $Ra^c=10^5$, $T_0-T_c=1$ K, and $\Delta T_h=1$ mK have been shown in Figs. 3 and 4. Because of the large values of the fluid density and the small values of the fluid viscosity near the critical region, SCF flows are often turbulent at the normal values of acceleration due to gravity, i.e., $g=9.8$ m/s^2. This is the case even for a weak heating and small cavity length. To avoid turbulent flows, g is adjusted (microgravity conditions) in such a way that the Ra obtained from Eq. (21) does not exceed the values which correspond to laminar flows.

The calculated results demonstrate a qualitatively good agreement with the results of Accary and Raspo [3] obtained for the same flow conditions.

As stated earlier, due to large variation of the fluid properties at supercritical conditions, it is very difficult to model the flow in a cavity enclosure by means of a finite volume numerical scheme. This is why the LBM represents a more stable behavior and there would be no need to use the under relaxation coefficient. Consequently, the speed of convergence in the solutions by the LBM significantly increases.

4 Conclusions

A 2D numerical tool is developed in this study to predict the SCF buoyant flows inside the heated enclosures. The method is based on a lattice Boltzmann equation of the momentum and energy conservations. The conventional form of the van der Waals equation is used for the equation of state. The solver was validated on several benchmark tests available for natural convection inside a differentially heated cavity in the low Mach number approxima-

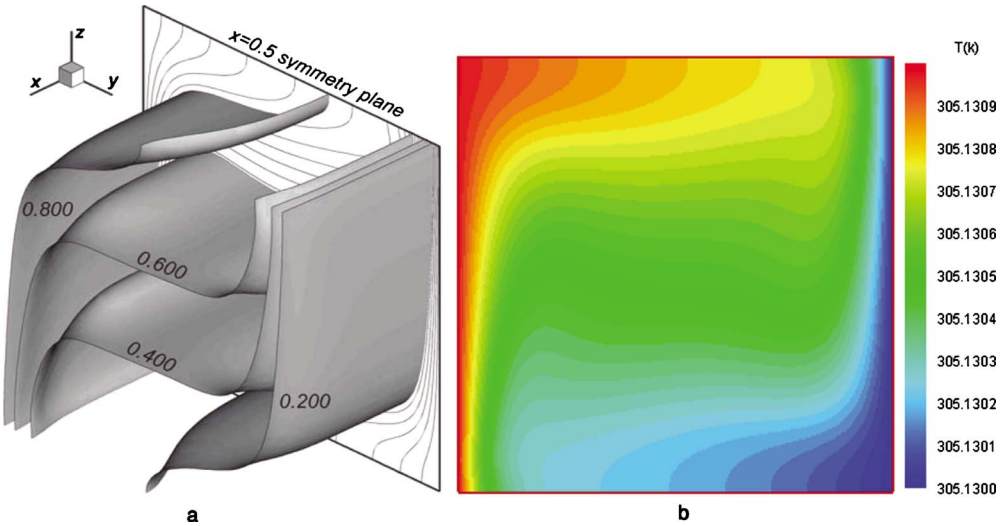

Fig. 4 Natural convection in a side heated cubical box filled with a SCF for $T_0-T_c=1$ K, $\Delta T_h=1$ mK, and $Ra^c=10^5$. (*a*) The results of Ref. [3] for isotherms $(T-T_0)/\Delta T_h$ for the half of the computational domain. (*b*) Temperature contour (present study).

tions. The comparison of the results shows that the LBM-FVM implemented in this study is more accurate and economic compared with the available data for the traditional numerical solutions as well as the results of LBM-LBM.

From the good agreement of the SCF buoyant flow results with the available data, it has been concluded that the LBM is a robust approach to model the supercritical fluid behavior in a cavity enclosure. The less number of grids, together with the fact that no under relaxation coefficient is needed in LBM, causes the convergence of the results to occur more rapidly compared with the conventional numerical solutions based on a finite volume scheme. The ability of parallelization of the lattice Boltzmann method also assists in accelerating the convergence of the results. There are no much data available on the running time and the convergence details of the numerical solutions in order to further assess the LBM characteristics in treating the supercritical fluids. This is left for further investigations in the future.

References

[1] Bazargan, M., and Fraser, D., 2009, "Heat Transfer to Supercritical Water in a Horizontal Pipe: Modeling, New Empirical Correlation, and Comparison Against Experimental Data," ASME J. Heat Transfer, **131**, p. 061702.

[2] Bazargan, M., Fraser, D., and Chatoorgan, V., 2005, "Effect of Buoyancy on Heat Transfer in Supercritical Water Flow in a Horizontal Round Tube," ASME J. Heat Transfer, **127**, pp. 897–902.

[3] Accary, G., and Raspo, I., 2006, "A 3D Finite Volume Method for the Prediction of a Supercritical Fluid Buoyant Flow in a Differentially Heated Cavity," Comput. Fluids, **35**, pp. 1316–1331.

[4] Guo, Z., Liu, H., Luo, L. S., and Xu, K., 2008, "A Comparative Study of the LBE and GKS Methods for 2D Near Incompressible Laminar Flows," J. Comput. Phys., **227**, pp. 4955–4976.

[5] Kuznik, F., Vareilles, J., Rusaoue, G., and Krauss, G., 2007, "A Double-Population Lattice Boltzmann Method With Non-Uniform Mesh for the Simulation of Natural Convection in a Square Cavity," Int. J. Heat Fluid Flow, **28**, pp. 862–870.

[6] Házi, G., and Márkus, A., 2008, "Modeling Heat Transfer in Supercritical Fluid Using the Lattice Boltzmann Method," Phys. Rev. E, **77**, p. 026305.

[7] He, X., and Luo, L.-S., 1997, "A Priori Derivation of the Lattice Boltzmann Equation," Phys. Rev. E, **55**(6), pp. R6333–R6336.

[8] Bhatnagher, P. L., Gross, E. P., and Krook, M., 1954, "A Model for Collision Processes in Gases. I. Small Amplitude Processes in Charged and Neutral One-Component Systems," Phys. Rev., **94**(3), pp. 511–525.

[9] Succi, S., 2001, *The Lattice Boltzmann Equation for Fluid Dynamics and Beyond*, Clarendon, Oxford.

[10] Sukop, M. C., and Thorne, D. T., 2006, *Lattice Boltzmann Modeling: An Introduction for Geoscientists and Engineers*, Springer, New York.

[11] Patankar, S. V., 1980, *Numerical Heat Transfer and Fluid Flow*, McGraw-Hill, New York.

[12] Zou, Q., and He, X., 1997, "On Pressure and Velocity Boundary Conditions for the Lattice Boltzmann BGK Model," Phys. Fluids, **9**, pp. 1591–1598.

[13] De Vahl Davis, G., 1983, "Natural Convection of Air in a Square Cavity: A Benchmark Numerical Solution," Int. J. Numer. Methods Fluids, **3**, pp. 249–264.

[14] Becker, R., and Braack, M., 2002, "Solution of a Stationary Benchmark Problem for Natural Convection With Large Temperature Difference," Int. J. Therm. Sci., **41**, pp. 428–439.

[15] Heuveline, V., 2003, "On Higher-Order Mixed FEM for Low Mach Number Flows: Application to a Natural Convection Benchmark Problem," Int. J. Numer. Methods Fluids, **41**(12), pp. 1339–1356.

[16] Dixit, H. N., and Babu, V., 2006, "Simulation of High Rayleigh Number Natural Convection in a Square Cavity Using the Lattice Boltzmann Method," Int. J. Heat Mass Transfer, **49**, pp. 727–739.

F. M. Ali
Department of Mathematics,
Universiti Putra Malaysia,
43400 UPM Serdang,
Selangor, Malaysia

R. Nazar[1]
School of Mathematical Sciences,
Faculty of Science and Technology,
Universiti Kebangsaan Malaysia,
43600 UKM Bangi,
Selangor, Malaysia
e-mail: rmn72my@yahoo.com

N. M. Arifin
Department of Mathematics,
and Institute for Mathematical Research,
Universiti Putra Malaysia,
43400 UPM Serdang,
Selangor, Malaysia

I. Pop
Faculty of Mathematics,
University of Cluj,
R-3400 Cluj CP 253, Romania

MHD Mixed Convection Boundary Layer Flow Toward a Stagnation Point on a Vertical Surface With Induced Magnetic Field

In this paper, the steady magnetohydrodynamic (MHD) mixed convection stagnation point flow of an incompressible, viscous, and electrically conducting fluid over a vertical flat plate is investigated. The effect of induced magnetic field is taken into account. Numerical results are obtained using an implicit finite-difference scheme. Both assisting and opposing flows are considered. The results for skin friction, heat transfer, and induced magnetic field coefficients are obtained and discussed for various parameters. The velocity, temperature, and induced magnetic field profiles are also presented. For the case of the opposing flow, it is found that dual solutions exist for a certain range of the buoyancy parameter. Dual solutions are also obtained for the assisting flow. [DOI: 10.1115/1.4002602]

Keywords: boundary layer, dual solutions, induced magnetic field, MHD, mixed convection

1 Introduction

The case of a steady magnetohydrodynamic (MHD) stagnation point flow of an electrically conducting fluid has many practical applications. Many metallurgical processes, such as drawing, annealing, and tinning of copper wires, involve the cooling of continuous strips or filaments by drawing them through a quiescent fluid. Another important application of hydromagnetics to metallurgy is the purification of molten metals from nonmetallic inclusions by the application of a magnetic field. The study of the MHD stagnation point flow of an electrically conducting fluid in the presence of a uniform magnetic field, which is applied normal to the infinite plane surface, was considered by Ariel [1]. Later, Mahapatra and Gupta [2] studied the MHD stagnation point flow over a stretching surface, and very recently Chen [3] considered the combined effects of Joule heating and viscous dissipation on MHD flow past a permeable stretching surface with free convection and radiative heat transfer. Further, the study of boundary layer flow against a vertical surface problem was considered by Cramer [4], Cobble [5], Raptis et al. [6,7], Soundalgekar et al. [8], Ramachandran et al. [9], Hossain and Ahmed [10], Kumari et al. [11], and Ishak et al. [12–15] in various ways. On the other hand, in micropolar fluid, Lok et al. [16] and Ishak et al. [17] solved the boundary layer flow near a stagnation point on a vertical surface. These are examples where the induced magnetic fields are not considered in their study. The study of the boundary layer flow under the influence of a magnetic field with the induced magnetic field was considered by a few authors. For example, Raptis and Perdikis [18] studied the MHD free convection boundary layer flow past an infinite vertical porous plate. Later, Kumari et al. [19] considered prescribed wall temperature or heat flux, and Takhar et al. [20] studied the time dependence of a free convection flow.

This present paper aims to study the problem of a MHD mixed convection boundary layer flow toward a stagnation point on a vertical flat plate in the presence of a magnetic field where the effect of the induced magnetic field is considered. The governing partial differential equations are reduced to similarity or nonlinear ordinary differential equations that are then solved numerically. The flow depends heavily on the magnetic parameter, the Prandtl number, and the reciprocal of the magnetic Prandtl number.

2 Mathematical Formulation

Consider a steady two-dimensional MHD stagnation point flow of an incompressible, viscous, and electrically conducting fluid past a vertical surface with a velocity proportional to the distance from the fixed origin O of a stationary frame of reference (x,y), as shown in Fig. 1. The assisting flow situation occurs if the upper half of the flat surface is heated while the lower half of the flat surface is cooled (see Fig. 1(a)). In this case, the flow near the heated flat surface tends to move upward, and the flow near the cooled flat surface tends to move downward; therefore, this behavior acts to assist the flow field. The opposing flow situation occurs if the upper half of the flat surface is cooled while the lower half of the flat surface is heated (see Fig. 1(b)). The frame of reference (x,y) is chosen such that the x-axis is along the direction of the surface and the y-axis is normal to the surface. It is assumed that the velocity of the external flow $u_e(x)$ and the temperature of the plate $T_w(x)$ are proportional to the distance of x from the stagnation point, where $u_e(x)=ax$ and $T_w(x)=T_\infty + T_0(x/L)$, where a is a constant, T_0 is the reference temperature, and T_∞ is the uniform ambient temperature. Such assumptions were considered by Ramachandran et al. [9], who studied the steady laminar mixed convection in two-dimensional flows around heated surfaces for both cases of an arbitrary wall temperature and arbitrary surface heat flux. They showed that mixed convection in stagnation flows becomes important when the buoyancy forces due to the temperature difference between the wall and the freestream become high, thereby modifying the flow and thermal fields significantly. It is also assumed that a uniform induced magnetic field of strength H_0 is applied in the normal di-

[1]Corresponding author.

Contributed by the Heat Transfer Division of ASME for publication in the JOURNAL OF HEAT TRANSFER. Manuscript received February 4, 2010; final manuscript received August 22, 2010; published online November 2, 2010. Assoc. Editor: Frank Cunha.

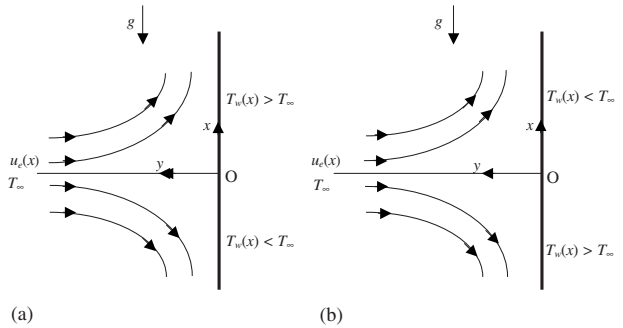

Fig. 1 Physical model and coordinate system for (*a*) assisting flow and (*b*) opposing flow

rection to the surface, while the normal component of the induced magnetic field H_2 vanishes when it reaches the wall and the parallel component H_1 approaches the value of H_0. Under these assumptions along with the Boussinesq and boundary layer approximations, the basic equations of the problem can be written as follows:

$$\frac{\partial u}{\partial x} + \frac{\partial v}{\partial y} = 0 \tag{1}$$

$$\frac{\partial H_1}{\partial x} + \frac{\partial H_2}{\partial y} = 0 \tag{2}$$

$$u\frac{\partial u}{\partial x} + v\frac{\partial u}{\partial y} = u_e\frac{du_e}{dx} + \nu\frac{\partial^2 u}{\partial y^2} + \frac{\mu_0}{\rho}\left(H_1\frac{\partial H_1}{\partial x} + H_2\frac{\partial H_1}{\partial y}\right) - \frac{\mu_0}{\rho}H_e\frac{\partial H_e}{\partial x} + g\beta(T - T_\infty)(x/L) \tag{3}$$

$$u\frac{\partial H_1}{\partial x} + v\frac{\partial H_1}{\partial y} - H_1\frac{\partial u}{\partial x} - H_2\frac{\partial u}{\partial y} = \alpha_1\frac{\partial^2 H_1}{\partial y^2} \tag{4}$$

$$u\frac{\partial T}{\partial x} + v\frac{\partial T}{\partial y} = \frac{\nu}{\mathrm{Pr}}\frac{\partial^2 T}{\partial y^2} \tag{5}$$

where u and v are the velocity components along the x-axis and y-axis, respectively, T is the fluid temperature, g is the gravity acceleration, ρ, ν, and β are the fluid density, kinematic viscosity, and thermal expansion coefficient, respectively, μ_0 is the magnetic permeability, α_1 is the magnetic diffusivity, L is the characteristic length, and Pr is the Prandtl number.

The boundary conditions for Eqs. (1)–(5) are

$$u = v = 0, \quad \frac{\partial H_1}{\partial y} = H_2 = 0, \quad T = T_w \quad \text{at } y = 0$$

$$u = u_e(x), \quad T = T_\infty, \quad H_1 = H_e(x) \quad \text{as } y \to \infty \tag{6}$$

where $H_e(x) = H_0(x/L)$.

Thus, we introduce the following similarity transformations:

$$\psi = (a\nu)^{1/2}xf(\eta), \quad \theta(\eta) = \frac{(T - T_\infty)}{(T_w - T_\infty)}, \quad \eta = (a/\nu)^{1/2}y$$

$$H_1 = H_0(x/L)h'(\eta), \quad H_2 = -\frac{H_0}{L}(\nu/a)^{1/2}h(\eta) \tag{7}$$

where ψ is the stream function, which is defined as $u = \partial\psi/\partial y$ and $v = -\partial\psi/\partial x$; hence, Eqs. (1) and (2) are satisfied.

By substituting Eq. (7) into Eqs. (3)–(5), we obtain the following similarity or ordinary nonlinear differential equations:

$$f''' + ff'' - (f')^2 + 1 + M(h'^2 - hh'' - 1) + \lambda\theta = 0 \tag{8}$$

$$\alpha h''' + fh'' - hf'' = 0 \tag{9}$$

Table 1 Variation in the skin friction coefficient for different values of Pr when $M=0$ and $\lambda=1$

			Ishak et al. [17]		Present results	
Pr	Ramachandran et al. [9]	Lok et al. [16]	Upper branch	Lower branch	Upper branch	Lower branch
0.7	1.7063	1.706376	1.7063	1.2387	1.7063	1.2388
1	–	–	1.6755	1.1332	1.6755	1.1332
7	1.5179	1.517952	1.5179	0.5824	1.5179	0.5824
10	–	–	1.4928	0.4958	1.4928	0.4958

$$\frac{1}{\mathrm{Pr}}\theta'' + f\theta' - f'\theta = 0 \tag{10}$$

and the boundary conditions (6) reduce to

$$f(0) = f'(0) = 0, \quad h(0) = h''(0) = 0, \quad \theta(0) = 1$$

$$f'(\infty) = 1, \quad h'(\infty) = 1, \quad \theta(\infty) = 0 \tag{11}$$

where primes denote differentiation with respect to η, $\alpha = \alpha_1/\nu$ is the reciprocal of the magnetic Prandtl number, and $M = \mu_0 H_0^2/(\rho L^2 a^2)$ is the magnetic parameter or Hartmann [21] number. Further,

$$\lambda = \frac{g\beta(T_w - T_\infty)L^3/\nu^2}{L^4a^2/\nu^2} = \frac{\mathrm{Gr}}{\mathrm{Re}^2} \tag{12}$$

is the constant buoyancy parameter with $\mathrm{Gr} = g\beta(T_w - T_\infty)L^3/\nu^2$ as the Grashof number and $\mathrm{Re} = L^2a/\nu$ as the Reynolds number, where $\lambda > 0$ and $\lambda < 0$ correspond to the buoyancy assisting and opposing flows, respectively, and $\lambda = 0$ is the pure forced convection flow.

In this study, the physical quantities of interest are the skin friction coefficient C_{fx} and the local Nusselt number Nu_x, which are defined as

$$C_{fx} = \frac{\tau_w}{\rho u_e^2}, \quad \mathrm{Nu}_x = \frac{xq_w}{k(T_w - T_\infty)} \tag{13}$$

where τ_w is the surface shear stress in the direction of y, while q_w is the surface heat flux, which are given by

$$\tau_w = \mu\left(\frac{\partial u}{\partial y}\right)_{y=0}, \quad q_w = -k\left(\frac{\partial T}{\partial y}\right)_{y=0} \tag{14}$$

with μ and k being the dynamic viscosity and thermal conductivity of the fluid, respectively. Using Eq. (7), we obtain

$$C_f\mathrm{Re}_x^{1/2} = f''(0), \quad \mathrm{Nu}_x/\mathrm{Re}_x^{1/2} = -\theta'(0) \tag{15}$$

3 Results and Discussion

Equations (8)–(10) subject to the boundary conditions (11) have been solved numerically using the Keller-box method as described by Cebeci and Bradshaw [22]. To validate the accuracy of the present method, the numerical result for the local skin friction coefficient when the magnetic parameter is absent in this study is found to be $f''(0) = 1.2326$, which is in very good agreement with Wang [23]. Comparison is also made with previously published results for the local skin friction coefficient and the local Nusselt number when $\lambda = 1$, as shown in Tables 1 and 2, where the dual solutions are also given, and the comparison is also found to be in very good agreement.

Figures 2–4 respectively display the effects of magnetic parameter on the velocity, temperature, and the induced magnetic field $h(\eta)$ profiles for both assisting ($\lambda = 4$) and opposing flow ($\lambda = -0.2$) cases when fixed λ and $\mathrm{Pr} = 0.7$ are applied. Velocity profiles decrease when magnetic parameter M increases, but the profiles increase with M after a certain point for the assisting flow. From

Table 2 Variation in the local Nusselt number for different values of Pr when $M=0$ and $\lambda=1$

Pr	Ramachandran et al. [9]	Lok et al.[16]	Ishak et al. [17] Upper branch	Ishak et al. [17] Lower branch	Present results Upper branch	Present results Lower branch
0.7	0.7641	0.764087	0.7641	1.0226	0.7641	1.0226
1	–	–	0.8708	1.1691	0.8708	1.1691
7	1.7224	1.722775	1.7225	2.2191	1.7225	2.2190
10	–	–	1.9448	2.4940	1.9448	2.4937

Fig. 3, it is seen that the temperature profiles are always increasing when M increases for both assisting and opposing flows, but the increase in M is not very significant for temperature profiles in the assisting flow. In the assisting flow, an increase in M leads to a decrease in $h(\eta)$ profiles, and these profiles increase with the increase in M after a certain point. On the other hand, an increase in M leads to an increase in $h(\eta)$ profiles for the opposing flow. These can be seen from Fig. 4.

Velocity profiles for the assisting flow ($\lambda=1$) and fixed $M=0.2$ decrease as Pr increases. However, the trend reverses for the opposing flow ($\lambda=-0.2$). These profiles are displayed in Fig. 5. Figure 6 shows the temperature profiles for fixed $M=0.2$ and $\lambda=1,-0.2$. Both assisting and opposing flows show that the thermal boundary layer thickness decreases as Pr increases. This phenomenon happened because when Pr is increased, the thermal diffusivity decreases; thus, it leads to the decrease of the energy transfer ability that decreases the thermal boundary layer. From Fig. 7, the Prandtl number shows the same effect as M on $h(\eta)$ profiles. In Figs. 8 and 9, the profiles are plotted for various values of the mixed convection parameter λ when the magnetic parameter and the Prandtl number are fixed at $M=0.2$ and $\mathrm{Pr}=0.7$, respectively. It can be seen that both the velocity profiles and the $h(\eta)$ profiles reduce with the increase in λ. Figure 10 shows the opposite trend for the temperature profiles.

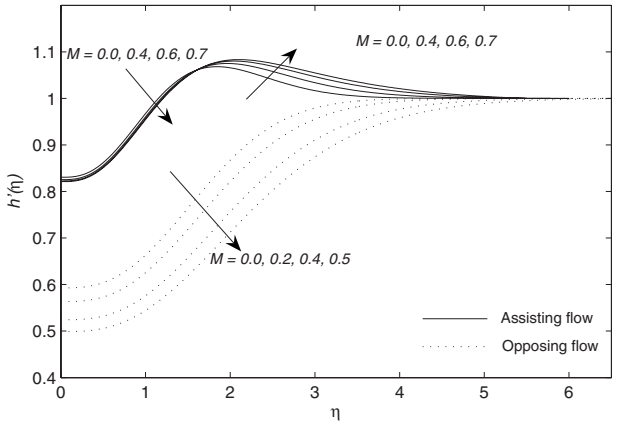

Fig. 4 Induced magnetic field profiles when $\mathrm{Pr}=0.7$ for fixed $\lambda=4$ (assisting flow) and $\lambda=-0.2$ (opposing flow)

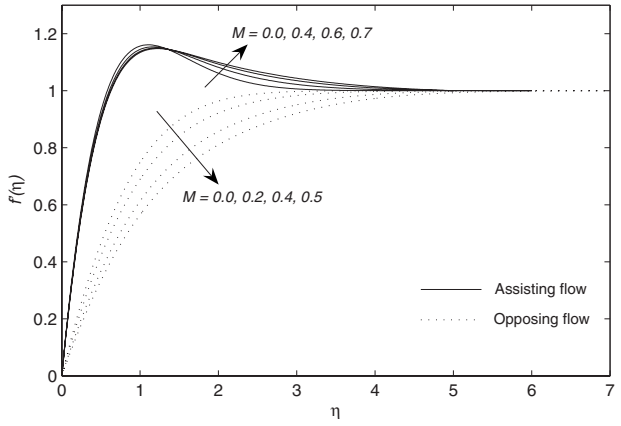

Fig. 2 Velocity profiles when $\mathrm{Pr}=0.7$ for fixed $\lambda=4$ (assisting flow) and $\lambda=-0.2$ (opposing flow)

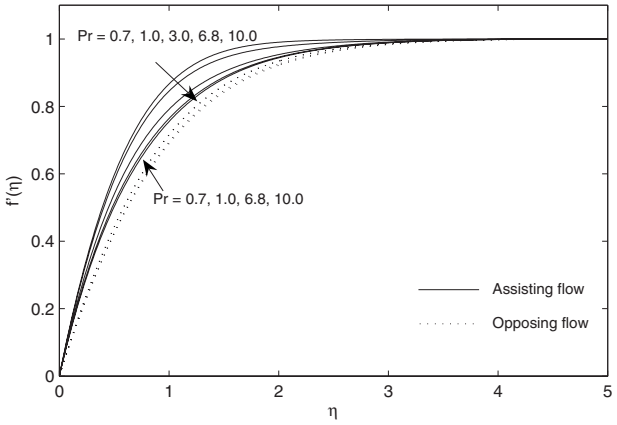

Fig. 5 Velocity profiles when $M=0.2$ for fixed $\lambda=1$ (assisting flow) and $\lambda=-0.2$ (opposing flow)

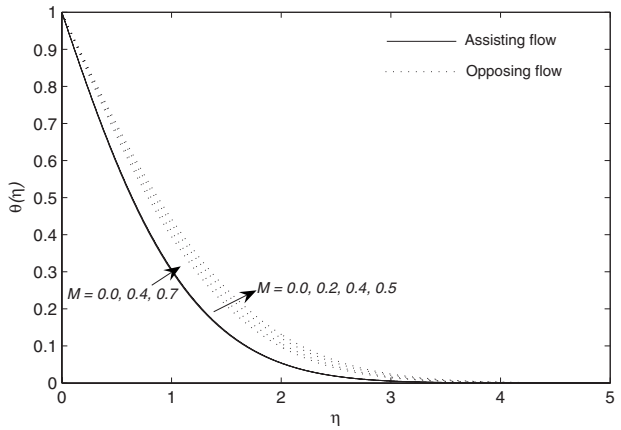

Fig. 3 Temperature profiles when $\mathrm{Pr}=0.7$ for fixed $\lambda=4$ (assisting flow) and $\lambda=-0.2$ (opposing flow)

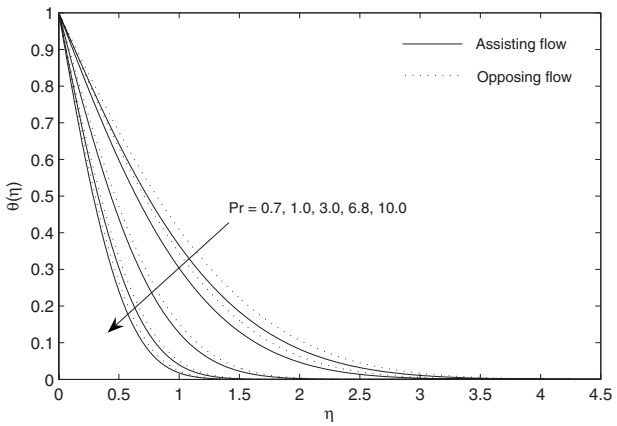

Fig. 6 Temperature profiles when $M=0.2$ for fixed $\lambda=1$ (assisting flow) and $\lambda=-0.2$ (opposing flow)

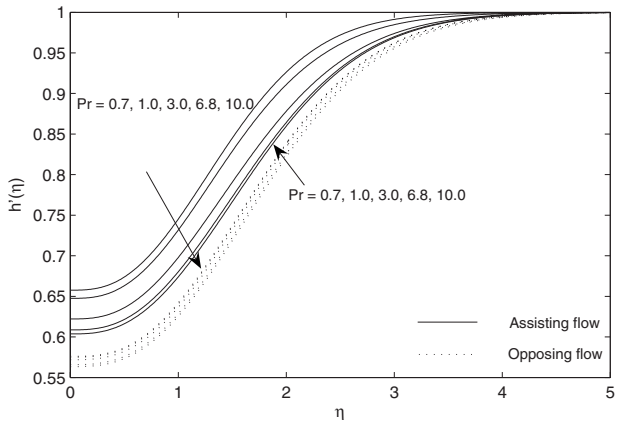

Fig. 7 Induced magnetic field profiles when $M=0.2$ for fixed $\lambda=1$ (assisting flow) and $\lambda=-0.2$ (opposing flow)

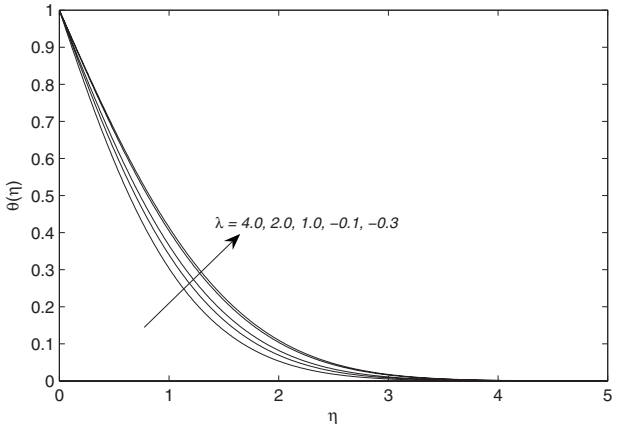

Fig. 10 Temperature profiles for fixed $M=0.2$ and $\Pr=0.7$

Figures 11 and 12 display the dual solutions for the quantities of physical interest, which are the skin friction coefficient $f''(0)$ and the local Nusselt number $-\theta(0)$. It can be seen that dual solutions of Eqs. (8)–(10) can be obtained for assisting and opposing flows for both $M=0.0$ and 0.3. For $\lambda>0$ (assisting flow), dual solutions exist for all λ, and the skin friction coefficient increases with λ as the pressure gradient due to the buoyancy forces accelerates the flow. For $\lambda<0$ (opposing flow), solutions do not exist beyond certain critical values of λ_c, dual solutions exist at $\lambda>\lambda_c$, and a unique solution is obtained when $\lambda=\lambda_c$. Hence, at $\lambda=\lambda_c$, the boundary layer separation occurs. In this study, for $M=0$, $\lambda_c=-2.2$, while for $M=0.3$, λ_c reduces to -1.6. The critical value $|\lambda_c|$ shown in Fig. 11 decreases as the magnetic parameter increases; therefore, the magnetic field induces earlier boundary layer separation or the boundary layer separation becomes faster when the magnetic field is applied. Numerical values of these results are presented in Table 3 for both assisting and opposing flows. Figure 12 shows that $-\theta'(0)$ becomes unbounded

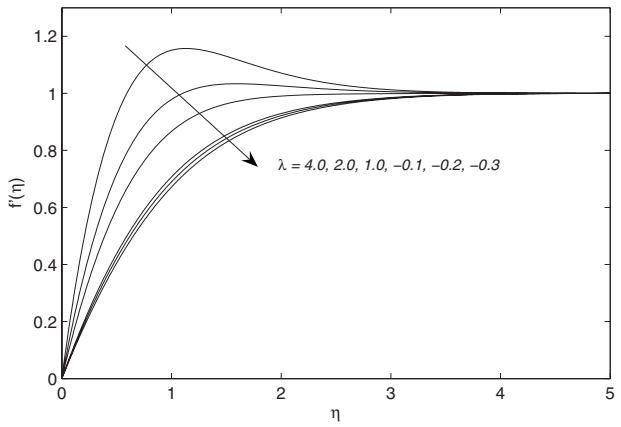

Fig. 8 Velocity profiles for fixed $M=0.2$ and $\Pr=0.7$

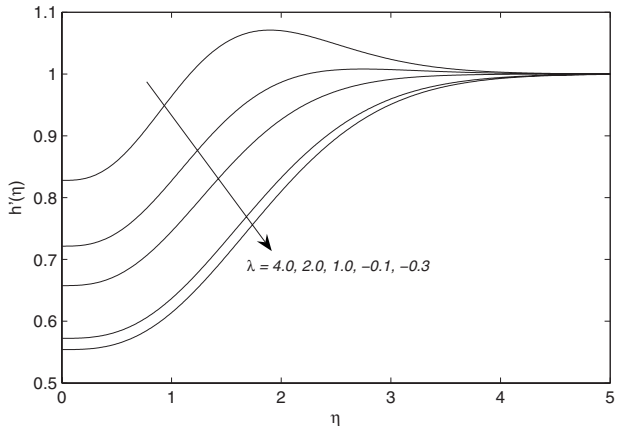

Fig. 9 Induced magnetic field profiles for fixed $M=0.2$ and $\Pr=0.7$

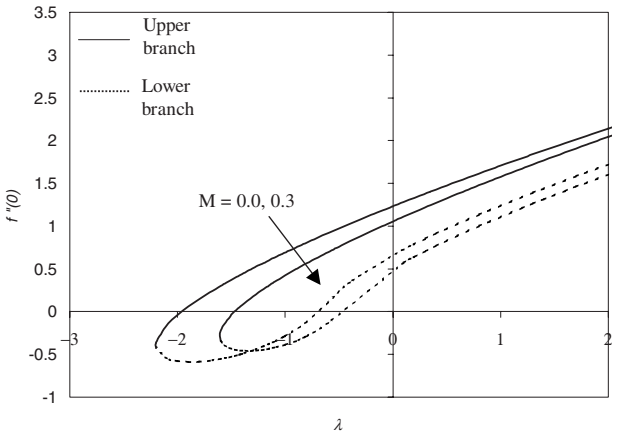

Fig. 11 Variation of the skin friction coefficient with λ for fixed $\Pr=0.7$ when $M=0$ and 0.3

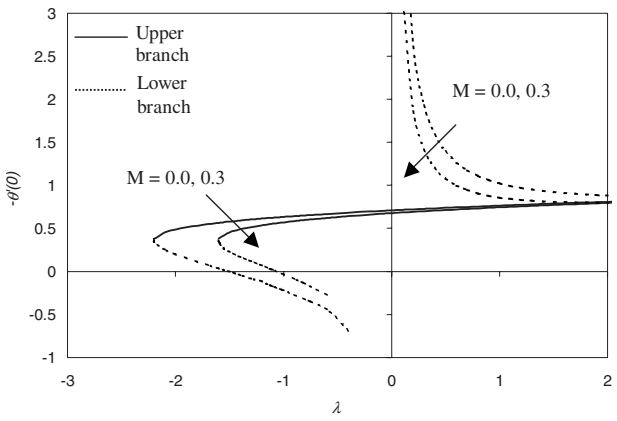

Fig. 12 Variation of the local Nusselt number with λ for fixed $\Pr=0.7$ when $M=0$ and 0.3

Table 3 Variation in the skin friction coefficient and the local Nusselt number with λ for fixed Pr=0.7 when $M=0$ and 0.3

	$M=0.0$		$M=0.3$		$M=0.0$		$M=0.3$	
λ	$f_1''(0)$	$f_2''(0)$	$f_1''(0)$	$f_2''(0)$	$-\theta_1'(0)$	$-\theta_2'(0)$	$-\theta_1'(0)$	$-\theta_2'(0)$
−0.6	0.1084	0.9194	−0.1316	0.6973	−0.4407	0.6673	−0.2719	0.6207
−0.8	−0.1193	0.8079	−0.2880	0.5651	0.3262	0.6510	−0.1437	0.5973
−1.0	−0.2851	0.6917	−0.3882	0.4225	−0.2222	0.6332	−0.0339	0.5698
−1.1	−0.3501	0.6315	−0.4224	0.3460	−0.1742	0.6236	0.0167	0.5539
−1.2	−0.4059	0.5696	−0.4463	0.2646	−0.1154	0.6134	0.0659	0.5358
−1.3	−0.4536	0.506	−0.4592	0.1765	−0.0857	0.5964	0.1154	0.5148
−1.4	−0.4941	0.4401	−0.4582	0.0783	−0.0444	0.5909	0.167	0.489
−1.5	−0.5277	0.3718	−0.4357	−0.0382	−0.0044	0.5632	0.2256	0.4543
−1.6	−0.5544	0.3003	−0.3443	−0.2208	0.0349	0.5574	0.3443	0.3852
0.1	0.7276	1.2823	0.5714	1.1105	4.6975	0.7157	3.2286	0.6844
0.5	0.9691	1.4755	0.8280	1.3242	1.3926	0.7383	1.0775	0.7130
0.9	1.1868	1.6610	1.0544	1.5268	1.0604	0.7591	0.8783	0.7382
1.6	1.5348	−0.1566	1.4125	1.8614	0.9112	0.7916	0.8041	0.7764
2.0	1.7209	2.1407	1.6029	2.0436	0.8843	0.8084	0.7970	0.7957

when $\lambda \to 0^+$ and $\lambda \to 0^-$ for the second solution, and for a certain value of the magnetic field M, the heat transfer coefficient for the first solution increases with λ. It is worth mentioning that as in similar physical situations, the upper branch (first) solutions are physically stable and occur in practice, while the lower branch (second) solutions are not physically obtained. This can be verified by performing a stability analysis, but this is beyond the scope of the present paper. Such an analysis was done by Merkin [24], Weidman et al. [25], and Harris et al. [26].

Table 4 shows the effect of the reciprocal of the magnetic Prandtl number α on the skin friction, the induced magnetic field, and the heat transfer coefficients. All three coefficients increase with α for both assisting and opposing flows. It can be seen that the induced magnetic field coefficients are affected the most by α as it appears in the induced magnetic field equation.

4 Conclusions

A numerical study is performed for the problem of the steady laminar mixed convection boundary layer flow on a vertical surface in the presence of a magnetic field. The induced magnetic field is also taken into account. The velocity, temperature, and the induced magnetic field profiles are affected by the magnetic parameter, the Prandtl number, and the buoyancy parameter for both assisting and opposing flows. In this study, it is also found that the induced magnetic field are affected the most by the reciprocal of the magnetic Prandtl number α compared with the skin friction and heat transfer coefficients. Dual solutions are also obtained for opposing and assisting flows in this study. It is also found that the magnetic field induces earlier boundary layer separation; i.e., the boundary layer separation becomes faster when the magnetic field is applied.

Acknowledgment

The authors gratefully acknowledge the financial support received in the form of a fundamental research grant (FRGS) from the Ministry of Higher Education, Malaysia. The authors also wish to express their very sincere thanks to the anonymous reviewers for their valuable comments and suggestions.

Table 4 Variation in the $f''(0)$, $h'(0)$, and $-\theta'(0)$ for different values of α when Pr=0.7

	$\lambda=0.2$			$\lambda=-0.2$		
α	$f''(0)$	$h'(0)$	$-\theta'(0)$	$f''(0)$	$h'(0)$	$-\theta'(0)$
1	1.0262	0.5453	0.6644	0.7769	0.4988	0.6238
5	1.1046	0.7032	0.6777	0.8620	0.6649	0.6403
10	1.1436	0.7639	0.6851	0.9260	0.7567	0.6541
20	1.1813	0.8172	0.6925	0.9724	0.8178	0.6638

Nomenclature

a = constant
C_{fx} = skin friction coefficient
$f(\eta)$ = dimensionless stream function
g = acceleration due to gravity
Gr = Grashof number
$h(\eta)$ = dimensionless induced magnetic field
H_0 = applied magnetic field
H_1, H_2 = induced magnetic field components along the x and y directions, respectively
k = thermal conductivity
L = characteristic length
M = magnetic parameter
Nu = Nusselt number
Pr = Prandtl number
q_w = surface heat flux
Re = Reynolds number
T = fluid temperature
$T_w(x)$ = temperature of the surface
T_∞ = ambient temperature
u, v = velocity components along the x and y directions, respectively
$u_e(x)$ = velocity of the external flow
x, y = Cartesian coordinates along the surface and normal to it, respectively

Greek

α = reciprocal of the magnetic Prandtl number
α_1 = magnetic diffusivity
β = thermal expansion coefficient
η = similarity variable
θ = dimensionless temperature
λ = buoyancy or mixed convection parameter
μ = dynamic viscosity
μ_0 = magnetic permeability
ν = kinematic viscosity
ρ = fluid density
ψ = stream function
τ_w = surface shear stress

References

[1] Ariel, P. D., 1994, "Hiemenz Flow in Hydromagnetics," Acta Mech., **103**, pp.

31–43.
[2] Mahapatra, T. R., and Gupta, A. S., 2001, "Magnetohydrodynamic Stagnation Point Flow Towards a Stretching Sheet," Acta Mech., **152**, pp. 191–196.
[3] Chen, C. H., 2010, "Combined Effects of Joule Heating and Viscous Dissipation on Magnetohydrodynamic Flow Past a Permeable, Stretching Surface With Free Convection and Radiative Heat Transfer," ASME J. Heat Transfer, **132**, p. 064503.
[4] Cramer, K. R., 1963, "Several Magneto-Hydrodynamic Free Convection Solutions," ASME J. Heat Transfer, **85**, pp. 35–40.
[5] Cobble, M. H., 1979, "Free Convection With Mass Transfer Under the Influence of a Magnetic Field," Nonlinear Anal. Theory, Methods Appl., **3**, pp. 135–143.
[6] Raptis, A., Perdikis, C., and Tzivanidis, G., 1981, "Effects of Free Convection Currents on the Flow of an Electrically Conducting Fluid Past an Accelerated Vertical Infinite Plate With Variable Suction," J. Appl. Math. Mech., **61**, pp. 341–342.
[7] Raptis, A., Tzivanidis, G., and Perdikis, C., 1981, "Hydromagnetic Free Convection Flow Past an Accelerated Vertical Infinite Plate With Variable Suction and Heat Flux," Lett. Heat Mass Transfer, **8**, pp. 137–143.
[8] Soundalgekar, V. M., Singh, M., and Takhar, H. S., 1983, "MHD Free Convection Past a Semi-Infinite Vertical Plate With Suction and Injection," Nonlinear Anal. Theory, Methods Appl., **7**, pp. 941–944.
[9] Ramachandran, N., Chen, T. S., and Armaly, B. F., 1988, "Mixed Convection in Stagnation Flows Adjacent to Vertical Surfaces," ASME J. Heat Transfer, **110**, pp. 373–377.
[10] Hossain, M. A., and Ahmed, M., 1990, "MHD Forced and Free Convection Boundary Layer Flow Near the Leading Edge," Int. J. Heat Mass Transfer, **33**, pp. 571–575.
[11] Kumari, M., Slaouti, A., Takhar, H. S., Nakamura, S., and Nath, G., 1996, "Unsteady Free Convection Flow Over a Continuous Moving Vertical Surface," Acta Mech., **116**, pp. 75–82.
[12] Ishak, A., Nazar, R., and Pop, I., 2006, "Magnetohydrodynamic Stagnation-Point Flow Towards a Stretching Vertical Sheet," Magnetohydrodynamics, **42**, pp. 17–30.
[13] Ishak, A., Nazar, R., and Pop, I., 2007, "Mixed Convection on the Stagnation Point Flow Toward a Vertical, Continuously Stretching Sheet," ASME J. Heat Transfer, **129**, pp. 1087–1090.
[14] Ishak, A., Nazar, R., Arifin, N. M., and Pop, I., 2007, "Dual Solutions in Magnetohydrodynamic Mixed Convection Flow Near a Stagnation-Point on a Vertical Surface," ASME J. Heat Transfer, **129**, pp. 1212–1216.
[15] Ishak, A., Nazar, R., and Pop, I., 2008, "Hydromagnetic Flow and Heat Transfer Adjacent to a Stretching Vertical Sheet," Heat Mass Transfer, **44**, pp. 921–927.
[16] Lok, Y. Y., Amin, N., Campean, D., and Pop, I., 2005, "Steady Mixed Convection Flow of a Micropolar Fluid Near the Stagnation Point on a Vertical Surface," Int. J. Numer. Methods Heat Fluid Flow, **15**, pp. 654–670.
[17] Ishak, A., Nazar, R., and Pop, I., 2008, "Magnetohydrodynamic (MHD) Flow of a Micropolar Fluid Towards a Stagnation Point on a Vertical Surface," Comput. Math. Appl., **56**, pp. 3188–3194.
[18] Raptis, A., and Perdikis, C., 1984, "Free Convection Under the Influence of a Magnetic Field," Nonlinear Anal. Theory, Methods Appl., **8**, pp. 749–756.
[19] Kumari, M., Takhar, H. S., and Nath, G., 1990, "MHD Flow and Heat Transfer Over a Stretching Surface With Prescribed Wall Temperature or Heat Flux," Waerme- Stoffuebertrag., **25**, pp. 331–336.
[20] Takhar, H. S., Kumari, M., and Nath, G., 1993, "Unsteady Free Convection Flow Under the Influence of a Magnetic Field," Arch. Appl. Mech., **63**, pp. 313–321.
[21] Hartmann, J., 1937, "Theory of the Laminar Flow of an Electrically Conducting Liquid in a Homogeneous Magnetic Field," Mat. Fys. Medd. K. Dan. Vidensk. Selsk., **15**, pp. 1–28.
[22] Cebeci, T., and Bradshaw, P., 1984, *Physical and Computational Aspects of Convective Heat Transfer*, Springer, New York.
[23] Wang, C. Y., 2006, "Stagnation Slip Flow and Heat Transfer on a Moving Plate," Chem. Eng. Sci., **61**, pp. 7668–7672.
[24] Merkin, J. H., 1985, "On Dual Solutions Occurring in Mixed Convection in a Porous Medium," J. Eng. Math., **20**, pp. 171–179.
[25] Weidman, P. D., Kubitschek, D. G., and Davis, A. M. J., 2006, "The Effect of Transpiration on Self-Similar Boundary Layer Flow Over Moving Surfaces," Int. J. Eng. Sci., **44**, pp. 730–737.
[26] Harris, S. D., Ingham, D. B., and Pop, I., 2009, "Mixed Convection Boundary-Layer Flow Near the Stagnation Point on a Vertical Surface in a Porous Medium: Brinkman Model With Slip," Transp. Porous Media, **77**, pp. 267–285.

Mixed Convective Heat Transfer Past a Heated Square Porous Cylinder in a Horizontal Channel With Varying Channel Height

Horng-Wen Wu[1]
Professor
e-mail: z7708033@email.ncku.edu.tw

Ren-Hung Wang
Post Doctor

Department of Systems and Naval Mechatronic Engineering,
National Cheng Kung University,
Tainan, 701 Taiwan, R.O.C.

The laminar mixed convection flow across the porous square cylinder with the heated cylinder bottom at the axis in the channel has been carried out numerically in this paper using a semi-implicit projection finite element method. The governing equations with the Brinkman–Forcheimer-extended Darcy model for the region of square porous cylinder were solved. The parameter studies including Grashof number, Darcy number, and channel-to-cylinder height ratio on heat transfer performance have been explored in detail. The results indicate that the heat transfer is augmented as the Darcy number and channel-to-cylinder height ratio increase. The buoyancy effect on the local Nusselt number is clearer for $B/H=0.1$ than for $B/H=0.3$ and $B/H=0.5$.
[DOI: 10.1115/1.4002632]

Keywords: heat transfer, square porous cylinder, buoyancy, Darcy number, channel-to-cylinder height ratio

1 Introduction

Unsteady mixed convection flows through a porous medium in a horizontal channel has been practically applicable such as electronic component cooling system, heat exchangers, light emitting diode (LED) backlight module cooling system, LED streetlamp cooling equipment, thermal insulation, and drying processes. The designs of the configuration require a thorough understanding of the influence of the transport phenomena through porous cylinder. Many studies discussed the characteristics of heat transfer for porous media with various conditions including the Darcy number, Grashof number, Reynolds number, flow conditions, and shape and body conditions. Most of the previous heat transfer studies on laminar channel flow past the porous media were done for the forced convection case [1–9]. However, laminar mixed channel flow through the porous media is also an important fundamental problem of engineering interest and is thus investigated here.

Although many papers have investigated forced convection for the channel flow past the porous media with heat source mounted on one wall, there are few studies on mixed convection. One of the augmentation techniques is to modify the flow pattern induced by vortex shedding, but it is not applied much for mixed convection augmentation. Prasad et al. [10] investigated the steady mixed convection in a horizontal porous layer with localized heating on the channel bottom. Their results indicated that the overall heat transfer rate always increased with increasing Rayleigh number, but the effect of the Peclet number was not straightforward. Hwang and Chao [11] studied how the wall conduction and Darcy number influenced laminar mixed convection in the fully developed region of a horizontal square porous channel with a uniform heat input. They found that the flow and heat transfer characteristics were greatly affected by the peripherally nonuniform wall temperature distribution. Rachedi and Chikh [12] used electronic cooling with insertion foam materials to determine how the operating temperature can be maintained under the allowable level. Their results showed that the insertion of the foam between the blocks led to a temperature reduction of 0.5. Many studies presented that the significant heat transfer augmentation could be achieved through the use of porous media and buoyancy.

Bae et al. [13] numerically studied an enhancement of a mixed convection heat transfer for multiple porous blocks on the wall of a channel with heating the block bottom. The heat flux from the most upstream heater varied in a sinusoidal form, while other heaters have a constant heat flux. Jaballah et al. [14,15] used the SIMPLER algorithm to investigate mixed convection in a channel partially filled with porous media. They determined the stability curve and optimal values of Rayleigh, Reynolds, and Darcy numbers permitting the maximum heat transfer from solid to fluid. Cimpean et al. [16] investigated steady, fully developed mixed convection flow between inclined parallel plates filled with a porous medium. Analytical results were obtained by a mixed convection parameter, Peclet number, and inclination angle.

With reference to the experiments, very few studies were reported. Chou et al. [17] experimentally and analytically investigated the fully developed non-Darcian mixed convection in horizontal packed-sphere channels. Kurtbas and Celik [18] experimentally investigated forced and mixed convection heat transfer in a foam horizontal rectangular channel. About unsteady vortex flow, Jue [19] used a semi-implicit projection finite element method to solve unsteady two-dimensional flow over a porous square cylinder. He found that as the flow passed a higher permeability cylinder, the vortex shedding occurred later and the shedding period was shorter.

Many previous studies on channel-confined flow across a square cylinder were considered as the forced convection problem [20,21]. Sharma and Eswaran [22] showed how the channel confinement and buoyancy influenced the 2D laminar flow and heat transfer across a square cylinder. Perng and Wu [23] investigated how the aiding/opposing buoyancy affected the turbulent flow field and heat transfer across a square cylinder in a vertical channel by changing the level of wall confinement.

Although the transport phenomena through porous media have been studied, there is little work on unsteady-state mixed convective heat transfer across a porous square cylinder at the axis in the channel. The purpose of this paper is to numerically realize the

[1]Corresponding author.

Contributed by the Heat Transfer Division of ASME for publication in the JOURNAL OF HEAT TRANSFER. Manuscript received November 13, 2009; final manuscript received September 23, 2010; published online November 3, 2010. Assoc. Editor: Patrick H. Oosthuizen.

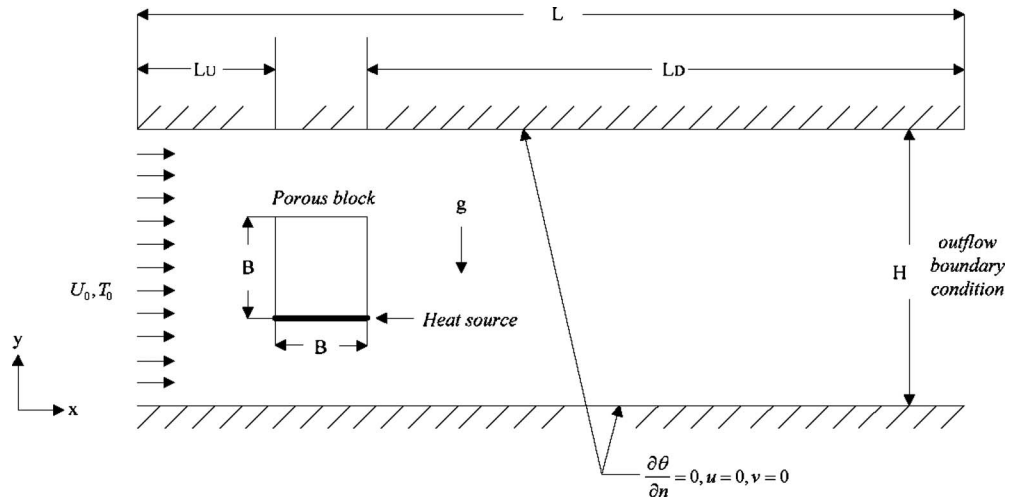

Fig. 1 Schematic of the physical domain

features of laminar mixed flow across a porous square cylinder with the heated cylinder bottom at the axis in the channel with cylinder-to-channel height ratios. The numerical method applied here is a semi-implicit projection finite element method, which is a powerful numerical method for unsteady incompressible thermal flows. This paper investigates how the permeability, Grashof number, and channel-to-cylinder height ratios influence the heat transfer under steady-state values and time history of global quantities with vortex shedding involved. The results of this paper may be of interest to engineers attempting to develop thermal control of heat exchangers or electronic devices and to researchers interested in the flow and heat transfer across a square cylinder at the axis in the channel.

2 Mathematical Formulation

The geometry and the relevant dimensions considered for analysis are schematically shown in Fig. 1. This model involves a two-dimensional, unsteady, laminar, mixed convection, and incompressible flow past a porous square cylinder with a uniform heat generation mounted on the nonpermeable bottom surface. The model is treated further subject to the following assumptions [24].

(1) The fluid is Newtonian, and the properties of the fluid are constant.
(2) The effective thermal conductivity of the fluid-saturated porous region is equal to the thermal conductivity of the fluid.
(3) The thermophysical properties of the porous medium are constant.
(4) The effective viscosity equals the fluid viscosity.
(5) The porous square cylinder is homogeneous, isotropic, and saturated with a single-phase fluid.

The nondimensional governing equations for continuity, the general Darcy–Brinkman–Forchheimer [3], and the energy equations are as follows:

$$\frac{\partial u}{\partial x}+\frac{\partial v}{\partial y}=0 \tag{1}$$

$$\frac{1}{\varepsilon}\frac{\partial u}{\partial t}+\frac{1}{\varepsilon^2}\left(u\frac{\partial u}{\partial x}+v\frac{\partial u}{\partial y}\right)=-\frac{\partial p}{\partial x}+\frac{1}{\varepsilon \mathrm{Re}}\left(\frac{\partial^2 u}{\partial x^2}+\frac{\partial^2 u}{\partial y^2}\right)-\frac{1}{\mathrm{DaRe}}u-\frac{1.75}{\sqrt{150}}\frac{1}{\sqrt{\mathrm{Da}}}\frac{|u|}{\varepsilon^{3/2}}u \tag{2}$$

$$\frac{1}{\varepsilon}\frac{\partial v}{\partial t}+\frac{1}{\varepsilon^2}\left(u\frac{\partial v}{\partial x}+v\frac{\partial v}{\partial y}\right)=-\frac{\partial p}{\partial y}+\frac{1}{\varepsilon \mathrm{Re}}\left(\frac{\partial^2 v}{\partial x^2}+\frac{\partial^2 v}{\partial y^2}\right)-\frac{1}{\mathrm{DaRe}}v-\frac{1.75}{\sqrt{150}}\frac{1}{\sqrt{\mathrm{Da}}}\frac{|u|}{\varepsilon^{3/2}}v+\frac{\mathrm{Gr}}{\mathrm{Re}^2}\theta \tag{3}$$

$$\sigma\frac{\partial \theta}{\partial t}+u\frac{\partial \theta}{\partial x}+v\frac{\partial \theta}{\partial y}=\frac{1}{\mathrm{RePr}}\left(\frac{\partial^2 \theta}{\partial x^2}+\frac{\partial^2 \theta}{\partial y^2}\right)+\frac{1}{\mathrm{RePr}}A \tag{4}$$

In this paper, σ is equal to 1, and Darcy number is set to a large value equal to 10^7 and $\varepsilon=1$ in the fluid region. The heat flux only exits on the bottom surface of the porous square cylinder. A harmonic mean is adopted to treat the sudden change between clear fluid and porous medium, as suggested by Patankar [25]. For fluid/porous interface, the construction of stiffness matrix for the points on the interface accumulates the influence from porous and clear areas. This procedure is similar to adopting a harmonic mean for the interfacial values. In addition, we place the finest mesh on the interface to reduce the sudden change in flow medium.

The relevant dimensionless boundary conditions are as follows:

$$\text{at } x=0,\quad 0<y<H/B,\quad u=1,\quad v=0,\quad \theta=0 \tag{5}$$

$$\text{at } y=0,\quad 0<x<L/B,\quad u=0,\quad v=0,\quad \left.\frac{\partial \theta}{\partial y}\right|_{y=0}=0 \tag{6}$$

$$\text{at } y=H/B,\quad 0<x<L/B,\quad u=0,\quad v=0,\quad \left.\frac{\partial \theta}{\partial y}\right|_{y=L/B}=0 \tag{7}$$

3 Numerical Methods

To solve the dimensionless conservation equations, this paper has used the Galerkin finite element method, which produces linear equations solved by a direct method, and the construction of stiffness matrix for the points on the interface covers porous and clear areas. In order to reduce the sudden variation on the interface between the fluid and the porous region, the authors use the finest mesh next to the interface and enlarged gradually off the porous medium. Applying the standard Galerkin finite element to the spatial discretization of Eqs. (1)–(4) leads to the following systems of couple ordinary equations:

$$\mathrm{H}_{\alpha i \beta}u_{\beta i}=0 \tag{8}$$

$$M_{\alpha\beta}\left(\frac{du_{\beta i}}{\varepsilon dt}+\frac{1}{\mathrm{DaRe}}u_{\beta j}+\frac{1.75}{\sqrt{150}}\frac{|U|}{\varepsilon^{3/2}\sqrt{\mathrm{Da}}}u_{\beta j}\right)+H_{\alpha i\beta}p_{\beta}$$
$$+\frac{1}{\varepsilon\mathrm{Re}}S_{\alpha i\beta j}u_{\beta j}+\frac{1}{\varepsilon^2}K_{\alpha\beta\gamma j}u_{\beta j}u_{\gamma j}=\frac{\mathrm{Gr}}{\mathrm{Re}^2}M_{\alpha\beta}\theta_{\beta}\delta_{i1} \quad (9)$$

$$M_{\alpha\beta}\frac{d\theta_{\beta}}{dt}+\frac{1}{\mathrm{PrRe}}A_{\alpha\beta}\theta_{\beta}+K_{\alpha\beta\gamma j}u_{\beta j}\theta_{\gamma}=\frac{1}{\mathrm{PrRe}}\sum\nolimits_{\alpha} \quad (10)$$

where

$$H_{\alpha i\beta}=\int_{\Omega}(\phi_{\alpha,i}\phi_{\beta})d\Omega,\quad M_{\alpha i\beta}=\int_{\Omega}(\phi_{\alpha}\phi_{\beta})d\Omega$$

$$S_{\alpha i\beta j}=\int_{\Omega}(\phi_{\alpha,i}\phi_{\beta,j})d\Omega$$

$$K_{\alpha\beta\gamma j}=\int_{\Omega}(\phi_{\alpha}\phi_{\beta,j}\phi_{\gamma})d\Omega,\quad A_{\alpha\beta}=\int_{\Omega}(\phi_{\alpha,j}\phi_{\beta,j})d\Omega$$

$$\sum\nolimits_{\alpha}=\int_{\Gamma}(\phi_{\alpha}\theta_{j})n_{j}d\Gamma$$

This paper uses the concept of projection to solve the nonlinear simultaneous ordinary differential equations. The concept of projection consists of a second-order Adams–Bashforth scheme for the advection terms and an implicit Euler scheme for the diffusion terms [26]. The solution procedure is as follows.

3.1 Step 1. This step is to determine an intermediate velocity field $\hat{u}_{\beta j}^{n+1}$ from $u_{\beta i}^{n+1}$ starting with u_0 for $n=0$ using the explicit Adams–Bashforth method for the nonlinear convective term and a first-order implicit Euler time integration scheme for the diffusion term,

$$M_{\alpha\beta}\hat{u}_{\beta i}^{n+1}=M_{\alpha\beta}\hat{u}_{\beta i}^{n}-\varepsilon\Delta t\left(\frac{3}{2}K_{\alpha\beta\gamma j}(u^{n})u_{\gamma i}^{n}-\frac{1}{2}K_{\alpha\beta\gamma j}u_{\beta j}^{n-1}u_{\gamma i}^{n-1}\right)$$
$$-\frac{\Delta t}{\mathrm{Re}}S_{\alpha i\beta j}\hat{u}_{\beta j}^{n+1}-\frac{\varepsilon\Delta t}{\mathrm{DaRe}}\hat{u}_{\beta j}^{n+1}-\frac{1.75}{\sqrt{150}}\frac{\Delta t}{\sqrt{\mathrm{Da}}}\frac{|U|}{\varepsilon^{1/2}}\hat{u}_{\beta j}^{n+1}$$
$$+\frac{\Delta t\mathrm{Gr}}{\mathrm{Re}^2}M_{\alpha\beta}\theta_{\beta}^{n}\delta_{i1} \quad (11)$$

3.2 Step 2. This step is to obtain pressure from a Poisson equation including $\hat{u}_{\beta j}^{n+1}$; in this approach, only the pressure at time $t=0$ is necessary to solve the boundary pressure Poisson equation,

$$A_{\alpha\beta}p_{\beta}^{n+1}=\frac{1}{\varepsilon\Delta t}H_{\alpha i\beta}\hat{u}_{\beta i}^{n+1} \quad (12)$$

Correcting the provisional velocity with the pressure effect yields the real velocity

$$M_{\alpha\beta}^{D}u_{\beta i}^{n+1}=M_{\alpha\beta}^{D}\hat{u}_{\beta i}^{n+1}-\varepsilon\Delta tH_{\alpha i\beta}p_{\beta}^{n+1} \quad (13)$$

where $M_{\alpha\beta}^{D}$ denotes the diagonalized mass matrix obtained simply by summing across each row of the consistent mass matrix and placing the results in the diagonal.

3.3 Step 3. Using the same procedure as the velocity phase obtains the final temperature solutions from the energy equation,

$$M_{\alpha\beta}\theta_{\beta}^{n+1}=M_{\alpha\beta}\theta_{\beta}^{n}-\Delta t\left(\frac{3}{2}K_{\alpha\beta\gamma j}u_{\beta j}^{n}\theta_{\gamma i}^{n}-\frac{1}{2}K_{\alpha\beta\gamma j}u_{\beta j}^{n-1}\theta_{\gamma i}^{n-1}\right)$$
$$-\frac{\Delta t}{\mathrm{RePr}}A_{\alpha\beta}\theta_{\beta}^{n+1}+\frac{\Delta t}{\mathrm{RePr}}\sum\nolimits_{\alpha}^{n} \quad (14)$$

Employing the "traction free" condition [19] at the outflow plane instead of $p=0$ at one point in the outflow plane can find the temperature distribution earlier.

The local Nusselt number along the porous square cylinder surfaces is evaluated by

$$\mathrm{Nu}=-\frac{1}{\theta_{bw}}\theta_{n} \quad (15)$$

where subscript n denotes normal to the porous square cylinder surface.

4 Results and Discussion

In this paper, "the external fluid" means the fluid outside the square porous cylinder and next to the bottom surface, and "the internal fluid" means the fluid inside the square porous cylinder and next to the bottom surface. The Darcy–Brinkman–Forchheimer term appearing in Eqs. (2) and (3) displays the parameters under consideration. The geometric parameters are kept constant at values of $B/B=1$, $L_U/B=4$, and $L_D/B=15$. The following ranges of parameters are considered: channel-to-cylinder height ratios $B/H=0.1$, 0.3, and 0.5, Gr=0, 6250, 31,250, 62,500, 625,000, and 1,250,000, and Da=10^{-2}, 10^{-3}, 10^{-4}, and 10^{-5} when Pr is kept constant at 0.71, Re is kept at 250, and porosity ε is set to 0.8 in the analysis.

All the cases have been calculated by using an Intel® Core™ 2 Quad 2.33 GHz computer. A series of grid independent test runs includes 91×99, 101×109, and 111×119 at $B/H=0.1$, 57×171, 67×189, and 75×203 at $B/H=0.3$, and 41×175, 45×189, and 49×201 at $B/H=0.5$, where the former number is in the x-axis and the latter number is in the y-axis. These nonuniform meshes 101×109 for $B/H=0.1$, 67×189 for $B/H=0.3$, and 45×189 for $B/H=0.5$ were chosen in all cases by considering the computational cost and accuracy from the sensitivity results, as shown in Fig. 2(*a*). The time increment size is adjusted in this numerical code from stability and accuracy criteria with the initial time increment size given as an input. Three values of the time increments $\Delta t=0.002$, 0.001, and 0.0005 were chosen to test the time increment sensitivity, as indicated in Fig. 2(*b*). As a result, the time increment was set at 0.001 in the following calculations. In addition, the calculation in these cases required 250,000 time steps to obtain reasonably reliable statistics. The computation times were approximately from 10 h, 3 min, and 33 s to 22 h, 13 min, and 57 s in all cases. Comparing the local Nusselt number over each heated part with the results of the paper of Rachedi and Chikh [12] may verify the correctness of the program applied in this paper. The current analysis infers discrepancies less than 8.6%, as displayed in Fig. 3. These curves have the same trend. The results of present predictions agree fairly closely with the predictions of Rachedi and Chikh and give one confidence in the use of the program.

The calculation of local time-mean Nusselt number requires us to realize the temperatures on the surface of the square porous cylinder, the external fluid, and the internal fluid. For the square porous cylinder, the temperatures along the bottom surface (locations 4–6) are greater than those along other surfaces, as shown in Fig. 4; this result means that the bottom surface has significant temperature gradients for thermal convection. Furthermore, the temperatures along other surfaces are very small. Therefore, the heat transfer on the bottom of the heated square porous cylinder is used to discuss all cases.

In Fig. 5(*a*), the local Nusselt number along the surface almost has the same trend when Gr=0, 6250, and 31,250. It has a different trend at Gr=625,000. For the lower bottom surface, the local Nusselt number decreases approximately along the surface when Gr=6250 and 31,250, but it increases along the surface after $x=4.6$ when Gr=625,000. For the upper bottom surface, when Gr=625,000, the Nusselt number decreases up to 35% (at $x=4$, relative ratio between Gr=0 and Gr=625,000). The buoyancy influ-

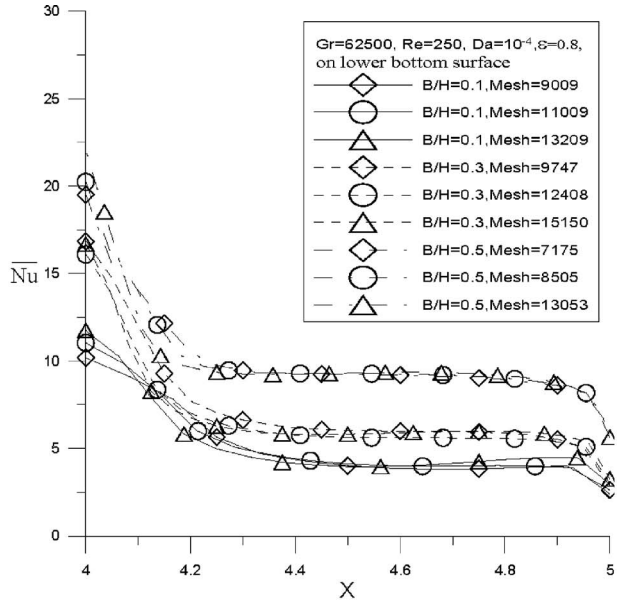

(a)

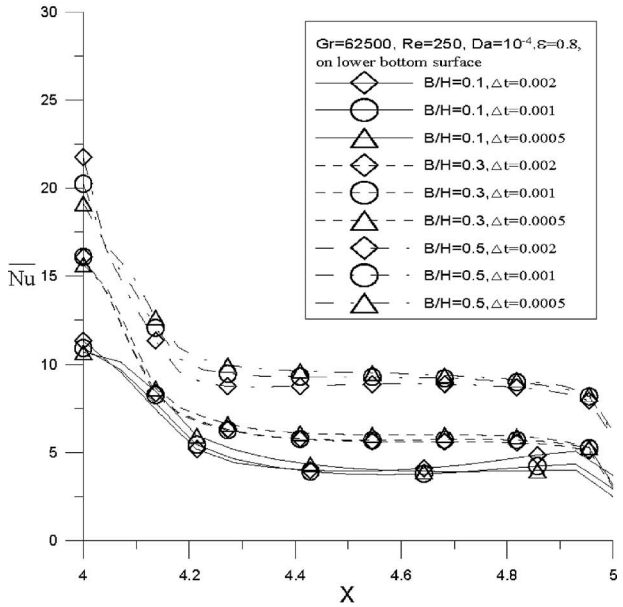

(b)

Fig. 2 (*a*) Grid sensitivity and (*b*) time-step size sensitivity at Gr=62,500, Re=250, Da=10^{-4}, and ε=0.8 with three different *B*/*H* on the local Nusselt number for the lower bottom surface

ences the local Nusselt number weakly when Gr=625,000; this phenomenon is because a larger vertical force blows the fluid a bit off the bottom surface, and there is less fluid to flow through along the bottom surface. The same trend is seen between $B/H=0.3$ and $B/H=0.5$ in Figs. 5(*b*) and 5(*c*) for the local Nusselt number. However, the buoyancy effect on the local Nusselt number becomes less clear for $B/H=0.3$ and $B/H=0.5$ than for $B/H=0.1$. Nevertheless, the heat transfer for the bottom surface is almost the same in Gr=0–625,000 for $B/H=0.3$ and 0.5. Furthermore, Figs. 6(*a*) and 6(*b*) show that Gr=0 generates a shorter length of wave flow than Gr=625,000, but the result in Fig. 6(*c*) scarcely exists because of the faster flow generated by less space between channel walls. A recirculating zone appears behind the square porous cylinder, and this area is lower and bigger under Gr=625,000 than under Gr=0, as shown in Figs. 6(*a*), 6(*a*), and 1. The heat is thus

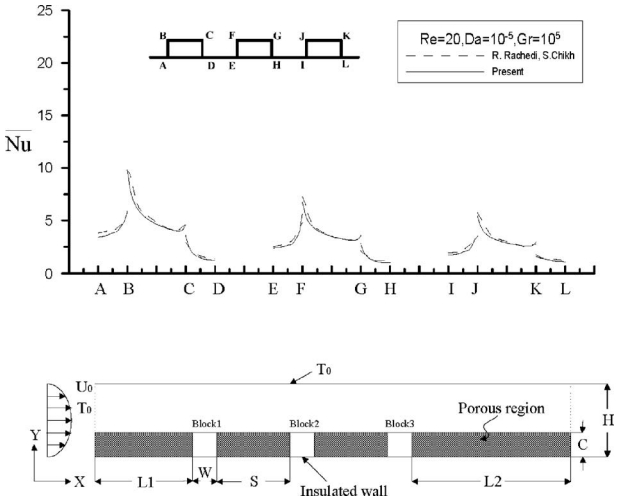

Fig. 3 Comparisons of $\overline{Nu}$ on each heat source with those of Rachedi and Chikh [12]

transferred more poorly from the recirculating zone fluid to the mainstream flow for Gr=625,000 than for Gr=0. The main pattern of Fig. 6(*b*) is similar to that of Fig. 6(*b*) and 1. Figures 6(*c*), 6(*c*), and 1 indicate a closed unsteady recirculating zone behind the square porous cylinder for $B/H=0.5$; this zone contains two vortices. The positions and sizes of vortices differ depending on buoyancy. Moreover, the sizes of the recirculating zone for $B/H=0.3$ and 0.5 on Gr=0 and 625,000 are similar, and then the Nusselt number along the bottom surface is almost the same (Figs. 5(*b*) and 5(*c*)).

In Fig. 7(*a*), as the channel-to-cylinder height ratio increases, the local Nusselt number increases. Specifically, the heat transfer effect is obvious at $B/H=0.5$. For the lower bottom surface, in-

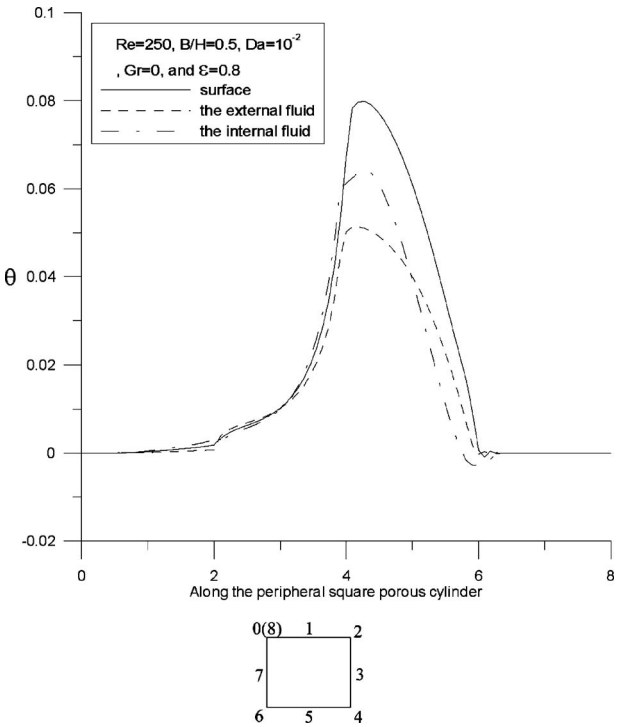

Fig. 4 Temperature distributions for the surface of the square porous cylinder, the external fluid, and the internal fluid at Re=250, Da=10^{-2}, *B*/*H*=0.5, Gr=0, and ε=0.8

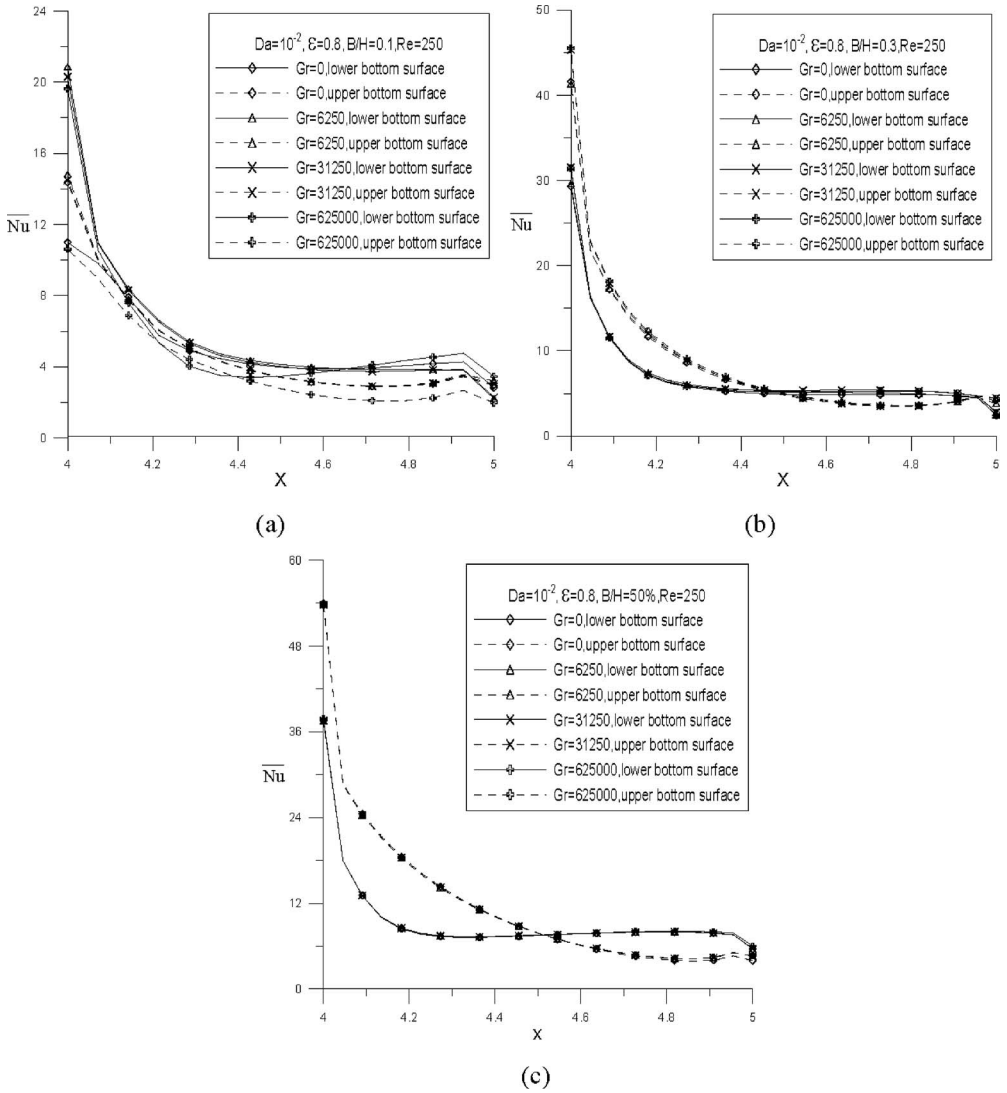

Fig. 5 Time-mean Nusselt number profiles along bottom surfaces of the square porous cylinder for four Gr values at Da=10^{-2}: (*a*) *B*/*H*=0.1, (*b*) *B*/*H*=0.3, and (*c*) *B*/*H*=0.5

creasing B/H greatly increases the Nusselt number (up to 227% at $x=4.2$, relative ratio between $B/H=0.1$ and $B/H=0.5$), while for the upper bottom surface, increasing B/H increases the Nusselt number up to 35% (at $x=4.05$, relative ratio between $B/H=0.1$ and $B/H=0.5$). In Fig. 7(*a*), the Nusselt number along the bottom surface with $B/H=0.5$ is the maximum among three channel-to-cylinder height ratios because of the interaction between the recirculating zone and the wall confinement in the wake region. As B/H increases, the total average time-mean Nusselt number including the lower bottom surface and the upper bottom surface increases. In Fig. 7(*b*), the internal fluid temperature is bigger than the external fluid temperature. By increasing the channel-to-cylinder height ratio from $B/H=0.1$ to 0.5, the difference between external and internal fluid temperatures is more prominent. Nevertheless, the temperature for the bottom surface decreases with an increase in B/H; this result is because the space between channel walls gradually narrows and increases fluid velocity in the wake region to enhance the heat transfer. A small recirculating zone is formed along the bottom surface of the square porous cylinder in Figs. 8(*a*) and 8(*b*), but the phenomenon in Fig. 8(*c*) scarcely exists. This recirculating zone poorly affects the heat transfer from the recirculating zone fluid to the mainstream flow. However, with a further increase in B/H value, the velocity of the fluid emanating from the gap between the top and bottom surfaces of the

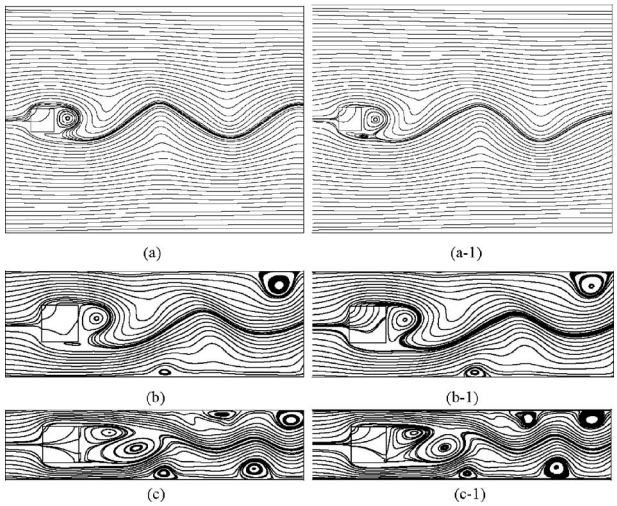

Fig. 6 Streamline contours at C_L=max and Da=10^{-2}: (*a*) *B*/*H*=0.1 and Gr=0, (*a-1*) *B*/*H*=0.1 and Gr=625,000, (*b*) *B*/*H*=0.3 and Gr=0, (*b-1*) *B*/*H*=0.3 and Gr=625,000, (*c*) *B*/*H*=0.5 and Gr=0, and (*c-1*) *B*/*H*=0.5 and Gr=625,000

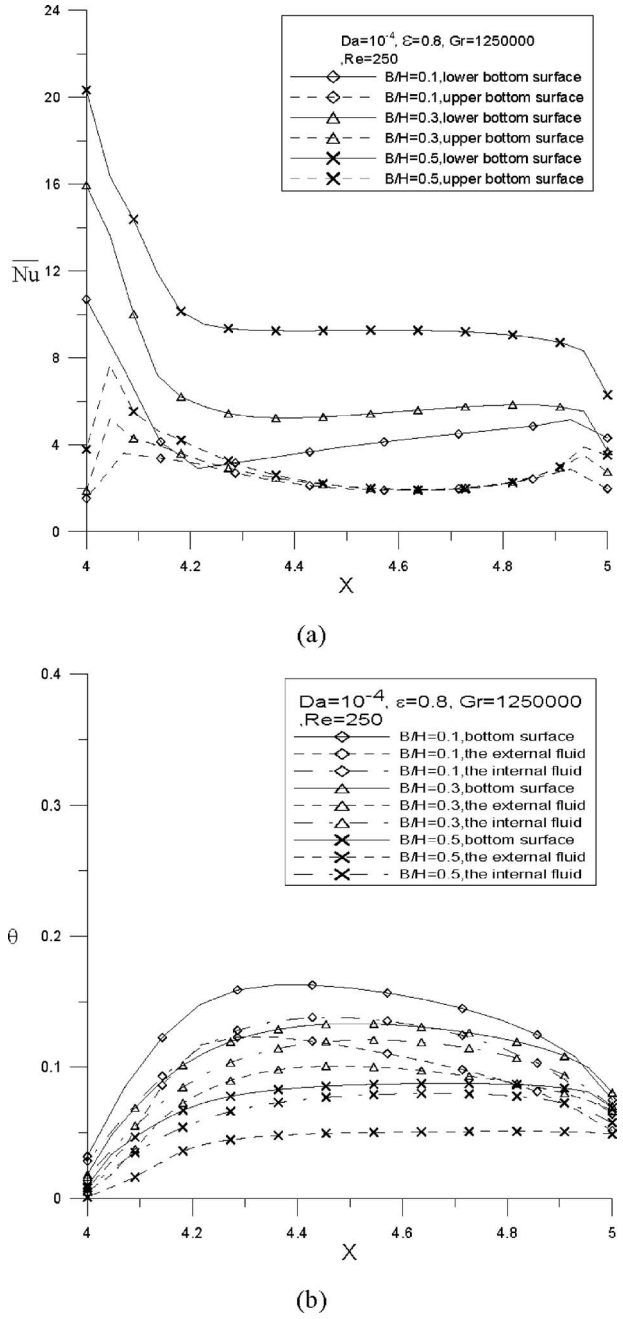

Fig. 7 Effects of B/H at the bottom of the square porous cylinder on heat transfer Gr=1,250,000, Da=10^{-4}, and ε=0.8: (*a*) local Nusselt number and (*b*) temperature distribution

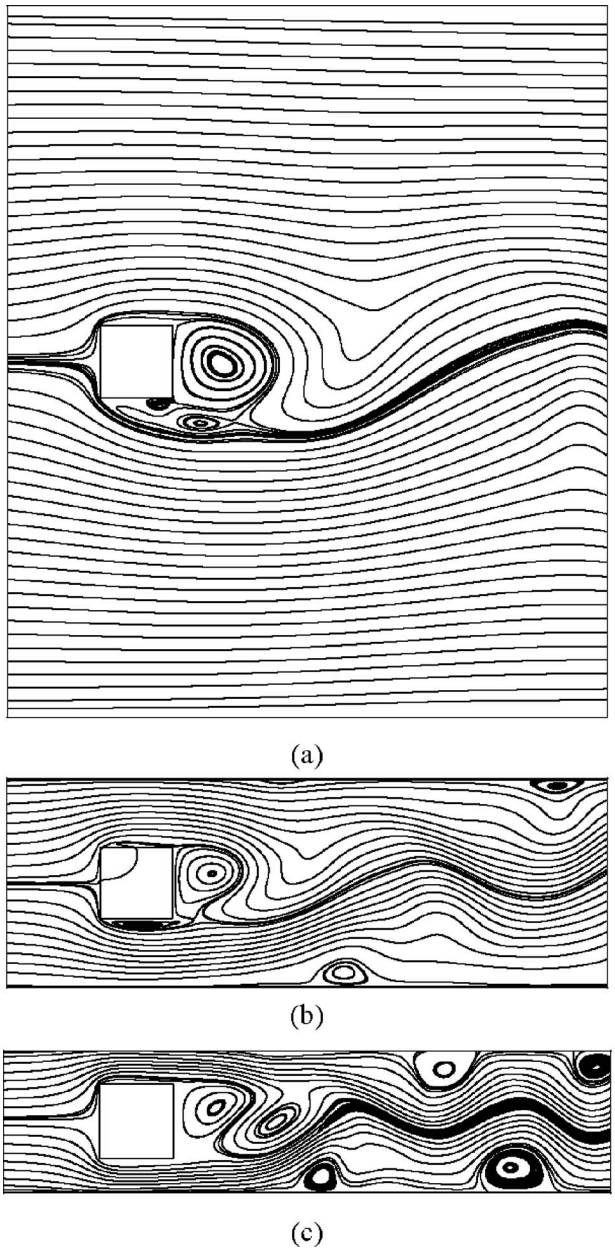

Fig. 8 Streamline contours at C_L=max, Re=250, Gr =1,250,000, Da=10^{-4}, and ε=0.8: (*a*) B/H=0.1, (*b*) B/H=0.3, and (*c*) B/H=0.5

square porous cylinder and the channel wall increases. The fastest flow moves rightward to make fluid particles flow into the wake region, so that the heat transfer from the bottom at $B/H=0.5$ is the best between three channel-to-cylinder height ratios. The flow motion is only noticeable near the square porous cylinder, and the fluid flow along the channel wall changes nothing for the square porous cylinder at $B/H=0.1$. While the channel-to-cylinder height ratio increases from 0.3 to 0.5, the flow along the channel wall becomes unsteady and several recirculating zones form along the channel wall.

This cycle demonstrates the event that begins with the shedding of a vortex from the leading tip and ends with the shedding of the next vortex from the same point, as demonstrated in Figs. 9 and 10. For different permeabilities with Gr=1,250,000 and $B/H=0.1$, the oscillatory nature of the wake behind the square porous cylinder is similar, but a higher permeability generates a shorter length of the wave flow than a lower permeability. With Gr =1,250,000, the higher permeability (Da=10^{-2}) thus generates a smaller recirculating zone in the wake region than the lower permeability (Da=10^{-5}). The study of flow evolution and characteristic values by varying Gr and B/H is interesting to researchers. In Fig. 11(*a*), the amplitude of temporal variation in C_L increases with increasing Gr, but the frequency is bigger when Gr =62,500 than when Gr=0. The amplitude and frequency of temporal variation in C_L are almost the same for different Gr values in Figs. 11(*b*) and 11(*c*). The buoyancy less affecting the oscillatory motion at $B/H=0.3$ and 0.5 is due to a larger variation in flow velocity generated by less space between channel walls. The oscillatory variation of the lift coefficient begins earlier when Gr increases for three B/H values.

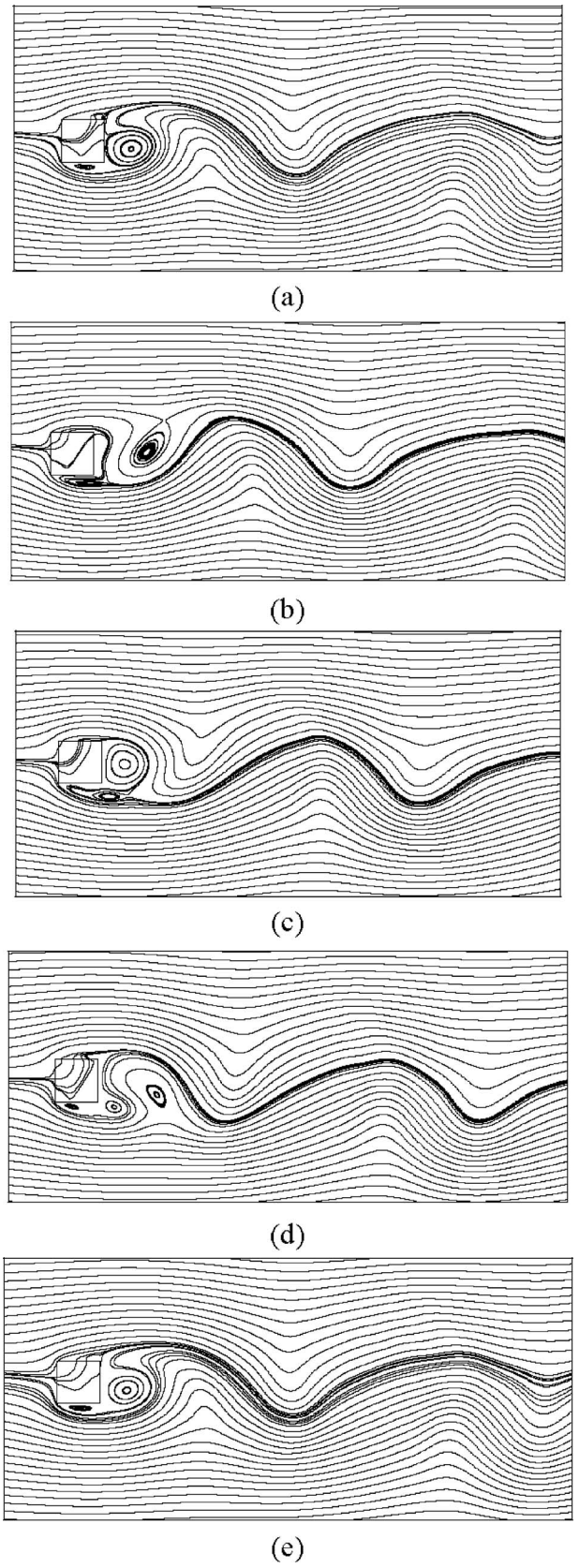

Fig. 9 Sequence of streamlines for the square porous cylinder under Da=10^{-2} at Gr=1,250,000 and B/H=0.1 during 1 cycle: (*a*) t=241.205, (*b*) t=242.767, (*c*) t=244.329, (*d*) t=245.859, and (*e*) t=247.389 for Re=250

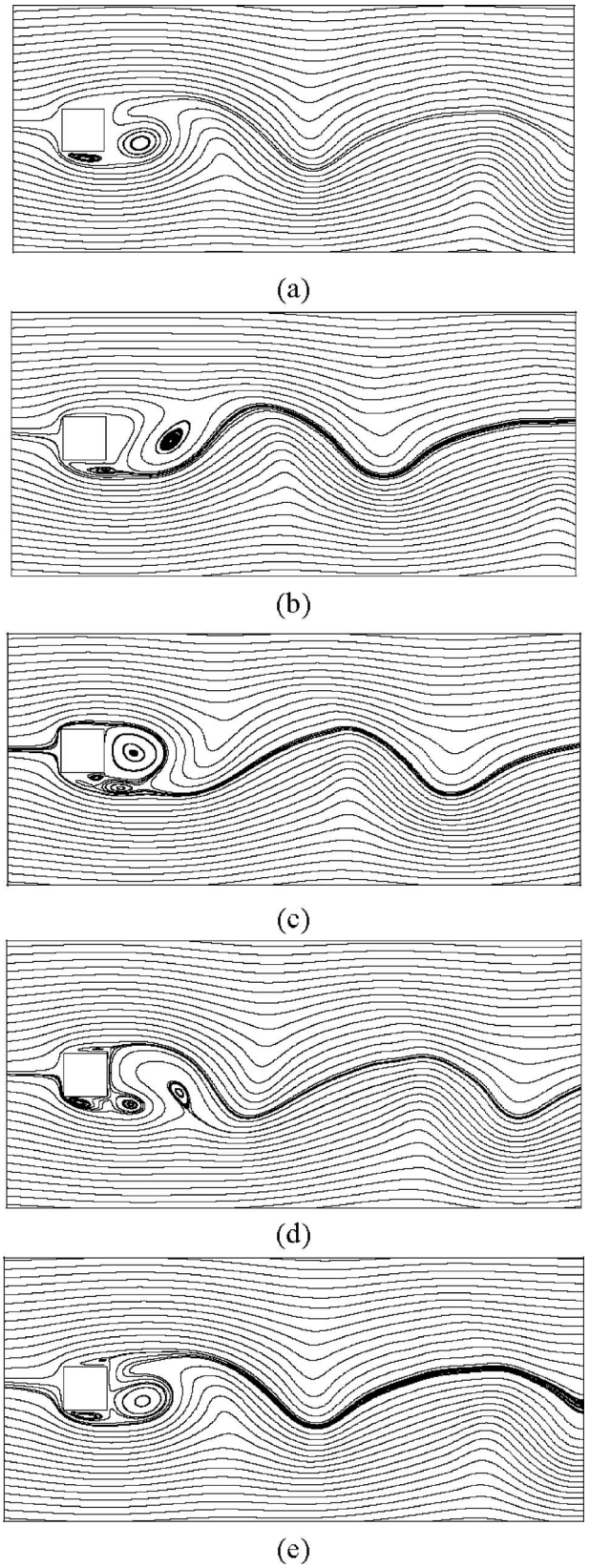

Fig. 10 Sequence of streamlines for the square porous cylinder under Da=10^{-5} at Gr=1,250,000 and B/H=0.1 during 1 cycle: (*a*) t=239.541, (*b*) t=241.21, (*c*) t=242.879, (*d*) t=244.421, and (*e*) t=245.962 for Re=250

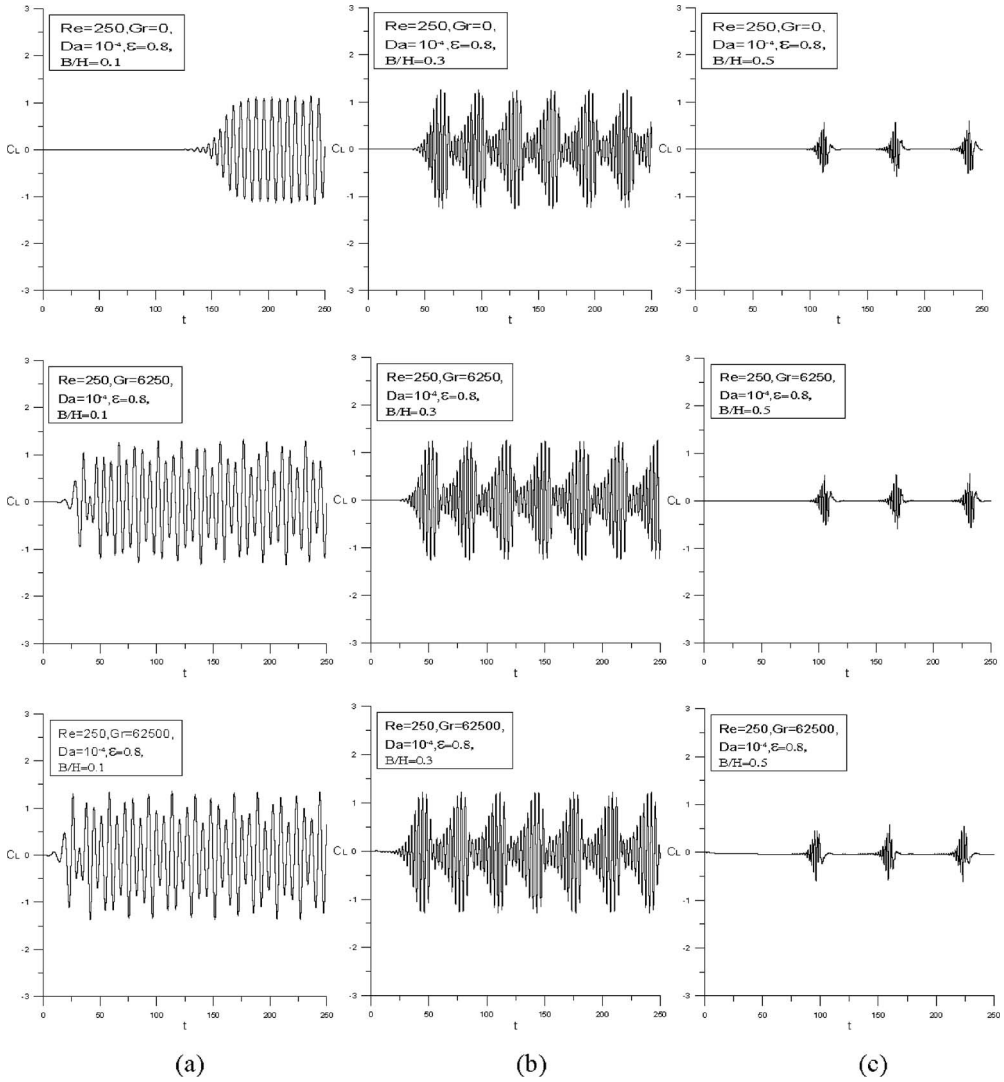

Fig. 11 Time histories of lift coefficient C_L for the square porous cylinder for Re=250 with different values of Gr at Da=10^{-4}: (*a*) *B*/*H*=0.1, (*b*) *B*/*H*=0.3, and (*c*) *B*/*H*=0.5

The average time-mean Nusselt number is calculated using the values of the time-mean Nusselt number on all node points of the bottom surface. For various Da and Gr, the values of the average time-mean Nusselt number on the bottom surface with the lower bottom surface and the upper bottom surface are listed in Table 1 at Da=10^{-2} and in Table 2 at Da=10^{-4}. The value of the average time-mean Nusselt number increases with an increase in channel-to-cylinder height ratio for the square porous cylinder. Increasing

Table 1 For different Gr and *B*/*H* at Re=250 and Da=10^{-2}, the values of the average time-mean Nusselt number on the bottom of the square porous cylinder with the lower bottom surface and the upper bottom surface

		Gr=0	Gr=6250	Gr=31,250	Gr=62,500	Gr=625,000	Gr=1,250,000
$B/H=0.1$	Lower bottom surface	5.96	6.07	5.97	5.93	5.76	5.74
	Upper bottom surface	5.11	5.15	5.12	5.03	4.12	3.07
	Total bottom surface	11.07	11.22	11.09	10.96	9.88	8.81
$B/H=0.3$	Lower bottom surface	7.32	7.32	7.34	7.35	7.37	7.25
		22.82%	*20.59%*	*22.95%*	*23.95%*	*27.95%*	*26.31%*
	Upper bottom surface	8.69	8.72	8.83	8.92	8.96	8.35
		70.06%	*69.32%*	*72.46%*	*77.34%*	*117.48%*	*171.99%*
	Total bottom surface	16.01	16.04	16.17	16.27	16.33	15.6
		44.63%	*42.96%*	*45.81%*	*48.45%*	*65.28%*	*77.07%*
$B/H=0.5$	Lower bottom surface	9.71	9.72	9.72	9.73	9.74	9.75
		62.92%	*60.13%*	*62.81%*	*64.08%*	*69.1%*	*69.86%*
	Upper bottom surface	12.23	12.27	12.28	12.27	12.29	12.3
		139.33%	*138.25%*	*139.84%*	*143.94%*	*198.3%*	*300.65%*
	Total bottom surface	21.94	21.99	22	22	22.03	22.05
		98.19%	*95.99%*	*98.38%*	*100.73%*	*122.98%*	*150.28%*

Values in italics denote the percentage change relative to $B/H=0.1$.

Table 2 For different Gr and B/H at Re=250 and Da=10^{-4}, the values of the average time-mean Nusselt number on the bottom surface of the square porous cylinder with the lower bottom surface and the upper bottom surface

		Gr=0	Gr=6250	Gr=31,250	Gr=62,500	Gr=625,000	Gr=1,250,000
B/H=0.1	Lower bottom surface	5.28	5.24	5.12	5.07	4.84	4.77
	Upper bottom surface	2.45	2.49	2.48	2.48	2.4	2.4
	Total bottom surface	7.73	7.73	7.6	7.55	7.24	7.17
B/H=0.3	Lower bottom surface	6.95	6.96	7.02	6.95	6.67	6.57
		31.63%	*32.82%*	*37.11%*	*37.08%*	*37.81%*	*37.74%*
	Upper bottom surface	2.86	2.87	2.86	2.87	2.78	2.74
		16.73%	*15.26%*	*15.32%*	*15.73%*	*15.83%*	*14.17%*
	Total bottom surface	9.81	9.83	9.88	9.82	9.45	9.31
		26.91%	*27.17%*	*0.3*	*30.07%*	*30.52%*	*29.85%*
B/H=0.5	Lower bottom surface	10.19	10.2	10.22	10.21	10.22	10.22
		92.99%	*94.66%*	*99.61%*	*101.38%*	*111.16%*	*114.26%*
	Upper bottom surface	3.13	3.14	3.2	3.2	3.2	3.2
		27.76%	*26.1%*	*29.03%*	*29.03%*	*33.33%*	*33.33%*
	Total bottom surface	13.32	13.34	13.42	13.41	13.42	13.42
		72.32%	*72.57%*	*76.58%*	*77.62%*	*85.36%*	*87.17%*

Values in italics denote the percentage change relative to B/H=0.1.

Da for three B/H values has a more significant total average Nusselt number. In Tables 1 and 2, the buoyancy affects the average Nusselt number weakly when Gr=1,250,000 and B/H=0.1. As B/H increases, the total average time-mean Nusselt number including the lower bottom surface and the upper bottom surface increases noticeably. In Table 1, the average Nusselt number for the upper bottom surface is greater than that for the lower bottom surface. In all cases, the maximum increase for the total average Nu is 150.28% at B/H=0.5 and Gr=1,250,000 with Da=10^{-2}, and the minimum increase is 26.91% at B/H=0.3 and Gr=0 with Da=10^{-4}. The channel confinement improves the heat transfer on the bottom because the velocity of the fluid emanating from the gap between the top and bottom surfaces of the square porous cylinder and the channel wall increases most for B/H=0.5. Moreover, the flow jets rightward into the wake region and causes the best heat transfer. However, an increase in Da or B/H can also increase heat transfer.

5 Conclusion

This paper has studied how the channel confinement affects the horizontal flow and heat transfer characteristics across the square porous cylinder with the heated cylinder bottom. The authors conclude the following from the results and discussion.

1. The value of the average time-mean Nusselt number increases with increasing channel-to-cylinder height ratio and Da for the square porous cylinder.
2. The buoyancy effect on the local Nusselt number is clearer for B/H=0.1 than for B/H=0.3 and B/H=0.5.
3. At B/H=0.1, the laminar flow motion is only noticeable near the square porous cylinder and the fluid flow along the channel wall changes nothing. While the channel-to-cylinder height ratio increases to 0.3 and 0.5, the flow along the channel wall becomes unsteady and some recirculating zones are generated.
4. The maximum increase for the total average Nu is 150.28% at B/H=0.5 and Gr=1,250,000 with Da=10^{-2}, and the minimum increase is 26.91% at B/H=0.3 and Gr=0 with Da=10^{-4}.

Acknowledgment

The authors gratefully acknowledge the partial financial support of this project by the National Council of the Republic of China.

Nomenclature

A = binary function
$A_{\alpha\beta}$ = diffusion matrix of energy equation
B = height of the cylinder (m)
C_L = lift coefficient ($=l/(\rho u_0^2 B/2)$)
Da = Darcy number ($=K/h^2$)
Gr = Grashof number
H = channel height (m)
$H_{\alpha i\beta}$ = pressure gradient matrix
K = permeability of the porous material
$K_{\alpha\beta\gamma j}$ = conduction matrix
l = lift force per unit length
L = channel length (m)
L_D = distance from right surface of square porous cylinder to exit plane (m)
L_U = distance from inlet plane to left surface of square porous cylinder (m)
$M_{\alpha i\beta}$ = mass matrix
$\underline{\mathrm{Nu}}$ = Nusselt number
$\overline{\mathrm{Nu}}$ = time-mean Nusselt number ($=\int \mathrm{Nu}\, dt/\int dt$)
p = dimensionless pressure ($=p^*/\rho u_0^2$)
p_a = pressure of nodal point
Pr = Prandtl number ($=\nu/\alpha$)
Re = Reynolds number ($=u_0 h/\nu$)
$S_{\alpha i\beta j}$ = diffusion matrix of the momentum equation
t = dimensionless time ($=t^*/(h/u_0)$)
$u_{\alpha i}$ = velocity of nodal point
$\hat{u}_{\alpha i}$ = intermediate velocity (m/s)
u,v = dimensionless velocity components ($u=u^*/u_0$, $v=v^*/u_0$)
x,y = dimensionless Cartesian coordinate
Δt = dimensionless time increment
θ = dimensionless temperature ($=(T^*-T_0)/(qh/k_f)$)
θ_{bw} = dimensionless porous cylinder wall temperature
ε = porosity of porous medium
ν = kinematic viscosity of fluid
ρ = density of fluid
Σ_α = surface integration in energy equation
σ = capacity ratio
η = tangential vector
ξ = normal vector

Superscripts

* = dimensional physical quantity
$n+1,n,n-1$ = $(n+1)$th, nth, $(n-1)$th time step

Subscripts

0 = inlet
e = effective

p = porous
f = fluid

References

[1] Hadim, A., 1994, "Forced Convection in Porous Channel With Localized Heat Sources," ASME J. Heat Transfer, **116**, pp. 465–472.
[2] Fu, W. S., Huang, H. C., and Liou, W. Y., 1996, "Thermal Enhancement in Laminar Channel Flow With a Porous Block," Int. J. Heat Mass Transfer, **39**, pp. 2165–2175.
[3] Chikh, S., Boumedien, A., Bouhadef, K., and Lauriat, G., 1998, "Analysis of Fluid and Heat Transfer in a Channel With Intermittent Heated Porous Blocks," Int. J. Heat Mass Transfer, **33**, pp. 405–413.
[4] Hyung-Jin, S., Seo-Young, K., and Jae-Min, H., 1995, "Forced Convection From an Isolated Heat Source in a Channel With Porous Medium," Int. J. Heat Fluid Flow, **16**, pp. 527–535.
[5] Huang, P. C., Yang, C. F., Hwang, J. J., and Chiu, M. T., 2005, "Enhancement of Forced-Convection Cooling of Multiple Heated Blocks in a Channel Using Porous Covers," Int. J. Heat Mass Transfer, **48**, pp. 647–664.
[6] Hwang, G. J., Wu, C. C., and Chao, C. H., 1995, "Investigation of Non-Darcian Forced-Convection in an Asymmetrically Heated Sintered Porous Channel," ASME J. Heat Transfer, **117**, pp. 725–732.
[7] Calmidi, V. V., and Mahajan, R. L., 2000, "Forced Convection in High Porosity Metal Foams," ASME J. Heat Transfer, **122**, pp. 557–565.
[8] Bejan, A., and Morega, A. M., 1993, "Optimal Arrays of Pin Fins and Plate Fins in Laminar Forced-Convection," ASME J. Heat Transfer, **115**, pp. 75–81.
[9] Cui, C., Huang, X. Y., and Liu, C. Y., 2001, "Forced Convection in a Porous Channel With Discrete Heat Sources," ASME J. Heat Transfer, **123**, pp. 404–407.
[10] Prasad, V., Lai, F. C., and Kulacki, F. A., 1988, "Mixed Convection in Horizontal Porous Layers Heated From Below," ASME J. Heat Transfer, **110**, pp. 395–402.
[11] Hwang, G. J., and Chao, C. H., 1992, "Effects of Wall Conduction and Darcy Number on Laminar Mixed Convection in a Horizontal Square Porous Channel," ASME J. Heat Transfer, **114**, pp. 614–621.
[12] Rachedi, R., and Chikh, S., 2001, "Enhancement of Electronic Cooling by Insertion of Foam Materials," Int. J. Heat Mass Transfer, **37**, pp. 371–378.
[13] Bae, J. H., Hyun, J. M., and Kim, J. W., 2004, "Mixed Convection in a Channel With Porous Multiblocks Under Imposed Thermal Modulation," Numer. Heat Transfer, Part A, **46**, pp. 891–908.
[14] Jaballah, S., Bennacer, R., Sammouda, H., and Belghith, A., 2006, "Simulation of Mixed Convection in a Channel Partially Filled With Porous Media," Prog. Comput. Fluid Dyn., **6**, pp. 335–341.
[15] Jaballah, S., Bennacer, R., Sammouda, H., and Belghith, A., 2008, "Numerical Simulation of Mixed Convection in a Channel Irregularly Heated and Partially Filled With a Porous Media," J. Porous Media, **11**, pp. 247–257.
[16] Cimpean, D., Pop, I., Ingham, D. B., and Merkin, J. H., 2009, "Fully Developed Mixed Convection Flow Between Inclined Parallel Plates Filled With a Porous Medium," Transp. Porous Media, **77**, pp. 87–102.
[17] Chou, F. C., Cheng, C. J., and Lien, W. Y., 1992, "Analysis and Experiment of Non-Darcian Convection in Horizontal Square Packed-Sphere Channels—II. Mixed Convection," Int. J. Heat Mass Transfer, **35**, pp. 1197–1207.
[18] Kurtbas, I., and Celik, N., 2009, "Experimental Investigation of Forced and Mixed Convection Heat Transfer in a Foam-Filled Horizontal Rectangular Channel," Int. J. Heat Mass Transfer, **52**, pp. 1313–1325.
[19] Jue, T. C., 2004, "Numerical Analysis of Vortex Shedding Behind a Porous Square Cylinder," Int. J. Numer. Methods Heat Fluid Flow, **14**, pp. 649–663.
[20] Yang, R. J., and Fu, L. M., 2001, "Thermal and Flow Analysis of a Heated Electronic Component," Int. J. Heat Mass Transfer, **44**, pp. 2261–2275.
[21] Turki, S., Abbassi, H., and Nasrallah, S. B., 2003, "Two-Dimensional Laminar Fluid Flow and Heat Transfer in a Built-In Square Cylinder," Int. J. Therm. Sci., **42**, pp. 1105–1113.
[22] Sharma, A., and Eswaran, V., 2005, "Effect of Channel-Confinement and Aiding/Opposing Buoyancy on the Two-Dimensional Laminar Flow and Heat Transfer Across a Square Cylinder," Int. J. Heat Mass Transfer, **48**, pp. 5310–5322.
[23] Perng, S. W., and Wu, H. W., 2007, "Buoyancy-Aided/Opposed Convection Heat Transfer for Unsteady Turbulent Flow Across a Square Cylinder in a Vertical Channel," Int. J. Heat Mass Transfer, **50**, pp. 3701–3717.
[24] Jue, T. C., 2003, "Analysis of Thermal Convection in a Fluid-Saturated Porous Cavity With Internal Heat Generation," Int. J. Heat Mass Transfer, **40**, pp. 83–89.
[25] Patankar, S. V., 1980, *Numerical Heat Transfer and Fluid Flow*, McGraw-Hill, New York.
[26] Chorin, A. J., 1968, "Numerical Solution of Navier–Stokes Equations," Math. Comput., **22**, pp. 745–762.

Enhanced Specific Heat of Silica Nanofluid

Donghyun Shin

Debjyoti Banerjee
e-mail: dbanerjee@tamu.edu

Department of Mechanical Engineering,
Texas A&M University,
Mail Stop 3123,
College Station, TX 77843-3123

Silica nanoparticles (1% by weight) were dispersed in a eutectic of lithium carbonate and potassium carbonate (62:38 ratio) to obtain high temperature nanofluids. A differential scanning calorimeter instrument was used to measure the specific heat of the neat molten salt eutectic and after addition of nanoparticles. The specific heat of the nanofluid was enhanced by 19–24%. The measurement uncertainty for the specific heat values in the experiments is estimated to be in the range of 1–5%. These experimental data contradict earlier experimental results reported in the literature. (Notably, the stability of the nanofluid samples was not verified in these studies.) In the present study, the dispersion and stability of the nanoparticles were confirmed by using scanning electron microscopy (SEM). Percolation networks were observed in the SEM image of the nanofluid. Furthermore, no agglomeration of the nanoparticles was observed, as confirmed by transmission electron microscopy. The observed enhancements are suggested to be due to the high specific surface energies that are associated with the high surface area of the nanoparticles per unit volume (or per unit mass). [DOI: 10.1115/1.4002600]

Keywords: nanofluid, specific heat, nanoparticle, molten salt, lithium carbonate, potassium carbonate, solar energy, thermal energy storage, phase change material

1 Introduction

Thermal energy storage (TES) systems at high temperatures are required to improve the operational efficiencies and reliability of solar thermal energy conversion systems. The materials that are compatible for these applications—such as alkali-nitrates, alkali-carbonates, and alkali-chlorides (as well as their eutectics)—have very low specific heat capacities, usually less than 2 J/g K (while, to compare, the specific heat of water is 4.2 J/g K at room temperature). The thermal conductivity of these materials is also low (usually, <1 W/m K). The thermophysical properties of molten salts can be improved by doping with small quantities of nanoparticles, thus realizing a high temperature nanofluid.

Solvents doped with minute concentrations of nanoparticles are termed as "nanofluids" [1–5]. Nanofluids were reported for the anomalous enhancement of thermal conductivity compared with the neat solvent. Thermal conductivities of water based nanofluids (that were doped with aluminum oxide and copper oxide nanoparticles) were reported to be enhanced by 30% and 60%, respectively [1]. Also, oil based nanofluids (doped with carbon nanotubes) showed 161% enhancement in thermal conductivity compared with pure oil [5]. Various models were reported in the literature to account for the anomalous enhancements in the thermophysical properties of nanofluids. Keblinski et al. [6] explored the contribution from various transport mechanisms such as the Brownian motion of nanoparticles, the semisolid layer of liquid molecules near nanoparticles, and the heat transfer within the nanoparticles. Prasher et al. [7] investigated the contributions from the localized convection due to Brownian motion. According to recent studies [8–10], the formation of percolation network within agglomerated nanoparticles may be primarily responsible for the observed enhancement of the thermal conductivity of nanofluids.

Similarly, the specific heat capacity of the fluid can also be enhanced by adding nanoparticles. Nelson et al. [11] reported that the specific heat of the nanofluid was enhanced by 50% when pure polyalphaolefin was doped with exfoliated graphite nanoparticles (100 nm thickness and nominal diameter of 20 μ) at 0.6% concentration by weight. However, contradictory reports in the literature demonstrate the degradation in specific heat of the fluids on doping with nanoparticles. Zhou and Ni [12] reported the reduction in specific heat of water by as much as 50%, when doped with aluminum oxide nanoparticles, with progressive increase in volume fraction from 0% to 21.7%. The nominal nanoparticle size used in this study was reported to be 45 nm (however, no SEM or transmission electron microscopy (TEM) images were provided to verify these data). Aluminum oxide is insoluble in water and has a propensity to agglomerate and precipitate if the pH of the water solution is not controlled within a tight margin. Hence, the alumina nanofluids are likely to be very unstable due to the propensity for agglomeration of the nanoparticles and precipitation of the agglomerated particles (especially at concentrations exceeding 1%)—leading to a degradation in the thermophysical properties of the resultant mixture. However, the authors did not report (or verify) if the nanoparticles agglomerated (or precipitated) in the nanofluid after mixing. Hence, it is possible that the alumina nanoparticles agglomerated (or precipitated) in the water solution, leading to the degradation in the thermal properties of the resulting nanofluid that was subsequently reported in their study.

In contrast, in this study we report an anomalous enhancement in the specific heat of nanofluids. Scanning electron microscopy (SEM) was used to verify that the nanoparticles were well dispersed even after the repeated thermocycling of the molten salt mixture from the solid phase to the liquid phase. A minimal agglomeration of the nanoparticles was observed by TEM for the samples after repeated thermocycling.

The objective of this study was to verify the stability and the applicability of the high temperature nanofluids (in the form of molten salts doped with nanoparticles) for realizing efficient TES platforms for solar thermal energy conversion systems. The enhancements of the specific heat of the high temperature nanofluids would enable the reduction in the size of the TES platforms. Use of these high temperature nanofluids can also help to enhance the operating temperature of the solar towers (currently operating at 400°C [13] to 500–600°C. This would raise the operating temperatures of the solar thermal systems, resulting in better thermal efficiencies for the overall system. If such an endeavor is successful, the operating costs for solar thermal systems can be competitive to that of coal based power generation technologies.

2 Nanofluid Synthesis and Measurements

In this study, SiO_2 nanoparticles were dispersed in a eutectic of lithium carbonate and potassium carbonate (62:38). This eutectic has a melting point of 488°C. The specific heat measurements were performed using a differential scanning calorimeter (DSC) (Q20, TA Instruments, Inc., New Castle, DE). The measurements were compared with the theoretical model of the effective specific heat for a mixture [12,14] as follows:

$$c_{p,t} = m_p c_{p,p} + m_f c_{p,f} \quad (1)$$

Contributed by the Heat Transfer Division of ASME for publication in the JOURNAL OF HEAT TRANSFER. Manuscript received December 21, 2009; final manuscript received September 2, 2010; published online November 2, 2010. Assoc. Editor: Patrick E. Phelan.

Table 1 Specific heat measurements of pure eutectic, using mixture of lithium carbonate and potassium carbonate (62:38), and silica nanofluids (silica nanoparticle concentration: 1% by weight; eutectic ratio: 61.5: 37.5). The enhancement varies from 19% to 24% for the three nanofluid samples (ε_1: standard deviation of measurements with change in temperature for the liquid phase for each measurement within an experiment; ε_2: standard deviations from all the measurements for a given sample).

Specific heat (J/g K)	Pure eutectic (ε_1)	Pure eutectic (ε_1)	Nanofluid (1) (ε_1)	Nanofluid (2) (ε_1)	Nanofluid (3) (ε_1)
First run	1.73 (0.0025)	1.73 (0.0015)	1.95 (0.0024)	1.85 (0.0109)	1.93 (0.0011)
Second run	1.63 (0.0030)	1.72 (0.0028)	1.97 (0.0029)	1.89 (0.0076)	2.00 (0.0031)
Third run	1.56 (0.0042)	1.62 (0.0043)	1.98 (0.0026)	2.00 (0.0111)	1.94 (0.0028)
Fourth run	1.56 (0.0038)	1.55 (0.0050)	2.00 (0.0030)	1.99 (0.0121)	1.84 (0.0008)
Fifth run			2.01 (0.0026)	2.10 (0.0145)	
Sixth run			2.00 (0.0022)	2.15 (0.0156)	
Seventh run			1.98 (0.0031)	2.10 (0.0168)	
Eighth run			1.97 (0.0027)	2.10 (0.0161)	
Ninth run			1.97 (0.0040)	2.10 (0.163)	
Average	1.62	1.65	1.98	2.03	1.93
Enhancement	–		21%	24%	19%
ε_2	0.08	0.09	0.019	0.104	0.070

where c_p is the specific heat and m is the mass fraction. The subscripts t, p, and f denote nanofluid, nanoparticle, and pure fluid (eutectic) properties, respectively.

The silica nanofluid is prepared by a simple two step liquid solution method. SiO_2 nanoparticle (nominal size: 10 nm) was supplied by Meliorum Technologies, Inc., Rochester, NY. Lithium carbonate and potassium carbonate were supplied by Spectrum Chemical Mfg. Corp., Gardena, CA. The mass fraction of the SiO_2 nanoparticles in the eutectic mixture was 1%. The protocol for synthesizing the nanofluids is as follows: 2 mg of SiO_2 nanoparticle is mixed with 92.25 mg of lithium carbonate and 105.75 mg of potassium carbonate (62:38 ratio for the pure eutectic and 61.5:37.5 ratio for the nanofluid). These measurements are performed on a mass balance (Sartorius Model: CPA26P). This mixture is then dissolved in 20 ml of distilled water. The water solution is then sonicated by an ultrasonicator (Branson 3510, Branson Ultrasonics Corporation, Danbury, CT) for ~100 min to obtain uniform dispersion of the nanoparticles. Then, the water in the solution is completely evaporated on a hot plate (C-MAG HP7, IKA) maintained at 200°C.

Standard DSC measurement protocol (ASTM-E1269) was used to measure the specific heat of the samples. The standard "Tzero™" hermetic pan and lid (TA Instruments, Inc., New Castle, DE) were used to mount the samples in the DSC. A custom temperature program was employed in accordance with the ASTM-E1269 standard measurement protocol. The temperature is held at 150°C for 10 min to thermally stabilize the instrument and to evaporate any absorbed moisture in the sample. Then, the temperature is ramped to 560°C at 20°C/min and held at 560°C for another 10 min. For each sample, an empty pan, the pan with the reference material (25.412 mg of sapphire), and the same pan with the sample material were subjected to the temperature cycles mentioned above and the heat transfer was recorded by the instrument. After each cool down—and for each analyte (i.e., empty pan, pan with sapphire, and pan with the sample)—the temperature program was cycled four to nine times to ensure the repeatability of the measurement.

3 Measurement Uncertainty

The precision of the heat flow measurements in the DSC instrument is 1 μW (10^{-6} J/s) and the accuracy of the heat flow measurements is of the order of 5 μW. The mass balance has a precision of 1 μg (10^{-6} g). The accuracy of the mass measurements is ~5 μg. It is shown in Table 1 that the standard deviation (ε_1) of the measurements for each specific heat measurement of each sample is less than 0.02 J/g K. The standard deviation in the measurement for all the cycles of measurement for a given nanofluid sample varies from 0.02 J/g K to 0.1 J/g K. Hence, the measurement uncertainty for the specific heat values in the experiments is estimated to be in the range of 1–5%. This shows that the heat capacity enhancements observed in this study are significantly higher than the measurement uncertainties.

4 Results and Discussion

The results from the measurements are shown in Fig. 1 and Table 1. To confirm the accuracy of the measurements, the specific heat of the neat (pure) eutectic was compared with the experimental data from the literature. According to Araki et al. [17], the specific heat of the eutectic at the liquid phase is constant with temperature and the value is 1.6 J/g K. It is shown in Table 1 that the standard deviation (ε_1) of the specific heat of each sample at temperature from 525°C to 555°C, which is the liquid phase of the eutectic, is less than 0.02 J/g K. This implies that the specific heat of the eutectic and the nanofluid is constant at the liquid phase. It is also shown in Fig. 1 that the average specific heat of the pure eutectic in the liquid phase is 1.62–1.65 J/g K. The difference in the measured values for the pure eutectic samples

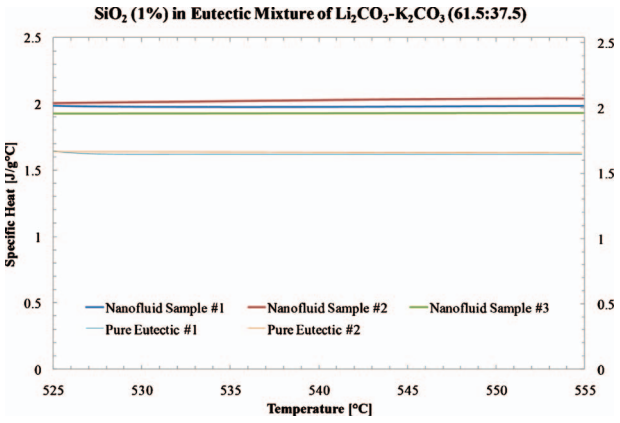

Fig. 1 Variation in specific heat of pure eutectic samples and nanofluid samples with temperature obtained from DSC measurements. The specific heat of the eutectic of lithium carbonate and potassium carbonate (62:38) is enhanced by 19–24% on addition of SiO_2 nanoparticles (at 1% by weight).

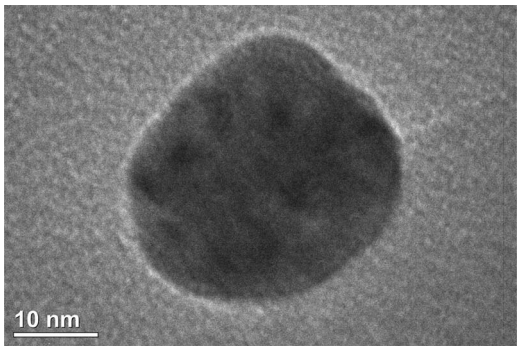

Fig. 2 TEM of silica nanoparticle after mixing with pure eutectic and before thermocycling in the DSC instrument. The nominal size of the nanoparticle in the figure is ~35 nm.

from the literature data is less than 3%. The melting point of the eutectic is observed to be depressed by ~1 °C on the addition of the nanoparticles to the eutectic.

The enhancement of the specific heat due to doping with nanoparticles varies between 18% and 24% for the three different silica nanofluid samples used in this study. Since the specific heat of the SiO_2 is less than the specific heat of the pure eutectic, according to the conventional model used in the literature (Eq. (1)), the effective specific heat of the mixture should be lower than the specific heat of the pure eutectic. The model used to formulate Eq. (1) predicts that at 1% loading of the silica nanoparticles, the degradation in specific heat capacity would be ~2%. Using Eq. (1), the specific heat of the silica nanofluid is predicted to be 1.58 J/g K. However, at 1% concentration the specific heat of the silica nanofluid (1.9–2.2 J/g K) is found to be significantly higher than that predicted by the theoretical model of Eq. (1). Accounting for the measurement uncertainties, the observed experimental measurements demonstrate a significant enhancement by ~18–24% (This is significantly larger than the measurement uncertainty of 1–5%.)

Since the nanoparticles have the propensity to agglomerate (e.g., due to variations in pH during synthesis of nanofluids, variations in concentration/nonhomogeneity, temperature cycling, temperature nonhomogeneity, etc.), it is necessary to verify if the nanoparticles are uniformly dispersed and not agglomerated after repeated cycles of melting/solidification. This is confirmed by transmission electron microscopy (TEM Model: JEOL JEM-2010) that the SiO_2 nanoparticles were not agglomerated before and after thermal cycling in the DSC (Figs. 2 and 3). A uniform dispersion of the nanoparticles was confirmed by observing the samples

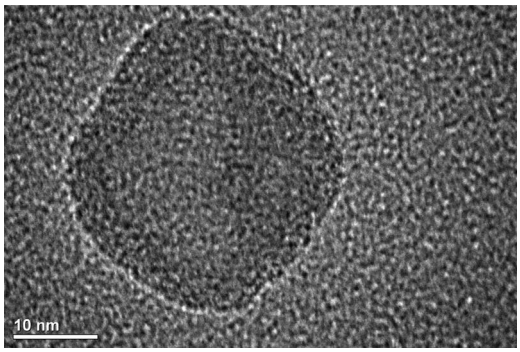

Fig. 3 TEM of silica nanoparticle after repeated thermocycling of melting and solidification of the nanofluid eutectic. The TEM image shows that the silica nanoparticles are not agglomerated and well dispersed in the pure eutectic after repeated thermal cycles of melting and solidification. The average size of the nanoparticle is ~35 nm.

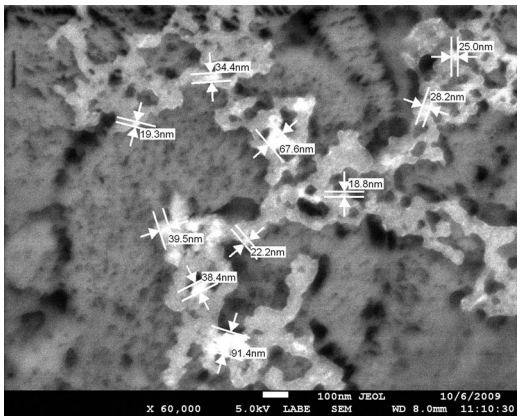

Fig. 4 SEM of silica nanoparticles after repeated thermocycling of melting and solidification. The SEM image shows that nanoparticles in the molten salt eutectic are well dispersed. The average size of the nanoparticles is 38.5 nm. A substructure (lighter color) is formed within the eutectic that forms an interconnected network (percolation network). This may enhance the effective thermal properties of the nanofluid due to more efficient heat transfer in the percolation network.

in scanning electron microscopy (SEM model: JEOL JSM-7500F) after measurements using the DSC, as shown in Fig. 4. A substructure within the eutectic is also observed in the SEM images at locations where the nanoparticles are dispersed in the eutectic. In the vicinity of the nanoparticles the eutectic seems to be of higher density (lighter color in the backscatter image of the SEM) and seems to form an intercalated network (percolation network). This network substructure of an interconnected high density eutectic impregnated with nanoparticles may form a percolation network that is more efficient for transferring heat across the mixture. This may be one of the factors that are responsible for enhancing the thermal properties of the nanofluid.

On a much smaller scale, the observed anomalous enhancement in specific heat can be explained to be due to the high surface energy of the nanoparticles arising from the high surface area per unit volume (or per unit mass) of the nanoparticles [15,16]. The high surface energy of the nanoparticles can also induce a phase transformation in the solvent material in the vicinity of the nanoparticle. For example, the layers of the adhered liquid molecules have lower intermolecular spacing on the crystalline surface than the liquid molecules in the bulk phase that are far away from the nanoparticle surface [6,18,19]. These adhered layers of liquid molecules thus exist in a highly "compressed phase" and can be expected to have semisolid properties (i.e., higher specific heat than in the bulk liquid phase for conventional solvent materials; whereas for water the ice phase has a lower specific heat). The number of adhered layers of the liquid molecules are expected to be a function of the surface energy of the crystalline interface. The mass fraction of the adhered "semisolid" molecules is expected to increase proportionally on a nanoparticle with a reduction in size. An optimum diameter of the nanoparticle can also be expected to exist in order to maximize the mass fraction of the adhered liquid molecules for a given concentration of the nanoparticles. (This is the subject of future studies by our research group.)

5 Conclusion

In summary, the specific heat data of the eutectic of lithium carbonate and potassium carbonate (62:38) along with their silica doped nanofluid (at concentration of 1% by weight) have been presented in this study. Accounting for the measurement uncertainties, the specific heat of the nanofluid was enhanced by ~25% compared with that of the pure eutectic. The stability of the high temperature nanofluids was also verified by using electron micros-

copy (SEM and TEM) after repeated thermocycling and melting/solidification. The microscopy results showed that the nanofluids were fairly stable with the minimal agglomeration of the nanoparticles after repeated thermocycling. A percolation network of a higher density eutectic material surrounding the nanoparticles was also observed in these microscopy images.

This result is contrary to a previous study in the literature, which showed a decrease in the specific heat of the nanofluid (possibly due to the agglomeration and precipitation of the particles in the mixture—which was not verified). The anomalous enhancement on the specific heat for the high temperature nanofluid samples can be potentially due to the high specific surface energy of the nanoparticles.

A significant enhancement of the specific heat of the high temperature nanofluids is an encouraging discovery for their application in thermal energy storage systems, especially for solar towers. Our research group is currently exploring the optimum concentration and the optimum size of various nanoparticles for the synthesis of high temperature nanofluids by using both experimental and numerical studies (e.g., using molecular dynamics simulations). The effect of synthesis conditions on the thermophysical properties of the high temperature nanofluids will also be explored in future experimental studies.

Acknowledgment

The authors acknowledge the support of the Department of Energy (DOE) Solar Energy Program (Golden, CO) under Grant No. DE-FG36-08GO18154 (Title: "Molten Salt-Carbon Nanotube Thermal Energy Storage For Concentrating Solar Power Systems").

References

[1] Eastman, J. A., Choi, U. S., Li, S., Thompson, L. J., and Lee, S., 1997, "Enhanced Thermal Conductivity Through the Development of Nanofluids," Mater Res. Soc. Symp. Proc., **457**, pp. 9–10.
[2] Lee, S., Choi, S. U.-S., Li, S., and Eastman, J. A., 1999, "Measuring Thermal Conductivity of Fluids Containing Oxide Nanoparticles," ASME J. Heat Transfer, **121**(2), pp. 280–289.
[3] Keblinski, P., Eastman, J. A., and Cahill, D. G., 2005, "Nanofluids for Thermal Transport," Mater. Today, **8**(6), pp. 36–44.
[4] Wang, X.-Q., and Mujumdar, A. S., 2007, "Heat Transfer Characteristics of Nanofluids: A Review," Int. J. Therm. Sci., **46**(1), pp. 1–19.
[5] Shaikh, S., Lafdi, K., and Rengasamy, P., 2007, "Thermal Conductivity Improvement in Carbon Nanoparticle Doped PAO Oil: An Experimental Study," J. Appl. Phys., **101**, p. 064302.
[6] Keblinski, P., Phillpot, S. R., Choi, S. U. S., and Eastman, J. A., 2002, "Mechanism of Heat Flow in Suspensions of Nano-Sized Particles (Nanofluids)," Int. J. Heat Mass Transfer, **45**(4), pp. 855–863.
[7] Prasher, R., Bhattacharya, P., and Phelan, P. E., 2006, "Brownian-Motion-Based Convective-Conductive Model for the Effective Thermal Conductivity of Nanofluids," ASME J. Heat Transfer, **128**, pp. 588–595.
[8] Keblinski, P., Prasher, R., and Eapen, J., 2008, "Thermal Conductance of Nanofluids: Is the Controversy Over?," J. Nanopart. Res., **10**, pp. 1089–1097.
[9] Evans, W., Prasher, R., Fish, J., Meakin, P., Phelan, P., and Keblinski, P., 2008, "Effect of Aggregation and Interfacial Thermal Resistance on Thermal Conductivity of Nanocomposites and Colloidal Nanofluids," Int. J. Heat Mass Transfer, **51**, pp. 1431–1438.
[10] Buongiorno, J., Venerus, D. C., Prabhat, N., McKrell, T., Townsend, J., Christianson, R., Tolmachev, Y. V., Keblinski, P., Hu, L., Alvarado, J. L., Bang, I. C., Bishnoi, S. W., Bonetti, M., Botz, F., Cecere, A., Chang, Y., Chen, G., Chen, H., Chung, S. J., Chyu, M. K., Das, S. K., Di Paola, R., Ding, Y., Dubois, F., Dzido, G., Eapen, J., Escher, W., Funfschilling, D., Galand, Q., Gao, J., Gharagozloo, P. E., Goodson, K. E., Gutierrez, J. G., Hong, H., Horton, M., Hwang, K. S., Iorio, C. S., Jang, S. P., Jarzebski, A. B., Jiang, Y., Jin, L., Kabelac, S., Kamath, A., Kedzierski, M. A., Kieng, L. G., Kim, C., Kim, J.-H., Kim, S., Lee, S. H., Leong, K. C., Manna, I., Michel, B., Ni, R., Patel, H. E., Philip, J., Poulikakos, D., Reynaud, C., Savino, R., Singh, P. K., Song, P., Sundararajan, T., Timofeeva, E., Tritcak, T., Turanov, A. N., Vaerenbergh, S. V., Wen, D., Witharana, S., Yang, C., Yeh, W.-H., Zhao, X.-Z., and Zhou, S.-Q., 2009, "A Benchmark Study on the Thermal Conductivity of Nanofluids," J. Appl. Phys., **106**, p. 094312.
[11] Nelson, I. C., Banerjee, D., and Rengasamy, P., 2009, "Flow Loop Experiments Using Polyalphaolefin Nanofluids," J. Thermophys. Heat Transfer, **23**(4), pp. 752–761.
[12] Zhou, S. Q., and Ni, R., 2008, "Measurement of the Specific Heat Capacity of Water-Based Al_2O_3 Nanofluid," Appl. Phys. Lett., **92**, p. 093123.
[13] Kearney, D., Herrmann, U., Nava, P., Kelly, B., Mahoney, R., Pacheco, J., Cable, R., Potrovitza, N., Blake, D., and Price, H., 2003, "Assessment of a Molten Salt Heat Transfer Fluid in a Parabolic Trough Solar Field," ASME J. Sol. Energy Eng., **125**, pp. 170–176.
[14] Buongiorno, J., 2006, "Convective Transport in Nanofluids," ASME J. Heat Transfer, **128**, pp. 240–250.
[15] Wang, B. X., Zhou, L. P., and Peng, X. F., 2006, "Surface and Size Effects on the Specific Heat Capacity of Nanoparticles," Int. J. Thermophys., **27**, pp. 139–151.
[16] Wang, L., Tan, Z. C., Meng, S. H., Liang, D., and Li, G. H., 2001, "Enhancement of Molar Heat Capacity of Nanostructured Al_2O_3," J. Nanopart. Res., **3**, pp. 483–487.
[17] Araki, N., Matsuura, M., Makino, A., Hirata, T., and Kato, Y., 1988, "Measurement of Thermophysical Properties of Molten Salts: Mixtures of Alkaline Carbonate Salts," Int. J. Thermophys., **9**, pp. 1071–1080.
[18] Oh, S. H., Kauffman, Y., Scheu, C., Kaplan, W. D., and Ruhle, M., 2005, "Ordered Liquid Aluminum at the Interface With Sapphire," Science, **310**(5748), pp. 661–663.
[19] Xue, L., Keblinski, P., Phillpot, S. R., Choi, S. U.-S., and Eastman, J. A., 2004, "Effect of Liquid Layering at the Liquid–Solid Interface on Thermal Transport," Int. J. Heat Mass Transfer, **47**, pp. 4277–4284.

Laminar Heat and Mass Transfer in Rotating Cone-and-Plate Devices

I. V. Shevchuk
MBtech Powertrain GmbH,
Salierstrasse 38,
70736 Fellbach-Schmiden, Germany

The convective diffusion of feeding culture and the effect of fluid shear stress on endothelial cells are frequently investigated in cone-and-plate devices. Laminar fluid flow and heat and mass transfer in a cone-and-plate device, with cone apex touching the plate/disk, were simulated. The disk-to-cone gap made 1–5 deg. Transport equations were reduced to a system of self-similar ordinary differential equations solved numerically. Cases studied were a rotating cone and a stationary plate, and vice versa. The cone was isothermal, while the disk temperature followed a power-law radial distribution; boundary concentrations were constant. Prandtl and Schmidt numbers varied from 0.1 to 800. Temperature/diffusion profiles in the gap and Nusselt and Sherwood numbers exhibit different regimes of heat/mass transfer, depending on the disk surface temperature distribution.
[DOI: 10.1115/1.4002606]

Keywords: cone-and-plate device, rotating disk, heat and mass transfer, efficiency

1 Introduction

Cone-and-plate devices, in which fluid flow develops in a conical gap with small angles $\gamma=1-5$ deg (Fig. 1), are known in viscosimetry [1] and bioengineering applications for growing endothelium cells located as a monolayer on the plate, while the slowly rotating cone enables the circulation of feeding culture in the gap [2,3].

Heat and mass transfer in different rotating-disk configurations is intensively studied as applied to different engineering and scientific applications [4–6]. Flow regimes in cone-and-plate devices were investigated experimentally [3], using computational fluid dynamics (CFD) methodology [3] and perturbation techniques [1,2]. The self-similar forms of the Navier–Stokes and energy equations were derived and solved by the author [6–8], with the results agreeing well with the experiments [1]. Different fluid flow and heat transfer regimes for rotating cone and stationary disk, and vice versa, corotating, contrarotating cone and disk, and stationary conical diffuser depend strongly on the radial temperature distribution on the disk. However, simulations were done only for air (Pr=0.71), while possible new phenomena in heat and mass transfer for other values of the Prandtl and Schmidt numbers remained not investigated.

The objectives of this paper consisted in the development of the previous research to study the effects of the Prandtl and Schmidt numbers in combination with different radial distributions of the disk temperature for an isothermal cone, and constant but different concentrations on the disk and the cone. The geometries chosen were a rotating cone and a stationary disk, and vice versa.

2 Self-Similar Equations and Numerical Procedure

Navier–Stokes, continuity, energy, and convective diffusion equations in cylindrical coordinates for an incompressible Newtonian fluid are

$$v_r\frac{\partial v_r}{\partial r}+v_z\frac{\partial v_r}{\partial z}-\frac{v_\varphi^2}{r}=-\frac{1}{\rho}\frac{\partial p}{\partial r}+\nu\left(\frac{\partial^2 v_r}{\partial r^2}+\frac{1}{r}\frac{\partial v_r}{\partial r}-\frac{v_r}{r^2}+\frac{\partial^2 v_r}{\partial z^2}\right) \tag{1}$$

$$v_r\frac{\partial v_\varphi}{\partial r}+v_z\frac{\partial v_\varphi}{\partial z}+\frac{v_r v_\varphi}{r}=\nu\left(\frac{\partial^2 v_\varphi}{\partial r^2}+\frac{1}{r}\frac{\partial v_\varphi}{\partial r}-\frac{v_\varphi}{r^2}+\frac{\partial^2 v_\varphi}{\partial z^2}\right) \tag{2}$$

$$v_r\frac{\partial v_z}{\partial r}+v_z\frac{\partial v_z}{\partial z}=-\frac{1}{\rho}\frac{\partial p}{\partial z}+\nu\left(\frac{\partial^2 v_z}{\partial r^2}+\frac{1}{r}\frac{\partial v_z}{\partial r}+\frac{\partial^2 v_z}{\partial z^2}\right) \tag{3}$$

$$\frac{\partial v_r}{\partial r}+\frac{v_r}{r}+\frac{\partial v_z}{\partial z}=0 \tag{4}$$

$$v_r\frac{\partial T}{\partial r}+v_z\frac{\partial T}{\partial z}=a\frac{\partial^2 T}{\partial z^2} \tag{5}$$

Equations (1)–(5) are not directly applicable to non-Newtonian fluids, but the solution can be nevertheless useful in estimating the effects of varying Pr and Sc numbers in a conical gap.

The boundary conditions are

$$z=0:\quad v_r=0,\quad v_z=0,\quad v_\varphi=\omega r$$

$$T_w-T_1=C_0 r^{n_*},\quad C_w=\text{const} \tag{6}$$

$$z=h:\quad v_r=0,\quad v_z=0,\quad v_\varphi=\Omega r,\quad T=T_1,\quad C=C_1 \tag{7}$$

The power exponent n_* in Eq. (6) accepts negative, zero, or positive values $n_*=-2$ to 4. This allows modeling different radially decreasing, constant, or increasing distributions of T_w on the disk surface, which is of primary interest in the engineering applications. Cone heat/mass transfer is unimportant for the current study; therefore, temperature T_1 and concentration C_1 on the cone are the accepted constants and equal to those of fluid at infinity. In case of the convective diffusion in bioengineering applications, the boundary concentration on the plate/disk C_w is lower than that on the cone/infinity C_1 because endothelium cells digest the feeding culture from the fluid.

Self-similar variables and functions used here are [6–8]

$$\eta=z/r,\quad F=v_r r/\nu,\quad G=v_\varphi r/\nu,\quad H=v_z r/\nu,\quad P=pr^2/(\rho\nu^2) \tag{8}$$

$$\theta=(T-T_1)/(T_w-T_1)\quad\text{or}\quad \theta=(C-C_1)/(C_w-C_1) \tag{9}$$

which transform Eqs. (1)–(7) to

$$F^2+G^2+2P+F'L+\eta P'+F''M=0 \tag{10}$$

$$G'L+G''M=0 \tag{11}$$

$$P'-H(1+F)-H'L-H''M=0 \tag{12}$$

$$H'-\eta F'=0 \tag{13}$$

$$\theta''=\text{Pr}[n_* F\theta+\theta'(H-\eta F)]\quad\text{or}\quad \theta''=\text{Sc}[n_* F\theta+\theta'(H-\eta F)] \tag{14}$$

$$\eta=0:\quad F=H=0,\quad G=G_w,\quad \theta=1 \tag{15}$$

$$\eta=\eta_1:\quad F=H=0,\quad G=G_1,\quad \theta=0 \tag{16}$$

where $M=1+\eta^2$, $L=3\eta+\eta F-H$, $\eta_1=h/r$, $G_w=\text{Re}_\omega$, $G_1=\text{Re}_\Omega$, and primes denote differentiation with respect to η.

Equations (10)–(14) were solved numerically using MATHCAD software (built-in shooting method).

The cone angle was $\gamma=4$ deg ($\eta_1=0.0698$); Pr=Sc=0.1–100 for the rotating cone and stationary disk, and Pr=Sc=0.1–800 for

Contributed by the Heat Transfer Division of ASME for publication in the JOURNAL OF HEAT TRANSFER. Manuscript received February 22, 2010; final manuscript received August 25, 2010; published online November 3, 2010. Assoc. Editor: Ali Ebadian.

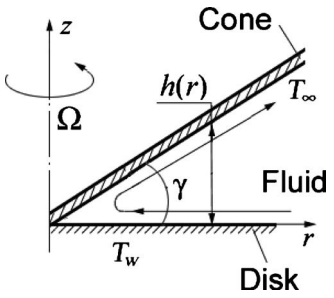

Fig. 1 Schematic of fluid flow in a conical gap, rotating cone and stationary disk

the stationary cone and rotating disk; the Reynolds number Re =1, which corresponds to $\mathrm{Re}_\omega=2463$ or $\mathrm{Re}_\Omega=2463$ for $\eta_1=0.0698$.

3 Disk Rotation, Stationary Cone

The tangential velocity $v_\varphi/(\omega r)$ varies almost linearly from unity on the disk to zero on the cone; the radial velocity $v_r/(\omega r)$ exhibits a radially outward flow between the disk and the middle of the gap and a radially inward flow further up to the cone (Fig. 2). The axial velocity $v_z/(\omega r)$ is an order of magnitude lower than the radial one [6–8].

For air flow over and $n_*=0$ at Pr=0.71, the profile of θ decreases almost linearly from unity (disk) to zero (cone). Following the increase in Pr, curves lie below each other, the variation in θ becomes nonlinear, owing to the decrease in heat conduction, and for $\mathrm{Pr}\geq 100$, the function θ is zero already inside the gap (Fig. 3). The profiles of θ for $n_*\geq 0$ exhibit qualitatively similar behavior.

For $n_*=-1$, the profiles of θ for increasing Pr numbers also lie below each other, flattening near the wall already for $\mathrm{Pr}\geq 20$, so that $d\theta/d\eta\to 0$ (Fig. 3).

By analogy to rotating-disk problems [6], the Nusselt number can be presented as

$$\mathrm{Nu}=-(d\theta/d\eta)_{\eta=0}=K_1\ \mathrm{Re}_\omega^{1/2} \tag{17}$$

$$K_1=\frac{-(d\theta/d\eta)_{\eta=0}}{\mathrm{Re}_\omega^{1/2}}=-\left(\frac{d\theta}{dz\sqrt{\omega/\nu}}\right)_{\zeta=0} \tag{18}$$

Here, the coefficient K_1 has an advantage of being independent of r and ω. For $n_*=0$ to 4 and $\mathrm{Re}_\omega=$const, the normalized Nusselt number $\mathrm{Nu}/\mathrm{Re}_\omega^{1/2}=K_1$ increases with the Prandtl number (Table 1), because the signs of v_r and dT_w/dr coincide [6–8]. This trend persists even for $n_*=-0.5$, where the temperature decrease in the radial direction is relatively weak.

Strongly negative dT_w/dr at $n_*=-1$ causes different signs of v_r and dT_w/dr and a decrease in K_1 with increasing Prandtl numbers.

Presenting K_1 for $n_*=0$ as

$$K_1=K_{1,\mathrm{Pr}=1}\mathrm{Pr}^{m_p} \tag{19}$$

where $K_{1,\mathrm{Pr}=1}=0.318$, one can obtain the dependence of the exponent m_p on the Prandtl number (Table 2), which tends to the asymptotic $m_p=0.372$ for a high Pr in analogy to a free rotating disk, where $m_p=1/3$ at $\mathrm{Pr}\to\infty$ [6].

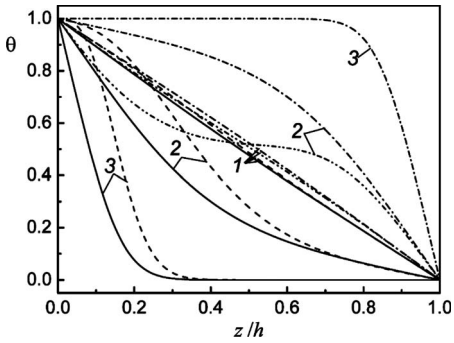

Fig. 3 Temperature profiles of θ in the gap. Rotating disk, stationary cone: solid lines for $n_*=0$, dashed lines for $n_*=-1$. Stationary disk, rotating cone: dashed-dotted lines for $n_*=0$, dashed-dotted-dotted lines for $n_*=-1$. (1) Pr=0.71, (2) Pr=10, and (3) Pr=100.

4 Cone Rotation, Stationary Disk

The radial and tangential velocities plotted in Fig. 2 look mirror opposite to the case of the disk rotating and cone stationary.

The profiles of θ for $n_*=0$ lie above each other with the growing Prandtl numbers and decrease from unity on the disk to zero on the cone, practically linear at Pr=0.71, becoming then nonlinear, owing to the reduced heat conduction (Fig. 3). For $\mathrm{Pr}\geq 100$, the derivative of function θ reaches zero values inside the gap.

The profiles of θ at different Prandtl numbers for $n_*>0$, $\mathrm{Pr}\leq 1$ and $n_*=-1$, $\mathrm{Pr}\leq 1$ practically collapse the curve for Pr

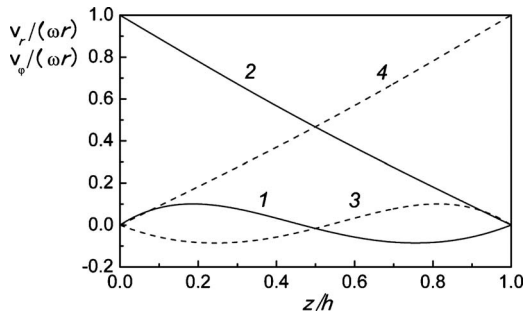

Fig. 2 Velocity profiles between rotating disk and stationary cone (1, 2) or stationary disk and rotating cone (3, 4). (1) $v_r/(\omega r)$, (2) $v_\varphi/(\omega r)$, (3) $v_r/(\Omega r)$, and (4) $v_\varphi/(\Omega r)$.

Table 1 Coefficient K_1, rotating disk and stationary cone

Pr (Sc)	$n_*=-1$	$n_*=-0.5$	$n_*=0$	$n_*=1$	$n_*=2$	$n_*=4$
0.1	0.2858	0.2887	0.2915	0.2972	0.3029	0.3141
0.3	0.2801	0.2888	0.2973	0.3142	0.3308	0.3630
0.5	0.2745	0.2890	0.3032	0.3309	0.3579	0.4094
0.71	0.2687	0.2892	0.3094	0.3483	0.3855	0.4556
1.0	0.2607	0.2898	0.3180	0.3718	0.4225	0.5155
5.0	0.1650	0.3155	0.4447	0.6552	0.8172	0.9048
10.0	0.0842	0.3829	0.6082	0.9265	0.9860	1.5737
50	0.00008	0.8744	1.3572	1.9492	2.3432	2.8986
100	0.0	1.1745	1.7882	2.5295	3.0225	3.7184
400	0.0	2.0005	2.9876	4.1627	4.9419	6.0423
800	0.0	2.5742	3.8435	5.3051	6.2862	7.6717

Table 2 Exponent m_p in Eq. (19) at $T_w=$const, rotating disk and stationary cone

Pr (Sc)	0.71	0.9	1.1	2	2.28	2.4	2.5	10	100	200	400	600	800
m_p	0.0805	0.0901	0.0978	0.1319	0.1409	0.1446	0.1476	0.2817	0.375	0.3752	0.3739	0.3729	0.3724

Table 3 Coefficient K_1, rotating cone and stationary disk

Pr (Sc)	$n_*=-1$	$n_*=-0.5$	$n_*=0$	$n_*=1$	$n_*=2$	$n_*=4$
0.1	0.2913	0.2887	0.2860	0.2807	0.2752	0.2643
0.5	0.3021	0.2889	0.2755	0.2479	0.2193	0.1587
0.71	0.3078	0.2892	0.2700	0.2302	0.1883	0.0971
0.9	0.3130	0.2894	0.2651	0.2140	0.1593	0.0373
1.0	0.3158	0.2896	0.2625	0.2054	0.1436	0.0040
2.0	0.3436	0.2924	0.2375			
10.0	0.5712	0.3679	0.0895			
50			0.0001			
100			0.0			

$=0.71$, $n_*=0$. For Pr$=1-10$ and $n_*=-1$, profiles of θ change their form (Fig. 3). For Pr>1, $n_*>0$ and Pr>10, $n_*=-1$, profiles of θ become nonphysical.

Following the increase in the Pr numbers, the normalized Nusselt numbers increase for $n_*<0$ because the signs of v_r and dT_w/dr coincide, and decrease for $n_*\geq 0$ because of the opposite signs of v_r and dT_w/dr (Table 3).

5 Application to the Cone-and-Plate Devices

To apply the results presented in Figs. 2 and 3 and Tables 1–3 to mass transfer, one should substitute T, Pr, and Nu with C, Sc, and Sh, respectively, and consider the values of K_1 for $n_*=0$ in Tables 1–3 [6]. Obviously, the values of K_1 for the rotating disk and stationary cone are always higher than those for the stationary disk and rotating cone. These differences increase with the Schmidt numbers and reach 14.6% for Sc$=0.71$, 2.6 times for Sc$=5$, 46.1 times for Sc$=20$, and tend to infinity for higher Sc.

Thus, the efficiency of a cone-and-plate device must be higher for a fixed cone and a rotating disk/plate rather than vice versa, which needs, however, experimental validation.

6 Conclusions

Laminar fluid flow and heat/mass transfer in a cone-and-plate device were simulated using self-similar transport equations. The cone-to-plate gap was 1–5 deg. The cases of rotating cone and stationary plate/disk, and vice versa, were studied. The cone was isothermal, and the radial distribution of the disk temperature followed a power law. Prandtl and Schmidt numbers varied from 0.1 to 800 for the rotating disk case, and from 0.1 to 100 for the rotating cone case.

Different regimes of heat/mass transfer were revealed, depending on the disk temperature distribution, with the values of the normalized Nusselt and Sherwood numbers either increasing or decreasing with the increase in the Prandtl/Schmidt numbers.

An applied conclusion is that the efficiency of a cone-and-plate device used in bioengineering applications for growing endothelium cells located as a monolayer on the plate can be higher for a fixed cone and rotating plate/disk rather than vice versa. This conclusion is valid independently of the rotational speed of the disk or cone.

Nomenclature

a = thermal diffusivity, m^2/s
D_m = diffusion coefficient, m^2/s
F, G, and H = dimensionless velocity components, Eq. (8)
$h=r\tan\gamma$ = gap height, m
$\mathrm{Nu}=\alpha r/\lambda$ = local Nusselt number, disk
n_* = exponent, Eq. (6)
p = pressure, Pa
$\mathrm{Pr}=a/\nu$ = Prandtl number
$q_w=-\lambda(dT/dz)_{z=0}$ = heat flux, disk value, W/m^2
r, φ, and z = cylindrical polar coordinates, m, rad
$\mathrm{Re}_\omega=\omega r^2/\nu$ = local Reynolds number, rotating disk
$\mathrm{Re}_\Omega=\Omega r^2/\nu$ = local Reynolds number, rotating cone
$\mathrm{Re}=\mathrm{Re}_\Omega\ \eta_1^2/12$ = Reynolds number
$\mathrm{Sc}=\nu/D_m$ = Schmidt number
$\mathrm{Sh}=\alpha_m r/D_m$ = Sherwood number
T = temperature, K
v_r, v_φ, and v_z = velocity components, m/s
$\alpha=q_w/(T_w-T_1)$ = heat transfer coefficient, W/m^2 K
α_m = mass transfer coefficient, m/s
γ = angle of conicity
$\eta=z/r$ = dimensionless coordinate
θ = dimensionless temperature/concentration, Eq. (9)
λ = thermal conductivity, W/m K
ν = kinematic viscosity, m^2/s
ω, Ω = angular velocities of rotation of a disk and a cone, 1/s

Subscripts

1 = value at the cone
w = value at the disk

References

[1] Sdougos, H. P., Bussolari, S. R., and Dewey, C. F., 1984, "Secondary Flow and Turbulence in a Cone-and-Plate Device," J. Fluid Mech., **138**, pp. 379–404.
[2] Buschmann, M. H., Dieterich, P., Adams, N. A., and Schnittler, H.-J., 2005, "Analysis of Flow in a Cone-and-Plate Apparatus With Respect to Spatial and Temporal Effects on Endothelial Cells," Biotechnol. Bioeng., **89**(5), pp. 493–502.
[3] Sucosky, P., Padala, M., Elhammali, A., Balachandran, K., Jo, H., and Yoganathan, A. P., 2008, "Design of an Ex Vivo Culture System to Investigate the Effects of Shear Stress on Cardiovascular Tissue," ASME J. Biomech. Eng., **130**(3), p. 035001.
[4] Turkyilmazoglu, M., 2010, "Heat and Mass Transfer on the Unsteady Magnetohydrodynamic Flow Due to a Porous Rotating Disk Subject to a Uniform Outer Radial Flow," ASME J. Heat Transfer, **132**(6), p. 061703.
[5] Arikoglu, A., Komurgoz, G., Ozkol, I., and Gunes, A. Y., 2010, "Combined Effects of Temperature and Velocity Jump on the Heat Transfer, Fluid Flow, and Entropy Generation Over a Single Rotating Disk," ASME J. Heat Transfer, **132**(11), p. 111703.
[6] Shevchuk, I. V., 2009, *Convective Heat and Mass Transfer in Rotating Disk Systems*, Springer-Verlag, Berlin, Heidelberg.
[7] Shevchuk, I. V., 2004, "A Self-Similar Solution of Navier–Stokes and Energy Equations for Rotating Flows Between a Cone and a Disk," High Temp., **42**(1), pp. 104–110.
[8] Shevchuk, I. V., 2004, "Laminar Heat Transfer of a Swirled Flow in a Conical Diffuser. Self-Similar Solution," Fluid Dyn., **39**(1), pp. 42–46.

Analytical Solution for Thermally Fully Developed Combined Electroosmotic and Pressure-Driven Flows in Narrow Confinements With Thick Electrical Double Layers

Ranabir Dey

Debapriya Chakraborty

Suman Chakraborty[1]
e-mail: suman@mech.iitkgp.ernet.in
Department of Mechanical Engineering,
Indian Institute of Technology Kharagpur,
Kharagpur 721 302, West Bengal, India

In the present paper, closed form solutions for the Nusselt number are obtained for hydrodynamically and thermally fully developed combined electroosmotic and pressure-driven flows in narrow confinements for the constant wall heat flux boundary condition. Overcoming the constraints of the standard models that are valid only within thin electrical double layer (EDL) limits, the effects of thick electric double layers are accounted for as a distinctive feature of this model. Along with Joule heating, viscous dissipation effects, which are particularly important for ultrathin channel dimensions (typically conforming to the cases of thick EDLs), are taken into account. The results are presented in terms of appropriate nondimensional parameters depicting the relative EDL thickness with respect to the channel height, as well as relative strengths of Joule heating and viscous dissipation effects.
[DOI: 10.1115/1.4002607]

Keywords: thermally fully developed, narrow confinements, thick electric double layer, viscous dissipation, Joule heating, Nusselt number

1 Introduction

Presently, convective heat transport in narrow confinements is an agenda of intensive research owing to its manifold applications in diverse fields of applied sciences and engineering such as heat sinks for microelectronic devices, microelectromechanical systems (MEMS), and chemical separation devices, to name a few. In this regard, Maynes and Webb [1,2] executed an analytical study of microscale heat transfer characteristics for hydrodynamically and thermally fully developed pure electroosmotic flow and combined pressure-driven and electroosmotic flow for both constant wall heat flux and constant wall temperature boundary conditions. In their studies, they parametrically evaluated the normalized temperature profiles and the Nusselt numbers for a wide range of dimensionless Joule heating parameter and channel diameter to Debye length ratio for relatively thin EDLs and for channel heights not small enough to render the viscous dissipation effects to be of significant consequence. The same authors [3] also assessed the implications of viscous dissipation in thermal transport of pure electroosmotic flows in microchannels, while being restrained within thin EDL limits. Chakraborty [4] derived closed form expressions for the Nusselt number variation in a thermally fully developed microtube flow for the constant wall heat flux boundary condition, while neglecting the effects of viscous dissipation. Similar parametric studies, within thin EDL limits and neglecting viscous dissipation effects, were also performed by Zade et al. [5] and Jain and Jensen [6]. Very recently, Chen [7] analyzed the heat transfer characteristics of thermally fully developed mixed electroosmotic and pressure-driven microflows with only the Joule heating effect for the constant wall heat flux condition, considering both constant, as well as variable fluid properties. Beyond the standard assumptions/approximations of the thin EDL limits, the heat transfer characteristics produce several nonintuitive phenomena, which are very significant for the design of miniaturized heat exchangers.

Going beyond the standard heat transfer analysis presented for electroosmotic flows in thin EDL limits [8], the present study considers a finite EDL thickness and offers a detailed accounting of the corresponding potential (hence, velocity) distribution in the Nusselt number calculation. Furthermore, for analyzing the heat transfer characteristics, the effects of viscous dissipation have also been considered along with the Joule heating effects, as the former plays an influential role for such narrow channels having channel height-to-Debye length ratio lower than 10 [3].

2 Mathematical Analysis

We consider a combined electroosmotically and pressure-driven transport of a symmetric electrolyte ($z^+=z^-=z$) through a long parallel plate narrow channel (narrow confinement) of height $2H$, and width W, with $W \gg 2H$. The flow is actuated by the combined effects of an axial electric field of strength E_x and a constant axial pressure gradient $P_x=-dP/dx$. For the present mathematical analysis, the following simplifying assumptions and approximations are made: steady, incompressible, and laminar flow of a Newtonian fluid is considered, the thermophysical properties of the electrolyte are considered to be constant, the ionic species behave as point charges, the zeta potential (ζ) is uniform throughout the channel walls, but the magnitude of this zeta potential is very small (≤ 25 mV), and the Boltzmann distribution of ionic concentration remains valid as the EDLs do not overlap and the flow Peclet number is sufficiently small ($\mathrm{Pe} \ll 1$). Development of such small ζ-potential is very common in practical applications using substrates such as polydimethylsiloxane (PDMS) and polymethylmethacrylate (PMMA). Hence, this assumption does not contradict the generality of the problem [9]. Moreover, this renders the Debye–Hückel linearization to be valid [10].

The velocity distribution of combined electroosmotic and pressure-driven flow can be obtained by solving the Navier–Stokes equation, which under the present assumptions along with the consideration of low Reynolds number flow, reduces to the following form:

$$-\frac{dP}{dx}+\mu\frac{d^2u}{dy^2}+\rho_c E_x=0 \tag{1}$$

where u is the axial velocity component, μ is the fluid viscosity, and ρ_c is the net volumetric charge density in the diffuse layer or the Gouy–Chapman layer of the EDL. From the simultaneous solution of Poisson's equation of potential distribution in conjunction with the Boltzmann equation of ionic concentrations in the diffuse layer, and considering the Debye–Hückel linearization, ρ_c can be evaluated as

$$\rho_c=-\frac{\kappa^2\varepsilon_0\varepsilon\zeta}{H^2}\frac{\cosh(\kappa\eta)}{\cosh(\kappa)} \tag{2}$$

where ε is the dielectric constant of the medium, ε_0 is the permittivity of free space, $\eta=y/H$ is the nondimensional transverse coordinate, and $\kappa=H/\lambda_D$ (half channel height-to-Debye length ratio). The Debye length (λ_D) is the characteristic length scale for

[1]Corresponding author.

Contributed by the Heat Transfer Division of ASME for publication in the JOURNAL OF HEAT TRANSFER. Manuscript received April 23, 2010; final manuscript received August 25, 2010; published online November 3, 2010. Assoc. Editor: Ali Ebadian.

the EDL thickness and can be estimated by the Debye–Hückel parameter:

$$\omega = \frac{1}{\lambda_D} = \left(\frac{2n_0 z^2 e^2}{\varepsilon\varepsilon_0 k_B T}\right)^{1/2}$$

where e is the electronic charge, n_0 is the average number of positive or negative ions in the electrolytic solution, k_B is the Boltzmann constant, and T is the absolute temperature of the electrolyte. Utilizing Eq. (2), the following solution for the velocity field can be obtained from Eq. (1):

$$\frac{u}{u_{\mathrm{HS}}} = \left[1 - \frac{\cosh(\kappa\eta)}{\cosh(\kappa)}\right] + \Omega(1-\eta^2) \tag{3}$$

where $u_{\mathrm{HS}} = -\zeta\varepsilon_0\varepsilon E_x/\mu$ is a reference electroosmotic velocity known as the Helmholtz–Smoluchowski velocity [11] and $\Omega = -dP/dxH^2/2\mu u_{\mathrm{HS}}$ is a nondimensional parameter depicting the relative strength of the electroosmotic and pressure-driven flow actuations. It can be noted here that in the limit of thin EDL ($\kappa \gg 100$), the electroosmotic velocity distribution within the EDL may be neglected, and "pluglike" velocity profile is justified across the channel cross-section. In such cases, the effects of EDL are considered using an effective slip-velocity at the wall given by u_{HS} as described above. In the present analysis, however, as the effects of thick EDL are being considered, such an approximation cannot be justified and an explicit description of the velocity profile in the EDL is essential for the analysis.

Based on the assumptions considered for the present analysis, the energy equation with axial conduction, volumetric heat generation, and viscous dissipation terms can be written as

$$\rho c_P u\frac{\partial T}{\partial x} = k\left(\frac{\partial^2 T}{\partial x^2} + \frac{\partial^2 T}{\partial y^2}\right) + \mu\left(\frac{\partial u}{\partial y}\right)^2 + S \tag{4}$$

where ρ is the density of the fluid, c_P is the specific heat capacity at constant pressure, T is the temperature of the fluid, k is the thermal conductivity, and $S = \sigma E_x^2$ is the volumetric heat generation due to Joule heating effect. Since this analysis is concerned with the effects of thick EDL in a narrow confinement, characterized by lower values of κ, the influence of viscous dissipation may not be trivially precluded compared with Joule heating effects. If the flow is thermally fully developed, then the classical dimensionless temperature $\theta = (T - T_W)/(T_M - T_W)$ becomes invariant with x, where T_W is the wall temperature and T_M is the bulk mean temperature defined as

$$T_M = \frac{\int_{-H}^{H} uT\ dy}{\int_{-H}^{H} u\ dy}$$

The definition of thermally fully developed flow stems from the more fundamental consideration that for a thermally fully developed flow, the Nusselt number ($\mathrm{Nu}_H = hH/k$) has to be invariant with x, where h is the convective heat transfer coefficient. Using the classical dimensionless temperature θ, coupled with the constant wall heat flux boundary condition ($q_W'' = \text{const}$), it can be shown that $\partial T/\partial x = dT_M/dx = dT_W/dx = \text{const}$. Now, from this condition, it follows that $\partial^2 T/\partial x^2 = 0$. Hence, the axial conduction term gets mathematically dropped from Eq. (4) for the constant wall heat flux boundary condition. Moreover, an overall energy balance on an elemental control volume yields

$$\frac{dT_M}{dx} = \frac{q_W''}{\rho\bar{u}Hc_P} + \frac{S}{\rho\bar{u}c_P} + \frac{\mu}{2\rho\bar{u}c_P}\int_{-1}^{1}\left(\frac{\partial u}{\partial y}\right)^2 d\eta \tag{5}$$

Evaluating the definite integral on the right-hand side, which originates due to the viscous dissipation effects, and then substituting Eq. (5) into Eq. (4), a nondimensional form of the energy equation can be written as

$$\frac{d^2\theta}{d\eta^2} = \mathrm{Nu}_H\left[g_1 - F_1(\eta)\left(1 + g_1 + g_2\frac{V}{2}\right) + g_2 F_2(\eta)\right] \tag{6}$$

where $g_1 = SH/q_W''$ is the ratio of the Joule heating effect to the applied heat flux, $g_2 = \mu u_{\mathrm{HS}}^2/Hq_W''$ is the ratio of the viscous dissipation to the applied heat flux,

$$F_1(\eta) = U = \frac{\left[\left\{1 - \frac{\cosh(\kappa\eta)}{\cosh(\kappa)}\right\} + \Omega(1-\eta^2)\right]}{\left[1 + \frac{2}{3}\Omega - \frac{\tanh(\kappa)}{\kappa}\right]}$$

is the axial velocity nondimensionalized by the average velocity,

$$F_2(\eta) = \left[2\Omega\eta + \kappa\frac{\sinh(\kappa\eta)}{\cosh(\kappa)}\right]^2$$

is the contribution of the viscous dissipation effects, and

$$V = \frac{8\Omega^2}{3} + 8\Omega\left[1 - \frac{\tanh(\kappa)}{\kappa}\right] + \frac{\kappa^2}{\cosh^2(\kappa)}\left[\frac{\sinh(2\kappa)}{2\kappa} - 1\right]$$

Integrating Eq. (6) twice analytically, subjected to the boundary conditions: at $\eta = 0$, $d\theta/d\eta = 0$ (symmetry condition at channel centerline), and at $\eta = 1$, $\theta = 0$, the dimensionless temperature profile can be obtained as

$$\theta = \mathrm{Nu}_H\left[A(1-\eta^2) - \frac{B}{12}\Omega(1-\eta^4) - \frac{B}{\kappa^2}\left(1 - \frac{\cosh(\kappa\eta)}{\cosh(\kappa)}\right) - g_2 F_3(\eta)\right] \tag{7}$$

where

$$A = \frac{\left(1 + g_1 + g_2\frac{V}{2}\right)(1+\Omega)}{2\left(1 + \frac{2}{3}\Omega - \frac{\tanh(\kappa)}{\kappa}\right)} - \frac{g_1}{2}$$

$$B = \frac{\left(1 + g_1 + g_2\frac{V}{2}\right)}{\left(1 + \frac{2}{3}\Omega - \frac{\tanh(\kappa)}{\kappa}\right)}$$

and

$$F_3(\eta) = \frac{\Omega^2}{3}(1-\eta^4) + \frac{4\Omega}{\cosh(\kappa)}\left[\left\{\frac{\sinh(\kappa)}{\kappa} - \frac{\eta\sinh(\kappa\eta)}{\kappa}\right\} - \frac{2}{\kappa^2}\{\cosh(\kappa) - \cosh(\kappa\eta)\}\right] + \frac{\kappa^2}{2\cosh^2(\kappa)}\left[\frac{1}{4\kappa^2}\{\cosh(2\kappa) - \cosh(2\kappa\eta)\} - \frac{1}{2}(1-\eta^2)\right]$$

It is quite evident from Eq. (7) that the function $F_3(\eta)$ will influence the nondimensional temperature profile only when viscous dissipation is being considered for the analysis, i.e., $g_2 \neq 0$. The unknown Nusselt number (Nu_H) in Eq. (7) is determined by utilizing the definition of bulk mean temperature and using $T = \theta(T_M - T_W) + T_W$ to obtain

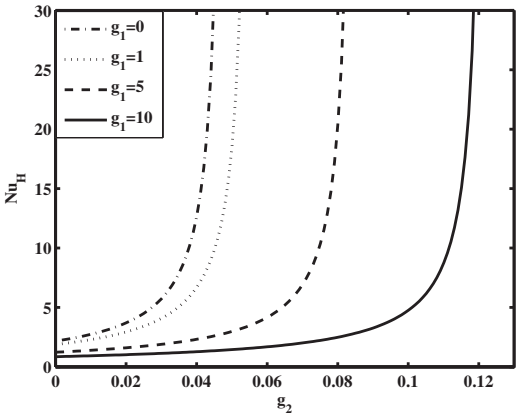

Fig. 1 Variation of Nusselt number with viscous dissipation parameter for different values of Joule heating parameter with thick EDL effects (κ=4) and Ω=1

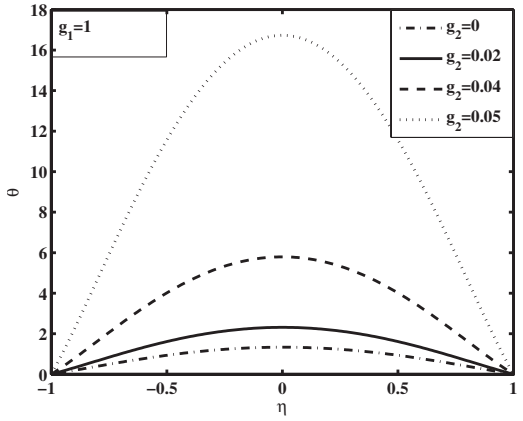

Fig. 2 Variations of nondimensional temperature profile θ with wall normal coordinate η for different values of viscous dissipation parameter (g_2) for κ=4 and Ω=1 with Joule heating parameter g_1=1

$$\mathrm{Nu}_H = 2\left(\int_{-1}^{1} F_1(\eta)\left[A(1-\eta^2) - \frac{B}{12}\Omega(1-\eta^4) - \frac{B}{\kappa^2}\left(1 - \frac{\cosh(\kappa\eta)}{\cosh(\kappa)}\right) - g_2 F_3(\eta)\right] d\eta\right)^{-1} \quad (8)$$

The parameters intrinsic to this analysis are κ, Ω, g_1, and g_2. The influence of these parameters on the nondimensional temperature θ and the Nusselt number Nu_H are discussed in detail subsequently.

3 Results and Discussions

Accuracy of the analytical solution presented here is first validated by comparing it with the classical solutions for constant wall heat flux boundary condition, in the limit of no volumetric Joule heating and viscous dissipation. The classical values of Nusselt number (Nu_H), based on half channel height, for a Poiseuille flow velocity profile and a slug-flow condition are 2.057 and 3, respectively, for the parallel plate channel flow [12], and the corresponding values obtained by the present analytical solution as $\Omega \to \infty$ and $\kappa \to \infty$, and $\Omega = 0$ and $\kappa \to \infty$ turn out to be 2.058 and 2.97, respectively. The wall heat flux (q''_W) is considered to be positive when it is directed into the fluid, as appropriate for the fluid heating problem. In conformation to the physical situation of thick but nonoverlapping EDL in narrow confinements, the value of κ (half channel height-to-Debye length ratio) has been considered to be equal to 4, which is an appropriate representative of this interesting physical limit for generating the pertinent results. The variation of Nusselt number (Nu_H) with g_2 for different values of g_1 has been shown in Fig. 1. From the figure, it is evident that for a chosen value of the Joule heating parameter g_1, the value of Nu_H increases monotonically for increasing values of the viscous dissipation parameter g_2 until it reaches an asymptote for a particular value of g_2. This value of g_2 can be considered as a critical or a threshold value for a given value of the Joule heating parameter, i.e., for a particular level of applied electric field, beyond which the problem of fluid heating by a constant wall heat flux cannot be physically posed, maintaining a steady state condition, in such narrow confinements. This critical value of g_2 goes on increasing with increasing values of the parameter g_1. To fully comprehend the significance of the existence of the critical value for g_2 for a particular value of g_1, it is imperative to consider here the equation for steady state energy balance as given by the following equation [12]:

$$q''_W = k \left.\frac{\partial T}{\partial y}\right|_{y=H} = h(T_W - T_M)$$

First, it should be recognized that Joule heating, due to the electrical current and the resistivity of the electrolyte, results in uniform volumetric heat generation. On the other hand, the viscous dissipation, being dependent on the gradient of velocity, results in a spatially nonuniform volumetric heat generation. In narrow confinements with the characteristic EDL thickness of the order of the channel half height, the effects of viscous heating are prominently felt almost over the entire channel section, unlike for the cases with infinitesimally thin EDLs, where the viscous dissipation is restricted to a small region inside the EDL near the walls. For a particular value of g_1, as the value of g_2 is gradually increased, the electrolyte temperature gradually increases over majority of the channel cross-section, resulting in an appreciable increase in the bulk mean temperature T_M as compared with the wall temperature T_W. Thus, with an increasing value of g_2, the difference ($T_W - T_M$) gradually decreases. However, to maintain isoheat flux boundary condition at the wall, the convective heat transfer coefficient increases, resulting in monotonically increasing values of the Nusselt number with increasing g_2. As the value of g_2 exceeds a critical limit, which is unique for a given value of the Joule heating parameter g_1, T_M exceeds T_W, and hence ($T_W - T_M$) becomes negative. From the energy balance condition at the wall, it is evident that beyond this critical limit of g_2, a positive q''_W cannot be maintained. Importantly, with an increasing Joule heating parameter (g_1), T_W also increases along with T_M in order to maintain the fluid heating condition by the supplied constant heat flux. Under these conditions, a greater critical value of the viscous dissipation parameter (g_2) is necessary for enabling T_M to exceed T_W. Thus, the critical value of g_2 increases with increasing g_1. Figure 2 depicts variations in the normalized temperature profile (θ) with the nondimensional transverse coordinate (η) for increasing values of g_2 within the physical domain of the fluid heating problem corresponding to a particular value of g_1, as inferred from Fig. 1, with Ω=1 and κ=4. This figure clearly demonstrates the appreciable change in the local temperature across almost the entire channel cross section with increasing magnitude of the viscous dissipation parameter for a given Joule heating condition, as attributed to appreciable penetration of the EDL into the bulk fluid, unlike the cases characterized with a thin EDL limit.

The variation of the Nusselt number with increasing values of Ω, implying increasing relative strength of pressure-driven actuation, is shown in Fig. 3. Increasing strength of the imposed pressure gradient results in greater axial velocity component, which

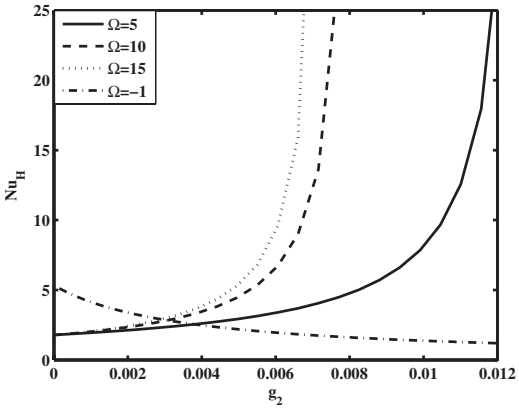

Fig. 3 Variation of Nusselt number with viscous dissipation parameter for varying flow actuation strengths considering thick EDL effects (κ=4) and g_1=1

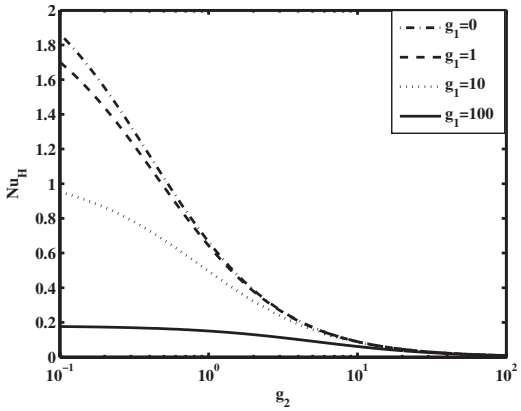

Fig. 4 Variation of Nusselt number with viscous dissipation parameter for different values of Joule heating parameter considering thin EDL limits ($\kappa \sim O(10)$) and Ω=1

culminates in increasing bulk mean temperature (T_M). This results in T_M to exceed T_W at relatively lower values of viscous dissipation parameter with increasing values of Ω. As a consequence, the critical value of g_2, beyond which the fluid heating problem cannot be physically sustained by an imposed wall heat flux, gradually decreases with increasing strength of pressure-driven actuation. However, it is of essence to note here that the existence of a critical value of g_2 will not be observed for very large values of Ω; as for such cases, the electrokinetic effects are suppressed by the dominating imposed pressure gradient. The interesting case of negative pressure gradient ($\Omega=-1$) has also been shown in Fig. 3. For this case, the stagnating core flow results in a greatly decreased value of T_M as compared with T_W and hence results in higher value of Nu_H with no viscous dissipation effects ($g_2=0$) as compared with the other cases. However, as the value of the viscous dissipation parameter increases, Nu_H gradually decreases for this case. Due to the negative pressure gradient, there is an adverse flow at the core, which arrests the convective thermal transport in that region. As a consequence, in accordance with the conservation of energy, the increasing heat generation due to viscous dissipation results in a greater increase of temperature near the wall, which culminates in T_W being greater than T_M. However, to maintain the constant wall heat flux condition in conjunction with the resulting increasing value of (T_W-T_M), the convective heat transfer coefficient decreases with an increasing value of g_2, affecting the gradually decreasing value of Nu_H. Finally, it is to be appreciated here that the heat transfer characteristics mentioned as above are exclusive to cases with thick EDL effects. Thus, if the value of the inverse EDL thickness parameter, κ, is increased by at least one order of magnitude, i.e., $\kappa \sim O(10)$, the fully developed Nusselt number does not exhibit any singularity for the entire operating regimes of g_1 and g_2 for comparable strength of pressure-driven and electroosmotic actuations, as shown by Fig. 4. On the contrary, for such cases, the Nusselt number approaches an asymptotic limit for higher values of g_2, irrespective of the value of g_1. This is because for larger values of κ, the effect of viscous dissipation is restricted to a region only in immense proximity to the wall, bearing an insignificant consequence on the overall heat transfer characteristics.

4 Conclusion

The outcome of this study may be of immense consequence for heat transfer analysis for nanochannel flows within the continuum regime for which the traditional models based on thin EDL limits may cease to work. From the interpretation of the results obtained for this study, it can be inferred that a distributed viscous dissipation over majority of the channel cross section, on account of strongly distributed velocity gradients due to substantial penetration of the EDL into the bulk, results in considerable increase of the bulk mean temperature compared with the wall temperature. To maintain the isoflux boundary condition at the wall, the convective heat transfer coefficient increases, resulting in monotonically increasing values of the Nusselt number with increasing strength of the viscous dissipation. However, for different levels of Joule heating, there exists a threshold limit of the viscous dissipation parameter beyond which the supplied wall heat flux fails to maintain the fluid heating condition. The heat transfer characteristics within the thick EDL limit is also strongly dependent on the relative strength of electroosmotic and pressure-driven actuations.

Nomenclature

c_p = specific heat capacity at constant pressure
E_x = externally applied electric field
e = electronic charge
g_1 = ratio of Joule heating to constant wall heat flux
g_2 = ratio of viscous dissipation to constant wall heat flux
H = half channel height
h = convective heat transfer coefficient
k = thermal conductivity of the fluid
k_B = Boltzmann constant
Nu_H = Nusselt number based on half channel height
n_0 = average number of positive or negative ions in the electrolytic solution or the buffer solution
P_x = externally applied pressure gradient
q''_W = channel wall heat flux
S = volumetric heat generation due to Joule heating
T = temperature of the electrolyte
T_W = channel wall temperature
T_M = Bulk mean temperature or the mixing cup temperature
u = combined electroosmotic and pressure-driven flow velocity
u_{HS} = Helmholtz–Smoluchowski velocity
W = Width of the channel
z = valency of the ions in the electrolyte

Greek Symbols

α = thermal diffusivity
ε = permittivity of the medium
ε_0 = permittivity of free space
ζ = zeta potential

η = nondimensional transverse coordinate
θ = nondimensional fully-developed temperature profile
κ = half channel height-to-Debye length ratio
λ_D = Debye length
μ = viscosity of the electrolyte
ρ = density of the medium
ρ_c = net charge density per unit volume in the diffuse layer
σ = Conductivity of the electrolyte
Ω = Normalized pressure gradient
ω = Debye–Hückel parameter

References

[1] Maynes, D., and Webb, B. W., 2003, "Fully Developed Electro-Osmotic Heat Transfer in Microchannels," Int. J. Heat Mass Transfer, **46**, pp. 1359–1369.
[2] Maynes, D., and Webb, B. W., 2003, "Fully Developed Thermal Transport in Combined Pressure and Electro-Osmotically Driven Flow in Microchannels," ASME J. Heat Transfer, **125**, pp. 889–895.
[3] Maynes, D., and Webb, B. W., 2004, "The Effect of Viscous Dissipation in Thermally Fully Developed Electro-Osmotic Heat Transfer in Microchannels," Int. J. Heat Mass Transfer, **47**, pp. 987–999.
[4] Chakraborty, S., 2006, "Analytical Solutions of Nusselt Number for Thermally Fully Developed Flow in Microtubes Under a Combined Action of Electroosmotic Forces and Imposed Pressure Gradients," Int. J. Heat Mass Transfer, **49**, pp. 810–813.
[5] Zade, A. Q., Manzari, M. T., and Hannani, S. K., 2007, "An Analytical Solution for Thermally Fully Developed Combined Pressure-Electroosmotically Driven Flow in Microchannels," Int. J. Heat Mass Transfer, **50**, pp. 1087–1096.
[6] Jain, A., and Jensen, M. K., 2007, "Analytical Modeling of Electrokinetic Effects on Flow and Heat Transfer in Microchannels," Int. J. Heat Mass Transfer, **50**, pp. 5161–5167.
[7] Chen, C.-H., 2009, "Thermal Transport Characteristics of Mixed Pressure and Electro-Osmotically Driven Flow in Micro- and Nanochannels With Joule Heating," ASME J. Heat Transfer, **131**, pp. 022401.
[8] Sharma, A., and Chakraborty, S., 2008, "Semi-Analytical Solution of the Extended Graetz Problem for Combined Electroosmotically and Pressure-Driven Microchannel Flows With Step-Change in Wall Temperature," Int. J. Heat Mass Transfer, **51**, pp. 4875–4885.
[9] Kirby, B. J., and Hasselbrink, E. F., Jr., 2004, "Zeta Potential of Microfluidic Substrates: 2. Data for Polymers," Electrophoresis, **25**, pp. 203–213.
[10] Karniadakis, G., Beskok, A., and Aluru, N., 2005, *Microflows and Nanoflows: Fundamentals and Simulation*, Springer Science Business Media, Inc., New York.
[11] Probstein, R. F., 1994, *Physicochemical Hydrodynamics: An Introduction*, 2nd ed., Wiley, New York.
[12] Bejan, A., 2004, *Convective Heat Transfer*, 3rd ed., Wiley, New York.